Institut für Erd- und Umweltwissenschaften
Mathematisch-Naturwissenschaftliche Fakultät
Universität Potsdam

The Geothermal Potential of Luxembourg:

Geological and thermal exploration for deep geothermal reservoirs in Luxembourg and the surroundings

Kumulative Dissertation

zur Erlangung des akademischen Grades
"doctor rerum naturalium"
(Dr. rer. nat.)
in der Wissenschaftsdisziplin "Geologie"

eingereicht an der
Mathematisch-Naturwissenschaftlichen Fakultät
der Universität Potsdam
von

Tom Vincent Schintgen

Potsdam, April 2015

Betreuer:
Prof. Dr. Maria Mutti (Universität Potsdam)

Gutachter:
Prof. Dr. Maria Mutti (Universität Potsdam)
Prof. Dr. Ulrich Glasmacher (Universität Heidelberg)
Prof. Noël Vandenberghe (Katholieke Universiteit Leuven)

Datum der Einreichung: 28. April 2015
Datum der Verteidigung: 2. Dezember 2015

Published online at the
Institutional Repository of the University of Potsdam:
URN urn:nbn:de:kobv:517-opus4-87110
http://nbn-resolving.de/urn:nbn:de:kobv:517-opus4-87110

Selbstständigkeitserklärung
Hiermit versiche ich, die vorliegende Arbeit selbstständig und nur unter Verwendung der angegebenen Quellen und Hilfsmittel angefertigt zu haben.
Declaration of independent work
Herewith I declare that I have written this thesis on my own, distinguished citations, and used no other than the named sources and aids.

Potsdam, im April 2015

The aim of this work is the evaluation of the geothermal potential of Luxembourg. The approach consists in a joint interpretation of different types of information necessary for a first rather qualitative assessment of deep geothermal reservoirs in Luxembourg and the adjoining regions in the surrounding countries of Belgium, France and Germany. For the identification of geothermal reservoirs by exploration, geological, thermal, hydrogeological and structural data are necessary. Until recently, however, reliable information about the thermal field and the regional geology, and thus about potential geothermal reservoirs, was lacking. Before a proper evaluation of the geothermal potential can be performed, a comprehensive survey of the geology and an assessment of the thermal field are required.

As a first step, the geology and basin structure of the Mesozoic Trier–Luxembourg Basin (TLB) is reviewed and updated using recently published information on the geology and structures as well as borehole data available in Luxembourg and the adjoining regions. A Bouguer map is used to get insight in the depth, morphology and structures in the Variscan basement buried beneath the Trier–Luxembourg Basin. The geological section of the old Cessange borehole is reinterpreted and provides, in combination with the available borehole data, consistent information for the production of isopach maps. The latter visualize the synsedimentary evolution of the Trier–Luxembourg Basin. Complementary, basin-wide cross sections illustrate the evolution and structure of the Trier–Luxembourg Basin. The knowledge gained does not support the old concept of the Weilerbach Mulde. The basin-wide cross sections, as well as the structural and sedimentological observations in the Trier–Luxembourg Basin suggest that the latter probably formed above a zone of weakness related to a buried Rotliegend graben. The inferred graben structure designated by SE-Luxembourg Graben (SELG) is located in direct southwestern continuation of the Wittlicher Rotliegend-Senke.

The lack of deep boreholes and subsurface temperature prognosis at depth is circumnavigated by using thermal modelling for inferring the geothermal resource at depth. For this approach, profound structural, geological and petrophysical input data are required. Conceptual geological cross sections encompassing the entire crust are constructed and further simplified and extended to lithospheric scale for their utilization as thermal models. The 2-D steady state and conductive models are parameterized by means of measured petrophysical properties including thermal conductivity, radiogenic heat production and density. A surface heat flow of 75 ± 7 (2σ) mW m^{-2} for verification of the thermal models could be determined in the area. The models are further constrained by the geophysically-estimated depth of the lithosphere–asthenosphere boundary (LAB) defined by the 1300 °C isotherm. A LAB depth of 100 km, as seismically derived for the Ardennes, provides the best fit with the measured surface heat flow.

The resulting mantle heat flow amounts to ~40 mW m^{-2}. Modelled temperatures are in the range of 120–125 °C at 5 km depth and of 600–650 °C at the crust/mantle discontinuity (Moho). Possible thermal consequences of the 10–20 Ma old Eifel plume, which apparently caused upwelling of the asthenospheric mantle to 50–60 km depth, were modelled in a steady-state thermal scenario resulting in a surface heat flow of at least 91 mW m^{-2} (for the plume top at 60 km) in the Eifel region. Available surface heat-flow values are significantly lower (65–80 mW m^{-2}) and indicate that the plume-related heating has not yet entirely reached the surface.

Once conceptual geological models are established and the thermal regime is assessed, the geothermal potential of Luxembourg and the surrounding areas is evaluated by additional consideration of the hydrogeology, the stress field and tectonically active regions. On the one hand, low-enthalpy hydrothermal reservoirs in Mesozoic reservoirs in the Trier–Luxembourg Embayment (TLE) are considered. On the other hand, petrothermal reservoirs in the Lower Devonian basement of the Ardennes and Eifel regions are considered for exploitation by Enhanced/Engineered Geothermal Systems (EGS). Among the Mesozoic aquifers, the Buntsandstein aquifer characterized by temperatures of up to 50 °C is a suitable hydrothermal reservoir that may be exploited by means of heat pumps or provide direct heat for various applications. The most promising area is the zone of the SE–Luxembourg Graben. The aquifer is warmest underneath the upper Alzette River valley and the limestone plateau in Lorraine, where the Buntsandstein aquifer lies below a thick Mesozoic cover. At the base of an inferred Rotliegend graben in the same area, temperatures of up to 75 °C are expected. However, geological and hydraulic conditions are uncertain. In the Lower Devonian basement, thick sandstone-/quartzite-rich formations with temperatures >90 °C are expected at depths >3.5 km and likely offer the possibility of direct heat use. The setting of the Südeifel (South Eifel) region, including the Müllerthal region near Echternach, as a tectonically active zone may offer the possibility of deep hydrothermal reservoirs in the fractured Lower Devonian basement. Based on the recent findings about the structure of the Trier–Luxembourg Basin, the new concept presents the Müllerthal–Südeifel Depression (MSD) as a Cenozoic structure that remains tectonically active and subsiding, and therefore is relevant for geothermal exploration. Beyond direct use of geothermal heat, the expected modest temperatures at 5 km depth (about 120 °C) and increased permeability by EGS in the quartzite-rich Lochkovian could prospectively enable combined geothermal heat production and power generation in Luxembourg and the western realm of the Eifel region.

Die Zielsetzung dieser Arbeit ist die Bewertung des geothermischen Potenzials in Luxemburg. Der Ansatz besteht aus einer gemeinsamen Ausdeutung verschiedener Daten die für eine erste eher qualitative Abschätzung der tiefen geothermischen Lagerstätten in Luxemburg und den angrenzenden Regionen in den benachbarten Ländern Belgien, Frankreich und Deutschland notwendig sind. Für die Erkennung geothermischer Lagerstätten durch Erkundung sind geologische, thermische, hydrogeologische und strukturgeologische Kenntnisse erforderlich. Bis vor kurzem jedoch waren verlässliche Informationen über das thermische Feld und die Geologie und somit über mögliche geothermische Lagerstätten nicht verfügbar. Bevor eine genaue Bewertung des geothermischen Potenzials durchgeführt werden kann müssen eine umfassende Untersuchung der regionalen Geologie und eine Abschätzung des thermischen Feldes erfolgen.

Als erstes wird die Geologie und Struktur des Mesozoischen Trier–Luxemburger Beckens (TLB) mittels kürzlich erschienenen Erkenntnissen über die Geologie und Strukturen sowie verfügbaren Bohrdaten in Luxemburg und den angrenzenden Gebieten überprüft und aktualisiert. Eine Bouguer Schwerekarte liefert einen Einblick in die Tiefe, Morphologie und Strukturen des variskischen Grundgebirges welches unter dem Trier–Luxemburger Becken verborgen ist. Die Schichtenfolge in der alten Bohrung Cessingen wird neu gedeutet und bietet in der Gesamtdeutung der verfügbaren Bohrdaten einheitliche Angaben für die Erzeugung von Mächtigkeitskarten. Diese veranschaulichen die synsedimentäre Entwickung des Trier–Luxemburger Beckens. Ergänzende, beckenübergreifende geologische Schnitte verdeutlichen die Entwicklung und Struktur des Trier–Luxemburger Beckens. Die gewonnenen Erkenntnisse widerlegen das alte Konzept der Mulde von Weilerbach. Die beckenumspannenden Schnitte, sowie die strukturgeologischen und sedimentologischen Beobachtungen im Trier–Luxemburger Becken legen nahe dass die Beckenentwicklung wahrscheinlich über einer Schwächezone stattgefunden hat die durch einen verborgenen Rotliegendgraben erzeugt wird. Die vermutete Grabenstruktur mit der Bezeichnung ‚Südost-Luxemburg Graben' befindet sich in unmittelbarer südwestlicher Fortsetzung der Wittlicher Rotliegend-Senke.

Das Fehlen von Tiefbohrungen und einer Vorhersage der Untergrundtemperaturen in der Tiefe wird durch thermische Modellierung als Mittel zur Bestimmung der tiefen geothermischen Resourcen umgangen. Für diese Herangehensweise werden tiefgreifende strukturgeologische, geologische und gesteinsphysikalische Eingangsdaten benötigt. Konzeptionelle geologische Krustenschnitte werden erstellt und dann für die Benutzung als thermische Modelle vereinfacht und auf Lithospärenmaßstab erweitert. Die thermisch stationären und konduktiven Modelle werden mittels im Labor gemessenen petrophysikalischen Eigenschaften wie der

Wärmeleitfähigkeit, der radiogenen Wärmeproduktion und der Gesteinsdichte parameterisiert. Ein terrestrischer Oberflächenwärmestrom von 75 ± 7 (2σ) mW m^{-2} zur Überprufung der thermischen Modelle konnte im Untersuchungsgebiet ermittelt werden. Die Modelle sind weiter begrenzt durch die geophysikalisch ermittelte Tiefe der Lithospäre-Asthenosphärengrenze (LAB) die sich durch die 1300 °C Isotherme definiert. Eine LAB-Tiefe von 100 km, wie seismisch für den Bereich der Ardennen bekannt, führt zur besten Übereinstimmung mit dem ermittelten Oberflächenwärmestrom. Der sich ergebende Mantelwärmestrom beträgt ~40 mW m^{-2}. Die Modelltemperaturen liegen im Bereich von 120–125 °C in 5 km Tiefe und 600–650 °C an der Krustenuntergrenze (Moho). Die möglichen thermischen Auswirkungen des 10–20 Ma alten, sogenannten Eifelplumes, der offenbar einen Aufstieg des asthenosphärischen Mantels bis in 50–60 km Tiefe verursacht hat, wurden mit Hilfe eines thermisch stationären Szenarios modelliert und ergeben einen Oberflächenwärmestrom von mindestens 91 mW m^{-2} (im Fall eines Plume Top in 60 km Tiefe) im Gebiet der Eifel. Die vorliegenden Wärmestromwerte sind deutlich niedriger (65–80 mW m^{-2}) und zeigen dass die durch den Plume bedingte Lithospären- und Krustenerwärmung die Oberfläche noch nicht erreicht hat.

Nach der Erstellung der konzeptionellen geologischen Modelle und der Berechnung des thermischen Feldes kann das geothermische Potenzial von Luxemburg und den angrenzenden Gebieten abgeschätzt werden. Die Bewertung geschieht durch die Einbeziehung der Hydrogeologie, des Stressfeldes und unter Berücksichtigung tektonisch aktiver Gebiete. Zum einen werden Niedrigenthalpie-Lagerstätten in mesozoischen Aquiferen in der Trier–Luxemburger Bucht (TLE) in Betracht gezogen. Andererseits werden petrothermale Lagerstätten im unterdevonischen Grundgebirge der Ardennen und der Eifel für die Erschließung durch EGS (Enhanced/Engineered Geothermal Systems) berücksichtigt. Unter den mesozoischen Aquiferen ist der Buntsandstein Aquifer mit Temperaturen bis 50 °C ein geeignetes hydrothermales Reservoir das mittels Wärmepumpen oder direkte Wärmebereitstellung für verschiedene Nutzungsmöglichkeiten in Frage kommen könnte. Das thermisch günstigste Gebiet befindet sich im Bereich des Südost-Luxemburg Graben unter dem oberen Alzettetal sowie dem Kalksteinplateau im nördlichen Lothringen wo der Buntsandstein Aquifer unter einer mächtigen Mesozoischen Bedeckung liegt. An der Basis des vermuteten Rotliegendgrabens in demselben Gebiet werden Temperaturen bis 75 °C erwartet. Allerdings sind die geologischen Verhältnisse und die hydraulischen Eigenschaften unbekannt. In dem unterdevonischen Grundgebirge werden mächtige sandsteinlastige beziehungsweise quarzitreiche geologische Formationen mit Temperaturen >90 °C in Tiefen >3,5 km erwartet

und ermöglichen wahrscheinlich eine direkte Wärmenutzung. Die geologische Situation der Südeifel einschliesslich der Region des Müllerthales nahe Echternach (Luxemburg) als tektonisch aktive Zone könnte tiefe hydrothermale Reservoire im geklüfteten unterdevonischen Grundgebirge zur Folge haben. Auf Basis der erarbeiteten Kenntnisse über das Trier–Luxemburger Becken in Luxemburg und speziell der Südeifel wurde das neue Konzept der Müllerthal–Südeifel Depression (MSD) aufgestellt. Es handelt sich um eine gegenwärtig tektonisch aktive und absinkende känozoische Struktur und hat deshalb eine große Bedeutung für die zukünftige geothermische Erkundung. Neben der direkten Nutzung geothermischer Wärme ermöglichen die mäßigen Temperaturen von 120 °C in 5 km Tiefe und eine verbesserte Durchlässigkeit der quarzitreichen Schichten des Lochkoviums mittels EGS potentiell die kombinierte Wärmebereitstellung und Stromproduktion in Luxemburg und im westlichen Bereich der Eifel.

Appendix A.1

Text

AAc	Ardenne Anticlinorium
ACT	Administration du Cadastre et de la Topographie
AD	Ardennes
AMA	Ardennes Margin Anomaly
BDLT	Boppard–Dausenau–Longuich Thrust
BGI	Bureau Gravimétrique International
BGR	Bundesanstalt für Geowissenschaften und Rohstoffe
BM	Brabant Massif
BRGM	Bureau de Recherches Géologiques et Minières
CLA	Central Luxembourg Anomaly
DF	Differdange Fault
ECRIS	European Cenozoic Rift System
ED	Eifel Depression
EDA	Eifel Depression Anomaly
EGS	Enhanced/Engineered Geothermal Systems
EP	Eifel plume
Esc	Eifel Synclinorium
FNR	Fonds National de la Recherche (National Research Fund), Luxembourg
GAc	Givonne Anticlinorium
GH	Grand-Halleux borehole
GFZ	Helmholtz Centre Potsdam – GFZ German Research Centre for Geosciences
GLS	Geologisches Landesamt des Saarlandes
GOMAc	Givonne–Oesling–Manderscheid Anticlinorium
HA	Hunsrück Anomaly
HBA	Hunsrück Boundary Anomaly
HBF	Hunsrück Boundary Fault
HDR	Hot-Dry-Rock Systems
HHMA	Hayange–Hettange–Mondorf Anomaly
HHMF	Hayange–Hettange–Mondorf Fault
HT	Herbeumont Thrust

ICGR	International Centre for Geothermal Research
IEA	International Energy Agency
KF	Koenigsmacker Fault
KLF	Konz–Longuich Fault
LAB	Lithosphere–Asthenosphere Boundary
LBF	Lorentzweiler–Bech Fault
LF	Luxembourg Fault
LGB	Landesamt für Geologie und Bergbau Rheinland–Pfalz
LRG	Lower Rhine Graben
LUA	Landesamt für Umwelt und Arbeitsschutz Saarland
LUWG	Landesamt für Umwelt, Wasserwirtschaft und Gewerbeaufsicht Rheinland–Pfalz
LZG	Luxemburger Zentralgraben
LZS	Luxemburger Zentralschwelle
L	Luxembourg (city)
M	Mersch borehole
Mac	Manderscheid Anticlinorium
MF	Metz Fault
MSc	Mosel Syncline
MSD	Müllerthal–Südeifel Depression
MST	Stavelot Massif/Stavelot–Venn Massif
Mz	Metz
NE	northeast
NSc	Neufchâteau Synclinorium
NW	northwest
NWESc	Neufchâteau–Wiltz–Eifel Synclinorium
OAc	Oesling Anticlinorium
ORC	Organic Rankine Cycle
OSc	Olkenbach Syncline
PT	Plein Thrust
RCMF	Roussy-le-Village–Canach–Machtum Fault
R&D	Research and development
RD&D	Research, development and demonstration
RHZ	Rhenohercynian Zone

RM	Rhenish Massif
RMS	Ridge of Mettlach–Sierck
Sb	Saarbrücken
SE	southeast
SELA	SE-Luxembourg Anomaly
SELG	SE-Luxembourg Graben
SGL	Service géologique du Luxembourg (Geological Survey of Luxembourg)
SKMF	Schoenfels–Keispelt–Mamer Fault
SMT	Siegen Main Thrust
SNB	Saar–Nahe Basin
STATEC	Institut national de la statistique et des études économiques du Grand-Duché du Luxembourg
STM	Stavelot Massif/Stavelot–Venn Massif
STZ	Saxothuringian Zone
SW	southwest
SWLA	SW-Luxembourg Anomaly
T	Temperature
TC	Thermal conductivity
TG	Thionville Graben
TLB	Trier–Luxembourg Basin
TLE	Trier–Luxembourg Embayment
TMT	Troisvierges–Malsbenden Thrust
Tr	Trier
TS	Tom Schintgen
URG	Upper Rhine Graben
USGS	United States Geological Survey
VF	Variscan Front
WEVF	West Eifel Volcanic Field
WMF	Wittlich Main Fault
WMS	Web Map Service
WOA	Western Oesling Anomaly
WS	Wittlicher (Rotliegend) Senke
WSc	Wiltz Synclinorium

Tables

C.	Couches
Calc.	Calculated
Fm.	Formation
Gn	Gneiss
Litho.	Lithotype
Max.	Maximum
M./Mbr.	Member
Min.	Minimum
O	Orientation
Q	Quartzite
Ref.	Reference
Sh	Shale
Sl	Slate
Ssl	Silty slate
Sst	Sandstone
Stst	Siltstone
TF	Transformation factor
Vol.	Volume fraction

m_{dry}	Mass of dry sample
m_{sat}	Mass of (water- or isooctane-) saturated sample
m_{im}	Mass of immersed sample
V_s	Sample volume
λ	Thermal conductivity
λ_m	Thermal conductivity of rock matrix
λ_p	Thermal conductivity of pore fluid
λ_{dry}	Thermal conductivity under dry conditions
λ_{sat}	Thermal conductivity under saturated conditions
λ_I, $\lambda_{//}$	Thermal conductivity measured parallel to bedding or cleavage
$\lambda_\perp$	Thermal conductivity measured perpendicular to bedding or cleavage
α	Standard error
α	Rock-specific coefficient for pressure correction of TC
σ	Standard deviation
q	Heat flow
q_s	Surface heat flow
q_m	Mantle heat flow
q_i	Interval heat flow
ϕ, ϕ_{tot}	Porosity (total porosity)
ρ, d	Density
A	Anisotropy
H	Radiogenic heat production (Chapter 3)
H	Thickness of geological units (Chapter 4)
T	Temperature
p	Pressure
X	Volume proportion/fraction
t	Volume fraction of lithotypes
S_0	Stratification/bedding
S_1	Cleavage
c	Concentration
x	Horizontal coordinate
z	Depth/vertical coordinate
gradT	Temperature gradient

a, b, c, d	Rock specific coefficients for temperature correction of TC
U	Uranium
Th	Thorium
K	Potassium (Chapter 3)
k_f	Hydraulic conductivity
K	Permeability (Chapter 4)
B	Belgium
D	Germany
F	France
L	Luxembourg
NL	The Netherlands
AM	Arithmetic mean
V_p	Seismic velocity
$\mu_{1/2}$	Median value

First, I would like to gratefully and cordially thank my co-supervisor Dr. Andrea Förster (GFZ German Research Centre for Geosciences) for first establishing contacts in January 2010 by listening to my proposal of a doctoral thesis about the geothermal potential of Luxembourg. Dr. A. Förster provided a salary for the first months of preparation of the project proposal. Together with Dr. A. Förster, the main content of the thesis was elaborated. The project proposal persuaded the National Reasearch Fund (Luxembourg) to finally provide funding. Dr. A. Förster supported the intention to write a cumulative thesis which asked a tremendous effort in preparing this work for publication in peer-reviewed journals. Without her devotion to the task, her continuous support and share of knowledge on surface heat flow and thermal regime, this doctoral thesis could not have been brought to this end. I also would like to thank Dr. Hans-Jürgen Förster (GFZ) who assisted with the petrological aspects of this work and supported the preparation of whole-rock samples for geochemical analyis.

I am thankful to Dr. Hans D. Zimmermann (Department of Geoscience, Aarhus University, Denmark) for first motivating discussions and his dedicated interest in the project of a doctoral thesis about the geothermal potential of Luxembourg. Those initial ideas as well as the scientific expertise learned in Aarhus represent the beginnings of the present thesis.

Dr. Ben Norden (GFZ) is thanked for the teamwork on the CLEAN project during my first months at GFZ Potsdam. Furthermore, Dr. Norden is gratefully acknowledged for the preparation of the field trip to Luxembourg and his assistance with temperature logging of boreholes in Mersch and Reisdorf. Dr. Norden and Dr. Dietrich Stromeyer implemented the algorithm for numerical modelling of the lithospheric thermal field based on the finite-element method using the MATLAB® software (Norden et al., 2008). Dr. Norden in particular is thanked for his help, explanations and troubleshooting during the implementation of the lithosphere thermal models.

The Helmholtz Centre Potsdam – GFZ German Research Centre for Geosciences (GFZ) and especially Prof. Dr. Ernst Huenges, head of section 4.1 Reservoir Technologies and head of the International Centre for Geothermal Research (ICGR), are cordially and sincerely acknowledged for the admission in their team as a doctoral student and the provision of the facilities necessary for the accomplishment of this work.

Furthermore, I would like to thank my supervisor Prof. Dr. Maria Mutti (Universität Potsdam) for supporting and reviewing this work.

Dr. Judith Sippel and Dr. Mauro Cacace (Section 4.4 Basin Analysis, GFZ) are gratefully acknowledged for the opportunity to practice teaching about thermal rock properties in the framework of the course 'Geologische 3D-Modellierung von Sedimentbecken'. The latter course was part of the module MGEW07 Geologische 3D-Modellierung lead by Prof. Dr. M. Mutti.

Constructive reviews by Dr. Doris Dittrich (LGB, Landesamt für Geologie und Bergbau Rheinland-Pfalz, Mainz), Prof. Dr. Jean Thein (Steinmann Institut, Bonn) and four anonymous reviewers helped to improve the three individual manuscripts within this doctoral thesis and are gratefully acknowledged. In particular, I would like to thank my colleague Dr. Dittrich for her expertise about the geology of the Trier–Luxembourg Embayment, her continuous interest in my work, her discerning and constructive discussions and her support by communicating me her most recent articles relevant to this work. L. Reinheimer (LGB) is thanked for the introduction about the state of knowledge of geothermal data in Rhineland–Palatinate and the permission to view the unpublished report about shallow geothermal applications in the Südeifel region by Häfner et al. (2007).

The Geological Survey of Luxembourg (SGL), in particular Robert Maquil and Robert Colbach, supported this work by granting access to the survey's library, archives and borehole database as well as by constructive discussions. The SGL also supported this work by granting access to their core-storage facility for sampling Mesozoic rock and by covering the costs for the geochemical analyses of whole-rock samples. Analysis was done at Acme Analytical Laboratories Ltd. (Acmelabs, Vancouver, Canada). The use of unpublished data by Prof. Dr. H.-G. Stosch (Karlsruher Institut für Technologie) about the geochemical composition of xenoliths from the Eifel region is gratefully acknowledged.

The Administration de la Gestion de l'Eau (Esch/Alzette, Luxembourg), in particular Tom Schaul, provided borehole data as well as information about hydrogeological aspects of this work.

The Geological Survey of Belgium (GSB), in particular Estelle Petitclerc, is thanked for the possibility of sampling and measuring core material from the Grand-Halleux borehole. Dr. M. Everaerts (GSB) is thanked for providing a Bouguer anomaly map of Luxembourg and adjacent areas. Dr. Michiel Dusar is acknowledged for providing information about the Grand-Halleux borehole. Dr. Isabelle Belanger is thanked for discussions about the new geological maps of Belgium and stratigraphical correlations between Belgium and Luxembourg.

The SEO (Société Electrique de l'Our SA, Vianden, Luxembourg), in particular N. Conrad, and the "Amis de l'Ardoise A.s.b.l." (Haut-Martelange, Luxembourg), in particular A. Hoogenhout and D. Thilmany, are thanked for the opportunity of rock sampling in their premises. Furthermore, the Groupe Spéléologique de l'Attert, in particular G. Beidler, is cordially acknowledged for his help in finding the Mersch borehole, and A. Strauch and G. Even for company during the collection of samples in the old mines in Schimpach (Luxembourg). G. Even is also thanked for the opportunity to see borehole cuttings stored by the DEA (Distribution d'Eau des Ardennes, Useldange, Luxembourg). The quarry of Consthum (premises of Rinnen constructions générales, Binsfeld, Luxembourg) is thanked for the possibility of collecting samples.

Agriconsult S.à.r.l. (Mersch, Luxembourg), in particular C. Pundel, is gratefully acknowledged for the permission to access and perform temperature logging in the Mersch borehole (FR-168-101) located in their premises. The municipality of Reisdorf, in particular C. Kraemer, is thanked for the permission to access and perform temperature logging in the Reisdorf borehole (FR-207-122). Moreover, M. Drake (LIM logging, Rodange, Luxembourg) is acknowledged for providing information and temperature data of the Reisdorf borehole for verification. Karsten Baumann and Werner Klink (BLM, Bohrlochmessung-Storkow, Germany) are gratefully acknowledged for the opportunity to view drilling reports of boreholes in Luxembourg measured by BLM.

Dr. Chrystel Dezayes (BRGM, Orléans) is thanked for borehole and temperature data as well as updates about geothermal energy in Lorraine, France. Dr. Bruno Werle (LUA, Landesamt für Umwelt und Arbeitsschutz Saarland, Saarbrücken) is thanked for hints about literature concerning the Cessange borehole and data about boreholes in Besch/Perl. Prof. Noël Vandenberghe (Katholieke Universiteit Leuven, Belgium) is acknowledged for information about the master thesis by Verkeyn (1995).

Prof. Dr. Onno Oncken (GFZ, Section 3.1 Lithosphere Dynamics) is acknowledged for explanations about reflection seismics and balanced sections in the Rhenohercynian Zone of the Variscan fold-and-thrust belt (Oncken et al., 1999; Oncken et al., 2000). Dr. James Mechie (GFZ, Section 2.2 Geophysical Deep Sounding) is thanked for discussing the refraction seismic profiles performed in the Rhenish Massif (Mechie et al., 1983) and for sharing available data. Prof. Dr. Inga Moeck (formerly GFZ, ICGR) and Prof. Dr. Kamil Ustaszewski (formerly GFZ, Section 3.1) are acknowledged for the opportunity to access the GOCAD® geomodelling software.

This work would have been unsuccessful without the help of numerous staff members, technicians and apprentices at GFZ. H. Liep and M. Ospald (Section 4.2 Inorganic and Isotope Geochemistry) supported the sample preparation by producing rock powder for whole-rock analysis. G. Arnold (Section 3.1 Lithosphere Dynamics) provided the facilities for cutting the rock samples. C.-T. Rach, S. Kienast, C. Rudolph and M. Oldman (Section 4.1 Reservoir Technologies) are acknowledged for their assistance during porosity and density determination, sample saturation and TC measurements. I also would like to thank Jörg Schrötter for lending the temperature logging equipment and Christian Cunow for performing the calibration of the temperature sensor used in the Mersch borehole.

My colleagues in section 4.1 Reservoir technologies and the International Centre for Geothermal Research (ICGR), in particular my former room mates Dr. Sven Fuchs, Dr. Gunther Baumann and Dr. Felina Schütz, are thanked for the pleasant working atmosphere. In particular, I would like to acknowledge Dr. Schütz for enriching discussions and sharing her knowledge about surface heat flow and thermal field modelling.

Moreover, I would like to thank Dr. Raymond Laugier (Paris, France), Prof. Hans-Balder Havenith and Marie Heeren (Université de Liège, Belgium), and Prof. Dr. Andreas Schäfer (Steinmann Institut, Bonn) for their interest in parts of the present work. In particular, Prof. Havenith is gratefully acknowledged for the opportunity to give a seminar about geothermics to geology students of the Université de Liège and for two visits at GFZ.

My partner Katrin, my flat mates Andreas, Robert, Martin and Marie-Luise as well as my friends in Potsdam are thanked for their company and support. I also would like to thank my fellow geology students Simon and Valentin for enriching and amicable discussions.

Finally, my parents Doris and Pierre, my brother Marc and my sisters Lynn and Joanne as well as my family are thanked for their continuous support and patience. In particular, I would like to thank my elder sister Lynn for her company during outcrop sampling near the Wartenstein castle in the SW-Hunsrück as well as for helping me during unearthing of the Mersch borehole and verification of its accessibility for temperature logging.

The project is supported by the National Research Fund (FNR – Fonds National de la Recherche, Luxembourg), the Helmholtz Centre Potsdam – GFZ German Research Centre for Geosciences (Germany) and the Geological Survey of Luxembourg.

1 Introduction

Geothermal energy currently represents a very low percentage of the national energy mix in Luxembourg and geothermal resources in the subsurface of Luxembourg and the surrounding areas are barely known. Its use is mainly restricted to heat pump systems (Biermayr et al., 2007; Häfner et al., 2007). In particular, the assessment of deep geothermal resources and their evaluation for different geothermal applications in Luxembourg and the adjoining areas was hampered by the absence of deep boreholes and the lack of temperature prognosis at depth. The aim of the present work is to combine different types of information necessary for a first rather qualitative assessment of deep geothermal reservoirs in the region of Luxembourg. The cornerstone consists in the assessment of the thermal field for the purpose of applied geothermics.

Within the geological framework, the study area encompasses Luxembourg and the surrounding areas of Belgium, Germany and France. On the one hand, the focus is laid on low-enthalpy hydrothermal reservoirs in Mesozoic aquifers in the Trier–Luxembourg Embayment. On the other hand, petrothermal reservoirs in the Devonian basement of the Ardennes and Eifel regions are considered for exploitation by Enhanced/Engineered Geothermal Systems (EGS). However, for the evaluation of the geothermal potential of Luxembourg and therewith the delineation of the different types of geothermal use, knowledge of subsurface temperatures is required to the depth to which geothermal boreholes can be drilled at costs that allow an economic use of the Earth's heat. In cases where subsurface temperature data are sparse, thermal modelling may be used as a tool for inferring the geothermal resource at depth but requires profound structural, geological, and petrophysical input data. The set-up of thermal models notably requires appropriate boundary conditions, reliable surface heat flow data for verification and, for characterization, a database of measured thermal rock properties (thermal conductivity, radiogenic heat production and density) and further literature data for the deeper parts of the crust and the lithosphere. The work envisaged for the area of Luxembourg profits from GFZ experience made in geothermal studies, e.g. in the Northeast German Basin, the Erzgebirge, Israel and Jordan (Fuchs and Förster, 2010; Fuchs and Förster, 2014; Fuchs et al., 2013; Förster, 2001; Förster et al., 2007; Förster et al., 2010; Norden and Förster, 2006; Norden et al., 2008; Schütz et al., 2011; Schütz et al., 2014). Before thermal modelling can be performed, a considerable task consists in the construction of conceptual geological models as a basis for the thermal models and further for the evaluation of subsurface conditions relevant for the identification of geothermal reservoirs and the exploitation of geothermal energy. A

major obstacle is the lack of deep boreholes and the scarcity of geophysical data with geological interpretations in the study area. Moreover, the geology of Luxembourg has last been addressed in its entirety and integrated in the regional geological and structural context by Lucius (1937, 1948, 1950). Since then, numerous relatively local, but essential studies about sedimentological and structural aspects were performed in Luxembourg and in the adjoining areas in Germany, Belgium and France. The focus was laid on new geological mapping in the Guttland (Geological Survey of Luxembourg, 1971 to present), in the Südeifel (South Eifel) in Germany (Dittrich, 2011), the Wittlicher Senke (Stets, 2004) and in the Wallonie in Belgium (Service géologique de Wallonie, 1988 to present; Bultynck and Dejonghe, 2001). Moreover, recent studies and state of knowledge about the South Eifel region and on a larger scale the Trier–Luxembourg Embayment is summarized by Wagner et al. (2012) and Dittrich (2014), and further for the entire Rhineland–Palatinate (Germany) by LGB (2005). Informative cross sections illustrating the geology of the South Eifel region are presented by Wagner and Dittrich (2010) and further the hydrogeological situation of the South Eifel region was investigated by LGB and LUWG (2010). Geological and geophysical investigations in the Rhenish Massif are presented by Fuchs et al. (1983) and summarized by Oncken et al. (2000). For the Lorraine region in France, a huge database of subsurface geological information is available publicly in form of borehole data (BRGM, 2015a) and comprehensive lithostratigraphic studies of the Triassic, Liassic and Middle Jurassic (Courel et al., 1980; Mouterde et al., 1980; Thierry et al., 1980), and for the Paris Basin in general (Mégnien, 1980). Based on the state of knowledge in the adjoining regions, the geology of Luxembourg had to be updated and greatly benefitted from a large database of selected boreholes that are available in the archives of the Geological Survey of Luxembourg. In particular, the old Cessange borehole needed reinterpretation. The consideration of the borehole data from Luxembourg and the adjoining regions of France, Belgium and Germany could be used for drawing of isopach maps and further to the construction of basin-wide cross sections of the Trier–Luxembourg Basin or rather Trier–Luxembourg Embayment. Besides borehole data, further insight in the depth and morphology of the Variscan basement as well as buried structures is gained by a semi-quantitative and qualitative interpretation of a Bouguer gravity map (M. Everaerts, pers. comm.).

In addition to conceptual geological models as a basis for the thermal models, a sophisticated parameterization of a thermal model requires a database of measured thermal rock properties. This involves field work for sampling of drill core at the geological surveys of Luxembourg and Belgium, and outcrop sampling in the Ardennes (Belgium and Luxembourg) and the Guttland in Luxembourg. For verification of thermal modelling, surface heat flow is crucial and

ideally has to be determined using high quality, continuous temperature logs in deep boreholes and appropriate thermal conductivity data. Although numerous surface heat flow values were determined in the areas surrounding Luxembourg (Bram, 1979; Haenel, 1971; Haenel, 1983; Hückel and Kappelmeyer, 1966; Vasseur, 1980; Vandenberghe, 2002), the terrestrial heat flow in Luxembourg was unknown prior to this study. It was therefore important to find appropriate temperature data or perform new temperature logging in accessible boreholes. Another important thermal input is radiogenic heat production of rocks that represent large proportions of the subsurface in the study area. Radiogenic heat production had to be determined on representative rock samples. Based on the preceding petrophysical properties and reliable boundary conditions, this work presents the first subsurface temperature prognosis for the greater Luxembourg region based on steady-state and conductive 2-D thermal modelling along the three crustal cross sections extended to englobe the entire lithosphere.

Once the necessary input data are generated, i.e. conceptual geological models and thermal models, the integrated study of geological, thermal, hydrogeological and structural information is necessary in exploration for deep geothermal reservoirs. The results of the thermal models can be used for the generation of temperature maps for 1 km depth steps between 1000 m and 6000 m (below mean sea level). The latter depth range corresponds to the realm to which geothermal boreholes can be drilled at costs that allow an economic use of the Earth's heat by combining heat production and power generation. However, besides the deep geological conditions and knowledge of the subsurface temperature distribution, the crustal stress field is particularly important in site selection for geothermal exploration and the development of EGS. Therefore, it was crucial to interprete the geographical location of Luxembourg and the surrounding regions in the geodynamical context of the ECRIS (European Cenozoic Rift System) (Bourgeois et al., 2007; Dèzes et al., 2004; Ziegler and Dèzes, 2007), the uplift of the Rhenish Massif (Fuchs et al., 1983; Meyer and Stets, 2007; Schmincke, 2007; and references therein), the Eifel plume (Ritter, 2007; and references therein), and the relatively young volcanism in the West Eifel Volcanic Field (Schmincke, 2007; and references therein).

The identification of possible geothermal reservoirs represents an important achievement for geothermal exploration and exploitation of geothermal energy in Luxembourg and the surroundings.

1.1 Regional geological setting

An adequate understanding of the geology and its structural/tectonic framework is of paramount importance for the evaluation of subsurface conditions relevant for exploitation of geothermal energy, notably temperature and permeability, and thus the identification of geothermal reservoirs. Despite the limited size of the study area, regional geology is multifaceted. It is characterized by various sedimentary rocks ranging mainly from Cambrian through Mesozoic to Quaternary volcanics. Lithotypes range from metasediments such as Lower Palaeozoic quartzite and slate, mostly diagenetically compacted Lower and Middle Devonian shale, sandstone, quartzitic sandstone and carbonates to Permian and Mesozoic claystone, siltstone, sandstone, conglomerate, marlstone and carbonates (Schintgen et al., 2015). Fig. 1.1 shows the major geological subunits of the study area and its location with respect to the Rhenish Massif (RM) and the European Cenozoic Rift System (ECRIS). The study area is characterized by two contrasting geological environments, the Mesozoic rock of the Trier–Luxembourg Embayment (TLE; in German: Trier–Luxemburger Bucht; Dittrich, 2011, 2014; Fig. 1.1) and the mostly Lower Devonian rock of the RM. The Wittlicher Rotliegend Senke (WS) represents a relatively narrow Permian Graben within the southwestern part of the RM (Stets, 2004).

The bulk of the Earth's crust in the study area was shaped in response to the amalgamation of Western Europe during the Caledonian and Variscan orogenic cycles, which involved the deposition of thick sediment piles and their subsequent deformation (Pharaoh, 1999; Pharaoh et al., 2006). The Variscan basement is largely composed of thick Lower Devonian (i.e. Lochkovian, Siegenian or Praguian and Emsian) syn-rift sediments characterized by a generally homogeneous, shale-rich, clastic rock assemblage, which often displays a pervasive cleavage (Furtak, 1965; Konrad and Wachsmut, 1973; Lucius, 1950; Wildberger, 1992). The total thickness of the Lower Devonian sediments increases rapidly from the margin towards the center of the Rhenohercynian basin, where maximum thicknesses of more than 10,000 m are reported (Meyer and Stets, 1996; Stets and Schäfer, 2002). Large and persistent fold structures are typical for the Ardennes and Eifel regions (e.g., Meyer and Stets, 1996), whereas thrusts are characteristic for the Hunsrück area (Fig. 1.1; e.g., Wildberger, 1992; Stets and Schäfer, 2011). The Eifel Depression (Eifeler-Nord-Süd Zone) is interpreted as an important cross fold within the RM, separating the Ardennes in the west from the Eifel region in the east (Murawski et al., 1983). The Lower Devonian unconformably overlies Cambrian and Ordovician metamorphic rocks that are only known from outcrops in the Ardennes, notably in the Stavelot–Venn Massif (or Stavelot Massif; STM; Fig. 1.1; e.g., Bless et al., 1990).

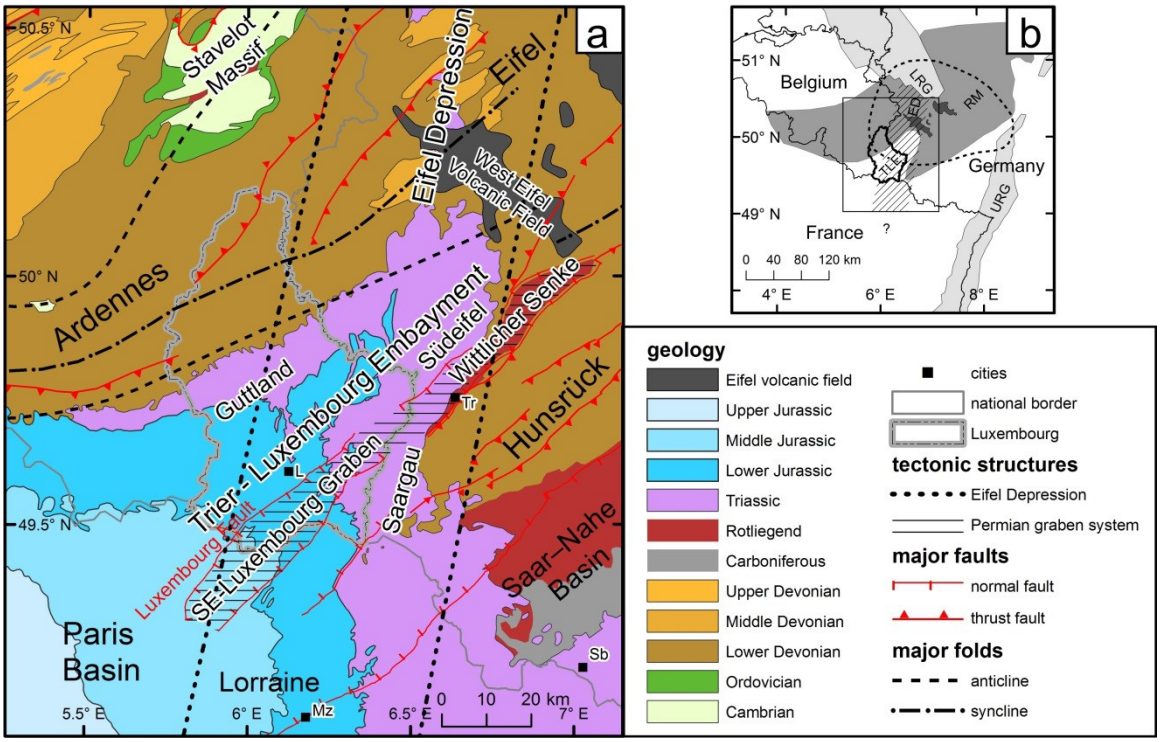

Fig. 1.1: a. Regional geological map of the study area. Geographical units are indicated. The location of the map within Western Europe is shown in b. Main cities are indicated in the text. b. Simplified basement tectonic map of Luxembourg and the surroundings. Rectangle indicates location of geological map shown in a. with indication of the Rhenish Massif (RM), the Lower and Upper Rhine Grabens (LRG and URG, respectively), the Eifel Depression (ED; hatched zone) and the Trier–Luxembourg Embayment (TLE). Dashed contour indicates the location of the Eifel plume according to Keyser et al. (2002).

The Mesozoic rock of the Trier–Luxembourg Embayment forms a northeastern extension of the Paris Basin reaching about 80 km into the RM, thus covering the Palaeozoic rock. The designation TLE specifically refers to the present-day structure and appearance of the Mesozoic sedimentary record (see Chapter 4), which constitutes a tectonically enhanced and partially eroded counterpart of the former Trier–Luxembourg Basin as it formed and evolved in the Mesozoic (TLB; Chapter 2; Schintgen and Förster, 2013). Sub-regions of the TLE are the Guttland region in Luxembourg, and the Südeifel (South Eifel) and Saargau regions in Germany. The TLB/TLE is characterized by subhorizontal layers of alternately hard and soft lithotypes of Triassic and Jurassic age (Schintgen and Förster, 2013).

During the Cenozoic to the present day, the TLE is undergoing active deformation (Dittrich, 2014; and references therein). At a larger scale, the RM and adjoining areas are deformed and uplifted due to the development and evolution of the ECRIS (European Cenozoic Rift System) since the Eocene about 40 Ma ago (Bourgeois et al., 2007; Demoulin and Hallot, 2009; Fuchs

et al., 1983; Schmincke, 2007; Dèzes et al., 2004; Ziegler and Dèzes, 2007; and references therein). In Fig. 1.1b, the ECRIS is represented by the LRG (Lower Rhine Graben) and URG (Upper Rhine Graben). Intensified tectonic activity in the last 700 ka is expressed by accelerated uplift of the RM and young volcanism in the Eifel region, in particular in the West Eifel Volcanic Field (WEVF) (Demoulin and Hallot, 2009; Fuchs et al., 1983; Meyer and Stets, 2002; Schmincke, 2007).

1.2 Methods and database

1.2.1 Existing data in Luxembourg and the surrounding areas

Numerous boreholes have been drilled in the TLE. The designation of 'deep' boreholes in Luxembourg is misleading since the deepest borehole is 750 m deep. In the entire Trier–Luxembourg Basin, maximum depth amounts to 2250 m in the Vacherauville borehole (France). In the South Eifel region in Germany maximum depth is 460 m in the Echternacherbrück borehole. In the Belgian Lorraine (or Gaume) maximum depth is 494 m in the Latour borehole (Schintgen and Förster, 2013). The deepest borehole in the study area outside the TLE is the 3225-m-deep Grand-Halleux borehole in the Stavelot Massif (Graulich, 1980). For Luxembourg, a digital borehole database exists, but detailed geological information had to be collected in the archive and library at the Geological Survey of Luxembourg. A number of borehole data also had to be collected at the Administration de la Gestion de l'Eau (Luxembourg). For France, borehole data are available to the public (BRGM, 2015a). For Belgium, borehole data were retrieved from the digital database of the Geological Survey of Belgium, and from Graulich (1980) for the Grand-Halleux borehole. For Germany, borehole data are either published (LGB and LUWG, 2010; Dittrich, 1989; Dittrich and Norbisrath, 2006; Dittrich et al., 1998, 2005) or available after permission at the Landesamt für Geologie und Bergbau Rheinland–Pfalz (LGB) and the Landesamt für Umwelt und Arbeitsschutz (LUA) Saarland. Information on the Altrich borehole is cited by Kopp (1955). Drill core of so-called reference boreholes as well as recent boreholes is available at the core storage at the Geological Survey of Luxembourg. The Geological Survey of Belgium stores drill core material from the Grand-Halleux borehole. In general, analog geophysical well logs were available for the deepest boreholes and had to be digitized for further use. Measured petrophysical rock properties are scarce. Rock sampling and the relevant measurements had to be performed for this study.

1.2.1.1 Set-up of the borehole database

For Luxembourg and surrounding areas in Belgium, France and Germany, the most informative boreholes, and generally boreholes deeper than 100 m, were selected for the isopach maps (Section 2.5.3; Schintgen and Förster, 2013). A selection of deep boreholes in the TLB is presented by Schintgen and Förster (2013) (see Table 2.1). A complete overview of the boreholes considered for the generation of the isopach maps is given in the Appendix: Table A.1.1 for Luxembourg (140 boreholes), Table A.1.2 for France (42 boreholes), Table A.1.3 for Belgium (7 boreholes) and Table A.1.4 for Germany (6 boreholes). The national coordinates in the respective countries were converted to latitude and longitude (WGS84) except for France for which latitude and longitude were available. Ground level and stratigrahical boundaries are expressed by reference to mean sea level. For the sake of simplicity, the small difference of altitude due to the various altimetric references in the countries of Luxembourg, France, Belgium and Germany and due to the age of the boreholes was omitted. For some boreholes, the stratigraphic interpretation has been corrected by stratigraphic correlations with nearby borehole data and gamma-ray logs in boreholes with a detailed and well-studied geological section. An extensive lithostratigraphical reinterpretation was necessary in case of the Cessange borehole (see Section 2.5.2).

1.2.1.2 Bouguer map

A Bouguer anomaly map of Luxembourg and surrounding areas (see Fig. 2.3, M. Everaerts, 2012, pers. comm.) was used to shed light on the Mesozoic basin structure and the topography/structure of the basement. For Luxembourg, the Bouguer map is based on 509 gravity measurements performed in 1996 for the Administration du Cadastre et de la Topographie (Everaerts, 1997). The coverage of one data point per 5 km^2 is comparable to the adjoining areas (Everaerts, 1997, 2002). The gravity points are tied to the reference point of Uccle, Belgium. The Bouguer anomalies are calculated with a standard density of 2.67×10^3 kg m^{-3} (Everaerts and De Vos, 2012: 42). Additional gravity data for countries adjacent to Luxembourg had been acquired for Belgium (Everaerts and De Vos, 2012), Germany (Skiba, 2011) and France (BGI, 2012).

1.2.2 Interpretation of existing data

1.2.2.1 Drawing of isopach maps

To delineate the geology and basin structure of the TLB, numerous isopach maps were drawn (see Fig. 2.5). They show most of the Triassic and Jurassic geological units and provide an overview of the existing borehole database which forms the basis for the generation of these maps. For a better visualization, in areas of high data density, only the most relevant data points are shown. In addition to borehole data, for the Keuper, thickness data by Dittrich (1989) were selected. For the Muschelkalk, complementary thickness data by Lucius (1948) and Dittrich (1989) were used. Along the northeastern border of Luxembourg, additional information from recently published cross sections in the adjoining Südeifel region was used (LGB and LUWG, 2010; Wagner and Dittrich, 2010). The isopachs were hand-contoured and honor the data points to show the large-scale morphology of the individual units. For the sake of clarity, small-scale thickness variations due to local synsedimentary tectonics and sediment deposition (e.g., Dittrich, 1989, 2008, 2009) are not honored. The uncertainty of the layout of the isopachs is strongly dependent on the availability of borehole data, which locally is very restricted. In those areas, the isopachs are concept-based and frequently show a certain structural continuity with the overlying and underlying geological units. For the sake of clarity, only the major synsedimentary faults are shown. As there is little data available about the largely concealed pre-Dogger units in SW-Guttland and northern Lorraine, relevant maps from the Paris Basin (Mégnien, 1980) were used to guide the isopach contouring.

1.2.2.2 Construction of cross sections across the TLB/TLE

The regional geological cross sections (see Fig. 6A–G) were generated based on the thickness information provided by the isopach maps and stratigraphical information supplied by the most recent geological map data. The basin-wide cross sections provide an overview of the geological structure of the TLB. The cross sections A to F are perpendicular to the SW–NE oriented Variscan elements, whereas cross section G is more or less parallel to the Variscan basement structures. The number and course of the cross sections generated depends on the availability of boreholes as a reference (see Tables 2.1 and A.1.5) and the representativity for illustration of the basin structure. The spacing of the NW–SE oriented sections ranges between 5 and 15 km. The trace of the sections was drawn in the software ArcMap™ 10 by considering the available boreholes and digitized, georeferenced geological maps for Luxembourg (SGL,

2015a), for France (BRGM, 2015b) and Germany (Dittrich, 2011; GLS, 1981). The geographical coordinates of the cross sections are provided in the Appendix (Table A.1.5). Along the trace of the cross section, the topography/altitude was extracted from a digital elevation model. Publicly available SRTM3 data with a resolution of 90 m (DEM90) were downloaded (USGS, 2015). These data were then converted using the software 3DEM and ArcCatalog™. A digital elevation of Luxembourg with a high resolution of 5 m was also available (SGL, 2015b). The latter was mainly used to verify elevation indicated in geological maps. The distance and elevation along each section were used as a basis for contructing the cross sections in an Excel® spreadsheet. The spreadsheet data were prepared with the intention of visualization as graph using the Matlab® 2010b software. However, as a first approach, the topography was printed and each geological cross section was drawn on paper. As an analog reference, for each cross section, starting from the origin, distance and elevation data of stratigraphical boundaries and faults as well as geographical reference points such as rivers/streams and villages/towns were then extracted from the geological maps and collected in a separate spreadsheet. The indicated faults are supposed to extend linearly with a constant dip of 70° assuming an extensional regime. A Matlab script was written to load text files, process them and visualize geological cross sections. Topography, geological map data and borehole data were the basic input data. Each cross section was built by switching between the main Excel spreadsheet in which the digital version of the cross section was build and Matlab for visualization of the stratigraphical data. At faults, fault equations had to be integrated in Excel (for calculation of boundaries) and in the Matlab script (for fault visualization). Stratigraphic boundaries, respectively geological units, were first ‘attached’ to outcropping boundaries at the surface, then to boreholes and faults. In segments were geological units had to follow a curvature, additional attachment points were created where necessary. In the Excel sheet, the thickness of geological units from the isopach maps was integrated manually by subtracting the local thickness value from the overlying boundary value. In Matlab, the ‘fill’ and ‘flipud’ commands were used to define each geological unit by its top and base boundaries and to colour units using the RGB code commonly used in Luxembourg. Frequent difficulties and errors occurred at the intersection of geological units with the surface (outcrop of stratigraphical boundaries) and at the intersection with faults. Whereas the Excel sheet contains alternately columns with cells containing altitude values and cells containing thickness values, only altitude values were exported to text and further imported into Matlab. Topography data and thus the digital cross section data theoretically have a resolution of 90 m. As the available and additionally constructed geological information is much less abundant and varies for each

boundary, the irrelevant cells were filled with zeros and later filtered in Matlab to extract the proper stratigraphical information. Attention had to be paid to slightly change real values of zero altitude. The major advantage of digital cross section data is that it can easily be adapted and updated and its visualization rapidly changed for example by using an exaggeration in the Matlab script. The spreadsheet data can also be plotted in ArcMap™ for the generation of e.g. top/base maps of individual formations/units (see Figue 4.7). Furthermore, as described in Section 4.4.2.2, the cross section data can easily be used for the analysis and reconstruction of sedimentary basins.

1.2.3 Generation of new data

1.2.3.1 Construction of conceptual, lithosphere-scale geological cross sections/models

The crustal geology is illustrated by three crustal cross sections (Figs. 1.2 and 3.2). Two of the sections (sections A and B) extend, perpendicular to the Variscan structures, from the Lower Palaeozoic Stavelot Massif in the Belgian Ardennes in the north to the Metz Fault/Hunsrück Boundary Fault in the south. These cross sections are representative of the slightly different geological situations in western and eastern Luxembourg. The main difference between cross sections A and B is an eastward increase in thickness of Emsian and Siegenian formations, changes in folding and thrusting and the generally greater depth of the Variscan/Caledonian unconformity in profile A in the east. The third section extends parallel to the Variscan structures approximately from the southwestern border of Luxembourg to the northeastern edge of the Mesozoic Trier–Luxembourg Basin (TLB) and the southwestern margin of the West Eifel Volcanic Field. The three crustal cross sections presented by Schintgen et al. (2015) are based on three shallow cross sections presented by Schintgen and Förster (2013) that have been extended laterally and downward into the mantle to encompass the entire crust (See Fig. 3.2; Section 3.3) and, for thermal modelling, the entire lithosphere (See Figs. 3.4 and 3.5; Section 3.5). Details about the geology are provided in Section 3.3. Here, the structural background relevant for the development of the crustal cross sections is presented. Similar to the construction of the basin-wide cross sections presented in Section 1.2.2.2, the construction of conceptual, lithosphere-scale geological cross sections/models was done using a combination of structural and stratigraphical data in spreadsheets and processing/visualization in the Matlab® 2010b software. In contrast to the relatively shallow basin-wide cross sections, the construction of digital versions of the crustal cross sections asked for a tremendous effort because the structure of the upper part of the crust is much more complicated due to the presence

of large thrust faults in the Rhenohercynian fold-and-thrust belt above the Eifel detachment (e.g., Oncken et al., 2000). However, as a major advantage of this approach, the later extraction of polylines for the set-up of the thermal models was considerably facilitated (see Section 3.5). For the implementation of the crustal cross sections, the upper part of the crust had to be subdivided into numerous crustal blocs, each one delimited by major thrust faults. A separate Excel spreadsheet containing the thrust data was prepared and imported to Matlab. The thrust data form the frame and provide the structure of the cross sections. A second spreadsheet contains the stratigraphical data discriminated in the different crustal blocs.

For Luxembourg and directly adjoining areas in France, Belgium and Germany, the lack of deep exploration boreholes and geophysical data, notably reflection seismic profiles, implicates that the only geological and structural data available stem from field studies and especially geological maps. The structure and geology of the upper part of the crust above the basal detachment can be constructed by extrapolating surface information. This approach greatly benefits from the investigations performed in the Rhenish Massif in order to understand the ongoing uplift (Fuchs et al., 1983) and from the relatively well known internal structure of the Rhenohercynian fold-and-thrust belt as modelled by Oncken et al. (1999) and summarized in Oncken et al. (2000). As shown in Fig. 1.2, the cross section of Hollmann (1997) ends in northern Luxembourg, while the balanced model by Oncken et al. (1999) based on the seismic reflection profile DEKORP1 (DEKORP Research Group, 1991) spans the entire Rhenohercynian Zone and is located just about 50 km east of Luxembourg. The Rhenohercynian Zone provides the structural framework with its generally northwest-vergent fold-and-thrust belt (Meyer, 1994; Meyer & Stets, 1980, 1996; Oncken et al., 1999). The balanced section through the Eifel shows that the Eifel detachment is located approximately at mid-crustal level at a depth of about 15 km from the collision zone at the Hunsrück Boundary fault in the southeast to the Siegen Main Thrust and then ascends by the means of a number of ramps first to a depth of about 12–14 km and then to 4–7 km depth underneath the Stavelot–Venn Massif. Hollmann (1997) assumes a depth of 13 km below the Wiltz Synclinorium. The fold-and-thrust belt therefore affects mostly Palaeozoic rock and probably leaves the lower part of the crust relatively unchanged (Oncken et al., 1999). Simplified cross sections adapted to the geology of the study area (Wagner et al., 2012; Zitzmann and Grünig, 1987) were also considered. Although the overall geometry of our conceptual geological model, visualized by the crustal cross sections A and B, is based on the balanced section by Oncken et al. (1999), the crustal cross sections are simplified and adapted to the geology of Luxembourg and surroundings using the lithostratigraphy and thickness estimations of the Lower Palaeozoic and

Lower Devonian successions. The structural viability of our sections in the sense of balanced cross sections is not relevant in thermal models. However, particular attention was paid to the lateral persistence of formations and their volume in fault/thrust zones. The velocity structure by Mechie et al. (1983) based on refraction seismic profiles (Fig.1.2) as well as existing petrological models based on xenoliths from the Eifel volcanic field and known velocity-depth profiles (Mengel et al., 1991, and references therein) are especially used to shed light on the compositon of the deeper part of the crust.

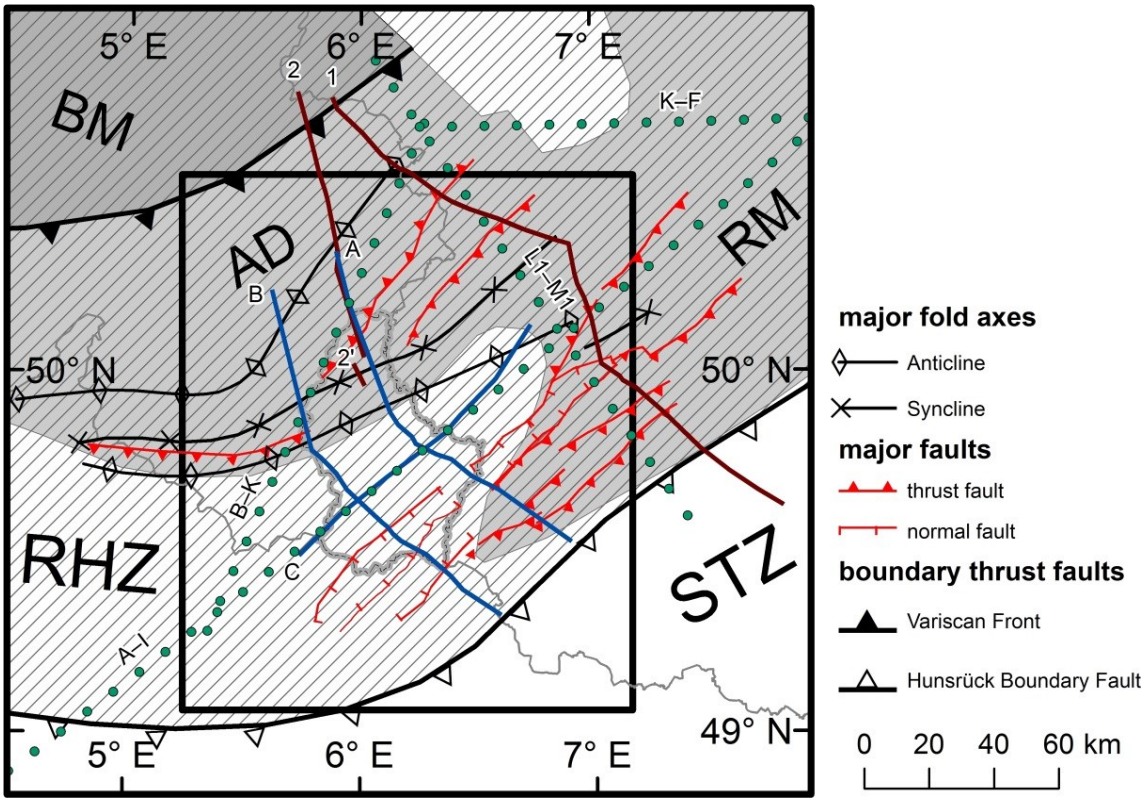

Fig. 1.2: Basement tectonic map of Luxembourg and surroundings with indication of cross sections and available profiles. Terranes pertaining to Eastern Avalonia are hatched. Dark and light grey areas mark the Brabant Massif (BM) and the Rhenish Massif (RM), respectively. The Ardennes (AD) to the northwest of the Trier–Luxembourg Embayment are indicated. Different elements of the Variscan orogenic belt are shown: RHZ = Rhenohercynian Zone, STZ = Saxothuringian Zone. Rectangle indicates the study area. Blue lines (A, B, C) correspond to lithosphere-scale cross sections presented in Chapter 3. Green-dotted transects (A–I, B–K, K–F, L1–M1) indicate refraction seismic profiles (Mechie et al., 1983) Dark red lines indicate (1) the DEKORP 1 reflection seismic profile (DEKORP Research Group, 1991) and the approximate location of a palinspastic reconstruction (Oncken et al., 1999; Oncken et al., 2000), and (2, 2') the balanced model constructed by Hollmann (1997).

1.2.3.2 Drill core and outcrop sampling

For the determination of the thermal conductivity, samples from the Palaeozoic basement and from the Mesozoic Trier–Luxembourg Basin have been collected (see Fig. 3.1; Section 3.3). In addition, a small number of samples of the highly metamorphic Wartenstein Gneiss (Meyer and Nagel, 2001) of Neoproterozoic age are available. These samples are representative for an up to 13-km-thick portion of the upper crust.

For the Cambrian to Devonian basement, only the lithologies characteristic for the Cambrian Deville and Revin groups could be sampled among the cores of the 3225-m-deep Grand-Halleux borehole (GH) located in the Stavelot Massif in the Belgian Ardennes (Fig. 2). Sampling locations were chosen using the newest geological maps, notably the sheet Bra–Lierneux (Geukens, 2008), containing valuable information about representative outcrops. Especially for the Revin Group, which contains black pyrite-rich slates, the quality of the outcrop samples is poor.

The Lower Devonian formations of Lochkovian (formerly Gedinnian) and Lower Praguian age (formerly Lower Siegenian) are not exposed in Luxembourg and therefore have been sampled in the Belgian Ardennes to the south and southwest of the Stavelot Massif according to recent geological maps (Dejonghe, 2008). The Lower Devonian formations of Middle Praguian to Upper Emsian age characteristic of the Luxembourgish Ardennes have generally been collected in the field. Exposures along roads, as well as ancient small quarries facilitated the collection of samples of good quality. In addition, it was also possible to sample roof slate, which usually shows a poor resistance to weathering, in the old mines of Schimpach (Sg2 formation) and Haut-Martelange (base of Sg3 formation). Samples from the E1b (Schuttbourg) Formation have been collected in an open quarry near Consthum. The excavation at the storage plant (SEO) near Vianden also permitted the collection of fresh rock samples from the E1b (Stolzembourg) Formation. The Lower Devonian formations of the Mosel Syncline and Hunsrück areas exist in the subsurface of SE-Luxembourg but are well known only from their regional exposure in Germany (LGB, 2005). They present a slightly different lithological composition and stratigraphy (e.g., LGB, 2005; Stets and Schäfer, 2002). These rocks have not been directly sampled, but assembled with lithostratigraphically similar samples from the Ardennes region.

The Mesozoic lithologies were sampled from drill cores of 12 different relatively shallow boreholes stored at the Geological Survey of Luxembourg. This way, also lithologies that are sensitive to weathering in outcrop areas, notably marl (-stone) and clay (-stone), could be collected. Lithologies that are not covered by available drill cores were sampled in areas with

good exposure. This was the case for the sandstones of the Schilfsandstein (Stuttgart Formation) and sandstones of Middle Buntsandstein age as well as the Minette ironstone and the overlying bioclastic limestones of Dogger age in southwestern Luxembourg. The geographical coordinates of the sampling/borehole locations of the various samples are given in the Appendix (Tables A.1.6–9).

1.2.3.3 Thermal conductivity

Thermal-conductivity (TC) measurements were performed with the Thermal Conductivity Scanning (TCS) device (Lippmann & Rauen, GbR Schaufling, Germany) (Fig. 1.3; Section 3.4.1). The measurement technique is based on high-resolution optical scanning with an inherent error of determination <3% (Popov et al., 1999). The TCS device uses a transient technique for contactless TC measurement by applying a constant heat pulse of known energy to the standards and samples.

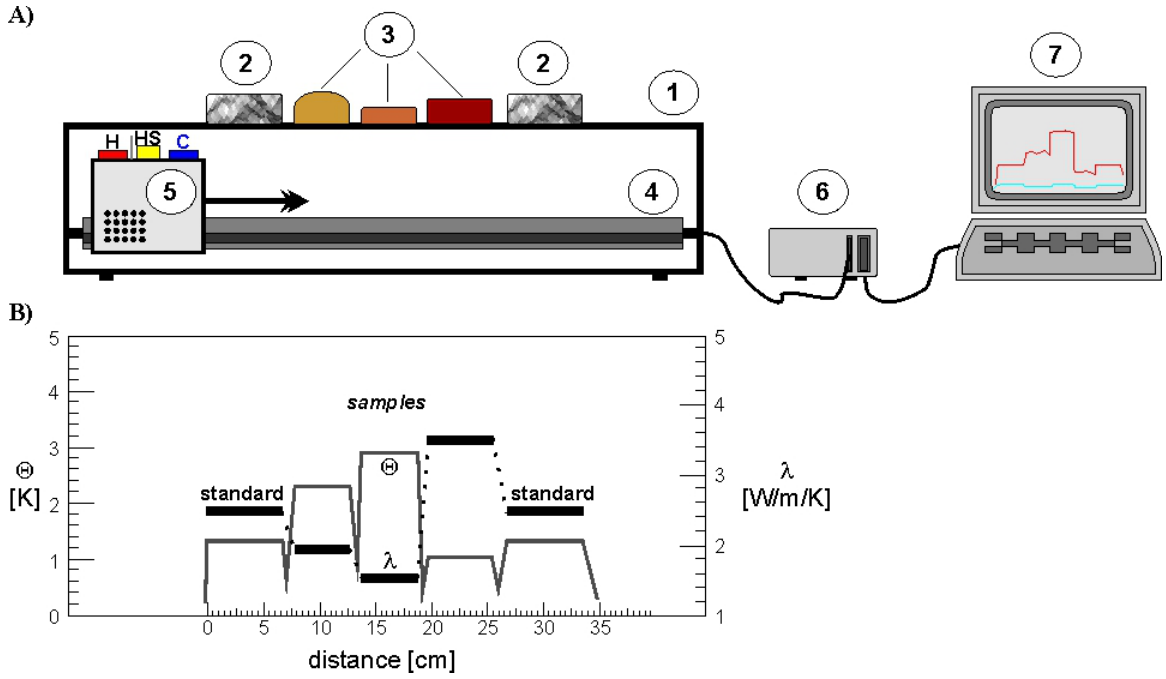

Fig. 1.3: (A) Schematic set-up of a TCS (Thermal Conductivity Scanning) device (after Lotz, 2004). (1) Scanning surface for standards and samples, (2) standards, (3) rock samples, (4) scanner with step motor, (5) optical scanning unit including the heat source (HS) and two infrared sensors (C = cold, and H = 'hot') for contactless temperature measurements, (6) electronic control unit, (7) computer with processing software. (B) Example of a measuring result obtained by the TCS device. Θ = temperature of the sensor H (continuous curve), λ = thermal conductivity (dotted lines and bars).

Anisotropy of TC can be determined with the TCS device by cutting anisotropic rocks parallel and perpendicular to cleavage or bedding, respectively. Heat absorption by the standards and samples is improved and homogenized for variegated and differently coloured samples by applying black paint (Fig 1.4). The minimum requirements for measurement of anisotropy are two flat, appropriately oriented surfaces characterized by a roughness <1 mm, measuring length >4 cm and a band width of black paint >2 cm. The TCS device also allows estimation of rock inhomogeneity.

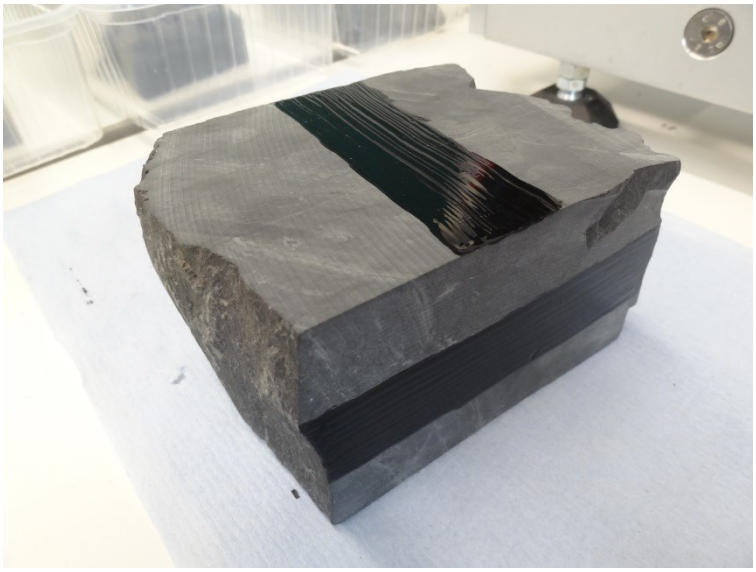

Fig 1.4: Example of a rock sample prepared for TC measurement.

The resulting temperature gradient produced within the standards of known TC and the rock samples with unknown TC permits to determine the thermal conductivity of the samples. By contrast to the steady-state (or rather stationary) technique, the transient technique does not need for a thermal equilibrium to be reached for TC determination. TC measurements using the TCS device therefore are relatively fast, so that the large number of samples usually needed for the appropriate characterization of the geology can be measured (Fig 1.5). Drill cores are preferable especially for TC measurement of sensitive lithotypes, e.g. clay/claystone and marl/marlstone (Fig. 1.6), but outcrop samples can easily be collected and prepared for TC measurement in the laboratory. TC measurements can be performed in dry and water-saturated conditions (see Section 3.4.1 for details). Isooctane instead of water can be used for saturation especially in the case of claystone and marlstone, to avoid clay swelling and damage to the samples (Fig 1.6; Fuchs et al., 2013). In this study, TC of samples was determined by comparison with standards (λ = 2.93 W m^{-1} K^{-1}) selected for the range of extreme TCs (irrespective of dry and fluid-saturated conditions) measured (0.9–7.7 W m^{-1} K^{-1}). The range

of median TCs for lithotypes ranges from 1.3 to 6.1 W m^{-1} K^{-1}. Thermal conductivity and additional petrophysical properties relevant to this study are detailed in Section 3.10.2 (Appendix A.3). TC and density of the Wartenstein Gneiss is provided in the Appendix (Table A.1.11).

Fig 1.5: Example of Palaeozoic rock samples measured in the TC laboratory.

Fig 1.6: Example of claystone/marlstone samples reacting to water and being damaged.

1.2.3.4 Porosity and density

In parallel to TC determination under dry and saturated conditions (see Section 3.4.1), porosity and density were determined using the Archimedes method. The rock samples were first oven-dried at 60 °C until constant mass was reached. The mass m_{dry} (in g) was then determined. Subsequently, samples were saturated with demineralized water under vacuum in a desiccator for a minimum of 48 hours. The mass of the saturated samples m_{sat} (in g) was measured. Then, the volume of the saturated samples was determined indirectly by suspending the sample in the

respective saturating fluid (demineralized water or isooctane; see Section 3.4.1) by measuring the mass of the immersed sample m_{im} (in g). For demineralized water, a density d (in g cm^{-3}) of 1, and for isooctane, a density of 0.698 was taken. Sample volume V_s (in cm^3) was determined:

$$V_s = \frac{m_{sat} - m_{dry}}{d} \tag{1.1}$$

Sample density d_s (in g cm^{-3}) was determined:

$$d_s = \frac{m_{dry}}{V_s} \tag{1.2}$$

Sample porosity ϕ [%] was determined:

$$\phi = \frac{m_{sat} - m_{dry}}{d \cdot V_s} \times 100 \tag{1.3}$$

Although absorption of humidity can not be entirely excluded, the compact Palaeozoic rock samples were not oven-dried before porosity/density determination and TC measurement under dry conditions. These samples were superficially dry shortly after the water-cooled and -lubrified cutting process, which showed that water absorption occurred predominantly through cracks. Drying took place in the laboratory in ambient air for at least 48 hours before porosity/density and TC determination under dry conditions. As a consequence, the mass under dry conditions m_{dry} may be slightly biased and thus may lead to weak underestimation of porosity. However, porosities of Palaeozoic rocks measured (51 samples) are very low (mostly in the range 1–4%) and consistent with the compactness expected from outcrop samples (42 samples; highest porosities 0.4–12.7%; average ~3%) and drill core samples (8 samples; lowest porosities 0.1–0.6%; average 0.3%), respectively (Schintgen et al., 2015).

1.2.3.5 Radiogenic heat production

For the Palaeozoic basement rocks, H was determined based on geochemical data since they form the major part of the crust in the study area (see Section 3.4.2). Bulk-rock geochemical analyses included the measurement of U, Th and K concentrations (Table 3.5) by X-ray fluorescence spectrometry and inductively coupled plasma-mass spectrometry on 20 rock samples representative for the Cambrian, Ordovician and Lower Devonian basement. The Geological Survey of Luxembourg covered the costs of geochemical analysis which was performed by Acmelabs in Vancouver, Canada. H was calculated according to the equation of

Rybach (1976, 1988):

$$H = 10^{-5} \cdot \rho\left(9.52c_U + 2.56c_{Th} + 3.48c_K\right) \quad (1.4)$$

where H is the radiogenic heat production (in μW m^{-3}), ρ is rock density (in kg m^{-3}), c_U and c_{Th} are the concentrations of uranium and thorium (in ppm), respectively, and c_K is the concentration of potassium (in wt %). The latter was calculated from the concentration of K_2O provided in wt % using the atomic mass of oxygen (M_O = 15.9994) and potassium (M_K = 39.0983).

$$c_K = c_{K_2O} \cdot \frac{2 \cdot M_K}{2 \cdot M_K + M_O} = c_{K_2O} \cdot 0.83 \quad (1.5)$$

The details about the calculation of radiogenic heat production are given in the Appendix (Table A.1.12).

1.2.3.6 Borehole temperature logging for surface heat flow determination

The terrestrial heat flow in Luxembourg was unknown prior to this study (Hurter and Haenel, 2002; Fig 1.7). To fill this gap in knowledge and to provide further input for the thermal modelling, heat flow was determined in the Mersch borehole (FR-168-101) (Fig. 1.8; see Section 3.4.3), located in the Alzette River valley in the Trier–Luxembourg Basin. This borehole was drilled in 1968 as an exploration borehole to a final depth of 328 m and mostly encountered rocks of the Lower Middle Keuper, the Muschelkalk and the Buntsandstein. Geophysical well logging was performed, but no temperature logging. The borehole then was then abandoned and rediscovered in summer 2011 (Fig. 1.9). It was possible to unearth the well head (Fig. 1.10). It became evident that, after completion, the borehole had been equipped with three piezometer tubes and the remaining open space cemented. It was possible to reopen the tubes for verification of the accessibility of the borehole (Fig. 1.11). However, the well head had to be cut off because it was scrunched (Fig. 1.12). The borehole was under thermal equilibrium when a continuous temperature (T) log was obtained in 09/2011 by an analog, electric-line system with a 28-mm-diameter sensor (Figs. 1.13, 1.14 and 1.15). A downward logging speed of 2 m min^{-1} was applied in order to compensate for the buoyancy of the sensor and, thus, a loss in cable tension during descent in the narrow water-filled tube. The water level in the borehole corresponds to terrain level. After temperature logging, the Mersch borehole could be secured by a manhole cover (Fig. 1.16).

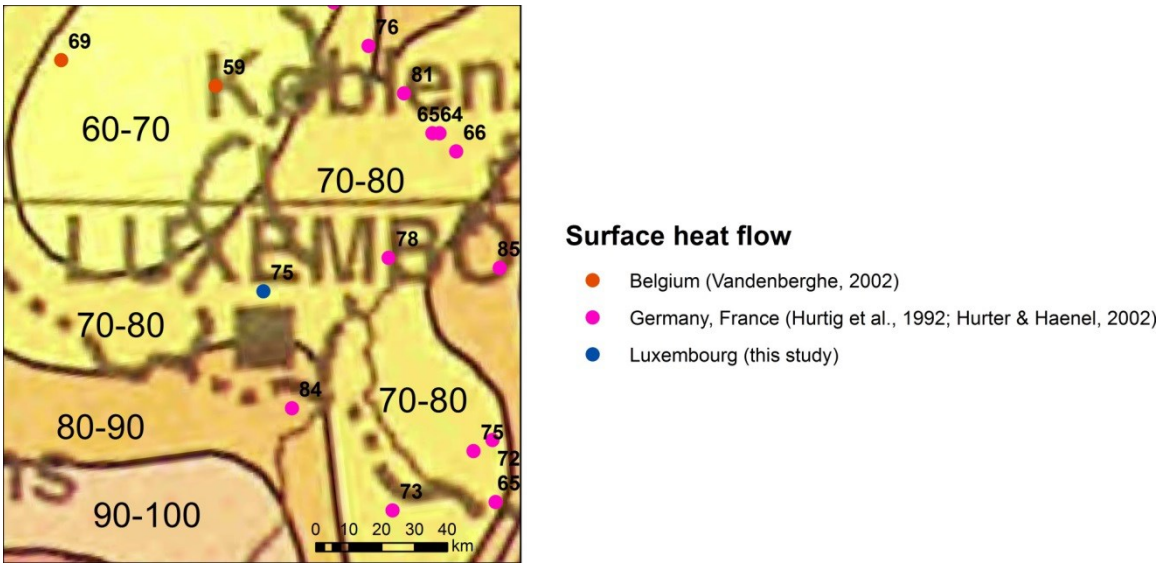

Fig. 1.7: Extract of the surface heat flow map by Hurter and Haenel (2002). Available terrestrial heat flow values (in mW m^{-2}) according to references in legend are indicated.

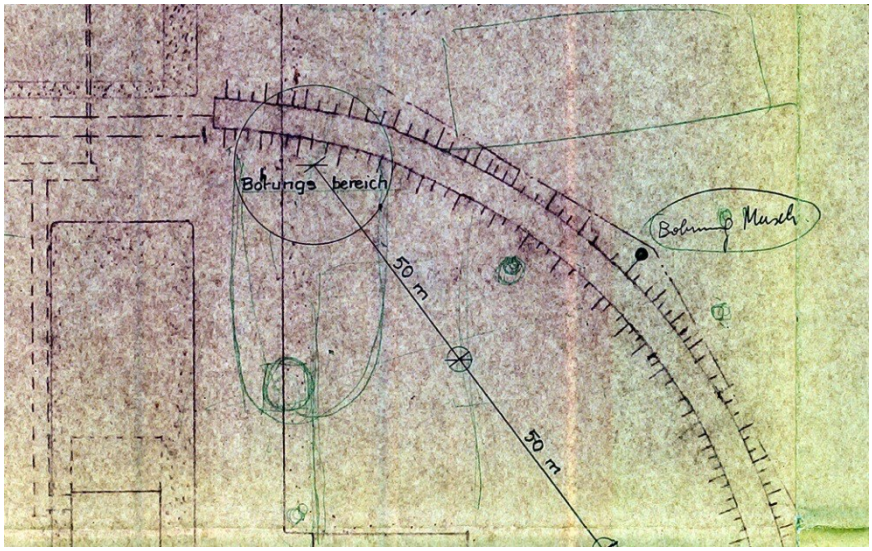

Fig. 1.8: Catasdral plan showing the location of the Mersch borehole. For geographical coordinates see Table 2.1.

Fig. 1.9: Mersch borehole after discovery by G. Beidler and T. Schintgen (TS) (6/29/2011).

Fig. 1.10: Unearthing of the Mersch borehole well head by L. Schintgen and TS (7/15/2011).

Fig. 1.11: Verification of the accessibility of the Mersch borehole with an electrical contact gauge by L. Schintgen and TS (7/15/2011).

Fig. 1.12: Cut-off of the well head by Dr. B. Norden (9/02/2011).

Fig. 1.13: Temperature logging in a 300-m-deep, narrow piezometric tube (9/02/2011).

Fig. 1.14: Electronic control unit and computer for regulating logging speed, data recording and processing (9/02/2011).

Fig. 1.15. Discussion between R. Colbach (Geological Survey of Luxembourg; hidden by left technician) and TS while temperature logging (9/02/2011).

Fig. 1.16. Manhole cover put in place by the Geological Survey and the Administration des Ponts et chaussées (Luxembourg) and now securing the Mersch borehole.

1.2.3.7 Temperature maps

As deep boreholes are scarce and temperature data are unavailable, the thermal regime was obtained by lithosphere-scale 2-D steady-state thermal modelling based on surface heat flow and a vast database of measured thermal rock properties, in particular thermal conductivity (see Section 4.4.1; Schintgen et al., 2015). The thermal model by Schintgen et al. (2015) provides

data for temperature maps (see Fig. 4.4) generated for 1 km depth steps between 1000 and 6000 m (below mean sea level). The temperature data are extracted from the thermal model for constant depths and then georeferenced for plotting using the ArcMap™ software. The geographical coordinates of the cross sections constructed for thermal modelling are provided in the Appendix (Table A.1.16; see also Figs. 1.2 and 3.1). As subsurface temperature is related to rock thermal conductivity and thus geology and structure, the temperature along transects was inter- and extrapolated by considering the geology, in particular the geometry of depth maps based on conceptual geological models (see Fig. 4.9). This approach helped to counteract the fact of using 2-D thermal models instead of a 3-D thermal model which would consider both geology and structure in space.

1.2.3.8 Top/base maps

The geometry or rather top/base maps of the Buntsandstein aquifer (see Fig. 4.7) and the Lochkovian succession (see Fig. 4.9) presented in Sections 4.4.3.1 and 4.4.3.4, respectively, are based on stratigraphical and structural data extracted from the conceptual geological models and, more specifically, the cross sections presented by Schintgen and Förster (2013) and by Wagner and Dittrich (2010) for the Mesozoic Trier–Luxembourg Embayment and by Schintgen et al. (2015) for the Lower Devonian basement. The extracted data is georeferenced for plotting using the ArcMap™ software. The geographical coordinates of the cross sections used as a basis for drawing the maps are given in the Appendix (Table A.1.16). For the sake of clarity, drawing of isodepth lines was performed by considering only a selection of major faults/thrusts. In addition, borehole data available in the Trier–Luxembourg Embayment as well as geological maps and existing maps by Coiffait and Ricour (1982) and Weiler (1972) were considered.

1.3 Overview of the manuscripts

Chapter	Publication/Main goal	Journal/Status
Chapter 2	Schintgen, T., Förster, A., 2013. Geology and basin structure of the Trier–Luxembourg Basin – implications for the existence of a buried Rotliegend graben. Main goal: Review of the geology of the Trier–Luxembourg Basin by inclusion of new data available in Luxembourg and adjoining areas in view of the exploration of Luxembourg's geothermal potential.	Zeitschrift der Deutschen Gesellschaft für Geowissenschaften published
Chapter 3	Schintgen, T., Förster, A., Förster, H.-J., Norden, B., 2015. Surface heat flow and lithosphere thermal structure of the Rhenohercynian Zone in the greater Luxembourg region. Main goal: Assessment of the thermal field by numerical modelling, provision of new data on surface heat flow for verification of the thermal models and presentation of a database of measured thermal rock properties. Schintgen, T., Förster, A., Förster, H.-J., Norden, B., 2015. Corrigendum to « Surface heat flow and lithosphere thermal structure of the Rhenohercynian Zone in the greater Luxembourg region » Main goal : Correct the errors in the cited T- and p-correction equations. The thermal models remain correct.	Geothermics published

Chapter 4	Schintgen, T., 2015. Geological exploration for deep geothermal reservoirs in Luxembourg and the surroundings – perspectives of geothermal energy use. Main goal: Combination of different types of information (geological, thermal, hydrogeological and structural) necessary for a first qualitative assessment of deep geothermal reservoirs in Luxembourg and the surroundings.	Geothermal Energy published

1.4 Author contributions

Chapter 2 *Geology and basin structure of the Trier–Luxembourg Basin – implications for the existence of a buried Rotliegend graben*

Tom Schintgen (TS) worked out the topic and content of this contribution. TS developed the conceptual model of the Trier–Luxembourg Basin as a consequence of the lack of an appropriate model for the exploration of Luxembourg's geothermal potential. TS collected borehole data in the archives of the Geological Survey of Luxembourg. Their joint interpretation (TS) showed the need to develop a new concept by means of isopach maps and cross sections (TS). The visualization technique and Matlab script to implement the basin-wide cross sections was developed and written by TS. The manuscript was written by TS with the help of Andrea Förster.

Chapter 3 *Surface heat flow and lithosphere thermal structure of the Rhenohercynian Zone in the greater Luxembourg region*

This Chapter represents the core of this work as it provides the thermal regime for the evaluation of the geothermal potential. Thermal modelling was necessary because subsurface temperature data in the study area are sparse. The assessment of the thermal regime at depth required profound structural, geological and petrophysical input data. The required petrophysical properties encompass thermal conductivity, radiogenic heat production and density. Rock sampling in the field and in the core storage at the geological surveys of Belgium and Luxembourg were planned and executed by TS. The samples were selected, cut and prepared for density, porosity and thermal conductivity determination by TS. The measurements were planned by TS and performed with the generous help of the laboratory assistants C.-T. Rach, S. Kienast, C. Rudolph and M. Oldman. TS interpreted the thermal conductivity data and selected the samples for determination of the radiogenic heat production. Hans-Jürgen Förster arranged the preparation of the rock powder for whole-rock analysis (done by H. Liep and M. Ospald) and provided information about the modalities for and the interpretation of the geochemical analysis which was performed by Acmelabs in Vancouver, Canada. TS calculated the radiogenic heat production. As surface heat flow was unknown prior to this study, TS searched for an undisturbed borehole in Luxembourg. Ben Norden and TS planned the field trip to Luxembourg and performed the temperature logging together. Andrea Förster helped with

the determination and interpretation of the surface heat flow. Ben Norden provided the thermal modelling algorith developed by him and Dietrich Stromeyer. Ben Norden also assisted with explanations and troubleshooting during the implementation of the conceptual models. The content and structure of this manuscript was discussed with Andrea Förster. TS wrote the manuscript together with Andrea Förster with contributions by Hans-Jürgen Förster (geochemistry, petrology) and Ben Norden (thermal modelling).

Chapter 4 *Exploration for deep geothermal reservoirs in Luxembourg and the surroundings – perspectives of geothermal energy use*

This Chapter aims at qualitatively assessing deep geothermal reservoirs in the greater region of Luxembourg. The concept and content of this contribution was worked out by TS. The approach consists in a joint interpretation of geological, thermal, hydrogeological and structural data necessary for the identification of geothermal reservoirs and the exploitation of geothermal energy. TS wrote the manuscript as a single author with critical comments and suggestions by Andrea Förster.

2 Geology and basin structure of the Trier–Luxembourg Basin – implications for the existence of a buried Rotliegend graben

Tom Schintgen, Andrea Förster

Published in:
Z. Dt. Ges. Geowiss. 164 (4), 615–637.
http://dx.doi.org/10.1127/1860-1804/2013/0025

2.1 Abstract

This paper presents the geology of the Trier–Luxembourg Basin (TLB) in a comprehensive and updated manner. It describes the structural and lithological features of the basin, which comprises sediments of Permian to Mesozoic age. The regional geological assessment profited from recently published information on the geology and regional tectonics, as well as from borehole data from Luxembourg and adjoining areas in France, Belgium and Germany. The paper specifically focuses on the location of major synsedimentary faults and weakness zones, which gave rise to a new conceptual model of basin structure and evolution. The total depth of the basin as well as the thickness estimates of the fault-controlled subunits are supported by the interpretation of a Bouguer gravity map. In addition, the stratigraphy of the Cessange borehole and the depositional conditions of the Luxembourg Sandstone have been reinterpreted in accordance with the new concept. Supported by numerous geological cross sections it is suggested that the TLB has developed along a SW–NE trending weakness zone above a Permian Graben in direct prolongation of the Wittlicher Senke.

2.2 Zusammenfassung

Dieser Beitrag befasst sich mit einer umfassenden und aktualisierten Überarbeitung der Geologie des Trier–Luxemburger Beckens (TLB). Die strukturellen und lithologischen Merkmale des Beckens, welches Sedimente permischen bis mesozoischen Alters enthält, werden beschrieben. Die regionale geologische Neubewertung stützt sich auf kürzlich veröffentlichte Daten über die Geologie und die regionale Tektonik sowie auf Bohrdaten aus Luxemburg und den angrenzenden Gebieten in Frankreich, Belgien und Deutschland. Der Beitrag konzentriert sich besonders auf die Lage der wichtigsten synsedimentären Störungen und Schwächezonen, woraus ein neues konzeptionelles Modell der Beckenstruktur und -entwicklung abgeleitet wurde. Die Gesamttiefe des Beckens und die geschätzten Mächtigkeiten der von Störungen beeinflussten Untereinheiten werden durch die Interpretation einer Schwerekarte gestützt. Außerdem wurde die Stratigraphie der Bohrung Cessingen und die Ablagerungsbedingungen des Luxemburger Sandsteins im Einklang mit dem neuen Konzept neu gedeutet. Gestützt durch zahlreiche geologische Profilschnitte wird vorgeschlagen, dass sich das TLB entlang einer SW–NE streichenden Schwächezone über einem permischen Graben in direkter Verlängerung der Wittlicher Senke gebildet hat.

2.3 Introduction

In this paper, the geology of the Trier–Luxembourg Basin (TLB) is reviewed by inclusion of new data available in Luxembourg and adjoining areas. The work is performed as a necessary first step to explore Luxembourg's geothermal potential and for the assessment of the thermal field to come.

The TLB is expressed as the northeastern extension of the Paris Basin (Fig. 2.1), designated by the descriptive terms Gulf of Luxembourg (Golfe du Luxembourg respectively Trier–Luxemburger Bucht) or Luxembourg Syncline (Synclinal du Luxembourg). As a sub-basin of the German Triassic Basin in the early Triassic and a sub-basin of the Paris Basin since the late Triassic, the TLB progressively increased its spatial extension covering most of the older Variscan basement except the highest regions of the Ardennes in the northwest and the Rhenish Massif in the east (e.g., Lucius, 1937; Murawski et al., 1983; Dittrich, 1989). After Tertiary and Quaternary uplift and erosion, the resulting Gulf of Luxembourg is again framed by exhumed parts of the basement, namely the Palaeozoic Ardennes Massif in the north and the Eifel and Hunsrück massifs in the east (Fig. 2.1). The western border of the TLB is set at the Meuse valley near Verdun (Fig. 2.1), where its signature fades (Le Roux, 1980, 1999, 2000). The southern border of the TLB is classically associated with the Ridge of Mettlach–Sierck ("Siercker Schwelle") consisting of particularly resistant Taunus Quartzite (Fig. 2.2; Müller, 1973; Muller, 1987). Lithostratigraphic studies in Lorraine (e.g., Courel et al., 1980; Mouterde et al., 1980), however, reveal that the southern border of the TLB is actually located at the Metz Fault, which also correlates with a major boundary between basement structures, namely the Rhenohercynian Zone in the north and the Saxothuringian Zone in the south (e.g., Prijac et al., 2000). The presented update of geology focuses on a more restricted area including the Luxembourgish part of the basin and its adjoining areas (Fig. 2.1). The study area encompasses the Guttland in Luxembourg, northern Lorraine in France, the Gaume (or Lorraine belge) in southeastern Belgium as well as the Südeifel (Rhineland-Palatinate) and Saargau (Rhineland-Palatinate and Saarland) in Germany.

The geology of Luxembourg has last been addressed as a whole and integrated in a regional context by Lucius (1937, 1948). Since then, several local studies were performed mainly focusing on new geological mapping and sedimentology (e.g., Dittrich, 1989; Wagner, 1989; Konrad and Wachsmut, 1973; Berners, 1985; Muller, 1987) as well as a sedimentology-based reassessment of tectonic structures (e.g., Dittrich, 1989, 2008, 2009, 2011b, 2012). In the older literature (i.e. prior to Dittrich 1989), the TLB is classically described to have a central syncline,

the so named “Mulde von Weilerbach”, forming the southwestern prolongation of the Eifel Depression (Fig. 2.2; e.g., Lucius, 1948; Bintz et al., 1985; Murawski et al., 1983; Muller, 1987). Detailed observations, mostly in the widely exposed series of the Keuper, by Dittrich (1989, 2011a) and Dittrich et al. (1997) describe a more complex setting leading to the rejection of the Weilerbach Mulde concept.

However, the link of this old concept with the present-day appearance of the Lower Liassic Luxembourg Sandstone and the initial interpretation of the geological section encountered by the Cessange borehole and vice-versa still remained. This paper questions these former interpretations by providing new geological insight into the basin geology based on the possibility of a southwestern prolongation of the Wittlicher Senke underneath the TLB. The new concept is based on information from a Bouguer gravity map and a reinterpretation of the Cessange borehole stratigraphy (Rost, 1839; Lucius, 1948). Additional information provided by borehole data (Table 2.1) from Luxembourg, France, Belgium and Germany are incorporated in a new comprehensive basin model visualized in several isopach maps and regional cross sections.

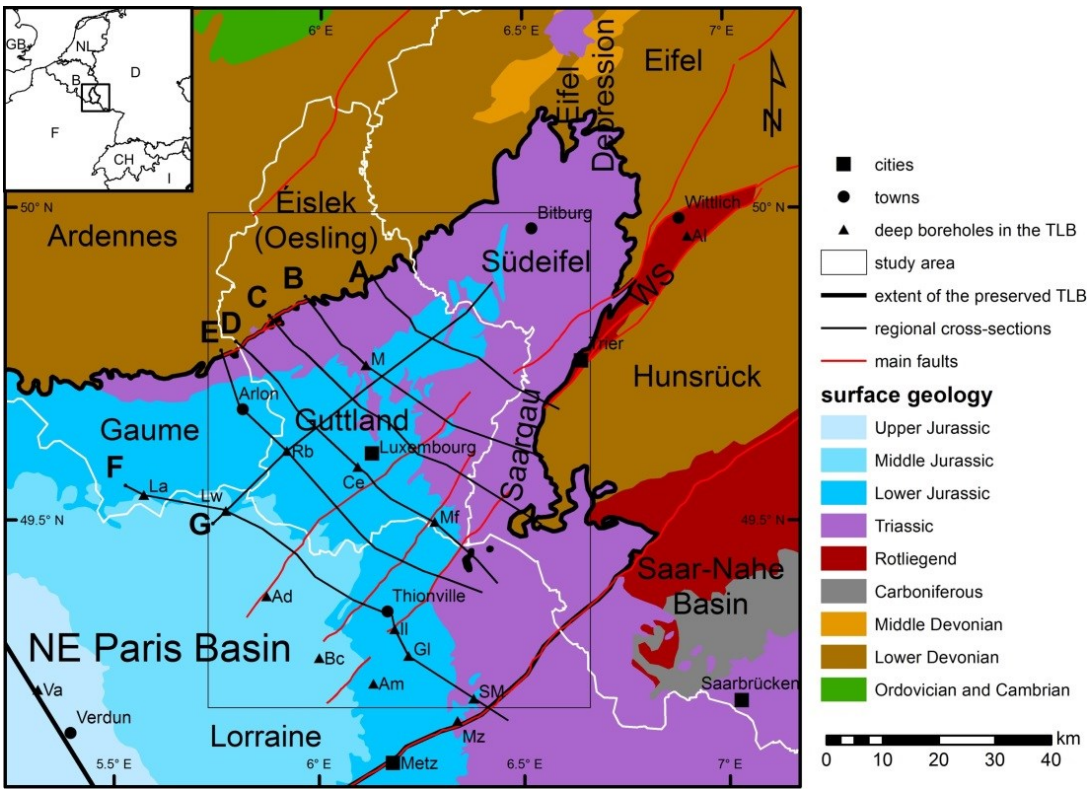

Fig. 2.1: Regional geological map of the study area and its surroundings with indication of the geographical units. The location of the map area within Western Europe is shown in the top left corner. National borders are shown as white lines. Black lines and bold letters correspond to the regional cross sections presented in Section 2.5.3. Locations of deep boreholes (Table 2.1) are shown with IDs.

Table 2.1: Deep boreholes in the TLB. The coordinates of the Cessange and Altrich boreholes are only indicative.

Borehole	ID	Year	TD	Stratigraphy	Latitude N	Longitude E	Target
Cessange	Ce	1839	534 m	Muschelkalk	49° 35.373' ?	6° 05.646' ?	rock salt
Mondorf KIND	Mf	1846	730 m	Devonian	49° 30.070'	6° 16.946'	rock salt
Altrich	Al	1890?	537 m	Permian	49° 57.423' ?	6° 54.538' ?	geology
Longwy	Lw	1908	922 m	Devonian	49° 31.117'	5° 46.217'	coal
Bois châté	Bc	1909	1100 m	Permian	49° 17.033'	6° 00.083'	coal
Mondorf ADELAIDE	Mf	1913	589 m	Buntsandstein	49° 30.109'	6° 16.985'	hydrothermal water
Vacherauville	Va	1953	2250 m	Devonian	49° 13.817'	5° 18.783'	iron, gas, oil
Audun-le-Roman	Ad	1957	1251 m	Permian	49° 22.933'	5° 52.333'	geology, oil
Metz	Mz	1961	1078 m	Devonian	49° 10.983'	6° 20.266'	geology
Mersch	M	1968	328 m	Devonian	49° 45.132'	6° 06.826'	geology, hydrogeology
Rebierg	Rb	1972	705 m	Devonian	49° 36.891'	5° 55.159'	geology, hydrogeology
Mondorf LUCIUS	Mf	1979	750 m	Devonian	49° 30.191'	6° 16.969'	hydrothermal water
Amnéville F1	Am	1979	900 m	Permian	49° 14.550'	6° 08.117'	hydrothermal water
Illange	Il	1982	538 m	Buntsandstein	49° 19.817'	6° 11.067'	oil
Guélange	Gl	1984	499 m	Buntsandstein	49° 17.250'	6° 13.133'	oil
St. Michel	SM	1985	857 m	Devonian	49° 13.133'	6° 22.667'	oil
Latour	La	1986	494 m	Devonian	49° 32.505'	5° 34.113'	geology
Amnéville F2	Am	1989	880 m	Permian	49° 14.633'	6° 07.767'	hydrothermal water

TD = total depth, Stratigraphy refers to stratigraphy at total depth.

2.4 Background on geology

2.4.1 Pre-Mesozoic basement structures

The evolution of the TLB is closely associated with inherited basement structures generated in different geodynamic contexts (e.g., Lucius, 1948; Le Roux, 1980; Berners, 1985; Dittrich, 1989). The basement of the TLB, being part of the Rhenohercynian Zone of the Variscan orogen, exibits a generally northwest-vergent fold-and-thrust belt consisting mostly of Devonian series. The Ardennes and Eifel massifs in the north are separated by a north–south-oriented depression or cross-fold, the so-called Eifel Depression ("Eifeler Nord-Süd-Zone", Fig. 2.1). The Eifel Depression is classically seen to continue in the TLB and thus to control its evolution (Murawski et al., 1983). The rather fold-dominated Eifel and thrust-dominated Hunsrück are separated by a Permian graben, the so-called Wittlicher Senke (WS) bound by normal faults (Fig. 2.2). The main known thrust faults from south (-west) to north (-east) are: the Metz Fault (MF) continued northeastwards by the Hunsrück Boundary Fault (HBF), the Boppard–Dausenau–Longuich Thrust (BDLT), the Siegen Main Thrust (SMT) and the Plein Thrust (PT; Fig. 2.2; Kölschbach, 1986; LGB, 2005). In the Ardennes–Eifel block, the most

important structures are: the Olkenbach Syncline (OSc), which is truncated by the Plein Thrust, the Givonne–Oesling–Manderscheid Anticlinorium (GAc–OAc–MAc) and the Neufchâteau–Wiltz–Eifel Synclinorium (NSc–WSc–ESc).

The late- to post-Variscan evolution of the area resulted in the formation of intramontane half-grabens such as the Permo-Carboniferous Saar–Nahe Basin (Korsch and Schäfer, 1996) and the Permian Wittlicher Senke (WS; Fig. 2.1; Fig. 2.2; Stets, 2004a). In the NW, the WS is bound by the Wittlich Main Fault (WMF; "Wittlicher Hauptverwerfung"; Kopp, 1955) which is a strike-slip fault with a throw of more than 1000 m. In the southeast, the WS is bound by the "Südrandstörung" or "südliche Randverwerfung" (also: "Störung Konz–Longuich" in [LGB and LUWG 2010]) for which a throw of 400 m is inferred (Stets, 2004b). Initially being part of a larger Permian sedimentation area (Lucius, 1948; Schäfer, 1986; Stets, 1990; LGB, 2005), the sediments of the WS are mainly preserved between the two border faults in a well-defined up to 7-km-wide and 40-km-long structure (Stets, 1990). In the Trier region (Fig. 2.1), the Buntsandstein and younger Mesozoic sediments overlying the Permian sediments mask the southwestern prolongation of the WS (Stets, 1990, 2004b; LGB and LUWG, 2010).

Although the main tectonic activity of the WS terminated by the end of the Rotliegend, post-Permian subsidence along the WMF also affected the Mesozoic cover in the TLB (Kopp, 1955; LGB, 2005; LGB and LUWG, 2010). According to Stets (2004b) and Dittrich (2011b), the WS was at least marginally incorporated during the formation of the TLB. However, as already mentioned, the structure and evolution of the TLB is classically assigned to the Weilerbach Mulde as a southwestern prolongation of the Eifel Depression (e.g., Lucius, 1948; Bintz et al., 1985; Murawski et al., 1983; Muller, 1987). The present-day appearance of the TLB as Gulf of Luxembourg is enhanced by the preferential preservation of the relatively resistant Luxembourg Sandstone framed by Triassic deposits in the northwest and east. The Ridge of Mettlach–Sierck, which is exposed in the Mosel valley at the southeastern tip of Luxembourg, is thereby considered to be the southern limit of the Eifel Depression (Muller, 1980). The post-Variscan tectonics is characterized primarily by fracture tectonics affecting the consolidated crust, which is well observable in the Mesozoic cover of the Südeifel (Stets, 2004b; LGB and LUWG, 2010), the Guttland (e.g., Lucius, 1948; Dittrich, 1989) and the northeastern Paris Basin (e.g., Le Roux, 2000). Whereas Variscan (N60–70°E) and Rhenish (N–S) fault systems are long known (Lucius, 1937), Dittrich (1989, 2008) reports also a SW–NE (N45°E) striking fault system. In particular the SW–NE striking faults play an important role in the TLB (Dittrich, 1989), which is also reported from the NE Paris Basin (Fig. 2.2; Le Roux, 1971, 1980, 2000).

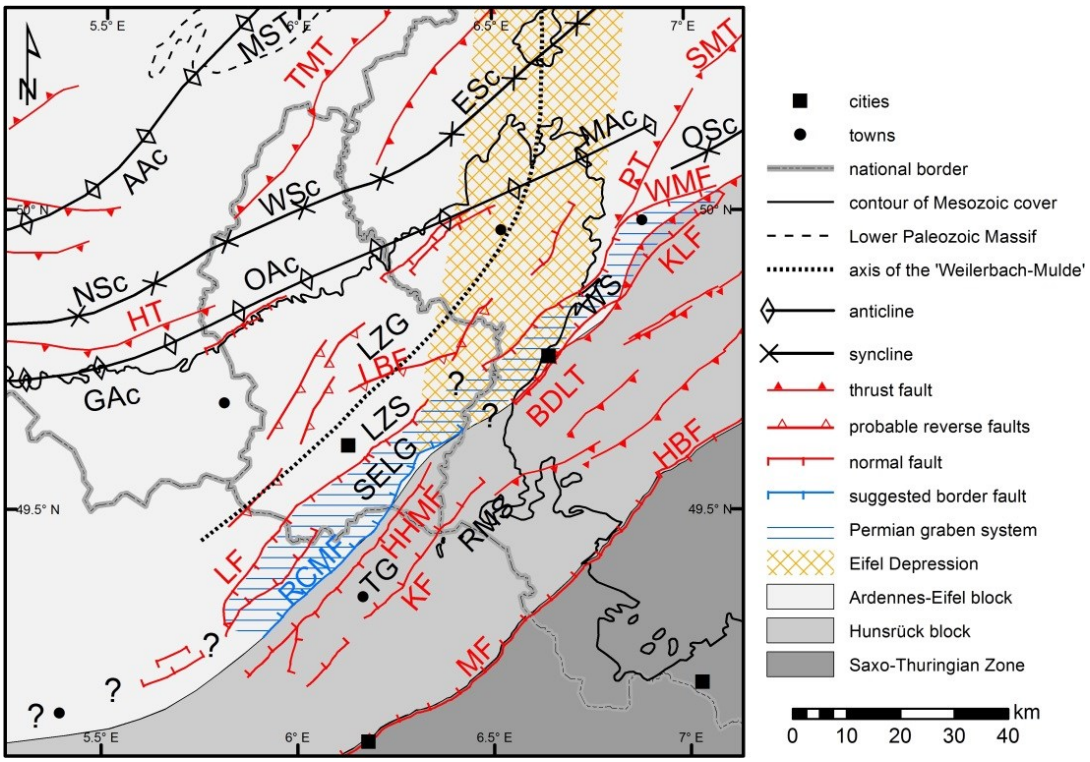

Fig. 2.2: Regional tectonic map with localities as in Fig. 2.1.

Tectonic structures: MST = Stavelot Massif, AAc = Ardenne Anticlinorium, NSc = Neufchâteau Synclinorium, WSc = Wiltz Synclinorium, ESc = Eifel Synclinorium, GAc = Givonne Anticlinorium, OAc = Oesling Anticlinorium, MAc = Manderscheid Anticlinorium, OSc = Olkenbach Syncline. TMT = Troisvierges–Malsbenden Thrust, HT = Herbeumont Thrust, SMT = Siegen Main Thrust, PT = Plein Thrust, WMF = Wittlich Main Fault, BDLT = Boppard–Dausenau–Longuich Thrust, KLF = Konz–Longuich Fault, LBF = Lorentzweiler–Bech Fault, LF = Luxembourg Fault, RCMF = Roussy-le-Village–Canach–Machtum Fault, HHMF = Hayange–Hettange–Mondorf Fault, KF = Koenigsmacker Fault, MF = Metz Fault, HBF = Hunsrück Boundary Fault, LZG = Luxemburger Zentralgraben, LZS = Luxemburger Zentralschwelle, SELG = SE-Luxembourg Graben, WS = Wittlicher Senke, TG = Thionville Graben, RMS = Ridge of Mettlach-Sierck.

2.4.2 Mesozoic evolution of the TLB and lithostratigraphic units

According to the present-day state of knowledge, the development of the TLB begins in the more or less N–S trending Eifel Depression where the oldest known post-Variscan deposits in Luxembourg are of Middle Buntsandstein age (e.g., Lucius, 1937; Muller, 1987). In the German Südeifel area, also deposits of Lower Buntsandstein age are known. However, limited Rotliegend is suggested underneath the TLB as reported from the Mondorf Kind borehole (Lucius, 1948). During the Triassic, progressive transgression resulted in the enlargement of the sedimentation area by roughly 50 km at the expense of the Ardennes (Lucius, 1948; Courel et al., 1980), and in the development of the so-called Germanic facies province with its tripartite subdivision into Buntsandstein, Muschelkalk and Keuper. In southern Luxembourg, the total

thickness of the Triassic series amounts to more than 600 m (655 m in the Mondorf Kind borehole). During the Buntsandstein and Muschelkalk, the TLB is characterized by a marginal position in the German Triassic Basin. In this context, a distinct margin facies formed in NW Guttland, and has also been recorded in the Rebierg and Longwy boreholes. A correlation of these typically more sandy and conglomeratic units with their counterparts in the basin facies is difficult (e.g., Lucius, 1948; Dittrich, 1989; Wagner, 1989).

The Buntsandstein, which consists typically of red-colored, fluviatile sandstone (e.g., Muller, 1987; Guillocheau et al., 2002), unconformably overlies the Devonian basement (Lucius, 1948; Dittrich, 2011a). It is largely concealed below younger units, and exposures of Upper Buntsandstein are restricted to the southern margin of the Ardennes in nortern Guttland, to an anticline near Born in eastern Guttland and to a small occurrence at the Ridge of Mettlach–Sierck in the Mosel valley to the south of Schengen. In the adjoining Südeifel region, the Buntsandstein shows a much more complete development and exposure. The Muschelkalk transgression results in marine conditions giving rise to the formation of the Lower Muschelkalk carbonates (mu; Table 2.2; Ziegler, 1982), which comprise various sandy-marly-dolomitic rock types (Dittrich, 2011a). The latter grade into Middle Muschelkalk evaporitic and dolomitic marls, typical of a lagoonal environment, and culminate in a dolomitic succession during the Late Muschelkalk. The Muschelkalk carbonate sedimentation is terminated by a regional regression (Ziegler, 1982), which triggers the return to a clastic-evaporitic environment typical for the Keuper.

In contrast to the Lower Triassic, the Keuper is characterized by a different make-up reflecting the birth of the Paris Basin (Guillocheau et al., 1999; Bourquin and Guillocheau, 1993). The intercalated sandstone channels of the Schilfsandstein (Stuttgart Fm.), which are mainly developed in eastern Guttland, are an important marker for the subdivision of the overall more or less monotonous, marl-dominated series of the Middle Keuper. The heterochronous Upper Keuper (Rhaetian) marks the transition from a clastic-evaporitic environment typical for the Keuper to a marine environment typical for the Liassic.

Table 2.2: Stratigraphy (in part simplified) of the Mesozoic in Luxembourg and adjacent areas. Grey areas mark eroded or non-existent units.

C. = Couches, M. = Membre, Fm. = Formation.

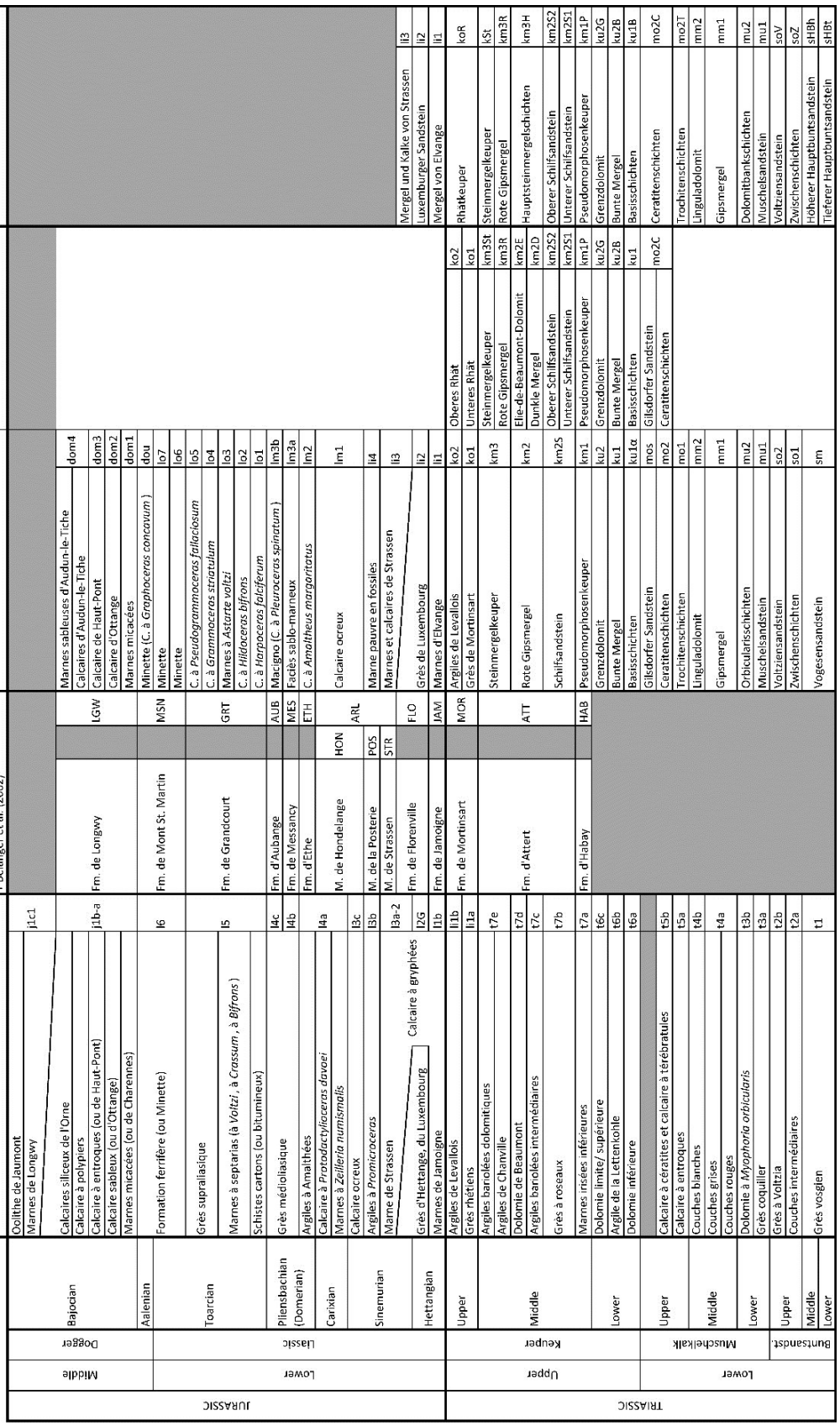

			FRANCE (N-Lorraine)		BELGIUM (E-Gaume)			LUXEMBOURG (Guttland)			GERMANY (Südeifel + Saargau)
			Le Roux (2007) + geological maps 1:50,000		Boulvain et al. (2001) + Belanger et al. (2002)			geological maps 1:25,000		Dittrich (1989), simplified	LGB (2005), simplified
JURASSIC	Middle	Bajocian	Oolithe de Jaumont	j1c1				Marnes sableuses d'Audun-le-Tiche	dom4		
			Marnes de Longwy					Calcaires d'Audun-le-Tiche			
			Calcaires siliceux de l'Orne		Fm. de Longwy		LGW	Calcaire de Haut-Pont	dom3		
			Calcaire à polypiers	j1b-a				Calcaire d'Ottange	dom2		
			Calcaire à entroques (ou de Haut-Pont)					Marnes micacées	dom1		
			Calcaire sableux (ou d'Ottange)					Minette (C. à *Graphoceras concavum*)	dou		
			Marnes micacées (ou de Charennes)					Minette	lo7		
	Lower	Aalenian	Formation ferrifère (ou Minette)	l6	Fm. de Mont St. Martin		MSN	Minette	lo6		
		Toarcian	Grès supraliasique					C. à *Pseudogrammoceras fallaciosum*	lo5		
			Marnes à septarias (à *Voltzi*, à *Crassum*, à *Bifrons*)	l5	Fm. de Grandcourt		GRT	C. à *Grammoceras striatulum*	lo4		
			Schistes cartons (ou bitumineux)					Marnes à *Astarte voltzi*	lo3		
								C. à *Hildoceras bifrons*	lo2		
		Pliensbachian (Domerian)	Grès médioliasique	l4c	Fm. d'Aubange		AUB	C. à *Harpoceras falciferum*	lo1		
			Argiles à Amalthées	l4b	Fm. de Messancy		MES	Macigno (C. à *Pleuroceras spinatum*)	lm3b		
					Fm. d'Ethe		ETH	Faciès sablo-marneux	lm3a		
		Carixian	Calcaire à *Prototdactylioceras davoei*	l4a	M. de Hondelange	HON		C. à *Amaltheus margaritatus*	lm2		
			Marnes à *Zelleria numismalis*				ARL	Calcaire ocreux	lm1		
		Sinemurian	Calcaire ocreux	l3c	M. de la Posterie	POS		Marne pauvre en fossiles	li4		
			Argiles à *Promicroceras*	l3b	M. de Strassen	STR		Marnes et calcaires de Strassen	li3		Mergel und Kalke von Strassen
			Marne de Strassen	l3a-2	Fm. de Florenville		FLO	Grès de Luxembourg	li2		Luxemburger Sandstein
			Grès d'Hettange, du Luxembourg	Calcaire à gryphées							
		Hettanglan	Marnes de Jamoigne	l2G	Fm. de Jamoigne		JAM	Marnes d'Elvange	li1		Mergel von Elvange
TRIASSIC	Upper	Upper	Argiles de Levallois	l1b	Fm. de Mortinsart		MOR	Argiles de Levallois	ko2	Oberes Rhät	Rhätkeuper
			Grès rhétiens	l1a				Grès de Mortinsart	ko1	Unteres Rhät	
	Keuper	Middle	Argiles bariolées dolomitiques	t7e				Steinmergelkeuper	km3	Steinmergelkeuper	Steinmergelkeuper
			Argiles de Chamville							Rote Gipsmergel	Rote Gipsmergel
			Dolomie de Beaumont	t7d	Fm. d'Attert		ATT	Rote Gipsmergel	km2	Elle-de-Beaumont-Dolomit	Hauptsteinmergelschichten
			Argiles bariolées intermédiaires	t7c						Dunkle Mergel	
			Grès à roseaux	t7b				Schilfsandstein	km2S	Oberer Schilfsandstein	Oberer Schilfsandstein
										Unterer Schilfsandstein	Unterer Schilfsandstein
			Marnes irisées inférieures	t7a	Fm. d'Habay		HAB	Pseudomorphosenkeuper	km1	Pseudomorphosenkeuper	Pseudomorphosenkeuper
		Lower	Dolomie limite/ supérieure	t6c				Grenzdolomit	ku2	Grenzdolomit	Grenzdolomit
			Argile de la Lettenkohle	t6b				Bunte Mergel	ku1	Bunte Mergel	Bunte Mergel
			Dolomie inférieure	t6a				Basisschichten	ku1α	Basisschichten	Basisschichten
	Muschelkalk	Upper	Calcaire à cératites et calcaire à térébratules	t5b				Gilsdorfer Sandstein	mo2	Gilsdorfer Sandstein	Cerattitenschichten
			Calcaire à entroques	t5a				Cerattitenschichten	mo2C	Cerattitenschichten	
		Middle	Couches blanches	t4b				Trochitenschichten	mo1		Trochitenschichten
			Couches grises	t4a				Linguladolomit	mm2		Linguladolomit
			Couches rouges					Gipsmergel	mm1		Gipsmergel
		Lower	Dolomie à *Myophoria orbicularis*	t3b				Orbicularisschichten	mu2		Dolomitbankschichten
			Grès coquiller	t3a				Muschelsandstein	mu1		Muschelsandstein
	Buntsandst.	Upper	Grès à Voltzia	t2b				Voltziensandstein	so2		Voltziensandstein
			Couches intermédiaires	t2a				Zwischenschichten	so1		Zwischenschichten
		Middle	Grès vosgien	t1				Vogesensandstein	sm		Höherer Hauptbuntsandstein
		Lower									Tieferer Hauptbuntsandstein

During the Jurassic, the sedimentation area is designated as the Luxembourg Basin (LB), instead of TLB because Jurassic deposits are at present almost completely eroded in the Trier area (Fig. 2.1). In the Paris Basin, the Liassic is characterized by a marine transgression from SW-Germany onto the old massifs which were already largely eroded. The sediments are generally very fine-grained, i.e. comprising clays and silts, especially in the most subsided part of the basin, and locally calcareous clays or even bioclastic limestones (Mouterde et al., 1980). The detritic material is provided from the north through the Eifel Depression (Berners, 1985). In the vicinity of the Ardennes mainland, some units are characterized by a more sandy facies, notably the Luxembourg Sandstone (li2) and the Grès médioliasique (lm3; Table 2.2). The Toarcian regression culminates in the uppermost Toarcian (lo6 and lo7) and Aalenian (dou) formation of oolithic ironstone known as Minette Formation in northern Lorraine and southwestern Luxembourg (Bubenicek, 1961; Teyssen, 1989; Guillocheau et al., 1999). The thickness of the whole Liassic succession in the LB amounts to more than 500 m (Mégnien, 1980: map L7). In contrast to the clay- and silt-dominated Lower Jurassic, the Middle Jurassic (Dogger) sedimentation is characterized by bioclastic and reef limestones (Thierry et al., 1980). The Mesozoic lithostratigraphic units of Luxembourg (Table 2.2) are addressed by the symbols widely used in the Luxembourgish geological maps (new series, scale 1:25,000). These symbols are used in this work instead of the new, more complex and detailed Upper Triassic (Keuper) stratigraphy of Dittrich (1989, 2011a) and LGB (2005), which is not yet established in Luxembourg.

2.5 Methodology

2.5.1 Interpretation of the Bouguer anomaly map

A Bouguer anomaly map of Luxembourg (Fig. 2.3; M. Everaerts, 2012, pers. comm.), which is based on 509 gravity measurements performed in 1996 for the Administration du Cadastre et de la Topographie (Everaerts, 1997), was used to shed light on the Mesozoic basin structure and the topography/structure of the basement. The coverage of one data point per 5 km^2 is comparable to the adjoining areas (Everaerts, 1997, 2002). The gravity points are tied to the reference point of Uccle, Belgium. The Bouguer anomalies are calculated with a standard density of 2.67×10^3 kg m^{-3} (Everaerts and De Vos, 2012: 42).

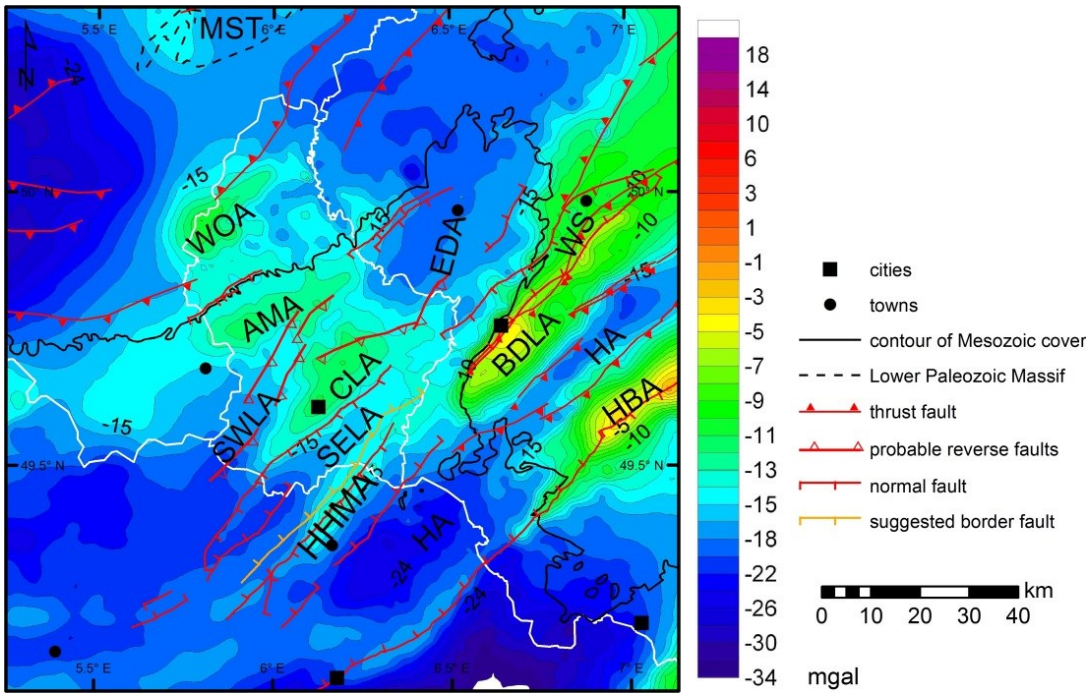

Fig. 2.3: Bouguer anomaly map with localities and areal extent of the TLB as in Fig. 2.1.
MST = Stavelot Massif, WS = Wittlicher Senke, WOA = Western Oesling Anomaly, AMA = Ardennes Margin Anomaly, CLA = Central Luxembourg Anomaly, SWLA = SW-Luxembourg Anomaly, SELA = SE-Luxembourg Anomaly, EDA = Eifel Depression Anomaly, HHMA = Hayange–Hettange–Mondorf Anomaly, BDLA = Boppard–Dausenau–Longuich Anomaly, HA = Hunsrück Anomaly, HBA = Hunsrück Boundary Anomaly.

In general, the most important Variscan structures, involving rock of different density, are well outlined by anomalies. Positive anomalies usually indicate thrusts or anticlines and negative anomalies synclines or depressions, respectively. The Bouguer map reveals the continuation of the main WSW–ENE to SW–NE striking Variscan structures below the TLB. Within the Rhenohercynian Zone, the structures belonging respectively to the Ardennes–Eifel block and Hunsrück block (Fig. 2.2) can thus be distinguished. The anomalies or the boundary between anomalies are often correlated with major faults observable at the surface. In addition, the Variscan structures are crossed by a more or less NW–SE arrangement of positive anomalies probably corresponding to exposed and buried Caledonian massifs, from the Stavelot Massif (Figs. 2.2 and 2.3) in the north to the CLA (Fig. 2.3) in the south. In contrast, the Eifel Depression is characterized by the relatively large negative anomaly EDA (Fig. 2.3). However, the Bouguer map also shows a fundamental problem with the "Variscan" (N60–70°E) and "diagonal" (SW–NE) structural directions in the Variscan basement first differentiated by Dittrich (1989) and defined as to have no particular genetic meaning. The anomalies and the associated main faults indicate that the Variscan direction, which is dominant in the Oesling (i.e. the Luxembourgish Ardennes) turns gradually into a dominantly SW–NE orientation

towards the south. Only to the west of Luxembourg, e.g. in the Belgian Ardennes, the structures in the Variscan orogenic belt turn into the W–E orientation (Fig. 2.2). This may be due to more southward contouring of more resistant, buried Caledonian massifs during the Variscan Orogeny (Autran et al., 1980; Keppie, 1994). Therefore, we put forward that both directions are actually inherently Variscan. Consequently, if not specified, by "Variscan" we mean a Variscan origin, not a Variscan direction or strike.

The Bouguer map does not only show the existence of major structures with higher density at depth, responsible for higher background gravity, but also provides hints about the depth of the basin itself when combined with available borehole data. A sufficiently thick Mesozoic succession with an average density lower than that of the basement generally produces a negative anomaly. This effect is best observed along the eastern margin of the TLB where the contrast between Mesozoic and Devonian rock also corresponds to a sharp gravimetric boundary.

Based on these findings, the Weilerbach Mulde (Fig. 2.2), which, in the older literature, is classically seen as the central syncline of the TLB and as the southwestern prolongation of the Eifel Depression, should have a gravimetric signature. The Bouguer map, however, shows a remarkable positive anomaly in the region classically expected to be the deepest area of the TLB (Lucius; 1948: Tafel III; Berners, 1985; Muller, 1987). This anomaly will hereafter be named Central Luxembourg Anomaly (CLA; Fig. 2.3). The regional context reveals that the CLA, as well as the other positive anomalies in the Variscan basement, are very likely buried Caledonian massifs similar to the exposed massifs in the Ardennes. At the surface, the CLA is well defined to the north and northwest by several fault segments and to the southeast by the so-called Luxembourg Fault (LF; Guillocheau et al., 1999) (Figs. 2.2 and 2.3), which is locally also known as Audun-le-Tiche Fault or Hesperange Fault. The LF separates the CLA from the gravity low named SE-Luxembourg Anomaly (SELA; Fig. 2.3), being a depositional trough, hereafter named SE-Luxembourg Graben (SELG; Fig. 2.2), that deepens towards the Paris Basin. Thus the Bouguer map does not indicate an independent depocentre in the Luxembourg City area with an axis traced from Weilerbach at the German border (Fig. 2.2), along the outcrops of thick Luxembourg Sandstone to the northwest of Luxembourg City and further to the vicinity of Longwy in the southwest. To the southeast, the narrow, but distinct, positive gravity anomaly, named Hayange–Hettange–Mondorf Anomaly (HHMA; Fig. 2.3), is likely linked to the Hayange–Hettange–Mondorf Fault (HHMF; Fig. 2.2). The northeastern prolongation of the latter structure in the Trier area likely is the so-called Boppard–Dausenau–Longuich Anomaly (BDLA; Fig. 2.3) which clearly is associated with the nearby thrust fault

(BDLT; Fig. 2.2). The Wittlicher Senke does not produce a particular negative anomaly, despite an up to 1000-m-thick infill of Rotliegend (Stets, 2004a), which is probably due to the superimposed effect of a denser basement related to the BDLA.

Most importantly, the Bouguer map allows for a parallelization of buried and exposed structures. In addition to their Variscan affinity, the LF–SE-Luxembourg Graben–HHMF structure shows a remarkable similarity to the WMF–Wittlicher Senke–BDLT structure and is located in the southwestern continuation of the latter. However, in a zone of intense Tertiary and Quaternary block faulting in the German-Luxembourgish border region some Variscan basement structures are probably partially overprinted. The negative SWLA anomaly (Fig. 2.3) in southeastern Belgium and southwestern Luxembourg may be caused by lower-density rock in the basement. Alternatively, an increased sediment accumulation during the Keuper and the Lower Liassic may be responsible as documented notably in the Rebierg borehole (Dittrich, 1989). The positive AMA anomaly to the south of the border of the Ardennes (Fig. 2.3) may correspond to the actual axis of the Givonne–Oesling–Manderscheid Anticlinorium (Fig. 2.2), which would then be concealed below the Mesozoic cover, instead of being located in the southern Oesling (e.g., Dittrich and Norbisrath, 2006). A relatively small but strong positive anomaly at the Belgian-Luxembourgish border, the Western Oesling Anomaly (WOA; Fig. 2.3), also likely corresponds to a body of dense Caledonian rock at depth.

2.5.2 Reinterpretation of the Cessange borehole section

The 534.85-m-deep Cessange borehole (Kind, 1842; Lucius, 1948), which is located just SW of the city of Luxembourg, was drilled from 1837 to 1839 and is still the only deep borehole in the vicinity of the (geographical) centre of the TLB (Fig. 2.1). It is among the first deep boreholes that were drilled for the purpose of finding salt deposits in the Keuper. Two lithological descriptions of the borehole section are known, one by Rost (1839), a business associate, and another by the head driller Kind (1842). No core was drilled, and the interpretation of the lithologies was based on the reading of drill cuttings. The lithology as well as the stratigraphic interpretation of Rost (1839) were used by Lucius (1948). His interpretation of the borehole geology has so far not been contested, except for some details (Dittrich, 1989). The existence of Liassic to Rhaetian sediments from the surface to about 171 m depth in the borehole is corroborated by nearby exposures. The Rhaetian rests on the 359-m-thick Middle Keuper, and the borehole section ends in the Lower Keuper (Fig. 2.4; Rost, 1839; Lucius, 1948; Dittrich, 1989).

However, a thickness of 359 m for the Middle Keuper is greater than what is expected from regional mapping. In the TLB, in particular in Luxembourg and northern Lorraine, the Middle Keuper is known to reach a maximum thickness of about 200 m in numerous boreholes. A Middle Keuper thickness as high as 359 m would require an independent depocentre in the Cessange area or, more generally, in the centre of the TLB. However, this is challenged by the Bouguer map (Fig. 2.3). Here, the Cessange area coincides with a remarkable positive gravity anomaly, not indicating any particularly deep basin. This calls for revisiting the borehole descriptions.

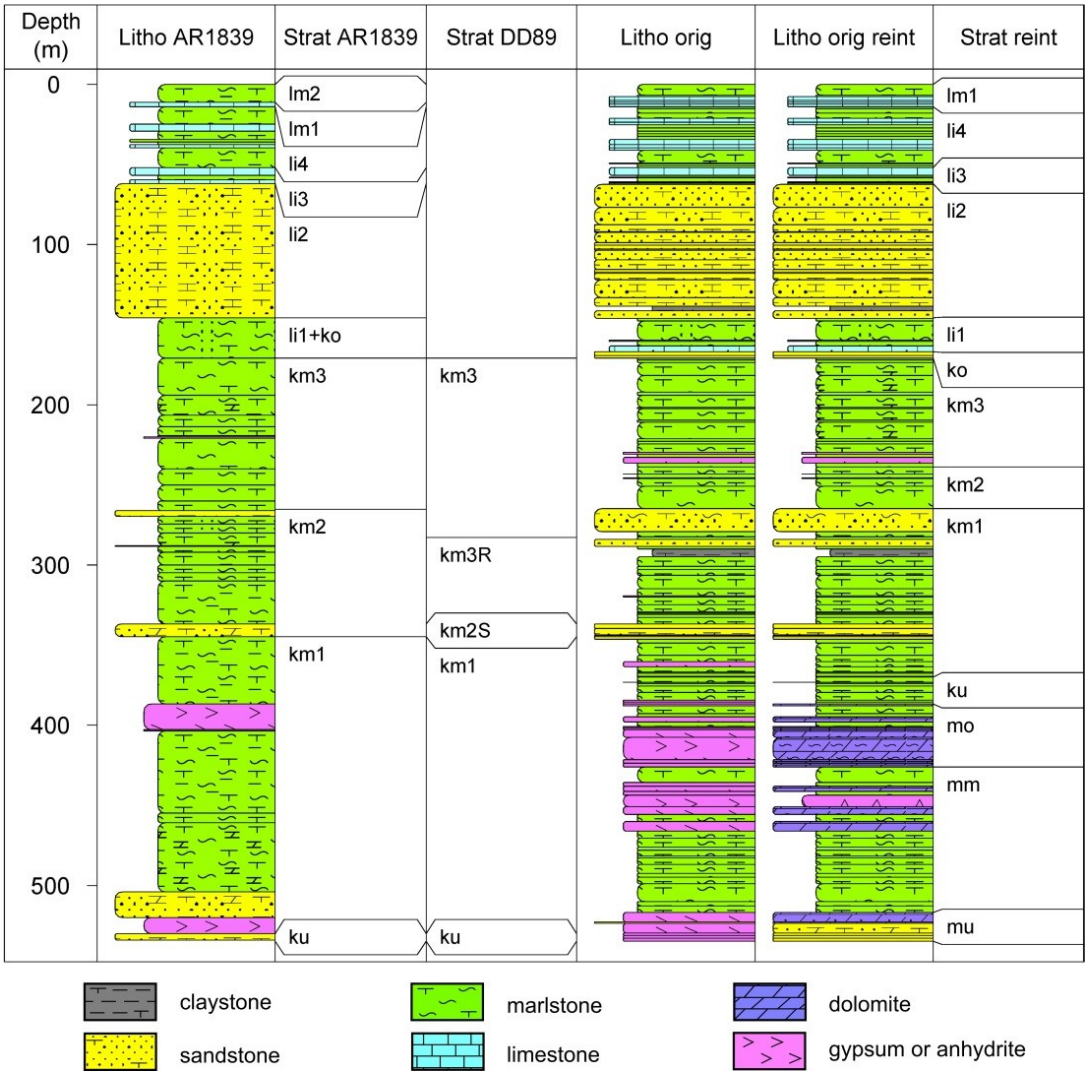

Fig. 2.4: Various stratigraphic (Strat) and lithologic (Litho) interpretations of the geological section in the Cessange borehole. Strat AR1839: Rost 1839 (after Lucius 1948), Strat DD89: Dittrich 1989, Litho AR1839: Rost 1839 (after Lucius 1948), Strat reint: stratigraphy reinterpreted in this study, Litho orig: lithology as originally reported in the drilling report (Kind, 1842), Litho orig reint: original lithology reinterpreted in this study.

The main problem with the Cessange borehole findings might be associated with a misidentification of specific lithotypes that was associated with the sketchy geological knowledge in the past. Especially the dolomitic rock types, frequently encountered in the Muschelkalk and Keuper, are not recognized or mentioned at that time. Arguing from an improved knowledge of the regional geological history of the TLB it is assumed that parts of the relatively abundant gypsum and anhydrite originally reported actually are dolomite, dolomitic marlstone or dolomitic sandstone, and therefore would require another stratigraphic labelling.

The new interpretation of the Cessange borehole stratigraphy uses the original description of Kind (1842) and centres in the replacement of the remarkable succession of anhydrite and gypsum from 387.02 to 425.90 m depth (38.88 m; Fig. 2.4) by relatively massive dolomite, typical for the Upper Muschelkalk (mo). The separation of 17.08 m of ku leaves 199.24 m to be classified as Middle Keuper. In contrast to the former interpretations, the occurrence of a sandstone facies, typical for the Schilfsandstein Formation in the E- and SE-Guttland, can be excluded. However, the Lower Middle Keuper (Pseudomorphosenkeuper; km1), ranging from 264.72 to 369.94 m depth (105.22 m), is differentiated due to a generally higher sand and sandstone content (Fig. 2.4). Lucius (1948) also notes a typically higher brine content in that section. The separation of the Steinmergelkeuper (km3) from the Rote Gipsmergel (km2) is more difficult. An alternation of blue and red marl from 224.63 to 238.70 m depth is correlated with the Argiles de Chanville (Table 2.2), which results in 68 m of km3 and 26.02 m of km2. Below the Upper Muschelkalk, the succession of blue-grey marls underlain by dominantly red marls (425.90 to 516.90 m) is classified as Middle Muschelkalk, resulting in a thickness of 91 m. The apparently sandy, relatively hard “gypsum” down to the bottom of the borehole likely corresponds to Lower Muschelkalk (mu; Fig. 2.4). In summary, despite the uncertain subdivision of the Middle Keuper, the reinterpretation of the geological section of the Cessange borehole yields relatively conservative thickness values which are also supported by the isopach maps presented in the following section.

2.5.3 Isopach maps and regional cross sections

To delineate the geology and basin structure of the TLB, several isopach maps were drawn (Fig. 2.5a–u). They show most of the Triassic and Jurassic geological units and provide an overview of the existing database. Borehole data from Luxembourg (Geological Survey of Luxembourg), France (http://infoterre.brgm.fr), Belgium (Geological Survey of Belgium) and Germany (LGB

and LUWG, 2010; Dittrich, 1989; Dittrich and Norbisrath, 2006; Dittrich et al., 1998, 2005; Landesamt für Umwelt und Arbeitsschutz [LUA] Saarland) form the basis on which these maps were generated. Where necessary, the stratigraphic interpretation has been corrected by comparison with nearby borehole data and gamma-ray logs. Due to the variable data density, only the most relevant data points are shown. The isopachs were hand-contoured and honor the data points to show the large-scale morphology of the individual units as well as cumulative thicknesses of subunits first defined by Dittrich (1989). The uncertainty of the layout of the isopachs is obviously strongly dependent on the availability of borehole data, which locally is very restricted. In those areas, the isopachs are concept-based and frequently show a certain structural continuity. Only the major synsedimentary faults are shown. For the sake of clarity, small-scale thickness variations due to local synsedimentary tectonics and sediment deposition (e.g., Dittrich, 1989, 2008, 2009) are not honored. Especially in the northwestern Guttland, where the stratigraphic interpretation of the Triassic margin facies is difficult and variably addressed by several authors, the isopachs are only indicative. In particular, the individual and largely differing thickness patterns of the subunits of the Middle Middle Keuper (Fig. 2.5h; Table 2.2) are summarized and thus extremely simplified because some of these units are locally very condensed or absent (e.g. Dittrich, 1989). Furthermore, there is little data available about the largely concealed pre-Dogger units in the southwestern Guttland and northern Lorraine. For this reason, relevant maps from the Paris Basin (Mégnien, 1980) were used to guide the isopach contouring. For the Luxembourg Sandstone, a modified version of the existing isopach map (Berners 1985, modified from Bintz and Muller 1966) is suggested by integrating additional data (Fig. 2.5m). For the ironstone formation, the map in Teyssen (1984) was used. In response to the progressive restructuration at the beginning of the Keuper, the throw at the MF is gradually inverted, which is clearly shown by the contrasting thickness patterns of the Triassic (Mégnien, 1980) and the Liassic deposits (Mouterde et al., 1980), respectively, on either side of the MF.

The Luxemburger Zentralschwelle (LZS; Fig. 2.2) has repeatedly influenced both thickness and facies patterns at least during the Triassic sedimentation in the TLB (e.g., Dittrich, 1989; Weiler, 1991). As shown on the Bouguer map (Fig. 2.3), the zone of the LZS is characterized by a positive anomaly (the CLA) which likely corresponds to a buried Caledonian massif. The tendency of passiveness or even relative uplift of the LZS within the overall subsiding basement of the TLB is often reflected by a spatially differentiated, slower increase (e.g., Fig. 2.5a, b) of thickness or even by no thickness changes (e.g., Fig. 2.5f–k) above the LZS.

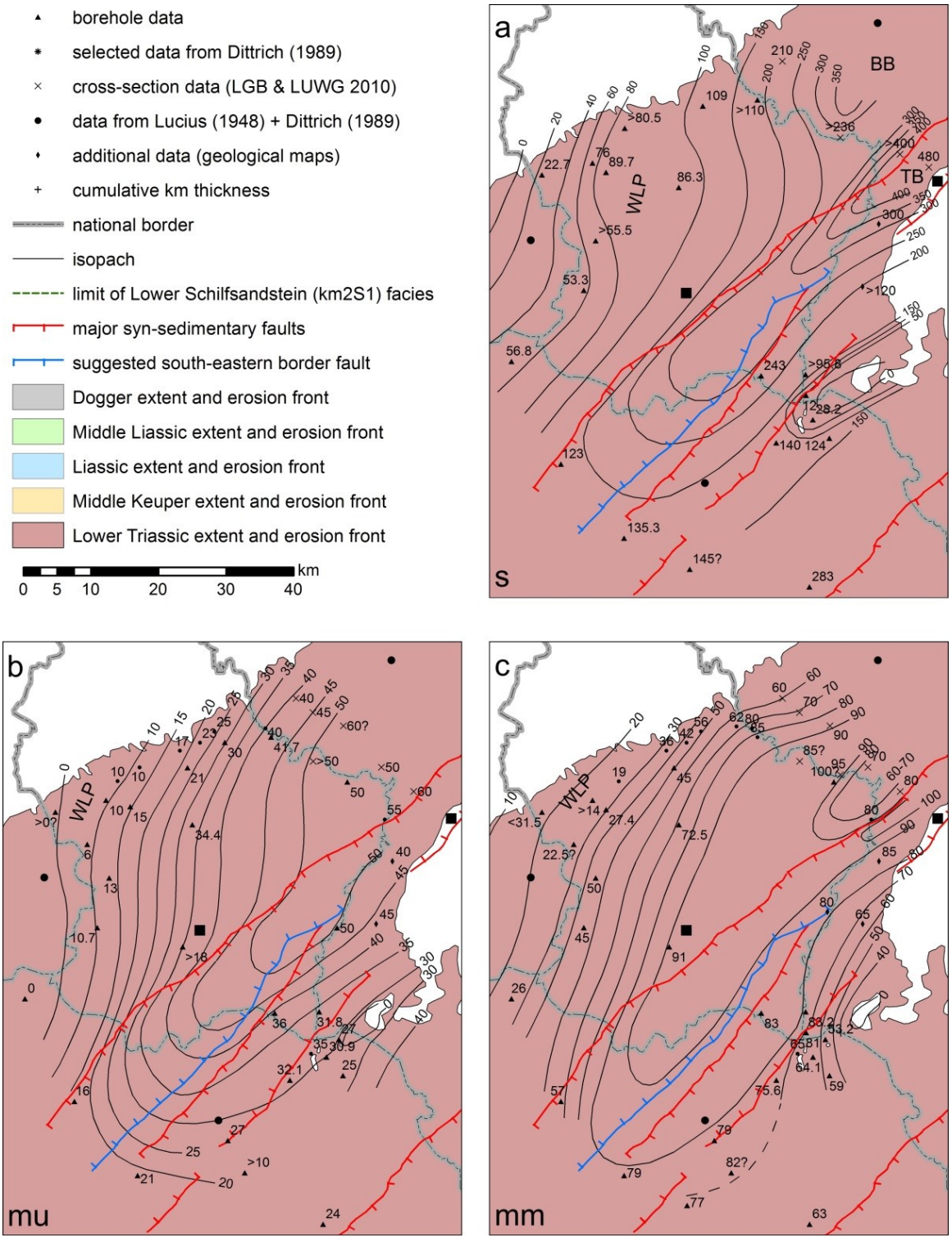

Fig. 2.5: Isopach maps (thickness values in meters). The indicated localities are the same as in Fig. 2.1. For the relative placement of the data points the extent and recent erosion front (simplified) of the relevant superordinate succession is indicated. The most important synsedimentary faults are plotted according to their contemporaneous slip tendency.

BB = Bitburg Basin, TB = Trier Basin, WLP = Western Luxembourg Plateau.

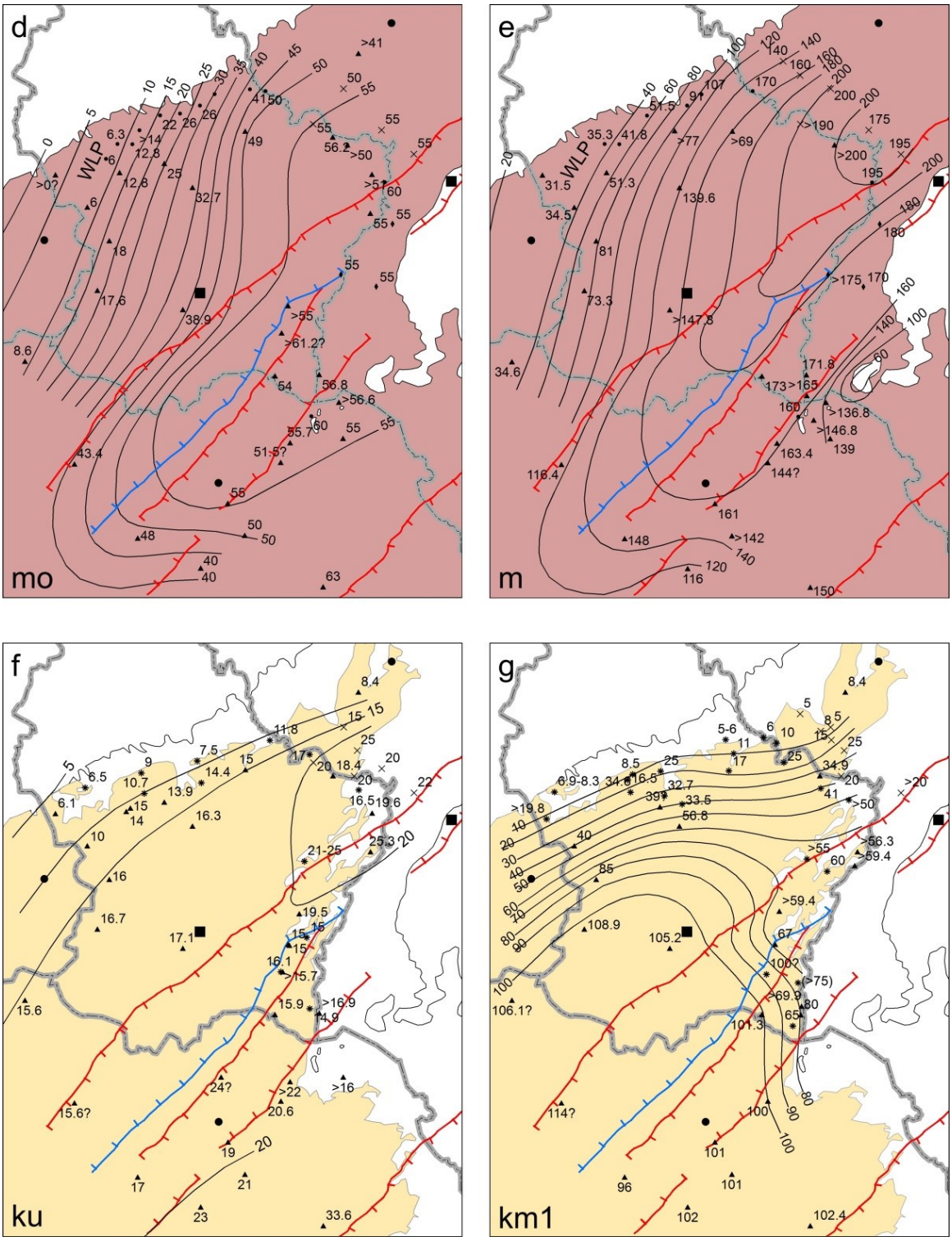

Fig. 2.5: cont.

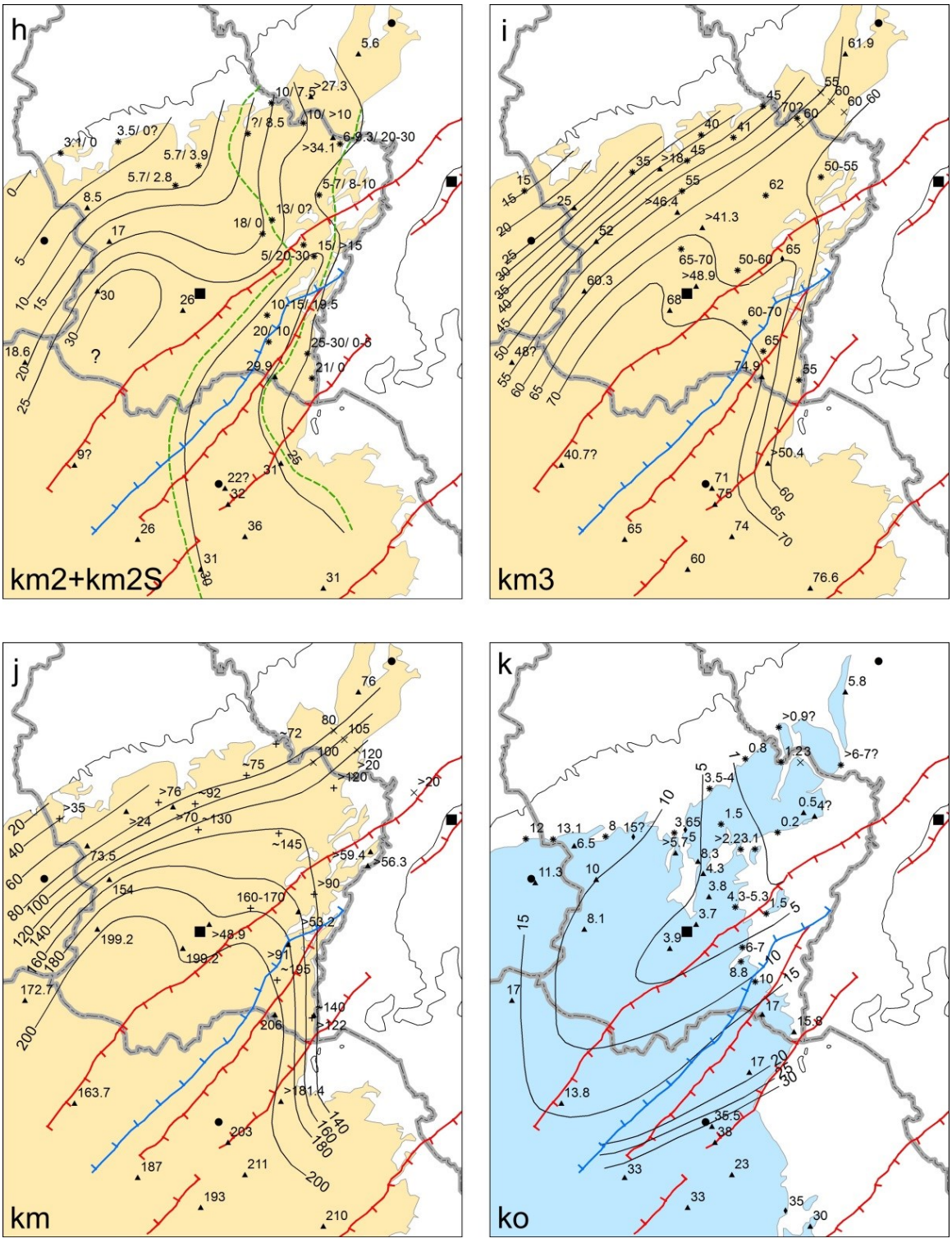

Fig. 2.5: cont.

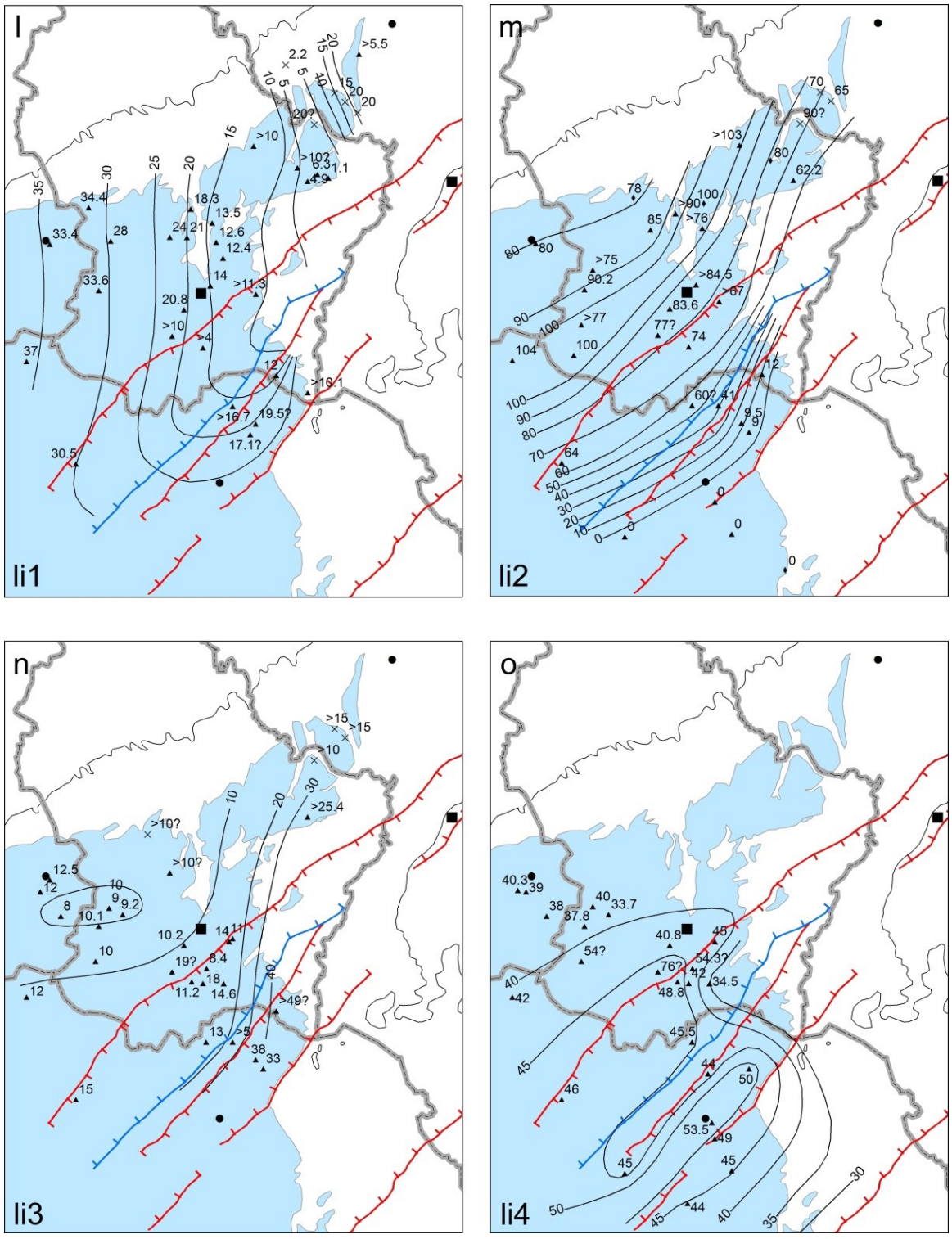

Fig. 2.5: cont.

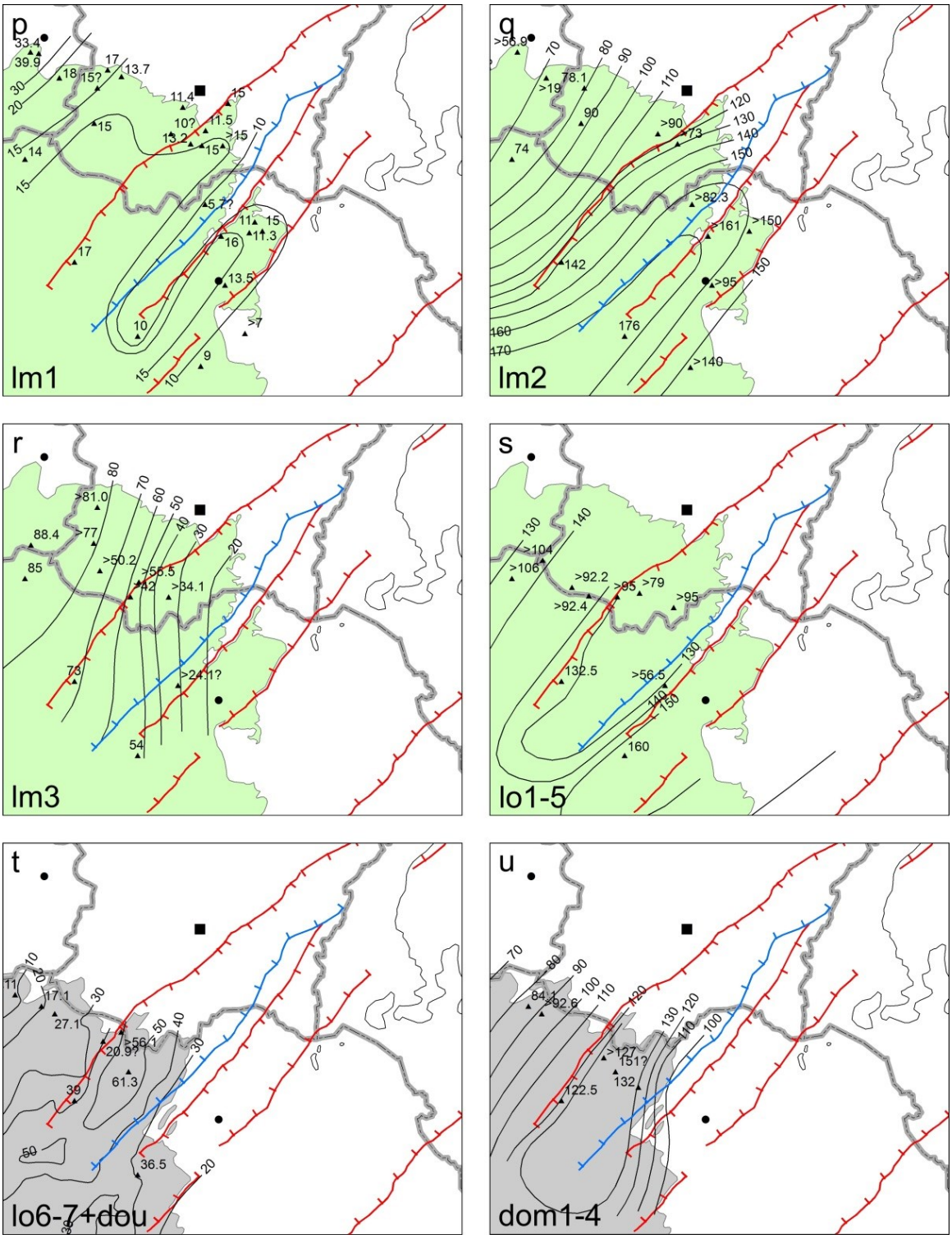

Fig. 2.5: cont.

It is also striking that contrasting thickness patterns in the TLB reflect major changes in the depositional environment. Certainly not all of the changes are of tectonic origin. Some changes may be caused by a coupling between structural processes and sedimentological effects. As an example, erosion obviously was important prior to and during the deposition of the fluvial channels of the Lower Schilfsandstein (km2S1; e.g., Barth et al., 1984; Dittrich, 1989; Dittrich et al., 2005). The transgression at the base of the Liassic, in addition to tectonic restructuration (Dittrich, 1989), then obviously also shapes the deposition of the Rhaetian deposits (Fig. 2.5k). Furthermore, changes in the thickness pattern are associated with geological formations that are defined by facies boundaries (the Luxembourg Sandstone [li2]) within the Lorrainian facies [li1–li3], the westward sanding up of the lm3, and the diachronous boundary between the lo1–5 and the Minette Fm.). Indeed, the gradation of the Grès supraliasique (lo4–5) into the overlying Minette Formation is progressive and depends on the palaeogeography (Le Roux in Thierry et al., 1980; Muller, 1987). In addition to considerable synsedimentary thickness changes, in particular within the Gipsmergel (mm1; LGB, 2005; Fig. 2.5c), local dissolution of some of their anhydrite and gypsum layers (e.g., Dittrich, 1989; LGB and LUWG, 2010) adds further complexity.

The regional geological cross sections (Fig. 2.6A–G), generated based on the information provided by the isopach maps and other geological map data, provide an overview of the geological structure in the TLB. For each cross section, the corresponding data are prepared in spreadsheet format and visualized as graph using Matlab®. The cross sections A to F are perpendicular to the SW–NE-oriented Variscan elements, whereas cross section G is more or less parallel to the Variscan basement structures, primarily showing the tilt from the German Triassic Basin towards the Paris Basin at the beginning of the Keuper. The indicated faults are obtained from the most recent geological maps and extended linearly with a constant dip of 70° assuming an extensional regime, although there is recent evidence of compressional phases in the Tertiary (including strike-slip faults with an offset of up to 3.5 km) in the adjoining Südeifel (Dittrich, 2008, 2009), SE-Luxembourg and the Saargau (Dittrich, 2011b, 2012). In particular, several reverse faults were probably formed due to the reactivation of the LZS during the Tertiary compression (Le Roux, 2000; Fig. 2.3).

Despite higher erosion levels towards the NE (i.e. towards the NE-Guttland and the Südeifel), the series of cross sections shows the rather homogeneous structure of the TLB. Before uplift, in particular of the Hunsrück in the east and consequent erosion, a transect through the TLB probably would have had much resemblance to cross section F, in which many units are preserved. The cross sections A to F also show the probable location of a Permian graben below

the Mesozoic TLB as will be discussed in the next section.

Except for the LZS, the depth of the TLB generally increases from the Ardennes in the NW towards the inferred Permian graben (SELG) and decreases again towards the Hunsrück in the SE. Interestingly, the axis of the TLB, which actually coincides with the location of the inferred Permian graben, is not simply inclined towards the Paris Basin as might be expected. Along the axis, the base of the TLB shows a break similar to the one observed along cross section G showing a relatively sub-horizontal position to the NE of cross section C (depth of about 400 m below mean sea level) and an increasing depth (i.e. 400 to about 900 m below mean sea level) between the cross sections C and F, towards the Paris Basin in the SW. This might have caused the preservation of a consistently larger amount of Liassic sediments in SW-Guttland. In southernmost Luxembourg, in the vicinity of Dudelange (Fig. 2.6E), the maximum thickness of preserved Mesozoic sediments may be on the order of about 1100 m, which is roughly 400 m greater than known from the Rebierg (Fig. 2.6E) and Mondorf (Fig. 2.6D) boreholes. In the same region, the Devonian basement may rest below the Permian deposits at about 2000 m depth.

The isopach maps and cross sections show that the Lower and Middle Buntsandstein have greater thicknesses in the Trier area, which is due to the synsedimentary activity of the Wittlich Main Fault (WMF) (Fig. 2.2; LGB and LUWG, 2010; Dittrich, 2011a). A contrast in thickness is also suggested on both sides of the Luxembourg Fault (LF). On the Ardennes block, typical Middle Buntsandstein (sm) is mostly restricted to the Bitburg Basin (BB; Fig. 2.5a), which likely extends roughly 10 km into E-Guttland. Deduced from the gravity map and the absence of typical sm (i.e. in a basin facies) in the Mersch borehole and assuming that the basement of the CLA has a similar synsedimentary behaviour than the basement underneath Mersch (cf. Fig. 2.3), the occurrences of typical sm are suggested to contour or slightly onlap the CLA, thus delimiting the Eifel Depression to the west. The Eifel Depression is suggested to be structurally bound only to the Ardennes-Eifel block and thus is geographically restricted to NE-Guttland and the Südeifel (Fig. 2.2). Although the Eifel Depression is only marginally included in this study, it is part of the western margin of the German Triassic Basin and acted as an important channel for river systems respectively sea gate during the Mesozoic sedimentation in the TLB. The interpretation of Wagner (1989), i.e. the existence of limited sm in a margin facies in the form of fluvial channels on the Western Luxembourg Plateau (WLP), hereby remains perfectly possible and is supported by Dittrich and Norbisrath (2006). Unfortunately, all boreholes between the major LF and HHMF faults did not penetrate neither the whole Buntsandstein nor the Permian succession, so that the maximum thicknesses in this crucial area remain unknown.

In comparison to the Trier Basin, the highest Buntsandstein thicknesses are to be expected close to the LF. Relatively thick Middle and Upper Buntsandstein along the eastern side of the TLB and the Mondorf Kind borehole (Lucius ,1948) suggest that the sedimentation area likely was far more extended in the Hunsrück area just to the southeast of Trier.

In comparison with the Buntsandstein, the Muschelkalk shows basically a very similar development (Fig. 2.5b–e). The thickness patterns of these lowermost units, where unconformably overlying the Devonian basement, are influenced by the palaeomorphology of the latter. It affects even the entire Middle Muschelkalk in the vicinity of the Ridge of Mettlach–Sierck (Fig. 2.5a–d) (e.g.; Müller, 1973; Dittrich, 2011a). A comparison of the Buntsandstein and Muschelkalk maps with the Middle Keuper maps shows the effect of the developing Paris Basin, which passes on to rapid expansion during the Upper Middle Keuper (Haguenauer and Hilly, 1987; Bourquin and Guillocheau, 1993; Guillocheau et al., 1999). The coarse clastics of the Lower Middle Keuper (Pseudomorphosenkeuper), in particular the sandstone- and conglomerate-rich horizons in the northwestern and western Guttland (e.g., Lucius, 1948; Dittrich, 1989), which coincide well with a newly formed high gradient in the latter region (Fig. 2.5g), very likely reflect the southwestward tilting of the TLB with reduced sedimentation at the northeastern margin and increased erosion of the exhumed lands at the northern and northwestern margins of the basin. Erosion goes along with a considerable westward enlargement with a high sedimentation rate in the direction of the new depocentre in the SW (Fig. 2.5g). In relation with the destabilization of the western margin of the TLB, the maps of the Keuper (Fig. 2.5f–j), and to some extent also those of the overlying Liassic, show that the sedimentation area is shifted by up to 10 km to the northwest in SW–Guttland. This evolution, however, is not explained by the formation of a new syncline, but rather is associated with a general northward shift of the sedimentation in the Paris Basin during the Triassic (Courel et al., 1980), whereby existing depressions, notably the SELG, remain active. The actual situation is exemplified by cross section F (Fig. 2.6F), in which the present-day structure illustrates that the latter process obviously went on beyond the Jurassic sedimentation. A strong argument for the sustained subsidence of the SELG is the distribution of fluvial deposits. The principal Lower Schilfsandstein (km2S1) channels (Barth et al., 1984; Dittrich, 1989; Dittrich et al., 2005) follow the orientation of different depocentres as they are directed first along the Eifel Depression as far as the LF, then turn to the southwest into the new depocentre to the southeast of the LF, i.e. the SELG, and continue in northern Lorraine

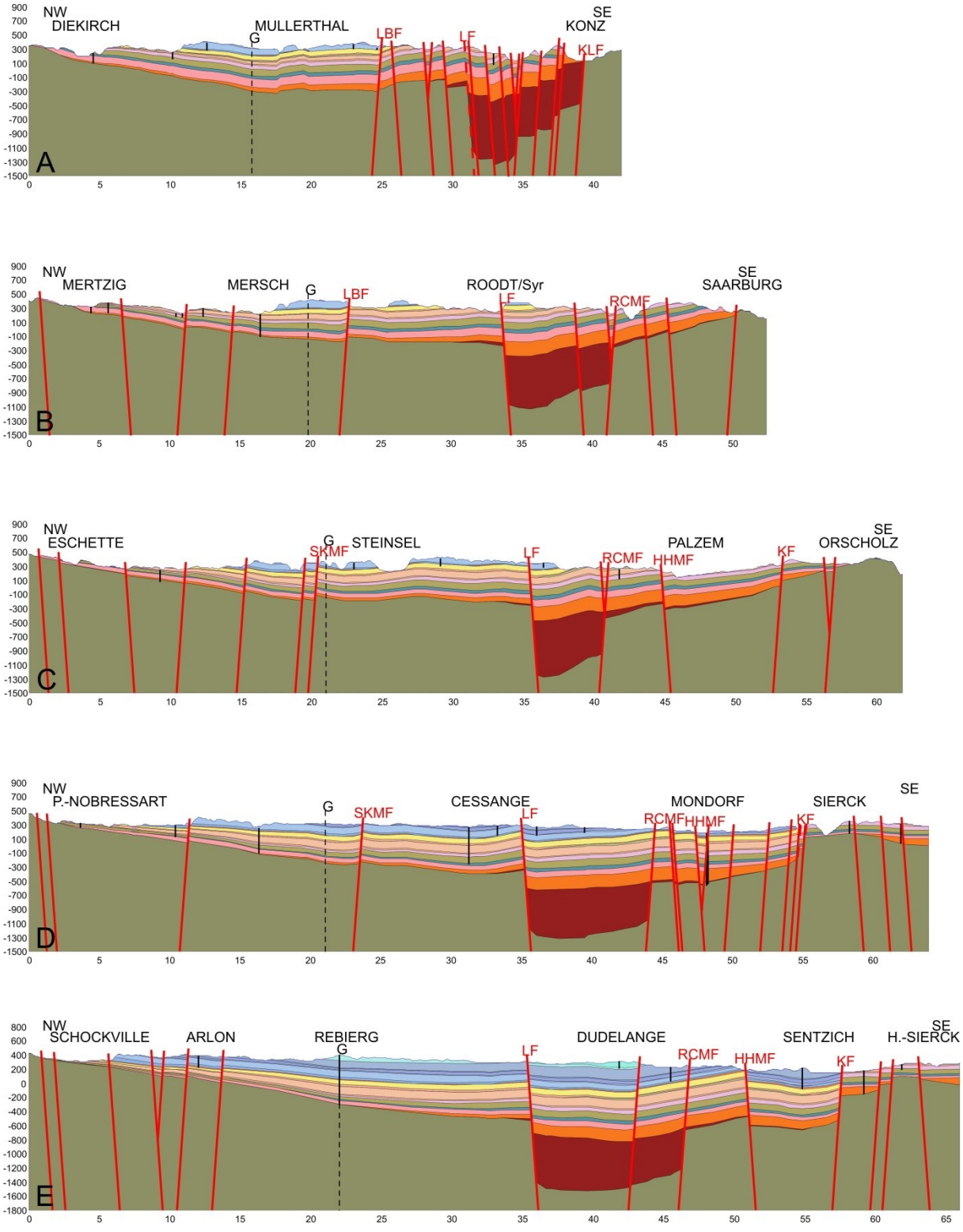

Fig. 2.6: Regional geological cross sections (horizontal axis in kilometers, vertical axis in meters). Traces of the sections are shown in Fig. 2.1. The vertical exaggeration is 5-fold for profiles A to E and 7.5-fold for profiles F and G. Black dashed lines correspond to intersection with the indicated cross section.

LBF = Lorentzweiler–Bech Fault, LF = Luxembourg Fault, KLF = Konz–Longuich Fault, SKMF = Schoenfels–Keispelt–Mamer Fault, RCMF = Roussy-le-Village–Canach–Machtum Fault, HHMF = Hayange–Hettange–Mondorf Fault, KF = Koenigsmacker Fault, DF = Differdange Fault, MF = Metz Fault.

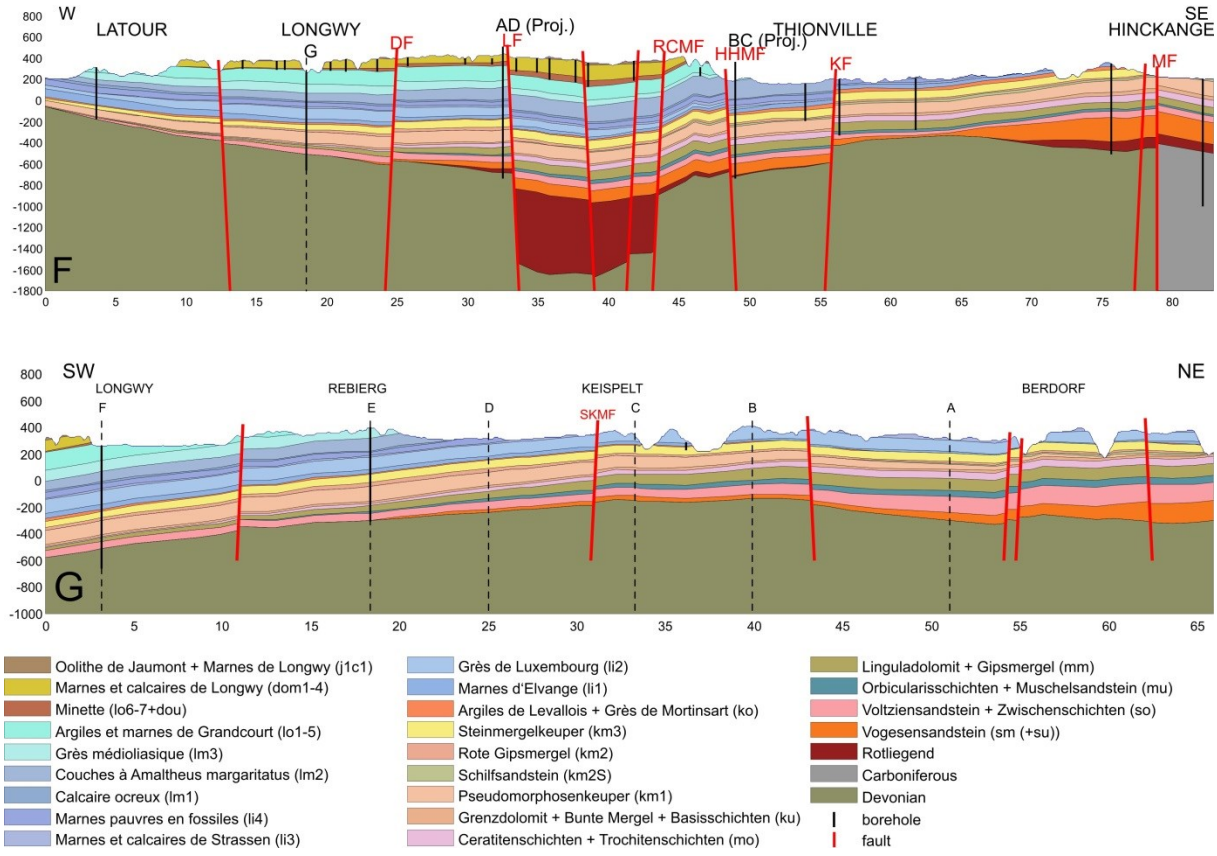

Fig. 2.6: cont.

as shown by Palain (1966) (Fig. 2.5h). The SELG corresponds roughly to a combination of two grabens defined by Dittrich (1989), namely the "Grabenzone Schifflange–Alzingen–Uebersyren–Betzdorf" and the "Grabenzone Volmerange–Aspelt–Gostingen". The southern border likely does not correspond to the HHMF, but rather follows several more or less well expressed fault segments located approximately 2.5–3 km to the northwest of the HHMF. The suggested southeastern border, named RCMF, strikes SW–NE from Bettainvillers, Fontoy, Roussy-le-Village, Canach til Machtum and forms the link with the KLF near Konz (Fig. 2.2). In the southeastern Guttland, the RCMF likely follows the southeastern border of the narrow grabens of Canach and Machtum, respectively. In the German-Luxembourgish border region, the complex tectonic situation (Dittrich, 2011b, 2012) obscures the connections of both the LF and the RCMF with the WMF and KLF, respectively. However, as the RCMF follows well the isolines in the gravity map (Fig. 2.3), it is supposed that it is a continuous major fault in the basement. Furthermore, the comparison of the km1 and km3 isopach maps (Fig. 2.5g, i) indicates a possible reduction of km1 thicknesses (by 20 to 30 m) in E-Guttland through erosional forces related to the deposition of the Lower Schilfsandstein. The Upper Schilfsandstein (km2S2) is subject to a different structuration and therefore more widespread

(e.g., Dittrich et al., 2005). In the TLB, the maximum thickness of the Middle Keuper commonly is in the range of 200 m (Fig. 2.5j). The untypically small Middle Keuper thickness of about 164 m in the AD101 borehole and of 187 m in the Bois-châté borehole (Fig. 2.5j) are probably artefacts associated with normal faults (the LF and HHMF respectively). Surprisingly, the thickness pattern of the Rhaetian deposits (Fig. 2.5k) is very different notably from the one of the underlying km3 (Fig. 2.5i), but resembles much the one of the overlying li1 (Fig. 2.5l). Berners et al. (1984) and Dittrich (1989) observed this phenomenon and concluded that the old subsidence zones again guided the emplacement of fluvial channels or marine currents through the Eifel Depression and thus the formation of conglomerate under high-energy erosive conditions. A relatively high thickness of the Rhaetian to the southeast of the HHMF may be linked to subsidence in the Thionville Graben (Dittrich, 1989).

The deposition of the Luxembourg Sandstone will be discussed in Section 2.6.3. The formation of the thick sandstone complex known as Grès médioliasique (lm3a+b; Table 2.2; Fig. 2.5r) due to a general regression at the end of the Domerian (Mouterde et al., 1980) to the northwest of the LF, also points to a change in bathymetry resulting from synsedimentary activity of the LF. During the Toarcian, the relatively thick succession (Fig. 2.5s), compared to frequent hiatuses towards the Ardennes, also reflects the ongoing creation of accommodation space in the centre of the Luxembourg Basin (Mouterde et al., 1980), with a markedly higher subsidence in the area southeast of the LF. This palaeotectonic setting is also strikingly well imaged by the accumulation of ironstone (Fig. 2.5t) in uppermost Toarcian and Aalenian time, and by the various Bajocian formations (Fig. 2.5u), detritic as well as calcareous, in northern Lorraine and SW–Luxembourg (Le Roux in Thierry et al. 1980).

Finally, in view of the relatively homogeneous thickness of the Liassic sediment pile in the Luxembourg Basin (Mégnien, 1980: map L7), it is most likely that the contrasting and remarkably complementary accumulation patterns of some formations, instead of reflecting changing subsidence, rather outbalance each other, e.g. the li2 and lm2 as well as the lm3 and lo1–lo5. Indeed, the coarse-grained formations are arranged exclusively close to the margin of the basin whereas clay-silt dominated formations are characterized by a homogenization of the depositional conditions and consequently a larger extension (Mouterde et al., 1980), thus filling up the remaining accommodation space.

2.6 Discussion

2.6.1 Permian sediments beneath the TLB

The concept of Permian (more specifically Rotliegend) sediments resting beneath the TLB is old and corroborated by the occurrence of those sediments in the surroundings of the TLB notably in the Wittlicher Senke and in the Saar valley. Although there is no direct confirmation of the presence of these sediments below the TLB by borehole or seismic data, those sediments were inferred in several studies and in numerous regional, relatively large-scale maps therein (e.g., Lucius, 1937; Autran et al., 1980; Mégnien, 1980; Donsimoni, 1981; Schäfer, 1986; Mascle, 1990; Perrodon and Zabek, 1990; Meyer, 1994; Prijac et al., 2000; Stets, 2004a; LGB, 2005). For example, Lucius (1937, 1948) suggests Permian sediments below the Mesozoic sedimentary cover, however playing only a minor role in the Luxembourgish sedimentation area, by linking the main Permian basins, namely the Wittlicher Senke in the north with the Saar-Nahe Senke in the south through the Weilerbach Mulde (see also Muller 1987). As a consequence, Lucius (1948) suspects Permian sediments in the Mondorf area (Fig. 2.1) and classifies the lowermost 8 m as Permian based on drill cores recovered during the restoration of the Kind borehole. At present, the latter occurrence still is the only indication of Permian sediments on Luxembourgish territory.

In the Longwy borehole (Table 2.1), which is located immediately to the southwest of Luxembourg (Fig. 2.1), Joly (1908) defines the 231-m-thick section above the Devonian basement as Permian overlain by only very little Buntsandstein, Muschelkalk and Keuper, which means a drastic reduction in thickness and hiatuses compared to the common regional thicknesses (Maubeuge, 1955). Van Werveke (1908), however, correctly correlates the relatively coarse facies in the Longwy borehole to similarly developed Triassic deposits south of the Luxembourgish Ardennes. Nevertheless, the original interpretation of Joly (1908) was still used in 1980 in a map compiling the Permian basins in France (Mégnien, 1980: map S4). In 1909, the Bois-châté borehole (Fig. 2.1) revealed the existence of Permian deposits below the high plateau (Pays-Haut) of Lorraine (Nicklès, 1914). However, barely 12 m of Permian deposits were drilled (Fig. 2.7). In the Audun-le-Roman borehole (Table 2.1; Mégnien, 1980: map S4) at least 125.7 m of Permian were drilled instead of the Devonian basement indicated in the initial report (Fig. 2.7). Furthermore, Autran et al. (1980) mention a more than 600-m-thick Permian deposit underneath the Luxembourg Basin, mostly on French territory. It extends some distance north and parallel to the southern boundary of the Rhenohercynian Zone. Autran et al. (1980) point out that except from local, fortuitous identification of Permian sediments in

boreholes, however, their spatial extent remains generally difficult to predict without having seismic data. Except the well-studied Permo-Carboniferous Saar–Nahe Basin (SNB; Fig. 2.1), the only exposed Permian deposits belong to the more than 1000-m-thick Permian succession of the Wittlicher Senke (WS) just east of the TLB (Fig. 2.1; for a complete description see Stets 2004a). The sedimentation in the WS began relatively late, namely in the higher Rotliegend (Saxonian, Nahe Sub-group) after termination of the Late Variscan Saalian phase (LGB, 2005; Autran et al., 1980). The depositional gap at the top comprises the uppermost Rotliegend, the Zechstein and variable amounts of the lowermost Buntsandstein (Stets, 2004a; LGB, 2005). For the formation of the WS, Stets (1990) suggests the development of a pull-apart basin in a sinistral regime based on the currently available observations, e.g. the s-shape of the basin and sedimentological aspects.

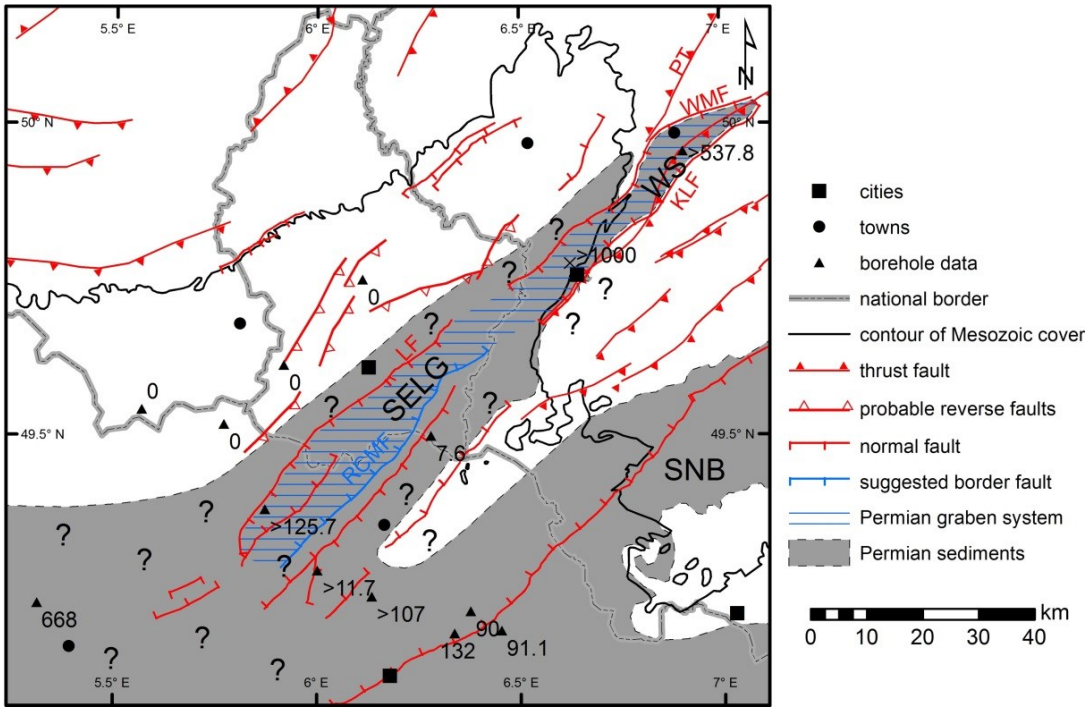

Fig. 2.7: Map showing the probable extent of preserved Permian deposits on exposure and below Mesozoic cover in Luxembourg and adjacent areas (modified after Mégnien [1980]: Map S4 and Prijac et al. [2000], and completed after Dittrich [2011a]). Only the deep boreholes that have reached the Permian respectively the Devonian basement are shown. The indicated localities are the same as in Fig. 2.1. The names of the main faults are the same as in Fig. 2.2.

According to the structural information deduced from geological and gravity data, the main Permian sedimentation area must be located on top of the elongate negative SELA anomaly (Fig. 2.3), between the Luxembourg Fault–Wittlich Main Fault system as master faults in the

northwest and the BDLA–HHMA lineament in the southeast (Figs. 2.2 and 2.7). Indeed, the thickness of preserved Permian sediments to the southeast of the latter lineament, for instance in the lower Saar valley (Lucius, 1948; Stets, 2004a) and in the Kind borehole in Mondorf (Lucius, 1948) is very restricted. Similarly, to the northwest of the WMF, the thin Permian record is known not to overlap largely the Eifel block with thicknesses not exceeding much more than several tens of meters (LGB, 2005; LGB and LUWG, 2010; Dittrich, 2011a).

In view of the new interpretation of the Cessange borehole and the gravity map, specifically the probable absence of an independent depocentre and the occurrence of rather conservative thicknesses, we suggest that possible Permian deposits likely are restricted in that region. The nearest borehole that drilled relatively thick Permian deposits is the French Audun-le-Roman borehole (Fig. 2.1; Table 2.1). As a consequence, it appears that the inferred SE-Luxembourg Graben (Fig. 2.2) has broadly the same structure as the WS. Its southeastern boundary fault is likely located at an unknown distance to the northwest of the HHMF (Fig. 2.6C–F). In southern Luxembourg the southeastern border fault of the SELG is suggested to be the RCMF, which is located 2–3.5 km to the northwest of the HHMF yielding a roughly 5- to 10-km-wide graben.

Further to the southwest in the Paris Basin, 668 m of Permian sediments were drilled in the Vacherauville borehole (Table 2.1; Figs. 2.1 and 2.6). Starting with an 11-m-thick rhyolite, the sedimentary succession resembles the formations defined in the WS. Field observations in the WS clearly indicate a southwestward sediment transport (Stets, 2004a), which means that the sediments eroded in the northeast were obviously channeled through the SELG–WS (Fig. 2.7) and may then have joined the Permian basin in the Vacherauville area (Mégnien, 1980). As confirmed by the new interpretation of the Longwy borehole, the Permian sediments however do not reach as far north onto the Ardennes–Eifel block (Fig. 2.7).

As a conclusion, in the WS and potentially the SELG, up to 1000-m-thick Permian sediments accumulated in a well-defined structure that is delimited by border faults. Considering the lack of convenient boreholes and seismic data, however, the existence of connections between individual Permian basins (e.g. with the Saar–Nahe Basin) is highly speculative and resulted in largely differing maps (e.g., Prijac et al., 2000; Mégnien, 1980). Because no transverse faults or folds are known in the Mesozoic cover and in the underlying basement, which would have an impact on the sediment deposition between the WS and the Vacherauville borehole, the thickness of the Permian sediments in the SELG probably ranges between 668 m (Vacherauville borehole) and more than 1000 m inferred by Stets (1990, 2004a: Abb. 4, 2004b) in the WS underneath Trier.

2.6.2 Structural concept of the Mesozoic Trier–Luxembourg Basin

The isopach maps, cross sections as well as structural and sedimentological observations in the Mesozoic sedimentary record of the TLB infer the influence of the Permian SELG as a major weakness zone during the development of the TLB. The concept presented by Dittrich (1989) does not consider the possibility of a single major weakness zone such as the SELG. Instead, she distinguished from sedimentological observations in the Upper Triassic (Keuper) three inherited, intersecting sets of faults giving rise to a more or less complex horst and graben structure. For parts of that structure synsedimentary activity is documented and evidence is perceptible in geological maps.

However, the new isopach maps, in particular the less facies-controlled sedimentation patterns of the Triassic, clearly suggest a long-lasting subsidence in the vicinity of the SELG, controlled mainly by a few major faults. The large variation in directions observed in the TLB (e.g., Dittrich, 1989) can actually be explained by heterogeneities in the basement whose tectonic behaviour likely is controlled not only by Variscan structures, but also to some point by the deeper Caledonian structures (e.g., the CLA) as well as the reactivation of those structures by a younger compressional regime (e.g., Guillocheau et al., 1999; Le Roux, 2000). As the superficial structures are often related to the structures of the basement (e.g., Lucius, 1948; Dittrich, 1989; Le Roux, 1971, 1980, 1999, 2000), it is rather unlikely that structures can be followed across the entire basin thereby indifferently cross-cutting major basement structures (Fig. 2.2), notably the internally differently structured Ardennes–Eifel block and the Hunsrück block (Fig. 2.2). In addition, the Ridge of Mettlach–Sierck (RMS; Fig. 2.2), an important synsedimentary high-ground (Courel et al., 1984) in the TLB, is here considered to be a relatively passive structural element in comparison to the actually active Luxembourg and Metz faults, respectively (Courel et al., 1980; Mouterde et al., 1980).

2.6.3 Implications for the Luxembourg Sandstone

The deposition of the well-studied Luxembourg Sandstone Formation (li2) is usually linked with the existence of the Weilerbach Mulde (e.g., Lucius, 1948; Bintz and Muller, 1966; Muller, 1980; Berners, 1983, 1985; Guérin–Franiatte et al., 1991). However, the existence of the Weilerbach Mulde has been structurally disproven by Dittrich (1989) for the Keuper and the present-day geological situation, which has important implications for understanding the deposition of the Luxembourg Sandstone (Table 2.2; Fig. 2.5m) of Lower Liassic age. It

consists of a diachronous sandstone body inserted in between Hettangian to Lower Sinemurian marls, clays and limestone pertaining to the Lorrainian facies (li1–3; Table 2.2). The sanding-up of the Lower Liassic took place along the NE–SW oriented coast of the Ardennes through the action of dominantly southwestward-directed littoral currents arriving through the marine channel of the Eifel Depression into the Paris Basin (Bintz and Muller, 1966; Berners, 1983, 1985). Instead of being fault-related (Berners, 1983), westward shifting of the sedimentation from the Hettangian to Lower Sinemurian can be explained by simple transgression as acknowledged by Guérin–Franiatte et al. (1991). The comparatively low position of the li2, notably in the Weilerbach area in the Lower Sauer valley likely has led to the more general interpretation that the Weilerbach Mulde is the central tectonic element of the "Gulf" of Luxembourg (Lucius, 1948; Muller, 1980, 1987). However, in addition to the arguments presented in section 2.5.1 and 2.5.3, there are more arguments to challenge the existence of the Weilerbach Mulde and its involvement in the deposition of the li2.

The straightforward structural interpretation of the present-day appearance of the sedimentary record is indeed misleading because it ignores a major phase of compression and folding in Upper Eocene and Miocene time related to the distant Alpine Orogeny (Le Roux, 2000). The LZS, which is a prominent feature in central Guttland and has facilitated the erosion of large portions of li2 in the eastern Guttland, likely was reactivated after the Mesozoic. At depth, in the basement, the bulge is well imaged by a positive Bouguer anomaly, namely the CLA. This fact, as well as the unusually arcuate course of the fault segments supports the hypothesis of its reactivation in the Tertiary due to compression of the basement northwest of the Luxembourg Fault along probably pre-existing basement structures and consequent deformation of the thin Mesozoic cover.

Despite only little information on the detailed thickness patterns notably for the Triassic units in central and SW-Guttland, the large-scale thickness pattern of the Steinmergelkeuper (Fig. 2.5i) is indicative for the basin structure during the formation of the overlying Lower Liassic succession. Indeed, Haguenauer and Hilly (1987) point out that the Paris Basin as a whole acquires already in the Upper Middle Keuper a configuration which is characteristic of the entire Liassic period. Instead of specifically controlling the accumulation of the Luxembourg Sandstone, the subsidence is known to affect the entire LB (Fig. 2.1) extending from the Metz Fault in the SE to the Ardennes mainland in the NW (Figs. 2.1 and 2.2; Mouterde et al., 1980: 92; Mégnien, 1980: map L7; Guillocheau et al., 1999). The lower Liassic transgression rapidly creates a marine environment in which the effects of sequence stratigraphy are even stronger than before. Probably for the first time during the development of the TLB, the accommodation

space created largely exceeds the volume of sediments provided. Considering only the thickness of the whole sandstone body irrespective of age, it is therefore significant that the li2, in contrast to the contemporaneous marly Lorrainian facies, is mostly developed in proximity to the Ardennes mainland and principally on the Ardennes block with a rapidly decreasing proportion to the southeast of the LF (Fig. 2.5m). Further to the SE, i.e. further away from the Ardennes, in the probably deeper parts of the basin, the supply of coarse material weakened and mainly marly and bioclastic material accumulated, resulting in the thinner Lorrainian facies. Comparison of the Lorrainian facies in the Thionville area with a typical Luxembourgish Lower Liassic profile shows that the difference in thickness is readily explained by the additional amount of sand (-stone), in accordance with a differentiated sedimentation and a higher accumulation rate along the Ardennes. The SE-Luxembourg Graben and probably also the Thionville Graben (Fig. 2.2) possibly contribute to the rapid thinning of the li2 towards the southeast (Fig. 2.5m). Finally, the occurrence of more than 100-m-thick li2 in a borehole near Medernach (Fig. 2.5m: > 103 m) further strengthens the strong sedimentological component in the formation of the Luxembourg Sandstone and shows that the maximum sedimentation is not associated with the Weilerbach Mulde as shown by Berners (1985). The regions of maximum thickness apparently imitate the direction of the palaeocurrents arriving from the north through the Eifel Depression.

2.7 Summary and conclusions

The paper aimed at a comprehensive structural and geological update of the Trier–Luxembourg Basin (TLB) as a first step for a geothermal resources assessment and a thermal model for drillable depths in Luxembourg. The incorporation of new data, e.g., a Bouguer map, and the reinterpretation of the Cessange borehole suggest that the Weilerbach Mulde, which has been disproven since Dittrich (1989) mainly for the Keuper, also does not control the deposition of the Luxembourg Sandstone and the development of a particularly thick Keuper succession in the Cessange area. The Bouguer map shows that the Luxemburger Zentralschwelle is probably related with a buried Caledonian Massif. Its present-day appearance as a structural high results likely from reactivation under a compressional regime in the Tertiary. The basin-wide cross sections, the structural and sedimentological observations in the TLB and the tectonic structures in the exposed basement strongly suggest that the TLB developed along a weakness zone related to a Permian graben. This roughly 5- to 10-km-large and more than 1000-m-deep, SW–NE trending SE-Luxembourg Graben (SELG), located between the Luxembourg Fault (LF) in the

northwest and the Roussy-le-Village–Canach–Machtum Fault (RCMF) in the southeast, corresponds very likely to the southwestern prolongation of the Permian Wittlicher Senke underneath the Mesozoic cover. According to this concept, the SELG, mainly controlled by the synsedimentary active LF, constitutes the central subsiding element of the TLB probably since Permian time.

2.8 Acknowledgements

This paper forms part of a doctoral thesis (TS) entitled “The Geothermal Potential of Luxembourg”. The project is supported by the National Research Fund (Luxembourg) and the GFZ German Research Centre for Geosciences (Potsdam, Germany). Michel Everaerts, Geological Survey of Belgium, is thanked for providing a Bouguer anomaly map of Luxembourg and adjacent areas. The Geological Survey of Luxembourg, in particular R. Maquil and R. Colbach, supported this work by granting access to the survey’s library, archives and borehole database as well as by constructive discussions. The authors would like to thank the reviewers Doris Dittrich (Mainz) and Jean Thein (Bonn) for critical comments and valuable suggestions.

2.9 References

Autran, A., Debeglia, N., Donsimoni, M., Feys, R., Greber, C. (1980). Socle du bassin. Mém. Bur. Rech. Géol. Min. 101, 17–36.

Barth, E., Bernecker, T., Berners H.-P., Bock, H., Kowalewski, J., Muller., A. (1984). Der Schilfsandstein Luxemburgs als tidal beeinflußte Rinnenfüllungen. Aspekte der Stratofazies und Sedimentologie des Profils Kinnett. Publ. Serv. Géol. Luxemb., Bull. 12, 25–43.

Belanger, I., Delsate, D., Ghysel, P., Laloux, M., Boulvain, F. (2002). Carte géologique de Wallonie 1/25.000, Saint-Léger – Messancy Musson – Le Fays Houwald., Notice explicative. Région Wallonne, Namur, 35 pp.

Berners, H.-P. (1983). A lower Liassic offshore bar environment, contribution to the sedimentology of the Luxemburg Sandstone. Ann. Soc. Géol. Belg. 106, 87–102.

Berners, H.-P. (1985). Der Einfluß der Siercker Schwelle auf die Faziesverteilungen meso-känozoischer Sedimente im NE des Pariser Beckens – Ein Sedimentationsmodell zum Luxemburger Sandstein (Lias), spezielle Aspekte zur strukturellen Änderung der Beckenkonfiguration und zum naturräumlichen Potential. Diss. R.W.T.H. Aachen, 321 pp.

Berners, H.-P., Bock, H., Courel, L., Demonfaucon, A., Hary, A., Hendriks, F., Müller, E., Muller, A., Schrader, E., Wagner J.F. (1984). Vom Westrand des Germanischen Trias-Beckens zum Ostrand des Pariser Lias-Beckens: Aspekte der Sedimentationsgeschichte. Jber. Mitt. Oberrhein. Geol. Ver. 66, 357–395.

Bintz, J., Muller, A. (1966). Sur la représentation du « Grès de Luxembourg » sur la nouvelle carte géologique générale du Grand-Duché. In: Arch. Inst. Grand-Ducal Luxemb., Sect. Sci. Nat., Phys. Math., Nouv. Sér. 32, 240–258.

Bintz, J., Maquil, R., Negendank, J.F.W., Wagner, W. (1985). Der Jura im Trier-Luxemburger Raum. Exkursionsführer, Jahrestagung 1985, Trier 16.5.–18.5.85, DUGW, Stratigr. Komm., Subkomm. Jura-Stratigr., 50 pp.

Boulvain, F., Belanger, I., Delsate, D., Ghysel, P., Godefroit, P., Laloux, M., Monteyne, R., Roche, M. (2001). Triassic and Jurassic lithostratigraphic units (Belgian Lorraine). In: Bultynck, P., Dejonghe, L. (Eds.), Guide to a Revised Lithostratigraphic Scale of Belgium, vol. 4 (1–2). Geol. Belgica, Brussels, pp. 113–119.

Bourquin, S., Guillocheau, F. (1993). Géométrie des séquences de dépôt du Keuper (Ladinien à Rhétien) du Bassin de Paris: implications géodynamiques. C. R. Acad. Sci. Paris 317

(2), 1341–1348.

Bubenicek, L. (1961). Recherches sur la constitution et la répartition du minerai de fer dans l'Aalénien de Lorraine. Sci. Terre 8 (1–2), 5–204.

Courel, L., Durand, M., Maget, P., Maiaux, C., Ménillet, C., Pareyn, C. (1980). Trias. Mém. Bur. Rech. Géol. Min. 101, 37–74.

Courel. L., Demonfaucan, A., Muller, A. (1984). Organisation des dépôts carbonatés de plate-forme du Muschelkalk supérieur luxembourgeois; Influence du Haut-Fond de Sierck-les-Bains. Publ. Serv. Géol. Luxemb., Bull. 12, 3–24.

Dittrich, D. (1989). Beckenanalyse der Oberen Trias der Trier-Luxemburger Bucht. Revision der stratigraphischen Gliederung und Rekonstruktion der Paläogeographie. Publ. Serv. Géol. Luxemb., vol. 26. Luxembourg, 223 pp.

Dittrich, D. (2008). Schertektonik im triassischen Deckgebirge der nordwestlichen Trierer Bucht – Teil I. Mainzer geowiss. Mitt. 36, 69–104.

Dittrich, D. (2009). Schertektonik im triassischen Deckgebirge der nordwestlichen Trierer Bucht – Teil II. Mainzer geowiss. Mitt. 37, 77–128.

Dittrich, D. (with contributions by Gad, J., Schäfer, P., Weidenfeller, M.) (2011a). Geologische Karte der Trierer Bucht 1: 50000 mit Erläuterungen. Landesamt für Geologie und Bergbau Rheinland-Pfalz, Mainz, 70 pp.

Dittrich, D. (2011b). Schertektonik im triassischen Deckgebirge der südöstlichen Trier-Luxemburger Bucht – Teil I. Mainzer geowiss. Mitt. 39, 7–86.

Dittrich, D. (2012). Schertektonik im mesozoischen Deckgebirge der südöstlichen Trier-Luxemburger Bucht – Teil II. Mainzer geowiss. Mitt. 40, 79–146.

Dittrich, D., Stets, J. (2008). Rotliegend-Vorkommen auf der Hunsrück-Scholle im Trierer Stadtgebiet. Mainzer Geowiss. Mitt. 36, 45–68.

Dittrich, D., Norbisrath, S. (2006). Konglomeratischer „Oberer" Buntsandstein in den Forschungsbohrungen Roth/Our und Körperich (Südeifel) – stratigraphische Neubewertung und geologisches Umfeld. Mainzer Geowiss. Mitt. 34, 73–112.

Dittrich, D., Bartels, L., Vogel, K. (1997). Neue Ergebnisse zur Geologie des Ferschweiler Plateaus und des Heiderückens (zentrale Trier-Bitburger Mulde) – Tektonik, Keuper- und Lias-Stratigraphie sowie ein Beitrag zur genetischen Deutung des Naturdenkmals „Irreler Wasserfälle". Mainzer geowiss. Mitt. 26, 55–98.

Dittrich, D., Himmerkus, J., Kobe, E. (1998). Stratigraphische und sedimentologische Ergebnisse der Forschungsbohrung Dockendorf im Zentrum der Trier-Bitburger Mulde (Oberer Muschelkalk, Keuper, Unterer Lias). Mainzer geowiss. Mitt. 27, 159–212.

Dittrich, D., Klösgen, M., Panknin, A. (2005). Gipskeuper und ardennisch geprägter Schilfsandstein in der Forschungsbohrung Kranzbach/Bollendorf (Südeifel) – Neue Befunde zum Faziesmuster. Mainzer geowiss. Mitt. 33, 245–294.

Donsimoni, M. (1981). Le bassin houiller lorrain. Synthèse géologique. Mém. Bur. Rech. Géol. Min. 117, 53–75.

Everaerts, M. (1997). Réseau gravimétrique à but géodésique du Grand-Duché de Luxembourg et calcul du géoïde local. Observ. Royal de Belgique, Bruxelles, 23 pp.

Everaerts, M. (2002). La gravimétrie au Grand-Duché de Luxembourg. In: Flick, J.A., Stomp, N. (Eds.), Sciences de la Terre au Luxembourg. Musée National d'Histoire Naturelle, Luxembourg, pp. 54–56.

Everaerts, M., De Vos, W. (2012). Gravity acquisition in Belgium and the resulting Bouguer anomaly map, vol. 58. Mem. Geol. Survey of Belgium, Brussels, 67 pp.

Guérin–Franiatte, S., Hary, A. and Muller, A. (1991). La formation des Grès du Luxembourg, au Lias inférieur: reconstitution dynamique du paléoenvironnement. Bull. Soc. Géol. France 162 (4), 763–773.

Guillocheau, F., Robin, C., Allemand, P., Bourquin, S., Brault, N., Dromart, G., Friedenberg, R., Garcia, J.-P., Gaulier, J.-M., Gaumet, F., Grosdoy, B., Hanot, F., Le Strat, P., Mettraux, M., Nalpas, T., Prijac, C., Rigollet, C., Serrano, O., Grandjean, G. (1999). Évolution géodynamique du Bassin de Paris: Apport d'une base de données stratigraphiques 3D. Bull. Inform. Géol. Bass. Paris 36 (4), 3–35.

Guillocheau, F., Péron, S., Bourquin, S., Dagallier, G., Robin, C. (2002). Les sédiments fluviatiles (faciès Buntsandstein) du Trias inférieur et moyen de l'est du Bassin de Paris. Bull. Inform. Bass. Paris 39 (3), 5–12.

Haguenauer, B., Hilly, J. (1987). Naissance et déclin du Bassin Parisien dans ses marches orientales. In: Cavelier, C. and Lorenz, J. (Eds.), Aspect et évolution géologiques du Bassin Parisien. Bull. Inform. Géol. Bass. Paris, Mém. hors sér. 6, 105–115.

Joly, H. (1908). Observations sur le sondage de Longwy. Bull. Soc. Sci. Nancy 9(2), 88–95.

Keppie, J.D. (Ed.) (1994). Pre-Mesozoic geology in France and related areas. Springer, Berlin, 514 pp.

Kind, C.G. (1842). Anleitung zum Abteufen der Bohrlöcher nach den neuesten und bewährtesten Erfahrungen, in's Besondere durch Anwendung der vom Verfasser selbst erfundenen, sich praktisch erwiesenen hölzernen Bohr-Gestänge. Michaelis, Luxemburg, 188 pp.

Kölschbach, K.-H. (1986). Eine nach SE gerichtete Aufschiebung auf der NW-Flanke der

Moselmulde (Liesertal, SW-Eifel). N. Jb. Geol. Paläont., Mh., 1986, 671–680.

Konrad, H.J., Wachsmut, W. (1973). Zur Lithologie und Tektonik des Unterdevons im südlichen Oesling Luxemburgs. Publ. Serv. Géol. Luxemb., Bull. 5, 1–20.

Kopp, K.-O. (1955). Die Wittlicher Rotliegend-Senke und ihre tektonische Stellung im Rheinischen Schiefergebirge. Geol. Rundsch. 44, 100–147.

Korsch, R.J., Schäfer, A. (1996). The Permo-Carboniferous Saar-Nahe Basin, south-west Germany and north-east France: basin formation and deformation in a strike-slip regime. Geol. Rundsch. 84, 293–318.

Le Roux, J. (1971). Structures tectoniques et anomalies gravimétriques dans l'est de la France. Bull. Bur. Rech. Géol. Min. 3, 137–141.

Le Roux, J. (1980). La tectonique de l'auréole orientale du Bassin de Paris. Ses relations avec la sédimentation. Bull. Soc. Géol. France 22 (4), 655–662.

Le Roux, J. (1999). Le contexte structural de l'est du Bassin Parisien et les relations avec la sédimentation. Bull. Inform. Géol. Bass. Paris 36 (1), 7–13.

Le Roux, J. (2000). Structuration du nord-est du Bassin de Paris. Bull. Inform. Géol. Bass. Paris. 37 (4), 13–34.

Le Roux, J. (2007). Introduction à la géologie de l'Alsace-Lorraine et des régions limitrophes. In: Cordier, S., Harmand, D., Occhietti, S. (Coord.), Excursion des 7, 8, 9 juin 2007, Livret-Guide. Univ. Nancy 2, Nancy, pp. 27–34.

LGB (Landesamt für Geologie und Bergbau Rheinland-Pfalz) (Ed.) (2005). Geologie von Rheinland-Pfalz. Schweizerbart, Stuttgart, 400 pp.

LGB (Landesamt für Geologie und Bergbau Rheinland-Pfalz), LUWG (Landesamt für Umwelt, Wasserwirtschaft und Gewerbeaufsicht Rheinland-Pfalz) (Eds.) (2010). Hydrogeologische Kartierung Bitburg-Trier. Mainz, 134 pp.

Lucius, M. (1937). Die Geologie Luxemburgs in ihren Beziehungen zu den benachbarten Gebieten. Publ. Serv. Géol. Luxemb., vol. 1. Luxembourg, 176 pp.

Lucius, M. (1948). Das Gutland. Erläuterungen zu der Geologischen Spezialkarte Luxemburgs. Publ. Serv. Géol. Luxemb., vol. 5. Luxembourg, 330 pp.

Mascle, A. (1990). Géologie pétrolière des bassins permiens français. Comparaison avec les bassins permiens du Nord de l'Europe. Chron. Rech. Min. 499, 69–86.

Maubeuge, P.L. (1955). Sur la géologie profonde de la Lorraine septentrionale et du Synclinal de Luxembourg. Arch., Inst. Grand-Ducal Luxemb., Sect. Sci. Nat., Phys. Math. 22, 47–55.

Mégnien, C. (Ed.) (1980). Synthèse géologique du Bassin de Paris. Mém. Bur. Rech. Gèol.

Min. 102.

Meyer, W. (1994). Geologie der Eifel. Schweizerbart, Stuttgart, 618 pp.

Mouterde, R., Tintant, H., Allouc, J., Gabilly, J., Hanzo, M., Lefavrais, A., Rioult, M. (1980). Lias. Mém. Bur. Rech. Géol. Min. 101, 75–123.

Müller, E. (1973). Die postsaalische Sedimentation im Bereich der Quarzitschwelle Mettlack-Sierck. Ann. Sci. Univ. Besançon, Géol., 3 (18), 55–58.

Muller, A. (1980). Luxembourg: Introduction à la géologie générale. 26th Int. Geol. Congr., excursion B1, Paris, 29 pp.

Muller, A. (1987). Structures géologiques et répartition des faciès dans les couches méso- et cénozoiques des confins nord-est du Bassin Parisien. In: Cavelier, C., Lorenz, J. (Eds.), Aspect et évolution géologiques du Bassin Parisien. Bull. Inform. Géol. Bass. Paris, Mém. hors sér. 6, 87–103.

Murawski, H., Albers, H.J., Bender, P., Berners, H.-P., Dürr, St., Huckriede, R., Kauffmann, G., Kowalczyk, G., Meiburg, P., Müller, R., Muller, A., Ritzkowski, S., Schwab, K., Semmel, A., Stapf, K., Walter, R., Winter, K.-P., Zankl, H. (1983). Regional tectonic setting and geological structure of the Rhenish Massif. In: Fuchs, K., von Gehlen, K., Mälzer, H., Murawski, H., Semmel, A. (Eds.), Plateau Uplift: The Rhenish Shield – A case history. Springer, Berlin, pp. 9–38.

Nicklès, R. (1914). Le sondage du Bois-châté. Bull. Soc. Sci. Nancy, sér. III, 15 (1), 197–214.

Palain, C. (1966). Contribution à l'étude sédimentologique du « Grès à roseaux » (Trias supérieur) en Lorraine. Sci. Terre 11 (3), 245–291.

Perrodon, A., Zabek, J. (1990). Paris Basin. In: Leighton, M.W., Kolata, D.R., Oltz D.F., Eidel J.J. (Eds.), Interior Cratonic Basin. Am. Assoc. Pet. Geol., Mem. 51, 633–678.

Prijac, C., Doin, M.P., Gaulier, J.M., Guillocheau, F. (2000). Subsidence of the Paris Basin and its bearing on the late Variscan lithosphere evolution: a comparison between Plate and Chablis models. Tectonophysics 323, 1–38.

Rost, H.G.A. (1839). Mittheilung über den Bohrversuch zu Cessingen bei Luxemburg: eine Vergleichung der durchsunkenen Gebirgsschichten mit dem ähnlichen Vorkommen an andern Orten. Henning und Hopf, Erfurt, 32 pp.

Schäfer, A. (1986). Die Sedimente des Oberkarbons und Unterrotliegenden im Saar-Nahe-Becken. Mainzer Geowiss. Mitt. 15, 239–365.

Stets, J. (1990). Ist die Wittlicher Rotliegend-Senke (Rheinisches Schiefergebirge) ein „pull-apart"-Becken? Mainzer geowiss. Mitt. 19, 81–98.

Stets, J. (2004a). Geologische Karte der Wittlicher Rotliegend-Senke 1: 50000 mit

Erläuterungen. Landesamt für Geologie und Bergbau Rheinland-Pfalz, Mainz, 82 pp.

Stets, J. (2004b). Zur Geologie der Wittlicher Rotliegend-Senke (Exkursion K am 17. April 2004). Jber. Mitt. Oberrhein. Geol. Ver. 86, 271–296.

Teyssen, T.A.L. (1984). Sedimentology of the Minette oolithic ironstones of Luxembourg and Lorraine: a Jurassic subtidal sandwave complex. Sedimentology 31, 195–211.

Teyssen, T. (1989). A depositional model for the Liassic Minette ironstones (Luxemburg and France), in comparison with other Phanerozoic oolitic ironstones. Spec. Publ. 46. Geol. Soc., London, pp. 79–92.

Thierry, J., Cariou, E., Dubois P., Fily, G., Gabilly, J., Laurin, B., Le Roux, J., Lorenz, J., Rioult, M., Yapaudjian, L. (1980). Jurassique Moyen. Mém. Bur. Rech. Géol. Min. 101, 125–190.

van Werveke, L. (1908). Zur Frage des Vorkommens von Kohle in der Gegend von Longwy sowie im Großherzogtum Luxemburg und über die Randausbildung der Trias in der Luxemburgischen Bucht. Mitt. Geol. Landesanst. Elsass-Lothr. 6 (2), 341–360.

Wagner, J.-F. (1989). Paläogeographische Entwicklung der triadischen Randfazies Luxemburgs. Z. Dt. Ges. Geowiss 140, 311–331.

Weiler, H. (1991). Das Grundwasser in der Bitburger Trias-Mulde, Beschreibung eines Aquifers, neue Ergebnisse. Mainzer geowiss. Mitt. 20, 9–42.

Ziegler, P.A. (1982). Triassic Rifts and Facies Patterns in Western and Central Europe. Geol. Rundsch. 71, 747–772.

3 Surface heat flow and lithosphere thermal structure of the Rhenohercynian Zone in the greater Luxembourg region

Tom Schintgen, Andrea Förster, Hans-Jürgen Förster, Ben Norden

Published in: Geothermics 56, 93–109.
http://dx.doi.org/10.1016/j.geothermics.2015.03.007
Supplementary data can be found online.

3.1 Abstract

Comprehensive knowledge of surface heat flow and subsurface temperature distribution is indispensable for the interpretation and quantification of crustal/mantle processes as well as for the evaluation of the geothermal potential of an area. In cases where subsurface temperature data are sparse, thermal modelling may be used as a tool for inferring the geothermal resource at depth but requires profound structural, geological, and petrophysical input data. The study area encompasses the Trier–Luxembourg Basin and the western realm of the Rhenish Massif, itself subdivided into the Ardennes region in the west as well as the Eifel and Hunsrück regions in the east. For the study area, 2-D steady-state and conductive thermal models were established based on geological models of lithosphere-scale which were parameterized using thermal rock properties including thermal conductivity, radiogenic heat production, and density. The thermal models are constrained by surface heat flow (q_s) and the geophysically-estimated depth of the lithosphere–asthenosphere boundary (LAB). A q_s of 75 ± 7 (2σ) mW m^{-2} was determined in the area. A LAB depth of 100 km, as seismically derived for the Ardennes, provides the best fit with the measured q_s. Modelled temperatures are in the range of 120–125 °C at 5 km depth and of 600–650 °C at the Moho, respectively. The mantle heat flow amounts to ~40 mW m^{-2}. Possible thermal consequences of the 10–20 Ma old Eifel plume, which caused elevation of the LAB to 50–60 km depth, were modelled in a steady-state thermal scenario resulting in a q_s of 91 mW m^{-2} in the Eifel region. Available q_s values (65–80 mW m^{-2}) are significantly lower and do indicate that the plume-related heating has not yet reached the surface in its entirety.

3.2 Introduction

Well-constrained thermal models help to evaluate the geothermal resources of a region. In general, structural data, representative thermal rock properties, and thermal boundary conditions represent the main input for the development of a thermal model. Logged subsurface temperature data are normally used for the calibration of a thermal model. For the greater Luxembourg region, only the Mersch borehole provides deep temperature data. In order to circumnavigate this fact, in-depth studies of the regional and local geology and of the thermal rock properties assigned to the geological units are required, providing reliable data for the parameterization of the geothermal model and for the definition of thermal boundaries. As a lower and upper boundary, the lithosphere-asthenosphere boundary (LAB) and the surface heat flow (q_s), respectively, could be used. The geology of the study area is well known in the upper

15 km but is generalized in the lower segment down to the crust/mantle discontinuity. The rock types of the geological units in the model were assessed from surface and borehole observations and, for the deeper portions of the model, from geophysical surveys and from xenolith data of the adjoining volcanic field in the Eifel region (Germany). Thermal rock properties assigned to geological units relate to a large number of measured laboratory data on outcrop and drill core samples for the upper part of the crust and are complemented by literature data for the lower part of the lithosphere.

The focus of the paper is threefold: It assesses the thermal field by numerical modelling, provides new data on surface heat flow for verification of the thermal models, and delivers a database of measured thermal rock properties (thermal conductivity, radiogenic heat production and density), which all are essential for any type of thermal simulation. The models constitute the basis for the assessment of geothermal resources of Luxembourg and adjoining areas.

3.3 Regional geology

The local and regional geological setting of the study area is shown in Fig. 3.1. The bulk of the Earth's crust in the study area was shaped in response to the amalgamation of Western Europe during the Caledonian and Variscan orogenic cycles, which involved the deposition of thick sediment piles and their subsequent deformation (Pharaoh, 1999; Pharaoh et al., 2006). Since about 40 Ma, part of the study area is undergoing deformation due to the development and evolution of the ECRIS (European Cenozoic Rift System), which is expressed by uplift and volcanism in the Rhenish Massif (Bourgeois et al., 2007; Demoulin and Hallot, 2009; Schmincke, 2007; Ziegler and Dèzes, 2007; and references therein).

The subsurface geology is illustrated by three crustal cross sections (Fig. 3.2). Two of the sections (sections A and B) extend, perpendicular to the Variscan structures, from the Lower Palaeozoic Stavelot Massif in the Belgian Ardennes in the north to the Metz Fault/Hunsrück Boundary Fault in the south. The third section extends parallel to the Variscan structures approximately from the southwestern border of Luxembourg to the northeastern edge of the Mesozoic Trier–Luxembourg Basin (TLB) and the southwestern margin of the West Eifel Volcanic Field.

The TLB is the youngest sedimentary record of the pre-Tertiary evolution of the area (Schintgen and Förster, 2013). The basement of the TLB and the Ardennes (AD), as well as

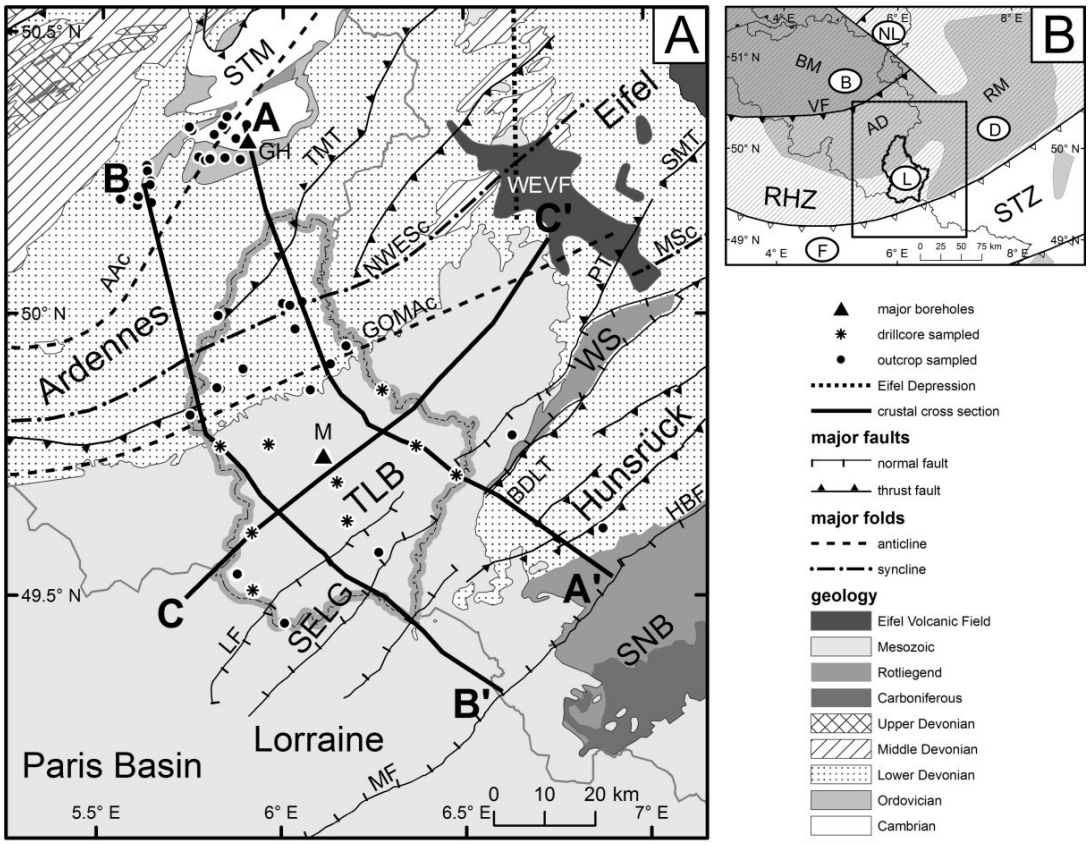

Fig. 3.1: (A) Regional geological map of the greater Luxembourg area (modified after Schintgen and Förster, 2013). Bold lines and letters indicate the three crustal cross sections shown in Fig. 3.2. Locations of the boreholes Grand-Halleux (GH) and Mersch (M) are indicated by triangles. Main structures: AAc = Ardennes Anticlinorium, NWESc = Neufchâteau–Wiltz–Eifel Synclinorium, GOMAc = Givonne–Oesling–Manderscheid Anticlinorium, MSc = Mosel Syncline, TMT = Troisvierges–Malsbenden Thrust, PT = Plein Thrust, SMT = Siegen Main Thrust, LF = Luxembourg Fault, SELG = SE-Luxembourg Graben, BDLT = Boppard–Dausenau–Longuich Thrust, MF = Metz Fault, HBF = Hunsrück Boundary Fault, STM = Stavelot Massif, TLB = Trier–Luxembourg Basin, WS = Wittlicher Senke and SNB = Saar–Nahe Basin; (B) Inset map: Basement tectonic map of Luxembourg and surroundings. B = Belgium, D = Germany, F = France, L = Luxembourg, NL = Netherlands. Terranes pertaining to Eastern Avalonia are hatched. Grey areas mark basins and platforms. AD = Ardennes, BM = Brabant Massif, RHZ = Rhenohercynian Zone, RM = Rhenish Massif, STZ = Saxothuringian Zone, VF = Variscan Front. Rectangle indicates location of geological map shown in the regional geological map.

the Eifel and the Hunsrück are part of the Rhenish Massif (RM). The latter belongs to the Variscan Rhenohercynian Zone (RHZ) (Fig. 3.1B). In the study area the RHZ is a generally northwest vergent fold-and-thrust belt, confined by the Variscan Front (VF) in the north (with its continuation at depth as the Eifel detachment) (Fig. 3.2) and the Saxothuringian Zone (STZ) in the south (Meyer, 1994; Meyer and Stets, 1980, 1996; Oncken et al., 1999). Large and persistent fold structures are typical for the Ardennes and Eifel regions (e.g., Meyer and Stets, 1996), whereas thrusts are characteristic for the Hunsrück area (e.g., Wildberger, 1992; Fig.

3.2, cross sections A and B). The orientation of the structures is dominantly WSW–ENE (N60–70°E) in the Ardennes–Eifel region and SW–NE (N45°E) in the Hunsrück, but turns to the west in a W–E direction in the Belgian Ardennes.

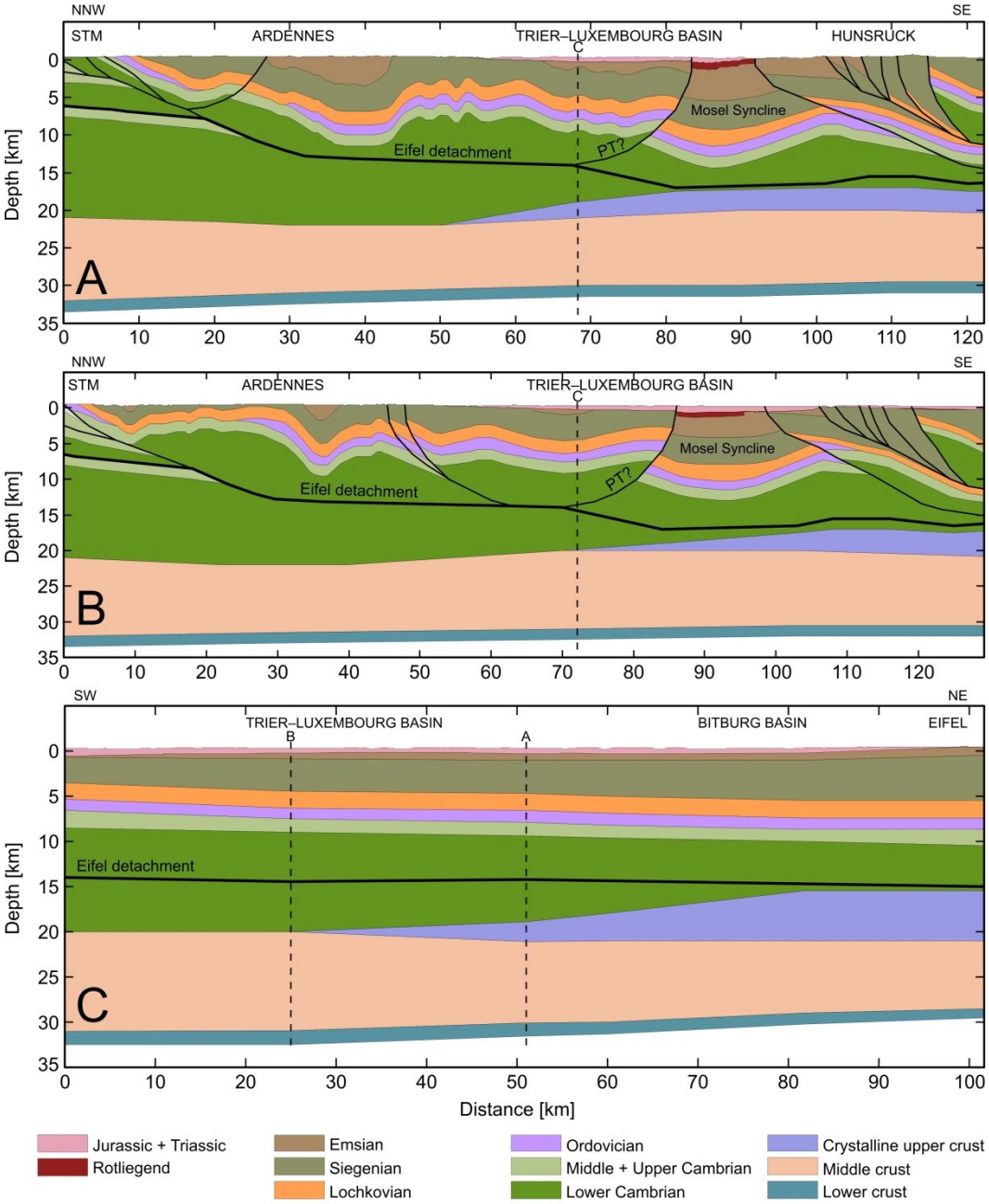

Fig. 3.2.: Geological cross sections (for location see Fig. 3.1A) developed to the depth of crust–mantle transition. Vertical dashed lines indicate the intersection with the indicated cross section. STM = Stavelot Massif, PT = Plein Thrust. For details, see text.

Except for the Wittlicher Senke (Fig. 3.1A), which constitutes a remarkable intramontane Permian (Rotliegend) graben (Stets, 2004), the Variscan basement is largely composed of thick

Lower Devonian (i.e. Lochkovian, Siegenian or Praguian and Emsian) syn-rift sediments characterized by a generally homogeneous, shale-rich, clastic rock assemblage, which often displays a pervasive cleavage (Furtak, 1965; Konrad and Wachsmut, 1973; Lucius, 1950; Wildberger, 1992). The total thickness of the Lower Devonian sediments increases rapidly from the margin towards the centre of the Rhenohercynian basin, where maximum thicknesses of more than 10,000 m are reported (Meyer and Stets, 1996; Stets and Schäfer, 2002). An apparent facies change in the Hunsrück and the Mosel Syncline (Stets and Schäfer, 2002; Zitzmann and Grünig, 1987) explains the different lithostratigraphic classification in Belgium and Luxembourg (Dejonghe, 2008; Bultynck and Dejonghe, 2001; Lucius, 1950) and further used in Germany (LGB, 2005; Mittmeyer, 2008).

The Lower Devonian unconformably overlies Cambrian and Ordovician metamorphic rocks that are only known from outcrops in the Ardennes, notably in the Stavelot–Venn Massif (or Stavelot Massif; e.g., Bless et al., 1990; Fig. 3.1A). It is characterized by dominantly E–W oriented structures, strongly north-verging folds, and a southward dipping main cleavage (Verniers et al., 2002) associated with Variscan processes that have largely overprinted a weaker Caledonian metamorphism and deformation (Bless et al., 1990; Fielitz and Mansy, 1999). The subsurface Cambrian–Ordovician succession is suggested to be stratigraphically complete in the study area. A high background density in the Bouguer map (Schintgen and Förster, 2013) indicates relatively dense Ordovician rock at about 5 km depth, in accordance with the estimated position of the Lower Palaeozoic/Lower Devonian unconformity (Meyer and Stets, 1980, 1996; LGB, 2005). The N–S-oriented Eifel Depression (Eifeler-Nord-Süd Zone) is an important cross fold separating the Ardennes in the west from the Eifel in the east (Fig. 3.1A; Murawski et al., 1983). Beneath the Ardennes, seismic velocities (Mechie et al., 1983) infer that the Lower Cambrian rift sediments are particularly thick (Hollmann, 1997; Verniers et al., 2002; Sintubin and Everaerts, 2002) and may extend down to the top of the cratonic basement at about 19 km depth as shown in the adjoining Brabant Massif (BM) (Fig. 3.1B).

The deep geology of the RHZ above the basal Eifel detachment at about mid-crustal level (Fig. 3.2) is constrained from numerous seismic refraction (Mooney and Prodehl, 1978; Mechie et al., 1983; Meissner et al., 1983) and seismic reflection profiles farther east through the Eifel area (DEKORP Research Group, 1991; Oncken et al., 1999, 2000). These seismic surveys allow a structural and to some point compositional subdivision of the crust in an upper part, largely composed of Palaeozoic rocks (known from the surface), and a lower part, consisting of Precambrian rocks known from xenolith samples of the Eifel volcanic field (e.g., Downes,

1993; Mengel et al., 1991; Stosch et al., 1991; Voll, 1983, Wörner et al., 1982). Simplified cross sections adapted to the geology of the study area (Wagner et al., 2012; Zitzmann and Grünig, 1987) were also considered. Still unresolved is the trace of the Plein thrust (Kölschbach, 1986), which appears to replace the Siegen Main Thrust, being an important thrust fault in the Rhenish Massif. Besides evidence from xenoliths, the small exposure of Wartenstein Gneiss of Neoproterozoic age (Meyer and Nagel, 2001) at the southern margin of the Hunsrück also shows the occurrence of Precambrian rock. In the Eifel region, xenoliths point towards large amounts of mica schists and paragneisses in between the Avalonian cratonic basement and the Cambrian rocks.

3.4 Analysis of thermal rock properties and surface heat flow

A sophisticated parameterization of a thermal model requires sample control for all major rock types. For the Mesozoic, drill core samples (66 samples) were obtained from 12 relatively shallow boreholes archived in the Geological Survey of Luxembourg. In addition, drill core (17 samples) from the Cambrian section of the 3225-m-deep Grand-Halleux borehole (GH in Fig. 3.1A; Graulich, 1980) was sampled in the archive of the Geological Survey of Belgium. To comprehensively characterize the major rock types of the Mesozoic–Palaeozoic and the Neoproterozoic geological formations on outcrop were also sampled (142 samples in the Palaeozoic and 9 in the Neoproterozoic; 12 samples in the Mesozoic; Fig. 3.1A). Table 3.1 provides the stratigraphic units and the sampled lithotypes. The Lower Devonian formations of the Mosel Syncline (Figs. 3.1A and 3.2), which is supposed to continue along strike underneath the Permian graben system (WS–SELG; Fig. 3.1A), and of the Hunsrück area are only exposed in Germany (e.g., LGB, 2005; Stets and Schäfer, 2002). Here, the Lower Devonian deposits differ with respect to their lithology and thus their stratigraphic subdivision from those in Belgium and Luxembourg (Dejonghe, 2008; Bultynck and Dejonghe, 2001; Lucius, 1950). As the formations in the Hunsrück were not sampled, they are characterized by a compilation of similar lithotypes sampled in the Ardennes. In the following, the methods applied for the determination of thermal conductivity and of radiogenic heat are described.

Table 3.1: Stratigraphic units and lithotypes sampled in different areas.

Sampling area	Stratigraphic unit	Lithotype	n
Stavelot Massif	Cambrian + Ordovician	Slate	25
		Silty slate	18
		Shale	1
		Siltstone	2
		Sandstone	9
		Quartzite	10
Ardennes	Lower Devonian	Slate	7
		Silty slate	5
		Shale	33
		Siltstone	18
		Sandstone	25
		Quartzite	3
Hunsrück	Lower Devonian	Slate	1
		Shale	1
		Quartzite	1
	Neoproterozoic	Gneiss	5
		Mica schist	2
		Quartzite	1
		Sandstone	1
Trier–Luxembourg Basin	Triassic + Jurassic	Claystone	4
		Siltstone	5
		Sandstone	22
		Marl/Marlstone	28
		Limestone	7
		Dolomite	8
		Anhydrite	1
		Gypsum + Anhydrite	1
		Conglomerate	2

n = number of samples

3.4.1 Thermal conductivity

Thermal-conductivity (TC) measurements were performed with the Thermal Conductivity Scanning (TCS) device (Lippmann and Rauen, GbR Schaufling, Germany). The measurement

technique is based on high-resolution optical scanning with an inherent error of determination <3% (Popov et al., 1999). TC of samples was determined by comparison with standards (λ = 2.93 W m^{-1} K^{-1}). The method allows a TC sampling interval of 0.1 mm at a scanning speed of 5 mm s^{-1}. Sample sizes were 5–10 cm in length and a minimum of 2 cm in width. Samples were first oven-dried at 60 °C until constant mass was reached before TC was measured under ambient temperature and pressure conditions. Subsequently, samples were saturated under vacuum in a desiccator for a minimum of 48 hours. The applied fluid-saturation with demineralized water allowed the determination of porosity and density using the Archimedes method (Tables 3.2 and 3.3, Table 3.4 for density).

Table 3.2: Porosity and transformation factor of thermal conductivity for different Palaeozoic lithotypes.

	Porosity [%]					Transformation factor			
Lithotype	Median	Mean	Min.	Max.	n_S	Median	Mean	1σ	n_m
Gneiss	4.5	4.5	2.8	6.2	2	1.19	1.20	0.05	6
Slate	2.6	3.1	1.8	6.5	7	1.24	1.23	0.11	14
Quartzite	6.0	6.4	0.5	12.7	3	1.37	1.38	0.09	6
Silty slate	2.6	2.5	1.1	3.8	8	1.16	1.19	0.08	16
Shale	2.7	3.3	1.4	8.0	10	1.17	1.19	0.11	20
Sandstone	2.3	2.3	0.4	3.5	7	1.15	1.17	0.10	14
Siltstone	1.8	2.9	1.3	8.1	6	1.13	1.17	0.10	12
All field samples	2.6	3.1	0.4	12.7					
Grand-Halleux slate	0.3	0.4	0.2	0.6	5	1.03	1.04	0.04	10
Grand-Halleux quartzite	0.1	0.2	0.1	0.3	3	1.10	1.12	0.06	6
All drill core samples	0.3	0.3	0.1	0.6					
Total					51				104

Min. = minimum, Max. = maximum, n_S = number of samples, σ = standard deviation, n_m = number of measurements.

For reduction of work load, not all the Palaeozoic samples were used for TC determination under saturated conditions. Only a subset was used as the Palaeozoic samples are characterized by low mean porosity values (<4%) in comparison to the Mesozoic samples (2–20%). Subsequently, transformation of dry-measured TC into water-saturated TC was accomplished by transformation factors derived from the measured subset (Table 3.2): First, ratios of saturated to dry TC were determined for every sample of the measured subset. Second, mean values of

these ratios were calculated for single lithotypes and used as transformation factors. Application of simple transformation factors seemed justified due to similar mean values (1.17–1.23) and their relatively small standard deviations (Table 3.2) owing to low and similar porosities. Exceptions are the quartzites (1.38), showing the highest porosity values of the Palaeozoic rock samples, and the drill core samples from Grand-Halleux (quartzites and slates) showing lower transformation factors (1.12 and 1.04), characterized by the lowest porosity values.

Table 3.3: Porosity of the Mesozoic lithotypes.

	Porosity [%]				
Lithotype	Median	Mean	Min.	Max.	n
Dolomite	1.6	1.8	0.9	3.1	8
Limestone	8.2	12.7	3.8	28.1	7
Marl/Marlstone	9.3	10.6	2.4	20.6	28
Sandstone	13.5	14.7	2.5	30.1	22
Siltstone	18.4	16.3	7.5	26.9	5
Claystone	19.4	17.9	11.9	20.9	4

Min. = minimum, Max. = maximum, n = number of samples.

All Mesozoic samples were measured either water-saturated or isooctane-saturated. Isooctane saturation was applied to claystone and marlstone, to avoid clay swelling (Fuchs et al., 2013). TC measured under isooctane-saturation was converted to water-saturated TC using the geometric-mean model developed for a two component system of pores and matrix (e.g., Brigaud et al., 1990):

$$\lambda = \lambda_m^{1-\phi} \cdot \lambda_p^{\phi} \qquad (3.1)$$

where λ is the TC of a sample (in W m^{-1} K^{-1}), λ_m is the TC of the rock matrix, λ_p is the TC of the pore fluid and ϕ is the porosity. The TC of saturating fluids (λ = 0.025 W m^{-1} K^{-1} for air, 0.095 W m^{-1} K^{-1} for isooctane and 0.604 W m^{-1} K^{-1} for water at room temperature) was taken according to Fuchs et al. (2013). The median, mean and range of TC for the different Palaeozoic and Mesozoic lithotypes are given in Table 3.4.

The anisotropy of TC ($A = \lambda_{\parallel}/\lambda_{\perp}$; e.g., Schön, 1996) was accounted for during sample preparation and orientation of the sample surfaces during the measurement, which allowed TC measurements parallel ($\lambda_{\parallel}$) and perpendicular ($\lambda_{\perp}$) to bedding (stratification; S_0) for layered sediments or schistosity (cleavage; S_1) for shale and slate (Table 3.4). Palaeozoic sandstone and quartzite, and shale are virtually isotropic. Siltstone commonly shows a minor anisotropy in the range of 1.0–1.3 (median 1.1). Silty slate ('quartzophyllade') is characterized by a range of 0.9–1.3 (median 1.2). Slate has the highest anisotropy, ranging from 0.9 to 2.0 (median 1.2). In the

Mesozoic rocks, anisotropy is usually small in limestone, dolomite, siltstone and sandstone, but increases in fine-grained clastic rocks, notably claystone and marlstone showing anisotropies in the range 1.0–1.6 (median 1.1 and 1.3, respectively) (Table 3.4). Even though variation of TC as a function of anisotropy for lithotype classes was small in general, orientation-dependent formation TC was determined in addition to mean formation TC values.

Table 3.4: Lithotype thermal conductivity under dry and water-saturated conditions, anisotropy of lithotype thermal conductivity and lithotype density.

Age	Lithology		λ_{dry}					λ_{sat}					A			ρ		
		n_S	Median	Mean	Min.	Q10	Q90	Max.	Median	Mean	Min.	Q10	Q90	Max.	Median	Min.	Max.	Median	Min.	Max.
			[W m^{-1} K^{-1}]						[W m^{-1} K^{-1}]							[10^3 kg m^{-3}]		
Paleozoic	Quartzite	13	4.7	4.8	3.7	4.1	5.6	5.6	6.1	6.1	5.1	5.4	6.9	7.7	1.0	1.0	1.1	2.64	2.35	2.71
	Sandstone	34	4.0	3.9	2.8	3.1	4.7	5.1	4.8	4.7	3.3	3.7	5.6	6.0	1.0	0.9	1.3	2.66	2.56	2.81
	Siltstone	20	2.7	2.8	1.8	2.3	3.3	3.7	3.2	3.3	2.1	2.7	3.9	4.3	1.1	1.0	1.3	2.69	2.43	2.80
	Slate	32	2.5	2.7	1.5	2.1	3.8	4.5	3.0	3.1	1.8	2.4	4.4	4.7	1.2	0.9	2.0	2.78	2.67	2.96
	Silty slate	23	2.5	2.5	1.7	2.0	3.2	3.8	2.9	3.0	2.0	2.3	3.8	4.5	1.2	0.9	1.3	2.75	2.64	2.94
	Shale	34	2.3	2.4	1.7	1.9	3.2	3.7	2.8	2.9	2.0	2.3	3.8	4.4	1.0	0.8	1.2	2.67	2.43	2.77
Mesozoic	Dolomite	8	3.8	3.8	3.2	3.4	4.3	4.5	3.8	3.9	3.4	3.4	4.4	4.6	1.0	0.9	1.1	2.78	2.66	2.82
	Limestone	7	2.0	1.9	1.1	1.3	2.3	2.7	2.3	2.3	2.0	2.1	2.6	2.9	1.0	1.0	1.1	2.51	1.97	2.62
	Marl/Marlstone	28	1.9	1.9	1.2	1.4	2.6	3.6	2.5	2.6	1.5	2.0	3.1	4.4	1.1	1.0	1.5	2.34	1.96	2.69
	Sandstone	22	2.2	2.2	0.9	1.5	3.0	3.8	3.2	3.3	1.9	2.7	3.9	5.0	1.0	0.8	1.2	2.29	1.85	2.60
	Siltstone	5	1.6	1.7	1.0	1.1	2.6	2.8	2.8	2.7	1.7	1.9	3.2	3.3	1.0	1.0	1.2	2.22	1.96	2.55
	Claystone	4	1.3	1.4	0.9	1.0	1.8	2.2	2.1	2.3	1.7	1.8	2.9	3.3	1.3	1.1	1.6	2.12	2.08	2.27

n_S = number of samples, λ_{dry} and λ_{sat} = thermal conductivity under dry and water-saturated conditions, respectively, A = anisotropy, ρ = density (dry state), Min. = minimum, Max. = maximum, Q10 = quantile 10, Q90 = quantile 90.

Calculation of formation TCs was done by applying a weighted arithmetic mean based on the proportion of different lithotypes in each formation:

$$\lambda_{Fm} = \sum_i^n \left(X_i \cdot \lambda_i \right) \quad (3.2)$$

where λ_{Fm} is the formation TC (orientation-specific) calculated from a number i out of n different lithotypes representing volume proportions X_i of the formation and characterized by an orientation-dependent lithotype TC λ_i specified for each formation.

For the Lower Devonian formations, anisotropy is negligible and mean formation TC values calculated using the two orientation-dependent values are sufficient to characterize a formation. Exceptions are the Lower Palaeozoic (Cambrian and Ordovician) formations showing at least a weak anisotropy of 1.1, with the highest value of 1.4 in the slate-rich formations. Anisotropy in Mesozoic formations generally does not exceed 1.1 except in more clay- and marl-/marlstone-rich formations (commonly 1.2–1.3). Details on thermal conductivity, anisotropy of TC, transformation factors, porosity and formation TC error calculation are given in the Supplementary material (Section 3.10).

3.4.2 Radiogenic heat production

Owing to the small thickness of the Mesozoic sedimentary succession (mostly 400–600 m increasing to about 1500 m only in the southwestern parts of the TLB in France) composed to 50–70% of marl/marlstone and claystone, the contribution of its radiogenic heat production (H) to surface heat flow is small (0.5–1 mW m^{-2}) and not considered. H of the thicker Rotliegend sediments is estimated from their lithological composition (Häfner et al., 2007) using lithotype-specific H values published by Vilà et al. (2010).

For the Palaeozoic basement rocks, H was determined based on geochemical data since they form the major part of the crust in the study area. Bulk-rock geochemical analyses included the measurement of U, Th and K concentrations (Table 3.5) by X-ray fluorescence spectrometry and inductively coupled plasma-mass spectrometry on 20 rock samples representative for the Cambrian, Ordovician and Lower Devonian basement. H was calculated according to the equation of Rybach (1976, 1988):

$$H = 10^{-5} \times \rho \left(9.52 c_U + 2.56 c_{Th} + 3.48 c_K \right) \quad (3.3)$$

where H is the radiogenic heat production (in μW m^{-3}), ρ is rock density (in kg m^{-3}), c_U and c_{Th} are the concentrations of uranium and thorium (in ppm), respectively, and c_K is the concentration of potassium (in wt%). For the Palaeozoic rocks, lab-measured densities mostly

range from 2.6 to 2.8 × 10^3 kg m^{-3} (Table 3.4). High density values between 2.8 and 2.96 × 10^3 kg m^{-3} refer to slate/silty slate samples from the Ordovician Salm Group.

The values of H are in the common range for the individual rock types (e.g., Schön, 1996; Vilà et al., 2010), with the lowest value for quartzite (0.6 μW m^{-3}) and the highest value for black slate (3.0 μW m^{-3}). For the Mesozoic–Palaeozoic upper crust, values of H for individual samples (Table 3.5) were then upscaled to formation H, ranging from 1.2 to 2.5 μW m^{-3} (median 1.9 μW m^{-3}) in the Cambrian to Ordovician formations, from 0.6 to 2.0 μW m^{-3} (median 1.8 and 1.6 μW m^{-3}, respectively) in the Ardennes and Hunsrück. The proportion of the different lithotypes in those formations was accounted for by applying a weighted arithmetic mean as done for the calculation of formation TC (Eq. (3.2)). The complete geochemical data and details on density and radiogenic heat production are given in the Supplementary material (Section 3.10).

Table 3.5: U, Th, K concentrations and resulting radiogenic heat production (H) of representative rock samples.

Region	Ardennes									Stavelot Massif				SE Hunsrück		Grand-Halleux borehole			
Sample	E1b-07	E1a-04	E1a-09	E1a-11	Sg3-03	Sg1-03	Sg1-07	OlG-13	FEP-07	BIH-06	COL-05	PLA-01	SPA-02	SLW-10	War-01	War-03	GH350	GH2331	GH3128	GH3216
Lithotype	Stst	Sh	Sh	Sst	Sh	Sl	Sst	Sh	Sh	Ssl	Sl	Sl	Ssl	Sl	Gn	Gn	Q	Sl	Sl	Q
K_2O [wt.%]	1.88	3.82	3.90	0.31	3.62	3.16	0.89	3.40	2.88	3.38	3.63	3.17	3.90	6.76	2.82	3.36	0.39	5.26	4.47	0.68
Th [ppm]	11.0	13.6	14.3	7.6	13.6	13.2	9.0	15.3	12.5	16.5	16.9	14.7	14.6	20.1	7.0	9.9	4.2	14.2	17.1	8.4
U [ppm]	3.1	2.9	3.2	1.6	2.9	3.1	2.0	3.5	2.5	2.4	2.9	1.8	2.7	3.7	1.7	2.4	1.1	1.8	5.3	2.2
H [mW m^{-3}]	1.7	2.0	2.2	1.0	2.0	2.0	1.2	2.3	1.7	2.1	2.3	1.9	2.0	2.9	1.1	1.6	0.6	1.9	3.0	1.2

Stst = siltstone, Sh = shale, Sst = sandstone, Sl = Slate, Ssl = silty slate, Gn = gneiss, Q = quartzite.

3.4.3 Determination of surface heat flow

The terrestrial heat flow in Luxembourg was unknown prior to this study. To fill this gap in knowledge and to provide further input for the thermal modelling, heat flow was determined in the Mersch borehole, located in the Alzette river valley in the Trier–Luxembourg Basin (M in Fig. 3.1A). This borehole was drilled in 1968 as an exploration borehole to a final depth of 328 m and mostly encountered rocks of the Lower Middle Keuper, the Muschelkalk and the Buntsandstein (see Schintgen and Förster, 2013, their cross section B).

After completion, the borehole had been equipped with three piezometer tubes and the remaining open space cemented. The borehole was under thermal equilibrium when a continuous temperature (T) log could be obtained in 2011 by an analog, electric-line system with a 28-mm-diameter sensor. A downward logging speed of 2 m min^{-1} was applied in order to compensate for the buoyancy of the sensor and, thus, a loss in cable tension during descent in the narrow water-filled tube. The water level in the borehole corresponds to terrain level.

The T-log has a precision of 0.01°C and an accuracy of 0.1 °C. The recording interval was 0.1 m. The T-log was processed by applying a running average over 21 records (i.e. 2 m) for smoothing the data. T-gradients were calculated between consecutive temperature-depth points. As could be expected for a borehole in thermal equilibrium, the T-gradient plot well reflects the changes in lithology resembled by the gamma-ray log (Fig. 3.3).

For the determination of the surface heat flow (q_s), the interval method was applied (Powell et al., 1988). Five depth intervals are selected for the heat-flow determination (Fig. 3.3). The intervals correspond more or less to lithostratigraphic units composed of up to three major lithotypes. The lithological changes between the intervals are also reflected in changes of the interval T-gradient, which indicates that they are linked to changes in TC. Values of measured TC assigned to the intervals are from drill core samples of the Mersch borehole (interval A) and from cores of the same lithostratigraphy from nearby boreholes (intervals B–E).

Table 3.6 lists the lithotypes, TC values and T-gradients used in the heat-flow calculation. The T-gradient is the arithmetic mean of individual gradients of the recording intervals. The standard error α of the T-gradient was determined as follows:

$$\alpha = \sigma \cdot (N-1)^{-\frac{1}{2}} \qquad (3.4)$$

where σ is the standard deviation and N the number of T-gradient values of the interval. TC of lithotypes corresponds to laboratory measurements under water-saturated conditions, performed perpendicular to bedding honoring the geological situation. The lithotype TC is

pressure corrected (after Fuchs and Förster, 2014) and T-corrected (after Somerton, 1992) to resemble in-situ conditions (see Eqs. (3.10)–(3.12) in Section 3.5). However, the cumulative effect of both corrections on the interval TC in this shallow borehole is minor (cf. Table 3.6). The interval TC is calculated as a weighted mean:

$$\lambda_{\text{int}} = \frac{\sum_{i}^{n}(t_i \cdot \lambda_i)}{\sum_{i}^{n} t_i} \tag{3.5}$$

where λ_{int} is the interval TC, λ_i the TC of individual pressure and T-corrected lithotype TC values, t_i the volume fraction of the individual lithotypes, and n the number of lithotypes considered. The 1σ error of TC of interval A is estimated to be 5% compared to 10% in intervals B, C and D and 15% in the most heterogeneous interval E (Table 3.6). The estimated errors are a reflection of the small number of samples per lithotype and uncertainties in the geology.

The interval heat flow q_i (in mW m^{-2}) is obtained by the Fourier equation of heat conduction:

$$q = -\lambda \cdot \frac{dT}{dz} \tag{3.6}$$

where λ is the TC (in W m^{-1} K^{-1}) and dT/dz is the T-gradient of the interval (in K km^{-1}). The 1σ error (Table 3.6) is determined by error propagation:

$$\sigma_q = \sqrt{\left(\frac{\partial q}{\partial \lambda} \cdot \sigma_\lambda\right)^2 + \left(\frac{\partial q}{\partial gradT} \cdot \sigma_{gradT}\right)^2} = \sqrt{(gradT \cdot \sigma_\lambda)^2 + (\lambda \cdot \sigma_{gradT})^2} \tag{3.7}$$

where σ_q is the standard deviation (or error) of interval heat flow q, σ_λ and $\sigma_{grad\ T}$ are the respective standard deviations of interval TC λ and interval thermal gradient grad T. Interval heat-flow values range from 68 to77 mW m^{-2}. The resulting q_s (± 2σ) for the borehole site averages to 75 ± 7 mW m^{-2}. The uncertainty of q_s is calculated by error propagation:

$$\sigma_{q_S} = \frac{1}{n}\sqrt{\sum_i^n \sigma_{q_i}^{\ 2}} \tag{3.8}$$

where σ_{qs} is the error on q_s resulting from a number n of intervals i characterized each by an error σ_{qi} of interval heat flow q_i.

The consideration of depth intervals in the shallower part of the borehole seemed inappropriate for the following reasons. The overall T-gradient in the upper part of the borehole to a depth of 125 m is remarkably low compared to the lower part of the section (Fig. 3.3). The TC values determined for this borehole section cannot compensate for this T-gradient reduction in a thermal regime that is purely conductive. It is supposed that regional water flow from a recharge area 10–15 km to the north is responsible for this situation. The first geological formation in

which the heat transfer is apparently purely conductive is the marl/marlstone aquitard in the Middle Muschelkalk (heat-flow interval A). This assumption is underpinned by similar heat-flow values determined in intervals B–D. The somewhat lower heat flow in interval E compared to the upper intervals can be explained by a larger error/uncertainty in determining the true interval TC.

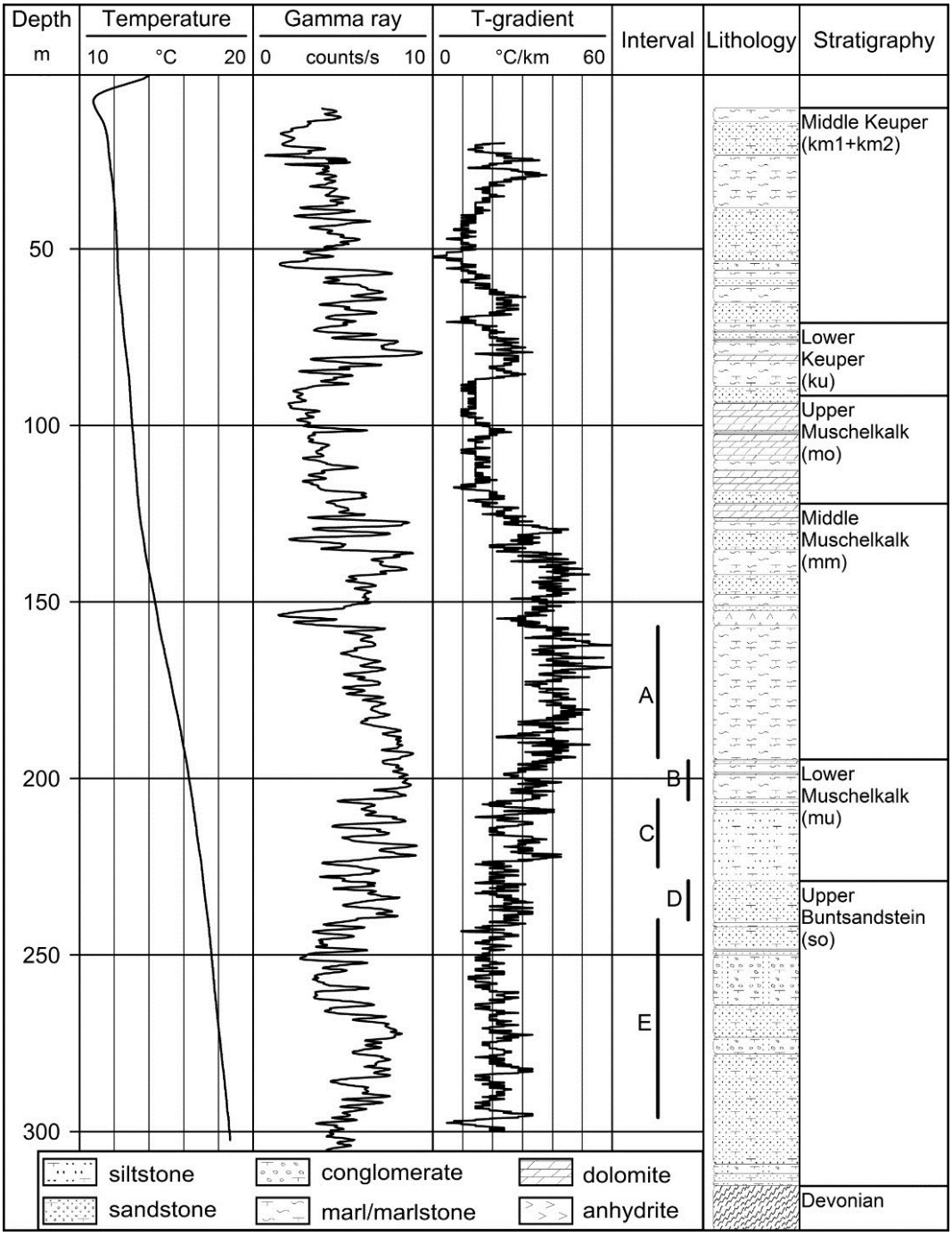

Fig. 3.3: Temperature, gamma ray, temperature gradient, simplified lithology, and stratigraphy of the Mersch borehole. Depth is given in meters below ground level. Black vertical bars mark the heat-flow intervals A–E (cf. Table 3.6).

The q_s of the Mersch borehole (75 ± 7 mW m^{-2}) is in accord with the bulk of data reported for areas adjacent to Luxembourg. In the Eifel and the Saar–Nahe Basin, q_s values between 64 and 76 mW m^{-2} have been determined (Bram, 1979; Haenel, 1971; Haenel, 1983; Hückel and Kappelmeyer, 1966). The adjoining northeastern part of the Lorraine region may have a slightly higher q_s of 73–84 mW m^{-2} (Vasseur, 1980). The value of 59 mW m^{-2} (Vandenberghe, 2002) reported in the Cambrian section of the Grand-Halleux borehole in the Stavelot Massif in Belgium is exceptionally low. This value is suggested to underestimate the heat flow due to a disturbed temperature profile (see also Section 3.6).

Table 3.6: Thermal data of the Mersch borehole.

					Litho λ_{sat}	Interval T-gradient			Interval λ_{sat}					q_i		q_s		
ID	Depth int.	Strat.	Lithology	Vol.		AM	σ	α	Unc.	Corr.	σ	σ		σ		AM	1σ	2σ
	[m]			[%]	[W m^{-1} K^{-1}]	[K km^{-1}]			[W m^{-1} K^{-1}]		[%]	[W m^{-1} K^{-1}]		[mW m^{-2}]		[mW m^{-2}]		
A	157–194	mm1	Silty, gypsum-rich marl	99.8	1.85	41.2	6.3	0.3	1.85	1.87	5	0.09		77	4	75	3	7
			Dolomite	0.2	4.32													
B	195–206	mu2	Dolomitic, sandy marlstone	27.6	2.42	33.1	5.0	0.5	2.29	2.34	10	0.23		77	8			
			Dolomitic clay-/marlstone	70.2	2.22													
			Sandy siltstone	2.2	2.76													
C	206–225	mu1	Sandy siltstone	85.3	2.76	27.8	6.5	0.5	2.68	2.78	10	0.28		77	8			
			Dolomitic clay-/marlstone	14.7	2.22													
D	229–240	so2	Dolomitic sandstone	66.1	2.99	24.9	4.5	0.4	2.87	3.00	10	0.30		75	8			
			Marly sandstone	33.7	2.75													
			Clayey siltstone	0.2	2.38													
E	240–296	so1	Sandy, dolomitic conglomerate	39.9	3.42	21.0	4.5	0.2	3.10	3.26	15	0.49		68	10			
			Dolomitic sandstone	46.2	2.94													
			Marly sandstone	13.7	2.75													
			Clayey siltstone	0.2	2.38													

ID = interval label, Depth int. = depth interval, Strat. = stratigraphy, Vol. = volume fraction of lithotype, Litho λ_{sat} = arithmetic mean of the lithotype thermal conductivity in saturated state, AM = arithmetic mean, σ = standard deviation, α = standard error, Interval λ_{sat} = interval thermal conductivity in saturated state, Unc. and Corr. = values uncorrected and corrected for T and p, q_i = interval heat flow, q_s = surface heat flow. Formations: mm1 = Gipsmergel, mu2 = Orbicularisschichten, mu1 = Muschelsandstein, so2 = Voltziensandstein, so1 = Zwischenschichten (see also Fig. 3.3).

3.5 Lithosphere thermal modelling

Figs. 3.4 and 3.5 show the conceptual models simplified from the geological cross sections A, B and C (see Fig. 3.2; location in Fig. 3.1A) with the polygons considered in the thermal modelling. The cross sections encompass the lithosphere down to the thermal lithosphere–asthenosphere boundary (LAB). Temperatures are calculated numerically by solving the equation for two-dimensional steady-state heat conduction:

$$\frac{\partial}{\partial x}\left(\lambda \frac{\partial T}{\partial x}\right)+\frac{\partial}{\partial z}\left(\lambda \frac{\partial T}{\partial z}\right)=-H \tag{3.9}$$

where H is the internal radiogenic heat production and the TC (λ) of the rock is assumed to be isotropic.

The temperature distribution T(x, z) within the lithosphere, x being the horizontal coordinate and z being the vertical coordinate, is determined based on temperature and pressure corrected TC λ(x, z), the distribution of radiogenic heat production H(x, z), and the appropriate thermal boundary conditions. Numerical calculations are based on a finite-element method using the MATLAB® R2010b software. For sedimentary rocks, the T-correction of ambient TC to in-situ conditions was performed separately for temperature and pressure (p). The combined correction equation is:

$$\lambda_{cor}=\lambda_{lab}+\Delta\lambda_T+\Delta\lambda_p \tag{3.10}$$

where λ_{cor} is the in-situ TC (in W m^{-1} K^{-1}), and $\Delta\lambda_T$ and $\Delta\lambda_p$ are the temperature and pressure corrections after Somerton (1992) and Fuchs and Förster (2014), respectively. T-correction after Somerton (1992) is expressed as follows:

$$\Delta\lambda_T=-10^{-3}\left(T-293\right)\cdot\left(\lambda_{lab}-1.38\right)\cdot\left[\lambda_{lab}\left(1.8\cdot10^{-3}T\right)^{\left(-0.25\lambda_{lab}\right)}+1.28\right]\cdot\lambda_{lab}^{-0.64} \tag{3.11}$$

where $\Delta\lambda_T$ is the contribution of T-correction (in W m^{-1} K^{-1}), λ_{lab} is the TC measured in the laboratory (in W m^{-1} K^{-1}) and T is the temperature (in K = °C +273). Pressure correction after Fuchs and Förster (2014) is expressed as follows:

$$\Delta\lambda_p=\left(1.095\cdot\lambda_{lab}-0.172\right)\cdot p^{\left(0.0088\lambda_{lab}-0.0067\right)}-\lambda_{lab} \tag{3.12}$$

Where $\Delta\lambda_p$ is the contribution of p-correction (in W m^{-1} K^{-1}), λ_{lab} is the TC measured in the laboratory (in W m^{-1} K^{-1}) and p is the assumed in-situ pressure (in MPa). For igneous and metamorphic rocks, lithotype-specific T- and p-corrections elaborated by Seipold (2001) were applied sequentially:

$$\lambda_T=\lambda_{lab}-a+\frac{1}{\left(b+c\cdot10^{-4}\cdot T\right)}+d\cdot10^{-9}\cdot T^3 \tag{3.13}$$

and for peridotite:

$$\lambda_T = \lambda_{lab} - a + \frac{T}{\left(b + c \cdot 10^{-4} \cdot T\right)} + d \cdot 10^{-9} \cdot T^3 \quad (3.14)$$

$$\lambda_{Tp} = \lambda_T \cdot \left(1 + \alpha \cdot 10^{-2} \cdot p\right) \quad (3.15)$$

where λ_T is the T-corrected TC (in W m^{-1} K^{-1}), λ_{lab} is the TC measured in the laboratory (in W m^{-1} K^{-1}), T is the temperature (in K), and a, b, c and d are rock-specific coefficients (a = 2.2849, b = 0.344, c = 3.27, d = 0.445 for mafic granulite, a = 4.1241, b = –42.9, c = 3890, d = 0.072 for peridotite and a = 2.9169, b = 0.191, c = 5.25, d = 0.670 for gneiss). λ_{Tp} is the T- and p-corrected TC (in W m^{-1} K^{-1}), p is the assumed in-situ pressure (in kbar) and α is a rock-specific coefficient (α = 0.44 for mafic granulite, 1.52 for peridotite and 1.34 for gneiss).

In-situ pressure in the thermal models was estimated considering the density of the overburden. Density values of the Palaeozoic formations and model units (Table 3.7) resulted from stepwise calculating a weighted arithmetic mean based on the density of representative samples. For the density of the Precambrian crustal units, typical lithotype-specific values, further constrained by seismic velocities (Mechie et al., 1983), were compared and adapted to densities or density contrasts obtained by gravity modelling in adjacent regions (Jacoby et al., 1983; Edel and Schulmann, 2009). For the lithospheric mantle, a density of 3.3 × 10^3 kg m^{-3} was assumed (Kukkonen and Peltonen, 1999; Norden et al., 2008).

3.5.1 Thermal boundaries

The upper boundary condition for thermal modelling is the annual surface T that generally ranges from 7.5 to 8 °C in the Ardennes and from 8 to 8.5 °C in the Guttland (Haenel et al., 1980; www.asta.etat.lu) and in areas of the TLB. Average surface T is lowest on the plateau of the Ardennes (7 °C) and highest in the Mosel valley (11 °C). The surface T is influenced by the topography, which varies by about 500 m along the cross sections A and B.

For modelling, the conceptual cross sections (Figs. 3.4 and 3.5) were extended horizontally by 50 km in order to reduce boundary effects on the calculated temperatures. Heat flow through the lateral boundaries is set to zero, thereby excluding any horizontal heat transfer. The lower boundary of the models (the thermal LAB) is defined by the 1300 °C isotherm (McKenzie and Bickle, 1988; Turcotte and Schubert, 2002). Different, geophysically constrained depth scenarios for the thermal LAB (80 km, 100 km, 130 km) were tested for validation by comparing the modelled with the measured q_s at the Mersch borehole (see Section 3.6).

Table 3.7: Petrophysical parameters for the crust and the lithospheric mantle used in the lithosphere thermal modelling.

Polygons in section			Age		Description	Major rock type(s)	V_P	λ ± 1σ	λ corr.		H	d
A	B	C					[km s^{-1}]	[W m^{-1} K^{-1}]	T	p	[μW m^{-3}]	[10^3 kg m^{-3}]
1	1, 2	1	Mesozoic		Jurassic – Triassic	Clay-/marlstone + limestone + sandstone + dolomite	/	2.5 ± 0.2	8	–	/	2.39
2	3		Permian		Rotliegend	Claystone + siltstone + sandstone + conglomerate	/	3.1	8	–	1.2	2.40
3, 4	4		Devonian (Eifel + Hunsrück)		Emsian – Upper Siegenian	Shale (+ slate) + siltstone + sandstone	2.6–5.6	3.4 ± 0.2	8	–	1.8	2.69
5	5, 6				Middle Siegenian	Sandstone (quartzite)		5.0 ± 0.5	8	–	0.6	2.66
6, 7	7, 8				Lower Siegenian – Lochkovian	Sandstone (quartzite) + siltstone + shale		3.9 ± 0.1	8	–	1.7	2.69
8	9	2	Devonian (Ardennes)		Emsian + Siegenian	Shale (+ slate) + sandstone		3.2 ± 0.2	8	–	1.8	2.68
9, 10	10, 11	3			Lochkovian	Sandstone + siltstone + shale		3.5 ± 0.1	8	–	1.7	2.64
11–15	12–15	4	Ordovician		Salm group	Slate/phyllite	6.1–6.35	3.1 ± 0.1	8	–	1.9	2.77
16–20	16–20	5	Upper + Middle Cambrian		Revin group	Slate/phyllite + quartzite		4.0 ± 0.1	8	–	2.0	2.73
21, 22	21, 22	6	Lower Cambrian		Deville group	Slate/phyllite + quartzite		4.3 ± 0.2	8	–	1.2	2.69
23	23	7	Neoproterozoic		Crystalline upper crust	Mica schist + gneiss	6.1–6.2	2.8	6	+	1.3	2.75
24	24	8			Middle crust	Tonalite + diorite + granodiorite	6.5–6.7	2.4	6	+	0.8	2.85
25	25	9			Lower crust	Hornblendite + pyroxenite	> 6.9	3.2	2	+	0.05	3.05
26	26	10			Lithospheric mantle	Lherzolite + harzburgite	8.0–8.5	4.2	4	+	0.02	3.30

Columns A, B and C refer to the corresponding cross sections with the polygon numbering as in Fig. 3.4 (A and B) and Fig. 3.5 (C). V_P = seismic velocity, λ = thermal conductivity at laboratory conditions (25 °C, atmospheric pressure), σ = standard deviation, λ corr. = correction of thermal conductivity for a temperature (T) and a pressure (p), H = radiogenic heat production, d = density. Numbers for T-correction (Eq. (3.13) and (3.14)) refer to specific categories by Seipold (2001) implemented in the used modelling algorithm: 2 mafic granulite, 4 peridotite and 6 gneiss. Category 8 refers to sediments to which a combination (Eq. (3.10)) of T-correction (Eq. (3.11)) after Somerton (1992) and p-correction (Eq. (3.12)) after Fuchs and Förster (2014) was applied. Pressure correction (Eq. (3.15)) was applied to the units marked by '+' according to Seipold (2001).

In addition to varying the LAB depth, the steady-state thermal effect of an uprised asthenospheric mantle, the Eifel plume (Budweg et al., 2006; Goes et al., 2000a; Seiberlich et al., 2013; Raikes, 1980; Raikes and Bonjer, 1983; Ritter, 2007), was modelled. Given the uncertainties with regard to the top of the plume, three scenarios were considered in the thermal

modelling for the easternmost part of cross section C: Top of plume at 60 km depth (e.g., Budweg et al., 2006), 50 km (Ritter, 2007; and references therein) or 40 km (Seiberlich et al., 2013). The transition from normal (100-km-thick) to thinned, plume-affected lithosphere apparently spans over 25–30 km and is located underneath northeastern Luxembourg and the eastern border of Belgium (Keyser et al., 2002; Walker et al., 2005).

3.5.2 Structure, composition and thermal properties of the lithosphere

Figs 3.4 and 3.5 show the conceptual models with the polygons considered in the modelling. In Fig. 3.4, the models are shown with a cut-off at 35 km depth. In Fig. 3.5, the full extent of the model beyond the crust–mantle boundary to a maximum depth of LAB scenarios (130 km) is shown. The crustal thickness along the models varies slightly between 33.5 km in the north (beneath the Ardennes) and 29.5 km in the northeast (beneath the western part of the Eifel region) (Ziegler and Dèzes, 2006, 2007). These values are close to those reported by Budweg et al. (2006) who provide values of about 32 km for the Ardennes and of 28 km for the Eifel region.

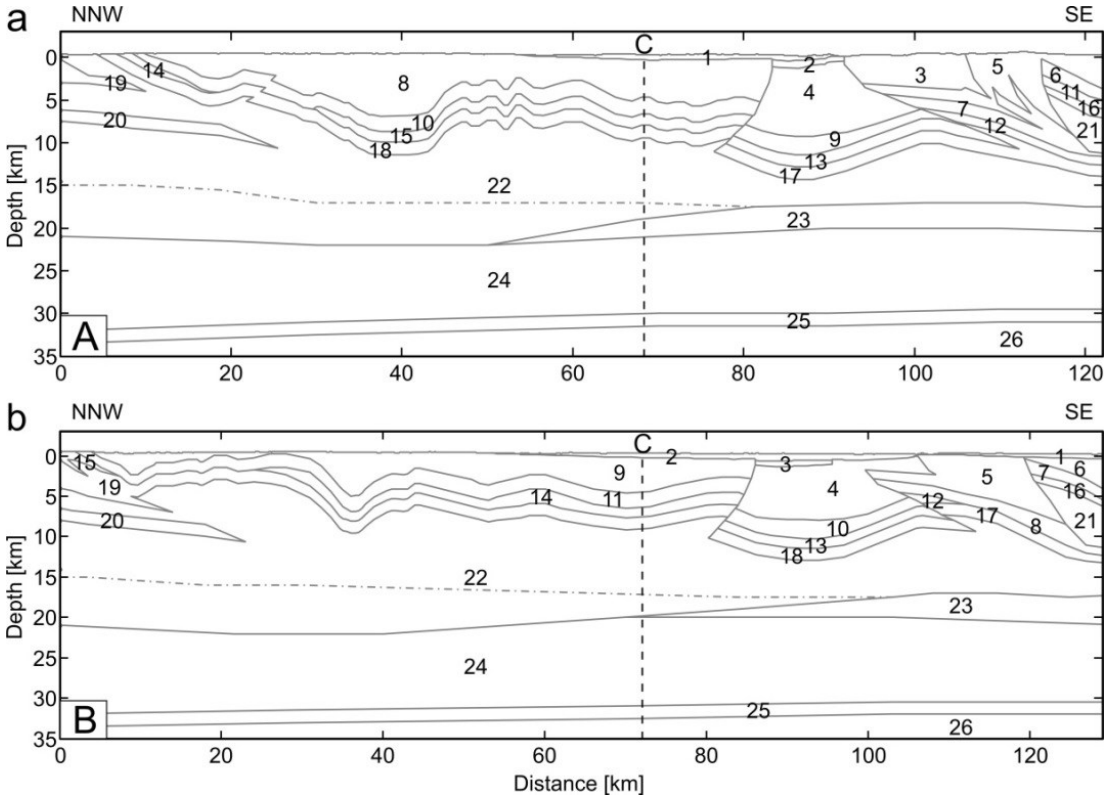

Fig. 3.4: Conceptual crustal models A and B (here cut off at 35 km depth) used in the thermal modelling. Vertical dashed lines indicate intersection with cross section C as shown in Fig. 3.2. Polygons marked with numbers denote units of different lithology and thermal properties (Table 3.7) extracted from the conceptual crustal cross sections shown in Fig. 3.2. The grey dash-dotted line marks a possible lateral extension of the gneiss in polygon 23.

The youngest unit of the crust is represented by the Mesozoic succession of the TLB (polygon 1, section A and C and polygons 1 and 2, section B, Figs. 3.4 and 3.5, Table 3.7). Modelling also considered a conceptual view according to which the central part of the TLB is underlain by a Permian graben (Schintgen and Förster, 2013), reflected in polygons 2 and 3 in sections A and B, respectively. The Lower Devonian succession is represented by polygons 3–10 (section A), 4–11 (section B) and polygon 2–3 (section C). Units of almost pure quartzite composition, even small, are delineated as single units owing to their exceptionally high TC values (polygon 5, section A, polygons 5 and 6, section B). The thick succession of parametamorphic Cambrian and Ordovician rocks (polygons 11–22, section A, 12–22, section B and 4–6, section C) has its base at about 22 km depth in the north, at 20 km in the southwest, at 17 km in the southeast, and at about 16 km in the northeast. In the latter two regions, i.e. underneath the Eifel and the Hunsrück, the succession is underlain by Proterozoic metasedimentary mica schist and gneiss (Mengel et al, 1991; attributed as crystalline upper crust in Table 3.7). The grey dash-dotted line within the crust (Figs. 3.4 and 3.5) indicates a possible lateral extension of the gneiss as a continuous and up to 6-km-thick layer. It replaces the lower part of Lower Cambrian metasediments below the dash-dotted line in Figs. 3.4 and 3.5 (extension of polygon 23, sections A and B and polygon 7, section C, respectively).

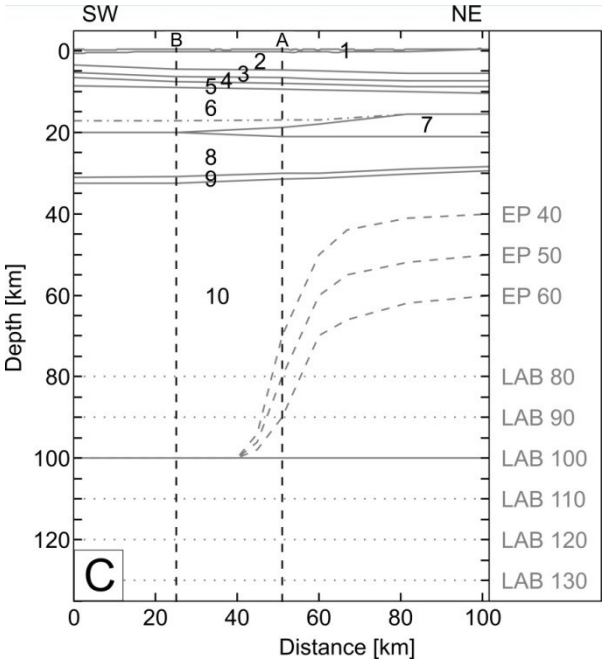

Fig. 3.5: Conceptual crustal model C used in the thermal modelling. Vertical dashed lines indicate intersection with cross sections A and B, respectively, as shown in Fig. 3.2. Polygons marked with numbers denote units of different lithology and thermal properties (Table 3.7). The dash-dotted line marks a possible lateral extension of the gneiss in polygon 7. Scenarios of variable LAB (lithosphere–asthenosphere boundary) depths are indicated as dotted lines. The location and variable depths of top of Eifel Plume (EP) are shown as dashed lines.

The middle crust (polygon 24, sections A and B and polygon 8, section C) encompasses the depth realm between approximately 19 and 30 km characterized by a seismic velocity of 6.5–6.7 km s^{-1} (Mechie et al., 1983). We interpret these velocities, which are typical of Palaeozoic middle crust, as representing metagranitoids (Rudnick and Fountain, 1995). Metaigneous gneiss xenoliths from the Eifel volcanic field support this assumption (Mengel et al., 1991; Stosch et al., 1991; and references therein). A relatively thin layer of pyroxenite and hornblendite (Voll, 1983; Mengel et al., 1991; Stosch et al., 1991) (polygon 25, sections A and B and polygon 9, section C) represents the lower crust. The present-day thin lower crust is the result of delamination in geological times, during which the crust lost more than 15 km of its original thickness (Wittenberg et al., 2000; Ziegler et al., 2004). The lithospheric mantle (polygon 26, sections A and B and polygon 10, section C) is likely made up of peridotite (spinel lherzolite and harzburgite) as indicated by xenoliths (Mengel et al., 1991; Shaw et al., 2005).

Thermal properties of the model units are compiled in Table 3.7. TC of the Mesozoic and Palaeozoic formations represents water-saturated conditions. The entire Mesozoic is represented by one TC value, which is the weighted average of TC measured perpendicular to bedding. For the isotropic Lower Devonian succession, mean TC values are assigned to model units. The TC values implemented for the Cambrian and Ordovician rocks refer to those measured perpendicular to cleavage. The TC of the crystalline upper crust, of the middle and lower crust, and of the lithospheric mantle was assigned based on literature TC data (Table 3.7; Norden et al., 2008; Schütz et al., 2014; and references therein). Details on thickness ranges of formations/stratigraphic units and error calculation used in the calculation of TC of model units are given in the Supplementary material (Section 3.10).

Radiogenic heat production (H) data of Mesozoic and Palaeozoic rocks were implemented in the models as discussed in Section 3.4.2. Xenoliths data supported mica schist and gneiss as major constituents of the crystalline upper crust, the H of which averages to 1.3 μW m^{-3} (considering geochemical data of Stosch et al., 1991). This average is consistent with the H of the Wartenstein Gneiss determined in this study. Xenoliths of diverse types of metagranitoid (tonalite, diorite, granodiorite) studied by Stosch et al. (1991) suggest a value of 0.8 μW m^{-3} for the middle crust (Table 3.7). Data for the lower crust and lithospheric mantle were taken from different literature sources reporting consistently low H values (Förster and Förster, 2000; Förster et al., 2010; Furlong and Chapman, 2013; Hasterok and Chapman, 2011).

3.5.3 Modelling results

Fig. 3.6 shows heat-flow patterns resulting from the 2-D thermal modelling along the three cross sections. Values of q_s are retrieved from the model at 1 km depth, to omit topography-related heat-flow refraction at the surface. On average, the 1-km-depth value is only about 1.4–1.5 mW m^{-2} lower than the modelled mean q_s.

The uncertainty range of q_s determined at the Mersch borehole (75 ± 7 mW m^{-2}) did not permit to establish the LAB depth below Luxembourg with statistical significance (see Fig. 3.6). However, a LAB depth of ~100 km, compatible with the Mersch heat-flow mean, is coincident with the bulk of modern geophysical LAB-depth estimates (90–110 km) for the wider area of Luxembourg except for the adjoining Eifel region where the present-day lithosphere is considerably thinned (Geissler et al., 2010; Seiberlich et al., 2013; and references therein). The following discussion considers a 100 km LAB-depth as apparent best-fit scenario, but we are aware of the fact that the actual depth may as well be slightly shallower or greater.

Lithosphere scenarios without a mantle plume result in q_s patterns that are highly variable along cross sections A and B (Fig. 3.6a and b) and more gentle along section C (Fig. 3.6c). Particularly high values are implied for the Stavelot Massif in the NNW (80–85 mW m^{-2}) and the Hunsrück (90–92 mW m^{-2}) in the SE of the sections A and B. By contrast, the mantle heat flow (q_m) is largely homogeneous along all sections (~40 mW m^{-2}).

The thermal models predict isotherms for the crust that are more densely spaced in the middle and lower crust compared to the upper crust (the upper 20 km of the models) (Fig. 3.7a–c) reflecting different geothermal gradients caused by different values of TC. The central part of the study area appears slightly warmer in the upper 20 km compared to the northern and southern parts. Below 20 km, isotherms are evenly spaced and homogeneous. Moho temperatures along cross sections A and B range between 605–630 °C and 620–640 °C, respectively (Fig. 3.7a and b). Moho temperatures are inferred to decrease from ~650 °C to ~620 °C towards the northeast (Fig. 3.7c).

Modelling the conductive responses of a long-lived Eifel plume along cross section C would result in q_s values that are only slightly increased in the SW, but rise to ~90–110 mW m^{-2} in the NE depending on the different top Eifel plume scenarios considered (Fig. 3.6d). The corresponding q_m value would remain virtually unchanged in the SW but increase to ~55–77 mW m^{-2} in the NE. Plume-triggered steady-state Moho temperatures at assumed 60, 50 or 40 km plume depth would increase from 680 to 710 °C in the SW to 820–1070 °C at the northeastern end of cross section C just above the plume (Fig. 3.7d).

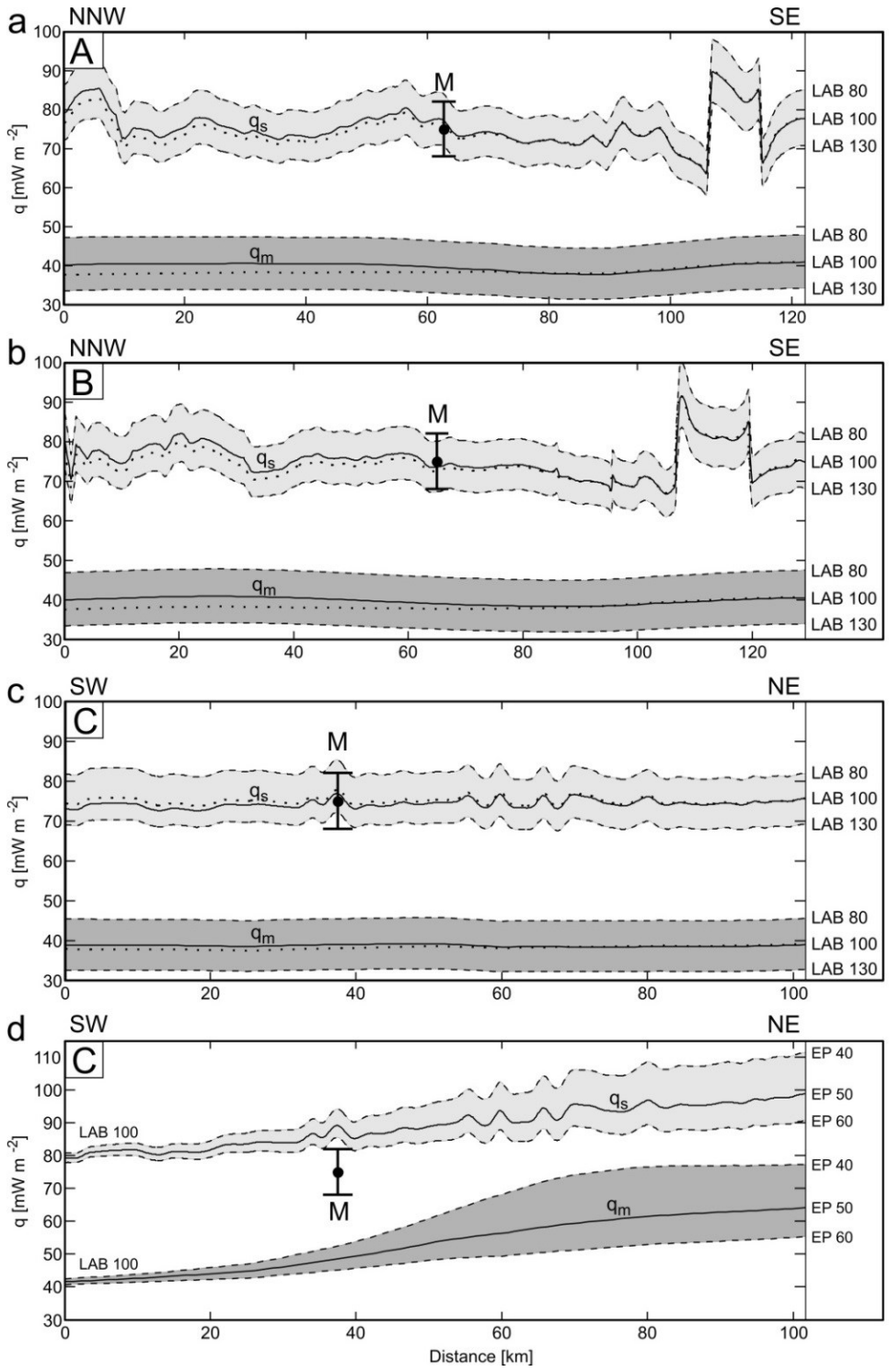

Fig. 3.6: (a–c) Modelled steady-state surface heat flow q_s (light grey zone) and mantle heat flow q_m (dark grey zone) according to three LAB-depth scenarios and (d) for the consideration of the Eifel plume (EP) at different depth. The q_s refers to 1 km depth below mean sea level to avoid heat refraction at the surface due to topography. This value is on average 1.4–1.5 mW m^{-2} lower than the q_s sensu stricto. The best-fit scenario of heat flow is indicated by a solid line. The dotted line in a–c shows the variation in q_s and q_m in case of a continuous gneiss layer (polygon 23 in cross sections A and B; polygon 7 in cross section C). The solid line (d) represents the scenario with the top of the Eifel plume at 50 km depth. Heat flow at the Mersch borehole location (denoted as M) with mean and standard deviation (2σ) is projected onto the sections.

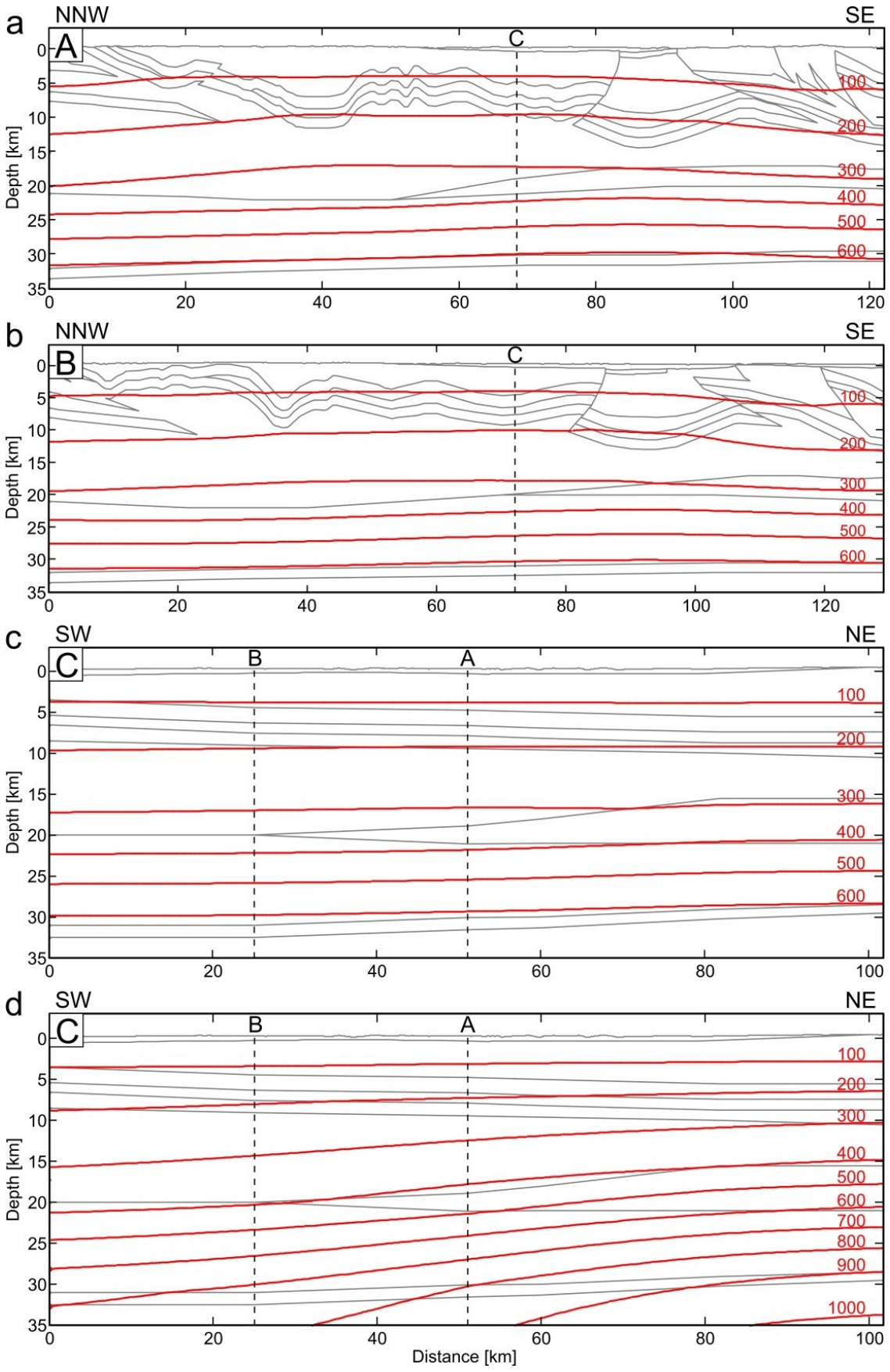

Fig. 3.7: (a–c) Modelled steady-state temperatures (in red and in °C) of sections A, B and C for the LAB-100-km-model; (d) Isotherms of cross section C for the top of the Eifel plume at 50 km depth.

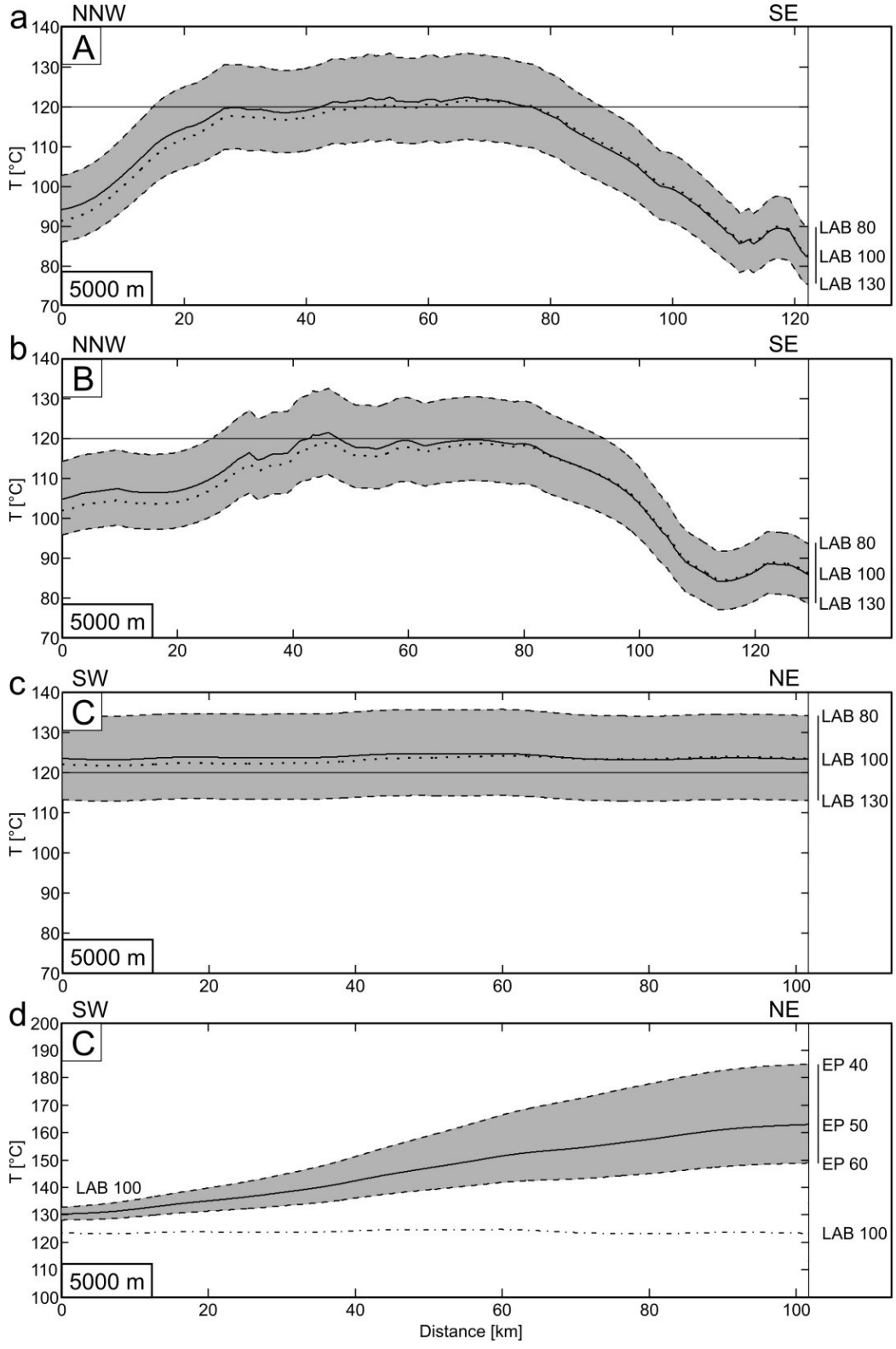

Fig. 3.8: (a–c) Modelled temperature at drillable depth of 5 km along cross sections A, B and C (dark grey zone) deduced from the LAB-100-km model (solid line) as well as from the LAB-80-km and LAB-130-km models (dashed lines). The 120 °C-isotherm is indicated by a solid line. The dotted line shows changes in T caused by a continuous gneiss layer (see Fig. 3.6). (d) Result for cross section C for a LAB at 100 km depth in the southwest and different Eifel plume (EP) scenarios at depths of 40, 50 and 60 km (see Fig. 3.5). A dash-dotted line is added for comparison with the LAB-100-km scenario in c.

For a borehole depth of 5 km, which may reflect a reasonable target depth for the development of deep geothermal energy applications, modelled temperatures are shown in Fig. 3.8a–c. In the central parts of cross section A (between 30 and 75 km; Fig. 3.8a) and B (between 40 and 85km; Fig. 3.8b), the LAB-100-km-model predicts a temperature plateau with an average T of 120 °C, about 5 °C lower than predicted T in section C (Fig. 3.8c). The high temperatures result from the volume of shale-dominated Lower Devonian in the Ardennes (Emsian and Siegenian; $\lambda \approx 3.2$ W m^{-1} K^{-1}; Table 3.7) as well as in the Eifel and the Mosel Syncline (Emsian and Upper Siegenian; $\lambda \approx 3.4$ W m^{-1} K^{-1}; Table 3.7). Towards the Stavelot Massif in cross section A (0–30 km; Fig. 3.8a) and B (0–40 km; Fig. 3.8b) T is inferred to rapidly decrease to minimum values of 95–105 °C. These low temperatures are explained by a high TC of the quartzite-rich Cambrian rocks of the Stavelot Massif (Revin and Deville groups; $\lambda > 4$ W m^{-1} K^{-1}; Table 3.7) in shallow position. Towards the Hunsrück region in cross section A (75–122 km; Fig. 3.8a) and B (85–127 km; Fig. 3.8b) T decreases to values of ~85 °C. Here, low temperatures are linked with the Middle Siegenian rocks (Taunusquarzit; $\lambda \approx 5$ W m^{-1} K^{-1}; Table 3.7) in shallow position. Compared to the LAB-100-km-model (Fig. 3.8a–c), variation of LAB depth (80 or 130 km) would result in temperatures that differ by only ~10 °C. In the steady-state Eifel-plume scenarios modelled in cross section C (Fig. 3.8d), T at 5 km would increase by about 40, 30 and 20 °C above the plume, resulting in absolute values of 165, 150 and 140 °C in the German–Luxembourgish border region (60 km).

3.6 Discussion

3.6.1 Surface heat flow and crustal temperature patterns

This paper presents the first subsurface T prognosis for the greater Luxembourg region based on steady-state 2-D thermal modelling. This prognosis benefitted from the determination of a reliable q_s value as well as from laboratory-measured TC and H data covering practically the entire Mesozoic–Palaeozoic succession.

The q_s value inferred from the Mersch borehole (75 ± 7 mW m^{-2}) and most values from neighbouring areas (64–85 mW m^{-2}) are higher than the average continental heat flow of 71 mW m^{-2} (Davies and Davies, 2010) and significantly exceed the average q_s value of 57–58 mW m^{-2} for Palaeozoic provinces (Jaupart and Mareschal, 2003). The q_s value of 75 ± 7 mW m^{-2} is consistent with a thermal model that shows the depth of the thermal LAB between 80 km and 130 km, with the mean value at the seismically favored 100 km depth (Geissler et al., 2010;

Jones et al., 2010). Given the properties of the crust and mantle in our conceptual models, the assumption of a lower q_s on the order of the Palaeozoic-province average (i.e., 60 mW m^{-2}) would require a LAB depth of 200 km, the upper end of lithospheric thickness range of Palaeozoic regions (150–200 km; Jaupart and Mareschal, 2003). Lithosphere thickness prior to Permo-Carboniferous delamination and thermal thinning is unknown but must have been higher than 100–120 km inferred for areas not affected by Cenozoic rifting (Ziegler et al., 2004; and references therein). Most of the granulitic base of the initially 45–60-km-thick crust is thought being removed shortly after the Variscan orogeny, which gave rise to the thin, extended crust imaged today (Christensen and Mooney, 1995; Wittenberg et al., 2000; Ziegler et al., 2004).

The variability of q_s modelled along the three cross sections (Fig. 3.6) is largely attributed to changes in the structure and composition of the crust in the uppermost 20 km. Thereby, changes in rock type, and therewith TC, exerted the major control on q_s, whereas the minor spread in H in the different model units imposed a negligible influence. The preferred LAB-100-km model results in q_m values of ~40 mW m^{-2} (Fig. 3.6), which coincide with values obtained for Palaeozoic extended crust in Europe (e.g., Balling, 1995; Norden et al., 2008). The crustal component of heat flow in our conceptual models is between 33 and 39 mW m^{-2} (Fig. 3.6a and b; cross sections A and B), with a mean of 36 mW m^{-2} (Fig. 3.6c; cross section C). These values, corresponding to an equivalent average crustal H of ~1.2 μW m^{-3}, are in the upper domain of bulk continental-crust averages (Rudnick et al., 1998).

As the deeper crustal structure and composition of the area are only incompletely known from geophysical surveys (e.g., seismics) and xenolith studies, it deemed valuable to test the sensitivity of the thermal models to slightly modified conceptual geological models. For example, the consideration of a continuous Precambrian gneiss layer (comparable H but λ = 2.8 instead of 4.3 W m^{-1} K^{-1}; Table 3.7) in cross section A (polygon 23; Fig. 3.4a) as an alternative to what is shown in Fig. 3.2 would negligibly affect the q_s and T patterns at 5 km depth (~–2.5 mW m^{-2} and –3 °C, respectively) and q_m (~–2.5 mW m^{-2}), but considerably affect the T pattern at the Moho (+40 °C). The same holds for varying the composition of the poorly known lowermost crust owing to the reduced thickness of this unit. In general, changes of parameters in the much less well known lower part of the crust (depth of ~15–30 km) have a relatively limited effect on the temperatures in the shallow subsurface (i.e. the upper 5 km).

Available borehole T-data as well as the modelled T from this study imply that the uppermost crust displays a rather normal T regime. Model temperatures between 120 °C and 125 °C at 5 km depth (Fig. 3.8) concur with T expectations resulting from large-scale extrapolation of T-

data and published as subsurface temperature maps (Haenel et al., 1980; Hurter and Haenel, 2002). By comparison, model-T results of about 120 °C at 5 km depth are higher than temperatures of ~110 °C measured at similar depth in deep wells in the Ardennes in Belgium (Vandenberghe and Fock, 1989). Given the estimated uncertainty in our modelled T in the upper 5 km (<5 °C), the higher temperatures inferred for greater Luxembourg may be real and related to the larger thickness of thermally less conductive Lower Devonian shale/slate layers. The presence of these rock types also tends to hamper large-scale groundwater circulation and, therefore, provide shielding from the near-surface effects and a thermal blanketing. Temperature estimates as high as 150–155 °C at 5 km depth in the adjoining Lorraine region (Bonté et al., 2010) in the southern part of the study area are not supported by the results presented in this study (i.e. a maximum of 120–125 °C at 5 km depth; Fig. 3.8). In addition, borehole T-measurements in the Variscan Ardennes yielded temperatures of 110 °C at 5 km depth (Vandenberghe and Fock, 1987). The higher temperatures provided by Bonté et al. (2010) are obviously related to an extrapolation of the thermal gradient of about 30 °C km^{-1} from the Mesozoic sedimentary cover into the Variscan basement, for which borehole data are scarce. Our study suggests such a thermal gradient only in the 1000–1500-m-thick Mesozoic and for the Pre-Mesozoic basement a gradient of 20 °C km^{-1}, also supported by measured T in the Ardennes.

With regard to q_s, the large contrasts in TC, in particular in the shallow subsurface, triggered significant heat refraction, which is well demonstrated by regionally elevated q_s values, notably in the Stavelot Massif (~10 mW m^{-2}; Fig. 3.6a) and the Hunsrück (~10–15 mW m^{-2}; Fig. 3.6a and b). Our results strongly question the reliability of the low q_s value of 59 mW m^{-2}, reported by Vandenberghe (2002) for the Stavelot Massif, which was determined in the Cambrian section of the Grand-Halleux borehole. The low q_s inferred from this borehole could be readily explained by a disturbed T-profile, indicated by a high T of 22 °C at 25 m depth compared to a mean annual surface T of 7.5 °C (Legrand, 1975). The perturbation is in response to a long drilling process (>5 years) and a short shut-in time (47 h) when the borehole was T-logged. Because the well is not cased (Graulich, 1980), topography-driven groundwater flow in the fractured quartzitic rocks may have overprinted the heat flow. Those processes are common in elevated areas (Deming, 1994; Deming et al., 1992; Smith and Chapman, 1983) and, thus, also may apply for the Stavelot Massif. In order to validate the q_s value determined for Grand-Halleux, a 1-D temperature profile was calculated in a ‘top down’ approach by inversion of the Fourier equation of heat conduction. TC (2.6 W m^{-1} K^{-1} for slate and 5.6 W m^{-1} K^{-1} for quartzite, this study) and H (1.94 μW m^{-3} for slate and 0.59 μW m^{-3} for quartzite) were

measured on drill cores from the same borehole (this study). A mean annual surface T of 7.5 °C and an undisturbed T of 52.5 °C at 2250 m depth are assumed (Graulich, 1980). Using a detailed lithological profile and applying to the TC a T-correction after Somerton (1992) and a p-correction after Fuchs and Förster (2014), the q_s required to match the undisturbed T at depth and the surface T equals 79 mW m^{-2}. The inverted q_s supports the result of our 2-D thermal modelling for the Stavelot Massif (~80 mW m^{-2}).

3.6.2 Temperature impact of the Eifel plume

The occurrence of the active volcanic area in Western Europe and thus also the Eifel plume heating in the upper mantle is inferred from seismic anomalies (Goes et al., 1999, 2000a, 2000b; Goes and van der Lee, 2002; Cammarano et al., 2003; Hieronymus et al., 2007). The resultant temperature increase in the upper mantle under the Rhenish Massif is supposed being as high as 100–300 ± 100 °C (Goes et al., 2000b). In this paper, the top of the Eifel plume (supposedly between 60 and 50 km depth) is associated with an increase of mantle temperatures on the order of 325–400 °C, thus corroborating the results of seismological studies. The present-day lithosphere in the Eifel region is evidently in thermal disequilibrium. Veins containing hydrous minerals hosted by mantle xenoliths are characterized by minimum equilibration temperatures of 850–900 °C (Shaw et al., 2005). The minimum present-day T at the crust/mantle boundary underneath the Eifel region is ~850 °C, which would corroborate a thermal LAB depth slightly shallower than 60 km.

In a steady-state thermal scenario, the plume-top at 60 km depth would result in a q_s of 91 mW m^{-2} (this study) along the western margin of the Eifel (Fig. 3.6d), which is significantly higher than the range of measured q_s (65–80 mW m^{-2}). From this observation, it follows that the plume-related heat pulse has not yet reached (at least entirely) the surface. This is corroborated by a study of Goes et al. (2000b) showing that the time span of heat diffusion through the crust from a heated mantle at 50 km depth is about 20 Ma. If heating has started 10–20 Ma ago (Goes et al., 2000b), the heat flow in the near-surface parts of the crust would not yet be affected. A further verification of this open question of plume heating and heat diffusion cannot be made with the available data set of q_s values.

On the other hand, measured q_s may be afflicted with several problems which render the discussion above problematic. Available q_s values in the Eifel region were measured exclusively in shallow boreholes (<200 m) and lakes (<70 m) (Bram, 1979; Haenel, 1971, 1983) at a depth range where water movements in the Mesozoic aquifers and in the Lower Devonian

succession may occur (e.g., Stober and Bucher, 2005), causing heat advection and eventually lowering of the conductive q_s value. As a consequence, the consideration and a quantification of possible advective processes (Manning and Ingebritsen, 1999; Smith and Chapman, 1983) cannot be made with the available data set of q_s values.

3.7 Conclusions

Numerical modelling of the thermal field strongly depends on the availability of reliable constraints and boundary conditions. The new surface heat flow of 75 ± 7 (2σ) mW m^{-2} determined for central Luxembourg represents a supplementary anchorpoint for verification of thermal models. A large database of measured thermal rock properties and values of thermal conductivity, radiogenic heat production and density are provided for virtually all geological formations exposed in the study area. These petrophysical properties represent substantial parameters for any type of thermal simulation. Our study underlines that surface heat flow determined in the shallow subsurface needs to be verified and corroborated by surface heat flow determined from high quality, continuous temperature logs in deep boreholes. Such recordings would shed light on the thermal regime as well as ongoing advective or convective processes linked to hydraulic conductivity in the Lower Devonian basement, in particular in the Eifel region. Considering the time lag of heat transfer of only several 10 Ma, another highly relevant but unresolved issue is the timing of the Eifel-plume emplacement relative to the onset of development of the ECRIS ~40 Ma ago. Our results show that the thermal effect caused by this heat pulse would be verifiable if already arrived at 5 km depth. The availability of suitable exploration data would lay the basis for quantification of various transient processes that may overprint purely steady-state conductive conditions.

3.8 Acknowledgements

This paper forms part of the doctoral thesis of TS entitled “The Geothermal Potential of Luxembourg”. The project is supported by the National Research Fund (Luxembourg) and the GFZ German Research Centre for Geosciences (Potsdam, Germany). The Geological Survey of Belgium is thanked for the possibility of sampling and measuring core material from the Grand-Halleux borehole. The Geological Survey of Luxembourg supported this work by granting access to their core-storage facility for sampling Mesozoic rock and by covering the costs for the geochemical analyses of whole-rock samples. The SEO (Société Electrique de l’Our) in Vianden (Luxembourg) and the “Amis de l’Ardoise” (Haut-Martelange, Luxembourg) are thanked for the opportunity of rock sampling in their premises. Constructive reviews by two anonymous reviewers helped to improve the manuscript and are gratefully acknowledged. H. Liep, M. Ospald and G. Arnold (GFZ) supported the sample preparation. C.-T. Rach, S. Kienast, C. Rudolph and M. Oldman (GFZ) are acknowledged for their assistance during TC measurements.

3.9 References

Balling, N. (1995). Heat flow and thermal structure of the lithosphere across the Baltic Shield and northern Tornquist Zone. Tectonophysics 244, 13–50.

Bless, M.J.M., Bouckaert, J., Camelbeeck, T., Dejonghe, L., Demoulin, A., Dupuis, C., Felder, P.J., Geukens, F., Gullentops, F., Hance, L., Jagt, J.W.M., Juvigné, E., Kramm, U., Ozer, A., Pissart, A., Robaszynski, F., Schumacker, R., Smolderen, A., Spaeth, G., Steemans, P, Streel, M., Vandenven, G., Vanguestaine, M., Walter, R., Wolf, M. (1990). The Stavelot Massif from Cambrian to Recent – a survey of the present state of knowledge. Ann. Soc. Géol. Belgique 113, 53–73.

Bonté, D., Guillou-Frottier, L., Garibaldi, C., Bourgine, B., Lopez, S., Bouchot, V., Lucazeau, F. (2010). Subsurface temperature maps in French sedimentary basins: new data compilation and interpolation. Bull. Soc. Géol. Fr. 181, 377–390.

Bourgeois, O., Ford, M., Diraison, M., Le Carlier de Veslud, C., Gerbault, M., Pik, R., Ruby, N., Bonnet, S. (2007). Separation of rifting and lithospheric folding signatures in the NW-Alpine foreland. Int. J. Earth Sci. 96, 1003–1031.

Bram, K. (1979). Heat flow measurements in the Federal Republic of Germany. In: Čermák, V., Rybach, L. (Eds.), Terrestrial Heat Flow in Europe. Springer, Berlin, Heidelberg, New York, NY, pp. 191–196.

Brigaud, F., Chapman, D.S., Le Douaran, S. (1990). Estimating thermal conductivity in sedimentary basins using lithological data and geophysical well logs. AAPG Bull. 74, 1459–1477.

Budweg, M., Bock, G., Weber, M. (2006). The Eifel Plume–imaged with converted seismic waves. Geophys. J. Int. 166, 579–589.

Bultynck, P., Dejonghe, L. (2001). Devonian lithostratigraphic units (Belgium). In: Bultynck, P., Dejonghe, L. (Eds.), Guide to a revised lithostratigraphic scale of Belgium. Geologica Belgica 4 (1–2). Brussels, pp. 39–69.

Cammarano, F., Goes, S., Vacher, P., Giardini, D. (2003). Inferring upper-mantle temperatures from seismic velocities. Phys. Earth Planet. Int. 138, 197–222.

Christensen, N.I., Mooney, W.D. (1995). Seismic velocity structure and composition of the continental crust: A global view. J. Geophys. Res. B100, 9761–9788.

Davies, J.H., Davies, D.R. (2010). Earth's surface heat flux. Solid Earth 1, 5–24.

Dejonghe, L. (2008). Carte géologique de Wallonie 1/25.000, feuille 55/5-6 Hotton–Dochamps. Notice explicative. Région Wallonne, Namur, 88 pp.

DEKORP Research Group (1991). Results of the DEKORP 1 (BELCORP-DEKORP) deep seismic reflection studies in the western part of the Rhenish Massif. Geophys. J. Int. 106, 203–227.

Deming, D. (1994). Fluid flow and heat transport in the upper continental crust. In: Parnell, J. (Ed.), Geofluids: Origin, Migration and Evolution of Fluids in Sedimentary Basins, Spec. Publ. 78. Geol. Soc., London, pp. 27–42.

Deming, D., Sass, J.H., Lachenbruch, A.H., De Rito, R.F. (1992). Heat flow and subsurface temperature as evidence for basin-scale ground-water flow, North Slope of Alaska. Geol. Soc. Am. Bull. 104, 528–542.

Demoulin, A., Hallot, E. (2009). Shape and amount of the Quaternary uplift of the western Rhenish shield and the Ardennes (western Europe). Tectonophysics 474, 696–708.

Downes, H. (1993). The nature of the lower continental crust of Europe: petrological and geochemical evidence from xenoliths. Phys. Earth Planet. Int. 79, 195–218.

Edel, J.-B., Schulmann, K (2009). Geophysical constraints and model of the „Saxothuringian and Rhenohercynian subductions – magmatic arc system" in NE France and SW Germany. Bull. Soc. Géol. Fr. 180, 545–558.

Fielitz, W., Mansy, J.-L. (1999). Pre- and synorogenic burial metamorphism in the Ardenne and neighbouring areas (Rhenohercynian zone, central European Variscides). Tectonophysics 309, 227–256.

Förster, A., Förster, H.-J. (2000). Crustal composition and mantle heat flow: Implications from surface heat flow and radiogenic heat production in the Variscan Erzgebirge (Germany). J. Geophys. Res. B 105, 27917–27938.

Förster, H.-J., Förster, A., Oberhänsli, R., Stromeyer, D. (2010). Lithospheric composition and thermal structure of the Arabian Shield in Jordan. Tectonophysics 481, 29–37.

Fuchs, S., Förster, A. (2014). Well-log based prediction of thermal conductivity of sedimentary successions: a case study from the North German Basin. Geophys. J. Int., 196, 291–311.

Fuchs, S., Schütz, F., Förster, H.-J., Förster, A. (2013). Evaluation of common mixing models for calculating bulk thermal conductivity of sedimentary rocks: Correction charts and new conversion equations. Geothermics 47, 40–52.

Furlong, K.P., Chapman, D.S. (2013). Heat flow, heat generation, and the thermal state of the lithosphere. Ann. Rev. Earth Planet. Sci. 41, 385–410.

Furtak, H., 1965. Die Tektonik der underdevonischen Gesteinsfolge im deutsch–belgisch–luxemburgischen Grenzgebiet. Geol. Mitt. 4, 273–332.

Geissler, W.H., Sodoudi, F., Kind, R. (2010). Thickness of the central and eastern European lithosphere as seen by S receiver functions. Geophys. J. Int. 181, 604–634.

Goes, S., van der Lee, S. (2002). Thermal structure of the North American uppermost mantle inferred from seismic tomography. J. Geophys. Res. B 107, 2050, http://dx.doi.org/10.1029/2000JB000049.

Goes, S., Spakman, W., Bijwaard, H. (1999). A lower mantle source for central European Volcanism. Science 286, 1928, http://dx.doi.org/10.1126/science.286.5446.1928.

Goes, S., Govers, R., Vacher, P. (2000a). Shallow mantle temperatures under Europe from P and S wave tomography. J. Geophys. Res. B105, 11153–11169.

Goes, S., Loohuis, J.J.P., Wortel, M.J.R., Govers, R. (2000b). The effect of plate stresses and shallow mantle temperatures on tectonics of northwestern Europe. Global Planet. Change 27, 23–38.

Graulich, J. M. (1980). Le sondage de Grand-Halleux. In: Professional Paper 175, Administration des Mines. Service géologique de Belgique, Brussels, 78 pp.

Hasterok, D., Chapman, D.S (2011). Heat production and geotherms for the continental lithosphere. Earth Planet. Sci. Lett. 307, 59–70.

Haenel, R. (1971). Heat flow measurements and a first heat flow map of Germany. Z. Geophys. 37, 975–992.

Haenel, R. (1983). Geothermal investigations in the Rhenish Massif. In: Fuchs, K., von Gehlen, K., Mälzer, H., Murawski, H., Semmel, A. (Eds.), Plateau Uplift: The Rhenish Shield – A Case History. Springer, Berlin, Heidelberg, New York, Tokyo, pp. 228–246.

Haenel, R., Legrand, R., Balling, N., Saxov, S., Bram, K., Gable, R., Meunier, J., Fanelli, M., Rossi, A., Salomone, M., Taffi, L., Prins, S., Burley, A.J., Edmunds, W.M., Oxburgh, E.R., Richardson, S.W., Wheildon, J. (1980), Atlas of Subsurface Temperatures in the European Community. Publ. No. EUR 6578 EN of the Commission of the European Communities, Directorate-General Telecommunication, Information Industries and Innovation, Luxembourg, 36 pp.

Häfner, F., Kött, A., Spindeldreher, J., Rein, B., Grubert, A. (2007). Nutzung von oberflächennaher Erdwärme für die Gebäudeheizung in Rheinland-Pfalz. Landesamt für Geologie und Bergbau Rheinland-Pfalz, Mainz, 97 pp., unpublished report.

Hieronymus, C.F., Shomali, Z.H., Pedersen, L.B. (2007). A dynamical model for generating sharp seismic velocity contrasts underneath continents: Application to the Sorgenfrei–Tornquist Zone. Earth Planet. Sci. Lett. 262, 77–91.

Hollmann, E.G. (1997). Der variszische Vorlandüberschiebungsgürtel der Ostbelgischen Ardennen – Ein bilanziertes Modell. Aachener Geowiss. Beitr. 25, 235 pp.

Hückel, B., Kappelmeyer, O. (1966). Geothermische Untersuchungen im Saarkarbon. Z. Dt. Geol. Ges. 117 (1), 280–311.

Hurter, S., Haenel (2002). Atlas of Geothermal Resources in Europe. Publ. No. EUR 17811 of the European Commission, Office for Official Publ. of the European Communities, Luxembourg, 91 pp.

Jacoby, W.R., Joachimi, H, Gerstenecker, C (1983). The gravity field in the Rhenish Massif, in: Fuchs, K., von Gehlen, K., Mälzer, H., Murawski, H., Semmel, A. (Eds.), Plateau Uplift: The Rhenish Shield – A case history. Springer, Berlin, Heidelberg, New York, Tokyo, pp. 247–258.

Jaupart, C., Mareschal, J.-C. (2003). Constraints on crustal heat production from heat flow data. Treatise on Geochem. 3, 65–84.

Jones, A.G., Plomerova, J., Korja, T., Sodoudi, F., Spakman, W. (2010). Europe from the bottom up: A statistical examination of the central and northern European lithosphere-asthenosphere boundary from comparing seismological and electromagnetic observations. Lithos 120, 14–29.

Keyser, M., Ritter, J.R.R., Jordan, M. (2002). 3D shear-wave velocity structure of the Eifel plume, Germany. Earth Planet. Sci. Lett. 203, 59–82.

Kölschbach, K.-H. (1986). Eine nach SE gerichtete Aufschiebung auf der NW-Flanke der Moselmulde (Liesertal, SW-Eifel). N. Jb. Geol. Paläont., Mh., 671–680.

Konrad, H.J., Wachsmut, W. (1973). Zur Lithologie und Tektonik des Unterdevons im südlichen Oesling Luxemburgs. Publ. Serv. Géol. Luxemb. 5, 1–20.

Kukkonen, I.T., Peltonen, P. (1999). Xenolith-controlled geotherm for the central Fennoscandian Shield: implications for lithosphere–asthenosphere relations. Tectonophysics 304, 301–315.

Legrand, R. (1975). Jalons géothermiques. Mém. Expl. Cartes Géol. et Minières de la Belgique, vol. 16. Service géologique de Belgique, Brussels, 46 pp.

LGB (Landesamt für Geologie und Bergbau Rheinland-Pfalz) (Ed.) (2005). Geologie von Rheinland-Pfalz. Schweizerbart, Stuttgart, 400 pp.

Lucius, M. (1950). Das Oesling – Erläuterungen zu der geologischen Spezialkarte Luxemburgs. Publ. Serv. Géol. Luxemb., vol. 6. Luxembourg, 174 pp.

Manning, C.E., Ingebritsen, S.E. (1999). Permeability of the continental crust: Implications of geothermal data and metamorphic systems. Rev. Geophys. 37, 127–150.

McKenzie, D., Bickle, M.J. (1988). The volume and composition of melt generated by extension of the lithosphere. J. Petrol. 29, 625–679.

Mechie, J., Prodehl, C., Fuchs, K. (1983). The Long-Range Seismic Refraction Experiment in the Rhenish Massif. In: Fuchs, K., von Gehlen, K., Mälzer, H., Murawski, H., Semmel, A. (Eds.), Plateau Uplift: The Rhenish Shield – A Case History. Springer, Berlin, Heidelberg, New York, Tokyo, pp. 260–275.

Meissner, R., Springer, M., Murawski, H, Bartelsen, H., Flüh, E.R., Dürschner, H. (1983). Combined seismic reflection-refraction investigations in the Rhenish Massif and their relation to recent tectonic movements. In: Fuchs, K., von Gehlen, K., Mälzer, H., Murawski, H., Semmel, A. (Eds.), Plateau Uplift: The Rhenish Shield – A Case History. Springer, Berlin, Heidelberg, New York, Tokyo, pp. 276–287.

Mengel, K., Sachs, P.M., Stosch, H.G., Wörner, G., Loock, G. (1991). Crustal xenoliths from Cenozoic volcanic fields of West Germany: Implications for structure and composition of the continental crust. Tectonophysics 195, 271–289.

Meyer, D.E., Nagel J. (2001). 4.20.3 Proterozoikum. In: Hoth, K., Leonhardt, D. (Eds.), Stratigraphie von Deutschland II – Ordovizium, Kambrium, Vendium, Riphäikum – Teil II: Baden-Württemberg, Bayern, Hessen, Rheinland-Pfalz, Nordthüringen, Sachsen-Anhalt, Brandenburg., vol. 234. Cour. Forsch.-Inst. Senckenberg, Frankfurt a.M, pp. 119–120 (Deutsche Stratigraphische Kommission).

Meyer, W. (1994). Geologie der Eifel, third edition. Schweizerbart (Nägele und Obermiller), Stuttgart, 618 pp.

Meyer, W., Stets, J. (1980). Zur Paläogeographie von Unter- und Mitteldevon im westlichen und zentralen Rheinischen Schiefergebirge. Z. Dt. Geol. Ges. 131, 725–751.

Meyer, W., Stets, J. (1996). Das Rheintal zwischen Bingen und Bonn. In: Sammlung geol. Führer 89. Borntraeger, Berlin, Stuttgart, 386 pp.

Mittmeyer, H.G. (2008). Unterdevon der Mittelrheinischen und Eifeler Typ-Gebiete (Teile von Eifel, Westerwald, Hunsrück und Taunus). In: Stratigraphie von Deutschland VIII, Devon. Schriftenreihe Dt. Ges. Geowiss., vol. 52. Deutsche Stratigraphische Kommission, Hannover, pp. 139–203.

Mooney, W.D., Prodehl, C. (1978). Crustal structure of the Rhenish Massif and adjacent areas; a reinterpretation of existing seismic-refraction data. J. Geophys. 44, 573–601.

Murawski, H., Albers, H.J., Bender, P., Berners, H.-P., Dürr, St., Huckriede, R., Kauffmann, G., Kowalczyk, G., Meiburg, P., Müller, R., Muller, A., Ritzkowski, S., Schwab, K., Semmel, A., Stapf, K., Walter, R., Winter, K.-P., Zankl, H. (1983). Regional tectonic

setting and geological structure of the Rhenish Massif. In: Fuchs, K., von Gehlen, K., Mälzer, H., Murawski, H., Semmel, A. (Eds.), Plateau Uplift: The Rhenish Shield – A Case History. Springer, Berlin, Heidelberg, New York, Tokyo, pp. 9–38.

Norden, B., Förster, A., Balling, N. (2008). Heat flow and lithospheric thermal regime in the Northeast German Basin. Tectonophysics 460, 215–229.

Oncken, O., von Winterfeld, C., Dittmar, U. (1999). Accretion of a rifted passive margin: The Late Palaeozoic Rhenohercynian fold and thrust belt (Middle European Variscides). Tectonics 18, 75–91.

Oncken, O., Plesch, A., Weber, J., Ricken, W., Schrader, S. (2000). Passive margin detachment during arc-continent collision (Central European Variscides). In: Franke, W., Haak, V., Oncken, O., Tanner, D. (Eds.), Orogenic processes: Quantification and Modelling in the Variscan Belt. Spec. Publ. 179, Geol. Soc., London, pp. 199–216.

Pharaoh, T.C. (1999). Palaeozoic terranes and their lithospheric boundaries within the Trans-European Suture Zone (TESZ): a review. Tectonophysics 314, 17–41.

Pharaoh, T.C., Winchester, J.A., Verniers, J., Lassen, A., Seghedi, A. (2006). The western accretionary margin of the East European Craton: an overview. In: Gee, D.G., Stephenson, R.A. (Eds.), European Lithosphere Dynamics, vol. 32. Mem. Geol. Soc. London, 291–311.

Popov, Y.A., Pribnow, D.F.C., Sass, J.H., Williams, C.F., Burkhardt, H. (1999). Characterization of rock thermal conductivity by high-resolution optical scanning. Geothermics 28, 253–276.

Powell, W.G., Chapman, D.S., Balling, N., Beck, A.E. (1988). Continental heat flow density. In: R. Haenel, L. Rybach, L. Stegena (Eds.), Handbook of Terrestrial Heat-Flow Density Determination. Kluwer Academic Press, Dordrecht, pp. 167–222.

Raikes, S. (1980). Teleseismic evidence for velocity heterogeneity beneath the Rhenish Massif. J. Geophys. 48, 80–83.

Raikes, S., Bonjer, K.-P. (1983). Large-scale mantle heterogeneity beneath the Rhenish Massif and its vicinity from teleseismic P-residuals measurements. In: Fuchs, K., von Gehlen, K., Mälzer, H., Murawski, H., Semmel, A. (Eds.), Plateau Uplift: The Rhenish Shield – A Case History. Springer, Berlin, Heidelberg, New York, Tokyo, pp. 315–331.

Ritter, J.R.R. (2007). The seismic signature of the Eifel Plume. In: Ritter, J.R.R., Christensen, U.R. (Eds.), Mantle Plumes. A Multidisciplinary Approach. Springer, Berlin, Heidelberg, pp. 379–404.

Rudnick, R.L., Fountain, D.M. (1995). Nature and composition of the continental crust: a lower crustal perspective. Rev. Geophys. 33, 267–309.

Rudnick, R.L., McDonough, W.F., O'Connell, R.J. (1998). Thermal structure, thickness and composition of continental lithosphere. Chem. Geol. 145, 395–411.

Rybach, L. (1976). Radioactive heat production; a physical property determined by the chemistry of rocks. In: Strens, R.G.J. (Ed.), The Physics and Chemistry of Minerals and Rocks. J. Wiley and Sons, London, New York, Sydney, pp. 309–318.

Rybach, L. (1988). Determination of heat production rate. In: R. Haenel, L. Rybach, L. Stegena (Eds.), Handbook of Terrestrial Heat-Flow Density Determination. Kluwer Academic Press, Dordrecht, pp. 125–142.

Schintgen, T., Förster, A. (2013). Geology and basin structure of the Trier–Luxembourg Basin – implications for the existence of a buried Rotliegend graben. Z. Dt. Ges. Geowiss. 164 (4), 615–637.

Schmincke, H.-J. (2007). The Quaternary volcanic fields of the east and west Eifel (Germany). In: Ritter, J.R.R., Christensen, U.R. (Eds.), Mantle Plumes. A Multidisciplinary Approach. Springer, Berlin, Heidelberg, pp. 241–322.

Schön, J.H. (1996). Physical properties of rocks: fundamentals and principles of petrophysics. In: Helbig, K., Teitel, S. (Eds.), Handbook of Geophysical Exploration, Section 8, Thermal Properties of Rocks. Pergamon, Oxford, UK, pp. 323–373.

Schütz, F., Förster, H.-J., Förster, A. (2014). Thermal conditions of the central Sinai Microplate inferred from new surface heat-flow values and continuous borehole temperature logging in central and southern Israel. J. Geodyn. 76, 8–24.

Seiberlich, C.K.A., Ritter, J.R.R., Wawerzinek, B. (2013). Topography of the lithosphere–asthenosphere boundary below the Upper Rhine Graben Rift and the volcanic Eifel region, Central Europe. Tectonophysics 603, 222–236.

Seipold, U. (2001). Der Wärmetransport in kristallinen Gesteinen unter den Bedingungen der kontinentalen Kruste. In: Scientific Technical Report STR 01/13. GeoForschungsZentrum Potsdam, Potsdam, 148 pp.

Shaw, C.S.J., Eyzaguirre, J., Fryer, B., Gagnon, J. (2005). Regional variations in the mineralogy of metasomatic assemblages in mantle xenoliths from the West Eifel Volcanic Field, Germany. J. Petrol. 46, 945–972.

Sintubin, M., Everaerts, M. (2002). A compressional wedge model for the lower Palaeozoic Anglo-Brabant Belt (Belgium) based on potential field data. In: Winchester, J.A.,

Pharaoh, T.C., Verniers, J. (Eds.), Palaeozoic Amalgamation of Central Europe, vol. 201. Geol. Soc., London, pp. 327–343.

Smith, L., Chapman, D.S. (1983). On the thermal effects of groundwater flow. J. Geophys. Res. B88, 593–608.

Somerton, W.H. (1992). Thermal Properties and Temperature Related Behaviour of Rock/Fluid Systems. In: Developments in Petroleum Sciences 37. Elsevier, Amsterdam, 256 pp.

Stets, J. (2004). Geologische Karte der Wittlicher Rotliegend-Senke 1:50000 mit Erläuterungen. Landesamt für Geologie und Bergbau Rheinland-Pfalz, Mainz, 82 pp.

Stets, J., Schäfer, A. (2002). Depositional environments in the Lower Devonian siliciclastics of the Rhenohercynian Basin (Rheinisches Schiefergebirge, W-Germany) – Case studies and a model. Contr. Sed. Geol. 22, 77 pp.

Stober, I., Bucher, K. (2005). The upper continental crust, an aquifer and its fluid: hydraulic and chemical data from 4 km depth in fractured crystalline basement rocks at the KTB test site. Geofluids 5, 8–19.

Stosch, H.-G., Schmucker, A., Reys, C. (1991). The nature and geological history of the deep crust under the Eifel, Germany. Terra Nova 4, 53–62.

Turcotte, D.L., Schubert, G. (2002). Geodynamics, second ed. Cambridge University Press, Cambridge, 456 pp.

Vandenberghe, N., Fock, W. (1989). Temperature data in the subsurface of Belgium. In: Čermák, V., Rybach, L., Decker, E.R. (Eds.), Heat Flow and Lithosphere Structure, vol. 164. Tectonophysics, pp 237–250.

Vandenberghe, N. (2002). Belgium. In: Hurter, S., Haenel, R., 2002 (Eds.), Atlas of Geothermal Resources in Europe. Publ. No. EUR 17811 of the European Commission, Office for Official Publ. of the European Communities, Luxembourg, pp. 23–24.

Vasseur, G. (1980). Some aspects of heat flow in France. In: Strub, A.S., Ungemach, P. (Eds.), Advances in European Geothermal Research, Second International Seminar on the Results of EC Geothermal Energy Research. Reidel Publ. Co., Dordrecht, pp. 170–175.

Verniers, J., Pharaoh, T., André, L., Debacker, T.N., De Vos, W., Everaerts, M., Herbosch, A., Samuelsson, J., Sintubin, M., Vecoli, M. (2002). The Cambrian to mid Devonian basin development and deformation history of Eastern Avalonia, east of the Midlands Microcraton: new data and a review. In: Winchester, J.A., Pharaoh, T.C., Verniers, J. 2002 (Eds.), Palaeozoic Amalgamation of Central Europe, Spec. Publ. 201. Geol. Soc., London, pp. 47–93.

Vilà, M., Fernández, M., Jiménez-Munt, I. (2010). Radiogenic heat production variability of some common lithological groups and its significance to lithospheric thermal modelling. Tectonophysics 490, 152–164.

Voll, G. (1983). Crustal xenoliths and their evidence for crustal structure underneath the Eifel volcanic district. In: Fuchs, K., von Gehlen, K., Mälzer, H., Murawski, H., Semmel, A. (Eds.), Plateau Uplift: The Rhenish Shield – A Case History. Springer, Berlin, Heidelberg, New York, Tokyo, pp. 336–342.

Wagner, H.W., Kremb-Wagner, F., Koziol, M., Negendank, J.F.W (2012). Trier und Umgebung, third edition. Gebr. Bornträger, Stuttgart, 396 pp.

Walker, K.T., Bokelmann, G.H.R., Klemperer, S.L., Bock, G. (2005). Shear-wave splitting around the Eifel hotspot: evidence for a mantle upwelling. Geophys. J. Int. 163, 962–980.

Wildberger, J. (1992). Zur tektonischen Entwicklung des südwestlichen Hunsrücks (SW-Deutschland). Mitt. Pollichia 79, 5–119.

Wittenberg, A., Vellmer, C., Kern, H., Mengel, K. (2000). The Variscan lower continental crust: evidence for crustal delamination from geochemical and petrophysical investigations. In: Franke, W., Haak, V., Oncken, O., Tanner, D. (Eds.), Orogenic Processes: Quantification and Modelling in the Variscan Belt, Spec. Publ. 179. Geol. Soc., London, pp. 401–414.

Wörner, G., Schminke, H.-U., Schreyer, W. (1982). Crustal xenoliths from the Quaternary Wehr volcano (East Eifel). Neues Jahrb. Miner. Abh. 144, 29–55.

Ziegler, P.A., Dèzes, P. (2006). Crustal evolution of Western and Central Europe. In: Gee, D.G., Stephenson, R.A. (Eds.), European Lithosphere Dynamics, vol. 32. Geol. Soc., London, Mem., pp. 43–56.

Ziegler, P.A., Dèzes, P. (2007). Cenozoic uplift of Variscan Massifs in the Alpine foreland: Timing and controlling mechanisms. Global Planet. Change 58, 237–269.

Ziegler, P.A., Schumacher, M.E., Dèzes, P., Van Wees, J.-D., Cloetingh, S. (2004). Post-Variscan evolution of the lithosphere in the Rhine Graben area: constraints from subsidence modelling. In: Wilson, M., Neumann, E.-R., Davies, G.R., Timmerman, M.J., Heeremans, M., Larsen, B.T. (Eds.), Permo-Carboniferous Magmatism and Rifting in Europe, Spec. Publ. 223. Geol. Soc., London, pp. 289–317.

Zitzmann, A., Grünig, S. (with contributions by Meyer, W., Stets, J., Mittmeyer, H.-G., Konrad, H.J., Ribbert, K.-H., Fuchs, G.) (1987). Geologische Übersichtskarte 1:200000, Blatt CC 6302 Trier. BGR (Bundesanstalt für Geowissenschaften und Rohstoffe), Hannover.

3.10 Supplementary material

3.10.1 Upscaling of thermal rock properties to geological formations

Thermal conductivity (TC) of samples was used to calculate TC of lithotypes. These TC values were transformed to formation TC by applying a weighted arithmetic mean based on the proportion of different lithotypes in each formation (Eq. 3.2; Section 3.4.1; Tables A.3.9–A.3.13 detailed in Tables A.3.4–A.3.8). Subsequently, the formation TC values were upscaled to thermal-model units (see Section 3.5.2; Table 3.7) by applying a weighted arithmetic mean similar to Eq. 3.2 (see Section 3.4.1), but accounting for the proportion/thickness of each formation within the model unit.

For the Mesozoic series, formation TC is characterized by anisotropy related to stratification. Due to the subhorizontal bedding in the Mesozoic succession, the orientation of anisotropy is constant. Therefore, anisotropy was accounted for throughout the upscaling procedure from sample TC, lithotype TC, formation TC to the TC of the model unit. The resulting anisotropy is relatively small. The uncertainty of TC of each geological unit is addressed by an error estimate (1σ) in the range of 5–15% for the basin facies (Table A.3.12) and 15–20% for the margin facies (Table A.3.13). The uncertainty/error is based on the quality of the borehole data, the lateral and vertical geological heterogeneity and the contrast in thermal conductivity of the lithotypes. The limited number of samples used per formation precluded the calculation of standard deviations. In addition, the bulk density of each formation was calculated using the corresponding values for the samples used for formation TC determination (Tables A.3.9–A.3.13 detailed in Tables A.3.4–A.3.6, A.3.2 and A.3.3). Similarly, for the Mesozoic, the bulk-formation porosity was determined without uncertainty indication (Tables A.3.2 and A.3.3).

In addition to anisotropy, for the Mesozoic sedimentary formations, two distinct facies types were discriminated (Schintgen and Förster, 2013): (1) for a basin facies and (2) for a margin facies. However, lateral variations and, thus, the geological complexity are difficult to adequately account for. The proportion of the different lithotypes in the formations was evaluated using relevant borehole sections if available (generally the case in the TLB). The resulting TC perpendicular to bedding for the entire Jurassic is 2.3 ± 0.1 W m^{-1} K^{-1}. The result for the Triassic is 2.7 ± 0.2 W m^{-1} K^{-1} for the basin and 2.8 ± 0.2 W m^{-1} K^{-1} for the margin facies, respectively. The resulting TC parallel to bedding for the entire Jurassic is 2.6 ± 0.1 W m^{-1} K^{-1}. The result for the Triassic is 3.0 ± 0.2 W m^{-1} K^{-1} and identical for both the basin and margin facies. TC of the margin facies in the Triassic succession is only insignificantly higher and an important observation is the fact that water saturation generally lowers the contrasts in

TC resulting from a large porosity range and, thus, reduces the impact of laterally heterogeneous geology on the overall TC.

For the thick and lithologically more homogeneous but intensively structured (folded/thrust) Lower Palaeozoic and Lower Devonian succession, estimations of the lithological composition are based on geological maps and bulk descriptions from field studies (Bultynck and Dejonghe, 2001; Dejonghe, 2008; Häfner et al., 2007, unpublished report; LGB, 2005; Lucius, 1950; Verniers et al., 2001). It is assumed that the proportions of lithotypes in the individual formations remain relatively constant, which is acceptable according to recent knowledge but, most importantly, a necessary assumption and simplification for the thermal model. A summary of the bulk TC values of the various Palaeozoic formations (in part subdivided into formation members) is reported in Tables A.3.9–A.3.11.

The anisotropy of TC has been considered in the calculation of formation TC. For the Palaeozoic series, variation of formation TC as a function of orientation due to anisotropy generally is small. For orientation-dependent variations of TC related to bedding for lithotypes such as Palaeozoic sandstone, quartzite, siltstone and silty slate mean lithotype TC was calculated. The reason is that, despite a higher anisotropy of siltstone and silty slate, the orientation/bedding of those rocks in the folded Palaeozoic basement cannot be assessed. By contrast, cleavage is more constant (e.g., Lucius, 1950; Graulich, 1980). Therefore, for orientation-dependent variations of TC related to cleavage for lithotypes such as shale and slate, TC parallel and perpendicular to cleavage was considered separately. The resulting TC (Eq. (3.2)) of the Lower Devonian formations in the Ardennes (Table A.3.10) as well as in the Eifel and Mosel Syncline/Hunsrück (Table A.3.11) is largely isotropic. This observation also was made by Häfner et al. (2007). In fact, slate presenting a relatively high anisotropy is a minor lithotype in the Lower Devonian, and shale is virtually isotropic. For these formations, mean formation TC values calculated using the two orientation-dependent values are sufficient to characterize a formation. Exceptions are the Lower Palaeozoic formations showing at least a weak anisotropy of 1.1, with the highest value of 1.4 in the slate-rich formations (Table A.3.9). Anisotropy in the Cambrian and Ordovician (Table A.3.9) is due to cleavage, which is practically horizontal at depth as described in the Lower Cambrian section of the 3,225-m-deep Grand-Halleux borehole (Graulich, 1980; Hollmann, 1997).

Values of formation thickness considered for the calculation of weighted arithmetic mean TC are variable (Tables A.3.9–A.3.13). Thickness estimates for the Belgian Ardennes (Bultynck and Dejonghe, 2001; Dejonghe, 2008; Verniers et al., 2001) are, in general, lower than those known for the central parts of the Rhenohercynian basin in the Eifel region and the Mosel

Syncline (e.g. Meyer and Stets, 1996; Stets and Schäfer, 2002). Especially for the buried and barely explored Lower Devonian units in the Luxembourgish Ardennes and the adjoining Eifel region, the available thickness values constitute rough estimates. This also pertains to the structurally complex thrust sheets of the Hunsrück, for which correct thickness values are difficult to obtain and associated with large lateral variations (e.g., LGB, 2005; Wildberger, 1992). The values preferred in this study (Tables A.3.9–A.3.11) are the most conservative, minimum thickness estimates published in literature, considering that the sum of the individual estimates honors the bulk thickness estimates for the Lochkovian, Siegenian and Emsian (LGB, 2005; Meyer and Stets, 1980, 1996) and the total estimated thickness of the Lower Devonian (10,000 m; Stets and Schäfer, 2002). In addition, the extremely high local thicknesses reported in literature for the Gladbach-Schichten, Kaub-Schichten (Hunsrückschiefer) and Taunusquarzit were reduced to values adaptable to the region of Luxembourg. Relative thickness variations within the sediment pile barely influence the calculated weighted average. Estimation of the uncertainty of formation TC is based on error propagation:

$$\sigma_{\lambda_{Fm}} = \lambda_{Fm} \sqrt{\sum_i^n \left(X_i \cdot \frac{\sigma_{\lambda_i}}{\lambda_i} \right)^2} \qquad (3.a1)$$

Where $\sigma_{\lambda_{Fm}}$ is the uncertainty of formation TC (in W m^{-1} K^{-1}), λ_{Fm} is the mean formation TC, X_i is the proportion of the different lithotypes within a formation and σ_{λ_i} is the standard deviation of TC λ_i of the different lithotypes. Uncertainties of formation TC were estimated by considering the standard deviations calculated for Palaeozoic formation TC. These uncertainties/errors frequently amount to 10–15% (Tables A.3.9–A.3.11) and depend on the homogeneity of the formation. Applying an error propagation law similar to Eq.(3.a1), the uncertainty (1σ) for a set of several formations generally is much smaller (i.e. 2–4%).

Table A.3.1: Supplement to Table 3.2. Details on calculation of the relationship between measured thermal conductivities of dry and saturated Paleozoic samples.

Sample	Litho	O	λ_{dry}					λ_{sat}					$\lambda_{sat}/\lambda_{dry}$				TF			A		ϕ		
			$\perp$	//	a	b	AM	$\perp$	//	a	b	AM	$\perp$	//	a	b	$\mu_{1/2}$	AM	σ	Dry	Sat		$\mu_{1/2}$	AM
			[W m^{-1} K^{-1}]					[W m^{-1} K^{-1}]														[%]		
War-01	Gn	L		3.17	2.92	2.81	2.97		3.67	3.58	3.34	3.53		1.16	1.23	1.19	1.19	1.20	0.05	1.1	1.1	2.8	4.5	4.5
War-04	Gs	L	2.02		2.91	2.10	2.34	2.41		3.30	2.70	2.80	1.19		1.13	1.28				1.4	1.4	6.2		
Sg3a-2	Sl	S_1	2.37	2.68				2.57	2.88				1.08	1.07			1.24	1.23	0.11	1.1	1.1	2.5	2.6	3.1
Sg1-003	Sl	S_1	2.42	2.69				2.72	3.11				1.12	1.16						1.1	1.1	1.8		
COL-02	Sl	S_1	2.44	2.60				3.04	3.39				1.25	1.30						1.1	1.1	1.8		
PLA-01	Sl	S_1	2.26	2.67				2.86	3.28				1.26	1.23						1.2	1.1	2.6		
PLA-06	Sl	S_1	2.01	2.41				2.78	3.13				1.38	1.30						1.2	1.1	6.5		
VEN-04	Sl	S_1	1.97	2.60				2.28	2.97				1.16	1.14						1.3	1.3	2.9		
BEL-03	Sl	S_1	2.42	2.74				3.34	3.81				1.38	1.39						1.1	1.1	3.4		
Sg1-007	Ssl	S_0	3.20	3.40				4.19	4.34				1.31	1.28			1.16	1.19	0.08	1.1	1.0	3.8	2.7	2.7
BIH-04	Ssl	S_0	2.10	2.48				2.67	2.82				1.27	1.14						1.2	1.1	3.0		
BIH-06	Ssl	S_0	1.96	2.47				2.41	2.91				1.23	1.18						1.3	1.2	2.4		
MEU-03	Ssl	S_0	2.60	2.88				2.80	3.31				1.07	1.15						1.1	1.2	2.8		
LIE-04	Ssl	S_0	2.17	2.23				2.60	3.06				1.20	1.37						1.0	1.2	3.7		
SPA-02	Ssl	S_0	2.41	3.12				2.66	3.58				1.11	1.15						1.3	1.3	1.1		
GLE-03	Ssl	S_0	2.76	2.42				3.20	2.80				1.16	1.16						0.9	0.9	2.6		
WAN-08	Ssl	S_0	2.21	2.68				2.54	3.12				1.15	1.16						1.2	1.2	1.8		
E3-001	Sh	S_1	2.28	1.94				2.43	2.43				1.07	1.25			1.17	1.19	0.11	0.9	1.0	2.8	2.7	3.3
E1a-003	Sh	S_1	2.11	2.39				2.42	2.61				1.14	1.10						1.1	1.1	2.0		
E1a-004	Sh	S_1	2.52	2.53				2.73	2.69				1.08	1.06						1.0	1.0	2.1		
E1a-010	Sh	S_1	2.50	3.05				2.59	3.24				1.03	1.06						1.2	1.3	1.4		
Sg3-003	Sh	S_1	2.52	2.45				2.98	2.84				1.18	1.16						1.0	1.0	3.4		
Sg3-011	Sh	S_1	2.52	2.30				2.75	2.61				1.09	1.13						0.9	1.0	4.3		
VIL-05	Sh	S_1	2.05	2.28				2.63	3.15				1.28	1.38						1.1	1.2	8.0		
OIG-13	Sh	S_1	2.48	2.38				3.16	3.26				1.27	1.37						1.0	1.0	2.6		
FEP-07	Sh	S_1	2.42	2.60				3.11	3.28				1.29	1.26						1.1	1.1	3.4		
gd-02	Sh	S_1	3.16	3.29				4.08	4.23				1.29	1.28						1.0	1.0	2.6		

Litho – lithotype, Gn – Gneiss, Gs – mica schist, Sl – slate, Ssl – sandy slate, Sh – shale, Stst – siltstone, Sst – sandstone, Q – quartzite, O – sample orientation, L – foliation, S_1 – cleavage, S_0 – bedding, λ_{dry} and λ_{sat} – thermal conductivity in dry and saturated states, respectively, TF – transformation factor, A – anisotropy of thermal conductivity, ϕ – porosity, $\perp$ and // – perpendicular and parallel to orientation, a and b – other oblique orientations, AM – arithmetic mean, $\mu_{1/2}$ – median value, σ – standard deviation.

Table A.3.1 continued

Sample	Litho	O	λ_{dry}					λ_{sat}					$\lambda_{sat}/\lambda_{dry}$				TF			A		ϕ		
			⊥	//	a	b	AM	⊥	//	a	b	AM	⊥	//	a	b	$\mu_{1/2}$	AM	σ	Dry	Sat		$\mu_{1/2}$	AM
			[W m^{-1} K^{-1}]					[W m^{-1} K^{-1}]														[%]		
E2-002	Stst	S_0	2.35	2.34				2.64	2.73				1.12	1.17			1.13	1.17	0.10	1.0	1.0	2.1	1.8	2.9
E2-007	Stst	S_0	2.84	3.15				3.49	3.45				1.23	1.10						1.1	1.0	1.6		
E1b-012	Stst	S_0	2.50	2.63				2.88	2.98				1.15	1.13						1.1	1.0	2.9		
STH-04	Stst	S_0	2.90	3.30				3.26	3.69				1.12	1.12						1.1	1.1	1.3		
OIG-01	Stst	S_0	2.64	2.75				3.54	3.85				1.34	1.40						1.0	1.1	8.1		
MEU-08	Stst	S_0	2.83	3.22				2.99	3.65				1.06	1.13						1.1	1.2	1.5		
E1b-008	Sst	S_0	3.19	3.47				3.78	3.95				1.19	1.14			1.15	1.17	0.10	1.1	1.0	2.0	2.0	2.1
E1a-011	Sst	S_0	4.08	4.39				4.61	5.28				1.13	1.20						1.1	1.1	0.4		
VIL-08	Sst	S_0	3.18	3.39				4.10	3.76				1.29	1.11						1.1	0.9	3.5		
STH-09	Sst	S_0	4.92	5.08				6.55	6.78				1.33	1.34						1.0	1.0	1.3		
FEP-02	Sst	S_0	4.59	4.77				5.57	5.25				1.21	1.10						1.0	0.9	1.6		
SPA-06	Sst	S_0	3.86	4.09				3.94	4.14				1.02	1.01						1.1	1.1	2.6		
SLW-08	Sst	S_0	3.69	3.98				4.27	4.59				1.16	1.15						1.1	1.1	3.1		
q-001	Q	S_0	3.73	3.99				5.62	5.38				1.50	1.35			1.37	1.38	0.09	1.1	1.0	12.7	6.0	6.4
WAN-06	Q	S_0	4.40	4.32				5.74	5.52				1.30	1.28						1.0	1.0	0.5		
HUR-12	Q	S_0	4.41	4.44				6.09	6.42				1.38	1.45						1.0	1.1	6.0		
GH835	Sl	S_1	2.49	2.51				2.56	2.55				1.03	1.01			1.03	1.04	0.04	1.0	1.0	0.6	0.3	0.4
GH2008	Sl	S_1	2.35	2.62				2.37	2.67				1.01	1.02						1.1	1.1	0.4		
GH2331	Sl	S_1	2.51	3.87				2.73	4.03				1.09	1.04						1.5	1.5	0.3		
GH2386	Sl	S_1	2.56	4.24				2.48	4.55				0.97	1.07						1.7	1.8	0.2		
GH2728	Sl	S_1	2.31	4.47				2.51	4.63				1.09	1.04						1.9	1.8	0.3		
GH350	Q	S_0	5.57	5.60				6.11	6.21				1.10	1.11			1.10	1.12	0.06	1.0	1.0	0.1	0.1	0.2
GH2021	Q	S_0	4.87	4.69				5.28	4.89				1.08	1.04						1.0	0.9	0.3		
GH2600	Q	S_0	5.06	5.15				6.01	6.10				1.19	1.18						1.0	1.0	0.1		

Table A.3.2: Details on samples used to compose the density and porosity of the Mesozoic geological formations (basin facies) of the Trier–Luxembourg Basin.

						Density						Porosity		
						Sample		Litho.		Unit		Sample	Litho.	Unit
Strat. unit	Lithology	Vol.	Sample	Unit	Lithotype	Dry	Sat	Dry	Sat	Dry	Sat			
		[%]				[10^3 kg m^{-3}]						[%]		
dom4b	Sandy marlstone	100	Ru2	dom4b	Calcareous marlstone	2.35	2.48	2.35	2.48	2.35	2.48	13.4	13.4	13.4
dom4a	Limestone	80	Ru6	dom4a	Limestone	1.98	2.24	1.98	2.24	2.09	2.31	26.7	26.7	22.4
	Reef limestone (corals)	20	Ru4	dom4a	Limestone	2.55	2.60	2.55	2.60			5.3	5.3	
dom3	Sandy limestone	100	M9	dom3	Limestone	2.51	2.59	2.51	2.59	2.51	2.59	8.2	8.2	8.2
dom2	Limestone	70	M9	dom3	Limestone	2.51	2.59	2.51	2.59	2.50	2.59	8.2	8.2	8.4
	Marlstone	30	M8	dom1	Calcareous marlstone	2.47	2.60	2.47	2.60			8.9	8.9	
dom1	Marlstone	10	M8	dom1	Calcareous marlstone	2.47	2.60	2.47	2.60	2.10	2.26	8.9	8.9	15.7
	Marl	90	Bv4	lo4	Silty marl	2.06	2.22	2.06	2.22			16.5	16.5	
lo6-7 + dou	Iron-rich limestone + calcareous sandstone	50	M3	dou	Limestone	2.48	2.60	2.53	2.62	2.25	2.43	11.9	8.4	18.2
			M6	dou	Limestone	2.58	2.63					4.8		
	Iron-rich + marly sst.	50	M5	dou	Iron-rich limestone	1.97	2.25	1.97	2.25			28.1	28.1	
lo5	Marl	100	Bv4	lo4	Silty marl	2.06	2.22	2.06	2.22	2.06	2.22	16.5	16.5	16.5
lo4	Sandstone	50	Bv2	lo4	Marly siltstone	1.96	2.23	1.96	2.23	2.01	2.23	26.9	26.9	21.7
	Sandy marl	50	Bv4	lo4	Silty marl	2.06	2.22	2.06	2.22			16.5	16.5	
lo3	Marl	83	Bv11	lo3	Claystone	2.08	2.29	2.08	2.29	2.06	2.27	20.8	20.8	20.8
	Sandy marl	17	Bv12	lo3	Silty marl	1.96	2.17	1.96	2.17			20.6	20.6	
lo2	Marly claystone	100	Bv14	lo2	Claystone	2.11	2.32	2.12	2.31	2.12	2.31	20.9	19.5	19.5
			Bv16	lo1	Claystone	2.12	2.30					18.0		
lo1	Marly claystone	100	Bv14	lo2	Claystone	2.11	2.32	2.12	2.31	2.12	2.31	20.9	19.5	19.5
			Bv16	lo1	Claystone	2.12	2.30					18.0		
lm3b	Marly sandstone	19	Rb34	lm3a	Silty sandstone	2.45	2.55	2.45	2.55	2.09	2.27	9.7	9.7	16.7
	Sandy claystone	81	Rb40	lm3b	Clayey siltstone	2.01	2.20	2.01	2.20			18.4	18.4	
lm3a	Clayey sandstone	2	Rb34	lm3a	Silty sandstone	2.45	2.55	2.45	2.55	2.16	2.35	9.7	9.7	19.2
	Silty marl	98	Rb35	lm2	Marl	2.16	2.34	2.16	2.35			18.8	19.4	
			Rb36	lm2	Marl	2.15	2.35					19.9		

Strat. unit – stratigraphic unit, Vol. – volume fraction, Dry and Sat – dry and saturated conditions, respectively, Litho. – lithotype, sst. – sandstone, marlst. – marlstone, calc. – calcareous, fibr. – fibrous. Composition of individual units is estimated from different borehole sections located in the basin facies of the Trier–Luxembourg Basin.

Table A.3.2 continued

Strat. unit	Lithology	Vol. [%]	Sample	Unit	Lithotype	Density Sample Dry [10^3 kg m^{-3}]	Density Sample Sat [10^3 kg m^{-3}]	Density Litho. Dry [10^3 kg m^{-3}]	Density Litho. Sat [10^3 kg m^{-3}]	Density Unit Dry [10^3 kg m^{-3}]	Density Unit Sat [10^3 kg m^{-3}]	Porosity Sample [%]	Porosity Litho. [%]	Porosity Unit [%]
lm3	Clayey sandstone	11	Rb34	lm3a	Silty sandstone	2.45	2.55	2.45	2.55	2.14	2.32	9.7	9.7	18.0
	Silty marl	89	Rb35	lm2	Marl	2.16	2.34	2.11	2.30			18.8	19.0	
			Rb36	lm2	Marl	2.15	2.35					19.9		
			Rb40	lm3b	Clayey siltstone	2.01	2.20					18.4		
lm2	Clayey marl	100	Rb35	lm2	Marl	2.16	2.34	2.16	2.35	2.16	2.35	18.8	19.4	19.4
			Rb36	lm2	Marl	2.15	2.35					19.9		
lm1	Limestone	23	Rb39	li3	Marly limestone	2.62	2.66	2.62	2.66	2.26	2.42	3.8	3.8	15.8
	Marl	77	Rb35	lm2	Marl	2.16	2.34	2.16	2.35			18.8	19.4	
			Rb36	lm2	Marl	2.15	2.35					19.9		
li4	Clayey, silty marl	87	Rb38	li4	Marly siltstone	2.25	2.35	2.25	2.35	2.30	2.39	9.9	9.9	9.1
	Limestone	13	Rb39	li3	Marly limestone	2.62	2.66	2.62	2.66			3.8	3.8	
li3	Marlstone	59	Rw13	li1	Marlstone	2.31	2.38	2.31	2.38	2.44	2.49	6.7	6.7	5.5
	Limestone	41	Rb39	li3	Marly limestone	2.62	2.66	2.62	2.66			3.8	3.8	
li2	Sandstone	45	Rw10	li2	Sandstone	1.94	2.21	1.94	2.21	2.21	2.38	26.3	26.3	16.9
	Calcareous sandstone	55	Kb2	li2	Calcareous sandstone	2.43	2.53	2.43	2.52			9.5	9.2	
			Rw2	li2	Marly, calc. sandstone	2.42	2.51					8.9		
li1	Marlstone	46	Rw13	li1	Marlstone	2.31	2.38	2.31	2.38	2.35	2.43	6.7	6.7	7.5
	Sandy marlstone	30	Gr6	li1	Sandy marlstone	2.21	2.33	2.21	2.33			11.8	11.8	
	Limestone	24	Rb39	li3	Marly limestone	2.62	2.66	2.62	2.66			3.8	3.8	
ko	Clayey marl	25	Rb5	km3	Clayey marl	2.44	2.50	2.38	2.46	2.30	2.40	6.5	8.1	9.3
			Rb9	km2	Marl	2.32	2.42					9.6		
	Sandstone + conglomerate	33	Gr7	ko1	Marly sandstone	2.23	2.37	2.23	2.37			13.6	13.6	
	Claystone	42	Rw13	li1	Marlstone	2.31	2.38	2.31	2.38			6.7	6.7	
km3	Dolomitic marlstone	45	Gr11	km3	Dolomitic marlstone	2.29	2.41	2.29	2.41	2.39	2.47	11.5	11.5	7.9
	Marl	39	Rb5	km3	Clayey marl	2.44	2.50	2.44	2.50			6.5	6.5	
	Anhydrite + gypsum	11	Rb16	km3	Anhydrite + fibr. gypsum	2.41	2.41	2.41	2.41			0.8	0.8	
	Dolomite	5	Rb17	km1	Dolomite	2.82	2.83	2.82	2.83			1.1	1.1	

Table A.3.2 continued

Strat. unit	Lithology	Vol. [%]	Sample	Unit	Lithotype	Density Sample Dry [10^3 kg m^{-3}]	Density Sample Sat [10^3 kg m^{-3}]	Density Litho. Dry [10^3 kg m^{-3}]	Density Litho. Sat [10^3 kg m^{-3}]	Density Unit Dry [10^3 kg m^{-3}]	Density Unit Sat [10^3 kg m^{-3}]	Porosity Sample [%]	Porosity Litho. [%]	Porosity Unit [%]
km2	Clayey marl	89	Rb9	km2	Marl	2.32	2.42	2.32	2.42	2.34	2.43	9.6	9.6	8.8
	Gypsum	0	Rb16	km3	Anhydrite + fibr. gypsum	2.41	2.41	2.41	2.41			0.8	0.8	
	Sandstone	11	Rb8	km2	Dolomitic sandstone	2.52	2.55	2.52	2.55			2.5	2.5	
km2S	Sandstone	90	Ki5	km2S	Silty, micaceous sst.	1.85	2.15	1.85	2.15	1.90	2.18	30.1	30.1	28.1
	Claystone	10	Rb9	km2	Marl	2.32	2.42	2.32	2.42			9.6	9.6	
km1	Clayey marl	4	Wb1	km1	Clayey marl	2.15	2.32	2.15	2.32	2.32	2.43	16.8	16.8	10.9
	Marl	30	Rb13	km1	Silty marl	2.27	2.39	2.27	2.39			12.3	12.3	
	Sandstone	6	Rb10	km1	Dolomitic sandstone	2.42	2.50	2.42	2.50			8.5	8.5	
	Dolomitic marlstone	60	Wb7	ku	Silty, dolomitic marlstone	2.35	2.45	2.35	2.45			10.0	10.0	
ku	Dolomite	7	Rb17	km1	Dolomite	2.82	2.83	2.82	2.83	2.30	2.43	1.1	1.1	12.0
	Marl	39	Wb1	km1	Clayey marl	2.15	2.32	2.15	2.32			16.8	16.8	
	Marlstone	54	Wb7	ku	Silty, dolomitic marlstone	2.35	2.45	2.35	2.45			10.0	10.0	
mos	Dolomitic sandstone	100	Id1	mos	Dolomitic sandstone	2.60	2.66	2.60	2.66	2.60	2.66	6.4	6.4	6.4
mo2	Marlstone	5	Wb15	mm1	Marlstone	2.53	2.55	2.53	2.55	2.74	2.77	2.4	2.4	2.3
	Dolomite	23	Wb8	mo1	Dolomite	2.81	2.82	2.81	2.82			1.0	1.0	
			Wb12	mo1	Dolomite	2.81	2.81					0.9		
	Dolomitic siltstone/marlstone	13	Wb9	mo1	Dolomitic siltstone	2.55	2.63	2.62	2.68			7.5	5.9	
			Wb10	mo1	Dolomitic marlstone	2.69	2.73					4.3		
	Marly dolomite	59	Wb11	mo1	Marly dolomite	2.77	2.79	2.77	2.79			2.2	2.1	
			Wb13	mo1	Marly dolomite	2.76	2.78					2.0		
mo1	Marlstone	0	Wb15	mm1	Marlstone	2.53	2.55	2.53	2.55	2.78	2.80	2.4	2.4	1.6
	Dolomite	52	Wb8	mo1	Dolomite	2.81	2.82	2.81	2.82			1.0	1.0	
			Wb12	mo1	Dolomite	2.81	2.81					0.9		
	Dolomitic siltstone/marlstone	3	Wb9	mo1	Dolomitic siltstone	2.55	2.63	2.62	2.68			7.5	5.9	
			Wb10	mo1	Dolomitic marlstone	2.69	2.73					4.3		
	Marly dolomite	45	Wb11	mo1	Marly dolomite	2.77	2.79	2.77	2.79			2.2	2.1	
			Wb13	mo1	Marly dolomite	2.76	2.78					2.0		

Table A.3.2 continued

Strat. unit	Lithology	Vol. [%]	Sample	Unit	Lithotype	Density						Porosity		
						Sample		Litho.		Unit		Sample	Litho.	Unit
						Dry	Sat	Dry	Sat	Dry	Sat			
						[10^3 kg m^{-3}]						[%]		
mm2	Marlstone	67	Wb15	mm1	Marlstone	2.53	2.55	2.44	2.48	2.56	2.59	2.4	4.7	3.5
			Me2	mm1	Silty, dolomitic marlstone	2.39	2.45					5.7		
			Me6	mm1	Dolomitic marlstone	2.39	2.45					6.1		
	Dolomite	33	Wb8	mo1	Dolomite	2.81	2.82	2.81	2.82			1.0	1.0	
			Wb12	mo1	Dolomite	2.81	2.81					0.9		
mm1	Marl (gypsum-rich)	45	Me12	mm1	Silty marl	2.22	2.27	2.30	2.37	2.43	2.48	5.2	7.1	5.3
			Me13	mm1	Silty marl	2.36	2.44					7.9		
			Me14	mm1	Silty marl	2.39	2.47					8.6		
			Me15	mm1	Silty marl	2.24	2.31					6.7		
	Dolomitic marlstone	27	Me2	mm1	Silty, dolomitic marlstone	2.39	2.45	2.44	2.48			5.7	4.7	
			Me6	mm1	Dolomitic marlstone	2.39	2.45					6.1		
			Wb15	mm1	Marlstone	2.53	2.55					2.4		
	Dolomite	3	Wb8	mo1	Dolomite	2.81	2.82	2.81	2.82			1.0	1.0	
			Wb12	mo1	Dolomite	2.81	2.81					0.9		
	Sandstone	13	Me7	mm1	Silty sandstone	2.47	2.53	2.47	2.53			5.8	5.8	
	Anhydrite	12	Me8	mm1	Anhydrite	2.74	2.74	2.74	2.74			0.1	0.1	
mu2	Dolomite	20	Rd18	mu	Marly dolomite	2.66	2.69	2.66	2.69	2.46	2.54	3.1	3.1	7.6
	Marlstone	55	Rd17	mu	Dolomitic marlstone	2.43	2.51	2.43	2.51			7.3	7.3	
	Sandy marlstone	25	Rd14	mu	Dolomitic, sandy marlstone	2.37	2.49	2.37	2.49			11.7	11.7	
mu1	Dolomite	2	Rd18	mu	Marly dolomite	2.66	2.69	2.66	2.69	2.39	2.50	3.1	3.1	10.2
	Marlstone	31	Rd17	mu	Dolomitic marlstone	2.43	2.51	2.43	2.51			7.3	7.3	
	Sandy marlstone	67	Rd14	mu	Dolomitic, sandy marlst.	2.37	2.49	2.37	2.49			11.7	11.7	
so2	Sandstone	46	Rd1	so1	Dolomitic sandstone	2.20	2.38	2.18	2.36	2.23	2.38	17.9	18.7	15.0
			Rd4	so1	Dolomitic sandstone	2.15	2.34					19.5		
	Claystone	54	Rd12	so1	Silty claystone	2.27	2.39	2.27	2.39			11.9	11.9	
so1	Dolomitic sandstone	71	Rd1	so1	Dolomitic sandstone	2.20	2.38	2.18	2.36	2.20	2.37	17.9	18.7	16.7
			Rd4	so1	Dolomitic sandstone	2.15	2.34					19.5		
	Clayey sst./sandy claystone	29	Rd12	so1	Silty claystone	2.27	2.39	2.27	2.39			11.9	11.9	

Table A.3.2 continued

Strat. unit	Lithology	Vol.	Sample	Unit	Lithotype	Density						Porosity		
						Sample		Litho.		Unit		Sample	Litho.	Unit
						Dry	Sat	Dry	Sat	Dry	Sat			
		[%]				[10^3 kg m^{-3}]						[%]		
sm (+ su)	Sandstone	81	Bi2	sm	Sandstone (soft)	2.05	2.27	2.05	2.27	2.08	2.29	21.9	21.9	20.6
	Sandstone (conglomeratic)	12	Bi5	sm	Sandstone (coarse, gravel)	2.20	2.36	2.20	2.36			16.6	16.6	
	Claystone	7	Rd12	so1	Silty claystone	2.27	2.39	2.27	2.39			11.9	11.9	

Table A.3.3: Details on samples used to compose the density and porosity of Mesozoic geological formations (margin facies) of the Trier-Luxembourg Basin.

						Density						Porosity		
						Sample		Litho.		Unit		Sample	Litho.	Unit
Strat. unit	Lithology	Vol. [%]	Sample	Unit	Lithotype	Dry	Sat	Dry	Sat	Dry	Sat			
						[10^3 kg m^{-3}]						[%]		
km2	Sandy marlstone	47	Rb12	km1	Sandy marlstone	2.38	2.45	2.34	2.43	2.34	2.43	6.7	9.7	9.8
+ km2S			Rb11	km1	Marly sandstone	2.35	2.41					6.3		
			El3	km1	Clayey sandstone	2.35	2.48					13.3		
	Sandy marl	35	Rb13	km1	Silty marl	2.27	2.39	2.27	2.39			12.3	12.3	
	Dolomitic sandstone	18	Rb10	km1	Dolomitic sandstone	2.42	2.50	2.47	2.53			8.5	5.5	
			Rb8	km2	Dolomitic sandstone	2.52	2.55					2.5		
km1	Sandy marlstone	51	Rb12	km1	Sandy marlstone	2.38	2.45	2.36	2.45	2.40	2.48	6.7	8.8	8.3
			Rb11	km1	Marly sandstone	2.35	2.41					6.3		
			El3	km1	Clayey sandstone	2.35	2.48					13.3		
	Conglomeratic dolomite	2	Rb17	km1	Dolomite (marly)	2.82	2.83	2.82	2.83			1.1	1.1	
	Dolomitic + sandy congl.	14	Rb19	km1	Sandy, dolomitic congl.	2.52	2.57	2.52	2.57			5.0	5.0	
	Marly sandstone	24	Rb10	km1	Dolomitic sandstone	2.42	2.50	2.42	2.50			8.5	8.5	
	Marl	9	Rb13	km1	Silty marl	2.27	2.39	2.27	2.39			12.3	12.3	
ku	Siltstone	21	Rb21	ku	Silty marlstone	2.44	2.51	2.44	2.51	2.39	2.49	7.3	7.3	9.7
	Marl + claystone	23	Ev1	ku	Sandy, dolomitic marlst.	2.30	2.45	2.26	2.43			14.9	16.9	
			Ev3	ku	Sandy, dolomitic marl	2.22	2.41					18.8		
	Sandstone	48	Rb12	km1	Sandy marlstone	2.38	2.45	2.36	2.45			6.7	8.8	
			Rb11	km1	Marly sandstone	2.35	2.41					6.3		
			El3	km1	Clayey sandstone	2.35	2.48					13.3		
	Sandy dolomite	8	Rb17	km1	Dolomite (marly)	2.82	2.83	2.82	2.83			1.1	1.1	

Strat. unit – stratigraphic unit, Vol. – volume fraction, Dry and Sat – dry and saturated conditions, respectively, Litho. – lithotype, congl. – conglomerate, marlst. – marlstone. Composition of individual units is estimated from different borehole sections located in the margin facies of the Trier–Luxembourg Basin.

Table A.3.3 continued

						Density						Porosity		
						Sample		Litho.		Unit		Sample	Litho.	Unit
Strat. unit	Lithology	Vol. [%]	Sample	Unit	Lithotype	Dry	Sat	Dry	Sat	Dry	Sat	[%]		
						[10^3 kg m^{-3}]								
mo(s)	Marly, sandy dolomite	24	Rb24	mo	Marly dolomite	2.69	2.72	2.69	2.72	2.50	2.59	3.1	3.1	9.4
(Rebierg +		15	Rb25	mo	Marly, sandy dolomite	2.79	2.80	2.79	2.80			1.0	1.0	
Everlange)	Dolomitic sandstone	23	Ev5	mo	Dolomitic sandstone	2.40	2.53	2.40	2.53			13.4	13.4	
		11	Id1	mos	Dolomitic sandstone	2.60	2.66	2.60	2.66			6.4	6.4	
	Sandstone + siltstone	11	Ev9	mg	Sandstone	1.98	2.24	1.98	2.24			26.9	26.9	
		6	Ev11	mg	Sandy siltstone	2.22	2.41	2.22	2.41			18.6	18.6	
		10	Me11	mm1	Silty sandstone	2.49	2.56	2.49	2.56			6.9	6.9	
mo(s)	Dolomitic sandstone	11	Id1	mos	Dolomitic sandstone	2.60	2.66	2.60	2.66	2.67	2.71	6.4	6.4	4.4
(Bissen +	Marlstone	5	Wb15	mm1	Marlstone	2.53	2.55	2.53	2.55			2.4	2.4	
Mersch)	Dolomite	19	Wb8	mo1	Dolomite	2.81	2.82	2.81	2.82			1.0	1.0	
			Wb12	mo1	Dolomite	2.81	2.81					0.9		
	Dolomitic siltstone/marlstone	54	Wb9	mo1	Dolomitic siltstone	2.55	2.63	2.62	2.68			7.5	5.9	
			Wb10	mo1	Dolomitic marlstone	2.69	2.73					4.3		
	Marly dolomite	11	Wb11	mo1	Marly dolomite	2.77	2.79	2.765	2.79			2.2	2.1	
			Wb13	mo1	Marly dolomite	2.76	2.78					2.0		
mg	Sandstone/conglomerate	27	Ev9	mg	Sandstone	1.98	2.24	1.98	2.24	2.24	2.38	26.9	26.9	13.5
(Rebierg +	Siltstone	11	Ev11	mg	Sandy siltstone	2.22	2.41	2.22	2.41			18.6	18.6	
Everlange)		12	Me11	mm1	Silty sandstone	2.49	2.56	2.49	2.56			6.9	6.9	
	Dolomite	4	Rd18	mu	Marly dolomite	2.66	2.69	2.66	2.69			3.1	3.1	
	Clay-/marlstone	46	Me12	mm1	Silty marl	2.22	2.27	2.30	2.37			5.2	7.1	
			Me13	mm1	Silty marl	2.36	2.44					7.9		
			Me14	mm1	Silty marl	2.39	2.47					8.6		
			Me15	mm1	Silty marl	2.24	2.31					6.7		

Table A.3.3 continued

Strat. unit	Lithology	Vol. [%]	Sample	Unit	Lithotype	Density Sample Dry [10^3 kg m^{-3}]	Density Sample Sat [10^3 kg m^{-3}]	Density Litho. Dry [10^3 kg m^{-3}]	Density Litho. Sat [10^3 kg m^{-3}]	Density Unit Dry [10^3 kg m^{-3}]	Density Unit Sat [10^3 kg m^{-3}]	Porosity Sample [%]	Porosity Litho. [%]	Porosity Unit [%]
mm	Marl (gypsum-rich)	70	Me12	mm1	Silty marl	2.22	2.27	2.30	2.37	2.37	2.43	5.2	7.1	6.3
(Mersch)			Me13	mm1	Silty marl	2.36	2.44					7.9		
			Me14	mm1	Silty marl	2.39	2.47					8.6		
			Me15	mm1	Silty marl	2.24	2.31					6.7		
	Dolomite	5	Wb8	mo1	Dolomite	2.81	2.82	2.81	2.82			1.0	1.0	
			Wb12	mo1	Dolomite	2.81	2.81					0.9		
	Dolomitic marlstone	21	Me2	mm1	Silty, dolomitic marlstone	2.39	2.45	2.42	2.48			5.7	5.9	
			Me6	mm1	Dolomitic marlstone	2.39	2.45					6.1		
			Me7	mm1	Silty sandstone	2.47	2.53					5.8		
	Anhydrite	4	Me8	mm1	Anhydrite	2.74	2.74	2.74	2.74			0.1	0.1	
mu	Sandy/marly dolomite	3	Rd18	mu	Marly dolomite	2.66	2.69	2.66	2.69	2.28	2.42	3.1	3.1	13.3
	Sandstone	6	Ev13	mu	Dolomitic sandstone	2.19	2.39	2.19	2.39			19.4	19.4	
	Sandy marlstone	3	Rd14	mu	Dolomitic, sandy marlst.	2.37	2.49	2.37	2.49			11.7	11.7	
	Dolomitic marlstone	11	Rd17	mu	Dolomitic marlstone	2.43	2.51	2.43	2.51			7.3	7.3	
	Claystone	51	Rd12	so1	Silty claystone	2.27	2.39	2.27	2.39			11.9	11.9	
	Siltstone	26	Ev11	mg	Sandy siltstone	2.22	2.41	2.22	2.41			18.6	18.6	
so2	Dolomitic sandstone	22	Rd1	so1	Dolomitic sandstone	2.20	2.38	2.18	2.36	2.22	2.36	17.9	18.7	14.5
			Rd4	so1	Dolomitic sandstone	2.15	2.34					19.5		
	Sandstone	24	Ev19	so	Marly sandstone	2.13	2.30	2.13	2.30			16.4	16.4	
	Claystone + (sandy) siltstone	54	Rd12	so1	Silty claystone	2.27	2.39	2.27	2.39			11.9	11.9	
so1	Conglomerate	25	Ev25	so	Sandy, dolomitic congl.	2.42	2.50	2.42	2.50	2.23	2.38	8.4	8.4	15.3
	Conglomeratic sandstone	43	Ev24	so	Sandstone (conglomeratic)	2.08	2.32	2.14	2.35			23.0	20.1	
			Rd1	so1	Sandstone (dolomitic)	2.20	2.38					17.9		
			Rd4	so1	Sandstone (dolomitic)	2.15	2.34					19.5		
	Marly sandstone	17	Ev19	so	Marly sandstone	2.13	2.30	2.13	2.30			16.4	16.4	
	Claystone + siltstone	15	Rd12	so1	Silty claystone	2.27	2.39	2.27	2.39			11.9	11.9	

Table A.3.4: Details on samples used to compose the petrophysical properties of the Cambrian and Ordovician groups, geological formations and their members in the Lower Paleozoic Stavelot Massif.

Group	Fm.	Mbr.	Lithology	Vol.	Sample	Lithotype	λ_{dry}			Litho. λ_{dry}				Fm. λ_{dry}			TF	λ_{sat} calc.		Litho. λ_{sat}			Fm. λ_{sat}			Density		
							O	⊥	//	⊥	//	AM	A	⊥	//	AM		⊥	//	⊥	//	AM	⊥	//	AM	Sample	Litho.	Fm.
				[%]				[W m^{-1}K^{-1}]										[W m^{-1}K^{-1}]								[10^{3} kg m^{-3}]		
SALM	BIH		Silty slate (includes slate 65% and minor sandstone 15 %)	100	BIH-01	Silty slate	S_0	1.88	2.34	2.0	2.4	2.2	1.2	2.0	2.4	2.2	1.18	2.22	2.76	2.3	2.8	2.6	2.3	2.8	2.6	2.78	2.78	2.78
					BIH-02	Silty slate	S_0	2.22	2.37								1.18	2.62	2.80							2.79		
					BIH-03	Silty slate	S_0	1.73	2.26								1.18	2.04	2.66							2.77		
					BIH-04	Silty slate	S_0	2.10	2.48								1.18	2.48	2.93							2.75		
					BIH-05	Silty slate	S_0	1.92	2.42								1.18	2.27	2.86							2.80		
					BIH-06	Silty slate	S_0	1.96	2.47								1.18	2.31	2.91							2.79		
	OTT	COL	Slate	100	COL-01	Slate	S_1	1.85	2.62	2.2	2.6	2.4	1.2	2.2	2.6	2.4	1.23	2.28	3.22	2.7	3.2	3.0	2.7	3.2	3.0	2.79	2.87	2.87
					COL-02	Slate	S_1	2.44	2.60								1.23	3.00	3.20							2.92		
					COL-04	Slate	S_1	2.41	2.88								1.23	2.96	3.54							2.90		
					COL-05	Slate	S_1	2.23	2.37								1.23	2.75	2.92							2.88		
		PLA	Slate	100	PLA-01	Slate	S_1	2.26	2.67	1.9	2.7	2.3	1.4	1.9	2.7	2.3	1.23	2.78	3.29	2.4	3.3	2.8	2.4	3.3	2.8	2.96	2.89	2.89
					PLA-02	Slate	S_1	2.04	3.67								1.23	2.51	4.51							2.90		
					PLA-06	Slate	S_1	2.01	2.41								1.23	2.47	2.96							2.86		
					PLA-07	Slate	S_1	1.48	1.85								1.23	1.82	2.28							2.84		
		MEU	Silty slate	90	MEU-01	Silty slate	S_0	2.00	2.46	2.4	2.8	2.6	1.2	2.4	2.9	2.6	1.18	2.36	2.90	2.8	3.4	3.1	2.9	3.4	3.1	2.94	2.92	2.91
					MEU-02	Silty slate	S_0	2.46	3.20								1.18	2.90	3.77							2.90		
					MEU-03	Silty slate	S_0	2.60	2.88								1.18	3.07	3.40							2.92		
			Sandstone	10	MEU-06	Sandstone	S_0	3.59	3.41	3.0	3.1	3.0	1.0				1.19	4.27	4.05	3.5	3.6	3.6				2.81	2.80	
					MEU-07	Siltstone	S_0	2.55	2.57								1.17	2.98	3.01							2.80		
					MEU-08	Siltstone	S_0	2.83	3.22								1.17	3.31	3.77							2.80		

Fm. – formation, Mbr. – Member, Vol. – volume fraction, λ_{dry} and λ_{sat} – thermal conductivity under dry and saturated conditions, respectively, Litho. – lithotype, O – orientation, S_0 and S_1 – bedding and cleavage, respectively, ⊥ and // – thermal conductivity perpendicular and parallel to orientation, AM – arithmetic mean, A – anisotropy, TF – transformation factor, sst. – sandstone. Lithological composition estimated after Geukens (2008) and Verniers et al. (2001).

Table A.3.4 continued

Group	Fm.	Mbr.	Lithology	Vol. [%]	Sample	Lithotype	λ_{dry} O	λ_{dry} ⊥ [W m^{-1}K^{-1}]	λ_{dry} // [W m^{-1}K^{-1}]	Litho. λ_{dry} ⊥ [W m^{-1}K^{-1}]	Litho. λ_{dry} // [W m^{-1}K^{-1}]	Litho. λ_{dry} AM [W m^{-1}K^{-1}]	Litho. λ_{dry} A [W m^{-1}K^{-1}]	Fm. λ_{dry} ⊥ [W m^{-1}K^{-1}]	Fm. λ_{dry} // [W m^{-1}K^{-1}]	Fm. λ_{dry} AM [W m^{-1}K^{-1}]	TF	λ_{sat} calc. ⊥ [W m^{-1}K^{-1}]	λ_{sat} calc. // [W m^{-1}K^{-1}]	Litho. λ_{sat} ⊥ [W m^{-1}K^{-1}]	Litho. λ_{sat} // [W m^{-1}K^{-1}]	Litho. λ_{sat} AM [W m^{-1}K^{-1}]	Fm. λ_{sat} ⊥ [W m^{-1}K^{-1}]	Fm. λ_{sat} // [W m^{-1}K^{-1}]	Fm. λ_{sat} AM [W m^{-1}K^{-1}]	Density Sample [10^3 kg m^{-3}]	Density Litho. [10^3 kg m^{-3}]	Density Fm. [10^3 kg m^{-3}]
	JAL	LIE	Silty slate	80	LIE-03	Silty slate	S_0	1.97	2.31	2.1	2.3	2.2	1.1	2.6	2.8	2.7	1.18	2.33	2.72	2.4	2.7	2.6	3.1	3.3	3.2	2.69	2.70	2.69
					LIE-04	Silty slate	S_0	2.17	2.23								1.18	2.56	2.63							2.70		
			Sandstone	20	LIE-01	Sandstone	S_0	4.68	4.79	4.7	4.8	4.7	1.0				1.19	5.57	5.70	5.6	5.7	5.6				2.68	2.68	
		SPA	Silty slate	40	SPA-01	Silty slate	S_0	2.76	2.98	2.6	3.1	2.8	1.2	3.3	3.5	3.4	1.18	3.25	3.52	3.0	3.6	3.3	3.9	4.1	4.0	2.74	2.75	2.69
					SPA-02	Silty slate	S_0	2.41	3.12								1.18	2.84	3.68							2.75		
			Quartzitic sst.	60	SPA-06	Quartzitic sst.	S_0	3.86	4.09	3.6	3.8	3.7	1.1				1.19	4.60	4.87	4.3	4.6	4.4				2.65	2.66	
					SPA-07	Quartzitic sst.	S_0	3.36	3.57								1.19	3.99	4.24							2.67		
		SLW	Slate	20	GH2386	Slate	S_1	2.56	4.24	2.4	4.4	3.4	1.9	3.2	3.7	3.4	1.04	2.67	4.41	2.5	4.6	3.5	3.7	4.2	3.9	2.78	2.78	2.72
					GH2585	Slate	S_1	2.36	4.52								1.04	2.46	4.70							2.78		
					GH2728	Slate	S_1	2.31	4.47								1.04	2.40	4.65							2.80		
					GH3072	Slate	S_1	2.27	4.52								1.04	2.36	4.70							2.76		
					GH3128	Slate	S_1	2.29	4.28								1.04	2.38	4.45							2.76		
			Silty slate	50	SPA-01	Silty slate	S_0	2.76	2.98	3.0	3.2	3.1	1.1				1.18	3.25	3.52	3.5	3.7	3.6				2.74	2.73	
					SPA-02	Silty slate	S_0	2.41	3.12								1.18	2.84	3.68							2.75		
					SLW-02	Silty slate	S_0	3.78	3.42								1.18	4.46	4.03							2.71		
			Quartzite	30	SLW-03	Quartzitic sst.	S_0	3.63	4.67	3.7	4.3	4.0	1.2				1.19	4.32	5.56	4.4	5.2	4.8				2.69	2.68	
					SLW-08	Sandstone	S_0	3.69	3.98								1.19	4.40	4.74							2.66		

Table A.3.4 continued

Group	Fm.	Mbr.	Lithology	Vol. [%]	Sample	Lithotype	λ_{dry} O	λ_{dry} ⊥ [W m^{-1}K^{-1}]	λ_{dry} // [W m^{-1}K^{-1}]	Litho. λ_{dry} ⊥ [W m^{-1}K^{-1}]	Litho. λ_{dry} // [W m^{-1}K^{-1}]	Litho. λ_{dry} AM [W m^{-1}K^{-1}]	Litho. λ_{dry} A [W m^{-1}K^{-1}]	Fm. λ_{dry} ⊥ [W m^{-1}K^{-1}]	Fm. λ_{dry} // [W m^{-1}K^{-1}]	Fm. λ_{dry} AM [W m^{-1}K^{-1}]	TF	λ_{sat} calc. ⊥ [W m^{-1}K^{-1}]	λ_{sat} calc. // [W m^{-1}K^{-1}]	Litho. λ_{sat} ⊥ [W m^{-1}K^{-1}]	Litho. λ_{sat} // [W m^{-1}K^{-1}]	Litho. λ_{sat} AM [W m^{-1}K^{-1}]	Fm. λ_{sat} ⊥ [W m^{-1}K^{-1}]	Fm. λ_{sat} // [W m^{-1}K^{-1}]	Fm. λ_{sat} AM [W m^{-1}K^{-1}]	Density Sample [10^3 kg m^{-3}]	Density Litho. [10^3 kg m^{-3}]	Density Fm. [10^3 kg m^{-3}]
REVIN	GLE	Rv5	Slate	50	GH2386	Slate	S_1	2.56	4.24	2.4	4.4	3.4	1.9	2.4	3.5	3.0	1.04	2.67	4.41	2.5	4.6	3.5	2.7	3.8	3.3	2.78	2.78	2.75
					GH2585	Slate	S_1	2.36	4.52								1.04	2.46	4.70							2.78		
					GH2728	Slate	S_1	2.31	4.47								1.04	2.40	4.65							2.80		
					GH3072	Slate	S_1	2.27	4.52								1.04	2.36	4.70							2.76		
					GH3128	Slate	S_1	2.29	4.28								1.04	2.38	4.45							2.76		
			Silty slate	50	GLE-03	Silty slate	S_0	2.76	2.42	2.5	2.6	2.6	1.0				1.18	3.26	2.85	3.0	3.1	3.0				2.72	2.73	
					GLE-04	Silty slate	S_0	2.58	2.77								1.18	3.04	3.27							2.70		
					GLE-05	Silty slate	S_0	2.25	2.62								1.18	2.66	3.10							2.76		
	VEN	Rv3 + 4	Slate	30	VEN-04	Slate	S_1	1.97	2.60	2.3	4.1	3.2	1.8	4.4	4.9	4.7	1.23	2.42	3.20	2.4	4.4	3.4	4.9	5.5	5.2	2.70	2.76	2.72
					GH2386	Slate	S_1	2.56	4.24								1.04	2.67	4.41							2.78		
					GH2585	Slate	S_1	2.36	4.52								1.04	2.46	4.70							2.78		
					GH2728	Slate	S_1	2.31	4.47								1.04	2.40	4.65							2.80		
					GH3072	Slate	S_1	2.27	4.52								1.04	2.36	4.70							2.76		
					GH3128	Slate	S_1	2.29	4.28								1.04	2.38	4.45							2.76		
			Quartzite	70	GH2600	Quartzite	S_0	5.06	5.15	5.2	5.4	5.3	1.0				1.12	5.66	5.77	5.8	6.0	5.9				2.68	2.70	
					GH3216	Quartzite	S_0	5.35	5.63								1.12	5.99	6.31							2.71		
	WAN	Rv1 + 2	Slate	40	GH2386	Slate	S_1	2.56	4.24	2.4	4.4	3.4	1.9	3.3	4.3	3.8	1.04	2.67	4.41	2.5	4.6	3.5	4.0	5.0	4.5	2.78	2.78	2.75
					GH2585	Slate	S_1	2.36	4.52								1.04	2.46	4.70							2.78		
					GH2728	Slate	S_1	2.31	4.47								1.04	2.40	4.65							2.80		
					GH3072	Slate	S_1	2.27	4.52								1.04	2.36	4.70							2.76		
					GH3128	Slate	S_1	2.29	4.28								1.04	2.38	4.45							2.76		
			Silty slate	20	WAN-07	Silty slate	S_0	2.26	2.55	2.3	3.0	2.6	1.3				1.18	2.67	3.00	2.7	3.6	3.2				2.77	2.85	
					WAN-08	Slate	S_1	2.21	2.68								1.23	2.71	3.29							2.88		
					WAN-09	Slate	S_1	2.33	3.74								1.23	2.86	4.60							2.89		
			Quartzite	40	WAN-02	Quartzite	S_0	4.42	4.50	4.8	4.9	4.8	1.0				1.38	6.10	6.21	6.1	6.2	6.1				2.62	2.67	
					WAN-06	Quartzite	S_0	4.40	4.32								1.38	6.07	5.97							2.67		
					WAN-10	Quartzite	S_0	4.68	4.81								1.38	6.46	6.64							2.66		
					GH2600	Quartzite	S_0	5.06	5.15								1.12	5.66	5.77							2.68		
					GH3216	Quartzite	S_0	5.35	5.63								1.12	5.99	6.31							2.71		

Table A.3.4 continued

Group	Fm.	Mbr.	Lithology	Vol. [%]	Sample	Lithotype	λ_{dry} O	λ_{dry} ⊥ [W m^{-1}K^{-1}]	λ_{dry} // [W m^{-1}K^{-1}]	Litho. λ_{dry} ⊥ [W m^{-1}K^{-1}]	Litho. λ_{dry} // [W m^{-1}K^{-1}]	Litho. λ_{dry} AM [W m^{-1}K^{-1}]	Litho. λ_{dry} A	Fm. λ_{dry} ⊥ [W m^{-1}K^{-1}]	Fm. λ_{dry} // [W m^{-1}K^{-1}]	Fm. λ_{dry} AM [W m^{-1}K^{-1}]	TF	λ_{sat} calc. ⊥ [W m^{-1}K^{-1}]	λ_{sat} calc. // [W m^{-1}K^{-1}]	Litho. λ_{sat} ⊥ [W m^{-1}K^{-1}]	Litho. λ_{sat} // [W m^{-1}K^{-1}]	Litho. λ_{sat} AM [W m^{-1}K^{-1}]	Fm. λ_{sat} ⊥ [W m^{-1}K^{-1}]	Fm. λ_{sat} // [W m^{-1}K^{-1}]	Fm. λ_{sat} AM [W m^{-1}K^{-1}]	Density Sample [10^3 kg m^{-3}]	Density Litho. [10^3 kg m^{-3}]	Density Fm. [10^3 kg m^{-3}]
DEVILLE	BEL		Slate/shale	50	BEL-01	Sandy shale	S_1	3.12	3.65	2.5	3.1	2.8	1.2	3.6	3.9	3.8	1.19	3.72	4.34	3.0	3.7	3.4	4.3	4.7	4.5	2.61	2.66	2.66
					BEL-02	Slate	S_1	1.98	2.81								1.23	2.44	3.45							2.67		
					BEL-03	Slate	S_1	2.42	2.74								1.23	2.98	3.37							2.69		
			Quartz. sst./ quartzite	50	BEL-06	Quartzitic sst.	S_0	4.63	4.83	4.6	4.8	4.7	1.0				1.19	5.50	5.75	5.5	5.7	5.6				2.66	2.66	
	HUR		Slate	45	GH516	Slate	S_1	2.15	2.54	2.4	3.2	2.8	1.3	3.6	4.0	3.8	1.04	2.24	2.64	2.5	3.3	2.9	4.3	4.6	4.5	2.81	2.79	2.70
					GH835	Slate	S_1	2.49	2.51								1.04	2.59	2.61							2.81		
					GH1453	Slate	S_1	2.34	4.32								1.04	2.43	4.49							2.79		
					GH2004	Slate	S_1	2.24	2.68								1.04	2.33	2.78							2.75		
					GH2008	Slate	S_1	2.35	2.62								1.04	2.45	2.72							2.77		
					GH2315	Slate	S_1	2.88	3.64								1.04	3.00	3.78							2.78		
					GH2331	Slate	S_1	2.51	3.87								1.04	2.61	4.03							2.82		
			Quartzite	55	GH350	Quartzite	S_0	5.57	5.60	4.6	4.7	4.6	1.0				1.12	6.24	6.27	5.7	5.8	5.8				2.63	2.63	
					GH2021	Quartzite	S_0	4.87	4.69								1.12	5.45	5.25							2.66		
					GH2355	Quartzitic sst.	S_0	3.48	4.17								1.12	3.90	4.67							2.73		
					HUR-03	Quartzite	S_0	4.82	5.15								1.38	6.65	7.11							2.65		
					HUR-05	Quartzite	S_0	4.62	4.49								1.38	6.37	6.19							2.64		
					HUR-06	Quartzitic sst.	S_0	4.29	4.33								1.19	5.11	5.15							2.60		
					HUR-12	Quartzite	S_0	4.41	4.44								1.38	6.08	6.12							2.51		

Table A.3.5: Details on samples used to compose the petrophysical properties of the Lower Devonian geological formations in the Belgian and Luxembourgish Ardennes.

Formation		Lithology	Vol.	Sample	Lithotype	λ_{dry}			Litho. λ_{dry}				Fm. λ_{dry}			TF	λ_{sat} calc.		Litho. λ_{sat}			Fm. λ_{sat}			Density		
Be	Lux		[%]			O	⊥	//	⊥	//	AM	A	⊥	//	AM		⊥	//	⊥	//	AM	⊥	//	AM	Sample	Litho.	Fm.
							[$Wm^{-1}K^{-1}$]		[$Wm^{-1}K^{-1}$]				[$Wm^{-1}K^{-1}$]				[$Wm^{-1}K^{-1}$]		[$Wm^{-1}K^{-1}$]			[$Wm^{-1}K^{-1}$]			[10^3 kg m^{-3}]		
	E3	Sandy shale	90	E3-001	Shale	S_1	2.28	1.94	2.1	1.8	1.9	0.9	2.2	2.0	2.1	1.19	2.71	2.31	2.5	2.2	2.3	2.6	2.4	2.5	2.66	2.60	2.62
				E3-002	Shale	S_1	1.87	1.83								1.19	2.22	2.18							2.55		
				E3-003	Shale	S_1	2.05	1.69								1.19	2.44	2.02							2.59		
			10	E3-005	Sandy shale	S_1	3.23	3.73	3.2	3.7	3.5	1.2				1.19	3.84	4.44	3.8	4.4	4.1				2.77	2.77	
	q	Quartzite	100	q-001	Quartzite	S_0	3.73	3.99	4.4	4.6	4.5	1.0	4.5	4.5	4.5	1.38	5.15	5.51	6.1	6.3	6.2	6.2	6.2	6.2	2.35	2.50	2.50
				q-002	Quartzite	S_0	*4.14*	4.14								1.38	5.71	5.71							2.55		
				q-003	Quartzite	S_0	5.31	5.56								1.38	7.33	7.67							2.59		
	E2	Shale/siltstone	70	E2-002	Siltstone	S_0	2.35	2.34	2.4	2.6	2.5	1.1	2.9	2.9	2.9	1.17	2.75	2.74	2.9	3.1	3.0	3.3	3.3	3.3	2.71	2.66	2.66
				E2-004	Siltstone	S_0	2.13	2.56								1.17	2.50	2.99							2.71		
				E2-007	Siltstone	S_0	2.84	3.15								1.17	3.32	3.68							2.70		
				E2-008	Siltstone	S_0	3.17	3.14								1.17	3.71	3.67							2.67		
				E2-010-1	Siltstone	S_0	2.32	2.61								1.17	2.71	3.06							2.51		
				E2-010-2	Siltstone	S_0	1.81	2.06								1.17	2.12	2.41							2.66		
		Sandstone	25	E1b-008	Sandstone	S_0	3.19	3.47	3.4	3.6	3.5	1.0				1.17	3.73	4.06	4.0	4.2	4.1				2.65	2.66	
				E1b-009	Sandstone	S_0	3.67	3.68								1.17	4.30	4.31							2.66		
		Quartzitic sst.	5	E2-001	Quartzitic sst.	S_0	3.96	4.30	4.0	4.3	4.1	1.1				1.17	4.63	5.03	4.6	5.0	4.8				2.66	2.66	
	E1b	Silty slate/siltstone	70	E1b-001	Siltstone	S_0	2.19	2.95	2.4	2.9	2.7	1.2	2.8	3.1	2.9	1.17	2.56	3.45	2.9	3.4	3.1	3.5	3.5	3.5	2.72	2.69	2.68
				E1b-003	Siltstone	S_0	2.35	2.40								1.17	2.75	2.80							2.68		
				E1b-004	Silty slate	S_0	2.70	3.54								1.19	3.21	4.21							2.71		
				E1b-006	Silty slate	S_0	1.97	2.26								1.19	2.34	2.69							2.74		
				E1b-007	Siltstone	S_0	2.81	3.29								1.17	3.29	3.85							2.66		
				E1b-010	Siltstone	S_0	2.54	3.01								1.17	2.98	3.52							2.65		
				E1b-012	Siltstone	S_0	2.50	2.63								1.17	2.92	3.07							2.67		
		Sandstone	20	E1b-008	Sandstone	S_0	3.19	3.47	3.4	3.6	3.5	1.0				1.17	3.73	4.06	4.0	4.2	4.1				2.65	2.66	
				E1b-009	Sandstone	S_0	3.67	3.68								1.17	4.30	4.31							2.66		
		Quarzitic sst.	10	E1b-002	Quartzitic sst.	S_0	4.01	4.25	3.7	4.0	3.8	1.1				1.17	4.69	4.97	4.3	4.7	4.5				2.68	2.66	
				E1b-005	Quartzitic sst.	S_0	3.38	3.72								1.17	3.95	4.35							2.64		

Be – Belgium, Lux – Luxembourg, Vol. – volume fraction, Litho. – lithotype, Fm. – formation, O – orientation, λ_{dry} and λ_{sat} – thermal conductivity under dry and saturated conditions, respectively, S_0 and S_1 – bedding and cleavage, respectively, ⊥ and // – thermal conductivity perpendicular and parallel to orientation, AM – arithmetic mean, A – anisotropy, TF – transformation factor, calc. – calculated, sst. – sandstone, congl. – conglomeratic. Composition of the individual formations is estimated after Dejonghe (2008) and Lucius (1950).

Table A.3.5 continued

Formation		Lithology	Vol.	Sample	Lithotype	λ_{dry}			Litho. λ_{dry}				Fm. λ_{dry}			TF	λ_{sat} calc.		Litho. λ_{sat}			Fm. λ_{sat}			Density		
Be	Lux		[%]			O	⊥	//	⊥	//	AM	A	⊥	//	AM		⊥	//	⊥	//	AM	⊥	//	AM	Sample	Litho.	Fm.
							[$Wm^{-1}K^{-1}$]		[$Wm^{-1}K^{-1}$]				[$Wm^{-1}K^{-1}$]				[$Wm^{-1}K^{-1}$]		[$Wm^{-1}K^{-1}$]			[$Wm^{-1}K^{-1}$]			[10^3 kg m^{-3}]		
	E1a	Sandy shale	94	E1a-003	Sandy shale	S_1	2.11	2.39	2.6	2.7	2.6	1.0	2.6	2.7	2.7	1.19	2.51	2.84	3.0	3.2	3.1	3.1	3.3	3.2	2.73	2.74	2.73
				E1a-004	Sandy shale	S_1	2.52	2.53								1.19	3.00	3.00							2.71		
				E1a-006	Sandy shale	S_1	3.21	2.95								1.19	3.82	3.51							2.75		
				E1a-007	Sandy shale	S_1	2.45	2.73								1.19	2.92	3.25							2.73		
				E1a-009	Sandy shale	S_1	2.56	2.41								1.19	3.04	2.86							2.75		
				E1a-010	Sandy shale	S_1	2.50	3.05								1.19	2.98	3.63							2.75		
		Quartzitic sst.	6	E1a-005	Sandstone	S_0	3.03	2.80	3.7	3.8	3.7	1.0				1.17	3.54	3.28	4.3	4.4	4.3				2.69	2.71	
				E1a-011	Quartzitic sst	S_0	4.08	4.39								1.17	4.78	5.14							2.71		
				E1a-013	Sandstone	S_0	3.86	4.10								1.17	4.51	4.80							2.72		
LAR	Sg3	Sandy shale	100	Sg3-001	Sandy shale	S_1	2.52	2.98	2.4	2.5	2.5	1.0	2.4	2.5	2.5	1.19	2.99	3.54	2.9	3.0	2.9	2.9	3.0	2.9	2.68	2.67	2.67
				Sg3-002	Sandy shale	S_1	2.30	2.58								1.19	2.74	3.07							2.67		
				Sg3-003	Sandy shale	S_1	2.52	2.45								1.19	3.00	2.91							2.69		
				Sg3-006	Sandy shale	S_1	2.21	2.24								1.19	2.63	2.67							2.59		
				Sg3-009	Sandy shale	S_1	1.95	1.95								1.19	2.32	2.32							2.63		
				Sg3-010	Sandy shale	S_1	2.06	2.32								1.19	2.46	2.75							2.67		
				Sg3-011	Sandy shale	S_1	2.52	2.30								1.19	3.00	2.74							2.65		
				Sg3-012	Sandy shale	S_1	3.13	3.48								1.19	3.72	4.14							2.75		
				Sg3-013	Sandy shale	S_1	2.55	2.33								1.19	3.03	2.77							2.71		
	Sg3a	Slate	100	Sg3a-1	Slate	S_1	2.50	2.71	2.4	2.9	2.6	1.2	2.4	2.9	2.6	1.23	3.07	3.34	2.9	3.5	3.2	2.9	3.5	3.2	2.75	2.73	2.73
				Sg3a-2	Slate	S_1	2.37	2.68								1.23	2.91	3.30							2.74		
				Sg3a-3	Slate	S_1	2.42	3.39								1.23	2.97	4.17							2.69		
				Sg3a-4	Slate	S_1	2.29	2.72								1.23	2.82	3.34							2.75		

Table A.3.5 continued

Formation		Lithology	Vol.	Sample	Lithotype	λ_{dry}			Litho. λ_{dry}				Fm. λ_{dry}			TF	λ_{sat} calc.		Litho. λ_{sat}			Fm. λ_{sat}			Density		
						O	⊥	//	⊥	//	AM	A	⊥	//	AM		⊥	//	⊥	//	AM	⊥	//	AM	Sample	Litho.	Fm.
Be	Lux		[%]				[$Wm^{-1}K^{-1}$]		[$Wm^{-1}K^{-1}$]				[$Wm^{-1}K^{-1}$]				[$Wm^{-1}K^{-1}$]		[$Wm^{-1}K^{-1}$]			[$Wm^{-1}K^{-1}$]			[10^3 kg m^{-3}]		
VIL	Sg2	Shale/siltstone	35	VIL-02	Shale	S_1	1.91	1.90	2.2	2.1	2.1	1.0	3.0	3.0	3.0	1.19	2.27	2.26	2.6	2.5	2.5	3.5	3.5	3.5	2.57	2.58	2.58
				VIL-05	Shale	S_1	2.05	2.28								1.19	2.44	2.71							2.57		
				VIL-06	Shale	S_1	2.27	2.11								1.19	2.70	2.52							2.56		
				VIL-09	Shale	S_1	1.93	1.88								1.19	2.29	2.24							2.61		
				VIL-11	Sandy shale	S_1	2.23	2.17								1.19	2.65	2.58							2.56		
				VIL-12	Sandy shale	S_1	2.75	2.29								1.19	3.27	2.73							2.61		
				VIL-14	Sandy shale	S_1	1.96	1.99								1.19	2.34	2.37							2.58		
		Siltstone + calc. sst/sandy limestone	65	VIL-04	Sandstone	S_0	4.42	4.17	3.5	3.5	3.5	1.0				1.17	5.17	4.88	4.1	4.1	4.1				2.56	2.59	
				VIL-08	Sandstone	S_0	3.18	3.39								1.17	3.73	3.96							2.63		
				VIL-10	Sandstone	S_0	*2.85*	2.85								1.17	3.33	3.33							2.57		
MIR	Sg1	Slate	80	Sg1-001	Slate	S_1	2.28	2.55	2.5	2.6	2.5	1.0	2.8	2.9	2.8	1.23	2.80	3.14	3.1	3.2	3.1	3.4	3.5	3.4	2.72	2.73	2.73
				Sg1-002	Slate	S_1	2.77	2.58								1.23	3.40	3.18							2.74		
				Sg1-003	Slate	S_1	2.42	2.69								1.23	2.98	3.31							2.73		
		Silty slate	5	Sg1-008	Silty slate	S_0	2.56	2.99	2.6	3.1	2.8	1.2				1.19	3.04	3.56	3.1	3.6	3.4				2.70	2.69	
				Sg1-010	Silty slate	S_0	2.14	2.79								1.19	2.55	3.32							2.73		
				Sg1-007	Silty slate	S_0	3.20	3.40								1.19	3.81	4.05							2.64		
		Quartz. sst./quartzite	15	Sg1-005	Quartzitic sst.	S_0	4.13	4.49	4.1	4.5	4.3	1.1				1.17	4.83	5.26	4.8	5.3	5.0				2.71	2.71	
STH		Shale/siltstone	80	STH-01	Shale	S_1	2.12	2.34	2.9	3.2	3.1	1.1	3.3	3.3	3.3	1.19	2.52	2.78	3.4	3.8	3.6	3.9	3.9	3.9	2.73	2.71	2.70
				STH-03	Shale	S_1	2.97	*2.97*								1.19	3.53	3.53							2.67		
				STH-04	Siltstone	S_0	2.90	3.30								1.17	3.39	3.86							2.72		
				STH-05	Siltstone	S_0	2.95	3.66								1.17	3.45	4.28							2.74		
				STH-10	Siltstone	S_0	3.39	3.38								1.17	3.96	3.95							2.74		
				STH-13	Sandy siltstone	S_0	3.25	3.62								1.17	3.80	4.23							2.67		
				STH-14	Siltstone	S_0	2.71	3.17								1.17	3.17	3.71							2.71		
		Sandstone	20	STH-07	Quartzitic sst.	S_0	4.00	4.04	4.3	4.4	4.4	1.0				1.17	4.68	4.73	5.1	5.2	5.1				2.71	2.67	
				STH-08	Quartzitic sst.	S_0	4.29	4.26								1.17	5.02	4.99							2.62		
				STH-09	Quartzitic sst.	S_0	4.92	5.08								1.17	5.76	5.94							2.66		
				STH-11	Sandstone	S_0	4.17	4.30								1.17	4.87	5.03							2.67		

Table A.3.5 continued

Formation		Lithology	Vol.	Sample	Lithotype	λ_{dry}			Litho. λ_{dry}				Fm. λ_{dry}			TF	λ_{sat} calc.		Litho. λ_{sat}			Fm. λ_{sat}			Density		
Be	Lux		[%]			O	⊥	//	⊥	//	AM	A	⊥	//	AM		⊥	//	⊥	//	AM	⊥	//	AM	Sample	Litho.	Fm.
							[$Wm^{-1}K^{-1}$]		[$Wm^{-1}K^{-1}$]				[$Wm^{-1}K^{-1}$]				[$Wm^{-1}K^{-1}$]		[$Wm^{-1}K^{-1}$]			[$Wm^{-1}K^{-1}$]			[10^3 kg m^{-3}]		
OIG		Siltstone	15	OIG-01	Siltstone	S_0	2.64	2.75	2.7	2.7	2.7	1.0	2.6	2.6	2.6	1.17	3.09	3.21	3.1	3.1	3.1	3.0	3.0	3.0	2.57	2.50	2.60
				OIG-05	Siltstone	S_0	2.70	2.63								1.17	3.16	3.08							2.43		
		Shale	60	OIG-10	Shale	S_1	2.00	2.15	2.2	2.2	2.2	1.0				1.19	2.38	2.56	2.6	2.6	2.6				2.66	2.61	
				OIG-12	Shale	S_1	2.18	2.13								1.19	2.59	2.53							2.43		
				OIG-13	Shale	S_1	2.48	2.38								1.19	2.95	2.84							2.74		
		Sandstone	25	OIG-04	Silty sandstone	S_0	3.31	3.17	3.3	3.3	3.3	1.0				1.17	3.87	3.71	3.9	3.9	3.9				2.63	2.62	
				OIG-07	Sandstone	S_0	2.80	2.90								1.17	3.27	3.40							2.57		
				OIG-08	Sandstone	S_0	3.99	4.15								1.17	4.66	4.85							2.57		
				OIG-09	Silty sandstone	S_0	3.10	3.11								1.17	3.63	3.64							2.70		
FEP		Shale/siltstone	50	FEP-05	Shale	S_1	3.24	*3.24*	2.8	2.9	2.9	1.0	3.7	3.7	3.7	1.19	3.85	3.85	3.4	3.5	3.4	4.3	4.4	4.3	2.70	2.70	2.67
				FEP-07	Shale	S_1	2.42	2.60								1.19	2.88	3.09							2.70		
		Sandstone	20	FEP-06	Sandstone	S_0	4.79	4.39	4.8	4.4	4.6	0.9				1.17	5.60	5.13	5.6	5.1	5.4				2.68	2.68	
		Congl. sandstone	30	FEP-01	Congl. sst.	S_0	3.99	3.72	4.4	4.4	4.4	1.0				1.17	4.66	4.35	5.2	5.1	5.2				2.63	2.62	
				FEP-02	Congl. sst.	S_0	4.43	4.60								1.17	5.19	5.39							2.63		
				FEP-03	Congl. sst.	S_0	4.88	4.74								1.17	5.71	5.54							2.61		
				FEP-04	Congl. sst.	S_0	4.43	4.45								1.17	5.18	5.21							2.60		

Table A.3.6: Details on samples used to compose the petrophysical properties of the Lower Devonian geological formations in the Eifel and Mosel Syncline/Hunsrück regions.

					λ_{dry}			Litho. λ_{dry}				Fm. λ_{dry}			TF	λ_{sat} calc.		Litho. λ_{sat}			Fm. λ_{sat}			Density		
Formation	Lithology	Vol.	Sample	Lithotype	O	⊥	//	⊥	//	AM	A	⊥	//	AM		⊥	//	⊥	//	AM	⊥	//	AM	Sample	Litho.	Fm.
(Code)		[%]			[W m^{-1} K^{-1}]			[W m^{-1} K^{-1}]				[W m^{-1} K^{-1}]				[W m^{-1} K^{-1}]		[W m^{-1} K^{-1}]			[W m^{-1} K^{-1}]			[10^{3} kg m^{-3}]		
Wissenbach-Schiefer	Shale	> 90	E3-001	Shale	S_1	2.28	1.94	2.4	2.3	2.3	1.0	2.5	2.5	2.5	1.19	2.71	2.31	2.8	2.7	2.8	3.0	2.9	3.0	2.66	2.64	2.64
(de/dzoWI)			E3-002	Shale	S_1	1.87	1.83								1.19	2.22	2.18							2.55		
			E3-003	Shale	S_1	2.05	1.69								1.19	2.44	2.02							2.59		
			E3-005	Sandy shale	S_1	3.23	3.73								1.19	3.84	4.44							2.77		
	Quartzitic sst.	< 10	E2-001	Quartzitic sst.	S_0	3.96	4.30	4.0	4.3	4.1	1.1				1.17	4.63	5.03	4.6	5.0	4.8				2.66	2.66	
Kieselgallenschiefer	Shale/shaly siltstone	> 90	E3-001	Shale	S_1	2.28	1.94	2.4	2.3	2.3	1.0	2.4	2.3	2.3	1.19	2.71	2.31	2.8	2.7	2.8	2.8	2.8	2.8	2.66	2.64	2.64
(dzo3KG)			E3-002	Shale	S_1	1.87	1.83								1.19	2.22	2.18							2.55		
			E3-003	Shale	S_1	2.05	1.69								1.19	2.44	2.02							2.59		
			E3-005	Sandy shale	S_1	3.23	3.73								1.19	3.84	4.44							2.77		
	Siltstone/ sandstone	< 10	E2-002	Siltstone	S_0	2.35	2.34	2.4	2.6	2.5	1.1				1.17	2.75	2.74	2.9	3.1	3.0				2.71	2.66	
			E2-004	Siltstone	S_0	2.13	2.56								1.17	2.50	2.99							2.71		
			E2-007	Siltstone	S_0	2.84	3.15								1.17	3.32	3.68							2.70		
			E2-008	Siltstone	S_0	3.17	3.14								1.17	3.71	3.67							2.67		
			E2-010-1	Siltstone	S_0	2.32	2.61								1.17	2.71	3.06							2.51		
			E2-010-2	Siltstone	S_0	1.81	2.06								1.17	2.12	2.41							2.66		
Sphärosideritschiefer	Shale/shaly siltstone	> 80	E3-001	Shale	S_1	2.28	1.94	2.4	2.3	2.3	1.0	2.6	2.5	2.6	1.19	2.71	2.31	2.8	2.7	2.8	3.1	3.0	3.0	2.66	2.64	2.65
(dzo3SS)			E3-002	Shale	S_1	1.87	1.83								1.19	2.22	2.18							2.55		
			E3-003	Shale	S_1	2.05	1.69								1.19	2.44	2.02							2.59		
			E3-005	Sandy shale	S_1	3.23	3.73								1.19	3.84	4.44							2.77		
	Sandstone	< 20	E1b-008	Sandstone	S_0	3.19	3.47	3.4	3.6	3.5	1.0				1.17	3.73	4.06	4.0	4.2	4.1				2.65	2.66	
			E1b-009	Sandstone	S_0	3.67	3.68								1.17	4.30	4.31							2.66		
Brauneisenstein	Sandstone	> 70	E1b-008	Sandstone	S_0	3.19	3.47	3.4	3.6	3.5	1.0	3.2	3.1	3.1	1.17	3.73	4.06	4.0	4.2	4.1	3.7	3.7	3.7	2.65	2.66	2.65
(dzo3BE)			E1b-009	Sandstone	S_0	3.67	3.68								1.17	4.30	4.31							2.66		
	Shale/shaly siltstone	< 30	E3-001	Shale	S_1	2.28	1.94	2.4	2.3	2.3	1.0				1.19	2.71	2.31	2.8	2.7	2.8				2.66	2.64	
			E3-002	Shale	S_1	1.87	1.83								1.19	2.22	2.18							2.55		
			E3-003	Shale	S_1	2.05	1.69								1.19	2.44	2.02							2.59		
			E3-005	Sandy shale	S_1	3.23	3.73								1.19	3.84	4.44							2.77		

Vol. – volume fraction, Litho. – lithotype, Fm. – formation, O – orientation, λ_{dry} and λ_{sat} – thermal conductivity under dry and saturated conditions, respectively, S_0 and S_1 – bedding and cleavage, respectively, ⊥ and // – thermal conductivity perpendicular and parallel to orientation, AM – arithmetic mean, A – anisotropy, TF – transformation factor, calc. – calculated, sst. – sandstone. Composition of the individual formations is taken from Häfner et al. (2007) and completed according to LGB (2005).

Table A.3.6 continued

Formation	Lithology	Vol.	Sample	Lithotype	λ_{dry}			Litho. λ_{dry}				Fm. λ_{dry}			TF	λ_{sat} calc.		Litho. λ_{sat}			Fm. λ_{sat}			Density		
(Code)		[%]			O	⊥	//	⊥	//	AM	A	⊥	//	AM		⊥	//	⊥	//	AM	⊥	//	AM	Sample	Litho.	Fm.
					[W m^{-1} K^{-1}]			[W m^{-1} K^{-1}]				[W m^{-1} K^{-1}]				[W m^{-1} K^{-1}]		[W m^{-1} K^{-1}]			[W m^{-1} K^{-1}]			[10^{3} kg m^{-3}]		
Rötelgallen-Schichten (dzo2RG)	Shale	50	E3-001	Shale	S_1	2.28	1.94	2.4	2.3	2.3	1.0	2.9	2.9	2.9	1.19	2.71	2.31	2.8	2.7	2.8	3.4	3.4	3.4	2.66	2.64	2.65
			E3-002	Shale	S_1	1.87	1.83								1.19	2.22	2.18							2.55		
			E3-003	Shale	S_1	2.05	1.69								1.19	2.44	2.02							2.59		
			E3-005	Sandy shale	S_1	3.23	3.73								1.19	3.84	4.44							2.77		
	Sandstone + limestone	50	E1b-008	Sandstone	S_0	3.19	3.47	3.4	3.6	3.5	1.0				1.17	3.73	4.06	4.0	4.2	4.1				2.65	2.66	
			E1b-009	Sandstone	S_0	3.67	3.68								1.17	4.30	4.31							2.66		
Höllenthal-Schichten (dzo2HÖ)	Shale	50	E3-001	Shale	S_1	2.28	1.94	2.4	2.3	2.3	1.0	2.9	2.9	2.9	1.19	2.71	2.31	2.8	2.7	2.8	3.4	3.4	3.4	2.66	2.64	2.65
			E3-002	Shale	S_1	1.87	1.83								1.19	2.22	2.18							2.55		
			E3-003	Shale	S_1	2.05	1.69								1.19	2.44	2.02							2.59		
			E3-005	Sandy shale	S_1	3.23	3.73								1.19	3.84	4.44							2.77		
	Sandstone	50	E1b-008	Sandstone	S_0	3.19	3.47	3.4	3.6	3.5	1.0				1.17	3.73	4.06	4.0	4.2	4.1				2.65	2.66	
			E1b-009	Sandstone	S_0	3.67	3.68								1.17	4.30	4.31							2.66		
Flußbach-Schichten (dzo1FL)	Shale/shaly siltstone	40	E3-001	Shale	S_1	2.28	1.94	2.4	2.3	2.3	1.0	3.4	3.4	3.4	1.19	2.71	2.31	2.8	2.7	2.8	3.6	3.6	3.6	2.66	2.64	2.65
			E3-002	Shale	S_1	1.87	1.83								1.19	2.22	2.18							2.55		
			E3-003	Shale	S_1	2.05	1.69								1.19	2.44	2.02							2.59		
			E3-005	Sandy shale	S_1	3.23	3.73								1.19	3.84	4.44							2.77		
	Quartzitic sst.	60	E2-001	Quartzitic sst.	S_0	3.96	4.30	4.0	4.3	4.1	1.1				1.17	4.63	5.03	4.0	4.3	4.1				2.66	2.66	
Emsquarzit (dzo1EQ)	Quartzitic sst./quartzite	> 90	q-001	Quartzite	S_0	3.73	3.99	4.4	4.6	4.5	1.0	4.3	4.3	4.3	1.38	5.15	5.51	6.1	6.3	6.2	5.8	5.8	5.8	2.35	2.50	2.51
			q-002	Quartzite	S_0	*4.14*	4.14								1.38	5.71	5.71							2.55		
			q-003	Quartzite	S_0	5.31	5.56								1.38	7.33	7.67							2.59		
	Shale	< 10	E3-001	Shale	S_1	2.28	1.94	2.4	2.3	2.3	1.0				1.19	2.71	2.31	2.8	2.7	2.8				2.66	2.64	
			E3-002	Shale	S_1	1.87	1.83								1.19	2.22	2.18							2.55		
			E3-003	Shale	S_1	2.05	1.69								1.19	2.44	2.02							2.59		
			E3-005	Sandy shale	S_1	3.23	3.73								1.19	3.84	4.44							2.77		

Table A.3.6 continued

Formation (Code)	Lithology	Vol. [%]	Sample	Lithotype	λ_{dry} O [W m^{-1} K^{-1}]	λ_{dry} ⊥ [W m^{-1} K^{-1}]	λ_{dry} // [W m^{-1} K^{-1}]	Litho. λ_{dry} ⊥ [W m^{-1} K^{-1}]	Litho. λ_{dry} // [W m^{-1} K^{-1}]	Litho. λ_{dry} AM [W m^{-1} K^{-1}]	Litho. λ_{dry} A [W m^{-1} K^{-1}]	Fm. λ_{dry} ⊥ [W m^{-1} K^{-1}]	Fm. λ_{dry} // [W m^{-1} K^{-1}]	Fm. λ_{dry} AM [W m^{-1} K^{-1}]	TF	λ_{sat} calc. ⊥ [W m^{-1} K^{-1}]	λ_{sat} calc. // [W m^{-1} K^{-1}]	Litho. λ_{sat} ⊥ [W m^{-1} K^{-1}]	Litho. λ_{sat} // [W m^{-1} K^{-1}]	Litho. λ_{sat} AM [W m^{-1} K^{-1}]	Fm. λ_{sat} ⊥ [W m^{-1} K^{-1}]	Fm. λ_{sat} // [W m^{-1} K^{-1}]	Fm. λ_{sat} AM [W m^{-1} K^{-1}]	Density Sample [10^3 kg m^{-3}]	Density Litho. [10^3 kg m^{-3}]	Density Fm. [10^3 kg m^{-3}]
Klerf-Schichten (dzu3KL)	Shale/shaly siltstone	30	E2-002	Siltstone	S_0	2.35	2.34	2.4	2.6	2.5	1.1	3.4	3.4	3.4	1.17	2.75	2.74	2.9	3.1	3.0	3.9	3.9	3.9	2.71	2.66	2.66
			E2-004	Siltstone	S_0	2.13	2.56								1.17	2.50	2.99							2.71		
			E2-007	Siltstone	S_0	2.84	3.15								1.17	3.32	3.68							2.70		
			E2-008	Siltstone	S_0	3.17	3.14								1.17	3.71	3.67							2.67		
			E2-010-1	Siltstone	S_0	2.32	2.61								1.17	2.71	3.06							2.51		
			E2-010-2	Siltstone	S_0	1.81	2.06								1.17	2.12	2.41							2.66		
	Sandstone/ quartzite	70	E1b-008	Sandstone	S_0	3.19	3.47	3.6	3.8	3.7	1.1				1.17	3.73	4.06	4.2	4.5	4.3				2.65	2.66	
			E1b-009	Sandstone	S_0	3.67	3.68								1.17	4.30	4.31							2.66		
			E2-001	Quartzitic sst.	S_0	3.96	4.30								1.17	4.63	5.03							2.66		
Gladbach-Schichten (dzu3GL)	Shale	60	E1a-003	Sandy shale	S_1	2.11	2.39	2.6	2.7	2.6	1.0	2.8	2.9	2.8	1.19	2.51	2.84	3.0	3.2	3.1	3.3	3.4	3.4	2.73	2.74	2.72
			E1a-004	Sandy shale	S_1	2.52	2.53								1.19	3.00	3.00							2.71		
			E1a-006	Sandy shale	S_1	3.21	2.95								1.19	3.82	3.51							2.75		
			E1a-007	Sandy shale	S_1	2.45	2.73								1.19	2.92	3.25							2.73		
			E1a-009	Sandy shale	S_1	2.56	2.41								1.19	3.04	2.86							2.75		
			E1a-010	Sandy shale	S_1	2.50	3.05								1.19	2.98	3.63							2.75		
	Siltstone	20	E1b-001	Siltstone	S_0	2.19	2.95	2.4	2.9	2.7	1.2				1.17	2.56	3.45	2.9	3.4	3.1				2.72	2.69	
			E1b-003	Siltstone	S_0	2.35	2.40								1.17	2.75	2.80							2.68		
			E1b-004	Silty slate	S_0	2.70	3.54								1.19	3.21	4.21							2.71		
			E1b-006	Silty slate	S_0	1.97	2.26								1.19	2.34	2.69							2.74		
			E1b-007	Siltstone	S_0	2.81	3.29								1.17	3.29	3.85							2.66		
			E1b-010	Siltstone	S_0	2.54	3.01								1.17	2.98	3.52							2.65		
			E1b-012	Siltstone	S_0	2.50	2.63								1.17	2.92	3.07							2.67		
	Sandstone	20	E1b-008	Sandstone	S_0	3.19	3.47	3.6	3.8	3.7	1.0				1.17	3.73	4.06	4.2	4.4	4.3				2.65	2.68	
			E1b-009	Sandstone	S_0	3.67	3.68								1.17	4.30	4.31							2.66		
			E1b-002	Quartzitic sst.	S_0	4.01	4.25								1.17	4.69	4.97							2.68		
			E1b-005	Quartzitic sst.	S_0	3.38	3.72								1.17	3.95	4.35							2.64		
			E1a-005	Sandstone	S_0	3.03	2.80								1.17	3.54	3.28							2.69		
			E1a-011	Quartzitic sst	S_0	4.08	4.39								1.17	4.78	5.14							2.71		
			E1a-013	Sandstone	S_0	3.86	4.10								1.17	4.51	4.80							2.72		

Table A.3.6 continued

Formation (Code)	Lithology	Vol. [%]	Sample	Lithotype	λ_{dry} O [W m^{-1} K^{-1}]	λ_{dry} ⊥ [W m^{-1} K^{-1}]	λ_{dry} // [W m^{-1} K^{-1}]	Litho. λ_{dry} ⊥ [W m^{-1} K^{-1}]	Litho. λ_{dry} // [W m^{-1} K^{-1}]	Litho. λ_{dry} AM [W m^{-1} K^{-1}]	Litho. λ_{dry} A [W m^{-1} K^{-1}]	Fm. λ_{dry} ⊥ [W m^{-1} K^{-1}]	Fm. λ_{dry} // [W m^{-1} K^{-1}]	Fm. λ_{dry} AM [W m^{-1} K^{-1}]	TF	λ_{sat} calc. ⊥ [W m^{-1} K^{-1}]	λ_{sat} calc. // [W m^{-1} K^{-1}]	Litho. λ_{sat} ⊥ [W m^{-1} K^{-1}]	Litho. λ_{sat} // [W m^{-1} K^{-1}]	Litho. λ_{sat} AM [W m^{-1} K^{-1}]	Fm. λ_{sat} ⊥ [W m^{-1} K^{-1}]	Fm. λ_{sat} // [W m^{-1} K^{-1}]	Fm. λ_{sat} AM [W m^{-1} K^{-1}]	Density Sample [10^3 kg m^{-3}]	Density Litho. [10^3 kg m^{-3}]	Density Fm. [10^3 kg m^{-3}]
"Singhofen-Schichten" (old: dzS)	Shale/sandy shale	90	E1a-003	Sandy shale	S_1	2.11	2.39	2.6	2.7	2.6	1.0	2.7	2.8	2.7	1.19	2.51	2.84	3.0	3.2	3.1	3.2	3.3	3.2	2.73	2.74	2.73
			E1a-004	Sandy shale	S_1	2.52	2.53								1.19	3.00	3.00							2.71		
			E1a-006	Sandy shale	S_1	3.21	2.95								1.19	3.82	3.51							2.75		
			E1a-007	Sandy shale	S_1	2.45	2.73								1.19	2.92	3.25							2.73		
			E1a-009	Sandy shale	S_1	2.56	2.41								1.19	3.04	2.86							2.75		
			E1a-010	Sandy shale	S_1	2.50	3.05								1.19	2.98	3.63							2.75		
	Sandstone	10	E1b-008	Sandstone	S_0	3.19	3.47	3.6	3.8	3.7	1.0				1.17	3.73	4.06	4.2	4.4	4.3				2.65	2.68	
			E1b-009	Sandstone	S_0	3.67	3.68								1.17	4.30	4.31							2.66		
			E1b-002	Quartzitic sst.	S_0	4.01	4.25								1.17	4.69	4.97							2.68		
			E1b-005	Quartzitic sst.	S_0	3.38	3.72								1.17	3.95	4.35							2.64		
			E1a-005	Sandstone	S_0	3.03	2.80								1.17	3.54	3.28							2.69		
			E1a-011	Quartzitic sst	S_0	4.08	4.39								1.17	4.78	5.14							2.71		
			E1a-013	Sandstone	S_0	3.86	4.10								1.17	4.51	4.80							2.72		
Kaubschichten (Hunsrückschiefer) (dzu1KA)	Shale	85	Sg3-001	Sandy shale	S_1	2.52	2.98	2.4	2.5	2.5	1.0	2.4	2.6	2.5	1.19	2.99	3.54	2.9	3.0	2.9	2.9	3.1	3.0	2.68	2.67	2.67
			Sg3-002	Sandy shale	S_1	2.30	2.58								1.19	2.74	3.07							2.67		
			Sg3-003	Sandy shale	S_1	2.52	2.45								1.19	3.00	2.91							2.69		
			Sg3-006	Sandy shale	S_1	2.21	2.24								1.19	2.63	2.67							2.59		
			Sg3-009	Sandy shale	S_1	1.95	1.95								1.19	2.32	2.32							2.63		
			Sg3-010	Sandy shale	S_1	2.06	2.32								1.19	2.46	2.75							2.67		
			Sg3-011	Sandy shale	S_1	2.52	2.30								1.19	3.00	2.74							2.65		
			Sg3-012	Sandy shale	S_1	3.13	3.48								1.19	3.72	4.14							2.75		
			Sg3-013	Sandy shale	S_1	2.55	2.33								1.19	3.03	2.77							2.71		
	Slate	10	Sg3a-1	Slate	S_1	2.50	2.71	2.4	2.9	2.6	1.2				1.23	3.07	3.34	2.9	3.5	3.2				2.75	2.73	
			Sg3a-2	Slate	S_1	2.37	2.68								1.23	2.91	3.30							2.74		
			Sg3a-3	Slate	S_1	2.42	3.39								1.23	2.97	4.17							2.69		
			Sg3a-4	Slate	S_1	2.29	2.72								1.23	2.82	3.34							2.75		
	Quartzitic sst.	5	Sg3-008	Sandstone	S_0	3.08	3.03	3.0	2.9	2.9	1.0				1.17	3.60	3.54	3.5	3.4	3.4				2.61	2.62	
			Sg3-007	Sandstone	S_0	2.88	2.70								1.17	3.37	3.16							2.62		

Table A.3.6 continued

Formation (Code)	Lithology	Vol. [%]	Sample	Lithotype	λ_{dry} O	λ_{dry} ⊥ [W m^{-1} K^{-1}]	λ_{dry} //	Litho. λ_{dry} ⊥ [W m^{-1} K^{-1}]	Litho. λ_{dry} //	Litho. λ_{dry} AM	Litho. λ_{dry} A	Fm. λ_{dry} ⊥ [W m^{-1} K^{-1}]	Fm. λ_{dry} //	Fm. λ_{dry} AM	TF	λ_{sat} calc. ⊥ [W m^{-1} K^{-1}]	λ_{sat} calc. //	Litho. λ_{sat} ⊥ [W m^{-1} K^{-1}]	Litho. λ_{sat} //	Litho. λ_{sat} AM	Fm. λ_{sat} ⊥ [W m^{-1} K^{-1}]	Fm. λ_{sat} //	Fm. λ_{sat} AM	Density Sample [10^3 kg m^{-3}]	Density Litho.	Density Fm.
Zerf-Schichten	Sandy shale	75	Sg3-001	Sandy shale	S_1	2.52	2.98	2.4	2.5	2.5	1.0	2.9	3.0	2.9	1.19	2.99	3.54	2.9	3.0	2.9	3.4	3.5	3.5	2.68	2.67	2.68
(dzu1ZE)			Sg3-002	Sandy shale	S_1	2.30	2.58								1.19	2.74	3.07							2.67		
			Sg3-003	Sandy shale	S_1	2.52	2.45								1.19	3.00	2.91							2.69		
			Sg3-006	Sandy shale	S_1	2.21	2.24								1.19	2.63	2.67							2.59		
			Sg3-009	Sandy shale	S_1	1.95	1.95								1.19	2.32	2.32							2.63		
			Sg3-010	Sandy shale	S_1	2.06	2.32								1.19	2.46	2.75							2.67		
			Sg3-011	Sandy shale	S_1	2.52	2.30								1.19	3.00	2.74							2.65		
			Sg3-012	Sandy shale	S_1	3.13	3.48								1.19	3.72	4.14							2.75		
			Sg3-013	Sandy shale	S_1	2.55	2.33								1.19	3.03	2.77							2.71		
	Quartzitic sst./	25	Sg1-005	Quartzitic sst.	S_0	4.13	4.49	4.1	4.5	4.3	1.1				1.17	4.83	5.26	4.8	5.3	5.0				2.71	2.71	
Dhrontal-Schichten	Sandy shale	70	Sg3-001	Sandy shale	S_1	2.52	2.98	2.4	2.5	2.5	1.0	3.0	3.1	3.0	1.19	2.99	3.54	2.9	3.0	2.9	3.6	3.6	3.6	2.68	2.67	2.67
(ds3DR)			Sg3-002	Sandy shale	S_1	2.30	2.58								1.19	2.74	3.07							2.67		
			Sg3-003	Sandy shale	S_1	2.52	2.45								1.19	3.00	2.91							2.69		
			Sg3-006	Sandy shale	S_1	2.21	2.24								1.19	2.63	2.67							2.59		
			Sg3-009	Sandy shale	S_1	1.95	1.95								1.19	2.32	2.32							2.63		
			Sg3-010	Sandy shale	S_1	2.06	2.32								1.19	2.46	2.75							2.67		
			Sg3-011	Sandy shale	S_1	2.52	2.30								1.19	3.00	2.74							2.65		
			Sg3-012	Sandy shale	S_1	3.13	3.48								1.19	3.72	4.14							2.75		
			Sg3-013	Sandy shale	S_1	2.55	2.33								1.19	3.03	2.77							2.71		
	Quartzitic sst./ quartzite	30	STH-07	Quartzitic sst.	S_0	4.00	4.04	4.3	4.4	4.4	1.0				1.17	4.68	4.73	5.1	5.2	5.1				2.71	2.67	
			STH-08	Quartzitic sst.	S_0	4.29	4.26								1.17	5.02	4.99							2.62		
			STH-09	Quartzitic sst.	S_0	4.92	5.08								1.17	5.76	5.94							2.66		
			STH-11	Sandstone	S_0	4.17	4.30								1.17	4.87	5.03							2.67		

Table A.3.6 continued

Formation	Lithology	Vol.	Sample	Lithotype	λ_{dry}			Litho. λ_{dry}				Fm. λ_{dry}			TF	λ_{sat} calc.		Litho. λ_{sat}			Fm. λ_{sat}			Density		
					O	⊥	//	⊥	//	AM	A	⊥	//	AM		⊥	//	⊥	//	AM	⊥	//	AM	Sample	Litho.	Fm.
(Code)		[%]			[W m^{-1} K^{-1}]			[W m^{-1} K^{-1}]				[W m^{-1} K^{-1}]				[W m^{-1} K^{-1}]		[W m^{-1} K^{-1}]			[W m^{-1} K^{-1}]			[10^{3} kg m^{-3}]		
Taunusquarzit	Shale	5	OIG-10	Shale	S_1	2.00	2.15	2.2	2.2	2.2	1.0	4.3	4.3	4.3	1.19	2.38	2.56	2.6	2.6	2.6	5.0	5.0	5.0	2.66	2.61	2.66
(ds2TQ)			OIG-12	Shale	S_1	2.18	2.13								1.19	2.59	2.53							2.43		
			OIG-13	Shale	S_1	2.48	2.38								1.19	2.95	2.84							2.74		
	Quartzitic sst./quartzite	95	STH-07	Quartzitic sst.	S_0	4.00	4.04	4.3	4.4	4.4	1.0				1.17	4.68	4.73	5.1	5.2	5.1				2.71	2.67	
			STH-08	Quartzitic sst.	S_0	4.29	4.26								1.17	5.02	4.99							2.62		
			STH-09	Quartzitic sst.	S_0	4.92	5.08								1.17	5.76	5.94							2.66		
			STH-11	Sandstone	S_0	4.17	4.30								1.17	4.87	5.03							2.67		
Hermeskeil-Schichten (ds1HE)	Shale	50	OIG-10	Shale	S_1	2.00	2.15	2.2	2.2	2.2	1.0	3.3	3.3	3.3	1.19	2.38	2.56	2.6	2.6	2.6	3.9	3.9	3.9	2.66	2.61	2.64
			OIG-12	Shale	S_1	2.18	2.13								1.19	2.59	2.53							2.43		
			OIG-13	Shale	S_1	2.48	2.38								1.19	2.95	2.84							2.74		
	Quartzitic sst.	50	STH-07	Quartzitic sst.	S_0	4.00	4.04	4.3	4.4	4.4	1.0				1.17	4.68	4.73	5.1	5.2	5.1				2.71	2.67	
			STH-08	Quartzitic sst.	S_0	4.29	4.26								1.17	5.02	4.99							2.62		
			STH-09	Quartzitic sst.	S_0	4.92	5.08								1.17	5.76	5.94							2.66		
			STH-11	Sandstone	S_0	4.17	4.30								1.17	4.87	5.03							2.67		
Züsch-Schiefer	Shale	80	gd-01	Slate	S_1	2.26	2.37	2.7	2.8	2.8	1.0	3.1	3.2	3.1	1.23	2.78	2.91	3.3	3.4	3.3	3.9	4.0	3.9	2.69	2.72	2.70
(gd)			gd-02	Sandy shale	S_1	3.16	3.29								1.19	3.76	3.92							2.74		
	Quartzitic sst.	20	gd-06	Quartzite	S_0	4.49	4.53	4.5	4.5	4.5	1.0				1.38	6.20	6.25	6.2	6.2	6.2				2.66	2.66	

Table A.3.7: Details on samples used to compose the thermal conductivity of the Mesozoic geological formations (basin facies) of the Trier–Luxembourg Basin.

						$\lambda_{\perp}$						$\lambda_{//}$						A	
						Sample		Litho.		Unit		Sample		Litho.		Unit		Litho.	
Strat. unit	Lithology	Vol.	Sample	Unit	Lithotype	Dry	Sat	Dry	Sat	Dry	Sat	Dry	Sat	Dry	Sat	Dry	Sat	Dry	Sat
		[%]				[W m^{-1}K^{-1}]						[W m^{-1}K^{-1}]							
dom4b	Sandy marlstone	100	Ru2	dom4b	Calcareous marlstone	2.14	2.54	2.14	2.54	2.1	2.5	2.11	2.47	2.11	2.47	2.1	2.5	1.0	1.0
dom4a	Limestone	80	Ru6	dom4a	Limestone	1.55	2.16	1.55	2.16	1.7	2.3	1.50	2.13	1.50	2.13	1.7	2.3	1.0	1.0
	Reef limestone (corals)	20	Ru4	dom4a	Limestone	2.40	2.68	2.40	2.68			2.65	2.85	2.65	2.85			1.1	1.1
dom3	Sandy limestone	100	M9	dom3	Limestone	2.11	2.49	2.11	2.49	2.1	2.5	2.09	2.48	2.09	2.48	2.1	2.5	1.0	1.0
dom2	Limestone	70	M9	dom3	Limestone	2.11	2.49	2.11	2.49	2.1	2.5	2.09	2.48	2.09	2.48	2.1	2.5	1.0	1.0
	Marlstone	30	M8	dom1	Calcareous marlstone	2.03	2.44	2.03	2.44			1.99	2.39	1.99	2.39			1.0	1.0
dom1	Marlstone	10	M8	dom1	Calcareous marlstone	2.03	2.44	2.03	2.44	1.5	2.3	1.99	2.39	1.99	2.39	1.6	2.5	1.0	1.0
	Marl	90	Bv4	lo4	Silty marl	1.40	2.27	1.40	2.27			1.54	2.49	1.54	2.49			1.1	1.1
lo6-7 + dou	Iron-rich limestone + calcareous sandstone	50	M3	dou	Limestone	1.82	2.31	1.92	2.31	1.5	2.2	1.89	2.33	2.02	2.40	1.6	2.2	1.1	1.0
			M6	dou	Limestone	2.01	2.30					2.14	2.46						
	Iron-rich + marly sst.	50	M5	dou	Iron-rich limestone	1.08	2.02	1.08	2.02			1.23	2.09	1.23	2.09			1.1	1.0
lo5	Marl	100	Bv4	lo4	Silty marl	1.40	2.27	1.40	2.27	1.4	2.3	1.54	2.49	1.54	2.49	1.5	2.5	1.1	1.1
lo4	Sandstone	50	Bv2	lo4	Marly siltstone	1.17	2.80	1.17	2.80	1.3	2.5	1.28	3.00	1.28	3.00	1.4	2.7	1.1	1.1
	Sandy marl	50	Bv4	lo4	Silty marl	1.40	2.27	1.40	2.27			1.54	2.49	1.54	2.49			1.1	1.1
lo3	Marl	83	Bv11	lo3	Claystone	0.93	1.71	0.93	1.71	1.0	1.9	1.56	2.82	1.56	2.82	1.6	2.8	1.7	1.6
	Sandy marl	17	Bv12	lo3	Silty marl	1.41	2.74	1.41	2.74			1.51	2.90	1.51	2.90			1.1	1.1
lo2	Marly claystone	100	Bv14	lo2	Claystone	1.06	1.87	1.08	1.82	1.1	1.8	1.21	2.11	1.26	2.10	1.3	2.1	1.2	1.2
			Bv16	lo1	Claystone	1.09	1.77					1.30	2.09						
lo1	Marly claystone	100	Bv14	lo2	Claystone	1.06	1.87	1.08	1.82	1.1	1.8	1.21	2.11	1.26	2.10	1.3	2.1	1.2	1.2
			Bv16	lo1	Claystone	1.09	1.77					1.30	2.09						
lm3b	Marly sandstone	19	Rb34	lm3a	Silty sandstone	2.43	2.69	2.43	2.69	1.3	1.9	2.18	2.64	2.18	2.64	1.3	2.1	0.9	1.0
	Sandy claystone	81	Rb40	lm3b	Clayey siltstone	0.99	1.73	0.99	1.73			1.12	1.95	1.12	1.95			1.1	1.1
lm3a	Clayey sandstone	2	Rb34	lm3a	Silty sandstone	2.43	2.69	2.43	2.69	1.2	2.1	2.18	2.64	2.18	2.64	1.7	2.8	0.9	1.0
	Silty marl	98	Rb35	lm2	Marl	1.17	2.03	1.23	2.09			1.61	2.75	1.64	2.81			1.3	1.3
			Rb36	lm2	Marl	1.28	2.15					1.67	2.87						

Strat. unit – stratigraphic unit, Vol. – volume fraction, $\lambda_{\perp}$ and $\lambda_{//}$ – thermal conductivity perpendicular and parallel to bedding, Dry and Sat – dry and saturated conditions, respectively, Litho. – lithotype, sst. – sandstone, marlst. – marlstone, calc. – calcareous, fibr. – fibrous. Composition of individual units is estimated from different borehole sections located in the basin facies of the Trier–Luxembourg Basin.

Table A.3.7 continued

						$\lambda_{\perp}$						$\lambda_{//}$						A	
						Sample		Litho.		Unit		Sample		Litho.		Unit		Litho.	
Strat. unit	Lithology	Vol. [%]	Sample	Unit	Lithotype	Dry	Sat	Dry	Sat	Dry	Sat	Dry	Sat	Dry	Sat	Dry	Sat	Dry	Sat
						[W m^{-1}K^{-1}]						[W m^{-1}K^{-1}]							
lm3	Clayey sandstone	11	Rb34	lm3a	Silty sandstone	2.43	2.69	2.43	2.69	1.3	2.0	2.18	2.64	2.18	2.64	1.5	2.5	0.9	1.0
	Silty marl	89	Rb35	lm2	Marl	1.17	2.03	1.15	1.97			1.61	2.75	1.47	2.52			1.3	1.3
			Rb36	lm2	Marl	1.28	2.15					1.67	2.87						
			Rb40	lm3b	Clayey siltstone	0.99	1.73					1.12	1.95						
lm2	Clayey marl	100	Rb35	lm2	Marl	1.17	2.03	1.23	2.09	1.2	2.1	1.61	2.75	1.64	2.81	1.6	2.8	1.3	1.3
			Rb36	lm2	Marl	1.28	2.15					1.67	2.87						
lm1	Limestone	23	Rb39	li3	Marly limestone	1.94	2.17	1.94	2.17	1.39	2.1	2.10	2.19	2.10	2.19	1.7	2.7	1.1	1.0
	Marl	77	Rb35	lm2	Marl	1.17	2.03	1.23	2.09			1.61	2.75	1.64	2.81			1.3	1.3
			Rb36	lm2	Marl	1.28	2.15					1.67	2.87						
li4	Clayey, silty marl	87	Rb38	li4	Marly siltstone	1.64	2.29	1.64	2.29	1.7	2.3	1.93	2.63	1.93	2.63	2.0	2.6	1.2	1.1
		13	Rb39	li3	Marly limestone	1.94	2.17	1.94	2.17			2.10	2.19	2.10	2.19			1.1	1.0
li3	Marlstone	59	Rw13	li1	Marlstone	1.28	1.50	1.28	1.50	1.6	1.8	1.88	2.24	1.88	2.24	2.0	2.2	1.5	1.5
	Limestone	41	Rb39	li3	Marly limestone	1.94	2.17	1.94	2.17			2.10	2.19	2.10	2.19			1.1	1.0
li2	Sandstone	45	Rw10	li2	Sandstone	1.77	3.87	1.77	3.87	2.3	3.6	1.71	3.73	1.71	3.73	2.3	3.6	1.0	1.0
	Calcareous sandstone	55	Kb2	li2	Calcareous sandstone	2.83	3.38	2.77	3.43			2.71	3.38	2.81	3.48			1.0	1.0
			Rw2	li2	Marly, calc. sandstone	2.70	3.48					2.90	3.57						
li1	Marlstone	46	Rw13	li1	Marlstone	1.28	1.50	1.28	1.50	1.5	1.8	1.88	2.24	1.88	2.24	1.9	2.3	1.5	1.5
	Sandy marlstone	30	Gr6	li1	Sandy marlstone	1.36	2.08	1.36	2.08			1.70	2.56	1.70	2.56			1.3	1.2
	Limestone	24	Rb39	li3	Marly limestone	1.94	2.17	1.94	2.17			2.10	2.19	2.10	2.19			1.1	1.0
ko	Clayey marl	25	Rb5	km3	Clayey marl	2.30	2.69	2.02	2.47	1.6	2.1	2.50	3.02	2.39	2.97	2.1	2.8	1.2	1.2
			Rb9	km2	Marl	1.73	2.25					2.27	2.92						
	Sandstone + conglomerate	33	Gr7	ko1	Marly sandstone	1.70	2.69	1.70	2.69			2.08	3.27	2.08	3.27			1.2	1.2
	Claystone	42	Rw13	li1	Marlstone	1.28	1.50	1.28	1.50			1.88	2.24	1.88	2.24			1.5	1.5
km3	Dolomitic marlstone	45	Gr11	km3	Dolomitic marlstone	1.57	2.19	1.57	2.19	2.0	2.4	1.67	2.32	1.67	2.32	2.1	2.6	1.1	1.1
	Marl	39	Rb5	km3	Clayey marl	2.30	2.69	2.30	2.69			2.50	3.02	2.50	3.02			1.1	1.1
	Anhydrite + gypsum	11	Rb16	km3	Anhydrite + fibr. gypsum	1.95	1.96	1.95	1.96			1.98	1.94	1.98	1.94			1.0	1.0
	Dolomite	5	Rb17	km1	Dolomite	3.20	3.39	3.20	3.39			3.39	3.37	3.39	3.37			1.1	1.0

Table A.3.7 continued

						$\lambda_{\perp}$						$\lambda_{//}$						A	
						Sample		Litho.		Unit		Sample		Litho.		Unit		Litho.	
Strat. unit	Lithology	Vol.	Sample	Unit	Lithotype	Dry	Sat	Dry	Sat	Dry	Sat	Dry	Sat	Dry	Sat	Dry	Sat	Dry	Sat
		[%]				[W m^{-1}K^{-1}]						[W m^{-1}K^{-1}]							
km2	Clayey marl	89	Rb9	km2	Marl	1.73	2.25	1.73	2.25	1.8	2.3	2.27	2.92	2.27	2.92	2.4	3.0	1.3	1.3
	Gypsum	0	Rb16	km3	Anhydrite + fibr. gypsum	1.95	1.96	1.95	1.96			1.98	1.94	1.98	1.94			1.0	1.0
	Sandstone	11	Rb8	km2	Dolomitic sandstone	2.68	3.04	2.68	3.04			3.03	3.20	3.03	3.20			1.1	1.1
km2S	Sandstone	90	Ki5	km2S	Silty, micaceous sst.	0.91	1.91	0.91	1.91	1.0	1.9	0.95	2.04	0.95	2.04	1.1	2.1	1.0	1.1
	Claystone	10	Rb9	km2	Marl	1.73	2.25	1.73	2.25			2.27	2.92	2.27	2.92			1.3	1.3
km1	Clayey marl	4	Wb1	km1	Clayey marl	1.29	2.04	1.29	2.04	1.6	2.2	1.45	2.31	1.45	2.31	1.9	2.6	1.1	1.1
	Marl	30	Rb13	km1	Silty marl	1.83	2.66	1.83	2.66			2.12	3.04	2.12	3.04			1.2	1.1
	Sandstone	6	Rb10	km1	Dolomitic sandstone	2.65	3.45	2.65	3.45			2.25	2.91	2.25	2.91			0.8	0.8
	Dolomitic marlstone	60	Wb7	ku	Silty, dolomitic marlstone	1.35	1.81	1.35	1.81			1.82	2.39	1.82	2.39			1.3	1.3
ku	Dolomite	7	Rb17	km1	Dolomite	3.20	3.39	3.20	3.39	1.5	2.0	3.39	3.37	3.39	3.37	1.8	2.4	1.1	1.0
	Marl	39	Wb1	km1	Clayey marl	1.29	2.04	1.29	2.04			1.45	2.31	1.45	2.31			1.1	1.1
	Marlstone	54	Wb7	ku	Silty, dolomitic marlstone	1.35	1.81	1.35	1.81			1.82	2.39	1.82	2.39			1.3	1.3
mos	Dolomitic sandstone	100	Id1	mos	Dolomitic sandstone	3.75	4.82	3.75	4.82	3.8	4.8	3.78	5.02	3.78	5.02	3.8	5.0	1.0	1.0
mo2	Marlstone	5	Wb15	mm1	Marlstone	2.60	2.77	2.60	2.77	3.6	3.7	3.14	3.45	3.14	3.45	3.8	3.8	1.2	1.2
	Dolomite	23	Wb8	mo1	Dolomite	4.17	4.36	4.23	4.32			4.21	4.34	4.27	4.33			1.0	1.0
			Wb12	mo1	Dolomite	4.28	4.28					4.32	4.32						
	Dolomitic siltstone/marlstone	13	Wb9	mo1	Dolomitic siltstone	2.60	3.07	2.76	3.09			2.77	3.16	2.80	3.12			1.0	1.0
			Wb10	mo1	Dolomitic marlstone	2.91	3.10					2.82	3.08						
	Marly dolomite	59	Wb11	mo1	Marly dolomite	3.68	3.80	3.61	3.65			3.83	3.82	3.83	3.83			1.1	1.0
			Wb13	mo1	Marly dolomite	3.53	3.50					3.83	3.83						
mo1	Marlstone	0	Wb15	mm1	Marlstone	2.60	2.77	2.60	2.77	3.9	4.0	3.14	3.45	3.14	3.45	4.0	4.1	1.2	1.2
	Dolomite	52	Wb8	mo1	Dolomite	4.17	4.36	4.23	4.32			4.21	4.34	4.27	4.33			1.0	1.0
			Wb12	mo1	Dolomite	4.28	4.28					4.32	4.32						
	Dolomitic siltstone/marlstone	3	Wb9	mo1	Dolomitic siltstone	2.60	3.07	2.76	3.09			2.77	3.16	2.80	3.12			1.0	1.0
			Wb10	mo1	Dolomitic marlstone	2.91	3.10					2.82	3.08						
	Marly dolomite	45	Wb11	mo1	Marly dolomite	3.68	3.80	3.61	3.65			3.83	3.82	3.83	3.83			1.1	1.0
			Wb13	mo1	Marly dolomite	3.53	3.50					3.83	3.83						

Table A.3.7 continued

						$\lambda_{\perp}$						$\lambda_{//}$						A	
						Sample		Litho.		Unit		Sample		Litho.		Unit		Litho.	
Strat. unit	Lithology	Vol.	Sample	Unit	Lithotype	Dry	Sat	Dry	Sat	Dry	Sat	Dry	Sat	Dry	Sat	Dry	Sat	Dry	Sat
		[%]				[W m^{-1}K^{-1}]						[W m^{-1}K^{-1}]							
mm2	Marlstone	67	Wb15	mm1	Marlstone	2.60	2.77	2.36	2.72	3.0	3.3	3.14	3.45	2.75	3.19	3.2	3.6	1.2	1.2
			Me2	mm1	Silty, dolomitic marlstone	2.32	2.84					2.61	3.12						
			Me6	mm1	Dolomitic marlstone	2.17	2.56					2.49	3.00						
	Dolomite	33	Wb8	mo1	Dolomite	4.17	4.36	4.23	4.32			4.21	4.34	4.27	4.33			1.0	1.0
			Wb12	mo1	Dolomite	4.28	4.28					4.32	4.32						
mm1	Marl (gypsum-rich)	45	Me12	mm1	Silty marl	1.73	1.94	1.52	1.85	2.4	2.7	1.94	2.15	1.95	2.37	2.7	3.1	1.3	1.3
			Me13	mm1	Silty marl	1.55	1.94					1.96	2.42						
			Me14	mm1	Silty marl	1.29	1.76					2.00	2.65						
			Me15	mm1	Silty marl	1.49	1.77					1.89	2.25						
	Dolomitic marlstone	27	Me2	mm1	Silty, dolomitic marlstone	2.32	2.84	2.36	2.72			2.61	3.12	2.75	3.19			1.2	1.2
			Me6	mm1	Dolomitic marlstone	2.17	2.56					2.49	3.00						
			Wb15	mm1	Marlstone	2.60	2.77					3.14	3.45						
	Dolomite	3	Wb8	mo1	Dolomite	4.17	4.36	4.23	4.32			4.21	4.34	4.27	4.33			1.0	1.0
			Wb12	mo1	Dolomite	4.28	4.28					4.32	4.32						
	Sandstone	13	Me7	mm1	Silty sandstone	3.02	3.61	3.02	3.61			3.12	3.78	3.12	3.78			1.0	1.0
	Anhydrite	12	Me8	mm1	Anhydrite	4.53	4.51	4.53	4.51			4.62	4.52	4.62	4.52			1.0	1.0
mu2	Dolomite	20	Rd18	mu	Marly dolomite	3.36	3.68	3.36	3.68	2.1	2.6	3.45	3.82	3.45	3.82	2.3	2.8	1.0	1.0
	Marlstone	55	Rd17	mu	Dolomitic marlstone	1.82	2.22	1.82	2.22			2.00	2.44	2.00	2.44			1.1	1.1
	Sandy marlstone	25	Rd14	mu	Dolomitic, sandy marlstone	1.66	2.42	1.66	2.42			1.95	2.67	1.95	2.67			1.2	1.1
mu1	Dolomite	2	Rd18	mu	Marly dolomite	3.36	3.68	3.36	3.68	1.7	2.4	3.45	3.82	3.45	3.82	2.0	2.6	1.0	1.0
	Marlstone	31	Rd17	mu	Dolomitic marlstone	1.82	2.22	1.82	2.22			2.00	2.44	2.00	2.44			1.1	1.1
	Sandy marlstone	67	Rd14	mu	Dolomitic, sandy marlst.	1.66	2.42	1.66	2.42			1.95	2.67	1.95	2.67			1.2	1.1
so2	Sandstone	46	Rd1	so1	Dolomitic sandstone	1.75	2.84	1.71	2.99	1.7	2.7	1.83	3.09	1.77	3.19	2.0	3.2	1.0	1.1
			Rd4	so1	Dolomitic sandstone	1.67	3.14					1.71	3.29						
	Claystone	54	Rd12	so1	Silty claystone	1.64	2.38	1.64	2.38			2.22	3.25	2.22	3.25			1.4	1.4
so1	Dolomitic sandstone	71	Rd1	so1	Dolomitic sandstone	1.75	2.84	1.71	2.99	1.7	2.8	1.83	3.09	1.77	3.19	1.9	3.2	1.0	1.1
			Rd4	so1	Dolomitic sandstone	1.67	3.14					1.71	3.29						
	Clayey sst./sandy claystone	29	Rd12	so1	Silty claystone	1.64	2.38	1.64	2.38			2.22	3.25	2.22	3.25			1.4	1.4

Table A.3.7 continued

						$\lambda_{\perp}$						$\lambda_{//}$						A	
						Sample		Litho.		Unit		Sample		Litho.		Unit		Litho.	
Strat. unit	Lithology	Vol.	Sample	Unit	Lithotype	Dry	Sat	Dry	Sat	Dry	Sat	Dry	Sat	Dry	Sat	Dry	Sat	Dry	Sat
		[%]				[W m^{-1}K^{-1}]						[W m^{-1}K^{-1}]							
sm (+ su)	Sandstone	81	Bi2	sm	Sandstone (soft)	1.77	2.95	1.77	2.95	1.9	3.0	1.84	3.10	1.84	3.10	2.0	3.2	1.0	1.1
	Sandstone (conglomeratic)	12	Bi5	sm	Sandstone (coarse, gravel)	2.86	3.83	2.86	3.83			2.77	3.79	2.77	3.79			1.0	1.0
	Claystone	7	Rd12	so1	Silty claystone	1.64	2.38	1.64	2.38			2.22	3.25	2.22	3.25			1.4	1.4

Table A.3.8: Details on samples used to compose the thermal conductivity of Mesozoic geological formations (margin facies) of the Trier–Luxembourg Basin.

						$\lambda_{\perp}$						$\lambda_{//}$						A	
						Sample		Litho.		Unit		Sample		Litho.		Unit		Litho.	
Strat. unit	Lithology	Vol.	Sample	Unit	Lithotype	Dry	Sat	Dry	Sat	Dry	Sat	Dry	Sat	Dry	Sat	Dry	Sat	Dry	Sat
		[%]				[W m^{-1} K^{-1}]						[W m^{-1} K^{-1}]							
km2	Sandy marlstone	47	Rb12	km1	Sandy marlstone	2.26	2.46	2.23	2.86	2.2	2.9	2.10	2.50	2.30	3.00	2.3	3.0	1.0	1.0
+ km2S			Rb11	km1	Marly sandstone	2.67	3.17					2.72	3.29						
			El3	km1	Clayey sandstone	2.16	3.15					2.15	3.17						
	Sandy marl	35	Rb13	km1	Silty marl	1.83	2.66	1.83	2.66			2.22	3.04	2.22	3.04			1.2	1.1
	Dolomitic sandstone	18	Rb10	km1	Dolomitic sandstone	2.65	3.45	2.67	3.25			2.25	2.91	2.64	3.06			1.0	0.9
			Rb8	km2	Dolomitic sandstone	2.68	3.04					3.03	3.20						
km1	Sandy marlstone	51	Rb12	km1	Sandy marlstone	2.26	2.46	2.36	2.93	2.6	3.3	2.10	2.50	2.32	2.99	2.5	3.2	1.0	1.0
			Rb11	km1	Marly sandstone	2.67	3.17					2.72	3.29						
			El3	km1	Clayey sandstone	2.16	3.15					2.15	3.17						
	Conglomeratic dolomite	2	Rb17	km1	Dolomite (marly)	3.20	3.39	3.20	3.39			3.39	3.37	3.39	3.37			1.1	1.0
	Dolomitic + sandy congl.	14	Rb19	km1	Sandy, dolomitic congl.	4.11	4.48	4.11	4.48			3.96	4.30	3.96	4.30			1.0	1.0
	Marly sandstone	24	Rb10	km1	Dolomitic sandstone	2.65	3.45	2.65	3.45			2.25	2.91	2.25	2.91			0.8	0.8
	Marl	9	Rb13	km1	Silty marl	1.83	2.66	1.83	2.66			2.22	3.04	2.22	3.04			1.2	1.1
ku	Siltstone	21	Rb21	ku	Silty marlstone	2.84	3.49	2.84	3.49	2.4	3.1	3.59	4.42	3.59	4.42	2.6	3.4	1.3	1.3
	Marl + claystone	23	Ev1	ku	Sandy, dolomitic marlst.	2.09	3.61	1.80	3.15			2.07	3.65	1.92	3.41			1.1	1.1
			Ev3	ku	Sandy, dolomitic marl	1.50	2.69					1.76	3.17						
	Sandstone	48	Rb12	km1	Sandy marlstone	2.26	2.46	2.36	2.93			2.10	2.50	2.32	2.99			1.0	1.0
			Rb11	km1	Marly sandstone	2.67	3.17					2.72	3.29						
			El3	km1	Clayey sandstone	2.16	3.15					2.15	3.17						
	Sandy dolomite	8	Rb17	km1	Dolomite (marly)	3.20	3.39	3.20	3.39			3.39	3.37	3.39	3.37			1.1	1.0

Strat. unit – stratigraphic unit, Vol. – volume fraction, $\lambda_{\perp}$ and $\lambda_{//}$ – thermal conductivity perpendicular and parallel to bedding, Dry and Sat – dry and saturated conditions, respectively, Litho. – lithotype, congl. – conglomerate, marlst. – marlstone. Composition of individual units is estimated from different borehole sections located in the margin facies of the Trier–Luxembourg Basin.

Table A.3.8 continued

						$\lambda_{\perp}$						$\lambda_{//}$						A	
						Sample		Litho.		Unit		Sample		Litho.		Unit		Litho.	
Strat. unit	Lithology	Vol.	Sample	Unit	Lithotype	Dry	Sat	Dry	Sat	Dry	Sat	Dry	Sat	Dry	Sat	Dry	Sat	Dry	Sat
		[%]				[W m^{-1} K^{-1}]						[W m^{-1} K^{-1}]							
mo(s)	Marly, sandy dolomite	24	Rb24	mo	Marly dolomite	3.50	4.09	3.50	4.09	3.0	3.9	3.54	3.83	3.54	3.83	3.0	3.9	1.0	0.9
(Rebierg +		15	Rb25	mo	Marly, sandy dolomite	4.47	4.58	4.47	4.58			4.09	4.15	4.09	4.15			0.9	0.9
Everlange)	Dolomitic sandstone	23	Ev5	mo	Dolomitic sandstone	2.66	4.11	2.66	4.11			2.70	4.20	2.70	4.20			1.0	1.0
		11	Id1	mos	Dolomitic sandstone	3.75	4.82	3.75	4.82			3.78	5.02	3.78	5.02			1.0	1.0
	Sandstone + siltstone	11	Ev9	mg	Sandstone	1.39	3.05	1.39	3.05			1.48	3.21	1.48	3.21			1.1	1.1
		6	Ev11	mg	Sandy siltstone	1.64	2.76	1.64	2.76			1.81	3.28	1.81	3.28			1.1	1.2
		10	Me11	mm1	Silty sandstone	2.32	2.98	2.32	2.98			2.57	3.30	2.57	3.30			1.1	1.1
mo(s)	Dolomitic sandstone	11	Id1	mos	Dolomitic sandstone	3.75	4.82	3.75	4.82	3.2	3.6	3.78	5.02	3.78	5.02	3.3	3.7	1.0	1.0
(Bissen +	Marlstone	5	Wb15	mm1	Marlstone	2.6	2.77	2.60	2.77			3.14	3.45	3.14	3.45			1.2	1.2
Mersch)	Dolomite	19	Wb8	mo1	Dolomite	4.17	4.36	4.23	4.32			4.21	4.34	4.27	4.33			1.0	1.0
			Wb12	mo1	Dolomite	4.28	4.28					4.32	4.32						
	Dolomitic siltstone/marlstone	54	Wb9	mo1	Dolomitic siltstone	2.60	3.07	2.76	3.09			2.77	3.16	2.80	3.12			1.0	1.0
			Wb10	mo1	Dolomitic marlstone	2.91	3.10					2.82	3.08						
	Marly dolomite	11	Wb11	mo1	Marly dolomite	3.68	3.80	3.61	3.65			3.83	3.82	3.83	3.83			1.1	1.0
			Wb13	mo1	Marly dolomite	3.53	3.50					3.83	3.83						
mg	Sandstone/conglomerate	27	Ev9	mg	Sandstone	1.39	3.05	1.39	3.05	1.7	2.5	1.48	3.21	1.48	3.21	1.9	2.9	1.1	1.1
(Rebierg +	Siltstone	11	Ev11	mg	Sandy siltstone	1.64	2.76	1.64	2.76			1.81	3.28	1.81	3.28			1.1	1.2
Everlange)		12	Me11	mm1	Silty sandstone	2.32	2.98	2.32	2.98			2.57	3.30	2.57	3.30			1.1	1.1
	Dolomite	4	Rd18	mu	Marly dolomite	3.36	3.68	3.36	3.68			3.45	3.82	3.45	3.82			1.0	1.0
	Clay-/marlstone	46	Me12	mm1	Silty marl	1.73	1.94	1.52	1.85			1.94	2.15	1.95	2.37			1.3	1.3
			Me13	mm1	Silty marl	1.55	1.94					1.96	2.42						
			Me14	mm1	Silty marl	1.29	1.76					2.00	2.65						
			Me15	mm1	Silty marl	1.49	1.77					1.89	2.25						

Table A.3.8 continued

						$\lambda_{\perp}$						$\lambda_{//}$						A	
						Sample		Litho.		Unit		Sample		Litho.		Unit		Litho.	
Strat. unit	Lithology	Vol.	Sample	Unit	Lithotype	Dry	Sat	Dry	Sat	Dry	Sat	Dry	Sat	Dry	Sat	Dry	Sat	Dry	Sat
		[%]				[W m^{-1} K^{-1}]						[W m^{-1} K^{-1}]							
mm	Marl (gypsum-rich)	70	Me12	mm1	Silty marl	1.73	1.94	1.52	1.85	2.0	2.3	1.94	2.15	1.95	2.37	2.3	2.7	1.3	1.3
(Mersch)			Me13	mm1	Silty marl	1.55	1.94					1.96	2.42						
			Me14	mm1	Silty marl	1.29	1.76					2.00	2.65						
			Me15	mm1	Silty marl	1.49	1.77					1.89	2.25						
	Dolomite	5	Wb8	mo1	Dolomite	4.17	4.36	4.23	4.32			4.21	4.34	4.27	4.33			1.0	1.0
			Wb12	mo1	Dolomite	4.28	4.28					4.32	4.32						
	Dolomitic marlstone	21	Me2	mm1	Silty, dolomitic marlstone	2.32	2.84	2.50	3.00			2.61	3.12	2.69	3.30			1.1	1.1
			Me6	mm1	Dolomitic marlstone	2.17	2.56					2.23	3.00						
			Me7	mm1	Silty sandstone	3.02	3.61					3.22	3.78						
	Anhydrite	4	Me8	mm1	Anhydrite	4.53	4.51	4.53	4.51			4.62	4.52	4.62	4.52			1.0	1.0
mu	Sandy/marly dolomite	3	Rd18	mu	Marly dolomite	3.36	3.68	3.36	3.68	1.7	2.5	3.45	3.82	3.45	3.82	2.1	3.2	1.0	1.0
	Sandstone	6	Ev13	mu	Dolomitic sandstone	1.65	3.04	1.65	3.04			1.70	3.07	1.70	3.07			1.0	1.0
	Sandy marlstone	3	Rd14	mu	Dolomitic, sandy marlst.	1.66	2.42	1.66	2.42			1.95	2.67	1.95	2.67			1.2	1.1
	Dolomitic marlstone	11	Rd17	mu	Dolomitic marlstone	1.82	2.22	1.82	2.22			2.00	2.44	2.00	2.44			1.1	1.1
	Claystone	51	Rd12	so1	Silty claystone	1.64	2.38	1.64	2.38			2.22	3.25	2.22	3.25			1.4	1.4
	Siltstone	26	Ev11	mg	Sandy siltstone	1.64	2.76	1.64	2.76			1.81	3.28	1.81	3.28			1.1	1.2
so2	Dolomitic sandstone	22	Rd1	so1	Dolomitic sandstone	1.75	2.84	1.71	2.99	1.6	2.6	1.83	3.09	1.77	3.19	2.0	3.2	1.0	1.1
			Rd4	so1	Dolomitic sandstone	1.67	3.14					1.71	3.29						
	Sandstone	24	Ev19	so	Marly sandstone	1.53	2.75	1.53	2.75			1.70	2.99	1.70	2.99			1.1	1.1
	Claystone + (sandy) siltstone	54	Rd12	so1	Silty claystone	1.64	2.38	1.64	2.38			2.22	3.25	2.22	3.25			1.4	1.4
so1	Conglomerate	25	Ev25	so	Sandy, dolomitic congl.	2.81	3.42	2.81	3.42	1.9	2.9	2.87	3.58	2.87	3.58	2.1	3.2	1.0	1.0
	Conglomeratic sandstone	43	Ev24	so	Sandstone (conglomeratic)	1.42	2.84	1.61	2.94			1.59	2.88	1.71	3.09			1.1	1.0
			Rd1	so1	Sandstone (dolomitic)	1.75	2.84					1.83	3.09						
			Rd4	so1	Sandstone (dolomitic)	1.67	3.14					1.71	3.29						
	Marly sandstone	17	Ev19	so	Marly sandstone	1.53	2.75	1.53	2.75			1.70	2.99	1.70	2.99			1.1	1.1
	Claystone + siltstone	15	Rd12	so1	Silty claystone	1.64	2.38	1.64	2.38			2.22	3.25	2.22	3.25			1.4	1.4

Table A.3.9: Summary of petrophysical properties of the Cambrian and Ordovician groups, geological formations and their members in the Lower Paleozoic Stavelot Massif.

Stratigraphy	Group	Formation	Code	Mbr.	Lithology	Vol.	Fm. λ_{dry}			Fm. λ_{sat}				Error	Formation		Thickness range				
							⊥	//	AM	⊥	//	AM	A		d	H	Min.	Ref.		Max.	Ref.
						[%]	[W m^{-1} K^{-1}]			[W m^{-1} K^{-1}]			[-]	[%]	[10^{3} kg m^{-3}]	[10^{-6} W m^{-3}]	[m]			[m]	
Ordovician	SALM	Bihain	BIH		Silty slate (includes slate 65% and minor sandstone 15 %)	100	2.0	2.4	2.2	2.3	2.8	2.6	1.2	10	2.78	2.1	200	a	–	300	a
		Ottré	OTT	COL	Slate	100	2.2	2.6	2.4	2.7	3.2	3.0	1.2	10	2.87	2.3	50	c	–	100	a
				PLA	Slate	100	1.9	2.7	2.3	2.4	3.3	2.8	1.4	15	2.89	1.9	30	c	–	50	a
				MEU	Silty slate	90	2.4	2.9	2.6	2.9	3.4	3.1	1.2	15	2.91	1.8	70	c	–	150	a
					Sandstone	10															
		Jalhay	JAL	LIE	Silty slate	80	2.6	2.8	2.7	3.1	3.3	3.2	1.1	10	2.69	1.9	80	c	–	100	a
					Sandstone	20															
				SPA	Silty slate	40	3.3	3.5	3.4	3.9	4.1	4.0	1.1	15	2.69	1.5	200	a		200	a
					Quartzitic sst.	60															
				SLW	Slate	20	3.2	3.7	3.4	3.7	4.2	3.9	1.1	15	2.72	2.0	60	c	–	250	a
					Silty slate	50															
					Quartzite	30															
Cambrian	REVIN	La Gleize	GLE	Rv5	Slate	50	2.4	3.5	3.0	2.7	3.8	3.3	1.4	5	2.75	2.5	> 300	a	>	300	a
(Upper)					Silty slate	50															
		La Venne	VEN	Rv3 + 4	Slate	30	4.4	4.9	4.7	4.9	5.5	5.2	1.1	5	2.72	1.7	500	c	>	500	a
					Quartzite	70															
		Wanne	WAN	Rv1 + 2	Slate	40	3.3	4.3	3.8	4.0	5.0	4.5	1.3	5	2.75	2.1	200	a	–	650	c
					Silty slate	20															
					Quartzite	40															
(Lower)	DEVILLE	Bellevaux	BEL		Slate/shale	45	3.6	3.9	3.8	4.3	4.7	4.5	1.1	10	2.66	1.3	150	a, c	–	250	a
					Quartz. sst./quartzite	55															
		Hour	HUR		Slate	40	3.6	4.0	3.8	4.3	4.6	4.5	1.1	15	2.70	1.2	> 150	a, c	>	1200	b
					Quartzite	60															
Total thickness																	1990		>	4050	

Mbr. – Member, Vol. – volume fraction, Fm. – formation, λ_{dry} and λ_{sat} – thermal conductivity under dry and saturated conditions, respectively, ⊥ and // – thermal conductivity perpendicular and parallel to cleavage, AM – arithmetic mean, A – anisotropy, d – density, H – radiogenic heat production, Ref. – literature reference, Quartz. – quartzitic, sst. – sandstone. Thickness range of the individual formations after a) Geukens (2008), b) Hollmann (1997) and c) Verniers et al. (2001). Lithological composition is estimated after Geukens (2008) and Verniers et al. (2001).

Table A.3.10: Summary of petrophysical properties of the Lower Devonian geological formations in the Belgian and Luxembourgish Ardennes.

Stratigraphy	Formation	Code		Lithology	Vol.	Fm. λ_{dry}			Fm. λ_{sat}				Error	Fm.		Thickness range							
						⊥	//	AM	⊥	//	AM	A		d	H	Min.	Ref.		Max.	Ref.		Max.	Ref.
		Be	Lux		[%]	[$Wm^{-1}K^{-1}$]			[$Wm^{-1}K^{-1}$]			[-]	[%]	[10^3 kg m^{-3}]	[10^{-6} W m^{-3}]	[m]			[m]			[m]	
Emsian	Wiltz		E3	Sandy shale	100	2.2	2.0	2.1	2.6	2.4	2.5	0.9	10	2.62	2.0	250	g	>	1200	e			
	Berlé		q	Quartzite	100	4.5	4.5	4.5	6.2	6.2	6.2	1.0	20	2.50	0.6	0	g	–	15	g			
	Clervaux		E2	Shale/siltstone	70	2.9	2.9	2.9	3.3	3.3	3.3	1.0	15	2.66	1.5	200	g	–	660	e	–	1400	d
				Sandstone	25																		
				Quartzitic sst.	5																		
	Schuttbourg		E1b	Silty slate/siltstone	70	2.8	3.1	2.9	3.5	3.5	3.5	1.0	15	2.68	1.5	750	g	–	1200	e	>	3500	f
				Sandstone	20																		
				Quarzitic sst.	10																		
	Stolzembourg		E1a	Sandy shale	94	2.6	2.7	2.7	3.1	3.3	3.2	1.0	15	2.73	2.0	700	c	–	900	e			
				Quartzitic sst.	6																		
Siegenian	La Roche	LAR	Sg3	Sandy shale	100	2.4	2.5	2.5	2.9	3.0	2.9	1.0	15	2.67	2.0	> 1400	e	–	1500	b			
(~Praguian)			Sg3a	Slate	100	2.4	2.9	2.6	2.9	3.5	3.2	1.2	10	2.73	2.0				400	b			
	Villé	VIL	Sg2	Shale/siltstone	35	3.0	3.0	3.0	3.5	3.5	3.5	1.0	15	2.58	1.5	250	a, c	–	550	c			
				Siltstone + calc. sst/ sandy limestone	65																		
	Mirwart	MIR	Sg1	Slate	80	2.8	2.9	2.8	3.4	3.5	3.4	1.0	10	2.73	1.8	700	a	–	1050	c			
				Silty slate	5																		
				Quartz. sst./quartzite	15																		

Be – Belgium, Lux – Luxembourg, Vol. – volume fraction, Fm. – formation, λ_{dry} and λ_{sat} – thermal conductivity under dry and saturated conditions, respectively, ⊥ and // – thermal conductivity perpendicular and parallel to cleavage, AM – arithmetic mean, A – anisotropy, d – density, H – radiogenic heat production, Ref. – literature reference, sst. – sandstone, calc. – calcareous, Quartz. – quartzitic, Congl. – conglomeratic. Composition of the individual formations is estimated after Dejonghe (2008) and Lucius (1950). The highly variable thickness estimates or ranges are retrieved from a) Bultynck & Dejonghe (2001), b) Colbach & Maquil (2003), c) Dejonghe (2008), d) Furtak (1965), e) Hollmann (1997) and f) Konrad & Wachsmut (1973) and g) Lucius (1950).

Table A.3.10 continued

Stratigraphy	Formation	Code		Lithology	Vol.	Fm. λ_{dry}			Fm. λ_{sat}				Error	Fm.		Thickness range						
						⊥	//	AM	⊥	//	AM	A		d	H	Min.	Ref.		Max.	Ref.	Max.	Ref.
		Be	Lux		[%]	[$Wm^{-1}K^{-1}$]			[$Wm^{-1}K^{-1}$]			[-]	[%]	[10^3 kg m^{-3}]	[10^{-6} W m^{-3}]	[m]			[m]		[m]	
Lochkovian	Saint-Hubert	STH		Shale/siltstone	80	3.3	3.3	3.3	3.9	3.9	3.9	1.0	15	2.70	1.8	550	a, c	–	700	a, c		
				Sandstone	20																	
	Oignies	OIG		Siltstone	15	2.6	2.6	2.6	3.0	3.0	3.0	1.0	10	2.60	1.7	700	c	–	1200	c		
				Shale	60																	
				Sandstone	25																	
	Fépin	FEP		Shale/siltstone	50	3.7	3.7	3.7	4.3	4.4	4.3	1.0	15	2.67	1.4	20	a, c	>	300	a		
				Sandstone	20																	
				Congl. sst.	30																	
Total thickness																5520		>	9675		> 12715	

Table A.3.11: Summary of petrophysical properties of the Lower Devonian and Proterozoic geological formations in the Eifel and Mosel Syncline/Hunsrück regions.

Region	Stratigraphy	Formation	Code	Lithology	Vol.	Fm. λ_{dry}			Fm. λ_{sat}				Error	Fm.		Thickness range				
						⊥	//	AM	⊥	//	AM	A		d	H	Min.	Ref.		Max.	Ref.
					[%]	[W m^{-1} K^{-1}]			[W m^{-1} K^{-1}]			[-]	[%]	[10^{3} kg m^{-3}]	[10^{-6} W m^{-3}]	[m]			[m]	
Eifel/ Mosel Syncline	Eifelian	Wissenbach-Schiefer	de/dzoWI	Shale	> 90	2.5	2.5	2.5	3.0	2.9	3.0	1.0	15	2.64	1.9	400	a	–	450	a
				Quartzitic sst.	< 10															
	Emsian	Kieselgallenschiefer	dzo3KG	Shale/shaly siltstone	> 90	2.4	2.3	2.3	2.8	2.8	2.8	1.0	15	2.64	2.0	50	a	–	500	a
	(Upper)			Siltstone/sandstone	< 10															
		Sphärosideritschiefer	dzo3SS	Shale/shaly siltstone	> 80	2.6	2.5	2.6	3.1	3.0	3.0	1.0	15	2.65	1.9	100	a	–	250	a
				Sandstone	< 20															
		Brauneisenstein	dzo3BE	Sandstone	> 70	3.2	3.1	3.1	3.7	3.7	3.7	1.0	15	2.65	1.2	30	a	–	40	a
				Shale/shaly siltstone	< 30															
		Rötelgallen-Schichten	dzo2RG	Shale	50	2.9	2.9	2.9	3.4	3.4	3.4	1.0	15	2.65	1.5	30	a	–	40	a
				Sandstone + limestone	50															
		Höllenthal-Schichten	dzo2HÖ	Shale	50	2.9	2.9	2.9	3.4	3.4	3.4	1.0	15	2.65	1.5	60	a	–	130	a
				Sandstone	50															
		Flußbach-Schichten	dzo1FL	Shale/shaly siltstone	40	3.4	3.4	3.4	3.6	3.6	3.6	1.0	15	2.65	1.4	20	a	–	200	a, b
				Quartzitic sst.	60															
		Emsquarzit	dzo1EQ	Quartzitic sst./quartzite	> 90	4.3	4.3	4.3	5.8	5.8	5.8	1.0	20	2.51	0.7	15	a	–	200	a
				Shale	< 10															
	(Lower)	Klerf-Schichten	dzu3KL	Shale/shaly siltstone	30	3.4	3.4	3.4	3.9	3.9	3.9	1.0	15	2.67	1.2	500	b	–	1200	b
				Sandstone/quartzite	70															
		Gladbach-Schichten	dzu3GL	Shale	50–70	2.8	2.9	2.8	3.3	3.4	3.4	1.0	10	2.72	1.9	3000	b	–	3000	b
				Siltstone/sandstone	30–50															
		"Singhofen-Schichten"	dzS	Shale/sandy shale	90	2.7	2.8	2.7	3.2	3.3	3.2	1.0	15	2.73	1.9	0		>	1000	b
				Sandstone	10															

Vol. – volume fraction, Fm. – formation, λ_{dry} and λ_{sat} – thermal conductivity under dry and saturated conditions, respectively, ⊥ and // – thermal conductivity perpendicular and parallel to cleavage, AM – arithmetic mean, A – anisotropy, d – density, H – radiogenic heat production, Ref. – literature reference, sst. – sandstone. Composition of the individual formations is taken from Häfner et al. (2007) and completed by LGB (2005). The regional thickness estimates are retrieved from a) Häfner et al. (2007), b) LGB (2005), c) Wildberger (1992) and d) own completing estimates.

Table A.3.11 continued

Region	Stratigraphy	Formation	Code	Lithology	Vol.	Fm. λ_{dry}			Fm. λ_{sat}				Error	Fm.		Thickness range				
						⊥	//	AM	⊥	//	AM	A		d	H	Min.	Ref.		Max.	Ref.
					[%]	[W m^{-1} K^{-1}]			[W m^{-1} K^{-1}]			[-]	[%]	[10^{3} kg m^{-3}]	[10^{-6} W m^{-3}]	[m]			[m]	
Hunsrück		Kaubschichten	dzu1KA	Shale	85	2.4	2.6	2.5	2.9	3.1	3.0	1.1	15	2.67	2.0	> 1500	c	>	1700	b
				Quartzitic sst.	15															
		Zerf-Schichten	dzu1ZE	Sandy shale	75	2.9	3.0	2.9	3.4	3.5	3.5	1.0	15	2.68	1.8	500	d	–	1000	d
				Quartzitic sst./quarzite	25															
	Siegenian (~Praguian)	Dhrontal-Schichten	ds3DR	Sandy shale	70	3.0	3.1	3.0	3.6	3.6	3.6	1.0	10	2.66	1.7	700	d	–	1000	c
				Quartzitic sst./quartzite	30															
		Taunusquarzit	ds2TQ	Quartzitic sst./quartzite	> 95	4.3	4.3	4.3	5.0	5.0	5.0	1.0	10	2.66	0.6	> 800	c	–	1200	c
		Hermeskeil-Schichten	ds1HE	Shale	50	3.3	3.3	3.3	3.9	3.9	3.9	1.0	10	2.64	1.5	150	b	–	600	b
				Quartzitic sst.	50															
	Gedinnian (~Loch-kovian)	Züsch-Schiefer	gd	Shale	80	3.1	3.2	3.1	3.9	4.0	3.9	1.0	20	2.70	1.8	> 1100	c	–	2000	b
				Quartzitic sst.	20															
	Neo-proterozoic	Wartenstein Gneiss	War	Gneiss	85			3.0			3.6			2.64	1.3	?			?	
				Quartzitic sst.	5															
				Quartzite	5															
				Micaschist	5															
Total thickness																> 8955		>	14510	

Table A.3.12: Summary of petrophysical properties of the Mesozoic geological formations (basin facies) of the Trier–Luxembourg Basin.

				Formation									Thickness range	
				$\lambda_\perp$		$\lambda_{//}$				d		ϕ	Unit	
Stratigraphy	Stratigraphic unit	Unit	Lithology	Vol.	Dry	Sat	Dry	Sat	A	Error	Dry	Sat	Min.	Max.
				[%]	[W m^{-1}K^{-1}]		[W m^{-1}K^{-1}]			[%]	[10^3 kg m^{-3}]		[%]	[m]	
Dogger	Marnes sableuses d'Audun-le-Tiche	dom4b	Sandy marlstone	100	2.1	2.5	2.1	2.5	1.0	15	2.35	2.48	13.4	15	15
	Calcaires d'Audun-le-Tiche	dom4a	Limestone	80	1.7	2.3	1.7	2.3	1.0	15	2.09	2.31	22.4	20	20
			Reef limestone (corals)	20											
	Calcaire de Haut-Pont	dom3	Sandy limestone	100	2.1	2.5	2.1	2.5	1.0	10	2.51	2.59	8.2	15	25
	Calcaire d'Ottange	dom2	Limestone	70	2.1	2.5	2.1	2.5	1.0	15	2.50	2.59	8.4	12	20
			Marlstone	30											
	Marnes micacées	dom1	Marlstone	10	1.5	2.3	1.6	2.5	1.1	15	2.10	2.26	15.7	8	12
			Marl	90											
Liassic + Aalenian	Minette	lo6-7 + dou	Iron-rich limestone + calc. sst.	50	1.5	2.2	1.6	2.2	1.0	15	2.25	2.43	18.2	11	68
			Iron-rich + marly sst.	50											
	C. à P. fallaciosum	lo5	Marl	100	1.4	2.3	1.5	2.5	1.1	15	2.06	2.22	16.5	10	10
	C. à G. striatulum	lo4	Sandstone	50	1.3	2.5	1.4	2.7	1.1	10	2.01	2.23	21.7	15	25
			Sandy marl	50											
	Marnes à A. voltzi	lo3	Marl	83	1.0	1.9	1.6	2.8	1.5	10	2.06	2.27	20.8	15	23
			Sandy marl	17											
	C. à H. bifrons	lo2	Marly claystone	100	1.1	1.8	1.3	2.1	1.2	5	2.12	2.31	19.5	20	30
	C. à H. falciferum	lo1	Marly claystone	100	1.1	1.8	1.3	2.1	1.2	5	2.12	2.31	19.5	25	35
	Macigno	lm3b	Marly sandstone	19	1.3	1.9	1.3	2.1	1.1	15	2.09	2.27	16.7	20	45
			Sandy claystone	81											
	Faciès sablo-marneux	lm3a	Clayey sandstone	2	1.2	2.1	1.7	2.8	1.3	15	2.16	2.35	19.2	15	35
			Silty marl	98											
	C. à P. spinatum	lm3	Clayey sandstone	11	1.3	2.0	1.5	2.5	1.2	15	2.14	2.32	18.0	25	35
			Silty marl	89											
	C. à A. margaritatus	lm2	Clayey marl	100	1.2	2.1	1.6	2.8	1.3	5	2.16	2.35	19.4	80	90
	Calcaire ocreux	lm1	Limestone	23	1.4	2.1	1.7	2.7	1.3	15	2.26	2.42	15.8	4	15
			Marl (calcareous)	77											

Vol. – volume fraction, $\lambda_\perp$ and $\lambda_{//}$ – thermal conductivity perpendicular and parallel to bedding, Dry and Sat – dry and saturated conditions, respectively, A – anisotropy, d – density, ϕ – porosity, C. – couches, calc. – calcareous, sst. – sandstone. Composition of individual units is an average of different borehole sections located in the basin facies of the Trier–Luxembourg Basin. Indicative thickness ranges are retrieved from the geological maps 1: 25,000 and completed after Schintgen & Förster (2013).

Table A.3.12 continued

				Formation									Thickness range	
					$\lambda_{\perp}$		$\lambda_{//}$				d		ϕ	Unit	
Stratigraphy	Stratigraphic unit	Unit	Lithology	Vol.	Dry	Sat	Dry	Sat	A	Error	Dry	Sat		Min.	Max.
				[%]	[W m^{-1}K^{-1}]		[W m^{-1}K^{-1}]			[%]	[10^{3} kg m^{-3}]		[%]	[m]	
	Marnes pauvres en fossiles	li4	Clayey, silty marl	87	1.7	2.3	2.0	2.6	1.1	10	2.30	2.39	9.1	30	40
			Limestone	13											
	Marnes et calcaires de Strassen	li3	Marlstone	59	1.6	1.8	2.0	2.2	1.3	10	2.44	2.49	5.5	8	10
			Limestone	41											
	Grès de Luxembourg	li2	Sandstone	45	2.3	3.6	2.3	3.6	1.0	5	2.21	2.38	16.9	10	105
			Calcareous sandstone	55											
	Marnes d'Elvange	li1	Marlstone	46	1.5	1.8	1.9	2.3	1.3	10	2.35	2.43	7.5	0	30
			Sandy marlstone	30											
			Limestone	24											
Keuper	Rhät	ko	Clayey marl	25	1.6	2.1	2.1	2.8	1.3	15	2.30	2.40	9.3	0	17
			Sandstone + conglomerate	33											
			Claystone	42											
	Steinmergelkeuper	km3	Dolomitic marlstone	45	2.0	2.4	2.1	2.6	1.1	10	2.39	2.47	7.9	50	75
			Marl	39											
			Anhydrite + gypsum	11											
			Dolomite	5											
	Rote Gipsmergel	km2	Clayey marl	89	1.8	2.3	2.4	3.0	1.3	15	2.34	2.43	8.8	15	30
			Gypsum	0											
			Sandstone	11											
	Schilfsandstein	km2S	Sandstone	90	1.0	1.9	1.1	2.1	1.1	15	1.90	2.18	28.1	0	50
			Claystone	10											
	Pseudomorphosen-keuper	km1	Clayey marl	4	1.6	2.2	1.9	2.6	1.2	15	2.32	2.43	10.9	50	100
			Marl	30											
			Sandstone	6											
			Dolomitic marlstone	60											
	Lettenkeuper	ku	Dolomite	7	1.5	2.0	1.8	2.4	1.2	15	2.30	2.43	12.0	15	28
			Marl	39											
			Marlstone	54											

Table A.3.12 continued

					Formation									Thickness range	
					$\lambda_{\perp}$		$\lambda_{//}$				d		ϕ	Unit	
Stratigraphy	Stratigraphic unit	Unit	Lithology	Vol.	Dry	Sat	Dry	Sat	A	Error	Dry	Sat		Min.	Max.
				[%]	[W m^{-1}K^{-1}]		[W m^{-1}K^{-1}]			[%]	[10^{3} kg m^{-3}]		[%]	[m]	
Muschelkalk	Gilsdorfer Sandstein	mos	Dolomitic sandstone	100	3.8	4.8	3.8	5.0	1.0	10	2.60	2.66	6.4	0	10
	Ceratitenschichten	mo2	Marl	5	3.6	3.7	3.8	3.8	1.0	10	2.74	2.77	2.3	20	30
			Dolomite	23											
			Dolomitic siltstone/marlstone	13											
			Marly dolomite	59											
	Trochitenschichten	mo1	Dolomite	52	3.9	4.0	4.0	4.1	1.0	10	2.78	2.80	1.6	20	34
			Dolomitic siltstone/marlstone	3											
			Marly dolomite	45											
	Linguladolomit	mm2	Marlstone	67	3.0	3.3	3.2	3.6	1.1	10	2.56	2.59	3.5	0	7
			Dolomite	33											
	Gipsmergel	mm1	Marl (gypsum-rich)	45	2.4	2.7	2.7	3.1	1.1	15	2.43	2.48	5.3	50	108
			Dolomitic marlstone	27											
			Dolomite	3											
			Sandstone	13											
			Anhydrite	12											
	Orbicularisschichten	mu2	Dolomite	20	2.1	2.6	2.3	2.8	1.1	15	2.46	2.54	7.6	0	7
			Marlstone	55											
			Sandy marlstone	25											
	Muschelsandstein	mu1	Dolomite	2	1.7	2.4	2.0	2.6	1.1	15	2.39	2.50	10.2	25	45
			Marlstone	31											
			Sandy marlstone	67											

Table A.3.12 continued

				Formation									Thickness range	
				$\lambda_{\perp}$		$\lambda_{//}$				d		ϕ	Unit	
Stratigraphy	Stratigraphic unit	Unit	Lithology	Vol.	Dry	Sat	Dry	Sat	A	Error	Dry	Sat	Min.	Max.
				[%]	[W m^{-1}K^{-1}]		[W m^{-1}K^{-1}]			[%]	[10^{3} kg m^{-3}]		[%]	[m]	
Buntsandstein	Voltziensandstein	so2	Sandstone	46	1.7	2.7	2.0	3.2	1.2	10	2.23	2.38	15.0	12	15
			Claystone	54											
	Zwischenschichten	so1	Dolomitic sandstone	71	1.7	2.8	1.9	3.2	1.1	10	2.20	2.37	16.7	75	150
			Clayey sst./sandy claystone	29											
	Vogesensandstein	sm (+ su)	Sandstone	81	1.9	3.0	2.0	3.2	1.1	15	2.08	2.29	20.6	15	340
			Sandstone (conglomeratic)	12											
			Claystone	7											

Table A.3.13: Summary of petrophysical properties of Mesozoic geological formations (margin facies) of the Trier–Luxembourg Basin.

					Formation									Thickness range	
					$\lambda_{\perp}$		$\lambda_{//}$				d		ϕ	Unit	
Stratigraphy	Stratigraphic unit	Unit	Lithology	Vol.	Dry	Sat	Dry	Sat	A	Error	Dry	Sat		Min.	Max.
				[%]	[W m^{-1}K^{-1}]		[W m^{-1}K^{-1}]			[%]	[10^{3} kg m^{-3}]		[%]	[m]	
Keuper	Rote Gipsmergel + Schilfsandstein	km2 + km2S	Sandy marlstone	47	2.2	2.9	2.3	3.0	1.1	15	2.34	2.43	9.8	2.5	19
			Sandy marl	35											
			Dolomitic sandstone	18											
	Pseudomorphosen-keuper	km1	Sandy marlstone	51	2.6	3.3	2.5	3.2	1.0	15	2.40	2.48	8.3	5	50
			Conglomeratic dolomite	2											
			Dolomitic + sandy conglomerate	14											
			Marly sandstone	24											
			Marl	9											
	Lettenkeuper	ku	Siltstone	21	2.4	3.1	2.6	3.4	1.1	15	2.39	2.49	9.7	6	15
			Marl + claystone	23											
			Sandstone	48											
			Sandy dolomite	8											
Muschelkalk	Gilsdorfer Sandstein	mo(s)	Marly, sandy dolomite	24	3.0	3.9	3.0	3.9	1.0	20	2.50	2.59	9.4	4	30
	+ Ceratitenschichten	(Rebierg +		15											
	+ Trochitenschichten	Everlange)	Dolomitic sandstone	23											
				11											
			Sandstone + siltstone	11											
				6											
				10											
		mo(s)	Dolomitic sandstone	11	3.2	3.6	3.3	3.7	1.0	20	2.67	2.71	4.4		
		(Bissen +	Marlstone	5											
		Mersch)	Dolomite	19											
			Dolomitic siltstone/marlstone	54											
			Marly dolomite	11											

Vol. – volume fraction, $\lambda_{\perp}$ and $\lambda_{//}$ – thermal conductivity perpendicular and parallel to bedding, Dry and Sat – dry and saturated conditions, respectively, A – anisotropy, d – density, ϕ – porosity. Composition of individual units is an average of different borehole sections located in margin facies of the Trier–Luxembourg Basin. Indicative thickness ranges are retrieved from the geological maps 1: 25,000.

Table A.3.13 continued

Stratigraphy	Stratigraphic unit	Unit	Lithology	Vol.	Formation $\lambda_{\perp}$ Dry	Formation $\lambda_{\perp}$ Sat	Formation $\lambda_{//}$ Dry	Formation $\lambda_{//}$ Sat	A	Error	d Dry	d Sat	ϕ	Thickness range Unit Min.	Thickness range Unit Max.
				[%]	[W m^{-1}K^{-1}]		[W m^{-1}K^{-1}]			[%]	[10^{3} kg m^{-3}]		[%]	[m]	
	Grobklastischer Muschelkalk	mg (Rebierg + Everlange)	Sandstone/ conglomerate	27	1.7	2.5	1.9	2.9	1.2	20	2.24	2.38	13.5	5	50
			Siltstone	11											
				12											
			Dolomite	4											
			Clay-/marlstone	46											
	Gipsmergel	mm (Mersch)	Marl (gypsum-rich)	70	2.0	2.3	2.3	2.7	1.2	20	2.37	2.43	6.3		
			Dolomite	5											
			Dolomitic marlstone	21											
			Anhydrite	4											
	Muschelsandstein	mu	Sandy/marly dolomite	3	1.7	2.5	2.1	3.2	1.2	20	2.28	2.42	13.3	0	25
			Sandstone	6											
			Sandy marlstone	3											
			Dolomitic marlstone	11											
			Claystone	51											
			Siltstone	26											
Buntsandstein	Voltziensandstein	so2	Dolomitic sandstone	22	1.6	2.6	2.0	3.2	1.2	15	2.22	2.36	14.5	0	12
			Sandstone	24											
			Claystone + (sandy) siltstone	54											
	Zwischenschichten	so1	Conglomerate	25	1.9	2.9	2.1	3.2	1.1	15	2.23	2.38	15.3	15	75
			Conglomeratic sandstone	43											
			Marly sandstone	17											
			Claystone + siltstone	15											

Table A.3.14: Details on samples used to compose the radiogenic heat production of the Cambrian and Ordovician groups, geological formations and their members in the Lower Paleozoic Stavelot Massif.

Group	Fm.	Mbr.	Lithology	Vol. [%]	Sample	Lithotype	H Sample [10^{-6} W m^{-3}]	H Litho.	H Fm.
SALM	BIH		Silty slate (includes slate 65% and minor sandstone 15 %)	100	BIH-06	Silty slate	2.09	2.1	2.1
	OTT	COL	Slate	100	COL-05	Slate	2.34	2.3	2.3
		PLA	Slate	100	PLA-01	Slate	1.89	1.9	1.9
		MEU	Silty slate	90	PLA-01	Slate	1.89	1.9	1.8
			Sandstone	10	Sg1-07	Quartzitic sst.	1.18	1.2	
	JAL	LIE	Silty slate	80	SPA-02	Silty slate	2.04	2.0	1.9
			Sandstone	20	Sg1-07	Quartzitic sst.	1.18	1.2	
		SPA	Silty slate	40	SPA-02	Silty slate	2.04	2.0	1.5
			Quartzitic sst.	60	Sg1-07	Quartzitic sst.	1.18	1.2	
		SLW	Slate	20	SLW-10	Slate	2.95	3.0	2.0
			Silty slate	50	SPA-02	Silty slate	2.04	2.0	
			Quartzite	30	GH3216	Quartzite	1.20	1.2	
REVIN	GLE	Rv5	Slate	50	GH3128	Slate	2.96	3.0	2.5
			Silty slate	50	SPA-02	Silty slate	2.04	2.0	
	VEN	Rv3 + 4	Slate	30	GH3128	Slate	2.96	3.0	1.7
			Quartzite	70	GH3216	Quartzite	1.20	1.2	
	WAN	Rv1 + 2	Slate	40	GH3128	Slate	2.96	3.0	2.1
			Silty slate	20	SPA-02	Silty slate	2.04	2.0	
			Quartzite	40	GH3216	Quartzite	1.20	1.2	
DEVILLE	BEL		Slate/shale	50	GH2331	Slate	1.94	1.9	1.3
			Quartz. sst./quartzite	50	GH350	Quartzite	0.59	0.6	
	HUR		Slate	45	GH2331	Slate	1.94	1.9	1.2
			Quartzite	55	GH350	Quartzite	0.59	0.6	
	War		Gneiss/mica shist	10	War-01	Gneiss	1.12	1.1	1.4
				80	War-03	Gneiss	1.55	1.6	
			Quartzitic sst./quartzite	10	GH350	Quartzite	0.59	0.6	

Fm. – formation, Mbr. – Member, Vol. – volume fraction, Litho. – lithotype, sst. – sandstone. Lithological composition is estimated after Geukens (2008) and Verniers et al. (2001).

Table A.3.15: Details on samples used to compose the radiogenic heat production of the Lower Devonian geological formations in the Belgian and Luxembourgish Ardennes.

Formation		Lithology	Vol.	Sample	Lithotype	H		
						Sample	Litho.	Fm.
Be	Lux		[%]			[10^{-6} W m^{-3}]		
	E3	Sandy shale	100	E1a-004	Sandy shale	1.99	2.0	2.0
				E1a-009	Sandy shale	2.15		
				Sg3-003	Sandy shale	1.96		
	q	Quartzite	100	GH350	Quartzite	0.59	0.6	0.6
	E2	Shale/siltstone	70	E1b-007	Siltstone	1.68	1.7	1.5
		Sandstone	25	E1a-011	Quartzitic sst.	0.96	1.0	
		Quartzitic sst.	5	E1a-011	Quartzitic sst.	0.96	1.0	
	E1b	Silty slate/siltstone	70	E1b-007	Siltstone	1.68	1.7	1.5
		Sandstone	20	E1a-011	Quartzitic sst.	0.96	1.0	
		Quarzitic sst.	10	E1a-011	Quartzitic sst.	0.96	1.0	
	E1a	Sandy shale	94	E1a-004	Sandy shale	1.99	2.0	2.0
				E1a-009	Sandy shale	2.15		
				Sg3-003	Sandy shale	1.96		
		Quartzitic sst.	6	E1a-011	Quartzitic sst.	0.96	1.0	
LAR	Sg3	Sandy shale	100	E1a-004	Sandy shale	1.99	2.0	2.0
				E1a-009	Sandy shale	2.15		
				Sg3-003	Sandy shale	1.96		
	Sg3a	Slate	100	Sg1-003	Slate	1.98	2.0	2.0
VIL	Sg2	Shale/siltstone	35	E1a-004	Sandy shale	1.99	2.0	1.5
				E1a-009	Sandy shale	2.15		
				Sg3-003	Sandy shale	1.96		
		Siltstone + calc. sst.	65	Sg1-07	Silty slate	1.18	1.2	
MIR	Sg1	Slate	80	Sg1-003	Slate	1.98	2.0	1.8
		Silty slate	5	Sg1-07	Silty slate	1.18	1.2	
		Quartz. sst./quartzite	15	E1a-011	Quartzitic sst.	0.96	1.0	
STH		Shale/siltstone	80	OIG-13	Shale	2.26	2.0	1.8
				FEP-07	Shale	1.73		
		Sandstone	20	E1a-011	Quartzitic sst.	0.96	1.0	
OIG		Siltstone	15	OIG-13	Shale	2.26	2.0	1.7
				FEP-07	Shale	1.73		
		Shale	60	OIG-13	Shale	2.26	2.0	
				FEP-07	Shale	1.73		
		Sandstone	25	E1a-011	Quartzitic sst.	0.96	1.0	
FEP		Shale/siltstone	50	OIG-13	Shale	2.26	2.0	1.4
				FEP-07	Shale	1.73		
		Sandstone	20	E1a-011	Quartzitic sst.	0.96	1.0	
		Congl. sandstone	30	GH350	Quartzite	0.59	0.6	

Be – Belgium, Lux – Luxembourg, Vol. – volume fraction, Litho. – lithotype, Fm. – formation, sst. – sandstone, calc. – calcareous, congl. – conglomeratic. Composition of the individual formations is estimated after Dejonghe (2008) and Lucius (1950).

Table A.3.16: Details on samples used to compose the radiogenic heat production of the Lower Devonian and Proterozoic geological formations in the Eifel and Mosel Syncline/Hunsrück regions.

Formation	Code	Lithology	Vol. [%]	Sample	Lithotype	H Sample [10^{-6} W m^{-3}]	H Litho. [10^{-6} W m^{-3}]	H Fm. [10^{-6} W m^{-3}]
Wissenbach-Schiefer	de/dzoWI	Shale	> 90	Sg3-003	Sandy shale	1.96	2.0	1.9
		Quartzitic sst.	< 10	E1a-011	Quartzitic sst.	0.96	1.0	
Kieselgallenschiefer	dzo3KG	Shale/shaly siltstone	> 90	E1a-004	Sandy shale	1.99	2.0	2.0
				E1a-009	Sandy shale	2.15		
				Sg3-003	Sandy shale	1.96		
		Siltstone/sandstone	< 10	E1b-007	Siltstone	1.68	1.7	
Sphärosideritschiefer	dzo3SS	Shale/shaly siltstone	> 80	E1a-004	Sandy shale	1.99	2.0	1.9
				E1a-009	Sandy shale	2.15		
				Sg3-003	Sandy shale	1.96		
		Sandstone	< 20	E1a-011	Quartzitic sst.	0.96	1.0	
Brauneisenstein	dzo3BE	Sandstone	> 70	E1a-011	Quartzitic sst.	0.96	1.0	1.2
		Shale/shaly siltstone	< 30	E1a-004	Sandy shale	1.99	2.0	
				E1a-009	Sandy shale	2.15		
				Sg3-003	Sandy shale	1.96		
Rötelgallen-Schichten	dzo2RG	Shale	50	E1a-004	Sandy shale	1.99	2.0	1.5
				E1a-009	Sandy shale	2.15		
				Sg3-003	Sandy shale	1.96		
		Sandstone + limestone	50	E1a-011	Quartzitic sst.	0.96	1.0	
Höllenthal-Schichten	dzo2HÖ	Shale	50	E1a-004	Sandy shale	1.99	2.0	1.5
				E1a-009	Sandy shale	2.15		
				Sg3-003	Sandy shale	1.96		
		Sandstone	50	E1a-011	Quartzitic sst.	0.96	1.0	
Flußbach-Schichten	dzo1FL	Shale/shaly siltstone	40	E1a-004	Sandy shale	1.99	2.0	1.4
				E1a-009	Sandy shale	2.15		
				Sg3-003	Sandy shale	1.96		
		Quartzitic sst.	60	E1a-011	Quartzitic sst.	0.96	1.0	
Emsquarzit	dzo1EQ	Quartzitic sst./quartzite	> 90	GH350	Quartzite	0.59	0.6	0.7
		Shale	< 10	E1a-004	Sandy shale	1.99	2.0	
				E1a-009	Sandy shale	2.15		
				Sg3-003	Sandy shale	1.96		
Klerf-Schichten	dzu3KL	Shale/shaly siltstone	30	E1b-007	Siltstone	1.68	1.7	1.2
		Sandstone/quartzite	70	E1a-011	Quartzitic sst.	0.96	1.0	
Gladbach-Schichten	dzu3GL	Shale	50–70	E1a-004	Sandy shale	1.99	2.0	1.9
				E1a-009	Sandy shale	2.15		
				Sg3-003	Sandy shale	1.96		
		Siltstone/sandstone	30–50	E1b-007	Siltstone	1.68	1.7	
"Singhofen-Schichten"	dzS	Shale/sandy shale	90	E1a-004	Sandy shale	1.99	2.0	1.9
				E1a-009	Sandy shale	2.15		
				Sg3-003	Sandy shale	1.96		
		Sandstone	10	E1a-011	Quartzitic sst.	0.96	1.0	

Vol. – volume fraction, Litho. – lithotype, Fm. – formation, sst. – sandstone. Composition of the individual formations is taken from Häfner et al. (2007) and completed according to LGB (2005).

Table A.3.16 continued

Formation	Code	Lithology	Vol. [%]	Sample	Lithotype	H Sample [10^{-6} W m^{-3}]	H Litho.	H Fm.
Kaubschichten	dzu1KA	Shale	85	E1a-004	Sandy shale	1.99	2.0	2.0
				E1a-009	Sandy shale	2.15		
				Sg3-003	Sandy shale	1.96		
		Slate	10	Sg1-003	Slate	1.98	2.0	
		Quartzitic sst.	5	E1a-011	Quartzitic sst.	0.96	1.0	
Zerf-Schichten	dzu1ZE	Sandy shale	75	E1a-004	Sandy shale	1.99	2.0	1.8
				E1a-009	Sandy shale	2.15		
				Sg3-003	Sandy shale	1.96		
		Quartzitic sst./quarzite	25	E1a-011	Quartzitic sst.	0.96	1.0	
Dhrontal-Schichten	ds3DR	Sandy shale	70	E1a-004	Sandy shale	1.99	2.0	1.7
				E1a-009	Sandy shale	2.15		
				Sg3-003	Sandy shale	1.96		
		Quartzitic sst./quartzite	30	E1a-011	Quartzitic sst.	0.96	1.0	
Taunusquarzit	ds2TQ	Quartzitic sst./quartzite	> 95	GH350	Quartzite	0.59	0.6	0.6
Hermeskeil-Schichten	ds1HE	Shale	50	OIG-13	Shale	2.26	2.0	1.5
				FEP-07	Shale	1.73		
		Quartzitic sst.	50	E1a-011	Quartzitic sst.	0.96	1.0	
Züsch-Schiefer	gd	Shale	80	OIG-13	Shale	2.26	2.0	1.8
				FEP-07	Shale	1.73		
		Quartzitic sst.	20	E1a-011	Quartzitic sst.	0.96	1.0	
Wartenstein Gneiss	War	Gneiss/mica schist	90	War-01	Gneiss	1.12	1.3	1.3
				War-03	Gneiss	1.55		
		Quartzite	10	GH350	Quartzite	0.59	0.6	

Table A.3.17: Geochemical data of representative rock samples.

Region	Ardennes									Stavelot Massif					SE Hunsrück		Grand-Halleux borehole			
Sample	E1b-07	E1a-04	E1a-09	E1a-11	Sg3-03	Sg1-03	Sg1-07	OIG-13	FEP-07	BIH-06	COL-05	PLA-01	SPA-02	SLW-10	War-01	War-03	GH350	GH2331	GH3128	GH3216
Lithotype	Stst	Sh	Sh	Sst	Sh	Sl	Sst	Sh	Sh	Ssl	Sl	Sl	Ssl	Sl	Gn	Gn	Q	Sl	Sl	Q
SiO_2 (wt%)	73.0	61.7	60.1	75.0	59.6	59.2	70.4	68.4	67.4	55.0	53.9	49.4	63.9	50.7	72.7	65.2	94.4	58.2	56.1	79.3
TiO_2	0.76	0.92	0.93	0.49	0.90	0.96	0.67	1.05	0.88	0.98	0.98	0.90	0.90	1.37	0.49	0.83	0.25	0.92	1.07	0.72
Al_2O_3	11.9	18.5	18.9	7.48	18.0	18.9	11.5	17.2	15.4	22.0	23.0	20.4	17.7	26.3	13.2	15.5	2.63	19.9	21.6	6.21
Fe_2O_3	5.32	6.29	6.82	8.11	6.62	7.92	8.91	4.68	6.88	9.53	9.62	15.47	5.60	6.00	3.84	6.36	0.76	7.99	7.38	6.40
MnO	0.02	0.07	0.13	0.15	0.10	0.14	0.15	<0.01	<0.01	0.34	0.82	1.61	0.14	0.06	0.05	0.08	<0.01	0.04	0.05	0.09
MgO	1.87	2.17	2.47	2.29	2.78	2.97	3.18	0.68	1.41	2.10	1.74	2.38	1.57	1.58	1.33	2.15	0.19	1.89	2.01	1.47
CaO	0.17	0.57	0.36	0.78	0.89	0.27	0.11	0.04	0.04	0.32	0.16	0.34	0.38	0.06	0.15	0.27	0.07	0.11	0.13	0.12
Na_2O	1.52	1.02	0.98	0.77	1.03	1.20	0.98	0.94	0.35	0.81	1.24	0.97	1.87	0.24	2.70	2.14	0.67	1.19	0.75	0.64
K_2O	1.88	3.82	3.90	0.31	3.62	3.16	0.89	3.40	2.88	3.38	3.63	3.17	3.90	6.76	2.82	3.36	0.39	5.26	4.47	0.68
Cr_2O_3	0.022	0.022	0.020	0.015	0.025	0.022	0.017	0.019	0.027	0.015	0.017	0.015	0.014	0.020	0.007	0.009	0.009	0.013	0.016	0.011
P_2O_5	0.10	0.14	0.16	0.23	0.13	0.17	0.08	0.07	0.07	0.26	0.13	0.24	0.10	0.09	0.08	0.19	0.02	0.07	0.06	0.03
LOI	3.36	4.66	5.01	3.62	6.01	4.57	3.65	3.11	3.57	4.77	4.03	4.14	3.48	5.99	2.35	3.39	0.57	3.63	6.08	3.49
Total	99.9	99.9	99.8	99.3	99.7	99.5	100.5	99.6	99.3	99.6	99.3	99.2	99.6	99.3	99.8	99.6	99.9	99.3	99.7	99.2
TOT/C	0.05	0.39	0.51	0.28	0.82	0.20	0.06	0.02	0.02	0.08	<0.02	<0.02	0.08	0.48	0.02	0.06	0.03	<0.02	1.39	0.44
TOT/S	<0.02	<0.02	0.05	<0.02	0.08	<0.02	<0.02	<0.02	0.07	<0.02	<0.02	<0.02	<0.02	<0.02	<0.02	<0.02	<0.02	<0.02	1.64	1.84
Ba (ppm)	319	495	541	54	480	608	171	638	3440	641	841	1360	844	1250	419	697	76	955	568	91
Be	2	3	3	<1	5	3	1	3	3	6	6	5	5	7	2	2	<1	6	6	1
Co	14.9	19.3	27.4	18.0	21.5	17.9	21.4	8.5	13.5	8.0	36.2	109	15.2	6.4	8.3	12.3	2.5	21.1	19.6	12.2
Cs	2.9	6.2	7.2	1.1	6.3	6.4	1.6	4.5	7.5	5.9	7.7	6.9	5.5	9.6	3.7	4.0	0.7	8.9	10.0	0.8
Ga	15.9	24.8	25.2	8.9	24.4	26.2	15.0	22.9	20.9	30.2	31.1	29.5	24.5	36.1	14.1	20.2	1.5	26.7	29.9	6.5
Hf	9.0	6.2	5.2	9.1	5.3	5.9	5.0	8.2	8.8	4.6	4.0	3.8	7.1	7.1	4.6	5.7	11.1	4.8	5.5	11.3
Nb	14.8	17.6	18.3	10.3	16.3	17.6	11.3	18.7	15.6	18.5	20.1	17.3	17.8	24.8	8.3	12.3	4.9	18.5	21.4	14.0
Rb	78	171	177	12	170	145	37	168	141	161	172	150	170	264	102	121	14	220	201	29
Sn	2	4	5	1	3	4	2	3	3	5	4	3	4	5	2	3	<1	3	4	1
Sr	67	108	108	119	117	110	51	136	171	158	321	295	136	77	42	47	31	125	114	24
Ta	1.2	1.1	1.3	0.6	1.1	1.2	0.9	1.4	1.2	1.5	1.5	1.1	1.4	1.9	0.6	0.8	0.4	1.3	1.6	1.0
Th	11.0	13.6	14.3	7.6	13.6	13.2	9.0	15.3	12.5	16.5	16.9	14.7	14.6	20.1	7.0	9.9	4.2	14.2	17.1	8.4
U	3.1	2.9	3.2	1.6	2.9	3.1	2.0	3.5	2.5	2.4	2.9	1.8	2.7	3.7	1.7	2.4	1.1	1.8	5.3	2.2
V	90	163	168	70	149	153	93	141	115	131	133	119	105	161	72	126	11	121	208	42
W	1.5	2.2	2.4	1.1	2.0	1.9	1.3	2.9	2.0	2.3	3.2	4.2	2.1	3.3	1.8	1.2	0.7	2.3	3.2	1.9
Zr	341	213	196	362	200	193	205	314	331	180	146	143	268	239	181	209	444	180	198	441

Table A.3.17 continued

Region	Ardennes									Stavelot Massif					SE Hunsrück		Grand-Halleux borehole			
Sample	E1b-07	E1a-04	E1a-09	E1a-11	Sg3-03	Sg1-03	Sg1-07	OIG-13	FEP-07	BIH-06	COL-05	PLA-01	SPA-02	SLW-10	War-01	War-03	GH350	GH2331	GH3128	GH3216
Lithotype	Ststt	Sh	Sh	Sst	Sh	Sl	Sst	Sh	Sh	Ssl	Sl	Sl	Ssl	Sl	Gn	Gn	Q	Sl	Sl	Q
Y	28.9	32.7	35.7	25.1	29.6	37.2	27.6	41.0	36.3	38.2	37.4	38.9	33.2	42.8	14.9	30.0	11.0	28.4	41.7	31.4
La	37.6	56.0	51.4	24.9	45.0	38.9	24.2	48.8	36.9	54.8	57.7	58.1	49.3	72.3	26.3	31.7	12.7	42.3	57.5	23.1
Ce	75.7	95.6	101	53.3	92.3	62.3	58.0	101	79.8	116	117	147	103	143	50.5	66.4	27.3	88.8	118	48.2
Pr	9.50	11.1	12.2	6.64	11.0	9.09	6.43	12.1	9.55	13.3	13.3	13.6	11.8	17.8	5.80	7.93	3.38	10.1	14.5	5.68
Nd	36.8	44.0	48.7	27.0	42.4	35.1	25.4	46.7	36.9	47.9	53.7	55.4	46.8	66.2	24.0	29.8	12.7	37.7	54.6	24.2
Sm	6.63	7.76	8.01	5.35	7.40	6.55	4.90	8.73	6.78	9.90	9.07	9.23	8.07	11.5	3.89	6.09	2.49	6.84	10.1	4.45
Eu	1.25	1.66	1.79	1.25	1.57	1.50	1.01	1.76	1.46	2.10	1.92	1.76	1.77	2.44	0.84	1.18	0.48	1.38	2.28	0.99
Gd	5.78	7.14	7.30	5.40	6.52	6.61	4.98	7.75	6.08	8.59	8.47	8.13	7.27	8.81	3.63	5.61	2.07	5.59	8.75	4.51
Tb	0.86	1.00	1.06	0.77	0.91	1.00	0.78	1.17	0.97	1.20	1.19	1.26	1.01	1.23	0.48	0.82	0.29	0.85	1.29	0.76
Dy	5.60	6.07	6.72	4.32	6.21	6.66	5.11	8.00	6.12	7.26	7.23	8.41	6.46	7.93	2.69	5.28	1.67	5.35	8.38	5.53
Ho	1.04	1.15	1.13	0.85	1.07	1.22	0.95	1.46	1.19	1.20	1.33	1.40	1.18	1.52	0.54	1.00	0.36	0.89	1.55	1.13
Er	3.05	3.42	3.42	2.62	3.30	3.58	2.59	4.22	3.51	3.50	3.82	4.07	3.39	4.57	1.54	2.98	1.15	2.88	4.19	3.30
Tm	0.46	0.51	0.53	0.34	0.47	0.52	0.39	0.61	0.54	0.50	0.53	0.55	0.48	0.67	0.25	0.44	0.17	0.40	0.64	0.51
Yb	2.97	3.25	3.59	2.43	3.07	3.31	2.56	4.55	3.27	3.03	3.26	3.70	3.32	4.39	1.67	3.05	1.29	3.13	4.33	3.35
Lu	0.44	0.50	0.48	0.34	0.47	0.51	0.38	0.61	0.54	0.45	0.50	0.51	0.48	0.64	0.25	0.42	0.18	0.43	0.62	0.52
Mo	<0.1	0.1	0.3	0.1	0.1	<0.1	<0.1	<0.1	<0.1	<0.1	<0.1	0.8	<0.1	0.3	<0.1	0.2	<0.1	0.1	3.2	0.3
Cu	12	12	43	9.9	26	26	26	5.1	2.2	20	17	8.1	24	32	8.3	40	3.1	41	52	18
Pb	7.3	9.9	2.5	8.7	21.7	9.3	6.0	4.9	4.8	9.4	6.7	7.9	11.6	23.9	10.6	14.9	1.1	2.4	8.4	19.9
Zn	66	74	66	67	91	102	112	35	63	128	76	116	82	92	37	85	10	80	93	54
Ag	<0.1	<0.1	<0.1	<0.1	<0.1	<0.1	<0.1	<0.1	<0.1	<0.1	<0.1	<0.1	<0.1	<0.1	<0.1	<0.1	<0.1	<0.1	0.2	<0.1
Ni	62.9	65.4	63.4	39.9	78.5	82.2	66.7	37.0	58.0	50.6	56.4	71.3	32.1	34.2	13.1	28.8	3.8	35.6	32.5	13.3
As	<0.5	3.0	16.0	3.9	10.4	10.3	0.6	<0.5	<0.5	22.2	2.6	17.3	1.4	36.5	2.8	12.8	<0.5	<0.5	<0.5	19.8
Cd	<0.1	<0.1	<0.1	<0.1	<0.1	<0.1	<0.1	<0.1	<0.1	<0.1	<0.1	<0.1	<0.1	<0.1	<0.1	<0.1	<0.1	<0.1	0.1	<0.1
Sb	<0.1	0.1	<0.1	0.4	<0.1	<0.1	<0.1	<0.1	<0.1	<0.1	<0.1	<0.1	<0.1	<0.1	<0.1	<0.1	<0.1	<0.1	0.2	0.3
Bi	0.1	0.2	0.3	<0.1	0.2	0.1	0.1	0.2	0.2	0.2	0.3	0.5	<0.1	0.1	<0.1	<0.1	<0.1	<0.1	0.3	0.3
Hg	0.02	<0.01	0.03	0.13	0.04	0.05	<0.01	0.05	0.03	<0.01	<0.01	<0.01	<0.01	<0.01	0.13	0.14	<0.01	<0.01	0.05	0.01
Tl	<0.1	<0.1	<0.1	<0.1	<0.1	<0.1	<0.1	0.1	<0.1	<0.1	<0.1	<0.1	0.1	<0.1	0.1	0.1	<0.1	<0.1	<0.1	<0.1
Se	0.5	<0.5	<0.5	0.6	<0.5	<0.5	<0.5	<0.5	<0.5	0.5	<0.5	0.6	<0.5	<0.5	<0.5	<0.5	<0.5	<0.5	<0.5	<0.5
Au (ppb)	<0.5	<0.5	<0.5	<0.5	<0.5	<0.5	<0.5	0.7	1.0	<0.5	<0.5	0.6	<0.5	<0.5	0.9	0.6	<0.5	<0.5	<0.5	0.9

3.10.3 References

Bultynck, P., Dejonghe, L. (2001). Devonian lithostratigraphic units (Belgium). In: Bultynck, P., Dejonghe, L. (Eds.), Guide to a Revised Lithostratigraphic Scale of Belgium, vol. 4 (1–2). Geologica Belgica, Brussels, pp. 39–69.

Colbach, R., Maquil, R. (2003). Carte géologique du Luxembourg 1:25000, feuille 7 Rédange. Serv. Géol. Luxemb., Luxembourg.

Dejonghe, L. (2008). Carte géologique de Wallonie 1/25.000, feuille 55/5–6 Hotton–Dochamps, notice explicative. Région Wallonne, Namur, 88 pp.

Furtak, H., (1965). Die Tektonik der underdevonischen Gesteinsfolge im deutsch–belgisch–luxemburgischen Grenzgebiet. Geol. Mitt. 4, 273–332.

Geukens, F. (2008). Carte géologique de Wallonie 1/25.000, feuille 55/3–4 Bra–Lierneux, notice explicative. Région Wallonne, Namur, 40 pp.

Graulich, J. M. (1980). Le sondage de Grand-Halleux. In: Professional Paper 175, Administration des Mines. Service géologique de Belgique, Brussels, 78 pp.

Häfner, F., Kött, A., Spindeldreher, J., Rein, B., Grubert, A. (2007). Nutzung von oberflächennaher Erdwärme für die Gebäudeheizung in Rheinland-Pfalz. Landesamt für Geologie und Bergbau Rheinland-Pfalz, Mainz, 97 pp., unpublished report.

Hollmann, E.G. (1997). Der variszische Vorlandüberschiebungsgürtel der Ostbelgischen Ardennen – Ein bilanziertes Modell. Aachener Geowiss. Beitr. 25, 235 pp.

Konrad, H.J., Wachsmut, W. (1973). Zur Lithologie und Tektonik des Unterdevons im südlichen Oesling Luxemburgs. Publ. Serv. Géol. Luxemb. 5, 1–20.

LGB (Landesamt für Geologie und Bergbau Rheinland-Pfalz) (Ed.) (2005). Geologie von Rheinland-Pfalz. Schweizerbart, Stuttgart, 400 pp.

Lucius, M. (1950). Das Oesling – Erläuterungen zu der geologischen Spezialkarte Luxemburgs. Publ. Serv. Géol. Luxemb., vol. 6. Luxembourg, 174 pp.

Meyer, W., Stets, J. (1980). Zur Paläogeographie von Unter- und Mitteldevon im westlichen und zentralen Rheinischen Schiefergebirge. Z. Dt. Geol. Ges. 131, 725–751.

Meyer, W., Stets, J. (1996). Das Rheintal zwischen Bingen und Bonn. In: Sammlung geol. Führer 89. Borntraeger, Berlin, Stuttgart, 386 pp.

Schintgen, T., Förster, A. (2013). Geology and basin structure of the Trier–Luxembourg Basin – implications for the existence of a buried Rotliegend graben. Z. Dt. Ges. Geowiss. 164 (4), 615–637.

Stets, J., Schäfer, A. (2002). Depositional environments in the Lower Devonian siliciclastics of

the Rhenohercynian Basin (Rheinisches Schiefergebirge, W-Germany) – Case studies and a model. Contr. Sed. Geol. 22, 77 pp.

Verniers, J., Herbosch, A., Vanguestaine, M., Geukens, F., Delcambre, B., Pingot J.-L., Belanger, I., Hennebert, M., Debacker, T., Sintubin, M., De Vos, W. (2001). Cambrian–Ordovician–Silurian lithostratigraphic units (Belgium). In: Bultynck, P., Dejonghe, L. (Eds.), Guide to a Revised Lithostratigraphic Scale of Belgium, vol. 4 (1–2). Geologica Belgica, Brussels, pp. 5–38.

Wildberger, J. (1992). Zur tektonischen Entwicklung des südwestlichen Hunsrücks (SW-Deutschland). Mitt. Pollichia 79, 5–119.

4 Exploration for deep geothermal reservoirs in Luxembourg and the surroundings – perspectives of geothermal energy use

Tom Schintgen

Published in: Geothermal Energy (2015), 3 (1).
http://dx.doi.org/10.1186/s40517-015-0028-2

4.1 Abstract

The aim of this paper is to combine different types of information necessary for a first rather qualitative assessment of deep geothermal reservoirs in the region of Luxembourg. Within the geological framework, the study area encompasses Luxembourg and the surrounding areas of Belgium, Germany and France. On the one hand, the focus is laid on low-enthalpy hydrothermal reservoirs in Mesozoic aquifers in the Trier–Luxembourg Embayment. On the other hand, petrothermal reservoirs in the Devonian basement of the Ardennes and Eifel regions are considered for exploitation by Enhanced/Engineered Geothermal Systems (EGS). Among the Mesozoic aquifers, the Buntsandstein aquifer characterized by temperatures of up to 50 °C is a suitable hydrothermal reservoir that could be exploited by means of heat pumps or provide direct heat for various applications. The most promising area is the zone of the SE–Luxembourg Graben. The aquifer is warmest underneath the upper Alzette valley and the limestone plateau in Lorraine, where the Buntsandstein aquifer lies below a thick Mesozoic cover. At the base of an inferred Rotliegend graben in the same area, temperatures of up to 75 °C are expected. However, geological and hydraulic conditions are uncertain.
In the Lower Devonian basement, thick sandstone-/quartzite-rich formations with temperatures >90 °C are expected at depths >3.5 km and likely offer the possibility of direct heat use. The setting of the Südeifel (South Eifel) region, including the Müllerthal region near Echternach, as a tectonically active zone may offer the possibility of deep hydrothermal reservoirs in the fractured Lower Devonian basement. Based on recent data on the structure of the Trier–Luxembourg Basin, the new concept presents the Müllerthal–Südeifel Depression as a Cenozoic tectonic structure that is still mobile and relevant for geothermal exploration. Beyond direct use of geothermal heat, the expected modest temperatures at 5 km depth (about 120 °C) and increased permeability by EGS in the quartzite-rich Lochkovian could prospectively enable combined geothermal heat production and power generation in Luxembourg and the western realm of the Eifel region.

4.2 Introduction

4.2.1 Status quo of geothermal energy use

Geothermal energy currently represents a very low percentage of the national energy mix in Luxembourg and geothermal resources in the subsurface of Luxembourg and the surrounding areas are barely known. Its use is mainly restricted to heat pump systems (Biermayr et al., 2007;

Häfner et al., 2007). A remarkable exception is hydrothermal water tapped since 1846 by means of deep wells in Mondorf (southeastern Luxembourg) and used for the local spa (Mf in Fig. 4.1a; Bintz, 2000; Lucius, 1923, 1948, 1949; Leichtle, 1980). The water originates from the Buntsandstein aquifer at depths between 600 and 700 m with temperatures in the range of 25–28 °C. Similarly, the French site of Amnéville (Am) exploits for the local spa warm water (36–42 °C) since 1979 by means of 900 m deep wells. In the more densely populated southern part of Luxembourg, large areas are concerned with the conflicting uses of groundwater for drinking purposes and geothermal exploitation. This particularly hinders the areal development of heat pump systems in the shallow subsurface. Protected areas are shown in the national geoportal (ACT, 2014). Two major aquifers, i.e. the sandstone-dominated Upper Buntsandstein and the Luxembourg Sandstone Formation, are used for provision of drinking water (Bintz, 2003; Bintz et al., 1982, Lucius, 1953). However, the exploited shallow groundwater resources (<200 m depth) are vulnerable for contamination.

Regarding the surrounding countries, the potential of geothermal energy in Belgium was assessed by Berckmans and Vandenberghe (1998), while the geothermal conditions of the Rhineland–Palatinate in Germany were presented by Storz (2007). Häfner et al. (2007) evaluated the possibility of using of geothermal energy for space heating in the adjoining Trier–Bitburg region. A comprehensive study of mineral and thermal springs in the Eifel and Ardennes regions for geothermal anomalies was performed by Langguth and Plum (1984). In a recent and comprehensive study of the deep subsurface of Hesse (Germany) by means of 3-D-modelling (Bär et al., 2011; and references therein), all types of deep geothermal applications, including hydrothermal and petrothermal systems as well as fault zones and deep borehole heat exhangers, were considered. At present, the adjoining areas of the Südeifel region in Germany (Fig. 4.1) are not considered as targets for exploitation of hydrothermal reservoirs (Kaltschmitt et al., 1999; Stober et al., 2009). By contrast, the Paris Basin and the underlying Variscan basement in France are considered as potential areas for the development of geothermal resources (Bonté et al., 2010). For the Lorraine region in particular, the geothermal potential of shallow aquifers using heat pumps is presented by Bourgine et al. (2007). In Belgium (Berckmans and Vandenberghe, 1998) and the German Rhineland–Palatinate (Storz, 2007), the development of petrothermal systems using EGS are also not yet effective.

Until recently, the assessment of geothermal resources and their evaluation for different geothermal applications in Luxembourg and the adjoining areas was hampered by the absence of deep boreholes (Schintgen and Förster, 2013) and lack of temperature prognosis at depth. Conceptual geological models incorporated into thermal models allow evaluating the

possibilities for different types of geothermal uses and to pinpoint the most promising areas for geothermal exploration. The regional and local surface geology and conceptual subsurface models presented by Schintgen and Förster (2013) and Schintgen et al. (2015) form the basis for geothermal exploration presented in this paper. Two main types of geothermal reservoirs are considered: (1) the low-enthalpy hydrothermal reservoirs and (2) the petrothermal reservoirs for exploitation by Enhanced/Engineered Geothermal Systems (EGS).

4.2.2 Background on different types of geothermal utilizations

Geothermal energy is stored as heat in rocks and trapped vapour or liquid such as water or brines (Muffler and Cataldi, 1978; IEA, 2011). The different possibilities for its utilization are also related to depth and subsurface temperatures and lead to the distinction of shallow and deep geothermal resources. Shallow geothermal energy refers to systems frequently using heat pumps for exploitation of near-surface environments characterized by temperatures <20°C and depths <400 m (Stober et al., 2009). Deep geothermal energy refers to direct use of geothermal heat at temperatures >20 °C (Líndal, 1973; Saadat et al., 2010). Major applications are in spas and swimming pools for balneological purposes, in industry for process heating, in agriculture for greenhouse or soil heating or in aquaculture for pond heating. For example, for greenhouse heating temperatures >40 °C are required, and for district and space heating, temperatures >60 °C (Pluymaekers et al., 2012). In order to efficiently use a wider temperature domain, different applications demanding successively lower temperatures are ideally implemented in a cascade (IEA, 2011; Líndal, 1973). Space cooling is also possible using geothermal heat with a minimum temperature of 60–70 °C as an energy source for heat-driven sorption chillers instead of electrically-driven compression chillers (IEA, 2011; Líndal, 1973; Saadat et al., 2010). Another important field of application related to geothermal energy is the seasonal storage of solar energy or spare heat in deep aquifers (e.g., Stober and Bucher, 2012).

In contrast to volcanologically active regions, low- and medium-enthalpy reservoirs, characterized by temperatures <200 °C, are widespread in Europe and gain increasing attention because their potential is large and expandable (Kramers et al., 2012; Tester et al., 2006). Hydrothermal and petrothermal systems are distinguished. Hydrothermal systems are systems of warm or hot water present in deep aquifers or hydraulically conductive fault zones (Muffler and Cataldi, 1978). Where natural permeability is too low for economic–technical use of geothermal energy, natural joints can be hydraulically stimulated or new fractures formed by injecting pressurized water to enhance permeability and create a heat exchanger, a procedure

designated by Enhanced/Engineered Geothermal Systems (EGS technology; Breede et al., 2013; Held et al., 2014; Huenges, 2010). These are called petrothermal systems, unconventional geothermal resources or Hot-Dry-Rock (HDR) systems (Breede et al., 2013; ENGINE Coordination Action, 2008). In contrast to hydrothermal systems, EGS predominantly makes accessible heat stored in rocks (Muffler and Cataldi, 1978; Tester et al., 2006). Numerous existing EGS projects are still at pilot/demonstration-scale (Breede et al. 2013) with a high proportion of R&D funding, especially during the cost-intensive drilling and stimulation phases associated with exploration and geological–technical risks (Rybach, 2010; Sperber et al., 2010; IEA, 2011). The most common and simple type of a hydrothermal system is a hydrothermal doublet (two-well-system), consisting of a reservoir heat exchanger commonly at a depth of several kilometers (<5–6 km depth) exploited by a warm/hot production well, a heat exchanger at the surface for transferring the heat to a secondary circuit and a cold injection well. For heat production only, it is possible to install deep coaxial pipes in a single borehole operating as closed systems independent from local geology.

The production of electricity in low- and medium-enthalpy systems is only possible in binary systems using working fluids with low boiling point, notably ORC (Organic Rankine Cycle) power plants or Kalina systems based on an ammonia-water mixture, reaching an efficiency of 10–15% with minimum temperatures of about 120 °C (ENGINE Coordination Action 2008). According to Garnish (2002) and Rybach (2010), for the deployment of EGS technology in petrothermal reservoirs, production rates of 50–100 l s^{-1} and fluid temperatures at wellhead of 150–200 °C are preferable. Most of the current European EGS projects are characterized by reservoir/bottomhole temperatures <165 °C (e.g., Bruchsal, Landau, Unterhaching, Insheim, Mauerstetten, Groß Schönebeck, Soultz; Breede et al., 2013) and worldwide operating flow rates frequently are <40 l s^{-1} (Breede et al. 2013). From an economic and ecological point of view, the heat remaining after power production should be used according to the principle of cogeneration or combined heat and power generation (IEA, 2011; Paschen et al., 2003). The technical lifetime of a doublet system usually is 30 years (e.g., Kramers et al., 2012), which is due to the fact that conductive heat flow within rock is too small to compensate heat extraction (Muffler and Cataldi, 1978).

4.3 Regional geology

An adequate understanding of the geology and its structural/tectonic framework is of paramount importance for the evaluation of subsurface conditions, notably temperature and permeability, relevant for the identification and exploitation of geothermal reservoirs. Despite the limited size of the study area, regional geology is multifaceted. It is characterized by various sedimentary rock ranging mainly from Cambrian through Mesozoic to Quaternary volcanics. Lithotypes range from metasediments such as Lower Palaeozoic quartzite and slate, Lower Devonian shale, sandstone, quartzitic sandstone and carbonates to Permian and Mesozoic claystone, siltstone, sandstone, conglomerate, marlstone and carbonates (Schintgen et al., 2015).

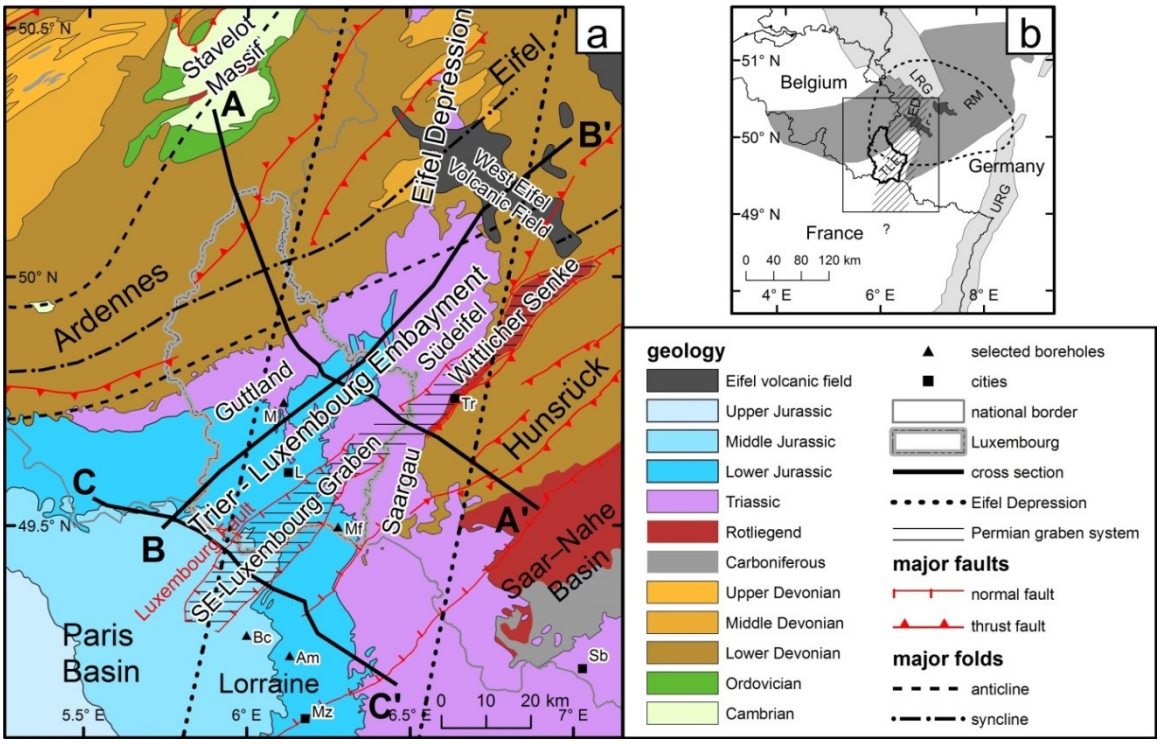

Fig. 4.1: (a) Regional geological map of the study area (modified from Schintgen and Förster, 2013). Geographical units are indicated. The location of the map within Western Europe is shown in b. Main cities and boreholes are mentioned in the text. Black bold lines and letters indicate the cross sections A–A', B–B' and C–C'. (b) Simplified basement tectonic map of Luxembourg and surroundings. Rectangle indicates location of geological map shown in a. with indication of the Rhenish Massif (RM), the Lower and Upper Rhine Grabens (LRG and URG, respectively), the Eifel Depression (ED; hatched zone) and the Trier–Luxembourg Embayment (TLE). Dashed contour indicates the location of the Eifel plume according to Keyser et al. (2002).

Fig. 4.1 shows the major geological subunits of the study area and its location with respect to the Rhenish Massif (RM) and the European Cenozoic Rift System (ECRIS). As a geographical orientation, the major cities of Luxembourg (L), Trier (Tr), Metz (Mz) and Saarbrücken (Sb) are indicated in Fig. 4.1. The Eifel Depression (Eifeler-Nord-Süd Zone) is interpreted as an important cross fold within the RM, separating the Ardennes (to the west side) from the Eifel region (to the east side) (Murawski et al., 1983). The study area is characterized by two contrasting geological environments, the Mesozoic rock of the Trier–Luxembourg Embayment (TLE) and the mostly Lower Devonian rock of the RM. The Wittlicher Rotliegend Senke (WS) represents a relatively narrow Permian Graben within the southwestern part of the RM (Stets, 2004).

4.3.1 Mesozoic and Rotliegend

The TLE (Fig. 4.1; in German: Trier–Luxemburger Bucht) refers to the present-day structure and appearance of the Mesozoic sedimentary record, which constitutes a tectonically enhanced and partially eroded counterpart of the former Trier–Luxembourg Basin (TLB; Dittrich, 2011a, 2014; Schintgen and Förster, 2013). As shown in Fig. 4.2, it is composed of subhorizontal layers of alternating hard and soft lithotypes of Triassic and Jurassic age. The TLE forms a northeastern extension of the Paris Basin reaching about 80 km into the RM. Sub-regions of the TLE are the Guttland in Luxembourg, and the Südeifel (South Eifel) and Saargau in Germany. The South Eifel region, encompassing the Bitburg and Trier sub-basins (Dittrich, 2011a), is a geologically and structurally integral part of the TLE though this region is frequently handled separately on either side of the German–Luxembourgish border. According to Schintgen and Förster (2013), the development of the Mesozoic TLB is attributed to a synsedimentary zone of weakness of SW–NE orientation along a Permian graben system. It consists of a buried part, the SE–Luxembourg Graben (SELG), and a relatively well known exposed part, the Wittlicher Senke. In the Trier–Wittlich area, the infill of the 5–10-km-wide graben is an about 1000-m-thick succession of Rotliegend sediments. The dominantly siliciclastic lithotypes are breccia/conglomerates, sandstones, siltstone and claystone of fluvial origin as well as an ignimbrite layer at its base (Stets, 2004).

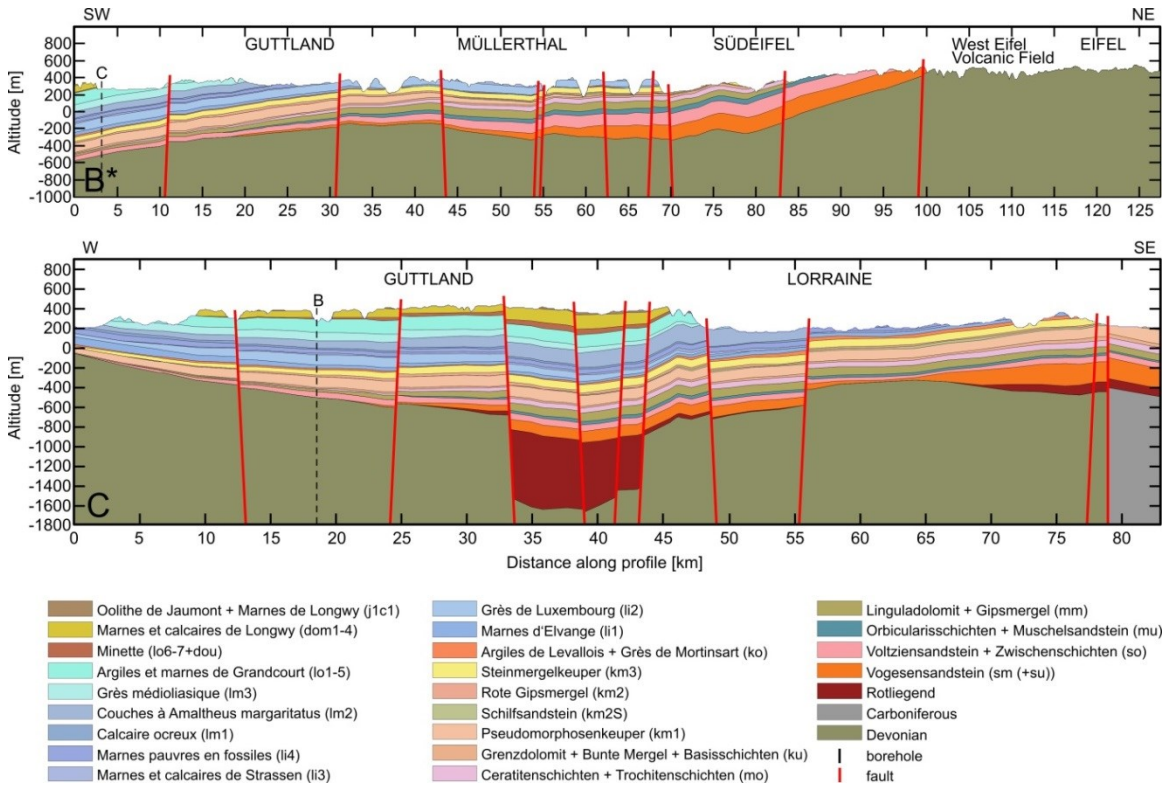

Fig. 4.2: Geological cross sections of the Trier–Luxembourg Embayment (modified from Schintgen and Förster, 2013). For location see Fig. 4.1a. Vertical exaggeration is 10-fold for profile B and 7.5-fold for profile C. Black dashed lines correspond to intersection with the indicated cross section.

4.3.2 Lower Devonian

The Variscan basement of the RM is exposed in the Ardennes in Belgium and Luxembourg, as well as in the adjoining Eifel and Hunsrück regions in Germany, and is buried below the TLE (Fig. 4.1a). The geology and structure of the study area are illustrated by cross sections in Fig. 4.3. It is predominantly composed of thick Lower Devonian sediments characterized by a relatively homogeneous, shale-rich clastic-rock assemblage. Numerous thrust faults characterize the Hunsrück, whereas persistent fold structures are typical for the Ardennes and Eifel regions. Besides shale, all Lower Devonian formations contain a certain proportion of sandstone or quartzitic sandstone, but significant amounts are represented by the Taunusquarzit in the Hunsrück (e.g., Wildberger, 1992; Stets and Schäfer, 2011) and are known towards the base of the Devonian in the Ardennes (Bultynck and Dejonghe, 2001; Dejonghe, 2008). The underlying Caledonian basement (Ordovician and Cambrian), which is well exposed in the Stavelot–Venn Massif to the north of Luxembourg (Fig. 4.1a), is not considered because its specific local geology is uncertain and it is mostly located too deep to be of interest for

geothermal energy use (Fig. 4.3). So far, the lack of deep boreholes precludes knowledge about the distribution of lithologies and the stratigraphical position of known formations buried in the Lower Devonian basement.

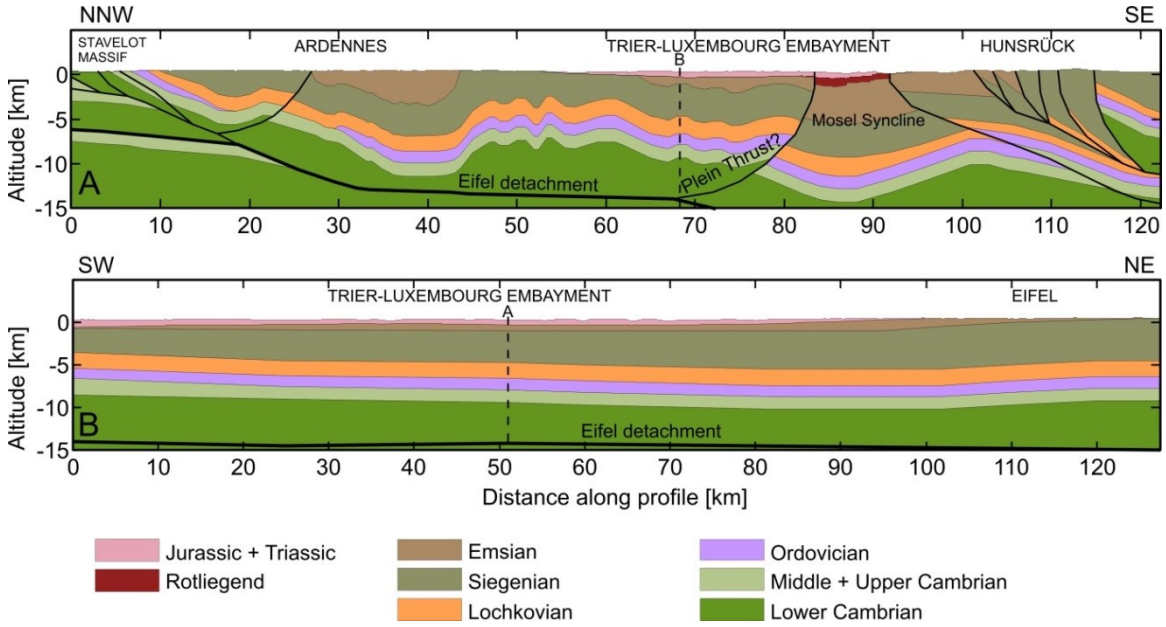

Fig. 4.3: Geological cross sections of the upper part of the crust (modified from Schintgen et al., 2015). For location see Fig. 4.1a. Vertical dashed lines indicate the intersection with the indicated cross section. Black lines represent thrust faults.

4.3.3 Cenozoic evolution

From the Cenozoic to the present day, the TLE is undergoing active deformation (Dittrich 2014; and references therein). On a larger scale, the RM and adjoining areas are deformed and uplifted due to the development and evolution of the ECRIS (European Cenozoic Rift System, represented by the LRG and URG in Fig. 4.1b) since the Eocene about 40 Ma ago (Bourgeois et al., 2007; Demoulin and Hallot, 2009; Fuchs et al., 1983; Schmincke, 2007; Dèzes et al., 2004; Ziegler and Dèzes, 2007; and references therein). Intensified tectonic activity in the last 700 ka is expressed by the accelerated uplift of the RM and young volcanism in the Eifel region (Demoulin and Hallot, 2009; Fuchs et al., 1983; Meyer and Stets, 2002; Schmincke, 2007).

4.4 Geothermal exploration

For geothermal exploration and exploitation purposes, geological, thermal, hydrogeological and structural data are necessary. In fact, especially in hydrothermal reservoirs, various lithologies and facies changes are responsible for a large range of porosities and permeabilities. Subsurface temperatures represent important information for the identification of geothermal reservoirs because the temperature domain determines the types of geothermal energy use and applications that can be implemented. Hydraulic properties, notably permeability and the associated transmissibility, are crucial parameters because they dictate the technical feasibility of specific applications by directly influencing achievable flow rates and thus power output of a geothermal plant (e.g., Schulte et al., 2010). In hydrothermal as well as petrothermal reservoirs, the crustal stress field influences or controls the creation and evolution of faults, fractures and joints, thus permeability, and therefore is particularly important for site selection for geothermal exploration and development of Enhanced Geothermal Systems (Cloetingh et al., 2010).

4.4.1 New temperature data

As deep boreholes are scarce and temperature data are unavailable, the thermal regime was obtained by lithosphere-scale 2-D steady-state thermal modelling based on surface heat flow and a vast database of measured thermal rock properties, in particular thermal conductivity (TC) (Schintgen et al., 2015). It is assumed that heat conduction is the main heat transfer mechanism in the lithosphere, which encompasses the crust and the lithospheric mantle. Possible convective as well as transient processes are so far unknown and were not quantified due to the lack of pertinent data. The thermal model by Schintgen et al. (2015) provides data for temperature maps (Fig. 4.4) generated for 1 km depth steps between 1000 and 6000 m (below mean sea level). Of particular interest are the temperatures encountered at a depth of 5–6 km to which geothermal boreholes can be drilled at costs that allow an economic use of the Earth's heat by combining heat production and power generation.

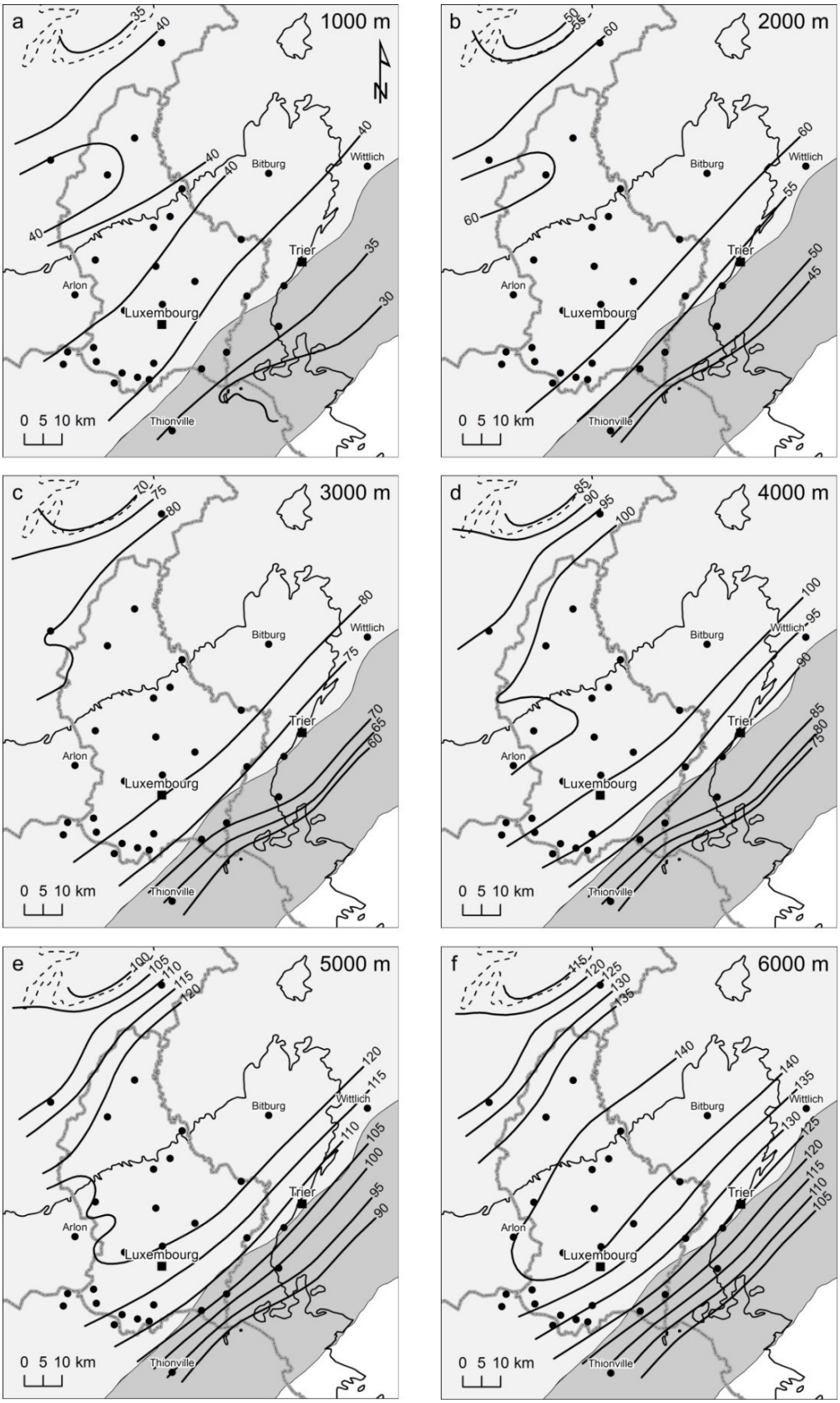

Fig. 4.4: Isodepth temperature maps (obtained from the thermal model by Schintgen et al., 2015). Temperature (°C) evaluated at a. 1000 m; b. 2000 m; c. 3000 m; d. 4000 m; e. 5000 m; f. 6000 m below mean sea level. Grey and light grey zones indicate the Hunsrück and Ardennes–Eifel blocks, respectively. Squares indicate major cities and full circles indicate towns of at least several thousand inhabitants.

In contrast to an evaluation by Biermayr et al. (2007), the geothermal potential in Luxembourg cannot be negated a priori. In the following, it is shown that temperature gradients for the Mesozoic are higher than about 18 °C km^{-1} specified by Biermayr et al. (2007). According to recent TC data for lithotypes and entire formations and a surface heat flow value of 75 mW m^{-2} evaluated by Schintgen et al. (2015), average thermal gradients amount to 27.8 °C km^{-1} in the Triassic and 32.6 °C km^{-1} in the Liassic and Dogger (or Lower and Middle Jurassic). The lower thermal gradient in the Triassic is related to a higher proportion of sandstone and evaporites such as dolomite presenting a high TC (median 3.2 and 3.8 W m^{-1} K^{-1}, respectively). Except for the Luxembourg Sandstone Formation (median TC 3.6 W m^{-1} K^{-1}), the Liassic marine sediments are generally more fine-grained and characterized by claystone, marlstone and limestone of relatively low TC (median 2.1, 2.5 and 2.3 W m^{-1} K^{-1}, respectively; Schintgen et al., 2015). The thermal gradient amounts to 30 °C km^{-1} for the entire Mesozoic represented in Luxembourg, which constitutes a value characteristic for similar geological environments e.g. in France and in the Netherlands (Bonté et al., 2010, 2012). In the Palaeozoic basement, temperature maps show at each depth a SW–NE-oriented plateau of maximum temperature (Fig. 4.4a–f). For example, maximum temperatures at 5 km depth amount to 120–125 °C according to the thermal model by Schintgen et al. 2015. Temperature in the plateau region exhibits a thermal gradient of about 20 °C km^{-1} due to a higher TC of compact rock in the basement in comparison to the Mesozoic sediments. In the northwest, in the Belgian Ardennes, temperatures are reduced by 5 °C at 1000 m depth increasing to 20 °C at 5000 and 6000 m depth. The reduced temperature is associated with the thinning of the Emsian and Siegenian cover of relatively low TC (3.2 W m^{-1} K^{-1}) and a shallow depth of the Cambrian–Ordovician basement of overall high TC (3.1–4.3 W m^{-1} K^{-1}; Schintgen et al., 2015). In the southeast, in the Hunsrück region, temperatures are lower by 10 °C at 1000 m depth increasing to 30 °C at 6000 m depth. The reduced temperature is related to the high TC of the Taunusquarzit (~5 W m^{-1} K^{-1}).

4.4.2 Implications from tectonics and stress field

Besides the deep geological conditions and knowledge of the subsurface temperature distribution, the crustal stress field is particularly important in site selection for geothermal exploration and development of Enhanced Geothermal Systems. Inherited structures such as lithosphere-scale weakness zones formed under palaeo-stress fields play a significant role in basin and lithosphere dynamics under present-day stress fields (Cloetingh et al., 2010). The

previous tectonics and current activity affecting the eastern part/margin of the TLE have recently been studied in detail and reveal a complex network of polygenetic faults (Dittrich, 2014; and references therein). The result is a subsided bloc mosaic where all types of faults, i.e. normal, inverted and strike-slip faults, and various combinations and reactivations, are observed (Dittrich, 2008, 2009, 2011a, 2011b, 2012, 2013, 2014; Wagner, 1996; Wagner et al., 2012; and references therein). The present-day NW–SE-oriented principal stress direction, which has remained practically unchanged since the early Miocene (Dèzes et al., 2004; Ziegler and Dèzes, 2007), is well expressed in the NW–SE orientation of the West Eifel Volcanic Field (WEVF) (Fig. 4.1; Schmincke, 2007). The TLE is currently characterized by a compressional tectonic regime (Dittrich, 2014).

4.4.2.1 New interpretation of the Müllerthal–Südeifel region

The Müllerthal region in Luxembourg and the adjoining Südeifel region in Germany correspond to the northeastern part of the TLE (Fig. 4.1). Both the present-day appearance of the TLE, in particular of the South Eifel region, as well as the development of the TLB were classically interpreted to be of practically identical origin and linked to the Eifel Depression (e.g., Lucius, 1948; Murawski et al., 1983; Wagner et al., 2012). Already challenged by Weiler (1972), this interpretation has been questioned (Dittrich, 1989; Schintgen and Förster, 2013). Detailed studies by Dittrich (2014; and references therein) show that the eastern part/margin of the TLE has been intensively deformed and subsided during the Cenozoic. In the following, the Cenozoic structural evolution of the Müllerthal–Südeifel region is reinterpreted for geothermal exploration using new data by Schintgen and Förster (2013). The present-day appearance of the TLE is likely the result of consecutive and superimposed large-scale structures formed in different geodynamic contexts. First, the Mesozoic TLB is suggested to have formed along the weakness zone of a Permian graben system (Schintgen and Förster, 2013). Second, the South Eifel region was intensively mobile during the Cenozoic (Dittrich, 2014; and references therein).

4.4.2.2 Cenozoic structural evolution of the Müllerthal–Südeifel Depression

In order to underpin the aforegoing reasoning about the young development of the Müllerthal–Südeifel Depression (MSD), Fig. 4.5a–c shows the palinspastic restoration of the South Eifel region to its probable Mesozoic synsedimentary structure by means of cross section B* (B–B’;

Fig. 4.1) showing the current bedding in the Trier–Luxembourg Embayment. For a clear visualization, the successive steps are shown with a ten-fold vertical exaggeration. Cross section B** shows the pre-Tertiary, relatively undisturbed stratigraphic layering (bedding) of the TLB as it likely was before the development of the Eifel Depression, more specifically, as it probably was prior to the inferred Cenozoic subsidence of the Müllerthal and South Eifel regions. The reconstruction of the TLB is now possible because the conceptual model of Schintgen and Förster (2013) infers a culmination of the base of the Mesozoic underneath the Alzette River valley (Fig. 4.5a; km 30–45) instead of the old concept of a subsided area underneath the central part of the Guttland.

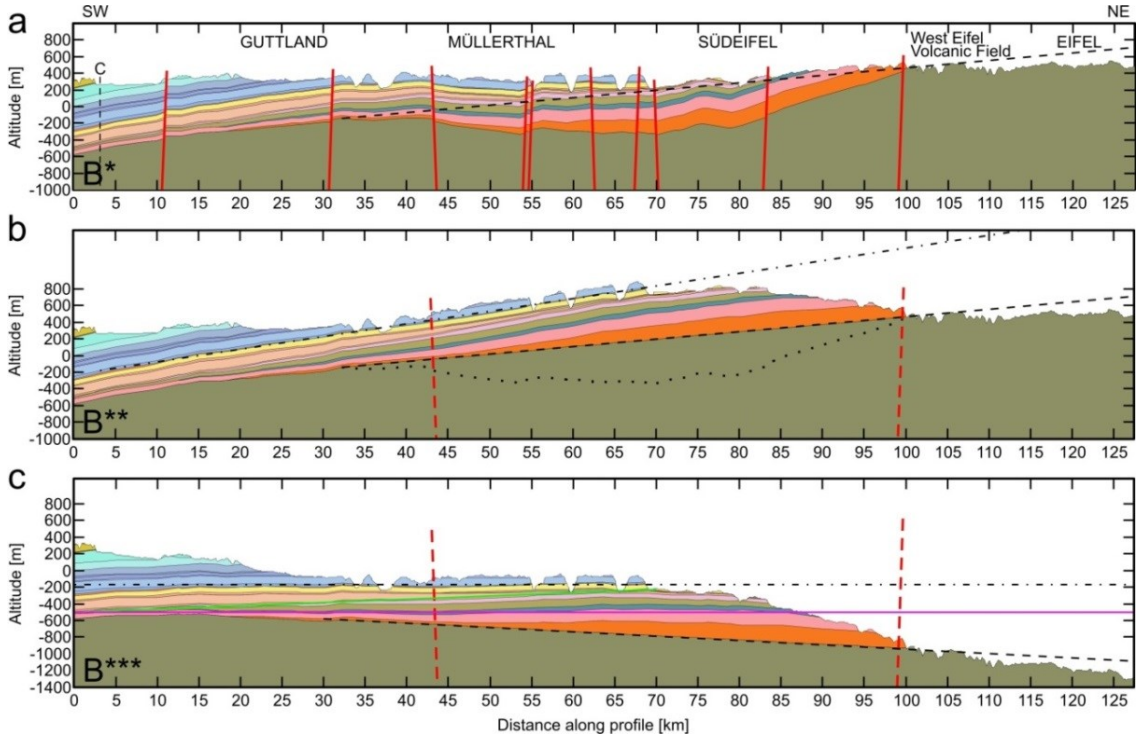

Fig. 4.5: Palinspastic reconstruction of the Mesozoic Trier–Luxembourg Basin. See Fig. 4.1 for the location of profile B* (B–B'). Vertical exaggeration is 10-fold. a. Cross section B*. b. Cross section B**. c. Cross section B***. Dash-dotted line in B** and B*** indicates the base of Liassic. Dashed line marks the postulated flat base of Buntsandstein in the Mesozoic. Dotted line in B** is a reference to the current base of Buntsandstein. Green line in B*** marks the reconstructed top of Muschelkalk. Pink line in B*** marks the reconstructed top of Buntsandstein. Dashed red lines in B** and B*** represent the border faults of the Eifel Depression.

This new vision leads to a different understanding of the regional geological evolution. Cross section B* is based on cross section G presented by Schintgen and Förster (2013). The latter is extended into the Eifel region using the cross section data by Wagner and Dittrich (2010). However, in large parts of the TLB the thickness of the Buntsandstein as the basal geological

unit remains speculative (Dittrich, 2011a; Wagner et al., 2012; and references therein). The reasons are the lack of appropriate boreholes in the deeper parts of the TLE and the locally complicated faulting e.g. to the north of Trier. In contrast to Kremb–Wagner et al. (2014), Wagner et al. (2012) and Weiler (1972), assumptions on Buntsandstein thicknesses adopted in this study are relatively conservative and retrieved from recent studies by Dittrich (2011a), LGB and LUWG (2010) and Wagner and Dittrich (2010). An important assumption is that the subsidence of the Müllerthal–Südeifel area affects a zone of about km 30–100 in cross section B* (Fig. 4.5a). According to the palinspastic reconstruction, it is postulated that the undisturbed top of the Devonian basement was flat prior to Buntsandstein deposition and thus in direct continuation of the undisturbed flat section in the southwestern part of Luxembourg (km 0–30 in cross section B*). The absolute difference in height, i.e. the supposed amount of subsidence, between the constructed line and present-day top of basement is added to the stratigraphical data. Interestingly, as shown in Fig. 4.5b, the reconstructed top of the Keuper succession is flat in the reconstructed basin geometry, which certainly was the case before marine transgression at the beginning of the Liassic. Cross section B*** in Fig. 4.5c shows the synsedimentary appearance of the Mesozoic Trier–Luxembourg Basin obtained after a northeastward rotation of 0.8°. The difference between Figs. 4.5b and 4.5c illustrates a simple tilting from the former western margin of the German Triassic Basin to the present-day northeastern realm of the Paris Basin at the beginning of the Keuper as described by Schintgen and Förster (2013). Northeastward tilting during the Lower Triassic, then southwestward tilting of the basin towards the centre of the Paris Basin during the Upper Triassic and Jurassic obviously compensated each other. If the preceeding assumptions are correct, the subsidence of the MSD and of the entire ED is entirely post-Liassic, and probably largely Cenozoic, i.e. comparatively young, as are the structures studied by Dittrich (2014; and references therein). The current stratigraphical inclination of 0.8° may be entirely attributed to the Cenozoic uplift of the RM in the northeastern realm of the study area, also represented as a rift signature by Bourgeois et al. (2007). Moreover, the inclination shown in Fig. 4.5b and the subsidence shown in Fig. 4.5a probably are contemporaneous Cenozoic processes. Fig. 4.5c clearly illustrates that the Triassic and Jurassic units covered large parts of the Eifel region prior to exhumation of the RM and consequent erosion. Conclusively, in case the sedimentary record of the TLE represents a simple western margin of the German Triassic Basin, the Buntsandstein thickness should more or less constantly decrease from the east to the west (Fig. 4.5c), which is basically not in contradiction with the newest thickness data reported by Dittrich (2011a). In the central part of the MSD, the average Cenozoic subsidence amounts to 470 m according to Fig. 4.5b, which is

comparatively more than the 350 m of Cenozoic subsidence in the Neuwied tectonic basin (Schmincke, 2007). A clear evidence for the current relative subsidence of the MSD within the uplifting Rhenish Massif is presented by Mälzer et al. (1983). During the last 40 Ma of evolution of the ECRIS, the average relative subsidence rate of the MSD amounts to 0.01 mm a^{-1}. If the relative subsidence is supposed to be 100 m in the last 700 ka according to Meyer and Stets (2002, 2007), the average relative subsidence rate amounts to 0.14 mm a^{-1}, i.e. a ten-fold acceleration. The latter rate corresponds to the instantaneous, relative height changes between the Eifel and the South Eifel regions determined by Mälzer et al. (1983). To sum up, it is not the development of the Mesozoic TLB itself, but the appearance of the present-day TLE, in particular the structure of the MSD, that is linked to the formation of the Eifel Depression.

4.4.3 Lithology and structure – implications on hydrogeology

The study area is characterized by two geologically and hydrogeologically contrasting environments, the Mesozoic rock of the TLE and the predominantly Lower Devonian rock of the RM. According to Bintz et al. (1982), Lucius (1953) and LGB and LUWG (2010), the exposed compact, often shale-rich, and folded and thrust rocks of the Ardennes, Eifel and Hunsrück are not capable of hosting large aquifers, whereas the subhorizontal and persistent layers of the TLE are composed of alternately permeable and impermeable lithologies suitable for the formation of significant aquifers.

4.4.3.1 Mesozoic of the Trier–Luxembourg Embayment

From top to bottom, six major aquifers are known in the TLE (Lucius, 1953; Bintz et al., 1982). Fig. 4.6 shows SW–NE- and W–SE-oriented hydrogeological cross sections across the TLE. Major aquifers are highlighted by their typical color codes and stratigraphical codes used in Luxembourg. Among those, the limestone and Minette complex (dom1–4 and lo6–7 + dou) and the Middle Liassic Sandstone (lm3) are the shallowest and only cover a small extent in the southwestern part of Luxembourg. The typical Schilfsandstein (km2S; Stuttgart Fm.) also has a limited extent in the eastern part of the TLE and is locally exposed. Three aquifers are more extensive in Luxembourg and adjoining areas: the Luxembourg Sandstone (li2), the Upper Muschelkalk dolomite (mo) and the Buntsandstein formations (so2 + so1 + sm).

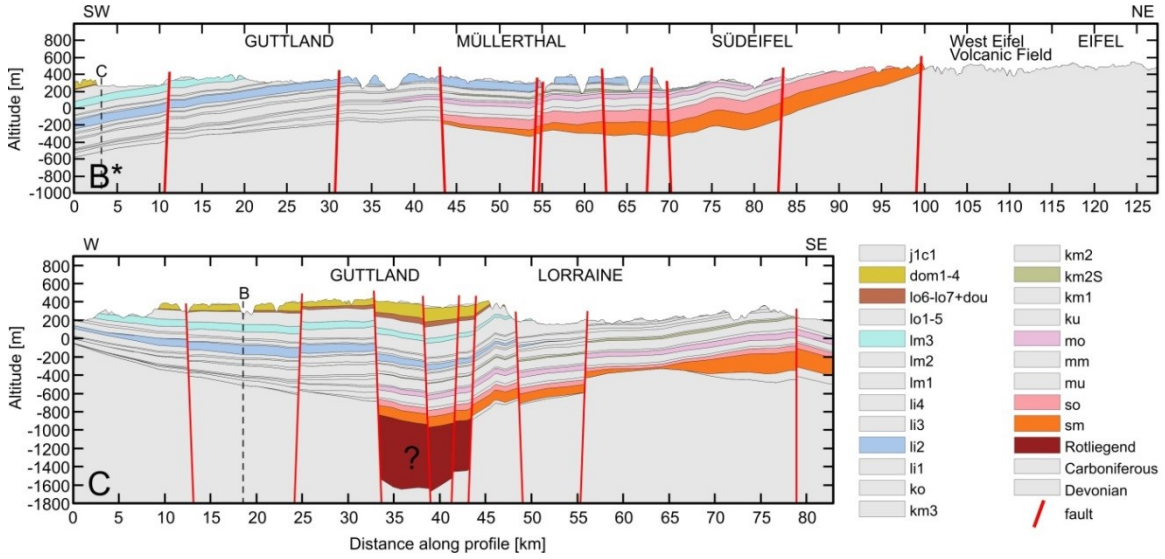

Fig. 4.6: Hydrogeological cross sections of the Trier–Luxembourg Embayment (modified from Schintgen and Förster, 2013). Traces of the sections are indicated in Fig. 4.1. Vertical exaggeration is 10-fold. Aquifers are highlighted in their typical color code. Low-permeability units are faded out (light grey). Stratigraphic codes are given in Table 4.1.

Table 4.1 summarizes the hydraulic properties of the Mesozoic formations including their degrees and values of hydraulic conductivity (k_f) adopted by LGB and LUWG (2010) for equivalent formations of the South Eifel region. The Luxembourg Sandstone Formation is a shallow aquifer in the northeastern part of the TLE (Fig. 4.6, cross section B*) and is significantly used as a drinking water resource, which creates a conflicting use (ACT, 2014). Therefore, the Luxembourg Sandstone may only be exploited in the southwestern part of Luxembourg where its thickness is in the range of 70–100 m and its top reaches a depth of 300–400 m (Fig. 4.6). The Upper Muschelkalk aquifer has a regional occurrence but presents both a relatively impermeable margin facies and a reduced thickness in the western part of the TLE. The basin facies generally presents a thickness in the range of 40–60 m with an average value of about 55 m in the southeastern part of the TLE. The natural porosity is very low (2%), except in the eastern part of the TLE where a dense fault network and shallow position lead to a locally very high permeability. The lowermost aquifer in the TLE is the Buntsandstein (Fig. 4.6) encompassing mainly three (locally four if the Lower Muschelkalk aquifer is considered) stratigraphical units, namely the Voltziensandstein (so2), the Zwischenschichten (so1) and the Vogesensandstein (sm + su; Table 4.1). The generally least permeable basin facies in the northwestern part of the TLE is up to 150 m thick, whereas the most permeable basin facies of the Buntsandstein in the southeastern part of the TLE is mostly about 150–300 m thick (Schintgen and Förster, 2013; Weiler, 1991).

Table 4.1: Hydraulic and thermal properties of the Mesozoic units.

Stratigraphy			Geological unit/formation		Hydraulic conductivity	k_f		K		Aquifer	H		ϕ_{tot}	λ	
											Min.	Max.		Dry	Sat.
						[m s^{-1}]		[m^2]	[mD]		[m]	[m]	[%]	[W m^{-1} K^{-1}]	
		Middle	Marnes sableuses d'Audun-le-Tiche	dom4	average to moderate*	$10^{-3} – 10^{-5}$	*	$10^{-10} – 10^{-12}$	$10^{5} – 10^{3}$	+	70	130	14	1.9	2.4
			Calcaires d'Audun-le-Tiche												
			Calcaire de Haut-Pont	dom3											
			Calcaire d'Ottange	dom2											
			Marnes micacées	dom1											
	Dogger	Lower	Minette	dou	average to moderate*	$10^{-3} – 10^{-5}$	*	$10^{-10} – 10^{-12}$	$10^{5} – 10^{3}$	+	11	68	18	1.5	2.2
		Upper		lo6–7											
			Argiles et marnes de Grandcourt	lo1–5	low*	$10^{-5} – 10^{-7}$	*	$10^{-12} – 10^{-14}$	$10^{3} – 10$	–	100	140?	20	1.1	2.0
		Middle	Grès médioliasique	lm3a+b	moderate to low*	$10^{-4} – 10^{-7}$	*	$10^{-11} – 10^{-14}$	$10^{4} – 10$	+/–	35	80	18	1.3	2.0
			Couches à *Amaltheus margaritatus*	lm2	low to very low*	$10^{-5} – 10^{-9}$	*	$10^{-12} – 10^{-16}$	$10^{3} – 10^{-1}$	–	80	150?	19	1.2	2.1
			Calcaire ocreux	lm1	low*	$10^{-5} – 10^{-7}$	*	$10^{-12} – 10^{-14}$	$10^{3} – 10$	–	4	15	16	1.4	2.1
		Lower	Marne pauvre en fossiles	li4	low*	$10^{-5} – 10^{-7}$	*	$10^{-12} – 10^{-14}$	$10^{3} – 10$	–	30	45	9	1.7	2.3
			Marnes et calcaires de Strassen	li3	low to very low	$10^{-5} – 10^{-9}$		$10^{-12} – 10^{-16}$	$10^{3} – 10^{-1}$	–	8	40	6	1.6	1.8
Jurassic	Liassic		Grès de Luxembourg	li2	moderate to low	$10^{-4} – 10^{-7}$		$10^{-11} – 10^{-14}$	$10^{4} – 10$	+	0	100	17	2.3	3.6
			Marnes d'Elvange	li1	low to very low	$10^{-5} – 10^{-9}$		$10^{-12} – 10^{-16}$	$10^{3} – 10^{-1}$	–	0	35	8	1.5	1.8

k_f – hydraulic conductivity by LGB and LUWG (2010), * – indication of hydraulic conductivity estimated according to bulk lithological composition, K – permeability for a temperature of 20°C, '+', '–' and '+/–' indicates whether an unit is known, not known, or partly known to have aquifer quality, respectively, H – common thickness range, ϕ_{tot} – total porosity, λ – thermal conductivity in dry (Dry) and water-saturated (Sat.) conditions measured perpendicular to bedding. Thickness, porosity and thermal conductivity values by Schintgen et al. (2015).

Table 4.1 continued

Stratigraphy		Geological unit/formation		Hydraulic conductivity	k_f	K		Aquifer	H		ϕ_{tot}	λ	
									Min.	Max.			
					$[m\ s^{-1}]$	$[m^2]$	[mD]		[m]	[m]	[%]	Dry $[W\ m^{-1}\ K^{-1}]$	Sat. $[W\ m^{-1}\ K^{-1}]$
Triassic	Upper	Argiles de Levallois	ko2	moderate to very low	$10^{-4} - 10^{-9}$	$10^{-11} - 10^{-16}$	$10^{4} - 10^{-1}$	+/–	0	17	9	1.6	2.1
		Grès de Mortinsart	ko1										
	Middle	Steinmergelkeuper	km3	low to very low	$10^{-5} - 10^{-9}$	$10^{-12} - 10^{-16}$	$10^{3} - 10^{-1}$	–	20	75	8	2.0	2.4
		Rote Gipsmergel	km2	low to very low	$10^{-5} - 10^{-9}$	$10^{-12} - 10^{-16}$	$10^{3} - 10^{-1}$	–	15	30	9	1.8	2.3
		Schilfsandstein	km2S	moderate to low	$10^{-4} - 10^{-7}$	$10^{-11} - 10^{-14}$	$10^{4} - 10$	+/–	0	50	28?	1.0	1.9
		Pseudomorphosenkeuper	km1	low to very low	$10^{-5} - 10^{-9}$	$10^{-12} - 10^{-16}$	$10^{3} - 10^{-1}$	–	20	100	11	1.6	2.2
Keuper	Lower	Grenzdolomit	ku	low to very low	$10^{-5} - 10^{-9}$	$10^{-12} - 10^{-16}$	$10^{3} - 10^{-1}$	–	10	25	12	1.5	2.0
		Bunte Mergel											
		Basisschichten											
Muschelkalk	Upper	Ceratitenschichten	mo2	average to moderate	$10^{-3} - 10^{-5}$	$10^{-10} - 10^{-12}$	$10^{5} - 10^{3}$	+	10	55	2	3.8	3.8
		Trochitenschichten	mo1										
	Middle	Linguladolomit	mm2	average to moderate	$10^{-3} - 10^{-5}$	$10^{-10} - 10^{-12}$	$10^{5} - 10^{3}$	+	0	7	4	3.0	3.3
		Gipsmergel	mm1	very low	$10^{-7} - 10^{-9}$	$10^{-14} - 10^{-16}$	$10 - 10^{-1}$	–	30	100	5	2.4	2.7
	Lower	Orbicularisschichten	mu2	moderate to low	$10^{-4} - 10^{-7}$	$10^{-11} - 10^{-14}$	$10^{4} - 10$	+	10	50	10	1.8	2.4
		Muschelsandstein	mu1										
Buntsandstein	Upper	Voltziensandstein	so2	moderate to low	$10^{-4} - 10^{-7}$	$10^{-11} - 10^{-14}$	$10^{4} - 10$	+	50	150	17	1.7	2.8
		Zwischenschichten	so1										
	Middle	Vogesensandstein	sm	moderate to low	$10^{-4} - 10^{-7}$	$10^{-11} - 10^{-14}$	$10^{4} - 10$	+	0	>150	21	1.9	3.0
	Lower		su	moderate to low	$10^{-4} - 10^{-7}$	$10^{-11} - 10^{-14}$	$10^{4} - 10$	+					

Fig. 4.7 presents the top and base, thus the geometry, of the Buntsandstein aquifer mapped using conceptual models in the form of cross sections for Luxembourg by Schintgen and Förster (2013), and LGB and LUWG (2010) and Wagner and Dittrich (2010) for Germany. Additional data is provided by boreholes in Luxembourg, France and Germany as well as the most recent geological maps of Luxembourg, Rhineland–Palatinate, Saarland and France. For the top of the Buntsandstein aquifer, additional depth maps by Coiffait and Ricour (1982) and Weiler (1972) were considered. Due to its appropriate depth and temperature, and known excellent hydraulic properties (Agence de l'eau Rhin–Meuse, 2002; Weiler, 1972, 1991; Weidenfeller et al., 2004), the Buntsandstein aquifer is important for geothermal use and considered in more detail. The amount of geothermal energy extractable from a hydrothermal reservoir is a function of fluid properties such as temperature and mineralization, but achievable flow rates are crucial.

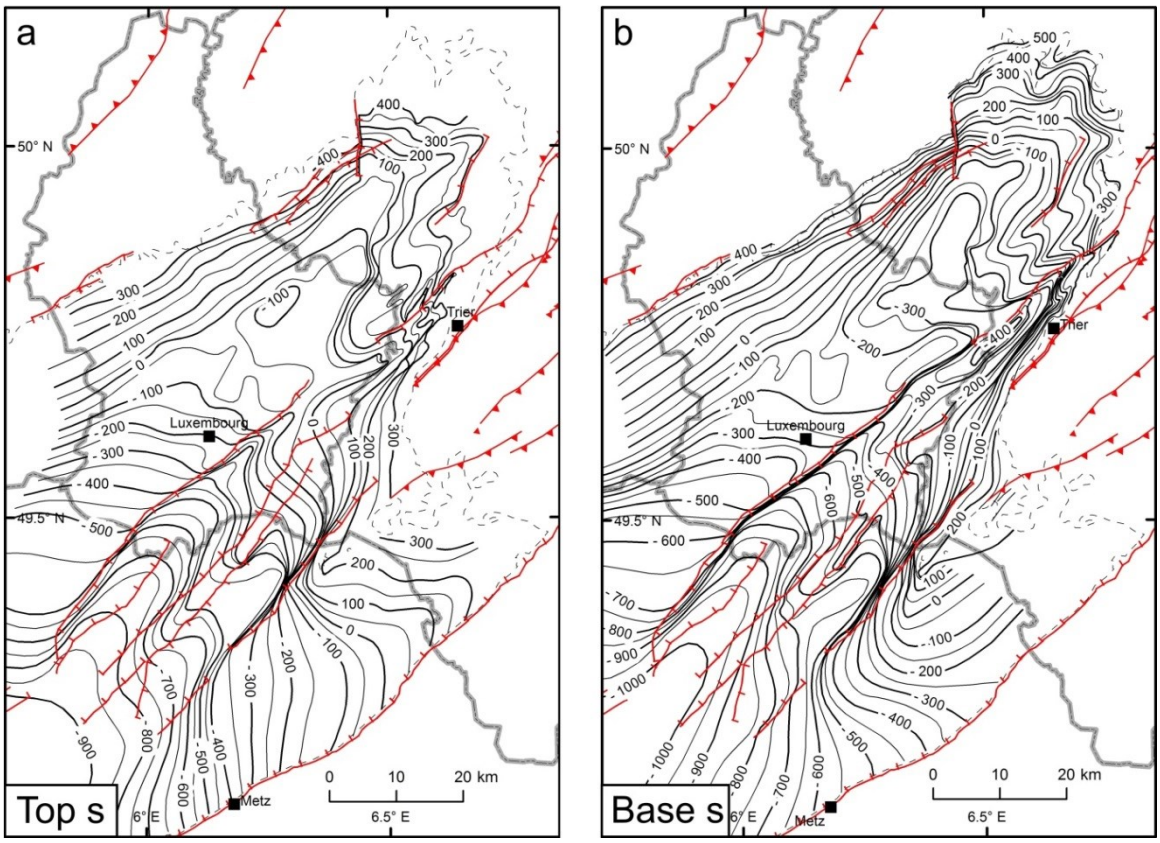

Fig. 4.7: Simplified geometry of the Buntsandstein aquifer. (a) Top and (b) Base. Depth (m) relative to mean sea level. Only major faults are shown.

4.4.3.2 Hydrogeology of the Buntsandstein aquifer

Among the aquifers of the TLB, the Buntsandstein aquifer is the deepest, thickest and has the largest extent. The sandstone-dominated Buntsandstein is a heterogeneous, mixed fracture/pore aquifer (Celle–Jeanton et al., 2009; LGB & LUWG, 2010; Weiler, 1991). Fig. 4.8 gives an overview of the hydrogeology of the Buntsandstein aquifer, including the water table as well as known permeable and impermeable zones. Data on the level of the water table in boreholes being scarce, equipotential lines in Luxembourg are completed using river levels in outcrop areas and available maps of the adjoining areas (Agence de l'eau Rhin–Meuse, 2002; Celle–Jeanton et al., 2009; Weidenfeller et al., 2004; Weiler, 1991).

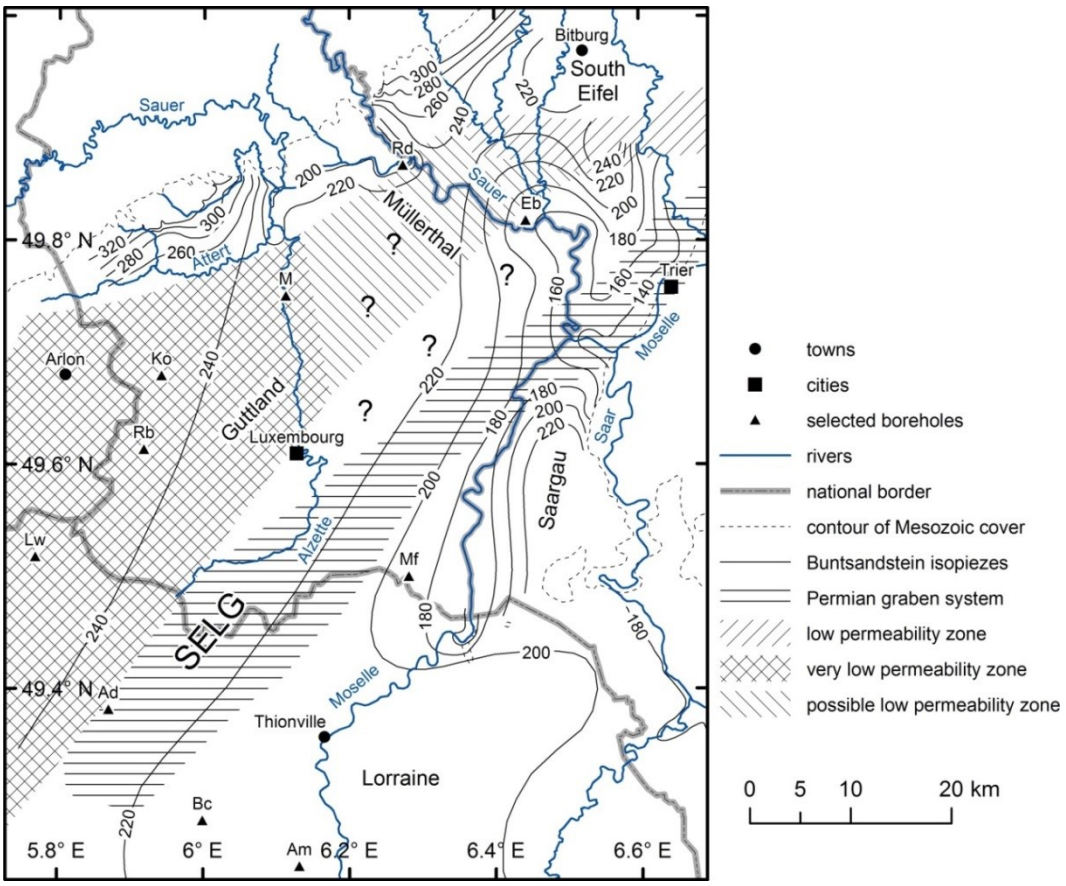

Fig. 4.8: Schematic hydrogeological map of the Buntsandstein aquifer. Isopiezes in m above mean sea level. Boreholes are mentioned in the text. Location of the Permian SE–Luxembourg Graben (SELG) according to Schintgen and Förster (2013) is shown. Diagonally hatched and cross-hatched zones indicate areas of low permeability in the Buntsandstein aquifer known from boreholes as well as from Kremb–Wagner (1996) and Weiler (1991).

A narrow zone along the northern margin of the TLE is intensively used as a drinking water resource (Lucius, 1953; Bintz, 2003). Fig. 4.8 shows a large zone of low permeability of the

Buntsandstein aquifer related to a clay-rich and well-cemented margin facies in most of the northwestern part of the TLE. According to borehole reports available at the Geological Survey of Luxembourg, low permeabilities of the Buntsandstein (productivity <10 $m^3 h^{-1}$) have been measured in the Rebierg (Rb), SES Koerich (Ko), Mersch (M) and Reisdorf (Rd) boreholes. Similarly low permeabilities are known in France in the Longwy (Lw) and Audun-le-Roman (Ad) boreholes (BRGM, 2015). The available data suggest that the Buntsandstein below the Müllerthal region in Luxembourg also has a low permeability. In the South Eifel region, low permeabilities are described by Kremb–Wagner (1996) and Weiler (1991). The W–E oriented zone of low permeability forms a major barrier for groundwater flow (Weiler, 1991). To the south, in the 460-m-deep Echternacherbrück (Eb) borehole located close to the German–Luxembourgish border (Fig. 4.8), the Buntsandstein productivity is significantly higher (40–50 $m^3 h^{-1}$). The Buntsandstein aquifer is drained beneath the southeastern part of the TLE towards the Moselle, Saar and Sauer valleys (Fig. 4.8). Evidence for drainage of the Buntsandstein is known in the Lower Sauer and Moselle valleys by ascending mineralized springs through faults even where the Buntsandstein is not directly exposed (Lucius, 1953). A well productivity of 30–150 $m^3 h^{-1}$ is observed in Lorraine (Agence de l'eau Rhin–Meuse, 2002) and in the Saargau (Weidenfeller et al., 2004). Average hydraulic conductivity in the South Eifel and Lorraine regions is practically the same and amounts to about 10^{-5}–5×10^{-5} m s^{-1} (permeability of 1–5 D) (Celle–Jeanton et al., 2009; LGB and LUWG, 2010). High permeabilities and productivities in those regions as well as in the southeastern part of the TLE are probably due to a high thickness of the Buntsandstein aquifer and a complex fault/fracture network (Dittrich, 2014; and references therein) that is hydraulically conductive. Effective porosities in Luxembourg are unknown, but effective porosities of the basin facies in the northeastern part of Lorraine are 2–5% according to Agence de l'eau Rhin–Meuse (2002) and relatively high, in the range of 10–15 % according to Celle–Jeanton et al. (2009). However, as porosity decreases due to compaction with depth, porosity is subordinate at greater depth and the presence of faults, fractures and joints is crucial for permeability (Ledru and Guillou–Frottier, 2010). The only location in Luxembourg where reliable hydraulic properties in the basin facies were determined using different techniques (Theis and Papadopoulos–Cooper) is the Mondorf Lucius borehole (Mf in Fig. 4.8). According to Leichtle (1980), the average hydraulic conductivity k_f is about 10^{-6} m s^{-1}, i.e. 10 to 50 times lower than in areas where the Buntsandstein is exposed (10^{-5}–5×10^{-5} m s^{-1}). This might be related to lower effective porosities due to a more fine-grained facies, a higher compaction, a lower fault density, as well as a higher mineralized fluid and higher rock cementation. The resulting average permeability (at 20 °C) amounts to 100 mD.

The measured productivity varies from 6.3 to 14.2 l s^{-1} (Leichtle, 1980). The productivity of the Lucius and Bois-châté boreholes (about 36 m^3 h^{-1}) thereby is in the lower zone of productivity of wells in the Buntsandstein (30–150 m^3 h^{-1}). Mineralization in the central and deeper parts of the TLE known from boreholes and springs is in the range 12–16 g l^{-1} (Lucius, 1948) with a maximum of about 23 g l^{-1} in the Bois-châté borehole (Nicklès, 1914).

4.4.3.3 Hydrogeology of the Rotliegend

Schintgen and Förster (2013) infer the existence of a 5–10-km-wide Rotliegend graben, designated by SE–Luxembourg Graben (SELG). It is located in direct southwestern prolongation of the Wittlicher Senke and buried below the TLE. By parallelization with the about 1000-m-thick succession of Rotliegend in the Trier area (Stets, 2004), a set of yet unknown deep aquifers may exist in the southeastern part of Luxembourg. Hydraulic properties of the Rotliegend formations according to LGB and LUWG (2010) for the Wittlicher Senke are summarized in Table 4.2. The hydrogeological conditions in the Rotliegend are essentially known from the Wittlicher Senke. The small-scale lithological contrasts are responsible for a relatively heterogeneous fracture (joint, fissure) aquifer characterized by a moderate to very low permeability (10^{-11}–10^{-16} m^2; LGB and LUWG, 2010). According to Stets (2004), the depositional environment in the Rotliegend consisted in a changeful fluviatile system and the siliciclastic infill of the graben structure is heterogeneous. It is therefore difficult to constrain permeable reservoirs. In contrast to the overlying Buntsandstein aquifer, the groundwater in the Rotliegend sediments is highly mineralized and the permeability is predominantly lower (LGB & LUWG, 2010). Due to the lack of exploration boreholes in-situ, porosity and permeability in these siliciclastic deposits of fluvial origin cannot be ascertained.

4.4.3.4 Lower Devonian of the Ardennes, Eifel and Hunsrück

Lower Devonian formations of the Eifel region including the South Eifel area were analyzed for their hydraulic properties by LGB and LUWG (2010). The resulting ranges of hydraulic conductivity (or conductivity classes) are summarized in Table 4.2. To the remaining Siegenian and Lochkovian formations for which hydraulic data is unavailable, estimates of hydraulic conductivity are assigned depending on their individual lithological composition. The shale-dominated Lower Devonian formations generally have permeabilities (or rather hydraulic conductivities) lower by several orders of magnitude with respect to those of the Buntsandstein

Table 4.2: Hydraulic and thermal properties of the Paleozoic formations.

Stratigraphy			Geological unit/formation		Hydraulic conductivity	k_f		K		Aquifer	H		ϕ_{tot}	λ	
											Min.	Max.		Dry	Sat.
						[m s^{-1}]		[m^2]	[mD]		[m]	[m]	[%]	[W m^{-1} K^{-1}]	
Permian	Rotliegend		Altrich-Formation	rA	moderate to very low	$10^{-4} – 10^{-9}$		$10^{-11} – 10^{-16}$	$10^{4} – 10^{-1}$	+/–	300	400	15	1.6	2.7
			Kinderbeuern-Formation	rK	moderate to low	$10^{-4} – 10^{-7}$		$10^{-11} – 10^{-14}$	$10^{4} – 10$	+	350	450	18	2.0	3.2
			Ürzig-Formation	rÜ	low to very low	$10^{-5} – 10^{-9}$		$10^{-12} – 10^{-16}$	$10^{3} – 10^{-1}$	–	200	350	12	2.1	2.9
Devonian	Lochkovian	Upper	Wiltz Fm.	E3	low to very low	$10^{-5} – 10^{-9}$		$10^{-12} – 10^{-16}$	$10^{3} – 10^{-1}$	–	250	>1200	-	2.1	2.5
			Berlé Fm.	q	moderate to low	$10^{-4} – 10^{-7}$		$10^{-11} – 10^{-14}$	$10^{4} – 10$	+/–	0	15	-	4.5	6.2
		Middle	Clervaux Fm.	E2	low to very low	$10^{-5} – 10^{-9}$		$10^{-12} – 10^{-16}$	$10^{3} – 10^{-1}$	–	200	660	-	2.9	3.3
		Lower	Schuttbourg Fm.	E1b	low to very low	$10^{-5} – 10^{-9}$		$10^{-12} – 10^{-16}$	$10^{3} – 10^{-1}$	–	750	1200	-	2.9	3.5
	Emsian		Stolzembourg Fm.	E1a	low to very low	$10^{-5} – 10^{-9}$		$10^{-12} – 10^{-16}$	$10^{3} – 10^{-1}$	–	700	900	-	2.7	3.2
		Upper	La Roche Fm.	Sg3/ LAR	low to very low	$10^{-5} – 10^{-9}$		$10^{-12} – 10^{-16}$	$10^{3} – 10^{-1}$	–	>1400	1500	-	2.5	2.9
				Sg3a/ LAR	low to very low*	$10^{-5} – 10^{-9}$	*	$10^{-12} – 10^{-16}$	$10^{3} – 10^{-1}$	–		400	-	2.6	3.2
		Middle	Villé Fm.	Sg2/ VIL	low to very low*	$10^{-5} – 10^{-9}$	*	$10^{-12} – 10^{-16}$	$10^{3} – 10^{-1}$	–	250	550	-	3.0	3.5
	Siegenian	Lower	Mirwart Fm.	Sg1/ MIR	low to very low*	$10^{-5} – 10^{-9}$	*	$10^{-12} – 10^{-16}$	$10^{3} – 10^{-1}$	–	700	1050	-	2.8	3.4
			Saint-Hubert Fm.	STH	low*	$10^{-5} – 10^{-7}$	*	$10^{-12} – 10^{-14}$	$10^{3} – 10$	+/–	550	700	-	3.3	3.9
			Oignies Fm.	OIG	low to very low*	$10^{-5} – 10^{-9}$	*	$10^{-12} – 10^{-16}$	$10^{3} – 10^{-1}$	–	700	1200	-	2.6	3.0
			Fépin Fm.	FEP	low*	$10^{-5} – 10^{-7}$	*	$10^{-12} – 10^{-14}$	$10^{3} – 10$	+/–	20	>300	-	3.7	4.3

k_f – hydraulic conductivity by LGB and LUWG (2010), * – indication of hydraulic conductivity estimated according to bulk lithological composition, K – permeability calculated for a temperature of 20 °C, '+', '–' and '+/–' indicates whether an unit is known, not known, or partly known to have aquifer quality, respectively, H – common thickness range, ϕ_{tot} – total porosity, λ – thermal conductivity in dry (Dry) and water-saturated (Sat.) conditions. Thickness, porosity and thermal conductivity values by Schintgen et al. (2015). For the Rotliegend formation, thickness and thermal conductivity are based on data by Häfner et al. (2007).

in the TLE (Table 4.1). The Lower Devonian basement therefore forms the impermeable base of the Buntsandstein aquifer where the Rotliegend is absent (LGB and LUWG, 2010; Lucius, 1948). Compact sedimentary rock can be used to create artificial heat exchangers using EGS technology (Breede et al., 2013; Schulte et al., 2010; Tester et al., 2006; Zimmermann et al., 2011). Lower Devonian lithologies best suited for geothermal exploitation are deep-lying, thick and laterally persistent layers with a high proportion of sandstone and/or quartzite with a possible fracture porosity/permeability. Most of the Lower Devonian formations contain a certain proportion of sandstone, frequently between 15 and 30%. However, the Saint-Hubert and Fépin formations of Lochkovian age at the base of the Devonian in the Ardennes contain large and relatively thick packages of sandstone/quartzite (Dejonghe, 2008) and therefore are described in more detail below. Fig. 4.9 shows a schematic map of the top and base of the Lochkovian succession based on the conceptual geological cross sections presented by Schintgen et al. (2015). Major thrust faults shown are located at their inferred positions. The nature and throw of the thrust fault to the southeast of the city of Luxembourg (i.e., the Luxembourg Fault and its prolongation at depth) is particularly uncertain. In the Hunsrück region in Germany, the Taunusquarzit of Middle to Upper Siegenian (Praguian) age consists

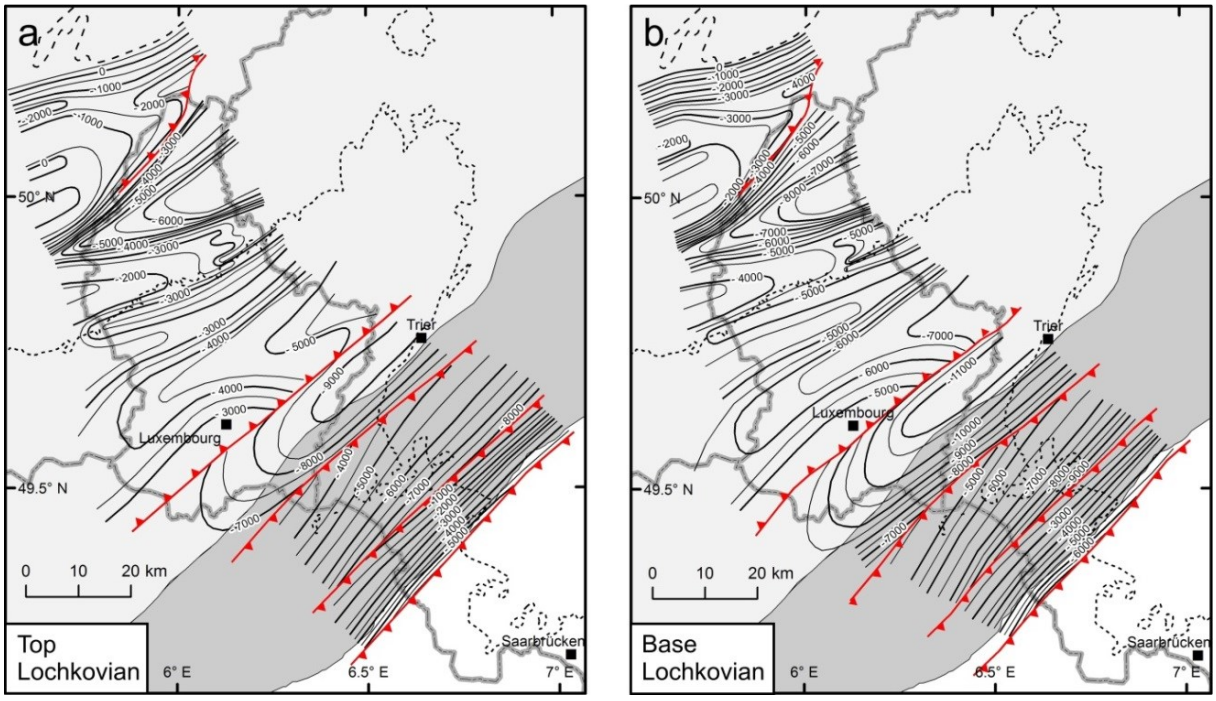

Fig. 4.9: Geometry of Lochkovian succession. (a) Top and (b) Base. Depth in m below mean sea level. Grey and light grey zones indicate the Hunsrück and Ardennes–Eifel blocks, respectively.

mainly of highly fractured quarzitic sandstone and hosts, together with the overlying Dhrontal-Schichten, the waterhead of numerous streams (Wildberger, 1992). It has a minimum thickness of about 1000 m (Wildberger, 1992; Stets and Schäfer, 2011). Due to complex tectonics and apparent facies changes (Meyer and Stets, 1996; Stets and Schäfer, 2002, 2011) the possible northwestern extension of the Taunusquarzit into the Eifel region remains unknown (e.g., Wierich, 1999; Wildberger, 1992; Zitzmann and Grünig, 1987).

4.4.3.5 Hydrogeology of the Lochkovian in the Ardennes

The depth position of the Lochkovian sediments in the geological and structural context is presented in Fig. 4.10 with a twofold exaggeration. The Fépin Formation at the base of the Lochkovian unconformably overlies the Caledonian basement (Cambrian–Ordovician). It is dominated by coarse to gravelly sandstones and conglomerates (Bultynck and Dejonghe, 2001; Dejonghe, 2008). To the south of the Stavelot Massif, a transitional facies predominantly containing shales and siltstones and subordinate gravelly to conglomeratic sandstone prevails. Due to its transgressional character, the thickness presents a wide range of tens of meters to several hundreds of meters (Dejonghe, 2008). If a correlation with the similar Bunte Schiefer at the southern border of the Hunsrück (LGB, 2005; Stets and Schäfer, 2002) is considered, the Fépin Formation may reach an even greater thickness. As an evidence of local aquifer quality at the southern border of the Stavelot Massif, springs occur in the Lower Devonian quartzitic sandstone and conglomerate at the contact with the underlying impermeable Caledonian rocks. The overlying Oignies Formation also contains sandstone beds. The Saint-Hubert Formation at the top of the Lochkovian locally contains massive lenses of quartzitic sandstone which is mined in large quarries (Dejonghe, 2008). However, the lack of deep boreholes in the Lower Devonian in the centre of the Rhenohercynian basin precludes further knowledge on the distribution of lithologies, thicknesses and extent of surface formations at depth (Stets and Schäfer, 2002, 2011). However, parallelization with the Belgian Ardennes suggests that the known Lower Devonian formations and their lateral equivalents extend southeastwards in the subsurface of Luxembourg and the western margin of the Eifel region. The total thickness of Lochkovian formations is in the range of 1300 to 2500 m (Table 4.2).

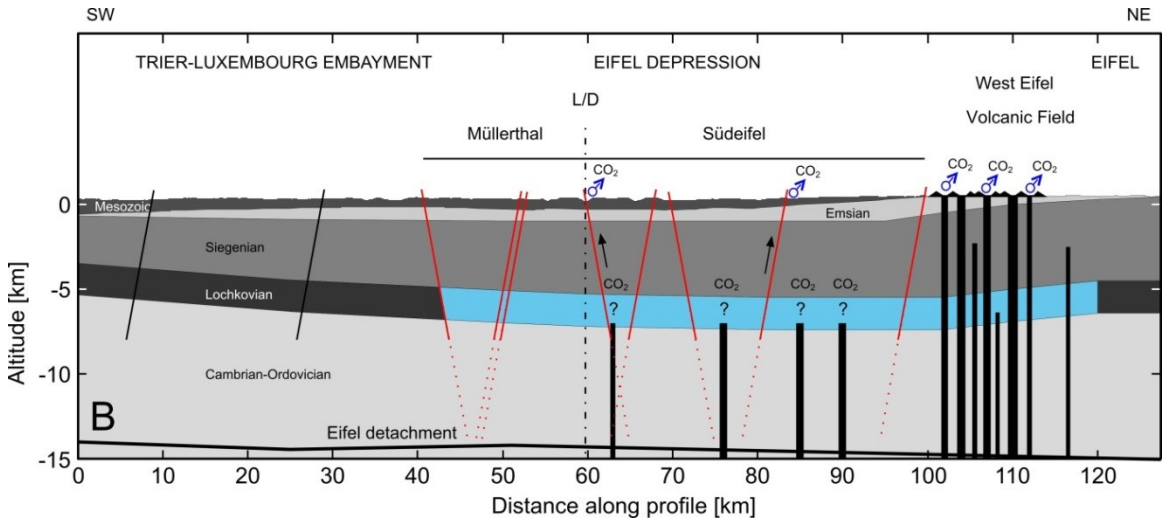

Fig. 4.10: Mesozoic and Palaeozoic upper crust with emphasis on the petrothermal Lochkovian reservoir (in blue). Cross section modified from Schintgen et al. (2015). For location of the cross section see Fig. 4.1. L/D and dash-dotted line mark the German–Luxembourgish border. Vertical exaggeration is twofold. Red faults represent faulting in the Eifel Depression. Black vertical colums (width not to scale) indicate schematic feeder dikes of Eifel volcanoes.

Measured porosity of the Lower Devonian rock samples generally is very low (1–4%; average about 3%; Schintgen et al., 2015), but fracture porosity/permeability of sandstone/quartzite formations is known from exposure (Wildberger, 1992). According to Lorenz (2003, 2007), hard rocks in the Eifel region are transected by joints and faults which frequently are hydraulically conductive. Further evidence that migration of fluids is generally possible in the Ardennes and the Eifel is the occurrence of numerous vein-type ore deposits (Dejonghe, 1998; Meyer, 1994; Philippo, 2007). Permeability of the Lower Devonian derived from LGB and LUWG (2010) is in the range of 10^{-12}–10^{-16} m^2. Under those conditions and the size of the hydraulic system, convection is generally possible (Manning and Ingebritsen, 1999), thus theoretically enabling the possibility of advective coupled fluid and heat flow. Consequently, convection driven heat advection may be more efficient then heat conduction (Clauser, 2009; Deming et al., 1992; Deming, 1994; Manning and Ingebritsen, 1999; Smith and Chapman, 1983). This may challenge the purely conductive thermal model presented by Schintgen et al. (2015). Furthermore, in-situ permeability depends on the amount and type of dissolved solids, pressure, gas content and temperature (Stober et al., 2009). Strong CO_2 degassing occurs at the intersection of WEVF and ED (Fig. 4.10; Griesshaber et al., 1992; Schmincke, 2007). In Fig. 4.10, sources of CO_2 in the South Eifel and West Eifel regions are schematically shown as vertical magmatic dikes. Arrows indicate ascent of CO_2-rich water to the mineral springs at the surface. According to Schmincke (2007), the ED represents a lithosphere-scale weakness zone

which apparently increased the volcano density, and influenced the distribution (fissure direction) and composition (xenolith types) of volcanism in the WEVF. In particular, more than 50 sites of mineral springs associated with CO_2 degassing are found in the South Eifel region, the West Eifel and the Moselle valley (Langguth and Plum, 1984; Lucius, 1959; Wagner et al., 2012; Werle, 2009). The springs are often located at the intersection of valleys and deep-reaching faults. Natural productivity of tapped springs is about 10 l s^{-1}. The highest measured spring temperatures are known in the Moselle valley to the south of the WEVF (>30 °C; Langguth and Plum, 1984). In general, however, mineral waters known at the surface are relatively cool, no particularly high heat flow due to the young volcanism in the WEVF was observed (Langguth and Plum, 1984; Griesshaber et al., 1992; LGB & LUWG, 2010). Groundwater from surface manifestations in the Lower Devonian is poorly mineralized (up to 4 g l^{-1}) but aggressive due to its content in carbonic acid (up to 3 g l^{-1}) (Griesshaber et al., 1992; Lucius, 1953, 1959). Mineralization of deeper reservoirs might be higher but so far remains unknown. The origin of CO_2 is local and bound to the presence of groundwater (Lucius, 1959; Meyer and Stets, 1996). This suggests that large-scale groundwater circulation is possible underneath the South Eifel area and that the CO_2 is related to the cooling magma due to unsuccessful attempts of small-volume magma batches to erupt on the surface (Fig. 4.10; Bräuer et al., 2013; Langguth and Plum, 1984; Lucius, 1959; Schmincke, 2007). Furthermore, recent tectonic mobility (see section 3.2.2), deep magma emplacement and CO_2 degassing are related to the fact that the South Eifel area is located above the western margin of the Eifel plume (Bräuer et al., 2013; Keyser et al., 2002; Seiberlich et al., 2013; Walker et al., 2005). The fact that the adjoining Müllerthal region in Luxembourg, which also lies within the ED, does not have any mineral springs may be related to the relatively thick and impermeable sedimentary cover and a lower number of faults.

4.5 Geothermal reservoirs

4.5.1 Hydrothermal reservoirs

4.5.1.1 Buntsandstein

The temperature distribution at the base of the Buntsandstein based on the thermal data by Schintgen et al. (2015) is shown in Fig. 4.11. If the possibility of convection and advective heat transport by fluid flow in the Buntsandstein aquifer is excluded, temperatures are related to depth, thus thickness of the sedimentary cover, and the thermal gradient. The latter depends on the thermal conductivities of the overlying formations (Table 4.1) and the regional surface heat

flow. The lowest temperature of about 10 °C (mean annual surface temperature) is encountered along the margins of the TLE where the Buntsandstein aquifer is exposed. The highest temperatures of about 50 °C are expected in the most southern part of Luxembourg in the Luxembourgish–French border region. The Bois-châté borehole in northern Lorraine provided about 50 °C warm water, while temperatures in the range of 36–42 °C were recorded in Amnéville (Am in Fig. 4.8) (C. Dezayes, pers. comm.). A 'top down' approach can be used to calculate temperatures in the subsurface up to several kilometers depth by applying the Fourier equation of heat conduction:

$$q = -\lambda \cdot \frac{dT}{dz} \tag{4.1}$$

where q is the surface heat flow (in mW m^{-2}), λ is the TC of a geological unit (in W m^{-1} K^{-1}) and dT/dz is the thermal gradient within each geological unit (in K km^{-1}). The thermal gradient corresponds to the temperature difference dT (in °C = K–273) at the top and base of each unit divided by the thickness dz (in m) of the unit. Temperatures of about 36–42 °C at the top and base of the Buntsandstein aquifer, respectively, were calculated in the southern part of the Alzette valley where the Buntsandstein reaches a maximum depth of about 850 m (top) and 1100 m (base) below surface. Just to the south of the city of Luxembourg, in the northern part of the upper Alzette valley, where the top and base are located in about 600 m and 850 m depth, respectively, inferred temperatures amount to about 27–33 °C. As a result, the warmest part of the Buntsandstein aquifer coincides with the region where it lies below the Liassic cover, more specifically the part of the SE–Luxembourg Graben beneath the upper Alzette valley. The warm zone extends further to the south below the Dogger limestone plateau in the southernmost part of Luxembourg and the northernmost part of Lorraine (Fig. 4.11). In consideration of the local elevation of the upper Alzette valley, the water table of the Buntsandstein aquifer is probably located 40–50 m below terrain level.

The key information to the selected reservoirs is presented in Table 4.3. Geothermal heat for district heating is of particular interest in the highly populated southwestern part of Luxembourg and the capital of Luxembourg (Fig. 4.11), making up 60% of the total population in 2014 (canton of Esch: 161,000; canton of Luxembourg: 167,000; STATEC, 2014). However, since the temperatures are <60 °C in the Buntsandstein aquifer, heat pumps have to be used to allow space and district heating (Bujakowski and Barbacki, 2004; Líndal, 1973). In the warmest and most permeable zones in the southeastern part of the TLE, minimum k_f values of 5×10^{-5} m s^{-1} are attained for successful exploitation of hydrothermal reservoirs according to Stober et al. (2009). In Mondorf, hydraulic conductivities measured (Leichtle, 1980) are 10 to 50 times

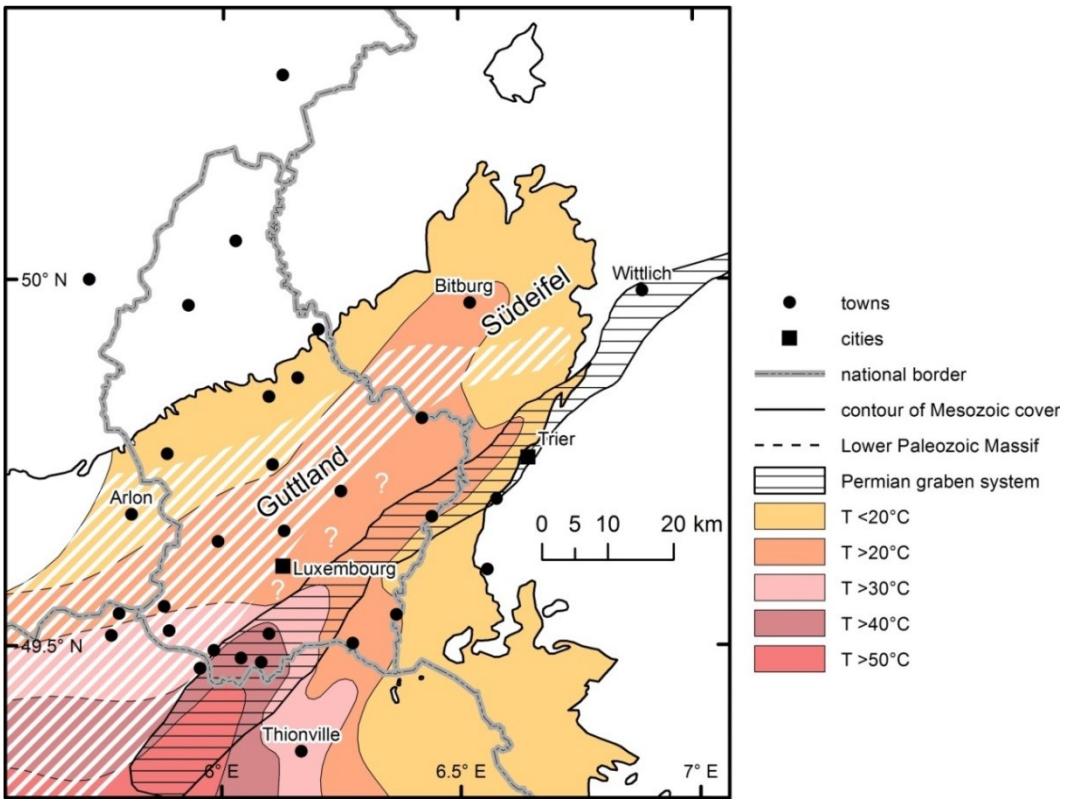

Fig. 4.11: Different temperature zones at the base of the Buntsandstein hydrothermal reservoir. Full circles indicate towns of at least several thousand inhabitants. White hatched zone characterized by low permeability. Question marks indicate a possible low permeability zone.

lower, but the corresponding average transmissibility with an about 240-m-thick Buntsandstein amounts to 24 Dm. According to Van Wees et al. (2012), transmissibilities >30 Dm are an excellent property of natural aquifers for geothermal energy use. Total mineralization also is comparatively low (12–23 g l^{-1}) and suitable for hydrothermal energy use.

4.5.1.2 Rotliegend

In the considered zone of the SELG beneath the upper Alzette valley, the inferred Rotliegend graben below the Buntsandstein aquifer may reach a maximum depth of about 2000 m in the northeast in the vicinity of the city of Luxembourg and 2500 m in the southwest in the Luxembourgish-French border region associated with calculated temperatures of about 63 °C and 75 °C at the base of the graben, respectively. A summary of relevant information is listed in Table 4.3. Geological and geophysical exploration is clearly needed to assess subsurface conditions (geology, structure, permeability, mineralization, temperature) in the inferred Rotliegend graben. Exploration data would shed light on the possibilities of direct use for space heating and cooling.

Table 4.3: Major hydrothermal and petrothermal reservoirs

Stratigraphy	Mesozoic	Permian	Devonian	Devonian
	Buntsandstein	Rotliegend	Upper Siegenian	Lochkovian
			Middle Siegenian	
Region	Trier–Luxembourg	SE-Luxembourg Graben	Hunsrück	Ardennes
	Embayment	+ Wittlicher Senke	+ Mosel region ?	+ NW Eifel ?
Formations	Voltziensandstein	Altrich	Taunusquarzit	Saint-Hubert
	Zwischenschichten	Kinderbeuern		Oignies
	Vogesensandstein	Ürzig		Fépin
Reservoir lithotype	Sandstone +	Sandstone +	Quartzite	Sandstone +
	conglomerate	breccia/conglomerate		quartzite
Reservoir type	Hydrothermal	Hydrothermal/	Petrothermal	Petrothermal
		petrothermal		
Depth [m]	0 – 1200	0 – 2500	0 – 4000	3500 – 6000
Thickness [m]	150 – 300	> 1000	> 1000	1300 – 2500
T [°C]	10 – 50	10 – 75	10 – 90	90 – 140
k_f [m s^{-1}]	$10^{-4} – 10^{-7}$	$10^{-4} – 10^{-9}$	$10^{-5} – 10^{-7}$	$10^{-5} – 10^{-7}$

T – temperature, k_f – hydraulic conductivity.

4.5.2 Petrothermal reservoirs

4.5.2.1 Lower Devonian

In the subsurface of Luxembourg and the surrounding areas, temperatures >120 °C and appropriate for efficient use in binary power plants are reached at depths >5000 m (below mean sea level; see Fig. 4.4; Schintgen et al., 2015). Fig. 4.12 shows the temperatures expected at the top of the Lochkovian, i.e. the Saint-Hubert Formation. The top of the sandstone-/quartzite-rich, ~1000–2000-m-thick Lochkovian formations is reached at depths >3000 m in the west and >5000 m in the east (see Fig. 4.9a). As the thermal gradient within the Lower Devonian amounts to about 20 °C km^{-1}, the temperature pattern shown in Fig. 4.12 is directly related to the depth of the Lochkovian. In the Hunsrück region, another possible petrothermal reservoir with a thickness >1000 m is the Taunusquarzit. However, the northwestward extension of the Taunusquarzit beyond the Hunsrück region where temperatures are best suited for EGS (>120 °C at 5000 m) remains unknown. Table 4.3 summarizes key information including ranges of depth, thickness, temperature and hydraulic conductivity for different petrothermal reservoirs.

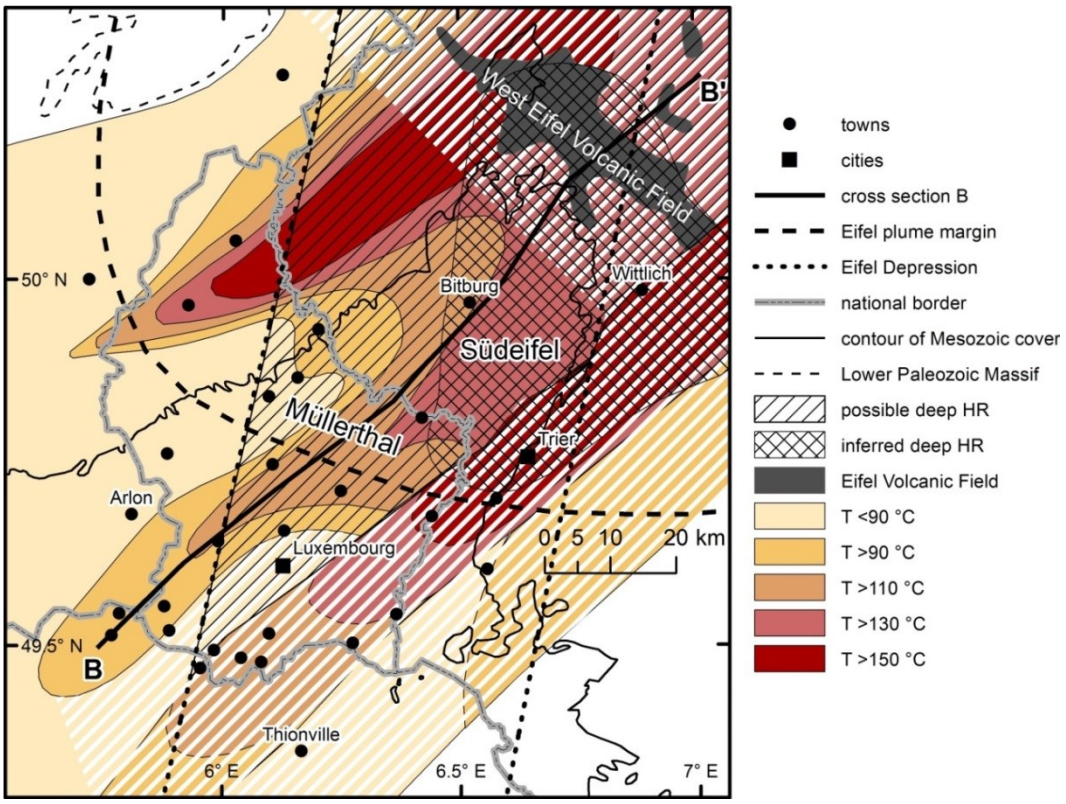

Fig. 4.12. Expected temperature zones at the top of the Lochkovian petrothermal reservoir. Full circles indicate towns of at least several thousand inhabitants. Hatched and cross-hatched areas mark possible and inferred deep hydrothermal reservoirs (HR), respectively. Contour of Eifel plume according to Keyser et al. (2002). In the white hatched zone temperatures are particularly uncertain due to missing thermal data or an unreliable geology.

A crucial factor in the production of geothermal energy is related to the large uncertainty of effective porosity/permeability and transmissivity/transmissibility values, which directly influence the achievable flow rates and thus doublet power in petrothermal systems (e.g., Schulte et al., 2010). Actively deforming areas characterized by extensional and strike-slip settings are favorable for EGS (Cloetingh et al., 2010). Furthermore, Garnish (2002) points out that the natural fracture system largely dominates induced fractures. Although the tectonic regime in the TLE is compressional at the surface (Dittrich, 2014), it most likely evolves towards a strike-slip regime with increasing depth under the weight of a sufficient overburden. As a positive aspect of the region of Luxembourg and the South Eifel, it may be considered that historical seismicity and present-day microearthquake activity related to the geodynamical processes in the RM is low (Ahorner, 1983; Cloetingh et al., 2009; Ziegler and Dèzes, 2007). The MSD, which corresponds to a zone of relatively high temperature (>120 °C at 5000 m), is likely characterized by a tectonically enhanced transmissibility and may therefore represent a deep hydrothermal reservoir. Deep fluid downflow preferentially along fault zones in the Eifel region (Lorenz, 2003, 2007) is a requirement to explain the origin of the hot springs in Aachen

(Bayer et al., 1996; Langguth and Plum, 1984; Pommerening, 1993). The entire zone of mineral springs in and around the South Eifel region might be the clearest indication of a hydrothermal reservoir at depth. If permeability of the Lochkovian formations is assumed to be low (corresponding to 10^3–10 mD according to LGB and LUWG, 2010), and an effective thickness of 500 m is adopted, i.e. 50–25% of the total thickness of the Lochkovian rock, the resulting transmissibility is in the range of 500–5 Dm. In contrast to petrothermal systems, this span in transmissibility would characterize a hydrothermal system (>5 Dm) according to Stober et al. (2009). However, the highest permeabilities are expected in tectonically active regions. Therefore, the zone of the ED and the MSD probably yield a higher productivity.

4.6 Conclusions

This paper aimed at combining different types of information necessary for a first rather qualitative assessment of deep geothermal reservoirs in Luxembourg and the adjoining regions in the surrounding countries of Belgium, France and Germany. Hydrothermal and petrothermal reservoirs were considered. Hydrothermal resources with temperatures up to 50 °C for use by means of heat pumps or direct use are found in the Buntsandstein aquifer. The most promising area is the part of the SE–Luxembourg Graben located below the Liassic cover, more specifically under the upper Alzette River valley. At the base of an inferred Rotliegend graben in the same zone, temperatures up to 75 °C are expected. However, geological and hydraulic conditions are largely unknown. Expected sandstone-/quartzite-rich formations in the Lochkovian towards the base of the Lower Devonian in the Ardennes–Eifel block offer the possibility of widespread use of EGS technology, despite a moderate temperature gradient of about 20 °C in the Palaeozoic basement. Based on recent data on the structure of the Trier–Luxembourg Basin, the new concept of the Müllerthal–Südeifel Depression is presented as a Cenozoic tectonic structure which is still mobile and potentially hydraulically conductive. The Müllerthal–Südeifel Depression therefore represents a particular target region for future geothermal exploration and implementation of EGS. In addition, numerous mineral springs with high CO_2 content in the WEVF and the South Eifel region suggest the existence of a large hydrothermal reservoir at a depth of several kilometers. Expected temperatures are at least 120–125 °C at 5 km depth. In the most permeable zones both in the Buntsandstein and the Lochkovian, the span of hydraulic conductivities varies approximately within a factor 100. Hydraulic conductivity therefore is a crucial parameter for determining flow rates and thus power output of a geothermal plant. The current lack of deep exploration boreholes and

geophysical data emphasizes the need for substantially more research, development and demonstration funding (RD&D) for geothermal exploration, resource assessment and potential exploitation of geothermal energy for base-load electricity generation and provision of heating and/or cooling.

4.7 Acknowledgements

This paper forms part of the doctoral thesis of TS entitled “The Geothermal Potential of Luxembourg”. The project is supported by the National Research Fund (Luxembourg) via an AFR research grant under the reference 866943 and the GFZ German Research Centre for Geosciences (Potsdam, Germany). The author would like to thank Andrea Förster (GFZ Potsdam) for critical comments which helped to improve the manuscript. Constructive reviews by two anonymous reviewers helped to significantly improve the manuscript and are gratefully acknowledged.

4.8 References

ACT (Administration du Cadastre et de la Topographie) (2014). Geoportal of the Grand-Duchy of Luxembourg, http://map.geoportail.lu/en/.

Agence de l'Eau Rhin–Meuse (2002). Atlas hydrogéologique du bassin Rhin–Meuse. Moulins-lès-Metz, pp. 71–77.

Ahorner, L. (1983). Historical seismicity and present-day microearthquake activity of the Rhenish Massif, Central Europe. In: Fuchs, K., von Gehlen, K., Mälzer, H., Murawski, H., Semmel, A. (Eds.), Plateau Uplift: The Rhenish Shield – A Case History. Springer, Berlin, Heidelberg, New York, Tokyo, pp 198–221.

Bär, K., Arndt, D., Fritsche, J.-G., Götz, A.E., Kracht, M., Hoppe, A., Sass, I. (2011). 3D-Modellierung der tiefengeothermischen Potenziale von Hessen – Eingangsdaten und Potenzialausweisung. Z. Dt. Ges. Geowiss. 162, 371–388.

Bayer, U., Lünenschloß, B., Springer, J., von Winterfeld, C. (1996). Thermal modelling at an ancient orogenic front with special regard to the uncertainty of heat-flow predictions. In: Förster, A., Merriam, D.F. (Eds.), Geologic Modelling and Mapping. Plenum Press, New York, pp 79–93.

Biermayr, P., Cremer, C., Faber, T., Kranzl, L., Ragwitz, M., Resch, G., Toro, F. (2007). Bestimmung der Potenziale und Ausarbeitung von Strategien zur verstärkten Nutzung von erneuerbaren Energien in Luxemburg. Endbericht, Fraunhofer Institut für System- und Innovationsforschung (Fh-ISI), Karlsruhe, Energy Economics Group (EEG), TU Wien, BSR-Sustainability, Karlsruhe, 235 pp.

Berckmans, A., Vandenberghe, N. (1998). Use and potential of geothermal energy in Belgium. Geothermics 27, 235–242.

Bintz, J., Frantz, M., Fried, J.J. (1982). Bilan des ressources en eau souterraine du Grand-Duché de Luxembourg. In: Atlas des Ressources en eaux Souterraines de la Communauté Européenne. CECA, CEE, CEEA, Bruxelles–Luxembourg, 46 pp.

Bintz, J. (2000). Le paysage géologique de Mondorf et la géologie de ses forages-captages. In: Gerges M (Ed.), Mondorf le domaine thermal: Mondorf – son passé, son présent, son avenir. Les publications mosellanes, Le domaine thermal, Mondorf, pp. 313–320.

Bintz, J. (2003). Géologie et hydrogéologie de la solution de rechange pour l'alimentation en eau potable du pays lors de la vidange du lac d'Esch-sur-Sûre. Bull. Soc. Nat. Luxemb. 103, 121–129.

Bonté, D., Guillou–Frottier, L., Garibaldi, C., Bourgine, B., Lopez, S., Bouchot, V., Lucazeau, F. (2010). Subsurface temperature maps in French sedimentary basins: new data compilation and interpolation. Bull. Soc. Géol. Fr. 181, 377–390.

Bonté, D., van Wees, J.-D., Verweij, J.M. (2012). Subsurface temperature of the onshore Netherlands: new temperature dataset and modelling. Neth. J. Geosci. 91, 491–515.

Bourgeois, O., Ford, M., Diraison, M., Le Carlier de Veslud, C., Gerbault, M., Pik, R., Ruby, N., Bonnet, S. (2007). Separation of rifting and lithospheric folding signatures in the NW–Alpine foreland. Int. J. Earth Sci. 96, 1003–1031.

Bourgine, B., Denis, L., Filhine–Tressarrieu, T., Monnot, P., Nguyen–Thé, D., Robelin, C. (2007). Atlas du potentiel géothermique des aquifères lorrains. Rapport BRGM/RP-54987-FR, Orléans, 83 pp, http://www.geothermie-perspectives.fr/sites/default/files/rp_54987_fr.pdf.

Bräuer, K., Kämpf, H., Niedermann, S., Strauch, G. (2013). Indications for the existence of different magmatic reservoirs beneath the Eifel area (Germany): A multi-isotope (C, N, He, Ne, Ar) approach. Chem. Geol. 356, 193–208.

Breede, K., Dzebisashvili, K., Liu, X., Falcone, G. (2013). A systematic review of enhanced (or engineered) geothermal systems: past, present and future. Geothermal Energy 1(4), http://dx.doi.org/10.1186/2195-9706-1-4.

BRGM (Bureau de Recherches Géologiques et Minières) (2015) Dossier du sous-sol (BSS), http://infoterre.brgm.fr.

Bujakowski, W., Barbacki, A. (2004). Potential for geothermal development in Southern Poland. Geothermics 33. 383–395.

Bultynck, P., Dejonghe, L. (2001). Devonian lithostratigraphic units (Belgium). In: Bultynck, P., Dejonghe, L. (Eds.), Guide to a Revised Lithostratigraphic Scale of Belgium, vol. 4(1–2). Geologica Belgica, Brussels, pp 39–69.

Celle–Jeanton, H., Huneau, F., Travi, Y., Edmunds, W.M. (2009). Twenty years of groundwater evolution in the Triassic sandstone aquifer of Lorraine: Impacts on baseline water quality. Applied Geochemistry 24, 1198–1213.

Clauser, C. (2009). Heat transport processes in the Earth's crust. Surv. Geophys. 30, 163–191, http://dx.doi.org/10.1007/s10712-009-9058-2.

Cloetingh, S., Thybo, H., Faccenna, C. (2009). TOPO-EUROPE: Studying continental topography and deep earth–surface processes in 4D. Tectonophysics 474, 4–32.

Cloetingh, S., van Wees, J.D., Ziegler, P.A., Lenkey, L., Beekman, F., Tesauro, M., Förster, A., Norden, B., Kaban, M., Hardebol, N., Bonté, D., Genter, A., Guillou–Frottier, L., Ter

Voorde, M., Sokoutis, D., Willingshofer, E., Cornu, T., Worum, G. (2010). Lithosphere tectonics and thermo-mechanical properties: An integrated modelling approach for Enhanced Geothermal Systems exploration in Europe. Earth-Science Reviews 102, 159–206.

Coiffait, B., Ricour, J. (1982). Forages aux Grès du Trias inférieur en Lorraine, analyse des archives disponibles, propositions pour une amélioration de la technologie de réalisation et d'équipement. Bur. Rech. Géol. Min., Serv. Géol. Rég. Lorraine., Vandoeuvre, 22 pp.

Dejonghe, L. (1998). Zinc–lead deposits of Belgium. Ore Geol. Rev. 12, 329–354.

Dejonghe, L. (2008). Carte géologique de Wallonie 1/25.000, feuille 55/5–6 Hotton–Dochamps. Notice explicative, Région Wallonne, Namur, 88 pp.

Deming, D. (1994). Fluid flow and heat transport in the upper continental crust. In: Parnell, J. (Ed.), Geofluids: Origin, Migration and Evolution of Fluids in Sedimentary Basins, Spec. Publ. 78. Geol. Soc., London, pp. 27–42.

Deming, D., Sass, J.H., Lachenbruch, A.H., De Rito, R.F. (1992). Heat flow and subsurface temperature as evidence for basin-scale ground-water flow, North Slope of Alaska. Geol. Soc. Am. Bull. 104, 528–542.

Demoulin, A., Hallot, E. (2009). Shape and amount of the Quaternary uplift of the western Rhenish shield and the Ardennes (western Europe). Tectonophysics 474, 696–708.

Dèzes, P., Schmid, S.M., Ziegler, P.A. (2004). Evolution of the European Cenozoic Rift System: interaction of the Alpine and Pyrenean orogens with their foreland lithosphere. Tectonophysics 389, 1–33.

Dittrich, D. (1989). Beckenanalyse der Oberen Trias der Trier–Luxemburger Bucht. Revision der stratigraphischen Gliederung und Rekonstruktion der Paläogeographie. Publ. Serv. Géol. Luxemb., vol. 26. Luxembourg, 223 pp.

Dittrich, D. (2008). Schertektonik im triassischen Deckgebirge der nordwestlichen Trierer Bucht – Teil I. Mainzer geowiss. Mitt. 36, 69–104.

Dittrich, D. (2009). Schertektonik im triassischen Deckgebirge der nordwestlichen Trierer Bucht – Teil II. Mainzer geowiss. Mitt. 37, 77–128.

Dittrich, D. (with contributions by Gad, J., Schäfer, P., Weidenfeller, M.) (2011a). Geologische Karte der Trierer Bucht 1:50000 mit Erläuterungen. Landesamt für Geologie und Bergbau Rheinland-Pfalz, Mainz, 70 pp.

Dittrich, D. (2011b). Schertektonik im triassischen Deckgebirge der südöstlichen Trier–Luxemburger Bucht – Teil I. Mainzer geowiss. Mitt. 39, 7–86.

Dittrich, D. (2012). Schertektonik im mesozoischen Deckgebirge der südöstlichen Trier–

Luxemburger Bucht – Teil II. Mainzer geowiss. Mitt. 40, 79–146.

Dittrich, D. (2013). Schertektonik im mesozoischen Deckgebirge der südöstlichen Trier–Luxemburger Bucht – Teil III. Mainzer geowiss. Mitt. 41, 123–212.

Dittrich, D. (2014). Schertektonik im mesozoischen Deckgebirge der südöstlichen Trier–Luxemburger Bucht – Teil IV. Mainzer geowiss. Mitt. 42, 27–98.

ENGINE Coordination Action (2008). Best Practice Handbook for the development of Unconventional Geothermal Resources with a focus on Enhanced Geothermal System 2008. Collection Actes/Proceedings, BRGM, Orléans, 97 pp., http://engine.brgm.fr/Documents/ENGINE_BestPracticeHandbook.pdf.

Fuchs, K., von Gehlen, K., Mälzer, H., Murawski, H., Semmel, A. (Eds.) (1983). Plateau Uplift: The Rhenish Shield – A Case History. Springer, Berlin, Heidelberg, New York, Tokyo, 411 pp.

Garnish, J. (2002). European activities in Hot Dry Rock research. In: Open Meeting on Enhanced Geothermal Systems, US Department of Energy, Reno/NV, 26–27 September 2002, http://geothermal.smu.edu.

Griesshaber, E., O'Nions, R.K., Oxburgh, E.R. (1992). Helium and carbon isotope systematics in crustal fluids from the Eifel, the Rhine Graben and Black Forest, FRG. Chem. Geol. 99, 213–235.

Häfner, F., Kött, A., Spindeldreher, J., Rein, B., Grubert, A. (2007). Nutzung von oberflächennaher Erdwärme für die Gebäudeheizung in Rheinland-Pfalz. Bericht, Landesamt für Geologie und Bergbau Rheinland-Pfalz, Mainz, 97 pp.

Held, S., Genter, A., Kohl, T., Kölbel, T., Sausse, J., Schoenball, M. (2014). Economic evaluation of geothermal reservoir performance through modelling the complexity of the operating EGS in Soultz-sous-Forêts. Geothermics 51, 270–280.

Huenges, E. (Ed.) (2010). Geothermal Energy Systems: Exploration, Development, and Utilization. Wiley-VCH, Berlin, 463 pp.

IEA (International Energy Agency) (2011). Technology Roadmap Geothermal Heat and Power. OECD/IEA, Paris, 45 pp., http://www.iea.org/publications/freepublications/publication/Geothermal_Roadmap.pdf.

Kaltschmitt, M., Huenges, E., Wolff, H. (Eds.) (1999). Energie aus Erdwärme. Deutscher Verlag für Grundstoffindustrie (DVG), Stuttgart, 265 pp.

Keyser, M., Ritter, J.R.R., Jordan, M. (2002). 3D shear-wave velocity structure of the Eifel plume, Germany. Earth Planet. Sci. Lett. 203, 59–82.

Kramers, L., van Wees, J.-D., Pluymaekers, M.P.D., Kronimus, A., Boxem, T. (2012). Direct

heat resource assessment and subsurface information systems for geothermal aquifers; the Dutch perspective. Neth. J. Geosci. 91, 637–649.

Kremb–Wagner, F. (1996). Zur Geologie und Hydrogeologie der Trier-Bitburger Mulde. Schriftenr. Schiefer-Fachverb. Deutschl., Sonderband 1996, Bonn, pp. 1–130.

Kremb–Wagner, F., Negendank, J.W.F., Wagner, H.W. (2014). Zur Struktur der Trier–Bitburger Mulde, der Fortsetzung des Trier–Wittlicher-Rotliegend-Grabens und weiterer Strukturen. Z. Dt. Ges. Geowiss. 165(3), 367–372.

Langguth, H.-R., Plum, H. (1984). Untersuchung der Mineral- und Thermalquellen der Eifel auf geothermische Indikationen. Forschungsbericht, BMFT–FB–T 84-019, Technologische Forschung und Entwicklung – Nichtnukleare Energietechnik, Lehr- und Forschungsgebiet für Hydrogeologie der RWTH Aachen, Aachen, 176 pp.

Ledru, P., Guillou–Frottier, L. (2010). Reservoir definition. In: Huenges, E. (Ed.), Geothermal Energy Systems: Exploration, Development, and Utilization. Wiley-VCH, Berlin, pp. 1–36.

Leichtle, T. (1980). Die Thermalwassertiefbohrung Michel-Lucius. Bericht, Bad Mondorf, Luxemburg, 46 pp.

LGB (Landesamt für Geologie und Bergbau Rheinland-Pfalz) (Ed.) (2005). Geologie von Rheinland-Pfalz. Schweizerbart, Stuttgart, 400 pp.

LGB, LUWG (Landesamt für Geologie und Bergbau Rheinland-Pfalz, Landesamt für Umwelt, Wasserwirtschaft und Gewerbeaufsicht Rheinland-Pfalz) (Eds.) (2010). Hydrogeologische Kartierung Bitburg–Trier. Mainz, 134 pp.

Líndal, B. (1973). Industrial and other applications of geothermal energy. In: Geothermal Energy. Review of Research and Development, LC No. 72-97138, UNESCO, Paris, pp. 135–148.

Lorenz, V. (2003). Maar-diatreme volcanoes, their formation, and their setting in hard-rock or soft-rock environments. Geolines 15, 72–83.

Lorenz, V. (2007). Syn- and posteruptive hazards of maar–diatreme volcanoes. J. Volc. Geoth. Res. 159, 285–312.

Lucius, M. (1923). La genèse des eaux thermo-minérales de Mondorf-les-bains. Bull. Soc. Nat. Luxemb. 1–2, 3–22.

Lucius, M. (1948). Das Gutland. Erläuterungen zu der Geologischen Spezialkarte Luxemburgs. Publ. Serv. Géol. Luxemb., vol. 5. Luxembourg, 408 pp.

Lucius, M. (1949). La remise en état de la source thermominérale Kind à Mondorf. Bull. Soc. belge Géol. Paléont. Hydrol. 58, 355–359.

Lucius, M. (1953). Quelques aspects de la géologie appliquée dans l'aire de sédimentation luxembourgeoise. Publ. Serv. Géol. Luxemb., vol. 9. Luxembourg, 279 pp.

Lucius, M. (1959). Hydrogéologie de l'eau minérale carbogazeuse dite « Source de Rosport ». Revue technique luxemb. 51(4), 203–207.

Mälzer, H., Hein, G., Zippelt, K. (1983). Height changes in the Rhenish Massif: Determination and analysis. In: Fuchs, K., von Gehlen, K., Mälzer, H., Murawski, H., Semmel, A. (Eds), Plateau Uplift: The Rhenish Shield – A Case History. Springer, Berlin, Heidelberg, New York, Tokyo, pp. 164–176.

Manning, C.E., Ingebritsen, S.E. (1999). Permeability of the continental crust: Implications of geothermal data and metamorphic systems. Rev. Geophys. 37, 127–150.

Meyer, W. (1994). Geologie der Eifel, third ed. Schweizerbart, Stuttgart, 618 pp.

Meyer, W., Stets, J. (1996). Das Rheintal zwischen Bingen und Bonn. In: Sammlung geol. Führer, vol. 89. Borntraeger, Berlin, Stuttgart, 386 pp.

Meyer, W., Stets, J. (2002). Pleistocene to recent tectonics in the Rhenish Massif (Germany). Neth. J. Geosci. 81, 217–221.

Meyer, W., Stets, J. (2007). Quaternary uplift in the Eifel area. In: Ritter, J.R.R., Christensen, U.R. (Eds.) Mantle Plumes. A Multidisciplinary Approach. Springer, Berlin, Heidelberg, pp. 369–376.

Muffler, P., Cataldi, R. (1978). Methods for regional assessment of geothermal resources. Geothermics 7, 53–89.

Murawski, H., Albers, H.J., Bender, P., Berners, H.-P., Dürr, S., Huckriede, R., Kauffmann, G., Kowalczyk, G., Meiburg, P., Müller, R., Muller, A., Ritzkowski, S., Schwab, K., Semmel, A., Stapf, K., Walter, R., Winter, K.-P., Zankl, H. (1983). Regional tectonic setting and geological structure of the Rhenish Massif. In: Fuchs, K., von Gehlen, K., Mälzer, H., Murawski, H., Semmel, A. (Eds.), Plateau Uplift: The Rhenish Shield – A Case History. Springer, Berlin, Heidelberg, New York, Tokyo, pp. 9–38.

Nicklès, R. (1914). Le sondage du Bois-châté. Bull. Soc. Sci. Nancy, sér. III, 15(1), 197–214.

Paschen, H., Oertel, D., Grünwald, R. (2003). Möglichkeiten geothermischer Stromerzeugung in Deutschland. Arbeitsbericht Nr. 84, Deutscher Bundestag Ausschuss für Bildung, Forschung und Technikfolgenabschätzung, Berlin, 124 pp., https://www.tab-beim-bundestag.de/de/pdf/publikationen/berichte/TAB-Arbeitsbericht-ab084.pdf.

Philippo, S. (Ed.) (2007). Inventaire minéralogique du Luxembourg Stolzembourg, Schimpach, Goesdorf. Ferrantia, vol. 49. Musée national d'histoire naturelle, Luxembourg, 146 pp.

Pluymaekers, M.P.D., Kramers, L., van Wees, J.-D., Kronimus, A., Nelskamp, S., Boxem, T.,

Bonté, D. (2012). Reservoir characterisation of aquifers for direct heat production: Methodology and screening of the potential reservoirs for the Netherlands. Neth. J. Geosci. 91, 621–636.

Pommerening, J. (1993). Hydrogeologie, Hydrogeochemie und Genese der Aachener Thermalquellen. Mitteilungen zur Ingenieurgeologie und Hydrogeologie, vol. 50. Lehrstuhl für Ingenieurgeologie und Hydrogeologie der RWTH Aachen, Aachen, 194 pp.

Rybach, L. (2010). "The future of geothermal energy" and its challenges. In: Proceedings of the World Geothermal Congress, 25–29 April 2010, Bali, Indonesia, pp. 1–4.

Saadat, A., Frick, S., Kranz, S., Regenpurg, S. (2010). Energetic use of EGS reservoirs. In: Huenges, E. (Ed.), Geothermal Energy Systems: Exploration, Development, and Utilization. Wiley-VCH, Berlin, pp. 303–372.

Schintgen, T., Förster, A. (2013). Geology and basin structure of the Trier–Luxembourg Basin – implications for the existence of a buried Rotliegend graben. Z. Dt. Ges. Geowiss. 164 (4), 615–637.

Schintgen, T., Förster, A., Förster, H.-J., Norden, B. (2015). Surface heat flow and lithosphere thermal structure of the Rhenohercynian Zone in the greater Luxembourg region. Geothermics 56, 93–109.

Schmincke, H.-U. (2007). The Quaternary volcanic fields of the east and west Eifel (Germany). In: Ritter, J.R.R., Christensen, U.R. (Eds.), Mantle Plumes. A Multidisciplinary Approach. Springer, Berlin, Heidelberg, pp. 241–322.

Schulte, T., Zimmermann, G., Vuataz, F., Portier, S., Tischner, T., Junker, R., Jatho, R., Huenges, E. (2010). Enhancing geothermal reservoirs. In: Huenges, E. (Ed.), Geothermal Energy Systems: Exploration, Development, and Utilization. Wiley-VCH, Berlin, pp. 173–243.

Seiberlich, C.K.A., Ritter, J.R.R., Wawerzinek, B. (2013). Topography of the lithosphere–asthenosphere boundary below the Upper Rhine Graben Rift and the volcanic Eifel region, Central Europe. Tectonophysics 603, 222–236.

Smith, L., Chapman, D.S. (1983). On the thermal effects of groundwater flow. J. Geophys. Res. B88, 593–608.

Sperber, A., Moeck, I., Brandt, W. (2010). Drilling into geothermal reservoirs. In: Huenges, E. (Ed.), Geothermal Energy Systems: Exploration, Development, and Utilization. Wiley-VCH, Berlin, pp. 113–171.

STATEC (Institut national de la statistique et des études économiques du Grand-Duché du Luxembourg) (2014). Le portail des statistiques du Grand-Duché du Luxembourg,

http://www.statistiques.public.lu/stat/TableViewer/tableView.aspx?ReportId=397andIF_Language=fra.

Stets, J. (2004). Geologische Karte der Wittlicher Rotliegend-Senke 1:50000 mit Erläuterungen. LGB (Landesamt für Geologie und Bergbau Rheinland-Pfalz), Mainz, 82 pp.

Stets, J., Schäfer, A. (2002). Depositional environments in the Lower Devonian siliciclastics of the Rhenohercynian Basin (Rheinisches Schiefergebirge, W-Germany) – Case studies and a model. Contr. Sed. Geol. 22, 77 pp.

Stets, J., Schäfer, A. (2011). The Lower Devonian Rhenohercynian rift – 20 Ma of sedimentation and tectonics (Rhenish Massif, W-Germany). Z. Dt. Ges. Geowiss. 162(2), 93–115.

Stober, I., Bucher, K. (2012). Geothermie. Springer, Berlin, Heidelberg, 287 pp.

Stober, I., Fritzer, T., Obst, K., Schulz, R. (2009). Nutzungsmöglichkeiten der tiefen Geothermie in Deutschland. BMU (Bundesministerium für Umwelt, Naturschutz und Reaktorsicherheit, Berlin, 73 pp.

Storz, R. (2007). Tiefe Geothermie in Rheinland-Pfalz – Ein Überblick über die geothermischen Verhältnisse und den aktuellen Stand der Nutzung. Mainzer geowiss. Mitt. 35, 135–158.

Tester, J.W., Anderson, B.J., Batchelor, A.S., Blackwell, D.D., DiPippo, R., Drake, E.M., Garnish, J., Livesay, B., Moore, M.C., Nichols, K., Petty, S., Toksöz, M.N., Veatch, R.W. Jr., Baria, R., Augustine, C., Murphy, E., Negraru, P., Richards, M. (2006). The Future of Geothermal Energy: Impact of Enhanced Geothermal Systems (EGS) on the United States in the 21st Century. MIT (Massachusetts Institute of Technology), Boston, http://www1.eere.energy.gov/geothermal/pdfs/future_geo_energy.pdf.

Van Wees, J.-D., Kronimus, A., van Putten, M., Pluymaekers, M.P.D., Mijnlieff, H., van Hooff, P., Obdam, A., Kramers, L. (2012). Geothermal aquifer performance assessment for direct heat production – Methodology and application to Rotliegend aquifers. Neth. J. Geosci. 91, 651–665.

Wagner, B., Dittrich, D. (2010). Profilschnitte A–A′ bis F–F′. In: LGB and LUWG (Landesamt für Geologie und Bergbau Rheinland-Pfalz and Landesamt für Umwelt, Wasserwirtschaft und Gewerbeaufsicht Rheinland-Pfalz) (Eds.), Hydrogeologische Kartierung Bitburg–Trier. LGB and LUWG, Mainz.

Wagner, H.W. (1996). Bemerkungen zur Tektonik der Trier–Bitburger Mulde (SW-Deutschland). Schriftenr. Schiefer-Fachverb. Deutschl., Sonderband 1996, pp. 131–140.

Wagner, H.W., Kremb–Wagner, F., Koziol, M., Negendank, J.F.W. (2012). Trier und Umgebung, third ed. Gebr. Bornträger, Stuttgart, 396 pp.

Walker, K.T., Bokelmann, G.H.R., Klemperer, S.L., Bock, G. (2005). Shear-wave splitting around the Eifel hotspot: evidence for a mantle upwelling. Geophys. J. Int. 163, 962–980.

Weidenfeller, M., Löhr, H., Weiler, H. (2004). Quartärgeologie, Hydrogeologie und Geoarchäologie in den Tälern von Mosel und unterer Saar (Exkursion G am 16. April 2004). Jber. Mitt. Oberrhein. Geol. Ver. 86, 203–235.

Weiler, H. (1972). Ergebnisse von Bohrungen im Buntsandstein im Raume Trier–Bitburg. Mainzer geowiss. Mitt. 1, 198–227.

Weiler, H. (1991). Das Grundwasser in der Bitburger Trias-Mulde, Beschreibung eines Aquifers, neue Ergebnisse. Mainzer geowiss. Mitt. 20, 9–42.

Werle, O. (2009). Mineralwasser im Sauertal: die Quellen von Ralingen und Rosport. Jb. Kreis Trier–Saarburg, pp. 56–62.

Wierich, F. (1999). Orogene Prozesse im Spiegel synorogener Sedimente; korngefügekundliche Liefergebietsanalyse siliziklastischer Sedimente im Devon des Rheinischen Schiefergebirges. Z. Marburger Geowiss. Ver., vol. 1. Marburg, 227 pp.

Wildberger, J. (1992). Zur tektonischen Entwicklung des südwestlichen Hunsrücks (SW–Deutschland). Mitt. Pollichia 79, 5–119.

Ziegler, P.A., Dèzes, P. (2007). Cenozoic uplift of Variscan Massifs in the Alpine foreland: Timing and controlling mechanisms. Global Planet. Change 58, 237–269.

Zimmermann, G., Blöcher, G., Reinicke, A., Brandt, W. (2011). Rock specific hydraulic fracturing and matrix acidizing to enhance a geothermal system – Concepts and field results. Tectonophysics 503, 146–154.

Zitzmann, A., Grünig, S. (with contributions by Meyer, W., Stets, J., Mittmeyer, H.-G., Konrad, H.J., Ribbert, K.-H., Fuchs, G.) (1987). Geologische Übersichtskarte 1:200000, Blatt CC 6302 Trier. BGR (Bundesanstalt für Geowissenschaften und Rohstoffe), Hannover.

5 Discussion

The evaluation of the geothermal potential of the region of Luxembourg envisaged in this study is evaluated by a joint interpretation of geological, thermal, hydrogeological and structural data. Although this study centres on the assessment of the thermal regime in the subsurface of Luxembourg, the study area encompasses, within the geological framework, the country of Luxembourg and the adjoining areas in France, Belgium and Germany (Fig. 1.1). For the evaluation of the geothermal potential of an area, comprehensive knowledge of surface heat flow and subsurface temperature distribution is indispensable. As subsurface temperature data in Luxembourg and adjoining regions is sparse, thermal modelling was chosen as a tool for elucidating the geothermal resource at depth. However, profound structural, geological and petrophysical input data are required.

During the initial search for the most recent geological and structural data of the study area (Fig. 2.2, it became evident that the geology and basin structure of the Trier–Luxembourg Basin (TLB) of Mesozoic age had to be reassessed. In Chapter 2, this task was mastered by setting up a borehole database for Luxembourg and the adjoining areas in France, Belgium and Germany (Table 2.1 and Tables A.1.1–4). The conceptual geological model developed for the TLB in Luxembourg was integrated into available and essential, recent geological/structural studies in the surrounding regions (Schintgen and Förster, 2013; and references therein). As a first step, the geology of Luxembourg is reviewed and stratigraphically correlated with the different parts of the TLB located outside of the territory of Luxembourg (Table 2.2). The geological setting accounts for the northern part of Lorraine, France, the Gaume region (or Belgian Lorraine) as well as the Südeifel region in Rhineland–Palatinate and the Saargau region in Rhineland–Palatinate and Saarland. In view of the lack of appropriate deep boreholes in the TLB, the actual depth of this basin was, and still remains, uncertain. However, in order to get further insight in the morphology/depth of the base of the Mesozoic basin, a Bouguer map (see Fig. 2.3; M. Everaerts, pers. comm.) was interpreted in combination with available borehole data (Schintgen and Förster, 2013). Positive and negative gravity anomalies are interpreted as contrasts in density imaging structural highs and lows in the Variscan basement, respectively. Most importantly, the Bouguer map allows the regional correlation of deep and shallow structures such as major faults known from the surface. The Bouguer map shows no gravimetric evidence for the old concept of the depression known as Weilerbach Mulde. In this respect, a major challenge but a necessity consisted in the reinterpretation of the geological section of the Cessange borehole (Fig. 2.4; Kind, 1842; Lucius, 1948; Rost, 1839). The latter was drilled from

1837 to 1839 and is still the only deep borehole in the geographical centre of the TLB. Inconsistencies with the present-day geological knowledge and a sketchy geological knowledge at the time when the borehole was drilled asked for revisiting the borehole descriptions. The new interpretation of the geological section centres in the replacement of the remarkable succession of anhydrite and gypsum by massive dolomite. The reinterpretation yields relatively conservative thickness values in accordance with the bulk of observations in the TLB. In order to visualize the geology and basin structure of the TLB, the Cessange borehole and numerous representative boreholes were used to generate isopach maps (Fig. 2.5; Schintgen and Förster, 2013). Thickness data were then further used to construct regional geological cross sections (Fig. 2.6). The six NW–SE-oriented sections show the synform shape of the basin, whereas the SW–NE-oriented section shows the tilt from the German Triassic Basin in the northeast towards the Paris Basin in the southwest at the beginning of the Keuper. A new and meaningful finding is the breakpoint/culmination of the base of the TLB below the Alzette River valley (Fig. 2.6G). The latter feature is further interpreted in Section 4.4.2. Furthermore, the occurrence of Permian sediments beneath the Mesozoic record of the TLB was inferred in numerous studies but still is a matter of debate. Based on the basin-wide cross sections, the structural and sedimentological observations in the TLB and the tectonic structures in the exposed basement, Schintgen and Förster (2013) suggest that the TLB developed along a weakness zone related to a Permian graben (Fig. 2.7). This central subsided structure buried underneath the TLB is designated by SE-Luxembourg Graben. The latter graben represents the direct southwestern prolongation of the Permian Wittlicher Senke (WS). In the area of Trier–Wittlich, the WS is a relatively well known narrow, 5–7-km-large and 40-km-long graben filled with an up to 1000-m-thick succession of Rotliegend sediments (Stets, 2004).

In Chapter 3, a tremendous effort was made to assess the thermal field of the study area by numerical modelling, which asked for the determination of a new surface heat flow value for verification of the thermal models and a database of measured thermal rock properties. Geological and structural data, reliable thermal rock properties and appropriate thermal boundary conditions are a prerequisite for the development, i.e. the construction and parameterization, of the thermal models. The geology of the study area (Fig. 3.1) is well known in the upper 15 km and is generalized in the lower part of the crust down to the Moho (Fig. 3.2). The lithotypes of the geological units in the model were assessed from surface and borehole observations and, for the deeper parts of the model, from geophysical surveys and from xenolith data of the adjoining volcanic field in the Eifel region (Germany). Thermal rock properties including thermal conductivity, radiogenic heat production and density assigned to the

geological or rather model units (Table 3.7) relate to measured laboratory data on field and drill core samples (246 in total; Table 3.1) for the upper part of the crust. Measured petrophysical properties (Tables 3.4 and 3.5) are complemented by literature data for the lower part of the crust. Temperature logs measured in deep boreholes are commonly used for the calibration of a thermal model. For the greater Luxembourg region, only the about 300-m-deep Mersch borehole located in the central part of Luxembourg provides appropriate temperature and geological data for surface heat-flow determination (Fig. 3.3; Table 3.6). The new q_s value amounts to 75 ± 7 (2σ) mW m^{-2} (Schintgen et al. 2015) and corroborates the bulk of data reported for the adjoining areas (64–84 mW m^{-2}). The lack of subsurface temperature data for greater depths was circumnavigated by performing in-depth studies of the regional and local geology and of the thermal rock properties assigned to the geological units. The relative scarcity of geological and geophysical data did not justify the contruction of a 3-D geothermal model so that conceptual, crustal cross sections (Figs. 3.1 and 3.2) served as a basis for the generation of 2-D steady-state and conductive lithosphere-scale thermal models (Figs. 3.4 and 3.5). The thermal models are constrained by surface heat flow (q_s) and the geophysically estimated depth of the lithosphere–asthenosphere boundary (LAB). A LAB depth of 100 km, as seismically derived for the Ardennes, provides the best fit with the measured q_s (Fig. 3.6a–c). The mantle heat flow amounts to ~ 40 mW m^{-2}. Possible thermal consequences of the 10–20 Ma old Eifel plume, which caused elevation of the LAB to 50–60 km depth, were modelled in a steady-state thermal scenario resulting in a q_s of 91 mW m^{-2} in the Eifel region (EP 60 in Fig. 3.6d). Available q_s values (65–80 mW m^{-2}) are significantly lower and indicate that the plume-related heating has not yet reached the surface in its entirety. Modelled temperatures are in the range of 120–125 °C at 5 km depth and of 600–650 °C at the Moho, respectively (Fig. 3.7a–c). Maximum temperatures at 5 km depth are reached only in a SW–NE-oriented zone beneath a cover of Siegenian to Emsian rock of low thermal conductivity ($\lambda \approx 3.2$ W m^{-1} K^{-1}). By contrast, high thermal conductivities in the Stavelot Massif in the northwest ($\lambda > 4$ W m^{-1} K^{-1}) and in the Hunsrück region in the southeast ($\lambda \approx 5$ W m^{-1} K^{-1}) cause significantly lower temperatures (Fig. 3.8a and b).

In Chapter 4, different types of information are presented that are necessary for a first rather qualitative assessment of deep geothermal reservoirs in the greater region of Luxembourg (Fig. 4.1). On the one hand, the focus is laid on low-enthalpy hydrothermal reservoirs in Mesozoic aquifers in the Trier–Luxembourg Embayment. On the other hand, petrothermal reservoirs in the Devonian basement of the Ardennes and Eifel regions are considered for exploitation by

Enhanced/Engineered Geothermal Systems (EGS). A major obstacle for the assessment of geothermal resources and their evaluation for different geothermal applications in Luxembourg and the adjoining areas is the absence of deep boreholes (Schintgen and Förster, 2013). As a consequence, subsurface temperature data are sparse. Moreover, prior to this study, a temperature prognosis based on a thermal model parameterized by measured thermal rock properties and constrained by appropriate boundary conditions was unavailable. At present, conceptual geological models (Figs. 4.2 and 4.3) incorporated into thermal models (Schintgen et al., 2015) allow evaluating the possibilities for different types of geothermal uses and to pinpoint the most promising areas for geothermal exploration. The thermal model by Schintgen et al. (2015) provides data for temperature maps generated for 1 km depth steps between 1000 and 6000 m (below mean sea level). In contrast to an evaluation by Biermayr et al. (2007), the geothermal potential in Luxembourg cannot be negated a priori. Maximum temperatures at 5 km depth are at least 120–125 °C (Fig. 4.4). Besides the deep geological conditions and knowledge of the subsurface temperature distribution, the crustal stress field and lithosphere-scale weakness zones are particularly important in site selection for geothermal exploration and the development of Enhanced Geothermal Systems (Cloetingh et al., 2010). Detailed studies of the geology and structure by Dittrich (2014; and references therein) revealed that the TLE is currently characterized by a NW–SE-orientated compressional tectonic regime that most likely evolves towards a strike-slip regime at greater depth. As an important outcome for geothermal exploration, the Cenozoic structural evolution of the Müllerthal–Südeifel region is reinterpreted using new data by Schintgen and Förster (2013) (Fig. 4.5). Their conceptual model of the Trier–Luxembourg Basin infers a culmination of the base of the Mesozoic underneath the Alzette River valley (Fig. 2.6G) instead of the old concept of a subsided area, i.e. the old concept of the Weilerbach Mulde, underneath the central part of the Guttland (e.g., Lucius, 1948; Bintz et al., 1985; Murawski et al., 1983; Muller, 1987). According to Schintgen and Förster (2013), the geology and basin structure of the Trier–Luxembourg Basin strongly suggests that the latter developed along a zone of weakness related to a Permian graben in direct southwestern continuation of the Wittlicher Rotliegend-Senke. In Section 4.4.2.1, it is further suggested that the Eifel Depression, more specifically the Müllerthal–Südeifel region (Fig. 4.2) likely is a Cenozoic structure. This would imply that the present-day appearance of the TLE is the result of consecutive and superimposed large-scale structures formed in different geodynamic contexts. The argumentation is mainly based on studies by Schintgen and Förster (2013) and Dittrich (2014; and references therein). For visualization of the concept, cross section B* in Fig. 4.5a shows the cross section G presented in Fig 2.6 and its extension into the Eifel region

using the cross section data by Wagner and Dittrich (2010). The postulation of a simple relatively flat Variscan basement below the Müllerthal–Südeifel region (Fig 4.5a and b) permits to reconstruct the former appearance of the Trier–Luxembourg Basin prior to uplift of the Rhenish Massif and consequent erosion. It is proposed that the present-day appearance of the TLE is the result of about 470 m of Cenozoic subsidence of the Müllerthal–Südeifel region, leading to the formation of the Müllerthal–Südeifel Depression (MSD). About 100 m of subsidence of the Müllerthal–Südeifel region according to Meyer and Stets (2007) in the last 700 ka (Schmincke, 2007) yields an average subsidence rate of 0.14 mm a^{-1}, which is supported by instantaneous height changes determined by Mälzer et al. (1983). The current mobility of the MSD has major implications for geothermal exploration. In fact, in site selection for geothermal exploration for hydrothermal as well as petrothermal reservoirs, the crustal stress field influences or controls the creation and evolution of faults, fractures and joints, thus fracture permeability. The latter becomes important particularly with increasing depth where the permeability of pores decreases notably by compaction and a higher cementation.

Among the Mesozoic aquifers, the Buntsandstein aquifer is the deepest, thickest, and has the largest extent (Figs. 4.6 and 4.7). It presents excellent hydraulic properties in the southeastern part of the TLE (Fig. 4.8; Table 4.1) and is characterized by temperatures of up to 50 °C (Fig. 4.11). It represents a suitable hydrothermal reservoir that could be used by means of heat pumps or provide direct heat for various applications.The most promising and warmest area is the zone of the SE–Luxembourg Graben, more specifically underneath the upper Alzette River valley and the limestone plateau in Lorraine where the Buntsandstein aquifer lies below a thick Mesozoic cover. At the base of an inferred Rotliegend graben in the same area, temperatures of up to 75 °C are expected. However, geological and hydraulic conditions are uncertain.

In the Lower Devonian basement, thick sandstone-/quartzite-rich formations with temperatures >90 °C are expected at depths >3.5 km (Fig. 4.9) and likely offer the possibility of direct heat use. The identification of the Müllerthal–Südeifel Depression as a Cenozoic tectonic structure that is still mobile is relevant for geothermal exploration and might offer the possibility of deep hydrothermal reservoirs in fractured Lower Devonian rock (Fig. 4.10). The entire zone of mineral springs in and around the South Eifel region (e.g., Langguth and Plum, 1984) might be the clearest indication of a hydrothermal reservoir at depth, though no particulary high temperatures of the groundwater are known. Despite expected modest temperatures at 5 km depth (about 120 °C), increased permeability by EGS in the quartzite-rich Lochkovian could prospectively enable combined geothermal heat production and power generation in Luxembourg and the western realm of the Eifel region (Fig. 4.12).

6 Conclusions

This work aimed at an evaluation of the geothermal potential of Luxembourg. It consists in combining different types of information necessary for a first rather qualitative assessment of deep geothermal reservoirs in Luxembourg and the adjoining regions in the surrounding countries of Belgium, France and Germany.

Until recently, reliable information about the thermal field and the geology, thus potential geothermal reservoirs, was lacking, which precluded an assessment of the technical potential of geothermal energy in general (Biermayr et al., 2007). In the past few years, work was done to overcome these shortcomings and lay the base for the regional development of geothermal energy. First, the geology and basin structure of the Mesozoic Trier–Luxembourg Basin was unraveled and gave rise to a new conceptual model postulating the existence of a zone of weakness along a buried Rotliegend graben (Schintgen and Förster, 2013).

Due to the lack of deep boreholes and thus subsurface temperature prognosis the temperature distribution in the subsurface of the greater Luxembourg region was assessed by thermal modelling (Schintgen et al., 2015). A surface heat flow value of 75 ± 7 mW m^{-2} determined for central Luxembourg and a database of measured petrophysical properties (thermal conductivity, radiogenic heat production, porosity and density), essential in any type of geothermal consideration, are available at present (Schintgen et al., 2015). For geothermal exploration, the temperatures encountered at depths <5–6 km, to which geothermal boreholes can be drilled at costs that allow an economic use of the Earth's heat, are of particular interest. It is shown that the available surface heat flow values in the region of Luxembourg measured in the shallow subsurface (<200 m) can be problematic and should be verified and corroborated by surface heat flow determined from high quality, continuous temperature logs in deep boreholes. Such recordings would shed light on the thermal regime as well as ongoing advective or convective processes linked to hydraulic conductivity in the Lower Devonian basement, in particular in the Eifel region. The temperature results show that the possible thermal effect caused by the relatively young Eifel plume would be verifiable if already arrived at 5 km depth. The availability of suitable exploration data would lay the basis for quantification of various transient processes that may overprint purely steady-state conductive conditions and thus challenge the thermal models by Schintgen et al. (2015).

For the evaluation of the geothermal potential of an area, i.e. the identification of geothermal reservoirs by exploration, geological, thermal, hydrogeological and structural data are necessary. Conceptual geological models are presented for the Mesozoic Trier–Luxembourg

Basin by Schintgen and Förster (2013) and for the Lower Devonian basement by Schintgen et al. (2015). Temperature maps for depth steps of 1 km up to 6000 m depth (below mean sea level) are now available for utilization in applied geothermics. Based on the revised knowledge about the geology as well as the surface heat flow, a database of measured thermal rock properties and the assessment of the thermal field, the present study does not support the evaluation by Biermayr et al. (2007) predicting an inexistent geothermal potential. Thermal gradients are about 30 °C km^{-1} in the Mesozoic and 20 °C km^{-1} in the Lower Devonian successions, respectively.

In this study, hydrothermal and petrothermal reservoirs were considered. Hydrothermal reservoirs with temperatures up to 50 °C for use by means of heat pumps or direct use are found in the Buntsandstein aquifer. The most promising area is the part of the SE–Luxembourg Graben located below the Liassic cover, more specifically under the upper Alzette River valley. At the base of an inferred Rotliegend graben in the same zone, temperatures up to 75 °C are expected. However, geological and hydraulic conditions are largely unknown. Despite a moderate temperature gradient of about 20 °C in the Palaeozoic basement, expected sandstone-/quartzite-rich formations in the Lochkovian towards the base of the Lower Devonian in the Ardennes–Eifel block offer the possibility of widespread use of EGS technology. Based on recent data on the structure of the Trier–Luxembourg Basin, the new concept of the Müllerthal–Südeifel Depression is presented as a Cenozoic tectonic structure that is still mobile and potentially hydraulically conductive. The Müllerthal–Südeifel Depression therefore represents a particular target region for future geothermal exploration and implementation of EGS. In particular, numerous mineral springs with high CO_2 content in the West Eifel Volcanic Field and the South Eifel region suggest the existence of a large hydrothermal reservoir at a depth of several kilometers.

Luxembourg's subsurface, like the conditions in the majority of Europe, is characterized by relatively modest temperatures destined primarily for direct heat applications. In the foreseeable future, deployment of low- and medium-temperature hydrothermal resources in deep aquifers and in particular exploitation of petrothermal reservoirs using EGS in the Lower Devonian basement can significantly reduce greenhouse gas emissions and increase the share of renewable energy in the energy mix of Luxembourg. IEA (2011) and Vuataz et al. (2003) put forward that the production of geothermal energy potentially improves energy security, strengthens the economy and creates employment opportunities. Expected temperatures obtained by steady-state conductive thermal models are at least 120–125 °C at 5 km depth. However, hydraulic conductivity is a crucial parameter in the identification of geothermal

reservoirs and the exploitation of geothermal energy, because it has an impact on flow rates and thus power output of a geothermal plant. In the most permeable zones both in the Buntsandstein and the Lochkovian, the span of hydraulic conductivities varies approximately within a factor 100. The current lack of deep exploration boreholes and geophysical data emphasizes the need for substantially more research, development and demonstration funding (RD&D) for geothermal exploration, resource assessment and potential exploitation of geothermal energy for base-load electricity generation and provision of heating and/or cooling. It is crucial to raise general awareness of the different types of utilization of geothermal energy, particularly of geothermal heat which can be used for various applications depending on available temperature (IEA, 2011; Kramers et al., 2012; Líndal, 1973; Vuataz et al., 2003).

7 References

BGI (Bureau Gravimétrique International), 2012. Formules de Réduction des données gravimétriques. Centre des données, Division de la gravité, de la géothermie et de la géodynamique, Direction de la Physique du Globe, Toulouse, http://bgi.omp.obs-mip.fr.

BGR (Bundesanstalt für Geowissenschaften und Rohstoffe) (2015). BGR Geologie : GUEK 200. WMS Service, http://www.bgr.de/service/geologie/guek200/?

Biermayr, P., Cremer, C., Faber, T., Kranzl, L., Ragwitz, M., Resch, G., Toro, F. (2007). Bestimmung der Potenziale und Ausarbeitung von Strategien zur verstärkten Nutzung von erneuerbaren Energien in Luxemburg. Endbericht, Fraunhofer Institut für System- und Innovationsforschung (Fh-ISI), Karlsruhe, Energy Economics Group (EEG), TU Wien, BSR-Sustainability, Karlsruhe, 235 pp.

Bintz, J., Maquil, R., Negendank, J.F.W., Wagner, W. (1985). Der Jura im Trier-Luxemburger Raum. Exkursionsführer, Jahrestagung 1985, Trier 16.5.–18.5.85, DUGW, Stratigr. Komm., Subkomm. Jura-Stratigr., 50 pp.

Bless, M.J.M., Bouckaert, J., Camelbeeck, T., Dejonghe, L., Demoulin, A., Dupuis, C., Felder, P.J., Geukens, F., Gullentops, F., Hance, L., Jagt, J.W.M., Juvigné, E., Kramm, U., Ozer, A., Pissart, A., Robaszynski, F., Schumacker, R., Smolderen, A., Spaeth, G., Steemans, P, Streel, M., Vandenven, G., Vanguestaine, M., Walter, R., Wolf, M. (1990). The Stavelot Massif from Cambrian to Recent – a survey of the present state of knowledge. Ann. Soc. Géol. Belgique 113, 53–73.

Bourgeois, O., Ford, M., Diraison, M., Le Carlier de Veslud, C., Gerbault, M., Pik, R., Ruby, N., Bonnet, S. (2007). Separation of rifting and lithospheric folding signatures in the NW-Alpine foreland. Int. J. Earth Sci. 96, 1003–1031.

Bram, K. (1979). Heat flow measurements in the Federal Republic of Germany. In: Čermák, V., Rybach, L. (Eds.), Terrestrial Heat Flow in Europe. Springer, Berlin, Heidelberg, New York, NY, pp. 191–196.

BRGM (Bureau de Recherches Géologiques et Minières) (2015a). Dossier du sous-sol (BSS), http://infoterre.brgm.fr.

BRGM (Bureau de Recherches Géologiques et Minières) (2015b). GéoServices: géologie, hydrogéologie et gravimétrie. WMS Service, http://geoservices.brgm.fr/geologie?

Bultynck, P., Dejonghe, L. (Eds.) (2001). Guide to a revised lithostratigraphic scale of Belgium. Geologica Belgica 4 (1–2). Brussels, pp. 39–69.

Cloetingh, S., van Wees, J.D., Ziegler, P.A., Lenkey, L., Beekman, F., Tesauro, M., Förster, A., Norden, B., Kaban, M., Hardebol, N., Bonté, D., Genter, A., Guillou–Frottier, L., Ter Voorde, M., Sokoutis, D., Willingshofer, E., Cornu, T., Worum, G. (2010). Lithosphere tectonics and thermo-mechanical properties: An integrated modelling approach for Enhanced Geothermal Systems exploration in Europe. Earth-Science Reviews 102, 159–206.

Coiffait, B., Ricour, J. (1982). Forages aux Grès du Trias inférieur en Lorraine, analyse des archives disponibles, propositions pour une amélioration de la technologie de réalisation et d'équipement. Bur. Rech. Géol. Min., Serv. Géol. Rég. Lorraine., Vandoeuvre, 22 pp.

Courel, L., Durand, M., Maget, P., Maiaux, C., Ménillet, C., Pareyn, C. (1980). Trias. Mém. Bur. Rech. Géol. Min. 101, 37–74.

Dejonghe, L. (2008). Carte géologique de Wallonie 1/25.000, feuille 55/5-6 Hotton–Dochamps. Notice explicative. Région Wallonne, Namur, 88 pp.

DEKORP Research Group (1991). Results of the DEKORP 1 (BELCORP-DEKORP) deep seismic reflection studies in the western part of the Rhenish Massif. Geophys. J. Int. 106, 203–227.

Demoulin, A., Hallot, E. (2009). Shape and amount of the Quaternary uplift of the western Rhenish shield and the Ardennes (western Europe). Tectonophysics 474, 696–708.

Dèzes, P., Schmid, S.M., Ziegler, P.A. (2004). Evolution of the European Cenozoic Rift System: interaction of the Alpine and Pyrenean orogens with their foreland lithosphere. Tectonophysics 389, 1–33.

Dittrich, D. (1989). Beckenanalyse der Oberen Trias der Trier-Luxemburger Bucht. Revision der stratigraphischen Gliederung und Rekonstruktion der Paläogeographie. Publ. Serv. Géol. Luxemb., vol. 26. Luxembourg, 223 pp.

Dittrich, D. (2008). Schertektonik im triassischen Deckgebirge der nordwestlichen Trierer Bucht – Teil I. Mainzer geowiss. Mitt. 36, 69–104.

Dittrich, D. (2009). Schertektonik im triassischen Deckgebirge der nordwestlichen Trierer Bucht – Teil II. Mainzer geowiss. Mitt. 37, 77–128.

Dittrich, D. (with contributions by Gad, J., Schäfer, P., Weidenfeller, M.) (2011). Geologische Karte der Trierer Bucht 1: 50000 mit Erläuterungen. – Landesamt für Geologie und Bergbau Rheinland-Pfalz, Mainz, 70 pp.

Dittrich, D. (2014). Schertektonik im mesozoischen Deckgebirge der südöstlichen Trier–Luxemburger Bucht – Teil IV. Mainzer geowiss. Mitt. 42, 27–98.

Dittrich, D., Norbisrath, S. (2006). Konglomeratischer „Oberer" Buntsandstein in den

Forschungsbohrungen Roth/Our und Körperich (Südeifel) – stratigraphische Neubewertung und geologisches Umfeld. Mainzer Geowiss. Mitt. 34, 73–112.

Dittrich, D., Himmerkus, J., Kobe, E. (1998). Stratigraphische und sedimentologische Ergebnisse der Forschungsbohrung Dockendorf im Zentrum der Trier-Bitburger Mulde (Oberer Muschelkalk, Keuper, Unterer Lias). Mainzer geowiss. Mitt. 27, 159–212.

Dittrich, D., Klösgen, M., Panknin, A. (2005). Gipskeuper und ardennisch geprägter Schilfsandstein in der Forschungsbohrung Kranzbach/Bollendorf (Südeifel) – Neue Befunde zum Faziesmuster. Mainzer geowiss. Mitt. 33, 245–294.

Everaerts, M. (1997). Réseau gravimétrique à but géodésique du Grand-Duché de Luxembourg et calcul du géoïde local. Observ. Royal de Belgique, Bruxelles, 23 pp.

Everaerts, M. (2002). La gravimétrie au Grand-Duché de Luxembourg. In: Flick, J.A., Stomp, N. (Eds.), Sciences de la Terre au Luxembourg. Musée National d'Histoire Naturelle, Luxembourg, pp. 54–56.

Everaerts, M., De Vos, W. (2012). Gravity acquisition in Belgium and the resulting Bouguer anomaly map, vol. 58. Mem. Geol. Survey of Belgium, Brussels, 67 pp.

Förster, A. (2001). Analysis of borehole temperature data in the Northeast German Basin: continuous logs versus bottom-hole temperatures. Petrol. Geosci. 7, 241–254.

Förster, A., Förster, H.-J. (2000). Crustal composition and mantle heat flow: Implications from surface heat flow and radiogenic heat production in the Variscan Erzgebirge (Germany). J. Geophys. Res. B105, 27917–27938.

Förster, A., Förster, H.-J., Masarweh, R., Masri, A., Tarawneh, K., DESERT Group (2007). The surface heat flow of the Arabian Shield in Jordan. J. Asian Earth Sci 30, 271–284.

Förster, H.-J., Förster, A., Oberhänsli, R., Stromeyer, D. (2010). Lithospheric composition and thermal structure of the Arabian Shield in Jordan. Tectonophysics 481, 29–37.

Fuchs, S., Förster, A. (2010). Rock thermal conductivity of Mesozoic geothermal aquifers in the Northeast German Basin. Chemie der Erde 70 (3), 13–22.

Fuchs, S., Förster, A. (2014). Well-log based prediction of thermal conductivity of sedimentary successions: a case study from the North German Basin. Geophys. J. Int., 196, 291–311.

Fuchs, S., Schütz, F., Förster, H.-J., Förster, A. (2013). Evaluation of common mixing models for calculating bulk thermal conductivity of sedimentary rocks: Correction charts and new conversion equations. Geothermics 47, 40–52.

Fuchs, K., von Gehlen, K., Mälzer, H., Murawski, H., Semmel, A. (Eds.) (1983). Plateau Uplift: The Rhenish Shield – A Case History. Springer, Berlin, Heidelberg, New York, Tokyo, 411 pp.

Furtak, H., 1965. Die Tektonik der underdevonischen Gesteinsfolge im deutsch–belgisch–luxemburgischen Grenzgebiet. Geol. Mitt. 4, 273–332.

Geukens, F. (2008). Carte géologique de Wallonie 1/25.000, feuille 55/3–4 Bra–Lierneux, notice explicative. Région Wallonne, Namur, 40 pp.

GLS (Geologisches Landesamt des Saarlandes) (1981). Geologische Karte des Saarlandes 1:50000. Geologisches Landesamt des Saarlandes, Saarbrücken.

Graulich, J. M. (1980). Le sondage de Grand-Halleux. In: Professional Paper 175, Administration des Mines. Service géologique de Belgique, Brussels, 78 pp.

Häfner, F., Kött, A., Spindeldreher, J., Rein, B., Grubert, A. (2007). Nutzung von oberflächennaher Erdwärme für die Gebäudeheizung in Rheinland-Pfalz. Bericht, Landesamt für Geologie und Bergbau Rheinland-Pfalz, Mainz, 97 pp.

Haenel, R. (1971). Heat flow measurements and a first heat flow map of Germany. Z. Geophys. 37, 975–992.

Haenel, R. (1983). Geothermal investigations in the Rhenish Massif. In: Fuchs, K., von Gehlen, K., Mälzer, H., Murawski, H., Semmel, A. (Eds.), Plateau Uplift: The Rhenish Shield – A Case History. Springer, Berlin, Heidelberg, New York, Tokyo, pp. 228–246.

Hollmann, E.G. (1997). Der variszische Vorlandüberschiebungsgürtel der Ostbelgischen Ardennen – Ein bilanziertes Modell. Aachener Geowiss. Beitr. 25, 235 pp.

Hückel, B., Kappelmeyer, O. (1966). Geothermische Untersuchungen im Saarkarbon. Z. Dt. Geol. Ges. 117 (1), 280–311.

Hurter, S., Haenel (2002). Atlas of Geothermal Resources in Europe. Publ. No. EUR 17811 of the European Commission, Office for Official Publ. of the European Communities, Luxembourg, 91 pp.

Hurtig, E., Čermák, V., Haenel, R. Zui, V. (1992). Geothermal Atlas of Europe, GeoForschungsZentrum Potsdam, Publ. 1. Haack, Gotha.

IEA (International Energy Agency) (2011). Technology Roadmap Geothermal Heat and Power. OECD/IEA, Paris, 45 pp., http://www.iea.org/publications/freepublications/publication/Geothermal_Roadmap.pdf.

Keyser, M., Ritter, J.R.R., Jordan, M. (2002). 3D shear-wave velocity structure of the Eifel plume, Germany. Earth Planet. Sci. Lett. 203, 59–82.

Kind, C.G. (1842). Anleitung zum Abteufen der Bohrlöcher nach den neuesten und bewährtesten Erfahrungen, in's Besondere durch Anwendung der vom Verfasser selbst erfundenen, sich praktisch erwiesenen hölzernen Bohr-Gestänge. Michaelis, Luxemburg, 188 pp.

Konrad, H.J., Wachsmut, W. (1973). Zur Lithologie und Tektonik des Unterdevons im südlichen Oesling Luxemburgs. Publ. Serv. Géol. Luxemb., Bull. 5, 1–20.

Kopp, K.-O. (1955). Die Wittlicher Rotliegend-Senke und ihre tektonische Stellung im Rheinischen Schiefergebirge. Geol. Rundsch. 44, 100–147.

Kramers, L., van Wees, J.-D., Pluymaekers, M.P.D., Kronimus, A., Boxem, T. (2012). Direct heat resource assessment and subsurface information systems for geothermal aquifers; the Dutch perspective. Neth. J. Geosci. 91, 637–649.

Langguth, H.-R., Plum, H. (1984). Untersuchung der Mineral- und Thermalquellen der Eifel auf geothermische Indikationen. Forschungsbericht, BMFT–FB–T 84-019, Technologische Forschung und Entwicklung – Nichtnukleare Energietechnik, Lehr- und Forschungsgebiet für Hydrogeologie der RWTH Aachen, Aachen, 176 pp.

LGB (Landesamt für Geologie und Bergbau Rheinland-Pfalz) (Ed.) (2005). Geologie von Rheinland-Pfalz. Schweizerbart, Stuttgart, 400 pp.

LGB, LUWG (Landesamt für Geologie und Bergbau Rheinland-Pfalz, Landesamt für Umwelt, Wasserwirtschaft und Gewerbeaufsicht Rheinland-Pfalz) (Eds.) (2010). Hydrogeologische Kartierung Bitburg–Trier. Mainz, 134 pp.

Líndal, B. (1973). Industrial and other applications of geothermal energy. In: Geothermal Energy. Review of Research and Development, LC No. 72-97138, UNESCO, Paris, pp. 135–148.

Lotz, B. (2004). Neubewertung des rezenten Wärmestroms im Nordostdeutschen Becken. In: Scientific Technical Report STR 04/04. GeoForschungsZentrum Potsdam, Potsdam, 226 pp.

Lucius, M. (1937). Die Geologie Luxemburgs in ihren Beziehungen zu den benachbarten Gebieten. Publ. Serv. Géol. Luxemb., vol. 1. Luxembourg, 176 pp.

Lucius, M. (1948). Das Gutland. Erläuterungen zu der Geologischen Spezialkarte Luxemburgs. Publ. Serv. Géol. Luxemb., vol. 5. Luxembourg, 330 pp.

Lucius, M. (1950). Das Oesling – Erläuterungen zu der geologischen Spezialkarte Luxemburgs. Publ. Serv. Géol. Luxemb., vol. 6. Luxembourg, 174 pp.

Mälzer, H., Hein, G., Zippelt, K. (1983). Height changes in the Rhenish Massif: Determination and analysis. In: Fuchs, K., von Gehlen, K., Mälzer, H., Murawski, H., Semmel, A. (Eds), Plateau Uplift: The Rhenish Shield – A Case History. Springer, Berlin, Heidelberg, New York, Tokyo, pp. 164–176.

Mechie, J., Prodehl, C., Fuchs, K. (1983). The Long-Range Seismic Refraction Experiment in the Rhenish Massif. In: Fuchs, K., von Gehlen, K., Mälzer, H., Murawski, H., Semmel,

A. (Eds.), Plateau Uplift: The Rhenish Shield – A Case History. Springer, Berlin, Heidelberg, New York, Tokyo, pp. 260–275.

Mégnien, C. (Ed.) (1980). Synthèse géologique du Bassin de Paris. Mém. Bur. Rech. Gèol. Min. 102.

Mengel, K., Sachs, P.M., Stosch, H.G., Wörner, G., Loock, G. (1991). Crustal xenoliths from Cenozoic volcanic fields of West Germany: Implications for structure and composition of the continental crust. Tectonophysics 195, 271–289.

Meyer, W. (1994). Geologie der Eifel, third edition. Schweizerbart (Nägele und Obermiller), Stuttgart, 618 pp.

Meyer, D.E., Nagel J. (2001). 4.20.3 Proterozoikum. In: Hoth, K., Leonhardt, D. (Eds.), Stratigraphie von Deutschland II – Ordovizium, Kambrium, Vendium, Riphäikum – Teil II: Baden-Württemberg, Bayern, Hessen, Rheinland-Pfalz, Nordthüringen, Sachsen-Anhalt, Brandenburg., vol. 234. Cour. Forsch.-Inst. Senckenberg, Frankfurt a.M, pp. 119–120 (Deutsche Stratigraphische Kommission).

Meyer, W., Stets, J. (1980). Zur Paläogeographie von Unter- und Mitteldevon im westlichen und zentralen Rheinischen Schiefergebirge. Z. Dt. Geol. Ges. 131, 725–751.

Meyer, W., Stets, J. (1996). Das Rheintal zwischen Bingen und Bonn. In: Sammlung geol. Führer 89. Borntraeger, Berlin, Stuttgart, 386 pp.

Meyer, W., Stets, J. (2002). Pleistocene to recent tectonics in the Rhenish Massif (Germany). Neth. J. Geosci. 81, 217–221.

Meyer, W., Stets, J. (2007). Quaternary uplift in the Eifel area. In: Ritter, J.R.R., Christensen, U.R. (Eds.) Mantle Plumes. A Multidisciplinary Approach. Springer, Berlin, Heidelberg, pp. 369–376.

Mouterde, R., Tintant, H., Allouc, J., Gabilly, J., Hanzo, M., Lefavrais, A., Rioult, M. (1980). Lias. Mém. Bur. Rech. Géol. Min. 101, 75–123.

Muller, A. (1987). Structures géologiques et répartition des faciès dans les couches méso- et cénozoiques des confins nord-est du Bassin Parisien. In: Cavelier, C., Lorenz, J. (Eds.), Aspect et évolution géologiques du Bassin Parisien. Bull. Inform. Géol. Bass. Paris, Mém. hors sér. 6, 87–103.

Murawski, H., Albers, H.J., Bender, P., Berners, H.-P., Dürr, St., Huckriede, R., Kauffmann, G., Kowalczyk, G., Meiburg, P., Müller, R., Muller, A., Ritzkowski, S., Schwab, K., Semmel, A., Stapf, K., Walter, R., Winter, K.-P., Zankl, H. (1983). Regional tectonic setting and geological structure of the Rhenish Massif. In: Fuchs, K., von Gehlen, K.,

Mälzer, H., Murawski, H., Semmel, A. (Eds.), Plateau Uplift: The Rhenish Shield – A Case History. Springer, Berlin, Heidelberg, New York, Tokyo, pp. 9–38.

Norden, B., Förster, A. (2006). Thermal conductivity and radiogenic heat production of sedimentary and magmatic rocks in the Northeast German Basin. Am. Assoc. Petrol. Geol. 90 (6), 939–962.

Norden, B., Förster, A., Balling, N. (2008). Heat flow and lithospheric thermal regime in the Northeast German Basin. Tectonophysics 460, 215–229.

Oncken, O., von Winterfeld, C., Dittmar, U. (1999). Accretion of a rifted passive margin: The Late Palaeozoic Rhenohercynian fold and thrust belt (Middle European Variscides). Tectonics 18, 75–91.

Oncken, O., Plesch, A., Weber, J., Ricken, W., Schrader, S. (2000). Passive margin detachment during arc-continent collision (Central European Variscides). In: Franke, W., Haak, V., Oncken, O., Tanner, D. (Eds.), Orogenic processes: Quantification and Modelling in the Variscan Belt. Spec. Publ. 179, Geol. Soc., London, pp. 199–216.

Pharaoh, T.C. (1999). Palaeozoic terranes and their lithospheric boundaries within the Trans-European Suture Zone (TESZ): a review. Tectonophysics 314, 17–41.

Pharaoh, T.C., Winchester, J.A., Verniers, J., Lassen, A., Seghedi, A. (2006). The western accretionary margin of the East European Craton: an overview. In: Gee, D.G., Stephenson, R.A. (Eds.), European Lithosphere Dynamics, vol. 32. Mem. Geol. Soc. London, 291–311.

Popov, Y.A., Pribnow, D.F.C., Sass, J.H., Williams, C.F., Burkhardt, H. (1999). Characterization of rock thermal conductivity by high-resolution optical scanning. Geothermics 28, 253–276.

Ritter, J.R.R. (2007). The seismic signature of the Eifel Plume. In: Ritter, J.R.R., Christensen, U.R. (Eds.), Mantle Plumes. A Multidisciplinary Approach. Springer, Berlin, Heidelberg, pp. 379–404.

Rost, H.G.A. (1839). Mittheilung über den Bohrversuch zu Cessingen bei Luxemburg: eine Vergleichung der durchsunkenen Gebirgsschichten mit dem ähnlichen Vorkommen an andern Orten. Henning und Hopf, Erfurt, 32 pp.

Rybach, L. (1976). Radioactive heat production; a physical property determined by the chemistry of rocks. In: Strens, R.G.J. (Ed.), The Physics and Chemistry of Minerals and Rocks. J. Wiley and Sons, London, New York, Sydney, pp. 309–318.

Rybach, L. (1988). Determination of heat production rate. In: R. Haenel, L. Rybach, L. Stegena (Eds.), Handbook of Terrestrial Heat-Flow Density Determination. Kluwer Academic Press, Dordrecht, pp. 125–142.

Schintgen, T., Förster, A. (2013). Geology and basin structure of the Trier–Luxembourg Basin – implications for the existence of a buried Rotliegend graben. Z. Dt. Ges. Geowiss. 164 (4), 615–637.

Schintgen, T., Förster, A., Förster, H.-J., Norden, B. (2015). Surface heat flow and lithosphere thermal structure of the Rhenohercynian Zone in the greater Luxembourg region. Geothermics 56, 93–109.

Schmincke, H.-U. (2007). The Quaternary volcanic fields of the east and west Eifel (Germany). In: Ritter, J.R.R., Christensen, U.R. (Eds.), Mantle Plumes. A Multidisciplinary Approach. Springer, Berlin, Heidelberg, pp. 241–322.

Schütz, F., Norden, B., Förster, A., DESIRE Group (2011). Thermal properties of sediments in southern Israel: a comprehensive data set for heat flow and geothermal energy studies. Basin Res. 23, 1–21.

Schütz, F., Förster, H.-J., Förster, A. (2014). Thermal conditions of the central Sinai Microplate inferred from new surface heat-flow values and continuous borehole temperature logging in central and southern Israel. J. Geodyn. 76, 8–24.

SGL (Service Géologique du Luxembourg) (2015a). Geo_auto. Carte géologique multi-échelles 1 :500'000 à 1 :25'000. WMS Service, http://gis.pch.etat.lu/arcgis/services/geologie/geo_auto/MapServer/WMSServer?

SGL (Service Géologique du Luxembourg) (2015b). Geologie_relief. MNT Luxembourg. WMS Service, http://gis.pch.etat.lu/arcgis/services/geologie/relief/MapServer/WMSServer?

Skiba, P., 2011. Homogene Schwerekarte der Bundesrepublik Deutschland (Bouguer-Anomalien) Technischer Bericht zur Fortführung der Datenbasis, deren Auswertung und Visualisierung, Leibniz-Institut für Angewandte Geophysik, Hannover, 89 pp.

Stets, J. (2004). Geologische Karte der Wittlicher Rotliegend-Senke 1: 50000 mit Erläuterungen. Landesamt für Geologie und Bergbau Rheinland-Pfalz, Mainz, 82 pp.

Stets, J., Schäfer, A. (2002). Depositional environments in the Lower Devonian siliciclastics of the Rhenohercynian Basin (Rheinisches Schiefergebirge, W-Germany) – Case studies and a model. Contr. Sed. Geol. 22, 77 pp.

Stets, J., Schäfer, A. (2011). The Lower Devonian Rhenohercynian rift – 20 Ma of sedimentation and tectonics (Rhenish Massif, W-Germany). Z. Dt. Ges. Geowiss. 162(2), 93–115.

Thierry, J., Cariou, E., Dubois P., Fily, G., Gabilly, J., Laurin, B., Le Roux, J., Lorenz, J., Rioult, M., Yapaudjian, L. (1980). Jurassique Moyen. Mém. Bur. Rech. Géol. Min. 101, 125–190.

USGS (United States Geological Survey) (2015). SRTM topography data, http://dds.cr.usgs.gov/srtm/version2_1/SRTM3/Eurasia/.

Vandenberghe, N. (2002). Belgium. In: Hurter, S., Haenel, R., 2002 (Eds.), Atlas of Geothermal Resources in Europe. Publ. No. EUR 17811 of the European Commission, Office for Official Publ. of the European Communities, Luxembourg, pp. 23–24.

Vasseur, G. (1980). Some aspects of heat flow in France. In: Strub, A.S., Ungemach, P. (Eds.), Advances in European Geothermal Research, Second International Seminar on the Results of EC Geothermal Energy Research. Reidel Publ. Co., Dordrecht, pp. 170–175.

Vuataz, F.-D., Gorhan, H.L., Geissmann, M. (2003). Promotion of geothermal energy in Switzerland: a recent programme for a long-term task. Geothermics 32, 789–797.

Wagner, H.W., Kremb–Wagner, F., Koziol, M., Negendank, J.F.W. (2012). Trier und Umgebung, third ed. Gebr. Bornträger, Stuttgart, 396 pp.

Wagner, B., Dittrich, D. (2010). Profilschnitte A–A′ bis F–F′. In: LGB and LUWG (Landesamt für Geologie und Bergbau Rheinland-Pfalz and Landesamt für Umwelt, Wasserwirtschaft und Gewerbeaufsicht Rheinland-Pfalz) (Eds.), Hydrogeologische Kartierung Bitburg–Trier. LGB and LUWG, Mainz.

Weiler, H. (1972). Ergebnisse von Bohrungen im Buntsandstein im Raume Trier–Bitburg. Mainzer geowiss. Mitt. 1, 198–227.

Wildberger, J. (1992). Zur tektonischen Entwicklung des südwestlichen Hunsrücks (SW-Deutschland). Mitt. Pollichia 79, 5–119.

Ziegler, P.A., Dèzes, P. (2007). Cenozoic uplift of Variscan Massifs in the Alpine foreland: Timing and controlling mechanisms. Global Planet. Change 58, 237–269.

Zitzmann, A., Grünig, S. (with contributions by Meyer, W., Stets, J., Mittmeyer, H.-G., Konrad, H.J., Ribbert, K.-H., Fuchs, G.) (1987). Geologische Übersichtskarte 1:200000, Blatt CC 6302 Trier. BGR (Bundesanstalt für Geowissenschaften und Rohstoffe), Hannover.

8 Appendix

A.1.1 Selected boreholes in Luxembourg

Table A.1.1: Selected boreholes in the Guttland region (Luxembourg).

Region	Borehole reference	Location	Details	LUREF			WGS84		
				x	y		Latitude N	Longitude E	
Liasplateau	TS-208-001	Steinsel	Plateau	75105	83488		49.68592525	6.10029078	
Liasplateau	FR-199-176	Schrassig		85325	75060		49.61014494	6.24180027	
Liasplateau	FR-203-015	Consdorf	Wolper	92970	91837		49.76086778	6.34813620	
Liasplateau	FR-204-201	Consdorf	Rosswinkel	94430	92835		49.76980710	6.36843656	
Liasplateau	FR-197-021	Medernach		82936	96018		49.79859293	6.20890567	
Liasplateau	FR-190-100	Medernach		84975	97050		49.80785652	6.23724114	
Liasplateau	FR-208-131	Consdorf	Millewues	91451	93833		49.77884425	6.32711308	
Liasplateau	FR-208-132	Consdorf	Millewues	91400	93845		49.77895311	6.32640535	
Liasplateau	FR-037-010	Cessange	Cessange	74648	72770	?	49.58955641	6.09410231	?
Liasplateau	FR-041-014	Mondorf	Mondorf Kind	88280	62943		49.50116662	6.28242957	
Liasplateau	FC-113-100	Mondorf	Mondorf Adelaide	88327	63015		49.50181334	6.28307995	
Liasplateau	FR-179-100	Mondorf	Mondorf Lucius	88308	63168		49.50318925	6.28282089	
Liasplateau	FR-172-010	Rebierg		62020	75610		49.61484854	5.91932441	
Liasplateau	FR-207-200	Koerich		63781	82951		49.68090194	5.94338405	
Liasplateau	FRE-1-16	Cloche d'Or		76289	71522		49.57834772	6.11680946	
Liasplateau	FC-190-010	Leudelange		72888	68836		49.55416769	6.06983135	
Liasplateau	FR-206-166	Keispelt		72552	83538		49.68634894	6.06491128	
Liasplateau	FR-206-167	Keispelt		71804	84479		49.69479971	6.05452611	
Liasplateau	FR-206-168	Keispelt		71909	84459		49.69462130	6.05598184	
Liasplateau	FR-209-100	Berchem		77462	67098		49.53857711	6.13305651	
Liasplateau	FR-191-094	Kockelscheuer	Eilbur	75798	67356		49.54088774	6.11006407	
Liasplateau	FR-191-125	Fentange	Weierfeld F5	77993	69311		49.55847634	6.14038187	
Liasplateau	FR-191-112	Schlammeste	Tréiergronn	80545	67080		49.53842001	6.17565106	
Liasplateau	FR-191-113	Schlammeste	Tréiergronn	80303	66321		49.53159595	6.17230690	
Liasplateau	FR-191-114	Schlammeste	Tréiergronn	80139	65724		49.52622832	6.17004110	
Liasplateau	FR-191-012	Mamer	Haebicht	65576	77320		49.63031794	5.96846769	

LUREF – Luxembourg Reference Frame (x,y in meters), SGL – Geological Survey of Luxembourg, AGE – Administration de la Gestion de l'Eau, * – thickness/stratigraphy reinterpreted, ? – thickness/stratigraphy reinterpreted and uncertain, dist. – thickness/stratigraphy disturbed by fault. Longitude and latitude in degrees. Ground level, total depth, thickness and stratigraphical boundaries by reference to mean sea level (national reference) in meters.

Table A.1.1 continued

Borehole reference	Location	Year	Ground level		Total depth	dom1–4	lo6–7+ dou	lo1–5	lm3	lm2		lm1		li4		li3		li2		li1
TS-208-001	Steinsel	2008	346	?	92													> 66.3		21
FR-199-176	Schrassig	1999	345.69		72.5													> 58.9		> 11.3
FR-203-015	Consdorf	2003	390		102											> 19.9		62.2		4.9
FR-204-201	Consdorf	2004	371.15		69.5													> 57.8		6.3
FR-197-021	Medernach	1997	352.23		70													> 61.7		> 8.3
FR-190-100	Medernach	1990	394		116													> 103		> 10
FR-208-131	Consdorf	2008	277.81		20													> 10.05		> 9.95
FR-208-132	Consdorf	2008	279.76		10													> 7.20		> 2.80
FR-037-010	Cessange	1839	272		534.85							> 12.64		39.59		10.15		83.57		20.76
FR-041-014	Mondorf	1846	191.33	?	730															dist.
FC-113-100	Mondorf	1913	190.62	?	589											> 49	?	12		12
FR-179-100	Mondorf	1979	190.15		750															
FR-172-010	Rebierg	1972	398		705				> 81.34	75.36	?	15	?	37.8		10.06		90.19		33.61
FR-207-200	Koerich	2007	261		363.5													> 19		28
FRE-1-16	Cloche d'Or	1986	292.3		148													84		
FC-190-010	Leudelange	1990	306		281					> 119	?	15	?	45	?	10	?	79	*	> 7
FR-206-166	Keispelt	2006	381		119											> 8		83		24
FR-206-167	Keispelt	2006	372.51		117											> 7.65		85		23.35
FR-206-168	Keispelt	2006	371.17		124											> 7.25		85.75		27.7
FR-209-100	Berchem	2009	266		202					> 49		15		42		18		74		> 4
FR-191-094	Kockelscheuer	1991	270.6		151.5					> 73		13.2		48.8		11.2		> 5.3		
FR-191-125	Fentange	1991	275.9		130					> 49		11.5		54.3	?	8.4	?	> 6.8		
FR-191-112	Schlammeste	1991	265.1		77.4					> 13.7		5.3		34.5		14.6		> 9.3		
FR-191-113	Schlammeste	1991	271		41					> 27.7		3.5		> 9.8						
FR-191-114	Schlammeste	1991	265.2		40					> 37		> 3								
FR-191-012	Mamer	1991	314.5		100					> 36.4	*	13.7	*	33.7	*	9.2		> 5.6		

Table A.1.1 continued

Borehole reference	Location	li1–3	ko2	ko1	ko	km3	km2	km2S	km2 tot	km1	km	ku	k
TS-208-001	Steinsel	> 87.3											
FR-199-176	Schrassig	> 70.2											
FR-203-015	Consdorf	> 92.5	9.5	> 0	> 9.5								
FR-204-201	Consdorf	> 64.1			0.5								
FR-197-021	Medernach	> 70											
FR-190-100	Medernach	> 113											
FR-208-131	Consdorf												
FR-208-132	Consdorf												
FR-037-010	Cessange	114.48	2.35	1.59	3.94	68	26.02	0	26.02	105.22	199.24	17.08	220.26
FR-041-014	Mondorf	dist.	dist.			74.88	24.86 *	5 *	29.86	101.28	206.02	15.87	> 234.5
FC-113-100	Mondorf	> 74	4	13	17	dist.	dist.	dist.	dist.	dist.	dist.		
FR-179-100	Mondorf					dist.	dist.	dist.	dist.	dist.	dist.		
FR-172-010	Rebierg	133.86	5.69	2.45	8.14	60.3 *	22.87 *	7.08 *	29.95 *	108.9 *	199.15	16.75	224.04
FR-207-200	Koerich	> 47	3	7	10	52	17	0	17	85	154	16	180
FRE-1-16	Cloche d'Or												
FC-190-010	Leudelange	> 106											
FR-206-166	Keispelt	> 115	> 2		> 2								
FR-206-167	Keispelt	> 116	> 1		> 1								
FR-206-168	Keispelt	> 120.7	> 1		> 1								
FR-209-100	Berchem	> 96											
FR-191-094	Kockelscheuer	> 16.5											
FR-191-125	Fentange	> 15.2											
FR-191-112	Schlammeste	> 23.9											
FR-191-113	Schlammeste												
FR-191-114	Schlammeste												
FR-191-012	Mamer	> 14.8											

Table A.1.1 continued

Borehole reference	Location	mo	mm	mu	m	so	sm	s	r
TS-208-001	Steinsel								
FR-199-176	Schrassig								
FR-203-015	Consdorf								
FR-204-201	Consdorf								
FR-197-021	Medernach								
FR-190-100	Medernach								
FR-208-131	Consdorf								
FR-208-132	Consdorf								
FR-037-010	Cessange	38.88	91	> 17.95	> 147.83				
FR-041-014	Mondorf	54	83	36	173	64	179	243	7.6
FC-113-100	Mondorf								
FR-179-100	Mondorf								
FR-172-010	Rebierg	17.6	45	10.67	? 73.27	53.33	0	53.33	0
FR-207-200	Koerich	18	50	13	81	> 55.5	0	> 55.5	0
FRE-1-16	Cloche d'Or								
FC-190-010	Leudelange								
FR-206-166	Keispelt								
FR-206-167	Keispelt								
FR-206-168	Keispelt								
FR-209-100	Berchem								
FR-191-094	Kockelscheuer								
FR-191-125	Fentange								
FR-191-112	Schlammeste								
FR-191-113	Schlammeste								
FR-191-114	Schlammeste								
FR-191-012	Mamer								

Table A.1.1 continued

Borehole reference	Location	Top dom4	Top dou	Top lo5	Top lm3	Top lm2	Top lm1	Top li4	Top li3	Top li2	Top li1	Top ko2	Top ko1	Top km3
TS-208-001	Steinsel										276	255		
FR-199-176	Schrassig										284.49			
FR-203-015	Consdorf									364.6	302.4	297.5		
FR-204-201	Consdorf										309.85			
FR-197-021	Medernach										290.53			
FR-190-100	Medernach										288			
FR-208-131	Consdorf										267.76			
FR-208-132	Consdorf										272.56			
FR-037-010	Cessange							259.36	219.77	209.62	126.05	105.24	102.89	101.3
FR-041-014	Mondorf													137.22
FC-113-100	Mondorf									141.62	129.62	117.62	113.62	100.62
FR-179-100	Mondorf													
FR-172-010	Rebierg					316.66	241.30 ?	226.30 ?	188.5	178.44	88.25	54.64	48.95	46.5
FR-207-200	Koerich										242	214	211	204
FRE-1-16	Cloche d'Or									240	156			
FC-190-010	Leudelange						181 ?	166 ?	121 ?	111 ?	32			
FR-206-166	Keispelt									371	288	264		
FR-206-167	Keispelt									364.86	279.86	256.51		
FR-206-168	Keispelt									361.62	275.87	248.17		
FR-209-100	Berchem						217	202	160	142	68			
FR-191-094	Kockelscheuer						197.6	184.4	135.6	124.4				
FR-191-125	Fentange						226.9	215.4	161.1 ?	152.7				
FR-191-112	Schlammeste						251.4	246.1	211.6	197				
FR-191-113	Schlammeste						243.3	239.8						
FR-191-114	Schlammeste						228.2							
FR-191-012	Mamer						278.1 *	264.4 *	230.7 *	221.5				

Table A.1.1 continued

Borehole reference	Location	Top km2	Top km2S	Top km1	Top km	Top ku	Top k	Top mo	Top mm	Top mu	Top m
TS-208-001	Steinsel										
FR-199-176	Schrassig										
FR-203-015	Consdorf										
FR-204-201	Consdorf										
FR-197-021	Medernach										
FR-190-100	Medernach										
FR-208-131	Consdorf										
FR-208-132	Consdorf										
FR-037-010	Cessange	33.3		7.28	101.3	−97.94	105.24	−115.02	−153.9	−244.9	−115.02
FR-041-014	Mondorf	62.34	37.48 *	32.48	137.22	−68.8	105.24	−84.67	−138.67	−221.67	−84.67
FC-113-100	Mondorf										
FR-179-100	Mondorf										
FR-172-010	Rebierg	−13.8 *	−36.67 *	−43.75 *	46.5	−152.65	54.64	−169.4	−187	−232.00 ?	−169.4
FR-207-200	Koerich	152		135	204	50	214	34	16	−34	34
FRE-1-16	Cloche d'Or										
FC-190-010	Leudelange										
FR-206-166	Keispelt										
FR-206-167	Keispelt										
FR-206-168	Keispelt										
FR-209-100	Berchem										
FR-191-094	Kockelscheuer										
FR-191-125	Fentange										
FR-191-112	Schlammeste										
FR-191-113	Schlammeste										
FR-191-114	Schlammeste										
FR-191-012	Mamer										

Table A.1.1 continued

Borehole reference	Location	Top so	Top sm	Top s	Top r	Top Dev	Source
TS-208-001	Steinsel						AGE
FR-199-176	Schrassig						SGL
FR-203-015	Consdorf						SGL
FR-204-201	Consdorf						SGL
FR-197-021	Medernach						SGL
FR-190-100	Medernach						SGL
FR-208-131	Consdorf						SGL
FR-208-132	Consdorf						SGL
FR-037-010	Cessange	< 262.9		< 262.9			Lucius (1948); Kind (1842)
FR-041-014	Mondorf	–257.67	–321.67	–257.67	–500.67	–508.27	Planche I Lucius (1948)
FC-113-100	Mondorf						SGL
FR-179-100	Mondorf						SGL
FR-172-010	Rebierg	–242.67		–242.67		–296	SGL
FR-207-200	Koerich	–47				< –102.5	SGL
FRE-1-16	Cloche d'Or						AGE
FC-190-010	Leudelange						SGL
FR-206-166	Keispelt						AGE
FR-206-167	Keispelt						AGE
FR-206-168	Keispelt						AGE
FR-209-100	Berchem						AGE
FR-191-094	Kockelscheuer						SGL
FR-191-125	Fentange						SGL
FR-191-112	Schlammeste						SGL
FR-191-113	Schlammeste						SGL
FR-191-114	Schlammeste						SGL
FR-191-012	Mamer						SGL

Table A.1.1 continued

Region	Borehole reference	Location	Details	LUREF		WGS84	
				x	y	Latitude N	Longitude E
Liasplateau	FC-191-064	Trois-Ponts		63539	78272	49.63882543	5.94023221
Liasplateau	FC-191-061	Trois-Ponts		63249	78508	49.64093933	5.93620736
Liasplateau	FC-191-063	Trois-Ponts		62687	78712	49.64275768	5.92841763
Liasplateau	FC-191-062	Trois-Ponts		62922	78590	49.64166746	5.93167656
Liasplateau	FR-189-044	Schaedhaff		81317	73333	49.59463990	6.18633885
Liasplateau	FR-189-043	Schaedhaff		81584	73552	49.59660826	6.19003285
Liasplateau	FR-189-042	Schaedhaff		81852	73772	49.59858550	6.19374099
Liasplateau	FR-189-041	Schaedhaff		81972	73848	49.59926842	6.19540133
Liasplateau	FR-208-702	Geyershof		96050	92294	49.76490191	6.39090215
Liasplateau	FR-205-051	Brouch		71019	89920	49.74370518	6.04352028
Liasplateau	FR-205-053	Brouch		72000	90021	49.74462761	6.05713189
Liasplateau	FR-208-006	Kirchberg		78533	76316	49.62146001	6.14782052
Alzette	FR-165-504	Gousselerbierg	Rte du Nord	75827	87425	49.72132560	6.11025768
Alzette	FR-165-505	Gousselerbierg	Rte du Nord	75679	87713	49.72391591	6.10819906
Alzette	FR-165-506	Gousselerbierg	Rte du Nord	75508	86901	49.71661151	6.10582983
Alzette	FR-195-112	Luxbg.–Lorentzweiler	Rte du Nord; Tronçon Luxembourg–Lorentzweiler	79436	82782	49.67959467	6.16030451
Alzette	FR-195-113	Luxbg.–Lorentzweiler	Rte du Nord; Tronçon Luxembourg–Lorentzweiler	79602	83846	49.68916145	6.16260977
Alzette	FR-195-115	Luxbg.–Lorentzweiler	Rte du Nord; Tronçon Luxembourg–Lorentzweiler	79473	84988	49.69942624	6.16081789
Alzette	FR-195-114	Luxbg.–Lorentzweiler	Rte du Nord; Tronçon Luxembourg–Lorentzweiler	79481	84399	49.69413242	6.16092808
Alzette	FR-198-007	Gousselerbierg	Rte du Nord; Tunnel Gousselerbierg	75799	87011	49.71760330	6.10987529
Alzette	FR-198-008	Gousselerbierg	Rte du Nord; Tunnel Gousselerbierg	75763	87256	49.71980616	6.10937195
Alzette	FR-201-222	Lorentzweiler	Rte du Nord; Tunnel Grouft	79723	84437	49.69448131	6.16427899
Alzette	FR-204-031	Lorentzweiler	Rte du Nord; Viaduc Lorentzweiler	78831	85636	49.70525597	6.15191836
Alzette	FR-204-032	Lorentzweiler	Rte du Nord; Tunnel Grouft	79452	84733	49.69713805	6.16052850
Alzette	FR-192-107	Stafelter	Rte du Nord	80430	80433	49.65847359	6.17407622
Alzette	FR-199-017	Gousselerbierg	Rte du Nord	75950	86677	49.71460605	6.11197145
Basse Sûre	FR-039-011	Echternach	Echternach Felsmühle	96837 ?	98306 ?	49.81893204 ?	6.40208696 ?
Basse Sûre	TS-165-005	Rosport	Rosport FC5	103545	97537	49.81179198	6.49525064
Basse Sûre	TS-165-001	Rosport	Rosport FC1	103455	97494	49.81140892	6.49399763
Basse Sûre	TS-165-002	Rosport	Rosport FC2	103599	97561	49.81200563	6.49600234

Table A.1.1 continued

Borehole reference	Location	Year	Ground level		Total depth	dom1–4	lo6–7+ dou	lo1–5	lm3	lm2		lm1		li4		li3	li2		li1	
FC-191-064	Trois-Ponts	1991	311.25		154					> 15	?	17	?	40	?	9	> 66			
FC-191-061	Trois-Ponts	1991	307.2		133.5									45	?	6	> 75			
FC-191-063	Trois-Ponts	1991	319.7		121.3									> 30		9	> 63			
FC-191-062	Trois-Ponts	1991	308.59		121									> 38		9	> 55			
FR-189-044	Schaedhaff	1989	284.01		139							> 15	?	45	?	14	> 65			
FR-189-043	Schaedhaff	1989	291.1		127							> 5	*	49	?	14	> 59			
FR-189-042	Schaedhaff	1989	289.69		125.3							> 6	*	49	?	11	> 59.3			
FR-189-041	Schaedhaff	1989	300.75		130							> 5	*	47	?	11	> 67			
FR-208-702	Geyershof	2008	322.43		38												> 27.6		1.1	
FR-205-051	Brouch	2005	330.86		35.5												> 30		> 5.5	
FR-205-053	Brouch	2005	371.89		79												> 71		> 8	
FR-208-006	Kirchberg	2008	329.5		150												> 84.5	*	14	*
FR-165-504	Gousselerbierg	1965	346.57		72												> 50.3		16.1	
FR-165-505	Gousselerbierg	1965	348.95		73.2												> 50.5		18.3	
FR-165-506	Gousselerbierg	1965	372.98		112												> 87		16.3	
FR-195-112	Luxbg.-Lorentzweiler	1995	385.28		83.5												> 46.8		12.6	
FR-195-113	Luxbg.-Lorentzweiler	1995	394.8		95												> 50.9		12.2	
FR-195-115	Luxbg.-Lorentzweiler	1995	406.1		115.5												> 51.5		11.9	
FR-195-114	Luxbg.-Lorentzweiler	1995	410.4		115.5												> 60.1		12.4	
FR-198-007	Gousselerbierg	1998	314.22		80												> 28.7		15.9	
FR-198-008	Gousselerbierg	1998	340.38		115												> 47.1		15.6	
FR-201-222	Lorentzweiler	2001	380.92		90												> 31.25		13.75	
FR-204-031	Lorentzweiler	2004	333.05		60												> 8.2		13.5	
FR-204-032	Lorentzweiler	2004	426.42		106												> 76		13.5	
FR-192-107	Stafelter	1992	407		105												> 45		25.4	
FR-199-017	Gousselerbierg	1999	287.76		60												> 9		17	
FR-039-011	Echternach	1840	171	?	235															
TS-165-005	Rosport	1965	160.5		64															
TS-165-001	Rosport	1965	156.7		70															
TS-165-002	Rosport	1965	160.1		70.6															

Table A.1.1 continued

Borehole reference	Location	li1–3	ko2	ko1	ko	km3	km2	km2S	km2 tot	km1	km	ku	k
FC-191-064	Trois-Ponts	> 75											
FC-191-061	Trois-Ponts	> 81											
FC-191-063	Trois-Ponts	> 72											
FC-191-062	Trois-Ponts	> 64											
FR-189-044	Schaedhaff	> 79											
FR-189-043	Schaedhaff	> 73											
FR-189-042	Schaedhaff	> 70.3											
FR-189-041	Schaedhaff	> 78											
FR-208-702	Geyershof	> 28.7			3.95	> 1.35							
FR-205-051	Brouch	> 35.5											
FR-205-053	Brouch	> 79											
FR-208-006	Kirchberg	> 98.5	0	3.7	3.7	> 49.8							
FR-165-504	Gousselerbierg	> 66.4	1.8	3.3	5.1	> 0.50							
FR-165-505	Gousselerbierg	> 68.8	1.35	> 3.05	> 4.40								
FR-165-506	Gousselerbierg	> 103.3	1.9	> 3.8	> 5.7								
FR-195-112	Luxbg.-Lorentzweiler	> 59.4	1.8	2	3.8	> 17.7							
FR-195-113	Luxbg.-Lorentzweiler	> 63.1	3.3	1	4.3	> 25.5							
FR-195-115	Luxbg.-Lorentzweiler	> 63.4	5.4	1.8	7.2	> 41.3							
FR-195-114	Luxbg.-Lorentzweiler	> 72.5	3.8	0.7	4.5	> 34.8							
FR-198-007	Gousselerbierg	> 44.6	2.45	3.15	5.6	> 29.8							
FR-198-008	Gousselerbierg	> 62.7	2.3	3.1	5.4	> 46.4							
FR-201-222	Lorentzweiler	> 45	2.4	0.7	3.1	> 41.9							
FR-204-031	Lorentzweiler	> 21.7	4.5	3.75	8.25	> 28.25							
FR-204-032	Lorentzweiler	> 89.5	3.7	1.25	4.95	> 11.55							
FR-192-107	Stafelter	> 70.4	3.3	0.5	3.8	> 26.8							
FR-199-017	Gousselerbierg	> 26	< 3.5	> 0	3.5	> 30.5							
FR-039-011	Echternach								> 34.13	34.87	> 69	18.4	> 87.4
TS-165-005	Rosport												
TS-165-001	Rosport												
TS-165-002	Rosport												

Table A.1.1 continued

Borehole reference	Location	mo	mm	mu	m	so	sm	s	r
FC-191-064	Trois-Ponts								
FC-191-061	Trois-Ponts								
FC-191-063	Trois-Ponts								
FC-191-062	Trois-Ponts								
FR-189-044	Schaedhaff								
FR-189-043	Schaedhaff								
FR-189-042	Schaedhaff								
FR-189-041	Schaedhaff								
FR-208-702	Geyershof								
FR-205-051	Brouch								
FR-205-053	Brouch								
FR-208-006	Kirchberg								
FR-165-504	Gousselerbierg								
FR-165-505	Gousselerbierg								
FR-165-506	Gousselerbierg								
FR-195-112	Luxbg.-Lorentzweiler								
FR-195-113	Luxbg.-Lorentzweiler								
FR-195-115	Luxbg.-Lorentzweiler								
FR-195-114	Luxbg.-Lorentzweiler								
FR-198-007	Gousselerbierg								
FR-198-008	Gousselerbierg								
FR-201-222	Lorentzweiler								
FR-204-031	Lorentzweiler								
FR-204-032	Lorentzweiler								
FR-192-107	Stafelter								
FR-199-017	Gousselerbierg								
FR-039-011	Echternach	56.19	> 91.41		> 147.6				
TS-165-005	Rosport					> 46.5		> 46.5	
TS-165-001	Rosport					> 52		> 52	
TS-165-002	Rosport		> 56.2	> 14.4	> 70.6				

Table A.1.1 continued

Borehole reference	Location	Top dom4	Top dou	Top lo5	Top lm3	Top lm2	Top lm1	Top li4	Top li3	Top li2	Top li1	Top ko2	Top ko1	Top km3
FC-191-064	Trois-Ponts						296.25 ?	279.25 ?	239.25	230.25	< 164.25			
FC-191-061	Trois-Ponts								262.2	256.2	< 181.2			
FC-191-063	Trois-Ponts								289.7	280.7	< 217.7			
FC-191-062	Trois-Ponts								270.59	261.59	< 206.59			
FR-189-044	Schaedhaff							269.01 ?	229.01	215.01	< 150.01			
FR-189-043	Schaedhaff							286.1 ?	237.1	223.1	< 164.1			
FR-189-042	Schaedhaff							283.69 ?	234.69	223.69	< 164.39			
FR-189-041	Schaedhaff							295.75 ?	248.75	237.75	< 170.75			
FR-208-702	Geyershof										290.83			285.78
FR-205-051	Brouch										300.86			
FR-205-053	Brouch										300.89			
FR-208-006	Kirchberg										245 *	231		227.3
FR-165-504	Gousselerbierg										296.27	280.17	278.37	275.07
FR-165-505	Gousselerbierg										298.45	280.15	278.8	< 275.75
FR-165-506	Gousselerbierg										282.98	266.68	264.78	< 260.98
FR-195-112	Luxbg.-Lorentzweiler										335.88	323.28	321.48	319.48
FR-195-113	Luxbg.-Lorentzweiler										341.8	329.6	326.3	325.3
FR-195-115	Luxbg.-Lorentzweiler										351	339.1	333.7	331.9
FR-195-114	Luxbg.-Lorentzweiler										346.6	334.2	330.4	329.7
FR-198-007	Gousselerbierg										285.52	269.62	267.17	264.02
FR-198-008	Gousselerbierg										293.28	277.68	275.38	272.28
FR-201-222	Lorentzweiler										349.67	335.92	333.52	332.82
FR-204-031	Lorentzweiler										323.05	309.55	305.05	301.3
FR-204-032	Lorentzweiler										350.42	336.92	333.22	331.97
FR-192-107	Stafelter										358	332.6	329.3	328.8
FR-199-017	Gousselerbierg										278.76	261.76	> 258.26	258.26
FR-039-011	Echternach													
TS-165-005	Rosport													
TS-165-001	Rosport													
TS-165-002	Rosport													

Table A.1.1 continued

Borehole reference	Location	Top km2	Top km2S	Top km1	Top km	Top ku	Top k	Top mo	Top mm	Top mu	Top m
FC-191-064	Trois-Ponts										
FC-191-061	Trois-Ponts										
FC-191-063	Trois-Ponts										
FC-191-062	Trois-Ponts										
FR-189-044	Schaedhaff										
FR-189-043	Schaedhaff										
FR-189-042	Schaedhaff										
FR-189-041	Schaedhaff										
FR-208-702	Geyershof										
FR-205-051	Brouch										
FR-205-053	Brouch										
FR-208-006	Kirchberg	< 177.5			227.3						
FR-165-504	Gousselerbierg										
FR-165-505	Gousselerbierg										
FR-165-506	Gousselerbierg										
FR-195-112	Luxbg.-Lorentzweiler										
FR-195-113	Luxbg.-Lorentzweiler										
FR-195-115	Luxbg.-Lorentzweiler										
FR-195-114	Luxbg.-Lorentzweiler										
FR-198-007	Gousselerbierg										
FR-198-008	Gousselerbierg										
FR-201-222	Lorentzweiler										
FR-204-031	Lorentzweiler										
FR-204-032	Lorentzweiler										
FR-192-107	Stafelter										
FR-199-017	Gousselerbierg										
FR-039-011	Echternach			136.87		102		83.6	27.41	< –64	83.6
TS-165-005	Rosport										
TS-165-001	Rosport										
TS-165-002	Rosport									103.9	

Table A.1.1 continued

Borehole reference	Location	Top so	Top sm	Top s	Top r	Top Dev	Source
FC-191-064	Trois-Ponts						SGL
FC-191-061	Trois-Ponts						SGL
FC-191-063	Trois-Ponts						SGL
FC-191-062	Trois-Ponts						SGL
FR-189-044	Schaedhaff						SGL
FR-189-043	Schaedhaff						SGL
FR-189-042	Schaedhaff						SGL
FR-189-041	Schaedhaff						SGL
FR-208-702	Geyershof						SGL
FR-205-051	Brouch						SGL
FR-205-053	Brouch						SGL
FR-208-006	Kirchberg						SGL
FR-165-504	Gousselerbierg						SGL
FR-165-505	Gousselerbierg						SGL
FR-165-506	Gousselerbierg						SGL
FR-195-112	Luxbg.-Lorentzweiler						SGL
FR-195-113	Luxbg.-Lorentzweiler						SGL
FR-195-115	Luxbg.-Lorentzweiler						SGL
FR-195-114	Luxbg.-Lorentzweiler						SGL
FR-198-007	Gousselerbierg						SGL
FR-198-008	Gousselerbierg						SGL
FR-201-222	Lorentzweiler						SGL
FR-204-031	Lorentzweiler						SGL
FR-204-032	Lorentzweiler						SGL
FR-192-107	Stafelter						SGL
FR-199-017	Gousselerbierg						SGL
FR-039-011	Echternach						Lucius (1948)
TS-165-005	Rosport						SGL
TS-165-001	Rosport						SGL
TS-165-002	Rosport						SGL

Table A.1.1 continued

Region	Borehole reference	Location	Details	LUREF		WGS84	
				x	y	Latitude N	Longitude E
Basse Sûre	TS-193-001	Rosport	Rosport BB1 Viva	103976	97290	49.80955422	6.50122338
Basse Sûre	TS-155-001	Rosport	Rosport B 0	103532	97565	49.81204423	6.49507173
Basse Sûre	TS-136-001	Echternach	Echternach Kreuzkapelle	98985	97164	49.80860047	6.43187843
Moselle–Syre	FR-177-100	Waldbredimus	Communes Waldbredimus et Dalheim; PZ1	89280	69300	49.55830850	6.29638543
Moselle–Syre	FR-195-100	Waldbredimus	Waldbredimus PZ2; FRE-138-05	89400	69270	49.55803690	6.29804329
Moselle–Syre	TS-199-001	Scheuerhof	Canach Scheuerhof (Golfplatz); Bohrung F2; Forage 2?	90385	73220	49.59353527	6.31176220
Moselle–Syre	FR-190-060	Scheuerhof	Golfplatz Canach; Forage 1	90220	73340	49.59461701	6.30948315
Moselle–Syre	FR-195-705	Markusbierg	Tunnel Markusbierg; FCV95-5	93007	60426	49.47845343	6.34760779
Moselle–Syre	FR-195-704	Markusbierg	Tunnel Markusbierg; FCV95-4	93341	60365	49.47789465	6.35220752
Moselle–Syre	TS-040-001	Besch-sous-Perl	Besch-sous-Perl 1840 F1	94884 ?	63719 ?	49.50801703 ?	6.37362940 ?
Moselle–Syre	FR-041-013	Besch-sous-Perl	Besch-sous-Perl 1840-1841 F2	94818 ?	63143 ?	49.50283977 ?	6.37269644 ?
Moselle–Syre	FR-196-900	Mertert	Bétons Feidt, port de Mertert; FCV1 11.96 ???	101995	84983	49.69898237	6.47300546
Moselle–Syre	FR-206-100	Boursdorf	Mompach-Boursdorf (AGE); FRE-116-20	102622	92782	49.76907734	6.48214978
Moselle–Syre	FR-198-100	Beyren	SIDERE Beyren; Piézomètre Sauerwis (AGE); FRE-123-13	91846	77884	49.63544210	6.33211129
Moselle–Syre	FR-196-001	Beyren	Piézomètre Doutboesch (AGE); FRE-123-14	90834	78255	49.63879683	6.31811219
Moselle–Syre	FC-199-200	Beyren	Forage-Captage Doutboesch (AGE); FCS-123-16	91730	78195	49.63824055	6.33051481
Moselle–Syre	FC-169-200	Wintrange	SESE Wintrange (F I); Wintrange I	94034	62926	49.50090741	6.36186495
Moselle–Syre	FR-171-199	Wintrange	FR;Forage de reconnaissance	94370	62912	49.50077364	6.36650300
Moselle–Syre	FC-176-200	Schwebsange	Schwebsange 1976 1FR (100 m) + 1 FC (135 m)	94120	64180	49.51218026	6.36309720
Moselle–Syre	FR-197-161	Wintrange	FR97-1 W (Wintrange)	94315	62044	49.49297065	6.36571215
Moselle–Syre	FR-197-162	Schengen	FR97-2 S (Schengen)	94325	60450	49.47863854	6.36579222
Moselle–Syre	TS-198-001	Wintrange	Greissen I (Wintrange)	94370	62571	49.49770767	6.36649056
Moselle–Syre	TS-198-002	Wintrange	Greissen II (Wintrange)	94353	62412	49.49627849	6.36625008
Moselle–Syre	TS-192-001	Wasserbillig	Dolomithartsteinwerk Wasserbillig; Bohrung Vormann	102385	87045	49.71750682	6.47852976
Moselle–Syre	TS-166-001	Wormeldange	Caves Coopératives de Wormeldange	97461 ?	75564 ?	49.61444644 ?	6.40973745 ?
Moselle–Syre	FR-178-002	Machtum	F2; Aménagement des vignobles à Machtum	99479	79996	49.65423208	6.43788171
Moselle–Syre	FR-178-006	Machtum	F6; Aménagement des vignobles à Machtum	99365	79728	49.65182622	6.43628970

Table A.1.1 continued

Borehole reference	Location	Year	Ground level		Total depth	dom1–4	lo6–7+ dou	lo1–5	lm3	lm2	lm1	li4	li3	li2	li1
TS-193-001	Rosport	1993	164		45										
TS-155-001	Rosport	1955	160		67										
TS-136-001	Echternach	1936	175		221										
FR-177-100	Waldbredimus	1977	179	?	130.4										
FR-195-100	Waldbredimus	1995	174.74	?	70										
TS-199-001	Scheuerhof	1999	259		148										
FR-190-060	Scheuerhof	1990	271		162										
FR-195-705	Markusbierg	1995	278.03		70										> 10.1
FR-195-704	Markusbierg	1995	248.48		55										
TS-040-001	Besch-sous-Perl	1840	153	?	166										
FR-041-013	Besch-sous-Perl	1841	153	?	290										
FR-196-900	Mertert	1996	148		83										
FR-206-100	Boursdorf	2006	285		62.1										
FR-198-100	Beyren	1998	288.4		94										
FR-196-001	Beyren	1996	289.4		86										
FC-199-200	Beyren	1999	294.1	?	127										
FC-169-200	Wintrange	1969	145		169.1										
FR-171-199	Wintrange	1971	143		42										
FC-176-200	Schwebsange	1976	142		135										
FR-197-161	Wintrange	1997	145		78										
FR-197-162	Schengen	1997	147		78										
TS-198-001	Wintrange	1998	142.5		85.5										
TS-198-002	Wintrange	1998	143.8		70.5										
TS-192-001	Wasserbillig	1992	238.4		160										
TS-166-001	Wormeldange	1966	154		121.5										
FR-178-002	Machtum	1978	182		51										
FR-178-006	Machtum	1978	179		62										

Table A.1.1 continued

Borehole reference	Location	li1–3	ko2	ko1	ko	km3	km2	km2S	km2 tot	km1	km	ku	k
TS-193-001	Rosport												
TS-155-001	Rosport												
TS-136-001	Echternach												
FR-177-100	Waldbredimus									> 54.2	> 54.2	15	69.2
FR-195-100	Waldbredimus									> 39.3	> 39.3	16.1	> 55.4
TS-199-001	Scheuerhof							> 3	> 3	67	> 70	15?	> 81
FR-190-060	Scheuerhof							> 10.5	> 10.5	80.5	> 91	15?	> 102
FR-195-705	Markusbierg	> 10.1	8	8.8	16.8	> 43.1							
FR-195-704	Markusbierg				> 6.90	> 44.1							
TS-040-001	Besch-sous-Perl											> 13.64	> 13.64
FR-041-013	Besch-sous-Perl											> 16.89	> 16.89
FR-196-900	Mertert									> 59.4	> 59.4	19.6	> 79
FR-206-100	Boursdorf												
FR-198-100	Beyren									> 38	> 38	19.5	> 57.5
FR-196-001	Beyren									> 59.4	> 59.4	19.6	> 79
FC-199-200	Beyren									> 53.2	> 53.2	19.6	> 72.8
FC-169-200	Wintrange					> 22	* 20	* 0	20	* 80	* > 122	13.6	> 135.6
FR-171-199	Wintrange									> 18.9	> 18.9	13.1	> 32
FC-176-200	Schwebsange									> 69.9	> 69.9	13	* > 82.9
FR-197-161	Wintrange									> 16.8	> 16.8	20.2	> 37
FR-197-162	Schengen												
TS-198-001	Wintrange												
TS-198-002	Wintrange												
TS-192-001	Wasserbillig									> 46.2	> 46.2	25.25	81.55
TS-166-001	Wormeldange												
FR-178-002	Machtum												
FR-178-006	Machtum												

Table A.1.1 continued

Borehole reference	Location	mo		mm	mu	m	so	sm	s	r
TS-193-001	Rosport			> 32.5	> 12.5	> 45				
TS-155-001	Rosport				> 46.7	> 46.7	> 20.3		> 20.3	
TS-136-001	Echternach	> 50		100	50	> 200	> 21			
FR-177-100	Waldbredimus	> 61.2	?			> 61.2				
FR-195-100	Waldbredimus	> 14.6				> 14.6				
TS-199-001	Scheuerhof	59	?	> 4		> 63				
FR-190-060	Scheuerhof	> 56	?			> 56				
FR-195-705	Markusbierg									
FR-195-704	Markusbierg									
TS-040-001	Besch-sous-Perl	56.84		82.17	> 11.69	> 150.70				
FR-041-013	Besch-sous-Perl	56.84		83.15	31.83	171.82	51.97	> 43.85	> 95.82	
FR-196-900	Mertert									
FR-206-100	Boursdorf	> 51		> 11.1		> 62.1				
FR-198-100	Beyren	> 36.5				> 36.5				
FR-196-001	Beyren	> 7				> 7				
FC-199-200	Beyren	> 54.2				> 54.2				
FC-169-200	Wintrange	> 33.5				> 33.5				
FR-171-199	Wintrange	> 10				> 10				
FC-176-200	Schwebsange	> 52				> 52				
FR-197-161	Wintrange	> 41								
FR-197-162	Schengen	> 46.5		> 31.5		> 78				
TS-198-001	Wintrange	> 49.5				> 49.5				
TS-198-002	Wintrange	> 34.5				> 34.5				
TS-192-001	Wasserbillig	54.95		> 23.5		> 78.45				
TS-166-001	Wormeldange			> 32	50	> 82	> 39.5		> 39.5	
FR-178-002	Machtum			> 39.3	> 11.7	> 51				
FR-178-006	Machtum			> 41.75	> 20.25	> 62				

Table A.1.1 continued

Borehole reference	Location	Top dom4	Top dou	Top lo5	Top lm3	Top lm2	Top lm1	Top li4	Top li3	Top li2	Top li1	Top ko2	Top ko1	Top km3
TS-193-001	Rosport													
TS-155-001	Rosport													
TS-136-001	Echternach													
FR-177-100	Waldbredimus													
FR-195-100	Waldbredimus													
TS-199-001	Scheuerhof													
FR-190-060	Scheuerhof													
FR-195-705	Markusbierg											267.93	259.93	251.13
FR-195-704	Markusbierg													237.58
TS-040-001	Besch-sous-Perl													
FR-041-013	Besch-sous-Perl													
FR-196-900	Mertert													
FR-206-100	Boursdorf													
FR-198-100	Beyren													
FR-196-001	Beyren													
FC-199-200	Beyren													
FC-169-200	Wintrange													
FR-171-199	Wintrange													
FC-176-200	Schwebsange													
FR-197-161	Wintrange													
FR-197-162	Schengen													
TS-198-001	Wintrange													
TS-198-002	Wintrange													
TS-192-001	Wasserbillig													
TS-166-001	Wormeldange													
FR-178-002	Machtum													
FR-178-006	Machtum													

Table A.1.1 continued

Borehole reference	Location	Top km2	Top km2S	Top km1	Top km	Top ku	Top k	Top mo	Top mm	Top mu	Top m
TS-193-001	Rosport									131.5	
TS-155-001	Rosport										
TS-136-001	Echternach								125	25	
FR-177-100	Waldbredimus					124.8		109.8	< 48.6 ?		
FR-195-100	Waldbredimus					135.44		119.34	< 63.94		
TS-199-001	Scheuerhof			256		189		174 ?	115		
FR-190-060	Scheuerhof			260.5		180		165 ?	< 109		
FR-195-705	Markusbierg										
FR-195-704	Markusbierg										
TS-040-001	Besch-sous-Perl							139.36	82.52	0.35	139.36
FR-041-013	Besch-sous-Perl							136.11	79.27	–3.88	136.11
FR-196-900	Mertert					88.6		69			
FR-206-100	Boursdorf								234		
FR-198-100	Beyren					250.4		230.9			
FR-196-001	Beyren					230		210.4			
FC-199-200	Beyren					240.9		221.3	< 167.1		
FC-169-200	Wintrange	123	*	103		23		9.4	< 24.1		
FR-171-199	Wintrange					124.1		111			
FC-176-200	Schwebsange					72.1		59.1 *	7.1		
FR-197-161	Wintrange					128.2		108	< 67		
FR-197-162	Schengen								< 100.5		
TS-198-001	Wintrange								< 93		
TS-198-002	Wintrange								< 109.3		
TS-192-001	Wasserbillig					182.1		156.85	101.9		
TS-166-001	Wormeldange									122	
FR-178-002	Machtum									142.7	
FR-178-006	Machtum									137.25	

Table A.1.1 continued

Borehole reference	Location	Top so	Top sm	Top s	Top r	Top Dev	Source
TS-193-001	Rosport						SGL
TS-155-001	Rosport	113.3		113.3			SGL
TS-136-001	Echternach	–25		–25			Lucius?
FR-177-100	Waldbredimus						SGL
FR-195-100	Waldbredimus						SGL
TS-199-001	Scheuerhof						SGL
FR-190-060	Scheuerhof						SGL
FR-195-705	Markusbierg						SGL
FR-195-704	Markusbierg						SGL
TS-040-001	Besch-sous-Perl						Kind (1842); 164.85 m
FR-041-013	Besch-sous-Perl	–35.71	–87.68	–35.71	< –131.53	< –131.53	Kind (1842); 286.5 m
FR-196-900	Mertert						SGL
FR-206-100	Boursdorf						AGE
FR-198-100	Beyren						AGE
FR-196-001	Beyren						AGE
FC-199-200	Beyren						AGE
FC-169-200	Wintrange						SGL
FR-171-199	Wintrange						SGL
FC-176-200	Schwebsange						SGL
FR-197-161	Wintrange						SGL
FR-197-162	Schengen						SGL
TS-198-001	Wintrange						SGL
TS-198-002	Wintrange						SGL
TS-192-001	Wasserbillig						SGL
TS-166-001	Wormeldange	72	< 32.5				SGL
FR-178-002	Machtum						SGL
FR-178-006	Machtum						SGL

Table A.1.1 continued

Region	Borehole reference	Location	Details	LUREF		WGS84	
				x	y	Latitude N	Longitude E
Trias Nord	FR-168-101	Mersch	Mersch 1968	76083	90858	49.75219468	6.11377086
Trias Nord	FR-210-055	Mertzig	F1 Mertzig	68095	99615	49.83082189	6.00265884
Trias Nord	FC-187-100	Useldange	DEA Useldange, Roubricht; FCS-811-01	66300	93020	49.77149042	5.97794156
Trias Nord	FC-204-100	Bissen	Commune Bissen; Forage Laaschert	73205	93679	49.77753227	6.07378549
Trias Nord	FR-207-122	Reisdorf	Commune Reisdorf	87730	103817	49.86866666	6.27565069
Trias Nord	FC-200-200	Reimberg	FCC-803-08; Commune Préizerdaul, Hieselgriecht	64940	96650	49.80409415	5.95892218
Trias Nord	FR-194-032	Beckerich	Beckerich; FR2; FRE-802-10	60530	87950	49.72574911	5.89809528
Trias Nord	FC-197-050	Beckerich	Ophélie Beckerich; FCP-802-08	60510	87920	49.72547874	5.89781939
Trias Nord	FR-203-480	Michelbuch	Michelbuch, DEA	68756	98573	49.82146633	6.01187606
Trias Nord	FR-203-490	Useldange	Useldange, DEA; Bohrung Bréimchen; FRE-811-19	67501	92978	49.77113885	5.99461515
Trias Nord	FR-208-300	Useldange	Useldange, DEA; Forage Ribbefeld; FRE-811-03	66894	93510	49.77590904	5.98617103
Trias Nord	FR-207-068	Diekirch	Diekirch Réservoir	79626	102912	49.86058077	6.16292579
Trias Nord	FR-208-070	Diekirch	Diekirch Stadion	79854	103168	49.86288244	6.16609666
Trias Nord	FC-189-100	Bissen	Trefil-ARBED Bissen; FCP-502-03	71558	94672	49.78643935	6.05089759
Trias Nord	TS-208-002	Bissen	Trefil-ARBED Bissen; F1	71923	94406	49.78405279	6.05597156
Trias Nord	FC-182-200	Eltz	Com. Redange; Kreschtebierg (1); FCC-809-10; Eltz	59870	93900	49.77922198	5.88863558
Trias Nord	FC-206-300	Eltz	Com. Rédange; Kreschtebierg 2; K2; FCC-809-25; Eltz2	59791	94083	49.78086462	5.88752927
Trias Nord	FR-186-100	Everlange	FPZ-811-07/ 86-026; Everlange EL 17-1	65318	93075	49.77196184	5.96430741
Trias Nord	FC-191-085	Everlange	SEBES, solution de rechange, Everlange EL-15-5; BR 5	65505	92955	49.77088747	5.96690781
Trias Nord	FC-191-081	Everlange	SEBES, solution de rechange, Everlange EL-15-4; BR 1	65320	93066	49.77188097	5.96433551
Trias Nord	FC-191-082	Everlange	SEBES, solution de rechange, Everlange EL-15-3; BR 2	65102	93084	49.77203746	5.96130854
Trias Nord	FC-191-083	Everlange	SEBES, solution de rechange, Everlange EL-15-2; BR 3	64940	93110	49.77226720	5.95905863
Trias Nord	FC-191-084	Everlange	SEBES, solution de rechange, Everlange EL-15-1; BR 4	64800	93212	49.77318075	5.95711116
Trias Nord	FR-183-100	Ell	Reconnaissance carrière Feidt à Ell	55812	92721	49.76847291	5.83236723
Trias Nord	FR-179-200	Platen	FPZ-803-04; SEBES; Platen, Commune de Préizerdaul	63310	94480	49.78454155	5.93637220
Trias Nord	FR-198-500	Reimberg	FRE-803-03; Reimberg, Commune de Préizerdaul	64950	96640	49.80400449	5.95906148
Trias Nord	FC-185-100	Schieren	FCC-713-06; Com de Schieren; Forage Pleiter ou Pleitert	75354	99279	49.82790037	6.10355567
Trias Nord	FC-178-100	Reckange	FCC-509-20; Puits Schwartz; Commune de Mersch	74075	91041	49.75382378	6.08590405
Trias Nord	FC-153-100	Ettelbruck	FCC-707-01; Puits Campingwee; Ville d'Ettelbruck	74346	101413	49.84707785	6.08951557
Trias Nord	FC-183-300	Ettelbruck	FCC-707-02; Puits Grondwee; Ville d'Ettelbruck	74213	101520	49.84803859	6.08766481

Table A.1.1 continued

Borehole reference	Location	Year	Ground level		Total depth	dom1–4	lo6–7+ dou	lo1–5	lm3	lm2	lm1	li4	li3	li2	li1
FR-168-101	Mersch	1968	218	?	328										
FR-210-055	Mertzig	2010	315		85										
FC-187-100	Useldange	1987	263.5		188										
FC-204-100	Bissen	2004	301.34		127										
FR-207-122	Reisdorf	2007	195		200										
FC-200-200	Reimberg	2000	376		144										
FR-194-032	Beckerich	1994	300		170									> 5.6	34.4
FC-197-050	Beckerich	1997	300		173										
FR-203-480	Michelbuch	2003	382.68	?	156										
FR-203-490	Useldange	2003	248		204										
FR-208-300	Useldange	2008	283		202										
FR-207-068	Diekirch	2007	243		151.5										
FR-208-070	Diekirch	2008	189.5		113										
FC-189-100	Bissen	1989	225		54										
TS-208-002	Bissen	2008	225		60										
FC-182-200	Eltz	1982	346		141										
FC-206-300	Eltz	2006	335.06		114										
FR-186-100	Everlange	1986	247.24		170										
FC-191-085	Everlange	1991	243.97		159										
FC-191-081	Everlange	1991	245.61		155.7										
FC-191-082	Everlange	1991	247.25		152.5										
FC-191-083	Everlange	1991	248.25		152										
FC-191-084	Everlange	1991	247.76		148										
FR-183-100	Ell	1983	325		67.4										
FR-179-200	Platen	1979	261.45		103										
FR-198-500	Reimberg	1998	375		125.25										
FC-185-100	Schieren	1985	251.35		113.6										
FC-178-100	Reckange	1978	230.33		45										
FC-153-100	Ettelbruck	1953	211		65										
FC-183-300	Ettelbruck	1983	222		84										

Table A.1.1 continued

Borehole reference	Location	li1–3	ko2	ko1	ko	km3	km2	km2S	km2 tot	km1	km	ku	k
FR-168-101	Mersch								> 6.15 *	56.88 *	> 63.03	16.34 *	> 79.37
FR-210-055	Mertzig												
FC-187-100	Useldange									> 24	> 24	14	> 38
FC-204-100	Bissen					> 18	13	0	13	39	> 70	13	> 83
FR-207-122	Reisdorf												
FC-200-200	Reimberg												> 26
FR-194-032	Beckerich	> 40	5	1.5	6.5	25	8.5	> 0	8.5	40	73.5	10	70
FC-197-050	Beckerich												
FR-203-480	Michelbuch												
FR-203-490	Useldange												
FR-208-300	Useldange											15 ?	> 15
FR-207-068	Diekirch												
FR-208-070	Diekirch												
FC-189-100	Bissen											> 9.7	> 9.7
TS-208-002	Bisen									> 12.36	> 12.36	13.85 *	> 26.21
FC-182-200	Eltz												
FC-206-300	Eltz												
FR-186-100	Everlange											> 8.7	> 8.7
FC-191-085	Everlange												
FC-191-081	Everlange												
FC-191-082	Everlange												
FC-191-083	Everlange												
FC-191-084	Everlange												
FR-183-100	Ell								4.6	11.2	> 15.8	6.1	> 21.9
FR-179-200	Platen												
FR-198-500	Reimberg												
FC-185-100	Schieren												
FC-178-100	Reckange					> 22	14	> 0	14	> 8	> 44		
FC-153-100	Ettelbruck												
FC-183-300	Ettelbruck												

Table A.1.1 continued

Borehole reference	Location	mo		mm		mu		m		so		sm		s		r
FR-168-101	Mersch	32.73	*	72.48		34.39	*	139.6		70.38	*	15.95	*	86.33	*	
FR-210-055	Mertzig									> 80.5		0		> 80.5		
FC-187-100	Useldange	16		26		15		57		89		0		89		
FC-204-100	Bissen	32.73		> 12.5				> 45.23								
FR-207-122	Reisdorf			> 48.35		41.65		> 90		> 110				> 110		
FC-200-200	Reimberg							38		> 80				> 80		
FR-194-032	Beckerich	6		22.5	?	6		34.5		> 5.5		0		> 5.5		
FC-197-050	Beckerich															
FR-203-480	Michelbuch									91						
FR-203-490	Useldange															
FR-208-300	Useldange	7		22	*	15	*	44	*	96	*	0		96	*	
FR-207-068	Diekirch			> 19		23		> 42		109		0		109		
FR-208-070	Diekirch									> 104.5		0		> 104.5		
FC-189-100	Bissen	23		> 14				> 37								
TS-208-002	Bissen	24.98		> 7.20				> 32.18								
FC-182-200	Eltz			< 42		0		42		62		0		62		
FC-206-300	Eltz															
FR-186-100	Everlange	12.8		27.35		11.15		51.3		89.67		0		89.67		
FC-191-085	Everlange															
FC-191-081	Everlange															
FC-191-082	Everlange															
FC-191-083	Everlange															
FC-191-084	Everlange															
FR-183-100	Ell							32.9		12.6		0		12.6		
FR-179-200	Platen			> 14		10		> 24		76		0		76		
FR-198-500	Reimberg															
FC-185-100	Schieren	> 8		45		21		> 74		> 36.6		0		> 36.6		
FC-178-100	Reckange															
FC-153-100	Ettelbruck									59.5		0		59.5		
FC-183-300	Ettelbruck									80		0		80		

Table A.1.1 continued

Borehole reference	Location	Top dom4	Top dou	Top lo5	Top lm3	Top lm2	Top lm1	Top li4	Top li3	Top li2	Top li1	Top ko2	Top ko1	Top km3
FR-168-101	Mersch													
FR-210-055	Mertzig													
FC-187-100	Useldange													
FC-204-100	Bissen													
FR-207-122	Reisdorf													
FC-200-200	Reimberg													
FR-194-032	Beckerich										294.4	260	255	253.5
FC-197-050	Beckerich													
FR-203-480	Michelbuch													
FR-203-490	Useldange													
FR-208-300	Useldange													
FR-207-068	Diekirch													
FR-208-070	Diekirch													
FC-189-100	Bissen													
TS-208-002	Bissen													
FC-182-200	Eltz													
FC-206-300	Eltz													
FR-186-100	Everlange													
FC-191-085	Everlange													
FC-191-081	Everlange													
FC-191-082	Everlange													
FC-191-083	Everlange													
FC-191-084	Everlange													
FR-183-100	Ell													
FR-179-200	Platen													
FR-198-500	Reimberg													
FC-185-100	Schieren													
FC-178-100	Reckange													
FC-153-100	Ettelbruck													
FC-183-300	Ettelbruck													

Table A.1.1 continued

Borehole reference	Location	Top km2	Top km2S	Top km1	Top km	Top ku	Top k	Top mo	Top mm	Top mu	Top m
FR-168-101	Mersch			201.85		144.97		128.63	95.9	23.42	128.63
FR-210-055	Mertzig										
FC-187-100	Useldange					239.5		225.5	209.5	183.5	225.5
FC-204-100	Bissen	283.34		270.34		231.34		218.34	185.61		218.34
FR-207-122	Reisdorf									146.65	
FC-200-200	Reimberg							350			350
FR-194-032	Beckerich	228.5		220	253.5	180	260	170	164 ?	141.5 ?	170
FC-197-050	Beckerich										
FR-203-480	Michelbuch										
FR-203-490	Useldange										
FR-208-300	Useldange					237 ?		222	215	193	222
FR-207-068	Diekirch									224	
FR-208-070	Diekirch										
FC-189-100	Bissen							208	185		208
TS-208-002	Bissen					211.03 *		197.18	172.2		197.18
FC-182-200	Eltz							319			319
FC-206-300	Eltz										
FR-186-100	Everlange							234.54	221.74	194.39	234.54
FC-191-085	Everlange										
FC-191-081	Everlange										
FC-191-082	Everlange										
FC-191-083	Everlange										
FC-191-084	Everlange										
FR-183-100	Ell			320.4		309		302.9			302.9
FR-179-200	Platen									244.45	
FR-198-500	Reimberg										
FC-185-100	Schieren								240.35	195.35	
FC-178-100	Reckange	207.33		193.33							
FC-153-100	Ettelbruck										
FC-183-300	Ettelbruck										

Table A.1.1 continued

Borehole reference	Location	Top so	Top sm	Top s	Top r	Top Dev	Source
FR-168-101	Mersch	–10.97	–81.35	–10.97		–97.3	SGL
FR-210-055	Mertzig					234.5	SGL
FC-187-100	Useldange	168.5		168.5		79.5	SGL
FC-204-100	Bissen						SGL
FR-207-122	Reisdorf	105	< –5				SGL
FC-200-200	Reimberg	312		312		< 232	SGL
FR-194-032	Beckerich	135.5					SGL
FC-197-050	Beckerich						SGL
FR-203-480	Michelbuch					232.68	SGL
FR-203-490	Useldange					47	SGL
FR-208-300	Useldange	178		178		82	SGL
FR-207-068	Diekirch	201		201		92	SGL
FR-208-070	Diekirch					79	SGL
FC-189-100	Bissen						SGL
TS-208-002	Bissen						SGL
FC-182-200	Eltz	277		277		215	SGL
FC-206-300	Eltz						SGL
FR-186-100	Everlange	183.24		183.24		93.57	SGL
FC-191-085	Everlange						SGL
FC-191-081	Everlange						SGL
FC-191-082	Everlange						SGL
FC-191-083	Everlange						SGL
FC-191-084	Everlange						SGL
FR-183-100	Ell	270		270		257.4	SGL
FR-179-200	Platen	234.45		234.45		158.45	SGL
FR-198-500	Reimberg						SGL
FC-185-100	Schieren	174.35		174.35		< 137.75	SGL
FC-178-100	Reckange						SGL
FC-153-100	Ettelbruck					151.5	SGL
FC-183-300	Ettelbruck					142	SGL

Table A.1.1 continued

Region	Borehole reference	Location	Details	LUREF		WGS84	
				x	y	Latitude N	Longitude E
Trias Nord	FC-175-100	Erpeldange	FCC-706-09; Commune d'Erpeldange	76389	102772	49.85931167	6.11790833
Trias Nord	FC-183-200	Erpeldange	FCP-706-10; LADUNO, Erpeldange	76580	101924	49.85168872	6.12057195
Trias Nord	FR-204-400	Diekirch	FPZ-704-41; Diekirch	78770	102894	49.86041788	6.15102098
Trias Nord	FC-165-200	Bettendorf	FCC-702-06; Commune de Bettendorf	83113	104690	49.87655771	6.21143600
Trias Nord	FC-171-300	Gilsdorf	FCC-702-04; Gilsdorf, Commune de Bettendorf	80867	103040	49.86173092	6.18018537
Trias Nord	FC-175-200	Ermsdorf	FCC-705-22; Commune de Ermsdorf	83883	99206	49.82724858	6.22209251
Minette	FR-191-131	Sanem	F1 Pafewé; Sanem – Differdange; Industriemülldeponie	61792	66849	49.53607186	5.91657325
Minette	FR-191-133	Sanem	F3 Pafewé; Sanem – Differdange; Industriemülldeponie	62407	66244	49.53065038	5.92509642
Minette	FR-191-135	Sanem	F5 Pafewé; Sanem – Differdange; Industriemülldeponie	61940	66573	49.53359475	5.91863047
Minette	FR-207-073	Belvaux	Tunnel ferroviaire Gaalgebierg, Belvaux	62193	64278	49.51297168	5.92222310
Minette	FR-207-079	Belvaux	Tunnel ferroviaire Gaalgebierg, Belvaux	62187	64279	49.51297556	5.92214368
Minette	FR-207-072	Belvaux	Tunnel ferroviaire Gaalgebierg, Belvaux	62001	64374	49.51382479	5.91957428
Minette	FR-182-001	Obercorn	S1; F1; 1/80 Obercorn	60192	63768	49.50832049	5.89462315
Minette	FR-182-002	Dudelange	S2; F2; 2/80 Dudelange I	75219	60775	49.48171276	6.10214283
Minette	FR-182-003	Differdange	S3; F3; 3/81 Differdange I	62080	66288	49.53103644	5.92057738
Minette	FR-182-004	Sanem	S4; F4; 4/81 Sanem	62572	68935	49.55484998	5.92725719
Minette	FR-182-005	Esch	S5; F5; 5/81 Esch corrigé Esch/Belval	68136	64534	49.51541415	6.00428592
Minette	FR-182-006	Kayl	S6; F6; 7/81 Kayl	70167	62905	49.50080369	6.03237305
Minette	FR-182-007	Rodange	S7; F7; 8/81 Rodange	55859	67777	49.54420889	5.83455200
Minette	FR-182-008	Belvaux	S8; F8; 6/81 Belval corrigé Belvaux	62917	63023	49.50170467	5.93228013
Minette	FR-175-054	Esch	Sondage 4; 4/75 Budersberg	64400	64100	49.51142785	5.95271130
Minette	FR-175-055	Esch	Sondage 5; 5/75 Raemerich	72550	62330	49.49566745	6.06528179
Minette	FC-186-010	Bascharage	Forage-captage 86-037 Bascharage Brasserie	61480	70296	49.56705443	5.91210156
Minette	FC-197-010	Bascharage	FCP-201-04 Brasserie Bofferding 1997	61556	70385	49.56785694	5.91314802
Minette	FC-133-100	Differdange	Forage Differdange Hadir 1933	60420	65850	49.52704722	5.89766834
Minette	FC-126-002	Esch	Weisen II	66901	62354	49.49578823	5.98730326
Minette	FC-202-500	Esch	Weisen III; FCC-304-04	66909	62348	49.49573445	5.98741389

Table A.1.1 continued

Borehole reference	Location	Year	Ground level		Total depth	dom1–4	lo6–7+ dou	lo1–5	lm3	lm2		lm1		li4		li3	li2	li1
FC-175-100	Erpeldange	1975	204		49													
FC-183-200	Erpeldange	1983	200.64		55													
FR-204-400	Diekirch	2004	211.59		64													
FC-165-200	Bettendorf	1965	199.91		103													
FC-171-300	Gilsdorf	1971	238.91		152													
FC-175-200	Ermsdorf	1975	260.6		90													
FR-191-131	Sanem	1991	294		40			> 17.8	22.2									
FR-191-133	Sanem	1991	331.8		100			> 49.8	> 50.2									
FR-191-135	Sanem	1991	295.7		40			> 23.2	> 16.8									
FR-207-073	Belvaux	2007	396.88		60.7													
FR-207-079	Belvaux	2007	397.08		80													
FR-207-072	Belvaux	2007	360.49		50													
FR-182-001	Obercorn	1982	328		103.8			> 92.2	> 11.6									
FR-182-002	Dudelange	1982	312.4		100.55			> 95	> 5.55									
FR-182-003	Differdange	1982	307.6		71			> 33.4	> 37.6									
FR-182-004	Sanem	1982	313.8		53			> 34.3	> 18.7									
FR-182-005	Esch	1982	288.5		80			> 24.5	> 55.5									
FR-182-006	Kayl	1982	352.8		79			> 79										
FR-182-007	Rodange	1982	320.8		113			> 104	> 9									
FR-182-008	Belvaux	1982	317.4		75.3			> 59	> 16.3									
FR-175-054	Esch	1975	312.3		71			> 55.5	> 15.5									
FR-175-055	Esch	1975	302.1		72.35			> 38.3	> 34.05									
FC-186-010	Bascharage	1986	286.27	?	81				> 77	> 4								
FC-197-010	Bascharage	1997	290.25		316				> 70	90	*	15	*	54	?	10	> 77	
FC-133-100	Differdange	1933	295		440												100	
FC-126-002	Esch	1926	289.06		137			> 95	> 42									
FC-202-500	Esch	2002	290.57		120													

Table A.1.1 continued

Borehole reference	Location	li1–3	ko2	ko1	ko	km3	km2	km2S	km2 tot	km1	km	ku	k
FC-175-100	Erpeldange												
FC-183-200	Erpeldange												
FR-204-400	Diekirch												
FC-165-200	Bettendorf												
FC-171-300	Gilsdorf												
FC-175-200	Ermsdorf									> 6	> 6	15	> 21
FR-191-131	Sanem												
FR-191-133	Sanem												
FR-191-135	Sanem												
FR-207-073	Belvaux												
FR-207-079	Belvaux												
FR-207-072	Belvaux												
FR-182-001	Obercorn												
FR-182-002	Dudelange												
FR-182-003	Differdange												
FR-182-004	Sanem												
FR-182-005	Esch												
FR-182-006	Kayl												
FR-182-007	Rodange												
FR-182-008	Belvaux												
FR-175-054	Esch												
FR-175-055	Esch												
FC-186-010	Bascharage												
FC-197-010	Bascharage	> 87											
FC-133-100	Differdange												
FC-126-002	Esch												
FC-202-500	Esch												

Table A.1.1 continued

Borehole reference	Location	mo	mm	mu	m	so	sm	s	r
FC-175-100	Erpeldange					40	0	40	
FC-183-200	Erpeldange					44.2	0	44.2	
FR-204-400	Diekirch					53	0	53	
FC-165-200	Bettendorf			> 3	> 3	99	0	99	
FC-171-300	Gilsdorf		> 20	30	> 50	100	0	100	
FC-175-200	Ermsdorf	49	> 20		> 69				
FR-191-131	Sanem								
FR-191-133	Sanem								
FR-191-135	Sanem								
FR-207-073	Belvaux								
FR-207-079	Belvaux								
FR-207-072	Belvaux								
FR-182-001	Obercorn								
FR-182-002	Dudelange								
FR-182-003	Differdange								
FR-182-004	Sanem								
FR-182-005	Esch								
FR-182-006	Kayl								
FR-182-007	Rodange								
FR-182-008	Belvaux								
FR-175-054	Esch								
FR-175-055	Esch								
FC-186-010	Bascharage								
FC-197-010	Bascharage								
FC-133-100	Differdange								
FC-126-002	Esch								
FC-202-500	Esch								

Table A.1.1 continued

Borehole reference	Location	Top dom4	Top dou	Top lo5	Top lm3	Top lm2	Top lm1	Top li4	Top li3	Top li2	Top li1	Top ko2	Top ko1	Top km3
FC-175-100	Erpeldange													
FC-183-200	Erpeldange													
FR-204-400	Diekirch													
FC-165-200	Bettendorf													
FC-171-300	Gilsdorf													
FC-175-200	Ermsdorf													
FR-191-131	Sanem				276.2	254								
FR-191-133	Sanem				282									
FR-191-135	Sanem				272.5									
FR-207-073	Belvaux													
FR-207-079	Belvaux													
FR-207-072	Belvaux													
FR-182-001	Obercorn				235.8									
FR-182-002	Dudelange				217.4									
FR-182-003	Differdange				274.2									
FR-182-004	Sanem				279.5									
FR-182-005	Esch				284									
FR-182-006	Kayl													
FR-182-007	Rodange				216.8									
FR-182-008	Belvaux				258.4									
FR-175-054	Esch				256.8									
FR-175-055	Esch				263.8									
FC-186-010	Bascharage					209.27								
FC-197-010	Bascharage					220.25	130.25	*	115.25	?	61.25	51.25	< –25.75	
FC-133-100	Differdange													
FC-126-002	Esch				194.06									
FC-202-500	Esch													

Table A.1.1 continued

Borehole reference	Location	Top km2	Top km2S	Top km1	Top km	Top ku	Top k	Top mo	Top mm	Top mu	Top m
FC-175-100	Erpeldange										
FC-183-200	Erpeldange										
FR-204-400	Diekirch										
FC-165-200	Bettendorf										
FC-171-300	Gilsdorf									218.91	
FC-175-200	Ermsdorf					254.6		239.6	190.6		239.6
FR-191-131	Sanem										
FR-191-133	Sanem										
FR-191-135	Sanem										
FR-207-073	Belvaux										
FR-207-079	Belvaux										
FR-207-072	Belvaux										
FR-182-001	Obercorn										
FR-182-002	Dudelange										
FR-182-003	Differdange										
FR-182-004	Sanem										
FR-182-005	Esch										
FR-182-006	Kayl										
FR-182-007	Rodange										
FR-182-008	Belvaux										
FR-175-054	Esch										
FR-175-055	Esch										
FC-186-010	Bascharage										
FC-197-010	Bascharage										
FC-133-100	Differdange										
FC-126-002	Esch										
FC-202-500	Esch										

Table A.1.1 continued

Borehole reference	Location	Top so	Top sm	Top s	Top r	Top Dev	Source
FC-175-100	Erpeldange					157	SGL
FC-183-200	Erpeldange					152.04	SGL
FR-204-400	Diekirch					152.59	SGL
FC-165-200	Bettendorf	196.91		196.91		97.91	SGL
FC-171-300	Gilsdorf	188.91		188.91		88.91	SGL
FC-175-200	Ermsdorf						SGL
FR-191-131	Sanem						SGL
FR-191-133	Sanem						SGL
FR-191-135	Sanem						SGL
FR-207-073	Belvaux						SGL
FR-207-079	Belvaux						SGL
FR-207-072	Belvaux						SGL
FR-182-001	Obercorn						SGL
FR-182-002	Dudelange						SGL
FR-182-003	Differdange						SGL
FR-182-004	Sanem						SGL
FR-182-005	Esch						SGL
FR-182-006	Kayl						SGL
FR-182-007	Rodange						SGL
FR-182-008	Belvaux						SGL
FR-175-054	Esch						SGL
FR-175-055	Esch						SGL
FC-186-010	Bascharage						SGL
FC-197-010	Bascharage						SGL
FC-133-100	Differdange						SGL
FC-126-002	Esch						SGL
FC-202-500	Esch						SGL

A.1.2 Selected boreholes in France

Table A.1.2: Selected boreholes in the Lorraine region (France).

Region	Borehole reference	Location	Details	WGS84	
				Latitude N	Longitude E
Lorraine	01133X0022/NB1	Audun-le-Tiche	NB1	49.43950513	5.95853770
Lorraine	01132X0129/S	Hussigny-Godbrange	S	49.49085245	5.85992452
Lorraine	01133X0029/BT	Audun-le-Tiche	Deutsch-Oth Mont-Rouge	49.47344618	5.96712159
Lorraine	01133X0012/BL	Aumetz	BL	49.41495424	5.96914678
Lorraine	01133X0052/P1	Tressange	GW1	49.41403302	5.98977681
Lorraine	01133X0008/S	Audun-le-Tiche	Bodenberg	49.44964985	5.94506332
Lorraine	01133X0095/E1	Aumetz	E1	49.43180617	5.96346376
Lorraine	01133X0053/GW2	Tressange	GW2	49.42083790	5.98241645
Lorraine	01138X0083/S	Rochonvillers		49.40009399	6.02888444
Lorraine	00905X0037/SN1	Mexy	SN1	49.51159726	5.79146122
Lorraine	00905X0034/SN2	Mexy	SN2	49.50742607	5.80450700
Lorraine	01131X0002/S23	Hussigny-Godbrange	S23	49.49761080	5.83152388
Lorraine	01132X0192/SC1THI	Thil	SC1	49.46737983	5.90260647
Lorraine	01132X0195/SC320	Villerupt	SC320	49.46142537	5.93036144
Lorraine	00898X0046/MS5	Cosnes-et-Romain	MS5	49.52372368	5.74285377
Lorraine	00898X0048/MS4	Cosnes-et-Romain	MS4	49.52272132	5.75059657
Lorraine	00898X0009/LE	Cosnes-et-Romain	Le Régla	49.52705785	5.70985581
Lorraine	01132X0161/L1	Rédange		49.49591423	5.92801118
Lorraine	00905X0003/S	Longwy	Sondage des Recollets	49.51879155	5.77053706
Lorraine	01373X0001/S	Bois-Châté	Source Perotin	49.28401737	6.00146681
Lorraine	01354X0131/VA-1	Vacherauville		49.23042728	5.31327139
Lorraine	01381X0243/F	Amnéville	Centre Loisirs	49.24253984	6.13528982
Lorraine	01381X0280/F2	Amnéville	Centre Thermal	49.24411732	6.12969481
Lorraine	01142X0102/F2	Cattenom	Camp militaire	49.42162710	6.22848253
Lorraine	01142X0018/S	Cattenom	Uttweiller	49.43583780	6.23963290
Lorraine	01142X0004/F	Sentzich		49.42361772	6.25481239
Lorraine	01141X0004/S	Hettange-Grande		49.41697608	6.17105822
Lorraine	01141X0016/F	Zoufftgen		49.45939122	6.13818155
Lorraine	01141X0002/F	Roussy-le-Village		49.45921768	6.19231565

BRGM – Bureau de Recherches Géologiques et Minières (France), * – thickness/stratigraphy reinterpreted, ? – thickness/stratigraphy reinterpreted and uncertain. Longitude and latitude in degrees. Ground level, total depth, thickness and stratigraphical boundaries by reference to mean sea level (national reference) in meters.

Table A.1.2 continued

Borehole reference	Location	Year	Ground level	Total depth	dom1–4	lo6–7 + dou	lo1–5	lm3	lm2	lm1	li4	li3	li2	li1
01133X0022/NB1	Audun-le-Tiche	1874	397	135.73	> 126	> 8.73								
01132X0129/S	Hussigny-Godbrange	1961	406.38	84	> 58.64	> 25.36								
01133X0029/BT	Audun-le-Tiche	1893	409.42	151.6	> 93.9	> 56.1								
01133X0012/BL	Aumetz	1910	385	228.96	> 168.38 ?	> 60.58								
01133X0052/P1	Tressange	1932	357.47	231.09	135.65 ?	56.01								
01133X0008/S	Audun-le-Tiche	1874	398	115.18	> 113.5	> 1.68								
01133X0095/E1	Aumetz	2001	402.49	210.49	142	> 58.49								
01133X0053/GW2	Tressange	1927	384.92	213.9	> 125 ?	> 63.9								
01138X0083/S	Rochonvillers	1874	373	189.6	> 132 ?	> 31.6								
00905X0037/SN1	Mexy	1955	361.85	83.5	> 61.8	15.64								
00905X0034/SN2	Mexy	1955	316.4	113	> 87.07	17.1								
01131X0002/S23	Hussigny-Godbrange	1962	392.34	119.64	> 92.56	27.08								
01132X0192/SC1THI	Thil	2001	399	55.7	> 38.37	> 15.03								
01132X0195/SC320	Villerupt	2006	399	57.65	> 34.95	20.85								
00898X0046/MS5	Cosnes-et-Romain	1965	374.88	87.87	> 71.29	14.11								
00898X0048/MS4	Cosnes-et-Romain	1965	378	91.08	> 71.58	11.03								
00898X0009/LE	Cosnes-et-Romain	1911	384.82	90.53	> 75	6.02								
01132X0161/L1	Rédange	1974	335	104			> 80.88	> 12.62						
00905X0003/S	Longwy	1908	259.78	922.17			> 106	85	74	14	42 *	12 *	104 *	37 *
01373X0001/S	Bois-Châté	1909	211.4	1100.3	> 11.5	36.5	160 *	54 *	176 *	10	45 *		0	
01354X0131/VA-1	Vacherauville	1953	195	2250.52	75	10	118	30	235 ?	0 ?	32.5 ?			
01381X0243/F	Amnéville	1979	209.04	900					> 139.8	10.2	44.8			
01381X0280/F2	Amnéville	1989	215	880					> 112.4	12	41			
01142X0102/F2	Cattenom	1978	182.08	205					> 74.45	11.3	52.25	40.5	5	17.1
01142X0018/S	Cattenom	1932	207	178.5					> 48.5	11 *	50 *	38	9.5	19.5
01142X0004/F	Sentzich	1932	214	301.5					> 149	15	50	33 *	9 *	22 *
01141X0004/S	Hettange-Grande	1933	217	380					> 161	16	44		fault	
01141X0016/F	Zoufftgen	1976	229	206.5					> 82	5.7 ?	45	13.5	> 60 ?	
01141X0002/F	Roussy-le-Village	1952	220	62.65								> 3.5	46	> 11.7

Table A.1.2 continued

Borehole reference	Location	li1–3	ko2	ko1	ko	km3	km2	km2S	km2 tot	km1	km	ku	k
01133X0022/NB1	Audun-le-Tiche												
01132X0129/S	Hussigny-Godbrange												
01133X0029/BT	Audun-le-Tiche												
01133X0012/BL	Aumetz												
01133X0052/P1	Tressange												
01133X0008/S	Audun-le-Tiche												
01133X0095/E1	Aumetz												
01133X0053/GW2	Tressange												
01138X0083/S	Rochonvillers												
00905X0037/SN1	Mexy												
00905X0034/SN2	Mexy												
01131X0002/S23	Hussigny-Godbrange												
01132X0192/SC1THI	Thil												
01132X0195/SC320	Villerupt												
00898X0046/MS5	Cosnes-et-Romain												
00898X0048/MS4	Cosnes-et-Romain												
00898X0009/LE	Cosnes-et-Romain												
01132X0161/L1	Rédange												
00905X0003/S	Longwy	153 *			17 *	48 ?	18.6 ?	0	18.6? ?	106.1 ?	172.7 *	15.6 *	205.3 *
01373X0001/S	Bois-Châté	75 *	14	19	33	65 *	26 *	0	? 26 *	96 *	187	17 *	237
01354X0131/VA-1	Vacherauville	94.5	5	38	43	115	15	2	17	107	239		282
01381X0243/F	Amnéville	58	8.5	24	32.5	57.5 *	35 *	0	35 *	112 *	204.5	32.5	269.5
01381X0280/F2	Amnéville	58.5	9	24	33	60	25	6	31	102.5	193.5	28.5	255
01142X0102/F2	Cattenom	62.6	> 4.4		> 4.4								
01142X0018/S	Cattenom	67	> 6.5		> 6.5								
01142X0004/F	Sentzich	64	7.5	9.5	17	> 5.5							
01141X0004/S	Hettange-Grande	> 46.75									> 101	24	> 125
01141X0016/F	Zoufftgen	> 73.5											
01141X0002/F	Roussy-le-Village	> 61.2											

Table A.1.2 continued

Borehole reference	Location	mo	mm	mu	m	so	sm	s	r
01133X0022/NB1	Audun-le-Tiche								
01132X0129/S	Hussigny-Godbrange								
01133X0029/BT	Audun-le-Tiche								
01133X0012/BL	Aumetz								
01133X0052/P1	Tressange								
01133X0008/S	Audun-le-Tiche								
01133X0095/E1	Aumetz								
01133X0053/GW2	Tressange								
01138X0083/S	Rochonvillers								
00905X0037/SN1	Mexy								
00905X0034/SN2	Mexy								
01131X0002/S23	Hussigny-Godbrange								
01132X0192/SC1THI	Thil								
01132X0195/SC320	Villerupt								
00898X0046/MS5	Cosnes-et-Romain								
00898X0048/MS4	Cosnes-et-Romain								
00898X0009/LE	Cosnes-et-Romain								
01132X0161/L1	Rédange								
00905X0003/S	Longwy	8.6 *	26 *	0	34.6 *			56.76	0
01373X0001/S	Bois-Châté	48 *	79	21 *	148	41 *	94.28	135.28	> 11.72
01354X0131/VA-1	Vacherauville				47			63.5	668
01381X0243/F	Amnéville	38.5	58	23	119.5	44	176	220	> 32
01381X0280/F2	Amnéville	34.5	53.5	22	110	58	183	241	> 43.5
01142X0102/F2	Cattenom								
01142X0018/S	Cattenom								
01142X0004/F	Sentzich								
01141X0004/S	Hettange-Grande	> 24							
01141X0016/F	Zoufftgen								
01141X0002/F	Roussy-le-Village								

Table A.1.2 continued

Borehole reference	Location	Top dom4	Top dou	Top lo5	Top lm3	Top lm2	Top lm1	Top li4	Top li3	Top li2	Top li1	Top ko2	Top ko1	Top km3
01133X0022/NB1	Audun-le-Tiche		270	< 261.27										
01132X0129/S	Hussigny-Godbrange		347.74	< 322.38										
01133X0029/BT	Audun-le-Tiche		313.92	< 257.82										
01133X0012/BL	Aumetz		216.62	< 156.04										
01133X0052/P1	Tressange	323.17 ?	187.52	131.51										
01133X0008/S	Audun-le-Tiche		284.5	< 282.82										
01133X0095/E1	Aumetz	392.49 ?	250.49	< 192										
01133X0053/GW2	Tressange		234.92	< 171.02										
01138X0083/S	Rochonvillers		215	< 183.4										
00905X0037/SN1	Mexy		300.05	284.41										
00905X0034/SN2	Mexy		229.33	212.23										
01131X0002/S23	Hussigny-Godbrange		299.78	272.7										
01132X0192/SC1THI	Thil		358.33	< 343.3										
01132X0195/SC320	Villerupt		362.55	341.7										
00898X0046/MS5	Cosnes-et-Romain		303.59	289.48										
00898X0048/MS4	Cosnes-et-Romain		306.42	295.39										
00898X0009/LE	Cosnes-et-Romain		308.82	302.8										
01132X0161/L1	Rédange				243.62									
00905X0003/S	Longwy				153.78	68.78	–5.22	–19.22	–61.22 *	–73.22 *	–177.22 *			–231.22
01373X0001/S	Bois-Châté		199.9	163.4 *	3.4 *	–50.6	–226.6	–236.6	–281.6 *			–356.6	–370.6	–389.6
01354X0131/VA-1	Vacherauville	–311.5	–386.5	–396.5	–514.5	–544.5	–779.5	–779.5	–812			–906.5	–911.5	–949.5
01381X0243/F	Amnéville						63.04	52.84	8.04			–49.96	–58.46	–82.46
01381X0280/F2	Amnéville						96	84	43			–15.5	–24.5	–48.5
01142X0102/F2	Cattenom						107.63	96.33	44.08	3.58	–1.42	–18.52		
01142X0018/S	Cattenom						158	147 *	97	59	49.5	30		
01142X0004/F	Sentzich						64	49	–1	–34	–43	–65	–72.5	–82
01141X0004/S	Hettange-Grande						56	40	–4					
01141X0016/F	Zoufftgen						146.7	141	96	82.5	< 22.5 ?			
01141X0002/F	Roussy-le-Village									215	169	< 157.35		

Table A.1.2 continued

Borehole reference	Location	Top km2	Top km2S	Top km1	Top km	Top ku	Top k	Top mo	Top mm	Top mu	Top m
01133X0022/NB1	Audun-le-Tiche										
01132X0129/S	Hussigny-Godbrange										
01133X0029/BT	Audun-le-Tiche										
01133X0012/BL	Aumetz										
01133X0052/P1	Tressange										
01133X0008/S	Audun-le-Tiche										
01133X0095/E1	Aumetz										
01133X0053/GW2	Tressange										
01138X0083/S	Rochonvillers										
00905X0037/SN1	Mexy										
00905X0034/SN2	Mexy										
01131X0002/S23	Hussigny-Godbrange										
01132X0192/SC1THI	Thil										
01132X0195/SC320	Villerupt										
00898X0046/MS5	Cosnes-et-Romain										
00898X0048/MS4	Cosnes-et-Romain										
00898X0009/LE	Cosnes-et-Romain										
01132X0161/L1	Rédange										
00905X0003/S	Longwy	−279.22 ?		−297.82 ?	−231.22	−403.92 *	−241.22	−419.52 *	−428.12 *	−454.12	−419.52 *
01373X0001/S	Bois-Châté	−454.6 *		−480.6 *	−389.6	−576.6	−356.6	−593.6 *	−641.6	−720.6	−593.6 *
01354X0131/VA-1	Vacherauville	−1064.5	−1079.5	−1081.5	−949.5	−1188.5	−906.5	−1188.5			
01381X0243/F	Amnéville	−139.96 *		−174.96 *	−82.46	−286.96	−49.96	−319.46	−357.96	−415.96	−319.46
01381X0280/F2	Amnéville	−108.5	−133.5	−139.5	−48.5	−242	−15.5	−270.5	−305	−358.5	−270.5
01142X0102/F2	Cattenom										
01142X0018/S	Cattenom										
01142X0004/F	Sentzich										
01141X0004/S	Hettange-Grande					−115		−139			
01141X0016/F	Zoufftgen										
01141X0002/F	Roussy-le-Village										

Table A.1.2 continued

Borehole reference	Location	Top so	Top sm	Top s	Top r	Top Dev	Source
01133X0022/NB1	Audun-le-Tiche						BRGM
01132X0129/S	Hussigny-Godbrange						BRGM
01133X0029/BT	Audun-le-Tiche						BRGM
01133X0012/BL	Aumetz						BRGM
01133X0052/P1	Tressange						BRGM
01133X0008/S	Audun-le-Tiche						BRGM
01133X0095/E1	Aumetz						BRGM
01133X0053/GW2	Tressange						BRGM
01138X0083/S	Rochonvillers						BRGM
00905X0037/SN1	Mexy						BRGM
00905X0034/SN2	Mexy						BRGM
01131X0002/S23	Hussigny-Godbrange						BRGM
01132X0192/SC1THI	Thil						BRGM
01132X0195/SC320	Villerupt						BRGM
00898X0046/MS5	Cosnes-et-Romain						BRGM
00898X0048/MS4	Cosnes-et-Romain						BRGM
00898X0009/LE	Cosnes-et-Romain						BRGM
01132X0161/L1	Rédange						BRGM
00905X0003/S	Longwy	−454.12		−454.12		−510.88	Joly (1908); van Werveke (1908)
01373X0001/S	Bois-Châté	−741.6 *	−782.6	−741.6 *	−876.88		Nicklès (1914); BRGM
01354X0131/VA-1	Vacherauville	−1235.5			−1299	−1956.5	BRGM
01381X0243/F	Amnéville	−438.96	−482.96	−438.96	−658.96		BRGM
01381X0280/F2	Amnéville	−380.5	−438.5	−380.5	−621.5		BRGM
01142X0102/F2	Cattenom						BRGM
01142X0018/S	Cattenom						BRGM
01142X0004/F	Sentzich						BRGM
01141X0004/S	Hettange-Grande						BRGM
01141X0016/F	Zoufftgen						BRGM
01141X0002/F	Roussy-le-Village						BRGM

Table A.1.2 continued

Region	Borehole reference	Location	Details	WGS84	
				Latitude N	Longitude E
Lorraine	01136X0065/AD-101	Audun-le-Roman		49.38240273	5.87228448
Lorraine	01146X0145/KOE1	Koenigsmacker		49.38496487	6.29242148
Lorraine	01145X0126/ILL1	Illange		49.33044178	6.18470564
Lorraine	01387X0037/SM1	St-Michel		49.21893573	6.37799000
Lorraine	01382X0017/GUELAN	Guélange		49.28759790	6.21907543
Lorraine	01138X0131/G1	Thionville	St-Michel	49.37717740	6.08342302
Lorraine	01145X0007/S	Thionville	Route Illange	49.35189327	6.17866523
Lorraine	01388X0001/HL478	Hinckange	Le Breuil	49.18749747	6.45355215
Lorraine	01144X0053/OUEST	Kirschnaumen		49.41664433	6.41961396
Lorraine	01144X0029/SI-04	Merschweiler		49.46493643	6.41133501
Lorraine	01143X0076/SI-06	Kirsch-les-Sierck		49.44141648	6.38618142
Lorraine	01143X0062/F	Contz-les-Bains		49.44923729	6.34787602
Lorraine	01143X0068/SI-07	Hunting		49.41096389	6.31149010

Table A.1.2 continued

Borehole reference	Location	Year	Ground level	Total depth	dom1–4	lo6–7 + dou	lo1–5	lm3	lm2	lm1	li4	li3	li2	li1
01136X0065/AD-101	Audun-le-Roman	1957	396.06	1251.7	122.5	39	132.5 *	73 *	142 *	17 *	46 *	15	64	30.5
01146X0145/KOE1	Koenigsmacker	1982	210	354										
01145X0126/ILL1	Illange	1982	204	538							45		0	
01387X0037/SM1	St-Michel	1985	344.38	857.21										
01382X0017/GUELAN	Guélange	1984	215	499						> 2 *	45 ?		0	
01138X0131/G1	Thionville	1974	315	83.05			> 56.50	> 24.12 ?						
01145X0007/S	Thionville	1934	159	355.4					> 89	13.5	53.5		0	
01388X0001/HL478	Hinckange	1965	203.23	1203.1										
01144X0053/OUEST	Kirschnaumen	1996	320	290										
01144X0029/SI-04	Merschweiler	1980	373	226.8										
01143X0076/SI-06	Kirsch-les-Sierck	1980	355	177.2										
01143X0062/F	Contz-les-Bains	1970	147	99.4										
01143X0068/SI-07	Hunting	1980	174	329.9										

Table A.1.2 continued

Borehole reference	Location	li1–3	ko2	ko1	ko	km3	km2	km2S	km2 tot	km1	km	ku	k
01136X0065/AD-101	Audun-le-Roman	109.5			13.8	40.7 ?	9 ?	0	9?	114 ?	163.7	15.6?	193.1
01146X0145/KOE1	Koenigsmacker					> 50.4 *	25 *	6 *	31 *	100 *	> 181.4	20.6	> 202
01145X0126/ILL1	Illange	52	12.5	25.5	38	75 *	27 *	0 ?	27 *	101	203	19	260
01387X0037/SM1	St-Michel	> 24.4 ?			30 ?	76.6 ?	31	< 31 ?	31	102.4 ?	210 ?	33.6	273.6 ?
01382X0017/GUELAN	Guélange	50 ?	6.5	16.5	23	74	36?	0 ?	36 ?	101 ?	211	27	261
01138X0131/G1	Thionville												
01145X0007/S	Thionville	57.5	7.3	28.2	35.5	71	10	12	22	> 7.4	> 100.4		> 135.9
01388X0001/HL478	Hinckange								> 13	135 ?	> 148	33.23	> 193
01144X0053/OUEST	Kirschnaumen											> 20	> 20
01144X0029/SI-04	Merschweiler												
01143X0076/SI-06	Kirsch-les-Sierck												
01143X0062/F	Contz-les-Bains												
01143X0068/SI-07	Hunting											> 18.85 *	> 18.85 *

Table A.1.2 continued

Borehole reference	Location	mo	mm	mu	m	so	sm	s	r
01136X0065/AD-101	Audun-le-Roman	43.4	57 *	16 *	116.4	53 *	70	123	> 125.7
01146X0145/KOE1	Koenigsmacker	51.5 ?	90.5 ?	> 10	> 152				
01145X0126/ILL1	Illange	55 *	79 *	30	164	> 14			
01387X0037/SM1	St-Michel	63	63 *	24 *	150 *	61 *	222	283	90
01382X0017/GUELAN	Guélange	35	91	> 10	> 136				
01138X0131/G1	Thionville								
01145X0007/S	Thionville								
01388X0001/HL478	Hinckange	63.77	68	21	152.77	55.4	202.48	257.88	91.07
01144X0053/OUEST	Kirschnaumen	56 *	54 *	25 *	135	33 ?	91	124	
01144X0029/SI-04	Merschweiler	> 55.2	53	27 *	> 136.8	36.8 ?	50.05 ?	86.85	
01143X0076/SI-06	Kirsch-les-Sierck	> 50.35	64.05	30.9 *	> 145.3	28.2		28.2	
01143X0062/F	Contz-les-Bains					> 21.24	70.41	> 91.65	
01143X0068/SI-07	Hunting	55.65 *	82.95 *	22.8 *	161.4 *	32.65 *	108.25 *	140.9	

Table A.1.2 continued

Borehole reference	Location	Top dom4	Top dou	Top lo5	Top lm3	Top lm2	Top lm1	Top li4	Top li3	Top li2	Top li1	Top ko2	Top ko1	Top km3
01136X0065/AD-101	Audun-le-Roman		262.56	223.56	91.06	18.06	−123.94	−140.94	−186.94	−201.94	−265.94	−296.44		−310.24
01146X0145/KOE1	Koenigsmacker													
01145X0126/ILL1	Illange							201	156			104	91.5	66
01387X0037/SM1	St-Michel											320 ?		290 ?
01382X0017/GUELAN	Guélange							208 ?	163 ?			113	106.5	90
01138X0131/G1	Thionville				258.5									
01145X0007/S	Thionville						64	50.5	−3			−60.5	−67.8	−96
01388X0001/HL478	Hinckange													
01144X0053/OUEST	Kirschnaumen													
01144X0029/SI-04	Merschweiler													
01143X0076/SI-06	Kirsch-les-Sierck													
01143X0062/F	Contz-les-Bains													
01143X0068/SI-07	Hunting													

Table A.1.2 continued

Borehole reference	Location	Top km2	Top km2S	Top km1	Top km	Top ku	Top k	Top mo	Top mm	Top mu	Top m
01136X0065/AD-101	Audun-le-Roman	−350.94 ?		−359.94 ?	−310.24	−473.94 ?	−296.44	−489.54	−532.94	−589.94	−489.54
01146X0145/KOE1	Koenigsmacker	159.6 *	134.6 *	128.6 *		28.6 *		8	−43.5 ?	−134 ?	8
01145X0126/ILL1	Illange	−9 *		−36	66	−137	104	−156	−211 *	−290 *	−156
01387X0037/SM1	St-Michel	213.38		182.38	290	80 ?	320 ?	46.38	−16.62	−79.62 *	46.38 *
01382X0017/GUELAN	Guélange	16		−20	90	−121	113	−148	−183	−274	−148
01138X0131/G1	Thionville										
01145X0007/S	Thionville	−167	−177	−189	−96						
01388X0001/HL478	Hinckange					48.23 *		15 ?	−48.77	−116.77 *	15 ?
01144X0053/OUEST	Kirschnaumen							300 *	244 *	190 *	300 *
01144X0029/SI-04	Merschweiler								316.4	263.4 *	
01143X0076/SI-06	Kirsch-les-Sierck								303.15	239.1	
01143X0062/F	Contz-les-Bains										
01143X0068/SI-07	Hunting							152.05 *	96.4 *	13.45 *	152.05 *

Table A.1.2 continued

Borehole reference	Location	Top so		Top sm		Top s		Top r		Top Dev		Source
01136X0065/AD-101	Audun-le-Roman	–605.94		–658.94		–605.94		–728.94				BRGM
01146X0145/KOE1	Koenigsmacker	< –144										beph.net
01145X0126/ILL1	Illange	–320										BRGM
01387X0037/SM1	St-Michel	–103.62	*	–164.62	*	–103.62	*	–386.62	*	–476.62		BRGM
01382X0017/GUELAN	Guélange	< –284										BRGM
01138X0131/G1	Thionville											BRGM
01145X0007/S	Thionville											BRGM
01388X0001/HL478	Hinckange	–137.77	*	–193.17	*	–137.77	*	–395.65		–486.72	*	BRGM
01144X0053/OUEST	Kirschnaumen	165	?	132						41		BRGM
01144X0029/SI-04	Merschweiler	236.4	*	199.6	?	236.4	*			149.55		BRGM
01143X0076/SI-06	Kirsch-les-Sierck	208.2	*			208.2				180		BRGM
01143X0062/F	Contz-les-Bains			118.41						< 48		BRGM
01143X0068/SI-07	Hunting	–9.35	*	–43.05	*	–9.35	*			–151.3		BRGM

A.1.3 Selected boreholes in Belgium

Table A.1.3: Selected boreholes in the Lorraine (or Gaume) region (Belgium).

Region	Borehole reference	Location	Details	Lambert 72		WGS84	
				x	y	Latitude N	Longitude E
Belgian Lorraine	219E0256	Arlon		254640	41380	49.66276084	5.810445435
Belgian Lorraine	219E0612	Weiler		254161	39967	49.66226199	5.811497186
Belgian Lorraine	219E0614	Toernich		252022	39756	49.66073530	5.781820934
Belgian Lorraine	219E0611	Sesselich		253246	39574	49.65888856	5.798721563
Belgian Lorraine	223E0501	Hondelange		256401	36012	49.62631572	5.841429090
Belgian Lorraine	223E0492	Aubange		252372	28860	49.56318742	5.784080289
Belgian Lorraine	225E0189	Latour		236840	26253	49.54175240	5.568209174

Lambert 72 – Belgian reference frame (x, y in meters), SGB – Geological Survey of Belgium, * – thickness/stratigraphy reinterpreted, ? – thickness/stratigraphy reinterpreted and uncertain. Longitude and latitude in degrees. Ground level, total depth, thickness and stratigraphical boundaries by reference to mean sea level (national reference) in meters.

Table A.1.3 continued

Borehole reference	Location	Year	Ground level	Total depth	dom1–4	lo6–7 + dou	lo1–5	lm3	lm2	lm1	li4	li3	li2	li1
219E0256	Arlon	1971	390 ?	176							> 17.5	12.5	80	33.4
219E0612	Weiler	1988	406.44	142.3						> 17.7 *	39.6 *	9 *	> 72	
219E0614	Toernich	1988	436.9	223					> 56.9	39.9 *	40.3 *	13.65 *	64.95	> 7.3
219E0611	Sesselich	1988	363.98	119						> 6.9 *	33.4 *	12 *	> 24	
223E0501	Hondelange	1990	330.12	140					> 19 *	18 *	38 *	8 *	> 57 *	
223E0492	Aubange	1986	295.5	145			> 24	88.4 *	> 32.6 *					
225E0189	Latour	1986	312	494			> 46 *	67.4 *	44.1 *	25.5 *	62.2 *	0	32.6	78.8

Table A.1.3 continued

Borehole reference	Location	li1–3	ko2	ko1	ko	km3	km2	km2S	km2 tot	km1	km	ku	k
219E0256	Arlon	125.9	2.1	9.2	11.3								
219E0612	Weiler	> 81 *											
219E0614	Toernich	> 85.9 *											
219E0611	Sesselich	> 36 *											
223E0501	Hondelange	> 65 *											
223E0492	Aubange												
225E0189	Latour	111.4			10	30.4	1.4	0	1.4	62.6	94.4	10.8	115.2

Table A.1.3 continued

Borehole reference	Location	mo	mm	mu	m	so	sm	s	r
219E0256	Arlon								
219E0612	Weiler								
219E0614	Toernich								
219E0611	Sesselich								
223E0501	Hondelange								
223E0492	Aubange								
225E0189	Latour	0	0	0	0	18.2	0	18.2	

Table A.1.3 continued

Borehole reference	Location	Top dom4	Top dou	Top lo5	Top lm3	Top lm2	Top lm1	Top li4	Top li3	Top li2	Top li1	Top ko2	Top ko1	Top km3
219E0256	Arlon								359.5	347	267			222.3
219E0612	Weiler							385.04 *	345.44 *	336.44 *	< 264.44			
219E0614	Toernich						380	340.1 *	299.1 *	286.15 *	221.2			
219E0611	Sesselich							353.38 *	319.98 *	307.98 *	< 283.98			
223E0501	Hondelange						311.12 *	293.12 *	255.12 *	247.12 *	< 190.12 *			
223E0492	Aubange				271.5	183.1 *								
225E0189	Latour				266 *	198.6 *	154.5 *	129 *		66.8 *	34.2			−54.6

Table A.1.3 continued

Borehole reference	Location	Top km2	Top km2S	Top km1	Top km	Top ku	Top k	Top mo	Top mm	Top mu	Top m
219E0256	Arlon										
219E0612	Weiler										
219E0614	Toernich										
219E0611	Sesselich										
223E0501	Hondelange										
223E0492	Aubange										
225E0189	Latour	−85	−86.4	−86.4	−54.6	−149	−44.6	−159.8	−159.8	−159.8	−159.8

Table A.1.3 continued

Borehole reference	Location	Top so	Top sm	Top s	Top r	Top Dev	Source
219E0256	Arlon						SGB
219E0612	Weiler						SGB
219E0614	Toernich						SGB
219E0611	Sesselich						SGB
223E0501	Hondelange						SGB
223E0492	Aubange						SGB
225E0189	Latour	−159.8		−159.8		−178	SGB

A.1.4 Selected boreholes in Germany

Table A.1.4: Selected boreholes in the Südeifel and Saargau regions (Germany).

Region	Borehole reference	Location	Details	DHDN 3 Degree Gauss Zone 2		WGS84	
				R	H	Latitude N	Longitude E
Suedeifel	/	Roth		2517100	5531575	49.92255704	6.239615590
Suedeifel	/	Körperich		2518800	5533750	49.94206288	6.263398840
Suedeifel	/	Dockendorf		2532590	5532570	49.93031998	6.455151340
Suedeifel	/	Kranzbach/Bollendorf		2525570	5526150	49.87347385	6.357221800
Saargau	/	Perl Maimühle		2526990	5481860	49.47515360	6.373917520
Suedeifel	58a	Echternacherbrück		2532150	5520220	49.81764329	6.446136630

DHDN 3 Degree Gauss Zone 2 – German reference frame in the considered region (R, H in meters) , LUA – Landesamt für Umwelt und Arbeitsschutz Saarland, LGB – Landesamt für Geologie und Bergbau Rheinland–Pfalz. Longitude and latitude in degrees. Ground level, total depth, thickness and stratigraphical boundaries by reference to mean sea level (national reference) in meters.

Table A.1.4 continued

Borehole reference	Location	Year	Ground level		Total depth	dom1–4	lo6–7 + dou	lo1–5	lm3	lm2	lm1	li4	li3	li2	li1
/	Roth	1999	254	?	46.9										
/	Körperich	1999	323	?	34.8										
/	Dockendorf	1993	277		137										> 5.45
/	Kranzbach/Bollendorf	1995	275		30.6										
/	Perl Maimühle	1951	172	?	178										
58a	Echternacherbrück	1974	180		460										

Table A.1.4 continued

Borehole reference	Location	li1–3	ko2	ko1	ko	km3	km2	km2S	km2 tot	km1	km	ku	k
/	Roth												
/	Körperich												
/	Dockendorf	> 5.45	5.03	0.81	5.84	61.91	5.25	0.36	5.61	8.43	75.95	8.44	90.23
/	Kranzbach/Bollendorf						> 5.20	22.05	> 27.25	> 3.35	> 30.60		
/	Perl Maimühle												
58a	Echternacherbrück									> 7	> 7	20	> 27

Table A.1.4 continued

Borehole reference	Location	mo	mm	mu	m	so	sm	s	r
/	Roth						> 45.30	> 45.30	
/	Körperich						> 34.80	> 34.80	
/	Dockendorf	> 41			> 41				
/	Kranzbach/Bollendorf								
/	Perl Maimühle	> 51.5	81	32.5	> 165	12	0	12	
58a	Echternacherbrück	59	89	47	195	135	> 101	> 236	

Table A.1.4 continued

Borehole reference	Location	Top dom4	Top dou	Top lo5	Top lm3	Top lm2	Top lm1	Top li4	Top li3	Top li2	Top li1	Top ko2	Top ko1	Top km3
/	Roth													
/	Körperich													
/	Dockendorf											271.55	266.52	265.71
/	Kranzbach/Bollendorf													
/	Perl Maimühle													
58a	Echternacherbrück													

Table A.1.4 continued

Borehole reference	Location	Top km2	Top km2S	Top km1	Top km	Top ku	Top k	Top mo	Top mm	Top mu	Top m
/	Roth										
/	Körperich										
/	Dockendorf	203.8	198.55	198.19	265.71	189.76	271.55	181.32	< 140.32		
/	Kranzbach/Bollendorf		269.8	247.75							
/	Perl Maimühle								120.5	39.5	
58a	Echternacherbrück					171	171	151	92	3	151

Table A.1.4 continued

Borehole reference	Location	Top so	Top sm	Top s	Top r	Top Dev	Source
/	Roth					< 208.7	Dittrich and Norbisrath (2006)
/	Körperich						
/	Dockendorf						Dittrich et al. (1998)
/	Kranzbach/Bollendorf						Dittrich et al. (2005)
/	Perl Maimühle	7		7		–5	LUA; 178 m
58a	Echternacherbrück	–44	–179	–44		< –280	LGB

A.1.5 Geographical coordinates of cross sections across the TLB

Table A.1.5: Geographical coordinates of the cross sections A–F across the Trier–Luxembourg Basin

	Breakpoints	Borehole reference	x	y	d
			[m]	[m]	[m]
Cross section A	Origin Friedhaff/Diekirch		77145	106700	0
	B. Diekirch Réservoir	FR-207-068	79626	102912	4528
	B. Ermsdorf	FC-175-200	83883	99206	10172
	B. Medernach	FR-190-100	84975	97050	12589
	Intersection G		87846	95615	15799
	B. Consdorf Millewues	FR-208-132	91400	93845	19769
	B. Rosswinkel	FR-204-201	94430	92835	22963
	B. Geyershof	FR-208-702	96050	92294	24671
	B. Wasserbillig	TS-192-001	102385	87045	32898
	End Konz		110521	83075	41951
Cross section B	Origin Turelbaach/Mertzig		65351	103089	0
	B. Mertzig	FR-210-055	68095	99615	4427
	B. Michelbuch	FR-203-480	68756	98573	5661
	B. Bissen FCP-502-03	FC-189-100	71558	94672	10464
	B. Bissen F1	TS-208-002	71923	94406	10916
	B. Laaschert	FC-204-100	73205	93679	12389
	B. Mersch	FR-168-101	76083	90858	16419
	Intersection G		78912	88901	19859
	Widdebierg		91475	80230	35124
	End Saarburg		107770	74567	52375
Cross section C	Origin Eschette		58911	99698	0
	B. Platen	FR-179-200	63310	94480	6825
	B. Everlange	FR-186-100	65318	93075	9276
	Intersection G		73685	84877	20989
	B. Steinsel Plateau	TS-208-001	75105	83488	22976
	B. Stafelter	FR-192-107	80430	80433	29115
	B. Schrassig	FR-199-176	85325	75060	36383
	B. Canach	TS-199-001	90385	73220	41767
	End Orscholz		107337	62579	61782
Cross section D	Origin Petit-Nobressart		52952	95065	0
	B. Ell	FR-183-100	55812	92721	3697
	B. Beckerich	FC-197-050	60510	87920	10415
	B. SES Koerich	FR-207-200	63781	82951	16364
	Intersection G		67214	79736	21067
	B. Cessange	FR-037-010	74648	72770	31255
	B. Cloche d'Or	FRE-1-16	76289	71522	33316
	B. F5 Weierfeld	FR-191-125	77993	69311	36108
	B. F2 Tréiergronn	FR-191-112	80545	67080	39498
	B. Mondorf Kind	FR-041-014	88280	62943	48269
	B. Kirsch-les-Sierck	01143X0076/SI-06	95814	56315	58304
	End Kirschnaumen		99534	52117	63913

Coordinates x and y according to the LUREF (Luxembourg Reference Frame), d – distance from the point of origin, B. – borehole .

Table A.1.5 continued

	Breakpoints	Borehole reference	x [m]	y [m]	d [m]
Cross section E	Origin Schockville		50349	93499	0
	Arlon		53581	83628	10387
	B. Rebierg/intersection G	FR-172-010	62020	75610	22027
	B. Dudelange I	FR-182-002	75219	60775	41884
	B. Zoufftgen	01141X0016/F	77830	58291	45488
	B. Sentzich	01142X0004/F	86290	54315	54836
	B. Hunting	01143X0068/SI-07	90404	52913	59182
	End Kerling-les-Sierck		96795	50497	66014
Cross section F	Origin Virton/Latour		33352	69485	0
	B. Latour	225E0189	36616	67804	3672
	Origin old		50680	65232	17969
	B. Longwy/intersection G	00905X0003/S	51211	64972	18561
	B. Hussigny-Godbrange S	01132X0129/S	57671	61835	25742
	B. Audun-le-Tiche Bodenberg	01133X0008/S	63826	57231	33428
	B. Tressange GW1	01133X0052/P1	67059	53261	38548
	B. Thionville St-Michel	01138X0131/G1	73850	49150	46486
	B. Thionville Route Illange	01145X0007/S	80766	46335	53953
	B. Illange	01145X0126/ILL1	81207	43949	56380
	B. Guélange	01382X0017/GUELAN	83706	39186	61759
	B. St. Michel	01387X0037/SM1	95290	31570	75622
	B. Hinckange Le Breuil	01388X0001/HL478	100812	28089	82150
	End Hinckange		101410	27702	82862
Cross section G	Origin Lexy		48925	62724	0
	Origin old		50620	64390	2377
	B. Longwy/intersection F	00905X0003/S	51211	64972	3207
	B. Rebierg/intersection E	FR-172-010	62020	75610	18372
	Intersection D		67214	79736	25006
	Intersection C		73685	84877	33270
	B. Gousselerbierg	FR-199-017	75950	86677	36164
	Intersection B		78912	88901	39868
	Intersection A		87846	95615	51043
	Berdorf		93942	100196	58668
	End Prümtal/Holsthum		98611	105684	65874

A.1.6 Geographical coordinates of Paleozoic outcrop and drill core samples

A.1.6: Coordinates of Paleozoic outcrop and drill core samples.

Sample	Lithotype	Be Formation	Lux Member	Lux Formation	Sampling location	GPS Position Latitude	GPS Position Longitude
E3-001	Shale	E3		Wiltz	To the south of the quarry off Neidhausen, at the wayside	N50 01.264	E6 03.418
E3-002	Shale					N50 01.363	E6 03.437
E3-003	Shale						
E3-005	Sandy shale				In road curve, large outcrop near Drauffelt	N50 01.312	E6 00.103
q-001	Quartzite	q		Berlé	Crossroads Routheck near Drauffelt	N50 01.156	E6 01.398
q-002	Quartzite						
q-003	Quartzite						
E2-001	Quartzitic sandstone	E2		Clervaux	Quarry to the west of Neidhausen	N50 01.524	E6 03.324
E2-002	Siltstone						
E2-004	Siltstone						
E2-007	Siltstone				20 m to the south of the quarry	/	/
E2-008	Siltstone				35 m to the south of the quarry	/	/
E2-010-1	Siltstone				Near crossroads Routheck near Drauffelt, down the way	N50 01.124	E6 01.357
E2-010-2	Siltstone						
E1b-001	Siltstone	E1b		Schuttbourg	Quarry of Consthum	N49 58.562	E6 01.960
E1b-002	Quartzitic sandstone					N49 58.563	E6 01.949
E1b-003	Siltstone					N49 58.562	E6 01.960
E1b-004	Silty slate					N49 58.563	E6 01.949
E1b-005	Quartzitic sandstone					N49 58.569	E6 01.969
E1b-006	Silty slate					N49 58.502	E6 01.841
E1b-007	Siltstone						
E1b-008	Sandstone					N49 58.597	E6 02.175
E1b-009	Sandstone						
E1b-010	Siltstone						
E1b-012	Siltstone						

Latitude and longitude are expressed in degrees and minutes.

A.1.6 continued

Sample	Lithotype		Be		Lux	Sampling location	GPS Position	
			Formation	Member	Formation		Latitude	Longitude
E1a-003	Sandy shale	E1a			Stolzembourg	SEO, Vianden, burden dump near football field	N49 56.739	E6 10.573
E1a-004	Sandy shale							
E1a-005	Sandstone							
E1a-006	Sandy shale							
E1a-007	Sandy shale							
E1a-009	Sandy shale							
E1a-010	Sandy shale							
E1a-011	Quartzitic sandstone							
E1a-013	Sandstone							
Sg3-001	Sandy shale	Sg3/LAR	La Roche		Radelange	Pont Misère, above parking place	N49 52.099	E5 49.947
Sg3-002	Sandy shale							
Sg3-003	Sandy shale					Pont Misère, behind sign of nature trail	N49 52.212	E5 49.936
Sg3-006	Sandy shale					Road from Pont Misère to Boulaide, old quarry above sharp curve	N49 52.335	E5 49.332
Sg3-009	Sandy shale					Road from Lultzhausen to Eschdorf, new road scarp	N49 54.325	E5 53.601
Sg3-010	Sandy shale					Road from Brandenbourg to Landscheid, new road scarp	N49 55.059	E6 07.840
Sg3-011	Sandy shale						N49 55.042	E6 07.851
Sg3-012	Sandy shale						N49 54.997	E6 07.894
Sg3-013	Sandy shale						N49 54.887	E6 08.038
Sg3a-1	Slate	Sg3a/LAR	La Roche		Martelange	Cavern Laura, Haut-Martelange, upper gallery and chamber	N49 49.380	E5 44.940
Sg3a-2	Slate							
Sg3a-3	Slate							
Sg3a-4	Slate							

A.1.6 continued

Sample	Lithotype		Be		Lux	Sampling location	GPS Position	
			Formation	Member	Formation		Latitude	Longitude
VIL-02	Shale	VIL	Villé			Outcrop in the valley to the southeast of Marcouray (near junction of faults)	N50 12.320	E5 33.183
VIL-05	Shale							
VIL-06	Shale							
VIL-08	Sandstone							
VIL-09	Shale							
VIL-10	Sandstone							
VIL-11	Sandy shale							
VIL-12	Sandy shale							
VIL-14	Sandy shale							
Sg1-001	Slate	Sg1/MIR	Mirwart			Abandoned roof slate gallery near old railway station of Schimpach	N49 59.990	E5 49.468
Sg1-002	Slate							
Sg1-003	Slate							
Sg1-005	Quartzitic sandstone					Near old railway station of Schimpach, quarry above the pasture	N49 59.906	E5 49.450
Sg1-007	Silty slate							
Sg1-008	Silty slate					Near old railway station of Schimpach, entry of the lower gallery	N49 59.990	E5 49.468
Sg1-010	Silty slate							
STH-01	Shale	STH	Saint-Hubert			Way scarp to the south of Samrée (near 30° southwest dip in map)	N50 11.877	E5 38.677
STH-03	Shale						N50 11.885	E5 38.565
STH-04	Siltstone					Old quarry to the south of Samrée (near 45° northwest dip in map)	N50 11.979	E5 38.360
STH-05	Siltstone							
STH-07	Quartzitic sandstone							
STH-08	Quartzitic sandstone							
STH-09	Quartzitic sandstone							
STH-10	Siltstone							
STH-11	Sandstone							
STH-13	Sandy siltstone					Rock pile to the east of the large quarry to the northeast of La Roche	N50 11.675	E5 36.054
STH-14	Siltstone							

A.1.6 continued

Sample	Lithotype		Be		Lux	Sampling location	GPS Position	
			Formation	Member	Formation		Latitude	Longitude
OIG-01	Siltstone	OIG	Oignies			Old quarry to the southeast of Dochamps (in map and note), upper level	N50 13.694	E5 38.543
OIG-04	Silty sandstone							
OIG-05	Siltstone							
OIG-07	Sandstone					Old quarry to the southeast of Dochamps (in map and note), lower level	N50 13.707	E5 38.518
OIG-08	Sandstone							
OIG-09	Silty sandstone					Road from La Roche to the motorway E25, above sharp curve in the valley of the stream 'ruisseau du Fond Honnet'	N50 12.532	E5 36.175
OIG-10	Shale							
OIG-12	Shale					Road from La Roche to the motorway E25, in the upper part of the same curve	N50 12.584	E5 36.151
OIG-13	Shale							
FEP-01	Conglomeratic sandstone	FEP	Fépin			To the west of 'Moulin de la Fosse, along the Aisne Stream	N50 15.941	E5 37.642
FEP-02	Conglomeratic sandstone						N50 15.953	E5 37.578
FEP-03	Conglomeratic sandstone							
FEP-04	Conglomeratic sandstone							
FEP-05	Shale					To the west of 'Moulin de la Fosse, along the Aisne Stream, near the rock crest	N50 15.953	E5 37.542
FEP-06	Sandstone						N50 15.953	E5 37.542
FEP-07	Shale						N50 15.953	E5 37.542
BIH-01	Silty slate	BIH	Bihain			To the west of Lierneux in the valley of the Grumont Stream, in the forest of 'Fond d'Oneu, indicated in map	N50 16.850	E5 46.149
BIH-02	Silty slate							
BIH-03	Silty slate							
BIH-04	Silty slate							
BIH-05	Silty slate							
BIH-06	Silty slate							
COL-01	Slate	COL	Ottré	Colanhan		Abandoned quarry to the southeast of Goronne (crest of 'Tier du Mont')	N50 16.635	E5 53.041
COL-02	Slate							
COL-04	Slate							
COL-05	Slate							
PLA-01	Slate	PLA	Ottré	Les Plattes		Quarry near Sart, at the crest of 'Tier dol Preu', indicated in map	N50 16.785	E5 50.505
PLA-02	Slate							
PLA-06	Slate							
PLA-07	Slate							

A.1.6 continued

Sample	Lithotype		Be		Lux	Sampling location	GPS Position	
			Formation	Member	Formation		Latitude	Longitude
MEU-01	Silty slate	MEU	Ottré	Meuville		Quarry to the south of Lierneux, indicated on map	N50 16.531	E5 47.279
MEU-02	Silty slate							
MEU-03	Silty slate							
MEU-06	Sandstone					To the east of the Lienne Stream, near the saw mill	N50 16.879	E5 48.149
MEU-07	Siltstone							
MEU-08	Siltstone							
LIE-01	Sandstone	LIE	Jalhay	Lierneux		Old quarry in the valley of the Lienne Stream near the saw mill to the east of Lierneux	N50 16.666	E5 48.011
LIE-03	Silty slate							
LIE-04	Silty slate							
SPA-01	Silty slate	SPA	Jalhay	Spa		Old quarry just to the east of Pont de Villettes, in the Lienne valley	N50 19.636	E5 45.147
SPA-02	Silty slate							
SPA-06	Quartzitic sandstone					Rock just to the north of Pont de Villettes, well exposed	N50 19.675	E5 44.993
SPA-07	Quartzitic sandstone							
SLW-02	Silty slate	SLW	Jalhay	Solwaster		Rock in the forest above the road from Pont de Villettes to Les trous de Bra, indicated by 50° southwest dip in map	N50 20.082	E5 44.136
SLW-03	Quartzitic sandstone							
SLW-08	Sandstone					Rock just next to the road Pont de Villettes – Les trous de Bra, indicated by 50 ° southwest dip in map	N50 20.057	E5 44.563
GLE-03	Silty slate	GLE	La Gleize			Way near Mâmont (indicated in map), between Fosse and Basse-Bodeux	N50 21.178	E5 50.841
GLE-04	Silty slate							
GLE-05	Silty slate							
VEN-04	Slate	VEN	La Venne			Old quarries to the northnortheast of Amcômont, first overgrown quarry	N50 19.270	E5 48.706
WAN-02	Quartzite	WAN	Wanne			Old quarry in the forest of Farnières (dip/strike indicated in map)	N50 18.780	E5 52.485
WAN-06	Quartzite					Water reservoir in the forest of Farnières	N50 18.764	E5 52.373
WAN-07	Silty slate					Above the water reservoir, at the crossroads	N50 18.770	E5 52.339
WAN-08	Slate					At the wayside, below the crossroads	N50 18.840	E5 52.323
WAN-09	Slate							
WAN-10	Quartzite							

A.1.6 continued

Sample	Lithotype		Be		Lux	Sampling location	GPS Position	
			Formation	Member	Formation		Latitude	Longitude
BEL-01	Sandy shale	BEL	Bellevaux			Near Rochinval, to the south of the entrance, close to the rails	N50 20.328	E5 54.102
BEL-02	Slate							
BEL-03	Slate							
BEL-06	Quartzitic sandstone							
HUR-03	Quartzite	HUR	Hour			Quarry of Hourt, burden dump to the right next to the entrance	N50 18.166	E5 54.693
HUR-05	Quartzite							
HUR-06	Quartzitic sandstone							
HUR-12	Quartzite					At the wayside just to the north of the quarry of Hourt	N50 18.292	E5 54.716
gd-01	Slate	gd	Züsch-Schiefer			Road from Grimburg to Kell am See, outcrop just to the west of Grimburg	N49 37.301	E6 52.703
gd-02	Sandy shale							
gd-06	Quartzite							
War-01	Gneiss	gn	Wartenstein			Wartenstein castle, in front of the castle	N49 48.196	E7 25.856
War-03	Gneiss					Wartenstein castle, at the wayside of the grass-covered way descending into the forest	N49 48.214	E7 25.888
War-04	Mica shist						N49 48.242	E7 25.956
War-05	Quartzite						N49 48.269	E7 25.997
War-07	Gneiss					Wartenstein castle, ascending the way in front of the castle	N49 48.226	E7 25.905
War-08	Gneiss						N49 48.246	E7 25.925
War-09	Quartzitic sandstone						N49 48.246	E7 25.925
War-10	Gneiss						N49 48.196	E7 25.812
War-11	Quartzite						N49 48.196	E7 25.856

A.1.6 continued

Sample	Lithotype		Be		Lux	Sampling location	GPS Position	
			Formation	Member	Formation		Latitude	Longitude
GH350	Quartzite	Dv	Hour			Grand-Halleux borehole, in the Massif of Stavelot, drill cores sampled at the Geological Survey of Belgium	N50 18.664	E5 54.302
GH516	Slate							
GH835	Slate							
GH1453	Slate							
GH2004	Slate							
GH2008	Slate							
GH2021	Quartzite							
GH2315	Slate							
GH2331	Slate							
GH2355	Quatzitic sandstone							
GH2386	Slate	Rn	Wanne/La Venne			Grand-Halleux borehole, in the Massif of Stavelot, drill cores sampled at the Geological Survey of Belgium	N50 18.664	E5 54.302
GH2585	Slate							
GH2600	Quartzite							
GH2728	Slate							
GH3072	Slate							
GH3128	Slate							
GH3216	Quartzite							

A.1.7 Geographical coordinates of Mesozoic outcrop and drill core samples (basin facies)

Table A.1.7: Coordinates of Mesozoic outcrop and drill core samples (basin facies).

Sample	Lithotype	Unit		Depth		Sampling location	Borehole	Reference	GPS Position		Sat.
				from	to				Latitude	Longitude	fluid
Ru2	Calcareous limestone	dom4	Marnes sableuses d'Audun-le-Tiche			Old quarry Weiss-Kaul to the west of Rumelange			N49 27.212	E6 00.600	W
Ru4	Limestone		Calcaire d'Audun-le-Tiche						N49 27.221	E6 00.572	W
Ru6	Limestone								N49 27.221	E6 00.572	W
M9	Limestone	dom3	Calcaire de Haut-Pont			Gielebotter, ca. 5 m below rim of the plateau			N49 32.413	E5 52.687	W
/		dom2	Calcaire d'Ottange			/	/	/	/	/	/
M8	Marlstone	dom1	Marnes micacées			Gielebotter			N49 32.457	E5 52.702	W
M3	Limestone	dou	Minette (calcareous)						N49 32.477	E5 52.864	W
M5	Iron-rich limestone								N49 32.482	E5 52.826	W
M6	Limestone								N49 32.503	E5 52.708	W
/		lo7	Minette			/	/	/	/	/	/
/		lo6	Minette			/	/	/	/	/	/
/		lo5	C. à *Pseudogrammoceras fallaciosum*			/	/	/	/	/	/
Bv2	Marly siltstone	lo4	C. à *Grammoceras striatulum*	26.32	26.45		Belvaux	FR-207-074	N49 30.742	E5 55.541	Iso.
Bv4	Silty marl			31.63	31.74						Iso.
Bv11	Claystone	lo3	Marnes à *Astarte voltzi*	51.24	51.31						Iso.
Bv12	Silty marl			59.75	59.83						Iso.
Bv14	Claystone	lo2	C. à *Hildoceras bifrons*	64.10	64.19		Belvaux	FR-207-079	N49 30.779	E5 55.329	Iso.
Bv16	Claystone	lo1	C. à *Harpoceras falciferum*	76.65	76.70						Iso.
Rb40	Clayey siltstone	lm3b	Macigno (C. à *Pleuroceras spinatum*)	38.88	38.98		Rebierg	FR-172-010	N49 36.891	E5 55.159	Iso.
Rb34	Silty sandstone	lm3a	Faciès sablo-marneux	66.21	66.28						W
Rb35	Marl	lm2	C. à *Amaltheus margaritatus*	117.47	117.55						Iso.
Rb36	Marl	lm2		141.33	141.43						Iso.
/		lm1	Calcaire ocreux			/	/	/	/	/	

Depth in meters. Latitude and longitude in degrees and minutes. Sat. fluid – Saturation fluid, W – water, Iso. – Isooctane, C. – couches, sst. – sandstone, mst. – marlstone, fibr. – fibrous.

Table A.1.7 continued

Sample	Lithotype	Unit		Depth from	to	Sampling location	Borehole	Reference	GPS Position Latitude	Longitude	Sat. fluid
Rb38	Marly siltstone	li4	Marne pauvre en fossiles	197.93	197.99		Rebierg	FR-172-010	N49 36.891	E5 55.159	Iso.
Rb39	Marly limestone	li3	Marnes et calcaires de Strassen	216.11	216.20						W
Kb2	Calcareous sandstone	li2	Grès de Luxembourg	10.51	10.60		Kirchberg	FR-211-136	N49 38.171	E6 10.751	W
Rw2	Marly, calcareous sst.	li2	Grès de Luxembourg	19.90	20.00		Rosswinkel	FR-204-201	N49 46.188	E6 22.106	W
Rw10	Sandstone			55	55.1			FR-204-201			W
Rw13	Marlstone	li1	Marnes d'Elvange	65.25	65.32			FR-204-201			Iso.
Gr6	Sandy marlstone	li1	Marnes d'Elvange	21.23	21.33		Grouft	FR-204-031	N49 42.315	E6 09.115	Iso.
/		ko2	Argiles de Levallois			/	/	/	/	/	
Gr7	Marly sandstone	ko1	Grès de Mortinsart	28.20	28.30		Grouft	FR-204-031	N49 42.315	E6 09.115	Iso.
Gr11	Dolomitic marlstone	km3	Steinmergelkeuper	51.55	51.63						Iso.
Rb5	Clayey marl	km3	Steinmergelkeuper	410.07	410.16		Rebierg	FR-172-010	N49 36.891	E5 55.159	Iso.
Rb16	Anhydrite + fibr. gypsum			383.14	383.25						Iso.
Rb8	Dolomitic sandstone	km2	Rote Gipsmergel	436.09	436.22						W
Rb9	Marl			442.62	442.73						Iso.
Ki5	Silty micaceous sst.	km2S	Schilfsandstein	/	/	Outcrop profile Kinett, to the east of Moutfort			N49 34.789	E6 15.987	W
Wb1	Clayey marl	km1	Pseudomorphosenkeuper	52.76	52.82		Wasserbillig	TS-192-001	N49 43.050	N6 28.712	Iso.
Wb7	Silty, dolomitic mst.	ku	Lettenkeuper	70.65	70.72						Iso.
/		ku2	Grenzdolomit			/	/	/	/	/	
/		ku1	Bunte Mergel			/	/	/	/	/	
/		ku1α	Basisschichten			/	/	/	/	/	

Table A.1.7 continued

Sample	Lithotype	Unit		Depth from	Depth to	Sampling location	Borehole	Reference	GPS Position Latitude	GPS Position Longitude	Sat. fluid
/		mo2	Ceratitenschichten			/	/	/	/	/	
Wb8	Dolomite	mo1	Trochitenschichten	111.00	111.09		Wasserbillig	TS-192-001	N49 43.050	N6 28.712	W
Wb9	Dolomitic siltstone	mo1		114.22	114.33						W
Wb10	Dolomitic marlstone	mo1		116.47	116.57						W
Wb11	Marly dolomite	mo1		120.89	121.00						W
Wb12	Dolomite	mo1		126.90	127.00						W
Wb13	Marly dolomite	mo1		130.82	130.93						W
/		mm2	Linguladolomit			/	/	/	/	/	
Wb15	Marlstone	mm1	Gipsmergel	150.14	150.22		Wasserbillig	TS-192-001	N49 43.050	N6 28.712	Iso.
/		mu2	Orbicularisschichten			/	/	/	/	/	
/		mu1	Muschelsandstein			/	/	/	/	/	
Rd14	Dolomitic, sandy mst.	mu	Muschelsandstein	87.64	87.73		Reisdorf	FR-207-122	N49 52.120	E6 16.539	W
Rd17	Dolomitic marlstone			60.08	60.18						Iso.
Rd18	Marly dolomite			56.00	56.15						W
/		so2	Voltziensandstein			/	/	/	/	/	
Rd1	Dolomitic sandstone	so1	Zwischenschichten	155.70	155.77		Reisdorf	FR-207-122	N49 52.120	E6 16.539	W
Rd4	Dolomitic sandstone			142.66	142.76						W
Rd12	Silty claystone			100.07	100.14						Iso.
Bi2	Sandstone (soft)	sm	Hauptbuntsandstein	/	/	Above the Erlenhof, in the forest above the rock at the side of the road					W
Bi5	Sst. (coarse, gravel)			/	/	Descending the small valley down to the road					W

Table A.1.7 continued

Sample	Lithotype	Unit		Depth		Sampling location	Borehole	Reference	GPS Position		Sat.
				from	to				Latitude	Longitude	fluid
/		mo2	Ceratitenschichten			/	/	/	/	/	
Wb8	Dolomite	mo1	Trochitenschichten	111.00	111.09		Wasserbillig	TS-192-001	N49 43.050	N6 28.712	W
Wb9	Dolomitic siltstone	mo1		114.22	114.33						W
Wb10	Dolomitic marlstone	mo1		116.47	116.57						W
Wb11	Marly dolomite	mo1		120.89	121.00						W
Wb12	Dolomite	mo1		126.90	127.00						W
Wb13	Marly dolomite	mo1		130.82	130.93						W
/		mm2	Linguladolomit			/	/	/	/	/	
Wb15	Marlstone	mm1	Gipsmergel	150.14	150.22		Wasserbillig	TS-192-001	N49 43.050	N6 28.712	Iso.
/		mu2	Orbicularisschichten			/	/	/	/	/	
/		mu1	Muschelsandstein			/	/	/	/	/	
Rd14	Dolomitic, sandy mst.	mu	Muschelsandstein	87.64	87.73		Reisdorf	FR-207-122	N49 52.120	E6 16.539	W
Rd17	Dolomitic marlstone			60.08	60.18						Iso.
Rd18	Marly dolomite			56.00	56.15						W
/		so2	Voltziensandstein			/	/	/	/	/	
Rd1	Dolomitic sandstone	so1	Zwischenschichten	155.70	155.77		Reisdorf	FR-207-122	N49 52.120	E6 16.539	W
Rd4	Dolomitic sandstone			142.66	142.76						W
Rd12	Silty claystone			100.07	100.14						Iso.
Bi2	Sandstone (soft)	sm	Hauptbuntsandstein	/	/	Above the Erlenhof, in the forest above the rock at the side of the road					W
Bi5	Sst. (coarse, gravel)			/	/	Descending the small valley down to the road					W

A.1.8 Geographical coordinates of Mesozoic drill core samples (intermediate between margin and basin facies)

Table A.1.8: Coordinates of Mesozoic drill core samples (intermediate between margin and basin facies).

Sample	Lithotype	Unit		Depth		Sampling location	Borehole	Reference	GPS Position		Sat.
				from	to				Latitude	Longitude	fluid
Rb12	Sandy marlstone	km1	Pseudomorphosenkeuper	487.79	487.92		Rebierg	FR-172-010	N49 36.891	E5 55.159	W
Rb17	Dolomite (marly)			506.60	506.70						W
Rb19	Sandy, dolomitic congl.			521.00	521.11						W
Rb10	Dolomitic sandstone			461.90	461.99						Iso.
Rb11	Marly sandstone			475.23	475.32						Iso.
Rb13	Silty marl			502.90	503.00						Iso.
Me2	Silty, dolomitic mst.	mm	Graue Gipsmergel	133.31	133.40		Mersch	FR-168-101	N49 45.132	E6 6.826	Iso.
Me6	Dolomitic marlstone			146.04	146.12						Iso.
Me7	Silty sandstone			148.34	148.40						Iso.
Me8	Anhydrite			155.27	155.38						Iso.
Me11	Silty sandstone			159.35	159.40						Iso.
Me12	Silty marl			160.38	160.44						Iso.
Me13	Silty marl			162.59	162.68						Iso.
Me14	Silty marl			165.58	165.67						Iso.
Me15	Silty marl			168.20	168.32						Iso.

Depth in meters. Latitude and Longitude in degrees and minutes. Sat. fluid – Saturation fluid, W – water, Iso. – Isooctane, congl. – conglomerate, mst. – marlstone.

A.1.9 Geographical coordinates of Mesozoic drill core samples (margin facies)

Table A.1.9: Coordinates of Mesozoic drill core samples (margin facies).

Sample	Lithotype	Unit		Depth		Sampling location	Borehole	Reference	GPS Position		Sat.
				from	to				Latitude	Longitude	fluid
El3	Clayey sandstone	km1	Pseudomorphosenkeuper	5.43	5.55		Ell	FR-183-100	N49 46.108	E5 49.942	Iso.
Ev1	Sandy, dolomitic mst.	ku	Lettenkeuper	6.88	6.98		Everlange	FR-186-100	N49 57.858	E5 46.318	Iso.
Ev3	Sandy, dolomitic marl			14.88	15.00						Iso.
Rb21	Silty marlstone	ku	Lettenkeuper	559.03	559.12		Rebierg	FR-172-010	N49 36.891	E5 55.159	Iso.
Id1	Dolomitic sandstone	mos	Gilsdorfer Sandstein	1.80	1.95	Sandstone bridge in Ingeldorf, FR-206-093					W
Rb24	Marly dolomite	mo	Oberer Muschelkalk	578.32	578.41		Rebierg	FR-172-010	N49 36.891	E5 55.159	W
Rb25	Marly, sandy dolomite			584.27	584.42						W
Ev5	Dolomitic sandstone	mo	Oberer Muschelkalk	18.67	18.75		Everlange	FR-186-100	N49 57.858	E5 46.318	W
Ev9	Sandstone	mg	Grobklastischer Muschelkalk	35.23	35.33		Everlange	FR-186-100	N49 57.858	E5 46.318	W
Ev11	Sandy siltstone			51.59	51.67						Iso.
Ev13	Dolomitic sandstone	mu	Muschelsandstein	59.60	59.69						W
Ev19	Marly sandstone	so	Oberer Buntsandstein	116.55	116.64		Everlange	FR-186-100	N49 57.858	E5 46.318	Iso.
Ev24	Sst. (conglomeratic)			140.25	140.35						W
Ev25	Sandy, dolomitic congl.			142.00	142.14						W

Depth in meters. Latitude and Longitude in degrees and minutes. Sat. fluid – Saturation fluid, W – water, Iso. – Isooctane, mst. – marlstone, sst. – sandstone, congl. – conglomerate.

A.1.10 Lithological composition of Mesozoic units (basin facies)

Table A.1.10 Lithological composition of Mesozoic units (basin facies) based on geological maps and boreholes.

Unit	Lithology	Reference	Sample	Unit	Lithotype	Composition [%]						
dom4b	Sandy marlstone + limest.	Map Esch/Alzette	Ru2	dom4b	Calcareous marlstone							100
dom4a	Bioclastic limestone	Map Esch/Alzette	Ru6	dom4a	Limestone							80
	Reef limestone (corals)		Ru4	dom4a	Coral							20
dom3	Sandy limestone	Map Esch/Alzette	M9	dom3	Limestone							100
dom2	Limestone	Map Esch/Alzette	M9	dom3	Limestone							70
	Marlstone		M8	dom1	Calc. marlstone							30
dom1	Marlstone	Map Esch/Alzette	M8	dom1	Calcareous marlstone							10
	Marl		Bv4	lo4	Silty marl							90
lo6–7 + dou	Iron-rich limest. + calc. sst.	Map Esch/Alzette	M3	dou	Limestone							50
			M6	dou	Limestone							
	Iron-rich + marly sst.		M5	dou	Iron-rich limestone							50
						FR-207-074	FR-207-079	FR-191-133	FR-182-002			AM
						Belvaux	Belvaux	Sanem	Obercorn			all
lo5	Marl	Map Esch/Alzette	Bv4	lo4	Silty marl							100
lo4	Sandy marl + sandstone	Map Esch/Alzette	Bv2	lo4	Marly siltstone	45			54			50
			Bv4	lo4	Silty marl	55			46			50
lo3	Sandy marl	Map Esch/Alzette	Bv11	lo3	Claystone	83	74		91			83
			Bv12	lo3	Silty marl	17	26		9			17
lo2	Marly claystone	Map Esch/Alzette	Bv14	lo2	Claystone	/	100		100			100
			Bv16	lo1	Claystone							
lo1	Marly claystone	Map Esch/Alzette	Bv14	lo2	Claystone	/	100	100	100			100
			Bv16	lo1	Claystone							
						FR-172-010	FR-182-005					AM
						Rebierg	Esch					all
lm3b	Marly sandstone	Map Esch/Alzette	Rb34	lm3a	Silty sandstone	19						19
(NW-facies)	+ sandy claystone		Rb40	lm3b	Clayey siltstone	81						81
lm3a	Clayey sandstone	Map Esch/Alzette	Rb34	lm3a	Silty sandstone	2						2
(NW-facies)			Rb35	lm2	Marl	98						98
			Rb36	lm2	Marl							
lm3	Marly, sandy claystone	Map Esch/Alzette	Rb34	lm3a	Silty sandstone	/	11					11
(SE-facies)			Rb35	lm2	Marl	/	89					89
			Rb36	lm2	Marl							
			Rb40	lm3b	Clayey siltstone							

Limest. – limestone, calc. – calcareous, sst. – sandstone, marlst. – marlstone, AM – arithmetic mean.

Table A.1.10 continued

lm2	Clayey marl	Map Esch/Alzette	Rb35	lm2	Marl						100
			Rb36	lm2	Marl						
						FR-172-010	FR-191-094	FR-191-125	FR-191-112	FR-191-113	AM
						Rebierg	Eilbur	Weierfeld	Treiergronn	Treiergronn	all
lm1	Limestone	Map Remich + Grevenmacher	Rb39	li3	Marly limestone	0	36	18	45	13	23
	Marl		Rb35	lm2	Marl	100	64	82	55	87	77
			Rb36	lm2	Marl						
						FR-172-010	FR-191-094	FR-191-125	FR-191-112	FR-191-012	AM
						Rebierg	Eilbur	Weierfeld	Treiergronn	Haebicht	all
li4	Clayey, silty marl	Map Remich + Grevenmacher	Rb38	li4	Marly siltstone	96	100	40	100	100	87
	Limestone		Rb39	li3	Marly limestone	4	0	60	0	0	13
						FR-172-010	FR-191-094	FR-191-112	FR-191-012		AM
						Rebierg	Eilbur	Treiergronn	Haebicht		all
li3	Marlstone	Maps Remich, Grevenmacher, Echternach, Beaufort, Mersch, Redange	Rw13	li1	Marlstone	70	52	56	57		59
	Limestone		Rb39	li3	Marly limestone	30	48	44	43		41
						Fr-172-010	FR-204-201	FR-190-100	FR-165-506		AM
						Rebierg	Consdorf Rw	Medernach	Rte du Nord		all
li2	Sandstone	Maps Remich, Grevenmacher, Echternach, Beaufort, Mersch, Redange	Rw10	li2	Sandstone	64	26	42	47		45
	Calcareous sandstone		Kb2	li2	Calcareous sst.	36	74	58	53		55
			Rw2	li2	Marly, calc. sst.						
						FR-172-010	FR-208-006	FR-192-107	FR-165-504	FR-195-114	AM
						Rebierg	Kirchberg	Stafelter	Rte du Nord	Rte du Nord	all
li1	Marlstone	Maps Remich, Grevenmacher, Echternach, Beaufort, Mersch, Redange	Rw13	li1	Marlstone	66	49	46	20	47	46
	Sandy marlstone		Gr6	li1	Sandy marlstone	25	29	11	43	42	30
	Limestone		Rb39	li3	Marly limestone	9	22	44	37	11	24
						FR-172-010	FR-208-006	FR-198-008	FR-195-115	FR-195-705	AM
						Rebierg	Kirchberg	Gousselerbierg	Rte du Nord	Markusbierg	all
ko	Claystone	Maps Remich, Grevenmacher, Echternach, Beaufort, Mersch, Redange	Rw13	li1	Marlstone	48	100	30	39	51	42
	Clayey marl		Rb5	km3	Clayey marl	0	0	24	44	33	25
			Rb9	km2	Marl						
	Sandstone + conglomerate		Gr7	ko1	Marly sandstone	52	0	46	17	16	33

Table A.1.10 continued

						FR-172-010 Rebierg	FR-208-006 Kirchberg	FR-198-008 Gousselerbierg	FR-195-115 Rte du Nord	AM all
km3	Dolomitic marlstone	Maps Remich, Grevenmacher, Echternach, Beaufort, Mersch, Redange	Gr11	km3	Dolomitic marlstone	43	48	39	50	45
	Marl		Rb5	km3	Clayey marl	49	39	39	31	39
	Anhydrite + gypsum		Rb16	km3	Anhydrite + fibrous gypsum	8	10	12	13	11
	Dolomite		Rb17	km1	Dolomite	0	3	10	6	5
						FR-172-010 Rebierg				
km2	Clayey marl	Maps Remich, Grevenmacher, Echternach, Beaufort, Mersch, Redange	Rb9	km2	Marl	89				89
	Gypsum		Rb16	km3	Anhydrite + fibrous gypsum	0				0
	Sandstone		Rb8	km2	Dolomitic sandstone	11				11
km2S	Sandstone	Maps Remich, Grevenmacher, Echternach, Beaufort	Ki5	km2S	Silty, micaceous sandstone					90
	Claystone		Rb9	km2	Marl					10
						TS-192-001 Wasserbillig	FR-177-100 Waldbredimus	FR-039-011 Echternach F		AM all
km1	Clayey marl	Maps Remich, Grevenmacher, Echternach, Beaufort	Wb1	km1	Clayey marl	2	11	0		4
	Marl		Rb13	km1	Silty marl	26	21	43		30
	Sandstone		Rb10	km1	Dolomitic sandstone	1	9	7		6
			Rb17	km1	Dolomite					
			Rb16	km3	Anhydrite + gypsum					
	Dolomitic marlstone		Wb7	ku	Silty, dolomitic marlstone	71	59	49		60
						TS-192-001 Wasserbillig	FR-177-100 Waldbredimus	FR-195-100 Waldbredimus	FC-175-200 Ermsdorf	AM all
ku	Dolomite	Maps Remich, Grevenmacher, Echternach, Beaufort	Rb17	km1	Dolomite	21	0	6	0	7
	Marl		Wb1	km1	Clayey marl	19	45	40	53	39
	Marlstone		Wb7	ku	Silty, dolomitic marlstone	60	55	54	47	54

Table A.1.10 continued

						TS-191-001 Wasserbillig	FR-177-100 Waldbredimus	FC-175-200 Ermsdorf	AM all
mo2	Marlstone	Maps Remich, Grevenmacher, Echternach, Beaufort	Wb15	mm1	Marl	10	0	0	5
	Dolomite		Wb8	mo1	Dolomite	16	30	39	23
			Wb12	mo1	Dolomite				
	Dolomitic siltstone/marlst.		Wb9	mo1	Dolomitic siltstone	25	0	30	13
			Wb10	mo1	Dolomitic marlstone				
	Marly dolomite		Wb11	mo1	Marly dolomite	49	70	30	59
			Wb13	mo1	Marly dolomite				
mo1	Dolomite	Maps Remich, Grevenmacher, Echternach, Beaufort	Wb8	mo1	Dolomite	49	55	0	52
			Wb12	mo1	Dolomite				
	Dolomitic siltstone/marlst.		Wb9	mo1	Dolomitic siltstone	1	6	0	3
			Wb10	mo1	Dolomitic marlstone				
	Marly dolomite		Wb11	mo1	Marly dolomite	50	39	100	45
			Wb13	mo1	Marly dolomite				
						TS-192-001 Wasserbillig	FR-041-014 M. Kind	FR-039-011 Echternach F	AM all
mm2	Marlstone	Maps Remich, Grevenmacher, Echternach, Beaufort	Me2	mm1	Silty dolomitic marlstone	58	49	92	67
			Me6	mm1	Dolomitic marlstone				
			Wb15	mm1	Dolomitic marlstone				
	Dolomite		Wb8	mo1	Dolomite	42	51	8	33
			Wb12	mo1	Dolomite				
mm1	Marl (gypsum-rich)	Maps Remich, Grevenmacher, Echternach, Beaufort, (Mersch)	Me12	mm1	Silty marl	/	56	34	45
			Me13	mm1	Silty marl				
			Me14	mm1	Silty marl				
			Me15	mm1	Silty marl				
	Dolomitic marlstone		Me2	mm1	Silty dolomitic marlstone	/	13	42	27
			Me6	mm1	Dolomitic marlstone				
			Wb15	mm1	Dolomitic marlstone				
	Dolomite		Wb8	mo1	Dolomite	/	5	0	3
			Wb12	mo1	Dolomite				
	Sandstone		Me7	mm1	Silty sandstone	/	13	13	13
	Anhydrite		Me8	mm1	Anhydrite	/	13	11	12

Table A.1.10 continued

						FR-207-122	TS-166-001	AM
						Reisdorf	Wormeldange	all
mu2	Dolomite	Maps Remich, Grevenmacher, Echternach, Beaufort	Rd18	mu	Marly dolomite	23	17	20
	Marlstone		Rd17	mu	Dolomitic clay-/marlstone	60	50	55
	Sandy marlstone		Rd14	mu	Dolomitic, sandy marlst.	17	33	25
mu1	Dolomite	Maps Remich, Grevenmacher, Echternach, Beaufort	Rd18	mu	Marly dolomite	3	0	2
	Marlstone		Rd17	mu	Dolomitic clay-/marlstone	36	27	31
	Sandy marlstone		Rd14	mu	Dolomitic, sandy marlst.	61	73	67
						FR-207-122	TS-166-001	AM
						Reisdorf	Wormeldange	all
so2	Sandstone	Map Echternach + Beaufort	Rd1	so1	Dolomitic sandstone	32	60	46
			Rd4	so1	Dolomitic sandstone			
	Claystone		Rd12	so1	Clayey siltstone	68	40	54
so1	Dolomitic sandstone	Map Echternach + Beaufort	Rd1	so1	Dolomitic sandstone	74	67	71
			Rd4	so1	Dolomitic sandstone			
	Clayey sst./sandy claystone		Rd12	so1	Clayey siltstone	26	33	29
						FR-179-100	FR-041-014	AM
						M. Lucius	M. Kind	all
sm		Mondorf	Bi2	sm	Sandstone (soft)	65	98	81
		Mondorf	Bi5	sm	Sandstone (coarse, gravel)	22	2	12
		Mondorf	Rd12	so1	Clayey siltstone	13	0	7

A.1.11 Lithological composition of Mesozoic units (margin facies)

Table A.1.11 Lithological composition of Mesozoic units (margin facies) based on geological maps and boreholes.

Unit	Lithology	Reference	Sample	Unit	Lithotype	Composition [%]					
						FC-204-100					
						Laaschert					
km25 + km2	Sandy marlstone	Map Rédange + Mersch	Rb12	km1	Sandy marlstone	47					47
			Rb11	km1	Marly sandstone						
			El3	km1	Clayey sandstone						
	Dolomitic sandstone		Rb10	km1	Dolomitic sandstone	18					18
			Rb8	km2	Dolomitic sandstone						
	Sandy marl		Rb13	km1	Silty marl	35					35
						FR-172-010	FC-204-100	FR-168-101			AM
						Rebierg	Laaschert	Mersch			all
km1	Sandy marlstone	Map Rédange + Mersch	Rb12	km1	Sandy marlstone	34	49	71			51
			Rb11	km1	Marly sandstone						
			El3	km1	Clayey sandstone						
	Conglomeratic dolomite		Rb17	km1	Dolomite (marly)	7	0	0			2
	Dolomitic + sandy conglomerate		Rb19	km1	Sandy, dolomitic conglomerate	9	29	4			14
	Marly sandstone		Rb10	km1	Dolomitic sandstone	31	22	18			24
	Marl		Rb13	km1	Silty marl	19	0	8			9
						FR-172-010	FR-186-100	FC-204-100	FR-168-101		AM
						Rebierg	Everlange	Laaschert	Mersch		all
ku	Siltstone	Map Rédange + Mersch	Rb21	ku	Silty marlstone	0	47	15	22		21
	Marl + claystone		Ev1	ku	Sandy, dolomitic marlstone	13	53	15	12		23
			Ev3	mos	Sandy, dolomitic marl						
	Sandstone		Rb12	km1	Sandy marlstone	87	0	69	35		48
			Rb11	km1	Marly sandstone						
			El3	km1	Clayey sandstone						
	Sandy dolomite		Rb17	km1	Dolomite (marly)	0	0	0	32		8

AM – arithmetic mean.

Table A.1.11 continued

						FR-172-010	FR-186-100			AM
						Rebierg	Everlange			all
mo(s)	Marly, sandy dolomite	Map Rédange + Mersch	Rb24	mo	Marly dolomite	49	0			24
(margin facies)			Rb25	mo	Marly, sandy dolomite	29	0			15
	Dolomitic sandstone		Ev5	mo	Dolomitic sandstone	0	46			23
			Id1	mos	Dolomitic sandstone	22	0			11
	Sandstone + siltstone		Ev9	mg	Sandstone	0	21			11
			Ev11	mg	Sandy siltstone	0	12			6
			Me11	mm1	Silty sandstone	0	20			10
								FC-204-100	FR-168-101	AM
								Laaschert	Mersch	all
mo(s)	Dolomitic sandstone	Map Rédange + Mersch	Id1	mos	Dolomitic sandstone			10	12	11
(margin/basin facies)	Marlstone		Wb15	mm1	Marlstone			0	10	5
	Dolomite		Wb8	mo1	Dolomite			30	7	19
			Wb12	mo1	Dolomite					
	Dolomitic siltstone/marlstone		Wb9	mo1	Dolomitic siltstone			38	71	54
			Wb10	mo1	Dolomitic marlstone					
	Marly dolomite		Wb11	mo1	Marly dolomite			22	0	11
			Wb13	mo1	Marly dolomite					
						FR-172-010	FR-186-100			AM
						Rebierg	Everlange			all
mg	Sandstone/conglomerate	Map Rédange + Mersch	Ev9	mg	Sandstone	18	37			27
(margin facies)	Siltstone		Ev11	mg	Sandy siltstone	0	22			11
			Me11	mm1	Silty sandstone	0	23			12
	Dolomite		Rd18	mu	Marly dolomite	6	1			4
	Clay-/marlstone		Me12	mm1	Silty marl	77	16			46
			Me13	mm1	Silty marl					
			Me14	mm1	Silty marl					
			Me15	mm1	Silty marl					

Table A.1.11 continued

								FR-168-101	
								Mersch	
mm	Marl (gypsum-rich)	Map Rédange + Mersch	Me12	mm1	Silty marl			70	70
(margin/basin facies)			Me13	mm1	Silty marl				
			Me14	mm1	Silty marl				
			Me15	mm1	Silty marl				
	Dolomite		Wb8	mo1	Dolomite			5	5
			Wb12	mo1	Dolomite				
	Dolomitic marlstone		Me2	mm1	Silty, dolomitic marlstone			21	21
			Me6	mm1	Dolomitic marlstone				
			Me7	mm1	Silty sandstone				
	Anhydrite		Me8	mm1	Anhydrite			4	4
						FR-172-010	FR-186-100	FR-168-101	AM
						Rebierg	Everlange	Mersch	all
mu	Sandy/marly dolomite	Map Rédange	Rd18	mu	Marly dolomite	0	9	0	3
	Sandstone		Ev13	mu	Dolomitic sandstone	0	17	0	6
	Sandy marlstone		Rd14	mu	Dolomitic, sandy marlstone	0	0	10	3
	Dolomitic marlstone		Rd17	mu	Dolomitic marlstone	0	0	32	11
	Claystone		Rd12	so1	Silty claystone	100	52	0	51
	Siltstone		Ev11	mg	Sandy siltstone	0	22	58	26
						FR-172-010	FR-186-100	FR-168-101	AM
						Rebierg	Everlange	Mersch	all
so2	Dolomitic sandstone	Map Rédange	Rd1	so1	Dolomitic sandstone	0	0	68	23
			Rd4	so1	Dolomitic sandstone				
	Sandstone		Ev19	so	Marly sandstone	39	0	32	24
	Claystone + sandy siltstone		Rd12	so1	Silty claystone	61	100	0	54
so1	Conglomerate	Map Rédange	Ev25	so	Sandy, dolomitic conglomerate	10	27	37	25
	Conglomeratic sandstone		Ev24	so	Sandstone (conglomeratic)	48	33	46	43
			Rd1	so1	Sandstone (dolomitic)				
			Rd4	so1	Sandstone (dolomitic)				
	Marly sandstone		Ev19	so	Marly sandstone	23	12	17	17
	Claystone + siltstone		Rd12	so1	Silty claystone	18	28	0	15

A.1.12 Summary of TC estimation of the Mesozoic formations (basin facies)

Table A.1.12: Summary of thermal-conductivity estimation of the Mesozoic formations (basin facies).

Unit or group	Borehole ref.	Location	Fm. $\lambda_\perp$					
					AM		1σ	
			Dry	Sat.	Dry	Sat.	Dry	Sat.
			[W m^{-1} K^{-1}]		[W m^{-1} K^{-1}]			
dom1–4			2.1	2.5	2.1	2.5		
lo6–7 + dou			1.5	2.2	1.5	2.2		
lo1–5 (comb.)	FR-207-074	Belvaux	1.2	2.2	1.2	2.2		
	FR-207-079	Belvaux						
	Fr-191-133	Sanem						
	FR-182-002	Obercorn						
lm3a + b	FR-172-010	Rebierg	1.3	2.0	1.5	2.1	0.3	0.1
	FR-191-133	Sanem	1.7	2.2				
lm3	FR-182-005	Esch	1.2	1.8	1.2	1.9	0.0	0.1
	FR-175-054	Budersberg	1.2	1.9				
lm2	FR-172-010	Rebierg	1.2	2.1	1.2	2.1		
lm1	FR-172-010	Rebierg	1.2	2.1	1.4	2.1	0.1	0.0
	FR-191-094	Eilbur	1.5	2.1				
	FR-191-125	Weierfeld	1.4	2.1				
	FR-191-112	Treiergronn	1.5	2.1				
	FR-191-113	Treiergronn	1.3	2.1				
li4	FR-172-010	Rebierg	1.7	2.3	1.7	2.3	0.1	0.0
	FR-191-094	Eilbur	1.6	2.3				
	FR-191-125	Weierfeld	1.8	2.2				
	FR-191-112	Treiergronn	1.6	2.3				
	FR-191-012	Haebicht	1.6	2.3				
li3	FR-172-010	Rebierg	1.5	1.7	1.6	1.8	0.1	0.1
	FR-191-094	Eilbur	1.6	1.8				
	FR-191-112	Treiergronn	1.6	1.8				
	FR-191-012	Haebicht	1.6	1.8				
li2	FR-172-010	Rebierg	2.1	3.7	2.3	3.6	0.2	0.1
	FR-204-201	Consdorf Rosswinkel	2.5	3.5				
	FR-190-100	Medernach	2.3	3.6				
	FR-165-506	Route du Nord	2.3	3.6				
li1	FR-172-010	Rebierg	1.4	1.7	1.5	1.8	0.1	0.1
	FR-208-006	Kirchberg	1.4	1.8				
	FR-192-107	Stafelter	1.6	1.9				
	FR-165-504	Route du Nord	1.6	2.0				
	FR-195-114	Route du Nord	1.4	1.8				

Borehole ref. – borehole reference, Fm. – Formation, $\lambda_\perp$ – thermal conductivity perpendicular to bedding, AM – arithmetic mean, σ – standard deviation, Dry and Sat. – dry and water-saturated conditions, respectively, comb. – thermal conductivity combined from several boreholes, ext. – lithology of the lower part of the borehole extrapolated by postulating a km3 thickness of 60 to 65 m.

Table A.1.12 continued

Unit or group	Borehole ref.	Location	Fm. $\lambda_\perp$					
					AM		1σ	
			Dry	Sat.	Dry	Sat.	Dry	Sat.
			[W m^{-1} K^{-1}]		[W m^{-1} K^{-1}]			
ko	FR-172-010	Rebierg	1.5	2.1	1.6	2.0	0.2	0.3
	FR-208-006	Kirchberg	1.3	1.5				
	FR-198-008	T Gousselerbierg	1.7	2.3				
	FR-195-115	Route du Nord	1.7	2.1				
	FR-195-705	T Markusbierg	1.6	2.0				
km3	FR-172-010	Rebierg	2.0	2.4	2.0	2.4	0.1	0.1
	FR-208-006	KA Kirchberg (ext.)	1.9	2.4				
	FR-198-008	T Gousselerbierg (ext.)	2.1	2.5				
	FR-195-115	Route du Nord (ext.)	1.9	2.4				
	FR-195-705	T Markusbierg (ext.)	1.9	2.5				
km2	FR-172-010	Rebierg	1.8	2.3	1.8	2.3		
km2S		Kinett profile	1.0	1.9	1.0	1.9		
km1	TS-192-001	Wasserbillig	1.5	2.1	1.6	2.2	0.1	0.1
	FR-177-100	Waldbredimus	1.6	2.2				
	FR-039-011	Echternach Felsmühle	1.7	2.3				
ku	TS-192-001	Wasserbillig	1.7	2.2	1.4	2.0	0.2	0.1
	FR-177-100	Waldbredimus	1.3	1.9				
	FR-195-100	Waldbredimus	1.4	2.0				
	FC-175-200	Ermsdorf	1.3	1.9				
mo	TS-192-001	Wasserbillig	3.7	3.8	3.5	3.7	0.3	0.2
	FR-177-100	Waldbredimus	3.8	3.9				
	FC-175-200	Ermsdorf	3.6	3.7				
	FC-204-100	Bissen Laaschert	3.5	3.7				
	FR-168-101	Mersch	3.0	3.4				
mm	FR-041-014	Mondorf Kind	2.4	2.8	2.3	2.6	0.2	0.3
	FR-039-011	Echternach Felsmühle	2.4	2.7				
	FR-168-101	Mersch	2.0	2.3				
mu	FR-207-122	Reisdorf	2.4	2.9	2.2	2.8	0.3	0.2
	TS-166-001	Wormeldange	2.0	2.6				
so	FR-207-122	Reisdorf	1.6	2.8	1.6	2.8	0.0	0.0
	TS-166-001	Wormeldange	1.6	2.8				
sm	FR-179-100	Mondorf Lucius	2.0	3.1	2.0	3.1	0.1	0.0
	FR-041-014	Mondorf Kind	1.9	3.1				

A.1.13 Summary of TC estimation of the Mesozoic formations (margin facies)

Table A.1.13: Summary of thermal-conductivity estimation of the Mesozoic formations (margin facies).

Unit or group	Borehole ref.	Location	Fm. $\lambda_{\perp}$					
					AM		1σ	
			Dry	Sat.	Dry	Sat.	Dry	Sat.
			[W m^{-1} K^{-1}]		[W m^{-1} K^{-1}]			
km2S	FC-204-100	Bissen Laaschert	2.2	2.9	2.2	2.9		
km1	FR-172-010	Rebierg	2.6	3.2	2.6	3.3	0.3	0.2
	FC-204-100	Bissen Laaschert	2.9	3.5				
	FR-168-101	Mersch	2.4	3.1				
ku	FR-172-010	Rebierg	2.3	3.0	2.4	3.1	0.2	0.2
	FR-186-100	Everlange	2.3	3.3				
	FC-204-100	Bissen Laaschert	2.3	3.0				
	FR-168-101	Mersch	2.7	3.2				
mo	FR-172-010	Rebierg	3.8	4.4	3.0	4.0	1.1	0.6
	FR-186-100	Everlange	2.2	3.5				
mg	FR-172-010	Rebierg	1.7	2.3	1.7	2.6	0.0	0.4
	FR-186-100	Everlange	1.7	2.8				
mu	FR-172-010	Rebierg	1.6	2.4	1.7	2.6	0.1	0.2
	FR-186-100	Everlange	1.8	2.7				
	FR-168-101	Mersch	1.7	2.6				
so	FR-172-010	Rebierg	1.7	2.8	1.9	2.9	0.2	0.2
	FR-186-100	Everlange	1.9	2.8				
	FR-168-101	Mersch	2.0	3.1				

Borehole ref. – borehole reference, Fm. – Formation, $\lambda_{\perp}$ – thermal conductivity perpendicular to bedding, AM – arithmetic mean, σ – standard deviation, Dry and Sat. – dry and water-saturated conditions, respectively.

A.1.14 Thermal conductivity and density of the Wartenstein Gneiss

Table A.1.14: Thermal conductivity and density of the Wartenstein Gneiss.

Formation	Lithology	Vol.	Sample	Lithotype	λ_{dry}						Litho. λ_{dry}	Fm. λ_{dry}	TF	λ_{sat} calc.	Litho. λ_{sat}	Fm. λ_{sat}	Density		
					O	⊥	//	a	b	AM	AM	AM			AM	AM	Sample	Litho.	Fm.
		[%]			[W m^{-1}K^{-1}]						[W m^{-1}K^{-1}]	[W m^{-1}K^{-1}]		[W m^{-1}K^{-1}]	[W m^{-1}K^{-1}]	[W m^{-1}K^{-1}]	[10^3 kg m^{-3}]		
War	Gneiss	85	War-01	Gneiss	L		3.17	2.92	2.81	2.97	2.9	3.0	1.20	3.56	3.5	3.6	2.65	2.64	2.64
			War-03	Gneiss	L	2.64	3.37			3.01			1.20	3.61			2.68		
			War-07	Gneiss	L	4.17	2.90			3.54			1.20	4.24			2.65		
			War-08	Gneiss	L	1.94	2.28			2.11			1.20	2.53			2.57		
			War-10	Gneiss	L	2.92		3.14	2.53	2.86			1.20	3.44			2.64		
	Quartzitic sst.	5	War-09	Quartzitic sst.	S_0		3.92	3.29	3.43	3.55	3.5		1.17	4.15	4.1		2.56	2.56	
	Quartzite	5	War-05	Quartzite	S_0	4.24	4.56			4.40	4.6		1.38	6.07	6.4		2.64	2.65	
			War-11	Quartzite	S_0	4.73	5.01			4.87			1.38	6.72			2.65		
	Mica shist	5	War-04	Mica shist	L	2.02		2.91	2.10	2.34	2.3		1.20	2.81	2.8		2.67	2.67	

Vol. – volume fraction, Litho. – lithotype, Fm. – Formation, O – orientation, λ_{dry} and λ_{sat} – thermal conductivity under dry and saturated conditions, respectively, L and S_0 – foliation and bedding, respectively, ⊥ and // – thermal conductivity perpendicular and parallel to orientation, AM – arithmetic mean, TF – transformation factor, calc. – calculated, sst. – sandstone. Composition of the Wartenstein Gneiss is estimated according to Meyer and Nagel (2001).

A.1.15 Radiogenic heat production

Table A.1.15: Calculation of radiogenic heat production (H).

Sample	Lithotype	ρ [10^3 kg m^{-3}]	U [ppm]	Th [ppm]	K_2O [wt. %]	K [wt. %]	H [10^{-6} W m^{-3}]
E1b-007	Stst	2.66	3.1	11.0	1.88	1.56	1.68
E1a-004	Sh	2.71	2.9	13.6	3.82	3.17	1.99
E1a-009	Sh	2.75	3.2	14.3	3.90	3.24	2.15
E1a-011	Sst	2.71	1.6	7.6	0.31	0.26	0.96
Sg3-003	Sh	2.69	2.9	13.6	3.62	3.01	1.96
Sg1-003	Sl	2.73	3.1	13.2	3.16	2.62	1.98
Sg1-07	Sst	2.64	2.0	9.0	0.89	0.74	1.18
OIG-13	Sh	2.74	3.5	15.3	3.40	2.82	2.26
FEP-07	Sh	2.70	2.5	12.5	2.88	2.39	1.73
BIH-06	Ssl	2.79	2.4	16.5	3.38	2.81	2.09
COL-05	Sl	2.88	2.9	16.9	3.63	3.01	2.34
PLA-01	Sl	2.96	1.8	14.7	3.17	2.63	1.89
SPA-02	Ssl	2.75	2.7	14.6	3.90	3.24	2.04
SLW-10	Sl	2.78	3.7	20.1	6.76	5.61	2.95
War-01	Gn	2.65	1.7	7.0	2.82	2.34	1.12
War-03	Gn	2.68	2.4	9.9	3.36	2.79	1.55
GH350	Q	2.63	1.1	4.2	0.39	0.32	0.59
GH2331	Sl	2.82	1.8	14.2	5.26	4.37	1.94
GH3128	Sl	2.76	5.3	17.1	4.47	3.71	2.96
GH3216	Q	2.71	2.2	8.4	0.68	0.56	1.20

Stst – siltstone, Sh – shale, Sst – sandstone, Sl – slate, Ssl – silty slate, Gn – gneiss, Q – quartzite, ρ – density, U, Th, K and O – uranium, thorium, potassium and oxygen, respectively, H – radiogenic heat production.

A.1.16 Geographical coordinates of the crustal cross sections and thermal models

Table A.1.16: Geographical coordinates of the lithosphere-scale cross sections and models.

		Break points	Borehole reference	x	y	d	WGS84	
				[m]	[m]	[m]	Latitude N	Longitude E
Cross section A		Stavelot Massif		60479	156417	0	50.34128214	5.89391620
		Grand-Halleux	171W0276	61529	153119	3461	50.31166754	5.90882667
		Gouvy		64657	139569	17367	50.18994318	5.95328552
		Troisvierges		67676	131622	25869	50.11856893	5.99581593
	a	Friedhaff/Diekirch		77145	106700	52529	49.89463067	6.12839384
	a	Diekirch Réservoir	FR-207-068	79626	102912	57057	49.86058077	6.16292579
	a	Ermsdorf	FC-175-200	83883	99206	62701	49.82724858	6.22209251
	a	Medernach	FR-190-100	84975	97050	65118	49.80785652	6.23724114
	a	Intersection C		87846	95615	68328	49.79492393	6.27709708
	a	Consdorf Millewues	FR-208-132	91400	93845	72298	49.77895311	6.32640535
	a	Rosswinkel	FR-204-201	94430	92835	75492	49.76980710	6.36843656
	a	Geyershof	FR-208-702	96050	92294	77200	49.76490191	6.39090215
	a	Wasserbillig	TS-192-001	102385	87045	85427	49.71750682	6.47852976
	a	Konz		110521	83075	94480	49.68145597	6.59103553
		Wadern		133191	67052	122241	49.53582962	6.90296756
Cross section B		Dochamps		40636	144603	0	50.23409069	5.61641061
	d	Petit-Nobressart		52952	95065	51046	49.78942521	5.79250538
	d	Ell	FR-183-100	55812	92721	54744	49.76847291	5.83236723
	d	Beckerich	FC-197-050	60510	87920	61461	49.72547874	5.89781939
	d	SES Koerich	FR-207-200	63781	82951	67410	49.68090015	5.94338960
	d	Intersection C		67214	79736	72113	49.65207668	5.99106222
	d	Cessange	FR-037-010	74648	72770	82301	49.58955642	6.09410231
	d	Cloche d'Or	FRE-1-16	76289	71522	84363	49.57834772	6.11680946
	d	Weierfeld	FR-191-125	77993	69311	87154	49.55847634	6.14038187
	d	Tréiergronn	FR-191-112	80545	67080	90544	49.53842001	6.17565106
	d	Mondorf Kind	FR-041-014	88280	62943	99316	49.50116662	6.28242957
	d	Kirsch-les-Sierck	01143X0076/SI-06	95814	56315	109350	49.44142296	6.38617322
	d	Kirschnaumen		99534	52117	114959	49.40356946	6.43725923
		Niedaltdorf		111476	44326	129218	49.33301835	6.60117560
Cross section C	g	Lexy		48925	62724	0	49.49846282	5.73914041
	g	Longwy	00905X0003/S	51211	64972	3206	49.51878693	5.77053367
	g	Rebierg	FR-172-010	62020	75610	18372	49.61484854	5.91932441
	g	Intersection B		67214	79736	25005	49.65207668	5.99106222
	g	Gousselerbierg	FR-199-017	75950	86677	36163	49.71460327	6.11196799
	g	Intersection A		87846	95615	51043	49.79492393	6.27709708
	g	Berdorf Hammhaff		93942	100196	58668	49.83599882	6.36192760
	g	Prümtal/Holsthum		98611	105684	65873	49.88521161	6.42709293
		Metternich		109623	117074	81716	49.98716603	6.58119377
		Weidenbach/Wallenborn/Schutz		120510	133807	101679	50.13695239	6.73476769

Coordinates x and y according to the LUREF (Luxembourg Reference Frame), d – distance from the point of origin of the cross sections. Longitude and latitude in degrees . Lowercase letters a, d and g mark break points identical to the respective cross sections A, D and G presented by Schintgen and Förster (2013).